Impacts of Glaciation on Petroleum Systems Offshore Northwest Greenland

---

A thesis submitted to the University of Manchester for the degree of Doctor of Philosophy in the Faculty of Science and Engineering.

2020

David R. Cox BSc MSc

School of Natural Sciences

Department of Earth and Environmental Sciences

Contents

Word count excluding references: 82,428

Figures List

Tables List

Abstract

Seismic investigations and 2D petroleum systems modelling were conducted across the Melville Bay glaciated margin, offshore northwest Greenland, to improve our understanding of the stratigraphy and structure, as well as the nature of the petroleum systems and the impacts of glaciation on them. The margin has experienced multiple episodes of shelf edge glaciation since ~2.7 Ma, leading to the erosion, transportation and re-deposition of vast amounts of sediment, isostatic compensation, and repeated ice loading and unloading on the shelf through glacial-interglacial cycles; processes that can cause extreme variations in the structure and subsurface conditions of sedimentary basins, and have likely significantly impacted any petroleum systems contained within.

Extensive 2D and 3D seismic reflection datasets across large areas of the complex paleo-rift topography of the Melville Bay margin were analysed, identifying an extensive gas-charged submarine landslide mass transport deposit reservoir along the crest of the Melville Bay Ridge (MBR) rift structure. Hydrocarbon anomalies were mapped across the study area within the top 1-2 km of Cenozoic stratigraphy, providing the first inventory of shallow gas and gas hydrates on the northwestern part of the Greenland margin. Evidence for historical fluid migration was also identified and showed the influence of paleo-rift topography and multiple shelf edge glaciations. Seismic anomalies were identified during a 3D seismic geohazards assessment for IODP Proposal 909; providing a workflow for future scientific drilling proposals.

2D petroleum systems modelling tested the evolution of the petroleum system in Melville Bay and provide a novel method for modelling glacial erosion, sediment re-deposition and multiple cycles of ice loading on the shelf. The modelling results suggest viable petroleum systems exist in Melville Bay, including both thermogenic and biogenic hydrocarbons, and that glaciation had a significant influence on margin evolution, causing substantial variations in subsurface pressure, temperature and sediment compaction across the shelf. These changes significantly impacted the petroleum systems, influencing source rock maturation and promoting reservoir leakage and fluid re-migration to reservoirs or through the overburden. Gas hydrate stability was impacted by variable pressure and temperature conditions, potentially causing dissociation at the phase boundary, but hydrate deposits at the seabed are predicted to remain stable throughout both past glaciations and future scenarios of global warming due to the relatively large water depths.

The additional knowledge provided by this thesis will help improve the success and limit the safety risks associated with scientific and applied drilling in this environmentally sensitive high latitude environment. The research also provides an important analogue for studies concerning the interaction of petroleum systems and climate change; providing critical insight into how near-surface hydrocarbons may respond to past and future climate and oceanic warming.

Declaration

No portion of the work referred to in the thesis has been submitted in support of an application for another degree or qualification of this or any other university or other institute of learning.

Copyright Statement

Acknowledgements

First and foremost, I would like to thank my PhD supervisory team for providing me with the support, guidance and encouragement required to help me survive the last 4 years. To my main supervisor Mads Huuse, I want to say a massive thank you for being my ever present guide into the unknowns of PhD life, for motivating me and for pulling me out the other side. Your enthusiasm, knowledge and (often last minute) ideas have always inspired me, pushed me to succeed, and you have managed to almost turn me into a real geophysicist. I also want to thank my external supervisor Paul Knutz for his support with research ideas and paper writing, and for keeping me excited about such a small part of Greenland. Thank you also for trusting me to be part of IODP Proposal 909, a project which allowed me to learn and develop myself considerably. Thank you to Jonathan Redfern and Erica Greenhalgh for their additional support and guidance. I want to give a special thanks to my unofficial supervisor, whose importance in this PhD cannot be fully expressed in such a short section, but to honour his contribution I use his full title, the Much Honoured Laird of Kincavel Dr Andrew Mark William Newton BSc (hons) MSc PhD FGS PgCHET FHEA. Thank you for keeping me sane, teaching me about glaciers, for so many fast paper reviews and most of all, for your friendship. San Francisco, Stavanger, Copenhagen, and the Amsterdam airport dash will all live long in the memory.

I would also like to thank my co-authors on all of the research presented in this thesis who are not mentioned above (Paul Gannon, John Clayburn, Arka D. Sarka, D. Calvin Campbell, John. R. Hopper, Karsten Gohl, Simone Salazar, Attila Bartha and Oliver Schenk). Without your input, this work would have been far less detailed, far less interesting and probably twice as long. I am extremely grateful to the University of Manchester and the British Geological Survey for funding this work, and to the Natural Environmental Research Council's Centre for Doctoral Training (CDT) in Oil and Gas for providing me with an important support network across the country and for such beneficial training courses. Within the CDT, I would like to thank Lorna Morrow, Anna Clark and John Underhill for their management, organization and unwavering support, along with all of my CDT colleagues for many fond memories. Additional thanks go to the staff at Cairn Energy PLC in Edinburgh and Stavanger for their support in this project, as well as the staff of the Geological Survey of Denmark and Greenland (GEUS) for making my time in their office an enjoyable learning experience. Finally, I would like to thank the staff at Schlumberger in Aachen, Germany, for being so welcoming and helpful during my time there. Without their expertise and support, especially from Simone Salazar, I would never have survived PetroMod and this PhD would be missing two chapters.

Thanks are also extended to all of my colleagues within the Basins research group, who have shared their knowledge, expertise and friendship with me throughout this PhD, as well as a few too many beers down the pub. Special thanks goes to Jack for teaching me scouse, to Euan for teaching me Scottish, to Arka for looking after the university for the last 10 years, to Chris for introducing me to Southend-on-Sea's pier, to Eggsy for letting me call him Eggsy, to Ross for getting me through the BP trials, to Max for epic food, giving me somewhere to live and for those California memories, to Zoe for spinning with me and for running Basins and finally to Kofi, for fixing so many technological problems in such a chaotic and amusing way.

I would also like to offer a special thanks to my family, who have supported me throughout over 8 years of university study by sending me food, saving me from being broke, for visiting me, for reading my work, for giving me someone to call on long walks and for generally being there for me whenever I needed it. I am especially thankful to my wife Hannah, who within the last 4 years, has moved to another continent to live with me, started a new career and has recently, for some unapparent reason, married me. I am so proud of all you have achieved and I thank you for everything you have done for me over the last 4 years. I could never have done this without you. Finally, I want to thank my parents Anne and Robert Cox, who have both supported me through all of the ups and downs of not only this PhD but my entire life. You are such dedicated and supportive parents and, if only to pay back a very small portion of what I owe you, this thesis is dedicated to you both.

The Author

I hold a first class BSc (Hons) in Geology (major) and Physical Geography (minor) from the University of Keele, as well as an MSc with Distinction in Petroleum Geoscience from the University of Manchester. In September 2014, I began employment on the Schlumberger UK Graduate Program in Aberdeen, Scotland, working within the Software Integrated Solutions team, providing software support and training courses for Petrel and Studio platforms. In September 2016, I started this PhD studying the impacts of glaciations on petroleum systems. The project is funded by the University of Manchester (50%) and the BGS (50%) as part of the British University Funding Initiative (BUFI), and forms part of the Natural Environmental Research Council (NERC) Centre for Doctoral Training (CDT) in Oil and Gas. This program provided 100 days of industry training during my 4 year PhD in a wide range of geoscience and professional development topics. In the summer of 2019, I completed an internship with BP in Aberdeen, working in the New Well Delivery team for the Clair field, UK North Sea. In January 2021, I will begin full time employment with BP.

The results from this thesis have been presented in 22 speaker and poster sessions across a wide range of national and international conferences, seminars, company presentations and workshops. The work presented has resulted in three first author publications in international journals, an additional first author publication within an Elsevier textbook, and three co-authored papers.

List of Publications

Cox, D. R., Huuse, M., Newton, A. M. W., Gannon, P., and Clayburn, J., 2020, Slip sliding away: enigma of large sandy blocks within a gas bearing mass transport deposit, offshore NW Greenland, AAPG Bulletin, v. 104, no. 5, pp. 1011-1043.

Cox, D. R., Huuse, M., Newton, A. M.W., Sarkar, A. D., and Knutz, P. C., 2021, Shallow gas and gas hydrate occurrences on the northwest Greenland shelf margin, Marine Geology, v. 432, pp. 1-21.

Cox, D. R., Knutz, P. C., Campbell, D. C., Hopper, J. R., Newton, A. M. W., Huuse, M., and Gohl, K., 2020, Geohazard detection using 3D seismic data to enhance offshore scientific drilling site selection, Scientific Drilling, v. 28, pp. 1-27.

Cox, D. R., Newton, A. M. W., and Huuse, M., 2020, An introduction to seismic reflection data: acquisition, processing and interpretation, in Scarselli, N., Adam, J., and Chiarella, D., eds., Regional Geology and Tectonics – Volume 1: Principles of Geologic Analysis, Second Edition, Elsevier, Amsterdam, Netherlands, Chapter 22, pp. 571-603.

Newton, A. M. W., Huuse, M., Knutz, P. C., and **Cox, D. R.**, 2020 Repeated ice streaming on the northwest Greenland continental shelf since the onset of the Middle Pleistocene Transition, The Cryosphere, 14, pp. 2303–2312.

Newton, A. M. W., Huuse, M., **Cox, D. R.**, and Knutz, P. C., 2021, Seismic geomorphology and evolution of the Melville Bugt Trough Mouth Fan, northwest Greenland, Quaternary Science Reviews, v. 255, pp. 1-23.

Nielsen, T., **Cox, D. R.**, and Jokat, W., accepted, Geophysical indications of gas hydrate occurrence in the Greenland continental margins. In: Mienert, J., Berndt, C., Tréhu, A., Camerlenghi, A., and Liu, C-S., World Atlas of submarine gas hydrates in continental margins, Springer (not presented in this thesis).

Published Abstracts

Newton, A. M. W., **Cox, D. R.**, Huuse, M., and Knutz, P. C. (2020), 3D seismic geomorphology offshore northwest Greenland, AGU Annual Fall Meeting, San Francisco.

Newton, A. M. W., Huuse, M., **Cox, D. R.**, and Knutz, P. C. (2019), Seismic geomorphology in northeast Baffin Bay: reconstructing the Pleistocene evolution of the northwest Greenland Ice Sheet, AGU Annual Fall Meeting, San Francisco.

Cox, D. R., Huuse, M., Newton A. M. W., and Knutz, P.C. (2019), The effect of glaciation on shallow gas and hydrates, offshore NW Greenland, AGU Annual Fall Meeting, San Francisco.

Huuse, M., **Cox, D. R.**, Newton, A. M. W., and Knutz, P. C. (2019), Identifying drilling hazards using high resolution 3D seismic data to aid site selection for IODP Proposal 909, AGU Annual Fall Meeting, San Francisco.

Cox, D. R., Huuse, M., Newton, A.M.W., Gannon, P., and Clayburn, J. (2019), Putting the pieces back together: landslide reconstruction of MTD mega-blocks, offshore NW Greenland, EGU Annual Meeting, Vienna.

Cox, D. R., Huuse, M., Newton, A.M.W., Gannon, P., and Clayburn, J. (2018), Slip sliding away: enigma of large sandy blocks within a gas bearing mass transport deposit, offshore NW Greenland, Symposium on Submarine Mass Movements, Victoria, Canada.

1

Introduction

Preamble

The principal aim of this thesis is to improve our understanding of the impacts of glaciation on petroleum systems. This topic has become increasingly studied over the past three decades, due to the push of exploration towards higher latitude, glaciated margins in the Arctic. This chapter will therefore begin with a review of this literature, to outline our current understanding, before detailing the research rationale and motivation, the key aims, objectives and methods of this thesis.

1.1. Introduction

Glaciated margins have experienced multiple episodes of glacial advance and retreat across the shelf during the Pliocene and Pleistocene, with these glaciations significantly impacting the landscape, bathymetry and subsurface conditions (Batchelor et al., 2019; De Schepper et al., 2014; Medvedev et al., 2019). Glaciations often cause the erosion, transportation and re-deposition of vast amounts of material, often leading to the exhumation of sedimentary basins, rapid burial, and isostatic adjustments in response to the variation in load across the shelf (Doré et al., 2002; Fjeldskaar and Amantov, 2018). Additionally, repeated ice loading and unloading on the shelf during glacial-interglacial cycles, causes considerable fluctuations in subsurface pressure and temperature (Cavanagh et al., 2006; Goffey et al., 2016; Grassmann et al., 2010), along with the repeated tilting of underlying stratigraphy due to differential vertical movements as the ice load expands and retreats (Kjemperud and Fjeldskaar, 1992; Stewart et al., 2000; Zieba and Grover, 2016). These extreme variations in the structure and subsurface conditions of sedimentary basins can have a major impact on petroleum systems contained within, and represents an essential consideration when exploring for oil and gas within glaciated margins (Fjeldskaar and Amantov, 2018; Medvedev et al., 2019).

For this reason, the impacts of glaciation on petroleum systems have become increasingly studied since the early 1990s, as exploration moved towards higher latitude glaciated margins in the Arctic, such as the Barents Sea, Arctic Alaska and offshore West and East Greenland. The rapid structural and subsurface stress changes associated with glaciation promotes fluid movement however, and is often associated with spill from traps and leakage to the surface (Goffey et al., 2016; Medvedev et al., 2019; Zieba and Grover, 2016). Therefore, fully understanding glacial processes prior to drilling can be integral to exploration success. Furthermore, hydrocarbon leakage into the water column, and potentially the atmosphere, as a result of glacial processes represents an important feedback with the climate system. Hydrocarbons such as methane represent a powerful greenhouse gas with many near surface methane deposits, such as gas hydrates, within the Arctic representing a major environmental concern (Krey et al., 2009; Reagan and Moridis, 2007; Ruppel and Kessler, 2017). Therefore, understanding the past conditions that led to the leakage or dissociation of these hydrocarbons is important for historical climate modelling, but also potentially reveals the sensitivity of such systems to environmental change; providing critical insight on how these systems may respond to future climate and oceanic warming.

Despite this importance, our understanding of the complex interaction between repeated glaciations and petroleum systems is in its infancy. It is only recently that dedicated basin modelling workflows have been developed for testing how different glacial scenarios may have resulted in a range of impacts on the subsurface (Cavanagh et al., 2006; Grassmann et al., 2010; Løtveit et al., 2019; Portnov et al., 2016; Zieba and Grover, 2016). Therefore, it is important to progress our knowledge of these processes, not only to understand more about the wider evolution of sedimentary basins within glaciated margins, but also to increase the success and limit the safety risks associated with exploration, if industry continues operating in the challenging, costly and environmentally sensitive environments of the high latitudes.

1.2. Background

1.2.1. Glaciations and Their Impact

Oxygen isotope records suggest that since the late Pliocene the global climate has experienced multiple periods of cooling and warming leading to repeated glacial-interglacial cycles (Fig. 1.1) (Lisiecki and Raymo, 2005; Miller et al., 2011). These climatic oscillations and associated glacial cycles varied in duration and magnitude through time, occurring in sync with the periodicities of orbital forces that affect the amount of solar radiation reaching the Earth (Maslin and Ridgwell, 2005; Shackleton and Opdyke, 1976). During the late Pliocene and Early Pleistocene, climatic oscillations were low amplitude, high frequency events occurring at pace with 41 kyr obliquity cycles, but transitioned into high amplitude, low frequency events during the Middle Pleistocene Transition (MPT) (~1.3-0.7 Ma) (Fig. 1.1), with cycles then occurring every 100 kyr at pace with eccentricity (Chalk et al., 2017; Huybers, 2011).

Eccentricity however, provides the weakest influence on Earth surface insolation of any of the orbital parameters and therefore, likely did not cause this transition of the dominant periodicity alone (Clark and Pollard, 1998; Maslin and Ridgwell, 2005). Several hypotheses have therefore been developed to explain this climatic evolution. One popular hypothesis is 'the regolith theory', which suggests that the pre-glacial landscape was covered by clay-rich regolith, providing a low resistance surface for over-riding ice sheets to glide across during early glacial cycles. This resulted in thinner, lower volume ice sheets which responded rapidly to climatic changes. After removal of this regolith through glacial erosion, ice sheet contact with bedrock would have provided additional basal resistance, leading to less mobile, thicker and greater volume ice sheets and importantly, slower response times to orbital forces, possibly causing the transition in periodicity (Clark and Pollard, 1998; Imbrie

et al., 1993). Additional theories surrounding the MPT include: (1) long term cooling throughout the Cenozoic allowing ice sheets to become thick enough to survive for longer than the 41 kyr cycle (Gildor and Tziperman, 2000; Raymo, 1997); (2) that the 100 kyr periodicity is instead defined by instability in the global atmospheric carbon cycle, and that the decline of CO^2 in the atmosphere throughout the late Cenozoic reached a threshold where the global climate begins to act non-linearly to orbital forces thereafter (Maslin and Ridgwell, 2005; Mudelsee and Stattegger, 1997); and (3) that reorganisation of ocean circulation during periods of climatic change caused warmer waters that destabilized gas hydrates, leading to methane release in to the atmosphere, accelerating deglaciations and amplifying glacial-interglacial cycles since the MPT (Fig. 1.1) (Kennett et al., 2003).

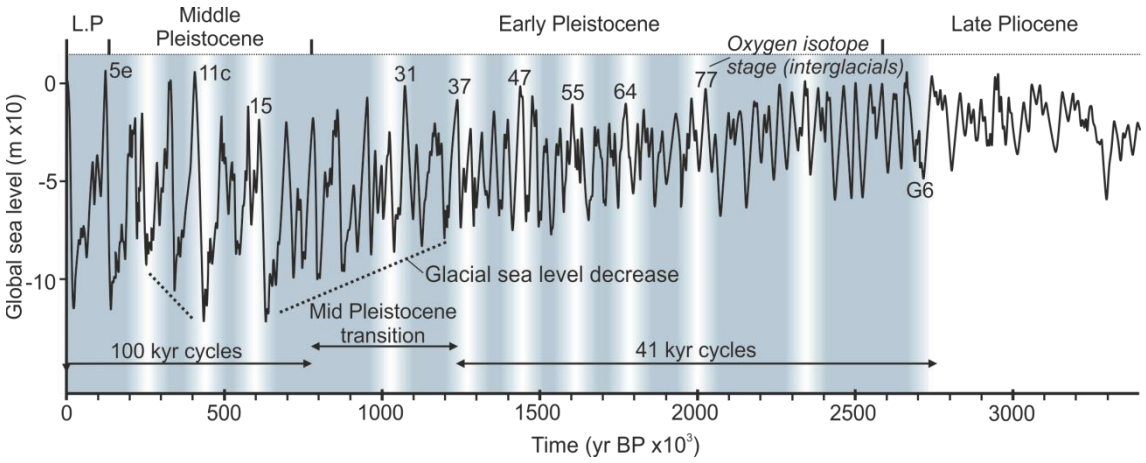

Figure 1.1. Global sea level curve | A global sea level curve constructed from the LR04 benthic δ18O stack (Lisiecki and Raymo, 2005), displaying the sea level response to numerous glacial-interglacial cycles and the switch from 41 kyr to 100 kyr cycles during the Middle Pleistocene Transition. The grey/blue areas represent the correlation of 11 glacigenic clinoforms interpreted on seismic data within Melville Bay, offshore northwest Greenland, with the sea level curve. The figure is modified from Knutz et al. (2019).

The consequence of climatic oscillations are glacial-interglacial cycles, and the repeated advance of thick grounded ice sheets across many high latitude continental shelves throughout this period (Cavanagh et al., 2006; Knutz et al., 2019; Winsborrow et al., 2010). Glaciations would have occurred as relatively short-lived but frequent events during much of the Early Pleistocene, characterised by thin but fast moving ice streams, extensive erosion and only brief periods of ice expansion onto the shelf. After the MPT however, glaciations were prolonged and intensified events with increased ice volumes, causing ice margins to advance progressively further across continental shelves, before retreat and possibly complete deglaciation (Clark and Pollard, 1998; Maslin and Ridgwell, 2005).

The development and expansion of these ice sheets throughout this period caused wide ranging effects to landscapes, ecosystems and subsurface geology. This impact is most commonly observed through glacial modification of landscapes, consisting of a wide range

of glacial landforms and features, from small scale striated rock surfaces to large scale cross-shelf troughs and trough mouth fans (Batchelor and Dowdeswell, 2014; Vorren and Laberg, 1997). High latitude continental margins are often transformed into these landscapes, through glacial processes that involve the erosion, transportation and re-deposition of extensive quantities of continental and marine sediments (Clayton and Moran, 1982; Weaver et al., 2000); with these sediments often observed throughout the rock record in a range of depositional structures and landforms including dunes, drapes and fans (Batchelor and Dowdeswell, 2014; Benn and Evans, 2010; Huuse et al., 2012).

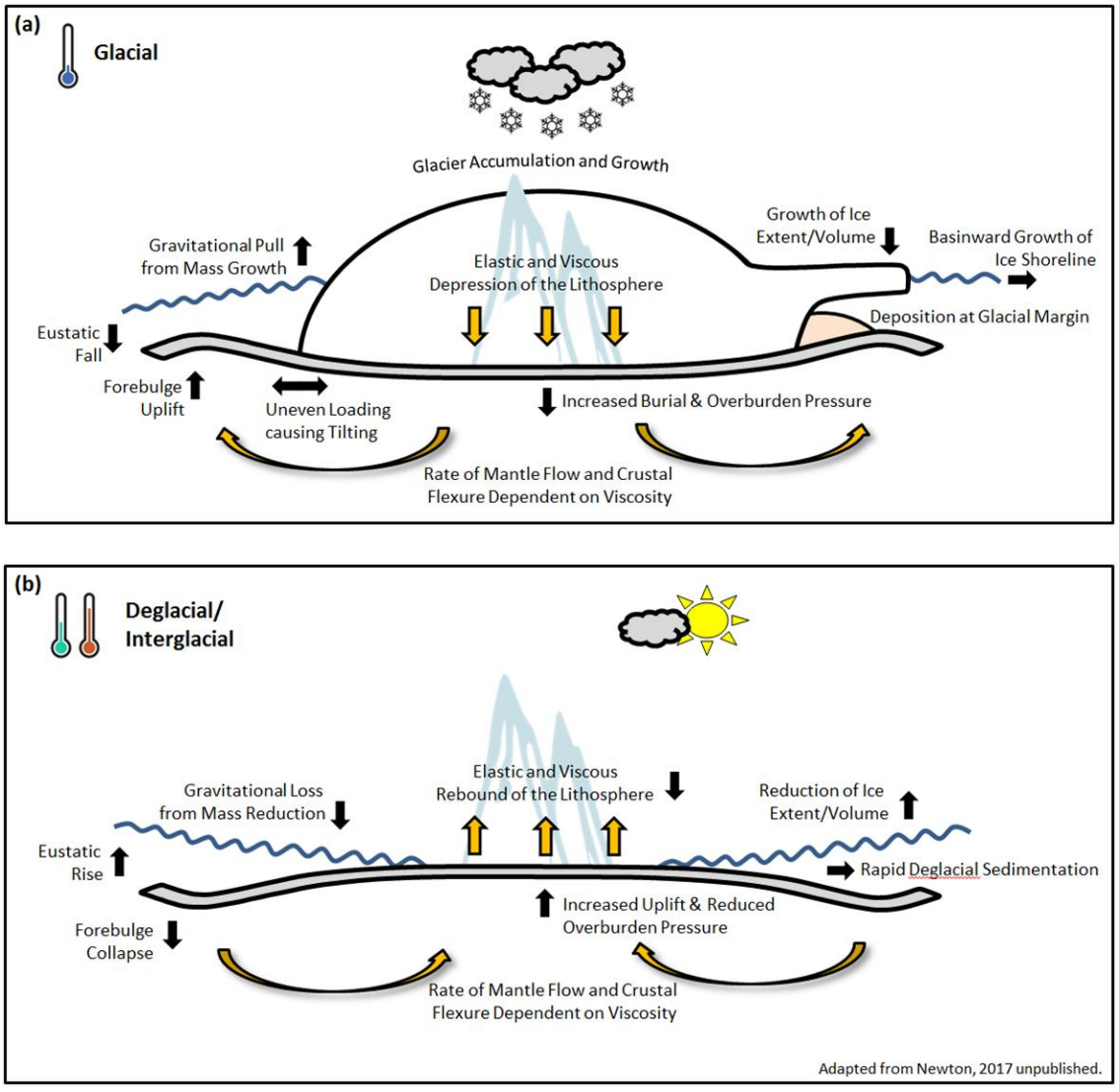

Figure 1.2. Glacial isostasy | Schematic diagrams displaying the impact of glacial loading on crustal flexure and sea level during glacial (a) and deglacial/interglacial (b) periods. The effects shown likely do not have time to re-equilibrate between glacial cycles and may overprint on one another creating a significantly complex interaction. The figure is modified from Newton (2017) and is not drawn to scale for ease of comparison.

Many other glacigenic impacts are not as easily observed at the surface however, and can have far reaching affects both deep into the subsurface and in laterally adjacent areas up to 200 km away (depending upon the size of the ice sheet and the viscosity of the

mantle) (Conrad, 2013; Fjeldskaar, 1994). A significant proportion of these effects descend from the equilibrium change and subsequent compensation of applying or removing an external load on the Earth's crust (Watts, 2001). The variation in load usually relates to not just the isostatic response of the crust to the mass of the ice sheet, but also extensive sediment erosion and re-deposition associated with ice sheet advance and retreat (Kjemperud and Fjeldskaar, 1992; Van den Berg et al., 2008). Repeated ice loading can influence crustal uplift and subsidence, sedimentation rates and the subsurface stress field (Fig. 1.2), with these effects lasting long after the glacier has been removed (Stewart et al., 2000).

The ice load will also cause the uplift of a forebulge in areas adjacent to the ice due to the lateral displacement of the asthenosphere beneath the ice sheet (Fig. 1.2) (Benn and Evans, 2010), with this forebulge collapsing during deglaciation and load removal. During periods of ice expansion and retreat, the variable distribution of the load across the shelf, can lead to laterally discontinuous compensation, tilting the subsurface stratigraphy (Tasianas et al., 2016; Zieba and Grover, 2016). Furthermore, the variations in load, uplift and subsidence will cause fluctuations in subsurface pressure, temperature and sediment compaction, leading to structural and stratigraphic changes, as well as variations in the condition and migration of fluids (Fjeldskaar and Amantov, 2018; Grassmann et al., 2010).

1.2.2. The Influence of Glaciation on Petroleum Systems

The impact of glaciations on subsurface geological conditions and structural positioning (Fig. 1.2) can have a large effect on the composition and stability of any petroleum system maintained within a subglacial and adjacent proglacial area (Fjeldskaar and Amantov, 2018; Medvedev et al., 2019). Such systems, for example, modern day Arctic glaciated margins, may exist within areas that have experienced numerous cycles of glacial advance and retreat throughout the Pleistocene alone, and the redistribution of substantial amounts of sediment through glacial processes. A petroleum system is sensitive to change, and could easily be compromised by the effects of these glaciations (Andreassen et al., 2017; Henriksen et al., 2011; Medvedev et al., 2019; Ostanin et al., 2017a). Alternatively, glaciations can also have a positive effect on petroleum systems, causing the system to remain in-balance and for hydrocarbons to remain trapped. The balance between positive and negative effects of glaciation on the different elements of a petroleum system are important as understanding these effects will allow better predictions on how the system has evolved through time and what is the most likely present day distribution and condition of hydrocarbons within the areas impacted by glaciation. This knowledge will not only provide key insights into resource assessments and exploitation, but also has implications

for understanding the interaction of high latitude hydrocarbon systems with climate change both in the past and future (Krey et al., 2009; Ruppel and Kessler, 2017).

The following sections will discuss the range of impacts that glacial processes, such as erosion, deposition and ice loading cycles, can have on petroleum systems (Fig. 1.3), using examples from several basins and hydrocarbon fields from across the Arctic region.

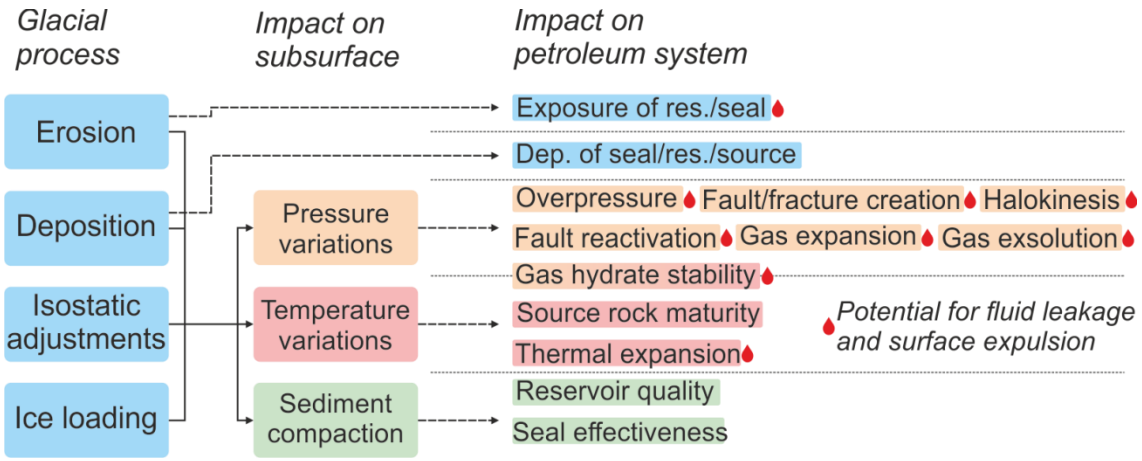

Figure 1.3. Effects of glaciation on petroleum systems | A flow chart displaying the main glacial processes experienced on a glaciated margin, the influence these processes have on the subsurface and how these variations may impact petroleum system elements.

1.2.2.1. Glacial Isostasy

Isostasy relates to how the Earth's lithosphere is in a buoyant equilibrium with the underlying mantle and that the addition or removal of mass will cause isostatic compensation, leading to the uplift or sinking of the crust into the asthenosphere (Benn and Evans, 2010; Watts, 2001). The cyclic nature of the expansion and removal of glacial ice, leads to a relatively short time scale variation in the addition and removal of mass on the crust (Peltier, 2004). These short time period variations have been detected from the analysis of oxygen isotope ratios which suggest cycle durations of 41 kyr (axial obliquity) and 100 kyr (orbital eccentricity) with the switch occurring during the Mid-Pleistocene transition (Fig. 1.1) (Bintanja and Van De Wal, 2008; Miller et al., 2011; Tziperman and Gildor, 2003). These short period variations suggest a large number of glaciations since the late Pliocene, and numerous, repeated cycles of isostatic compensation and rebound. Attempts to understand the impacts of these isostatic adjustments are complicated further by the lithosphere and asthenosphere taking in excess of 10,000 years to reach complete adjustment, meaning equilibrium between glacial and interglacial cycles may never be reached and a single cycle of isostatic rebound may be overprinted by a subsequent cycle (Benn and Evans, 2010; Le Meur and Huybrechts, 1996; Watts, 2001).

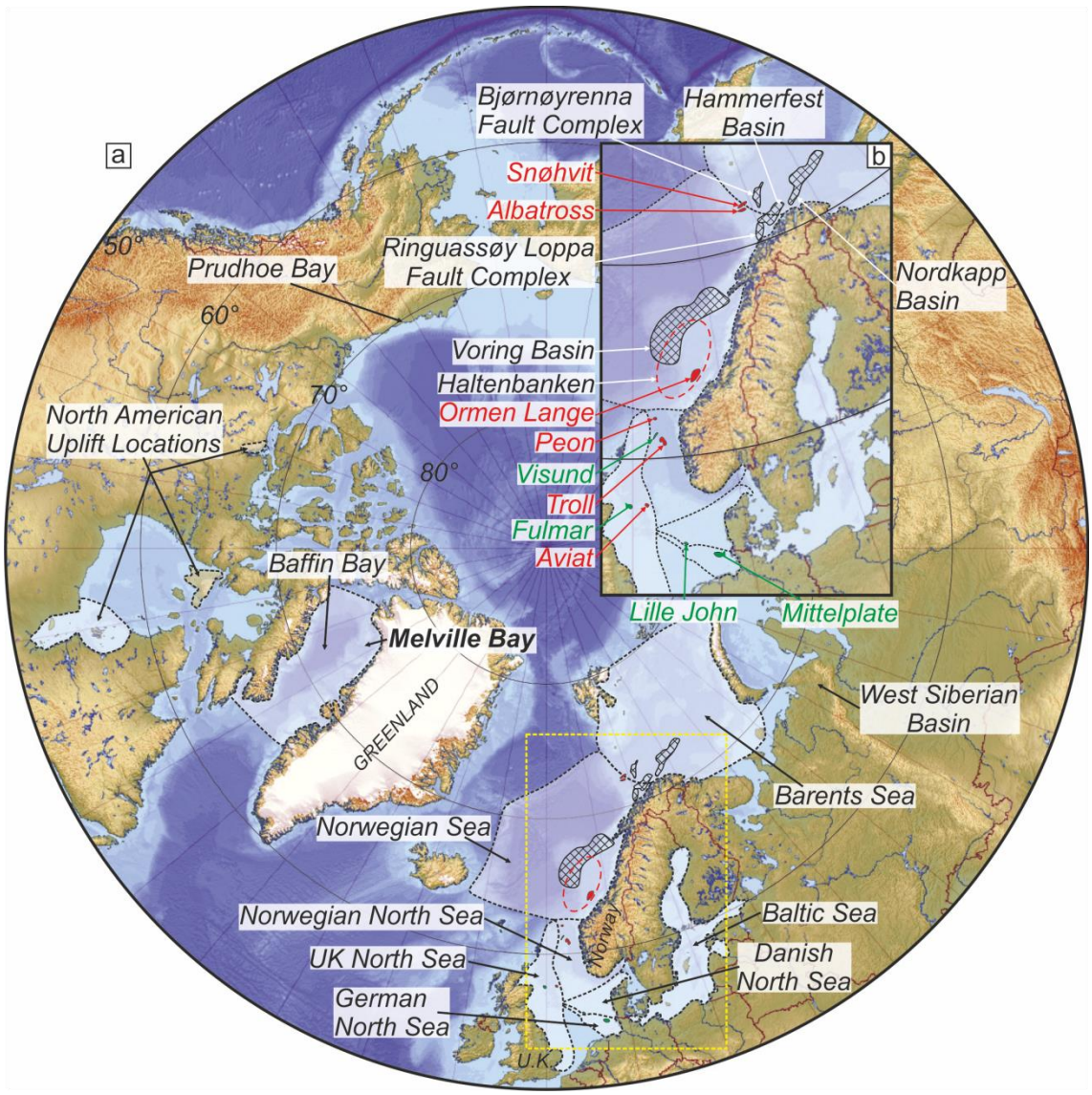

Figure 1.4. Arctic case studies | A map of the Arctic region from 50° northward (a), displaying the regions and specific oil (green) and gas (red) fields mentioned within the literature review. The Norwegian shelf (b) is the principal location for literature investigating the impact of glaciation on petroleum systems and a number of case study locations are shown along this margin. The oil and gas fields shown are not drawn to scale and are for location use only.

This complexity aside, glacial isostatic rebound has the ability to cause rapid and widespread uplift and erosion (Fig. 1.2), having a significant effect on the burial depth and nature of hydrocarbon systems (Doré et al., 2002). Such significant isostatic adjustments are often experienced across glaciated margins that are loaded by ice during glacial periods and return to ice free conditions during interglacials (Amantov et al., 2011; Kjemperud and Fjeldskaar, 1992). Such continental margins, such as the Norwegian shelf, are also commonly prolific hydrocarbon provinces; suggesting that these petroleum systems have experienced multiple episodes of isostatic rebound. Many areas of the Northern Hemisphere have undergone significant uplift and erosion during the last glacial cycle (Doré et al., 2002; Medvedev et al., 2019). Examples include the North Sea, where down-

warping and subsequent uplift of up to 400 m is suggested, with this process potentially having occurred several times throughout the last 2-3 million years (Kjemperud and Fjeldskaar, 1992). An estimated 32 m of post-glacial uplift is also predicted to have affected the Baltic Sea region from the last glacial cycle alone, contributing to the removal of an estimated 90,000 km^3 of eroded material throughout the Pliocene-Pleistocene from areas including the Black Sea Basin and the Poland-Belorussia region (Fig. 1.4) (Amantov, 1995; Amantov et al., 2011). This post-glacial isostatic uplift is estimated to have reached rates of 10-12 m/100 years immediately following deglaciation and is still in the range of 1.3 m/100 years at present day in areas of North America (Andrews, 1970).

Rapid rates of uplift and subsequent erosion across much of the Northern Hemisphere during the Pleistocene, have led to overburden removal and the exposure of sealing rocks and reservoirs, causing the subsequent loss of hydrocarbon fluids (Doré et al., 2002; Fjeldskaar and Amantov, 2018). An example of this is on the Norwegian part of the Barents Sea where ~3 km of overburden has been uplifted and removed. Fission track studies and biostratigraphic re-dating of sediments has attributed a significant part of this uplift to late Pliocene and Pleistocene post-glacial isostatic rebound (Nyland et al., 1992; Riis, 1992; Riis and Fjeldskaar, 1992). This uplift and erosion led to the thinning of seal lithologies and the exposure of reservoirs causing the loss of hydrocarbon fluids from previously completely filled traps. This is now evidenced by residual oil shows in several wells drilled in the Barents Sea (Skagen, 1993). Furthermore, glacial erosion from the inner margin (where ice sheets are more often grounded), causes more rapid isostatic uplift in these areas of the shelf after the ice has retreated, compared to the outer shelf, due to not just ice removal, but also sediment removal. This is often exacerbated by deposition of glacial sediments at the outer-shelf, which can restrict post-glacial rebound (if the area was ice covered) or cause subsidence (Doré and Jensen, 1996; Zieba and Grover, 2016). This difference between erosion and isostatic uplift on the inner shelf, and deposition and potentially less uplift (or even subsidence) at the outer shelf, can cause the shelf margin to tilt basinward (Fig. 1.5). This tilt can lead to changes in structural attitude and trap configuration, leading either to reservoir leakage or increased capacity. Such processes have been proposed for several hydrocarbon traps across the Norwegian shelf (Doré and Jensen, 1996; Løtveit et al., 2019).

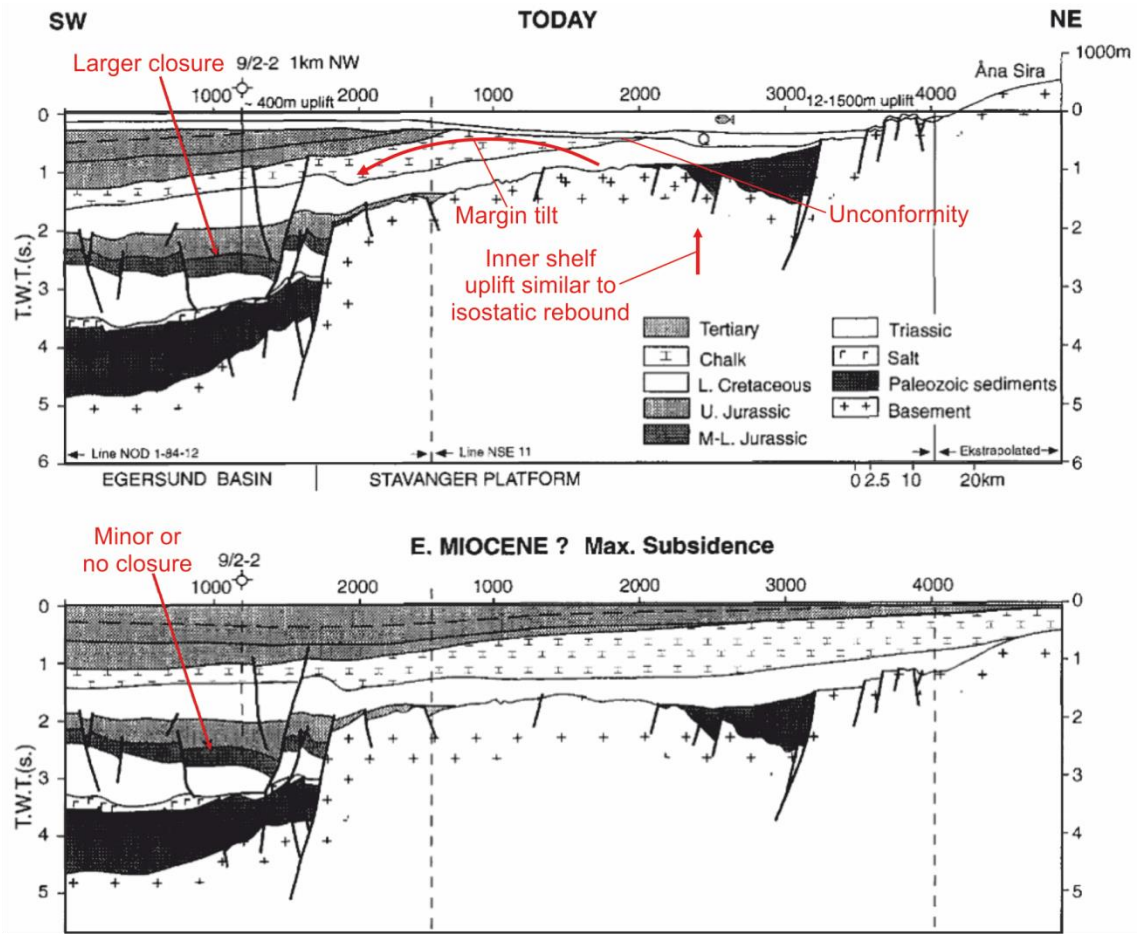

Figure 1.5. Margin tilt | Two cross sections across the Egersund Basin and Stavanger Platform at present day (a) and during the Early Miocene (b). The inner margin is shown to have been uplifted and exhumed at present day, similar to the response of isostatic rebound on many glaciated margins. This exhumation has caused the margin to tilt basinward, causing changes in structural attitude and trap configuration leading to variations in closure. The figure is modified from Doré and Jensen (1996).

During glacial periods and the expansion of ice sheets, the balance between eustatic sea level fall, isostatic crustal subsidence due to loading and adjacent forebulge uplift (Fig. 1.2), causes a complex mix of controls on accommodation and sediment deposition (Benn and Evans, 2010; Zachos et al., 2001). The net effect of glaciation is often subsidence however, the creation of local accommodation, and rapid deposition of potential reservoir formations; deposition which can further increase crustal load, leading to higher rates of subsidence. For example in the Baltic Sea region (Fig. 1.4), it is thought that glacigenic sedimentation produced an additional 155 m of subsidence during the last glacial cycle (Amantov et al., 2011). Reservoirs deposited in additional accommodation created by isostatic subsidence, can often be overlaid by shale lithologies, some of which may be organic rich, which are deposited due to rapid transgression of the depositional environment at the onset of deglaciation (Bechstadt et al., 2009; Fjeldskaar and Amantov, 2018). These shales may represent either important sealing lithologies for the underlying

reservoirs, or act as source rocks (if organic rich) for glacigenic hydrocarbon systems (Huuse et al., 2012). An example of this includes the lowermost Silurian organic-rich 'hot' shales that were deposited within the North African region during a period of transgression caused by the melting of the Late Ordovician ice cap (Bechstadt et al., 2009; Luning et al., 2000). The shales are thought to have sourced up to 90% of Palaeozoic sourced hydrocarbons in North Africa (Boote et al., 1998).

Source rock maturation is also affected by glacial isostasy due to the increased burial or uplift of the source rock interval, changing its position within the hydrocarbon generation window. This can cause source rocks to be at a higher degree of maturation than expected from current depths and can also cause generation to cease due to uplift and cooling (Doré et al., 2002). An example of this is within the Bjørnøyrenna Fault Complex, southwest Barents Sea, where source rock maturation modelling suggests that Pliocene-Pleistocene uplift of <1.5 km, part of which is associated with glacial isostatic rebound and erosion, has caused primary source rocks to show immature to early mature vitrinite reflectance values (Ro 0.59%) (sampled from wells in the region) (Stephenson et al., 1995). This is due to the duration of maximum burial being very short and the subsequent 'switching off' of the source rocks, in part due to isostatic uplift and erosion.

1.2.2.2. Isostatic Reservoir Tilt

Differential isostatic subsidence occurs across an area experiencing a variable load distribution (Kjemperud and Fjeldskaar, 1992; Zieba and Grover, 2016). On a glaciated margin, this effect often occurs between areas beneath and adjacent to the ice load with the transition point between the two areas on the shelf, changing throughout periods of ice sheet advance and retreat. Differential isostatic movements can cause the tilting of underlying stratigraphy and variations in trap geometry (Kjemperud and Fjeldskaar, 1992; Løtveit et al., 2019). This may affect reservoir volumes by changing the location of trap spill points, potentially leading to hydrocarbon leakage from reservoirs (Fig. 1.6) (Doré and Jensen, 1996; Kjemperud and Fjeldskaar, 1992; Nyland et al., 1992). Several efforts to model the effect of differential isostatic subsidence have been made on the Norwegian shelf. One of the first was made by Kjemperud and Fjeldskaar (1992), who discussed the uncertainty of understanding and modelling this process in depth, before going on to predict a 30% loss of hydrocarbon volume due to tilting on a hypothetical field in the Barents Sea (Fig. 1.6).

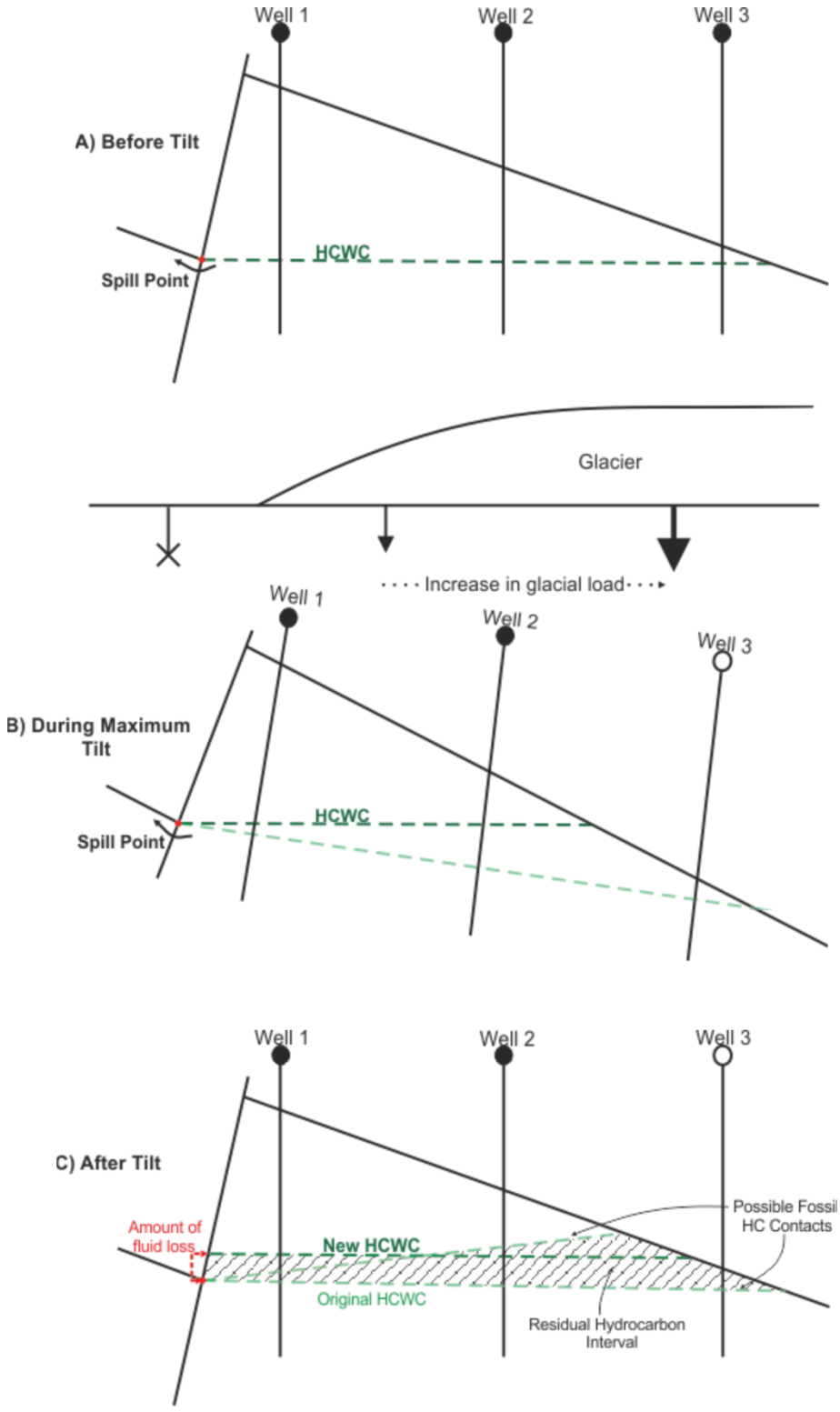

Figure 1.6. Reservoir tilt | A schematic diagram displaying the geometrical changes experienced by a theoretical reservoir during one cycle of glacial isostasy and differential loading. A simple tilted fault block reservoir is shown before tilt (a), during glaciation and tilting (b) and after tilt, with hydrocarbon leakage occurring during the geometrical change. This diagram is modified from Kjemperud and Fjeldskaar (1992).

Since then, Zieba and Grover (2016) attempted to model the impact of differential isostatic movements on hydrocarbon traps in the Bjørnøyrenna Fault Complex in the southwest Barents Sea (Fig. 1.4). They concluded that the Pleistocene burial history and

isostatically-driven depth changes and tilting led to an increase or decrease of trap capacities in the range of 5-14%. They also stated that tilt magnitude is the most controlling factor on trap capacity change and that any hydrocarbon loss was a result of tilting together with gas volume expansion. Nyland et al. (1992) and Doré and Jensen (1996), also suggested that the Albatross and Snøhvit fields, along with other low relief structures in hinge areas within the Barents Sea, have experienced secondary migration of hydrocarbons out of the trap, as shown by residual oil in the water leg. This is attributed to tilting of the reservoirs during the late Tertiary uplift and erosion, part of which is driven by differential isostatic rebound. This is further evidenced by modelling completed by Ostanin et al. (2017b), where reservoir tilt was shown to have caused episodes of hydrocarbon leakage since the last glacial maximum within the Snøhvit gas field (Fig. 1.4). Finally, it is suggested by Gray (1987) and Nyland et al. (1992), that the Troll field in the Norwegian North Sea was once an oil field with a minor gas cap (as suggested by the residual oil present) and differential isostatic reservoir tilting, along with gas expansion, is the cause for the secondary migration and loss of oil from the trap.

1.2.2.3. Subglacial Erosion and Deposition

In addition to uplift and erosion caused by post-glacial isostatic rebound (see Section 1.2.2.1), subglacial erosion by the ice sheet through processes such as abrasion and plucking, can lead to the removal of thick layers of sediment, commonly from areas on the inner continental shelf seabed (Benn and Evans, 2010; Boulton, 1979). The effect of this erosion on petroleum systems is similar to the impact of uplift and erosion associated with isostatic rebound (and they are somewhat linked through load removal), with stratigraphic burial depths, subsurface temperature and pressure, and trap geometries all potentially being influenced (Fjeldskaar and Amantov, 2018). Erosion may also have a greater effect on shallow petroleum systems through the removal of sealing lithologies or the exposure of reservoirs to the surface, resulting in fluid loss (Chand et al., 2012; Doré and Jensen, 1996; Medvedev et al., 2019).

In the southwest Barents Sea, the removal of thick layers of sediment due to subglacial erosion since 2.8 Ma, is predicted to have led to the migration and eventual escape of hydrocarbon fluids. This is evidenced by palaeo-pockmarked surfaces of glacial unconformities and the estimated removal of 600 m (thickness) of gas hydrate hosting sediments since the last glacial maximum (Fig. 1.6) (Chand et al., 2012; Solheim and Kristofferson, 1984). Vagnes et al. (1992), also showed evidence for subglacial erosion on the continental shelf for the northern Barents Sea and suggested that this led to the "significant reduction of the petroleum potential of the area". Repeated glacial erosion,

along with isostatic adjustment, has also caused deep exhumation within the Hammerfest and Nordkapp Basins within the Barents Sea, with the removal of <1500 m of sediment likely having a substantial effect on the petroleum potential within both basins (Doré et al., 2002; Nyland et al., 1992; Walderhaug, 1992).

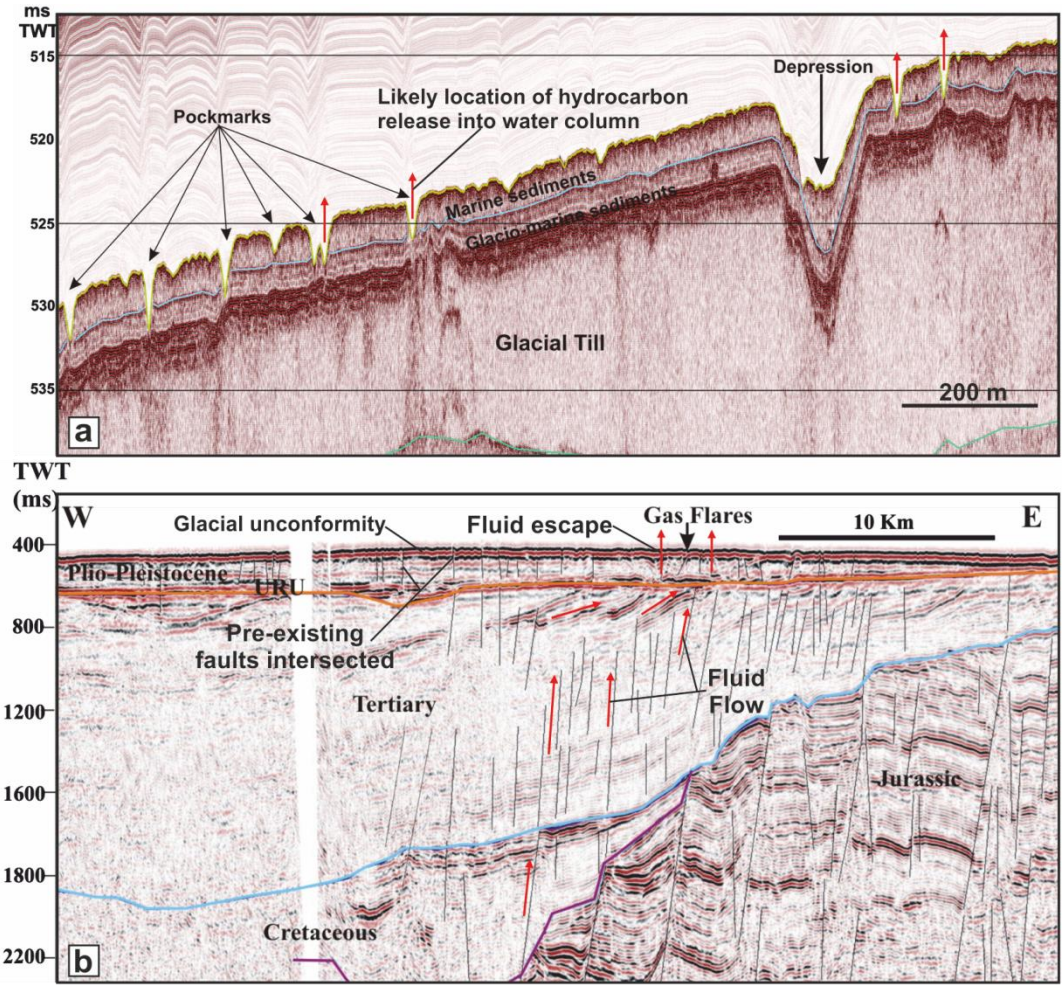

Figure 1.7. Fluid flow, faults and pockmarks caused by glaciation | A high resolution sub bottom profiler cross section (a), showing pockmarks created by fluid expulsion at the seabed as a result of glacial processes. A seismic cross section (b) showing inferred fluid flow through open faults as well as newly formed faults as a result of glaciation. Fluid expulsion at the seabed is supported by the presence of gas flares. Both a and b are modified from Chand et al. (2012).

Alternatively, subglacial erosion can also be associated with the creation of hydrocarbon reservoirs and traps. The Amenas field, within the South Illizi Basin, Algeria, is an example of this, where reservoir units consist of high-density turbidites that have infilled elongate incisions on a basal glacial erosion surface (Hirst, 2012). These incisions are interpreted to be created by subglacial meltwater channels and created a network of depressions up to 200 m deep that controlled post-glacial reservoir distribution. Another example is found in the form of shallow gas reservoirs within Haltenbanken, in mid-Norway. Here, a differing form of glacial erosion – icebergs scouring the seabed - has led to the trapping of shallow

gas pockets within ancient scour marks at certain stratigraphic levels (Gallagher and Braaten, 1990; Rise and Rokoengen, 1991).

The subglacial erosion, entrainment and transport of significant volumes of sediment towards the glacial margin, mean that reservoir deposition is also common across glaciated margins (Fjeldskaar and Amantov, 2018). However, for the most part, deposition in the modern day Arctic during the Pleistocene constitutes only shallow reservoirs with minor occurrences of shallow gas hosted in Pleistocene deposits in the North Sea and Canada (Huuse et al., 2012; Medvedev et al., 2019). These deposits are usually not volumetrically important and more often pose a risk to drilling operations rather than an economic resource (Buckley, 2012; Huuse et al., 2012). That said, within areas of extensive sedimentation, such as at the glacial margin, there is still potential for glacigenic petroleum systems to have formed throughout recent glaciations. An example of this is the Peon Gas field that is hosted within a glacial outwash fan overlain by glaci-marine sediments and tills; a system that is still only a few thousand years old (Huuse et al., 2012; Ottesen et al., 2012). Another example is the Aviat gas field, situated to the east of the Forties field in the North Sea, which is contained within a glacigenic reservoir deposited as a subaqueous glacial outwash fan during the Early Pleistocene (Rose et al., 2016). Significant volumes of hydrocarbons are also found within glacigenic reservoirs worldwide (e.g. Paleozoic sandstones in North Africa and the Middle East) where the impact of major past glaciations (300-350 Myr cycles) can also be considered (Huuse et al., 2012; Page et al., 2007).

1.2.2.4. Fault Effects

Faults often represent a key element of a petroleum system, commonly effecting fluid migration, with sealed faults creating the trapping mechanism for numerous hydrocarbon fields worldwide (Aydin, 2000), whilst open faults often provide pathways for the upward migration of hydrocarbons from deep source rocks into reservoirs or to the seafloor (Ostanin et al., 2017a; Wiprut and Zoback, 2002). Several fault properties that influence the ability of a fluid to flow through the fault plane, such as fault movement and slippage as well as fault plane permeability, are influenced by the state of the subsurface stress-field, and even slight variations can affect fault behaviour (Lund et al., 2009; Rouchet, 1981). Glacial processes such as isostatic adjustments, rapid burial or uplift and erosion, can all lead to faults becoming critically stressed, and may effect a fault's ability to either trap hydrocarbons or act as a fluid conduit (Aydin, 2000; Wiprut and Zoback, 2002). During glaciation, faults within areas beneath the ice load will commonly increase stability and 'stiffen', causing a reduction in reactivation and fluid flow, as evidenced by the aseismic

nature under the continental ice sheets of Greenland and Antarctica (Goffey et al., 2016; Johnston, 2000). This suggests that upon load removal during deglaciation, changes in the stress field will result in reduced fault stability, potentially leading to increased fluid flow and reservoir leakage (Fjeldskaar and Amantov, 2018; Lund et al., 2009). This is supported by offshore western Norway being characterised with some of the highest seismicity levels in northwest Europe, likely caused by stress field changes attributed to glacial flexural stresses (Goffey et al., 2016; Grollimund et al., 2001; Løtveit et al., 2019).

Several petroleum systems within glaciated margins have been affected by variable fault conditions in response to either ice load removal, isostatic adjustments or the erosion and re-deposition of sediment (Goffey et al., 2016; Medvedev et al., 2019; Ostanin et al., 2017a), with the majority of cases resulting in increased fluid leakage. For example, within the Barents Sea (Fig. 1.4), the removal of overburden due to erosion associated with deglaciation and isostatic rebound, resulted in the opening of many pre-existing faults and the creation of pathways for fluid flow (Nottvedt et al., 1988). This is also observed within the Ringvassøy Loppa Fault Complex, on the northern Norwegian shelf (Fig. 1.4), where glaciations have removed thick layers of sediment from the seabed resulting in the opening of pre-existing faults and the creation of new ones, allowing active fluid flow (Fig. 1.7) (Chand et al., 2012). Fluid migration and escape at the seabed is evidenced by several gas flares in the water column that are observed up to 200 m high, with the majority of flares observed in areas away from pockmarked regions, suggesting that present day gas escape is still controlled by the faults. Similarly, Tasianas et al. (2016), showed that fluid migration has taken place along faults for much of the Barents Sea and that these faults may have been reactivated by glacial-tectonic processes and are directly connected to reservoir spill points at depth. Additionally, Ostanin et al. (2017b), modelled the effect of Plio-Pleistocene glaciations on fault leakage from the Snøhvit gas field, southwest Barents Sea (Fig. 1.4). Fault dilation and seal bypass due to ice unloading and isostatic rebound was shown to account for a 60-80% reduction of initial accumulated mass in the reservoirs. Subsequent leakage events from succeeding glaciations caused further decrease from the remaining hydrocarbon mass from reservoirs in the range of 7-25%.

During deglacial periods, high pore pressures may remain within low permeability formations after the lithostatic load (the ice) is removed (Corcoran and Doré, 2002), with the excess pressure potentially causing faults to reactivate, allowing fluid leakage. This process is thought to have affected the Visund oil and gas field, Norwegian North Sea, which shows present day hydrocarbon leakage through a fault-valve mechanism that has been attributed to excess pore pressure within the deglacial stress regime, causing a

reduction in fault stability (Goffey et al., 2016; Grollimund and Zoback, 2003; Wiprut and Zoback, 2002). Furthermore, pore pressure changes are thought to have also caused a reduction in fault stability within offshore Denmark, leading to fault related seal breach of Late Cretaceous chalk reservoirs on the flanks of a Zechstein salt diaper (Fig. 1.8) (Goffey et al., 2016). This fluid remobilization has subsequently charged shallow Miocene reservoirs to spill creating the 'Lille John Field' which was discovered in 2011.

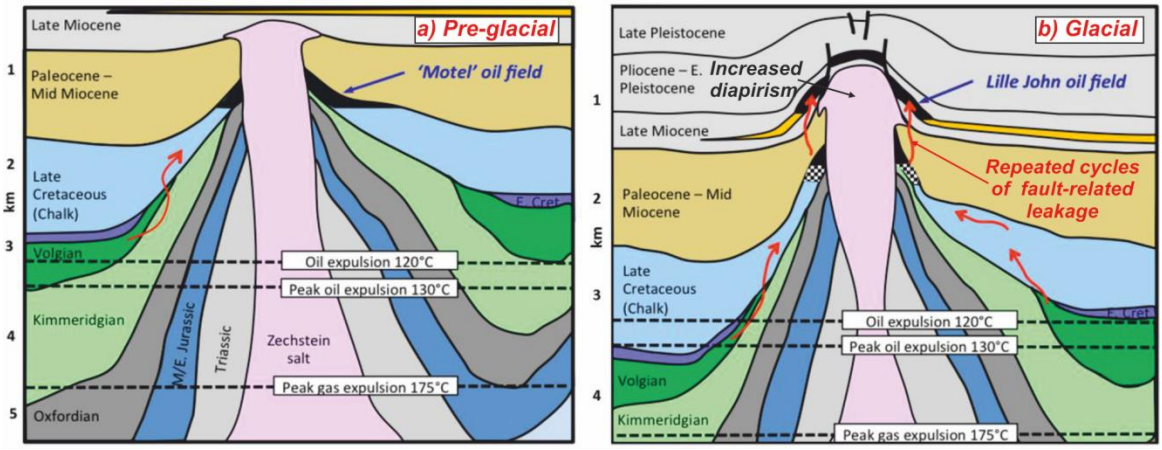

Figure 1.8. Lille John field | An interpreted cross section through the John diapir during the Late Miocene (a), showing the migration of oil from late Jurassic source rocks into a 'motel' chalk reservoir trapped against the salt. During late Pleistocene times (b), the interpreted cross-section shows how the top seal of the 'motel' reservoir has been breached, probably due to glacial forces, and the oil has re-migrated into Late Miocene reservoirs that were structured by increased salt diapirism likely in response to glacial loading. This figure has been modified from Goffey et al. (2016) with the length of the line approximately 22 km.

Polygonal faults commonly form within fine-grained sediments due to compaction and dewatering processes during burial (Cartwright et al., 2003; Cartwright and Lonergan, 1996), and have been observed within many petroleum seal formations worldwide (Cartwright, 2019; Cartwright et al., 2007), suggesting that polygonal fault networks are closed systems with regards to fluid flow. However, it is also suggested that polygonal fault systems may control fluid flow and create seal bypass pathways from underlying reservoirs (Berndt et al., 2003; Cartwright, 1994; Henriet et al., 1991). An example of this is the Ormen Lange gas field in the southern Norwegian Sea (Fig. 1.4), where numerous indications of polygonal fault controlled fluid flow exist, which has potentially caused 60% of the fluid volume to have leaked through the seal (Berndt et al., 2003; Verschuren, 1992). Therefore, for petroleum systems on glaciated margins, fluid migration through polygonally faulted seals may also be affected by glacially-induced variations in the subsurface stress-field. Ostanin et al. (2012); (2017b), showed that fault properties such as capillary entry pressure and permeability vary significantly during periods of glacial loading and unloading and that glacial cycles can cause the reactivation of polygonal fault systems, leading to the leakage of fluids through these networks. They also suggest that rapid glacigenic deposition

can cause the reactivation of polygonal faults and subsequent fluid flow to occur (Ostanin et al., 2012). Additionally, within the Vøring Basin, mid-Norwegian margin (Fig. 1.4), the rapid deposition of glacial debris flows has created intervals of polygonal faults that have penetrated into the underlying formation and are thought to cause the leakage of hydrocarbon fluids to shallower depths (Gay and Berndt, 2007). These examples suggest that glacial influences potentially cause a variation in the sealing potential of a polygonal fault system throughout certain parts of the glacial cycle.

1.2.2.5. Pressure and Temperature Conditions

Variable subsurface pressure and temperature conditions can significantly impact petroleum systems, influencing elements such reservoir quality, seal effectiveness and source maturation, whilst also affecting the nature and migration of hydrocarbon fluids (Fjeldskaar and Amantov, 2018; Medvedev et al., 2019). During periods of glaciation, subsurface pressure increases in response to ice loading, additional subsidence and rapid burial (Cavanagh et al., 2006; Grassmann et al., 2010). This often causes sediment compaction through mechanical and chemical compaction processes (Sclater and Christie, 1980; Walderhaug, 1992), leading to variations in reservoir quality and seal effectiveness, as well as creating overpressure (Osborne and Swarbrick, 1997). Overpressure is caused by the inability of pore fluid to escape as compaction occurs, and it often restricts compaction and instead retains reservoir porosity with burial, leading to anomalously high porosities compared to present-day depth (Hermanrud and Nordgard Bolas, 2002; Karlsen and Skeie, 2006). This process is thought to have affected the Upper Jurassic reservoirs of the Fulmar Fm. in the North Sea and several pre-Cretaceous fields in the central North Sea Graben (Gaarenstroom et al., 1993; Osborne and Swarbrick, 1999). Overpressured reservoirs can therefore, create tempting targets for hydrocarbon exploration and may occur more frequently in glaciated areas. However, leakage from overpressured reservoirs can also occur due to elevated buoyancy pressure promoting seal breach (Berg, 1975). Several shallow overpressured reservoirs at Haltenbanken, Norway, and also within the northern North Sea (Fig. 1.4), are predicted to have leaked as a result of fault reactivation and hydraulic fracturing of the seal formation, which created fluid leakage pathways. The breach is thought to have occurred due to both overpressure and increased horizontal stress due to lithospheric flexure from glacial advance and retreat (Hermanrud and Nordgard Bolas, 2002).

Overpressure is thought to have also affected the Lille John field, Danish North Sea (Fig. 1.8), where elevated pore pressures in Late Cretaceous chalk reservoirs have remained into the period of deglaciation and load removal, with the pressure difference causing fault

reactivation and repeated cycles of seal breach during multiple deglaciations (Goffey et al., 2016). Pressure within the deeper chalk reservoirs remain 900 psi higher than the post-leakage charge destination. Additionally, overpressure can also affect hydrocarbon expulsion and migration from source rocks. This is observed in the Yinggehai Basin, South China Sea, where abnormal organic-matter maturation has been attributed to overpressure within the source formation (Hao et al., 1998). This effect could theoretically occur due to glacially induced overpressure within source rocks formations on glaciated margins. Furthermore, glaciation can also affect sealing lithologies as rapid dewatering and compaction in response to loading causes a reduction in pore throat size within the sealing rock (Nordgard Bolas et al., 2005). This leads to a more effective seal with a higher capillary entry pressure limit whilst also adding to reservoir overpressure creation due to restricted vertical fluid flow. Moreover, overburden pressure variations can also impact salt tectonics, affecting hydrocarbon elements such as trap geometries and evaporitic seals. For example, salt diapirism at the Lille John field (Figs. 1.4 and 1.8) is thought to have increased in response to the additional vertical load during Late Pleistocene glaciation (Goffey et al., 2016). This is thought to have increased the trap capacity of the Miocene reservoirs.

Fluctuations in subsurface confining pressure in response to ice loading and isostatic adjustment will also cause significant variations in hydrocarbon volumes (Fjeldskaar and Amantov, 2018; Ostanin et al., 2017a; Tasianas et al., 2018). Deglaciation, uplift and erosion will cause a reduction in pressure and for hydrocarbon volumes to expand, whilst glacial expansion, subsidence and deposition, increase confining pressures, causing volumes to contract (Doré and Jensen, 1996; Tasianas et al., 2018). This will most significantly affect gas phase hydrocarbons, causing repeated cycles of gas expansion and contraction across several glaciations. This process can cause fluid leakage from reservoirs at the spill point, as an expanding gas volume can push underlying oil phase hydrocarbons out of the trap or gas itself can leak out if expansion occurs to depths below the spill point (Nyland et al., 1992; Ostanin et al., 2017a). This process is thought to have affected the Snøhvit field, Barents Sea (Fig. 1.4), where a paleo gas-oil contact has been detected shallower than the contact observed today. The oil was likely pushed out of the reservoir by the expanding gas leg due to a pressure reduction caused by 1000-1500 m of uplift, due in part to post-glacial isostatic rebound (Nyland et al., 1992; Ostanin et al., 2017a). Similar processes have been proposed for other reservoirs within the Haltenbanken and Skagerrak areas of the Norwegian shelf (Jensen and Schmidt, 1990; Riis and Fjeldskaar, 1992).

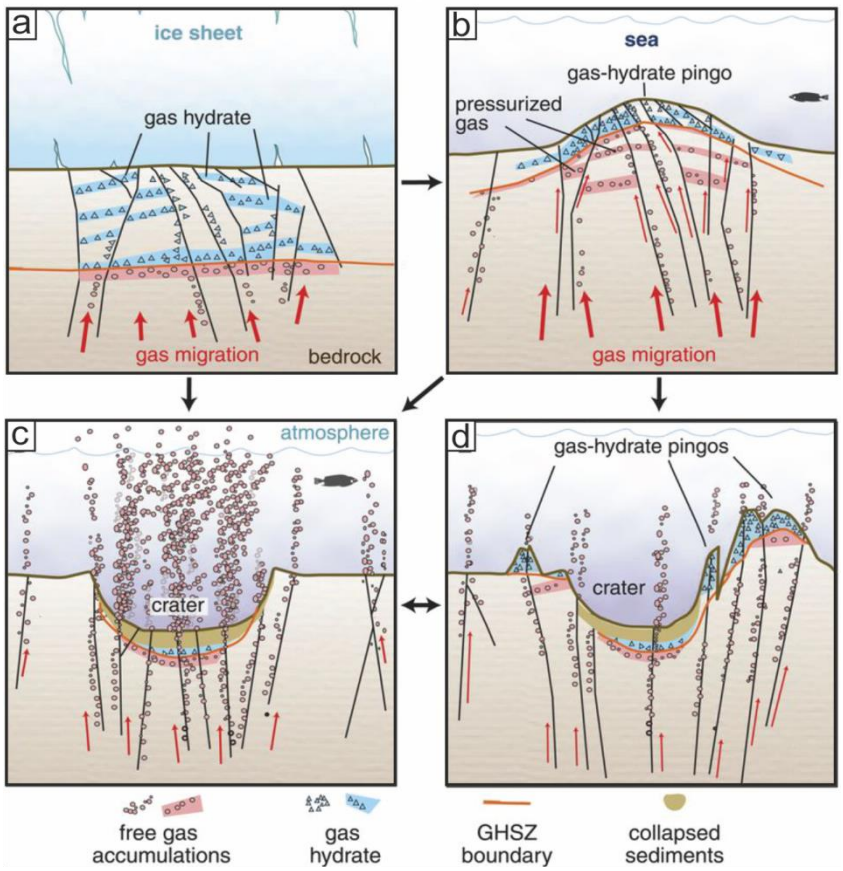

Figure 1.9. Glaciation impacting gas hydrate deposits | A conceptual sketch showing an example of how glaciation can cause the trapping of gas hydrates beneath an ice sheet (a), before deglaciation and continued gas migration causes increased pressure beneath the seabed (b), and eventual dissociation of gas hydrate pingos, causing the explosive release of gas at the seabed into the water column (c), and potentially the atmosphere, creating large craters that are still observed on the contemporary seabed (d). These diagrams are modified from Andreassen et al. (2017).

Glacially-induced variations in both pore pressure and temperature can affect the solubility of gas in both oil and water, possibly impacting hydrocarbon production (Goffey et al., 2016; Tasianas et al., 2016). These variations may also have a significant impact on source rock maturation and hydrocarbon generation, due to variations in the depth of maturity windows (Sweeney and Burnham, 1990). On top of this, pressure reduction may cause un-expelled oil retained in source rocks to exsolve and expel gas, possibly leading to late-stage gas charging of structures, often during uplift events in glacial environments (Doré and Jensen, 1996; Tasianas et al., 2016). Variations in subsurface temperature, can lead to the thermal expansion of hydrocarbons, possibly causing overlying seals to become fractured during rapid burial, causing episodic leakage (Hunt, 1990). The ice load on the seabed can also cause significant temperature fluctuations between glacial and interglacial periods; with sediment cooling from grounded ice often remaining into the subsequent interglacial (Cavanagh et al., 2006; Solheim et al., 1996). Glacially driven changes in subsurface reservoir temperature were modelled by Grassmann et al., (2010) for the

Mittelplate oil field, Germany, where they predicted a reduction in temperature by 3-7°C due to Pleistocene surface temperatures and the high thermal conductivity of permafrost. These thermal changes are an important consideration when calculating the formation volume factor of reservoir fluids.

Gas hydrates deposits often exist within high latitude shelf margins (Minshull et al., 2020; Sloan and Koh, 1990), with the deposits being particularly sensitive to glacially induced subsurface pressure and temperature variations (Andreassen et al., 2017; Mienert et al., 2000). Pressure and temperature conditions control the thickness of the gas hydrate stability zone, and the depth of the phase boundary (the free gas-gas hydrate transition), and therefore, varying these conditions between glacial-interglacial cycles can have a substantial impact on the accumulation, stability and dissociation of these deposits (Andreassen et al., 2017; Grassmann et al., 2010). During glacial periods, the base ice temperature in contact with the underlying sediment is commonly around -1 to 2°C (Andreassen et al., 2017; Cavanagh et al., 2006). This causes sediment cooling, alongside increased pressure from the ice load, which increases stability (shifting the phase boundary deeper) and promotes the formation and expansion of gas hydrate deposits. This stability is intensified by the low permeability of ice at the base of the glacier or the development of permafrost in shallow sediments, further increasing the trapping potential of gas (Andreassen et al., 2017). Increased hydrate stability during past glacial periods has been predicted for areas above the Prudhoe Bay oil field, Alaska (Fig. 1.4), and within the northern part of the West Siberian Basin, and in both localities, hydrate expansion is thought to have been great enough to convert shallow conventional gas reservoirs to gas hydrate (Collett, 1993; Cramer et al., 1997).

During deglaciation, temperature increase and the removal of load pressure causes the gas hydrate stability zone to contract, and can lead to the dissociation of gas hydrate deposits into free gas (Andreassen et al., 2017; Kvenvolden, 1993; Sloan and Koh, 1990). This will often occur at the phase boundary as it shifts upwards, but if temperature and pressure conditions change enough, hydrate dissociation can also occur at the seabed, releasing methane into the water column (Lerche and Bagirov, 1998; Ruppel and Kessler, 2017). For example, an increase in sea bed temperature of +4°C over a period of 100 kyr is thought to be enough to cause the complete dissociation of hydrate layers in water depths of 1200 m (Xu et al., 2001). This effect is observed on the sea bed of the Barents Sea where large craters are thought to have formed via the explosive release of dissociated hydrates in response to temperature and pressure changes experienced during deglaciation of the last glacial maximum (Fig. 1.9) (Andreassen et al., 2017; Solheim and Elverhoi, 1993). Hydrate

release into the water column and atmosphere through such processes, can act as a strong positive feedback mechanism for climate change, increasing greenhouse warming and further amplifying emissions at the sea bed (Krey et al., 2009; Nisbet, 1990; Ruppel and Kessler, 2017).

1.2.3. Melville Bay

Melville Bay represents the north-eastern part of Baffin Bay, offshore northwest Greenland (Fig. 1.10), and is characterised by an extensive continental shelf margin that has experienced multiple shelf-edge glaciations since ~2.7 Ma (Knutz et al., 2019; Newton et al., 2017). The area is thought to contain a complex subsurface geology including large basement structures and deep, unexplored sedimentary basins, which possibly comprise a frontier petroleum system (Bojesen-Koefoed, 2011; Gregersen et al., 2013; Henriksen et al., 2009; Schenk, 2011; Whittaker et al., 1997). With this potential for hydrocarbons and the recent history of glaciations, along with the dense coverage of both 2D and 3D seismic reflection data (Fig. 1.10; Section 1.3.5) (Gregersen et al., 2019), Melville Bay represents a suitable location to investigate the impacts of glaciation on underlying petroleum systems.

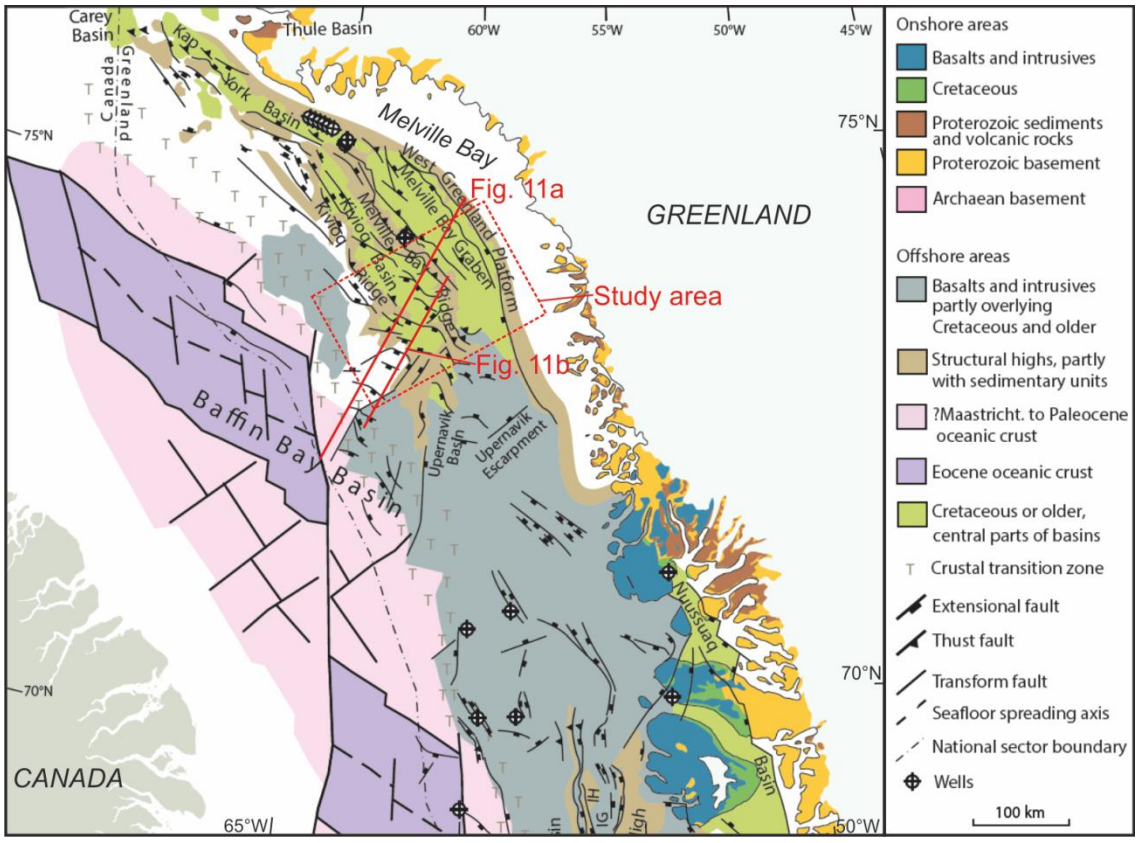

Figure 1.10. Geological map of Baffin Bay | A map of the tectonic elements of Baffin Bay, displaying the main structural highs including the Melville Bay Ridge, deep sedimentary basins including the South Kivioq Basin and Melville Bay Graben, major faults, oceanic crust and extensive volcanic deposits. The map has been modified from Gregersen et al. (2019) with the location of the spreading centre provided by Oakey and Chalmers (2012) and the map of onshore areas by Henriksen et al. (2009). The locations of Fig. 11a-b are shown along with the general study area of this thesis.

The subsurface geology of Melville Bay has been the focus of several studies since the early 1970's (Gregersen et al., 2019; 2008; 2013; 2016; Henderson et al., 1981; Keen et al., 1974; Knutsen et al., 2012; Knutz et al., 2012; 2015; 2019; Schenk, 2011; Skaarup and Pulvertaft, 2007; Whittaker et al., 1997), with basin formation occurring as a result of rifting and seafloor spreading between Greenland and Canada during the Cretaceous to Paleogene (Altenbernd et al., 2015; Oakey and Chalmers, 2012; Welford et al., 2018). Rifting is thought to have occurred during two phases; the first during the Early Cretaceous (145.5-99.6 Ma), and the second during the Campanian-Danian (83.6-61.6 Ma) after a period of rift quiescence (Gregersen et al., 2019; Oakey and Chalmers, 2012). This rifting has created the deep sedimentary basins of the Melville Bay Graben and South Kivioq Basin (Figs. 1.10 and 1.11) which are thought to contain syn- and post-rift sediments that can reach thicknesses of >10 km (Fig. 1.11) (Whittaker et al., 1997). The two sedimentary basins are separated by the Melville Bay Ridge, which, along with the Kivioq Ridge, represent northwest-southeast trending elongate inversion structures that likely formed during the second phase of rifting (Gregersen et al., 2019; Whittaker et al., 1997). Seafloor spreading is thought to have ceased during the late Eocene-Oligocene with the basin being infilled by post-rift sedimentation during and after post-drift tectonic relaxation (Knutz et al., submitted; Oakey and Chalmers, 2012; Welford et al., 2018). The Inversion structures possibly experienced periods of renewed uplift during the Cenozoic, potentially related to compressional tectonics that resulted from the Eurekan Orogeny as Greenland drifted northward and converged with the North American Plate (Gregersen et al., 2019; Japsen et al., 2006; Oakey and Stephenson, 2008). These processes have contributed to the development of several extensive tectonic faults that define the ridge structures and offset syn-rift stratigraphy (Fig. 1.11) (Gregersen et al., 2019; 2016).

The regional stratigraphy of north-eastern Baffin Bay, including Melville Bay, has been extensively mapped by Gregersen et al. (2013); (2016) and Knutz et al. (2015) using regional 2D seismic reflection data, with this work defining a seismic-stratigraphic nomenclature that will be used throughout this thesis. This framework divides the stratigraphy into ten seismic mega-units (mu-) (Hx-A from oldest to youngest) which are top bounded by regional unconformable horizons (hz) (hx-b1 from oldest to youngest) (Fig. 1.11). The geometry, distribution and internal seismic character of these units within Melville Bay is presented within the research chapters of this thesis, with a detailed description being provided within Chapter 5. In summary, mu-Hx and –H represent Proterozoic-Paleozoic crystalline basement and metamorphosed rocks (Acton, 2012; Gregersen et al., 2019; 2018; Nøhr-Hansen et al., 2018). The basement is overlain by Cretaceous-Paleogene syn-rift sedimentation, which is represented by mu-G, -F and the

lower part of –E, and most likely consists of a range of clastic lithologies including sands, shales and coals (Dam et al., 2009; Gregersen et al., 2013; Nøhr-Hansen et al., 2018). The mu-E package represents the transition from syn to post-rift sedimentation as the margin entered the tectonic drift phase (Gregersen et al., 2019; Knutz et al., submitted). The basin was subsequently infilled by Eocene-Pliocene aged post-rift units represented by mu-D, which comprises of sand-rich basin floor fans overlain by thick hemipelagic fine grained sediments (Knutz et al., 2012; Knutz et al., 2015), and mu-C and –B, which consist of Miocene-Pliocene aged thick muddy contourite deposits (Knutz et al., 2015; Nielsen et al., 2011).

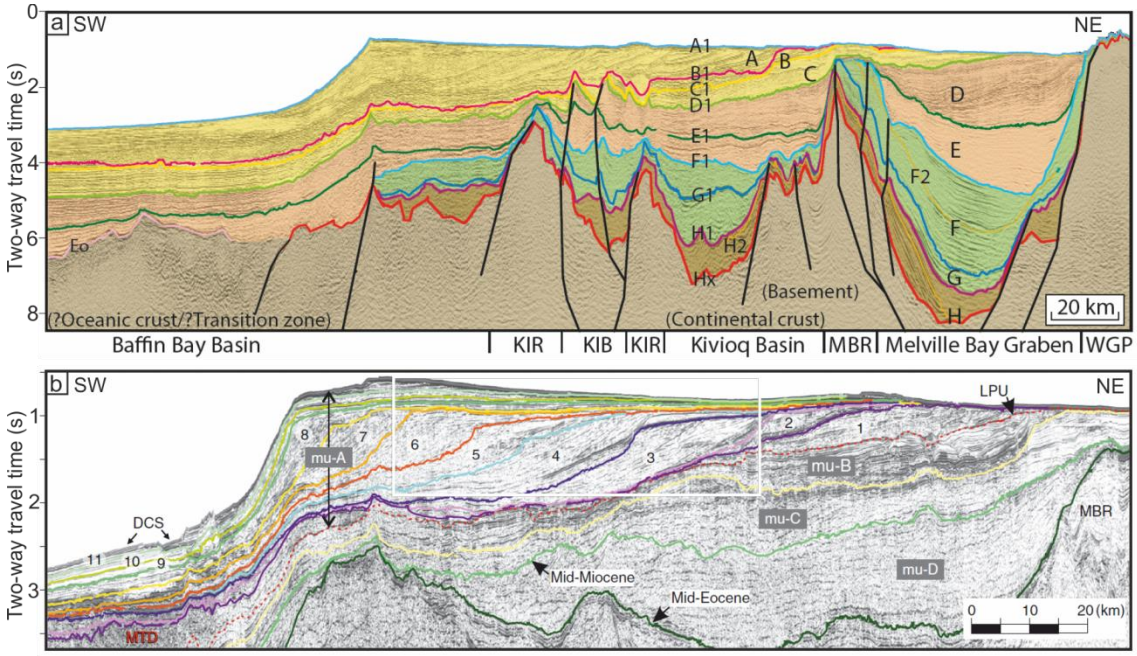

Figure 1.11. Regional seismic-stratigraphic framework | An interpreted seismic cross section NE-SW through Melville Bay (a), from Gregersen et al. (2019), displaying the regional stratigraphic framework for offshore northwest Greenland from Gregersen et al. (2013); (2017) and Knutz et al. (2015). A summary of the seismic units shown is provided in the text. Abbreviations include Kivioq Ridge (KIR), Kivioq Basin (KIB) and Melville Bay Ridge (MBR). An interpreted seismic cross section NE-SW through Melville Bay (b), from Knutz et al. (2019), displaying the division of mega unit (mu-) A into 11 glacigenic prograding units (1-11) that correspond to at least 11 shelf edge glaciations in Melville Bay since ~2.7 Ma. The paleo-shelf break positions for each of these units are shown on Fig. 1.12.

The uppermost post-rift unit is mu-A ,which represents a thick package of glacigenic sediments, deposited after the onset of glaciation across the shelf at ~2.7 Ma (Knutz et al., 2019; Newton et al., 2017). The Melville Bay continental margin has experienced at least eleven shelf-edge glaciations during this period (Fig. 1.12), with grounded ice causing extensive truncation by glacial erosion on the inner shelf which has contributed to the deposition of the Melville Bay Trough Mouth Fan at the shelf edge (mu-A). These processes have transformed the continental shelf in Melville Bay, with cross-shelf trough development causing over-deepening and a widespread glacial unconformity on the inner

shelf, whilst trough mouth fan deposition has caused over ~100 km of shelf edge progradation (Fig. 1.12) (Knutz et al., 2019; Newton et al., 2017).

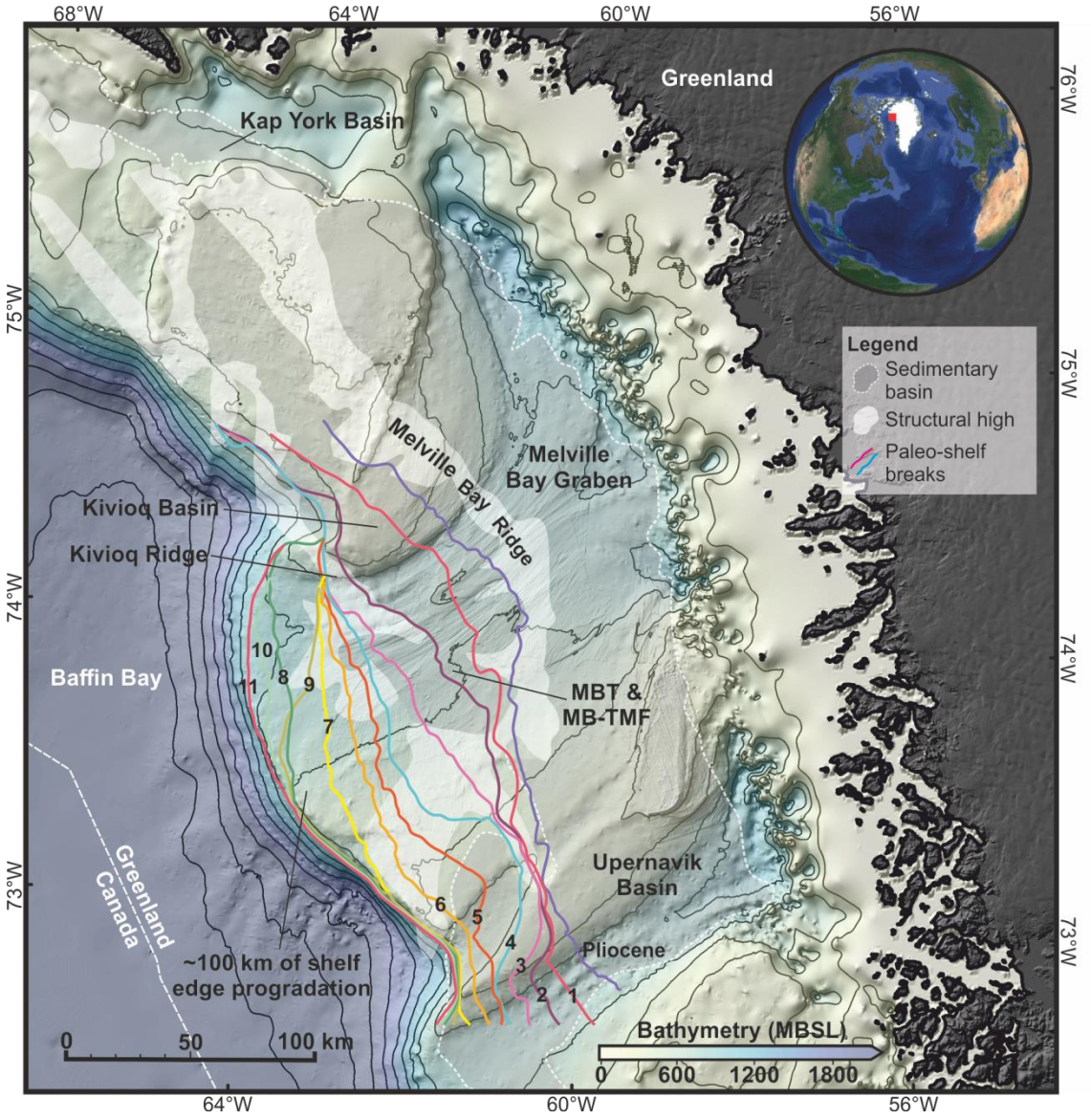

Figure 1.12. Glacial bathymetry of Melville Bay | A bathymetric map of the Melville Bay area in northwest Greenland, modified from Cox et al. (2020a) and displaying the bathymetry from Newton et al. (2017), highlighting the extensive influence of glaciation on the seabed including the Melville Bay Trough (MBT), Melville Bay Trough Mouth Fan (MB-TMF) and ~100 km of shelf edge progradation. The red square on the inset map shows the global location of the bathymetry. Annotations on the map include the distribution of regional rift elements, including sedimentary basins and structural ridges, as well as the location of paleo-shelf break positions of glacigenic prograding units from Knutz et al. (2019).

Interest in Melville Bay as a potential petroleum province began in the 1990s, after the discovery of gas on the Labrador shelf and southern West Greenland Shelf in the 1970-80s (Bell and Campbell, 1990; Rolle, 1985; Whittaker et al., 1997). This interest was accelerated after potential source rock horizons were identified on Ellesmere Island and in West Greenland (Bojesen-Koefoed, 2011; Bojesen-Koefoed et al., 1999; Christiansen et al., 1996; Núñez-Betelu, 1993), with these source rocks also expected to occur within northeast

Baffin Bay. Organic rich source rocks horizons are thought to have been deposited within the sedimentary basins of Melville Bay during a period of rift quiescence during the Cenomanian-Turonian (Gregersen et al., 2013; Nøhr-Hansen et al., 2018), and are potentially contained within the syn-rift unit mu-F (Fig. 1.11). Numerous reservoir horizons and trap styles were also predicted to occur within these basins (Whittaker et al., 1997). The potential existence of these petroleum system elements, along with renewed exploration interest in the Arctic as a result of increasing oil prices from 2002-2008, prompted an exploration license round from 2007-08 and 2010, which led to five licenses being awarded in northeast Baffin Bay alone. This led to extensive 2D and 3D seismic reflection data acquisition across the region (see Section 1.3.5). After falling oil prices in 2014 however, all five licenses in northeast Baffin Bay were relinquished without a single well being drilled.

1.3. This Thesis

1.3.1. Rationale

Glaciations can significantly affect the structure, stratigraphy and subsurface conditions within sedimentary basins on glaciated margins, with these changes often causing substantial impacts to any petroleum systems contained within. With oil and gas exploration moving towards higher latitude, Arctic environments, the need to fully understand these processes and how a particular petroleum system may have been affected in the past, is becoming increasingly important. The Arctic is predicted to contain 30% and 13% of the world's undiscovered gas and oil respectively (Gautier et al., 2009), meaning exploration is likely to continue. However, the majority of attention given to the effects of glaciation on petroleum systems has been focussed across the Norwegian Shelf (Fig. 1.4), so it is important to expand these investigations into other Arctic basins and glaciated margins which may have experienced a much different evolution, glacial scenario and importantly, impacts to the petroleum system.

This study is focussed within Melville Bay, offshore northwest Greenland, an area which is thought to represent a frontier petroleum system, existing within an Arctic basin predicted to contain significant untapped hydrocarbon resources (Gautier et al., 2009; Henriksen et al., 2009). This led to recent exploration interest in the area, resulting in the acquisition of wide coverage 2D and 3D seismic reflection surveys. The potential for hydrocarbons, the available data coverage, as well as the Melville Bay margin having been transformed by Pliocene-Pleistocene glaciations, makes this study area a suitable location to expand our understanding of the relationship between glaciation and petroleum systems.

Additionally, prior to this thesis, several regional studies have been produced, but a detailed assessment of the structure, stratigraphy and petroleum system within Melville Bay is mostly missing within current literature. Therefore, this thesis provides the opportunity to fill the gap in our understanding of the Melville Bay area, whilst expanding our knowledge on the influence that glaciations can have on petroleum systems; knowledge that can hopefully be applicable to petroleum provinces within glaciated margins worldwide.

1.3.2. Thesis Aims

The principal aim of this thesis is to investigate the impacts of glaciation on petroleum systems. This will be achieved by studying the Melville Bay area, offshore northwest Greenland, due to its glacial history, potential as a frontier petroleum province and wide coverage with seismic data sets (Section 1.3.5). A number of research aims have been designed to improve our understanding of the effects of glaciations on petroleum systems in this area. These aims are:

- To develop a more detailed understanding of the structural and stratigraphic framework across Melville Bay, including the Melville Bay Graben, Melville Bay Ridge and South Kivioq Basin, and to improve our knowledge of basin evolution and the chronology and potential lithology of seismic stratigraphic packages.

- To characterise potential petroleum systems in Melville Bay, by identifying and describing petroleum system elements, the contemporary distribution of hydrocarbons, and the history of hydrocarbon generation and migration.

- To understand the influence of Pliocene-Pleistocene glaciations on both margin evolution, and subsurface conditions (pressure, temperature and sediment compaction) across the shelf.

- To model and predict the impact that glacial erosion, sediment re-deposition and repeated ice loading has had on hydrocarbon generation, expulsion, migration, accumulation and preservation.

1.3.3. Thesis Objectives

A number of individual objectives have been identified that will allow the research aims to be achieved:

- Conduct a stratigraphic and structural interpretation of the seismic reflection data across the study area, expanding the regional framework set out by Gregersen et al. (2013); (2016) and Knutz et al. (2015) (Chapters 2-4).

- Evaluate the seismic data and interpreted framework to increase our understanding of basin evolution, including the chronology of seismic packages and their likely lithology and genesis (Chapters 1 and 2).
- Identify and characterise petroleum system elements throughout the seismic data, such as possible reservoirs, seals, traps and source rock intervals (Chapters 2-3).
- Map and document seismic anomalies that may represent the contemporary distribution of hydrocarbons, or evidence for historical fluid flow (Chapters 2-4).
- Evaluate the possible composition of the hydrocarbon fluids that are interpreted on seismic data (Chapters 2 and 5).
- Create a 2D petroleum systems model within a basin modelling software package (PetroMod) using the previous seismic interpretations, regional data and the understanding of basin evolution to predict hydrocarbon generation, expulsion, migration and accumulation across the Melville Bay shelf (Chapter 5).
- Conduct sensitivity modelling and compare results against seismic observations to calibrate and select realistic parameters for past conditions (Chapter 5).
- Create a modelling workflow within basin modelling software that allows for repeated cycles of ice loading, erosion and sediment re-deposition to be modelled across the shelf (Chapter 6).
- Apply this modelling workflow to the previously created 2D petroleum systems model to assess the potential impacts of glacial processes on subsurface conditions, and how these changes have influenced aspects of the hydrocarbon system (Chapter 6).

1.3.4. Thesis Structure – Journal Format

Journal Format, as outlined by the University of Manchester, has been used throughout this thesis and was deemed appropriate due to the submission of several of the presented research chapters for publication, as well as each chapter containing a specific research focus with individual aims and methodologies. The chapters are, however, interlinked, and are presented in a logical order that provides an increased understanding of the geology, petroleum systems and evolution of Melville Bay (Chapters 2-4); before using that understanding to simulate and analyse the effect of glaciation on this system (Chapters 5-6). Together, the research chapters not only improve our understanding of Melville Bay, but

consider multiple glacial impacts on petroleum systems that may be integral to a broader range of studies conducted within glaciated margins. The structure of the thesis is defined below:

- Chapter 1: *Introduction*. This chapter provides the rationale to the research topic of this thesis including a review of literature that considers the impacts of glaciation on the subsurface and petroleum systems, as well as a summary of the evolution, geology and glacial history of Melville Bay.

- Chapter 2: *Slip sliding away: enigma of large sandy blocks within a gas-bearing mass transport deposit, offshore northwestern Greenland.*

  Published in *AAPG Bulletin* (Cox, D. R., Huuse, M., Newton, A. M. W., Gannon, P., and Clayburn, J., 2020, Slip sliding away: enigma of large sandy blocks within a gas bearing mass transport deposit, offshore NW Greenland, AAPG Bulletin, v. 104, no. 5, pp. 1011-1043.), this chapter represents the documentation of the stratigraphy, structure and petroleum system elements of the Melville Bay Ridge and Melville Bay Graben areas. Specifically, the chapter documents the genesis, deformation and hydrocarbon charge history of a giant submarine landslide reservoir.

- Chapter 3: *Shallow gas and gas hydrate occurrences on the northwest Greenland shelf margin.*

  Published in *Marine Geology* (Cox, D. R., Huuse, M., Newton, A. M.W., Sarkar, A. D., and Knutz, P. C., 2021, Shallow gas and gas hydrate occurrences on the northwest Greenland shelf margin, Marine Geology, v. 432, pp. 1-21.), this chapter details the petroleum system across the entire study area, whilst focussing also on the migration history of these fluids and how the petroleum system may have been impacted by recent glaciations.

- Chapter 4: *Geohazard detection using 3D seismic data to enhance offshore scientific drilling site selection.*

  Published in *Scientific Drilling* (Cox, D. R., Knutz, P. C., Campbell, D. C., Hopper, J. R., Newton, A. M. W., Huuse, M., and Gohl, K., 2020, Geohazard detection using 3D seismic data to enhance offshore scientific drilling site selection, Scientific Drilling, v. 28, pp. 1-27.), this chapter details the methodology and results of a 3D seismic geohazard assessment that was used to aid site selection for IODP Proposal 909. This chapter further documents the stratigraphy, structure and

petroleum system, and assesses several geomorphological elements related to glaciation across the margin.

- Chapter 5: *Modelling basin evolution and petroleum systems along a 2D seismic section offshore northwest Greenland.*

  This chapter presents the results from a 2D petroleum systems modelling study that attempts to improve our understanding of the geological evolution and the nature of hydrocarbons through time in Melville Bay.

- Chapter 6: *The impacts of glaciation on arctic petroleum systems offshore northwest Greenland.*

  This chapter details a basin modelling workflow that models glacial erosion, sediment re-deposition and repeated cycles of ice loading on the shelf, as well as the impacts that these processes have on the subsurface and petroleum systems.

- Chapter 7: *Summary and Conclusions.*

Additional research (Appendices):

- Appendix A: *Repeated ice streaming on the northwest Greenland continental shelf since the onset of the middle Pleistocene transition.*

  Published in *The Cryosphere* (Newton, A. M. W., Huuse, M., Knutz, P. C., and Cox, D. R.: Repeated ice streaming on the northwest Greenland continental shelf since the onset of the Middle Pleistocene Transition, The Cryosphere, 14, pp. 2303–2312), this chapter describes six sets of glacigenic landforms that were formed by ice streams during the Pliocene-Pleistocene, providing evidence for grounded ice during this period and identifying glacial-related geohazards considered within Chapter 4. This chapter also provides estimates for glacial dynamics used within Chapters 5-6.

- Appendix B: *Seismic geomorphology and evolution of the Melville Bugt trough mouth fan, northwest Greenland.*

  Published in *Quaternary Science Reviews* (Newton, A. M. W., Huuse, M., Cox, D. R., and Knutz, P. C., 2021, Seismic geomorphology and evolution of the Melville Bugt Trough Mouth Fan, northwest Greenland, Quaternary Science Reviews, v. 255, pp. 1-23.), this chapter provides a detailed description of the Melville Bay Trough Mouth Fan, providing important insight into glacial dynamics, whilst

providing a more comprehensive understanding of glacial geomorphological features across the shelf and recent basin evolution.

- Appendix C: *An Introduction to Seismic Reflection Data: Acquisition, Processing and Interpretation.*

  Published in *Regional Geology and Tectonics (second edition)* (Cox, D. R., Newton, A. M. W., and Huuse, M., 2020, An introduction to seismic reflection data: acquisition, processing and interpretation, in Scarselli, N., Adam, J., and Chiarella, D., eds., Regional Geology and Tectonics – Volume 1: Principles of Geologic Analysis, Second Edition, Elsevier, Amsterdam, Netherlands, Chapter 22, pp. 571-603), this chapter provides a detailed description and critique of the seismic interpretation methodology conducted for this thesis.

1.3.5. Data and Methods

For each research chapter presented within this thesis, the specific data set and methodology used is discussed in sufficient detail to allow the recreation of that study. A summary of these data and methods are presented within this section.

1.3.5.1. Data

The research presented within this thesis predominantly uses 2D and 3D seismic reflection data that include four separate seismic surveys acquired between 2007 and 2019 (Figs 1.10, 1.13 and Table 1.1). The first of these surveys to be acquired is the BBRE11 regional 2D survey, which is comprised of four surveys (BB07, BB08, BB09 and BB10) that were acquired by the geophysical company TGS between 2007 and 2010 as part of the Baffin Bay 2D regional dataset. These surveys were re-processed and combined to create the BBRE11 survey used within this thesis. Seismic processing stacking velocities were provided alongside seismic intersections to allow for depth conversion.

The first 3D seismic reflection survey, the Pitu survey, was acquired by Cairn Energy in 2011, covering an area of 1,672 km^2 within the Pitu license block on the inner shelf margin (Fig. 1.13 and Table 1.1). The survey was also provided as a pre-stack depth migration (PSDM) volume, in the depth domain, along with an interval velocity cube across the survey extent. The survey was reprocessed by CGG in 2013, providing a sub-set high resolution (HR) 3D seismic survey, the Pitu HR survey, which covers an area of 1,135.5 km^2. Reprocessing increased the resolution of the Pitu 3D survey from 18 m at a depth of 1500 ms two-way-time to 11 m at the same depth. The second 3D seismic reflection survey, the Anu survey, was acquired by Shell in 2013 over an area of 8700 km^2 across the mid-to-outer shelf (Fig. 1.13 and Table 1.1). In 2019, a new ultra-high-resolution (UHR)

survey, the LAKO UHR survey (LAKO is an acronym for the research vessel *HDMS Lauge Koch*), was acquired across sections of the shelf margin and beyond the shelf edge within Baffin Bay. This survey provides UHR imaging of the upper 500 ms below the seabed in order to supplement the existing industry seismic.

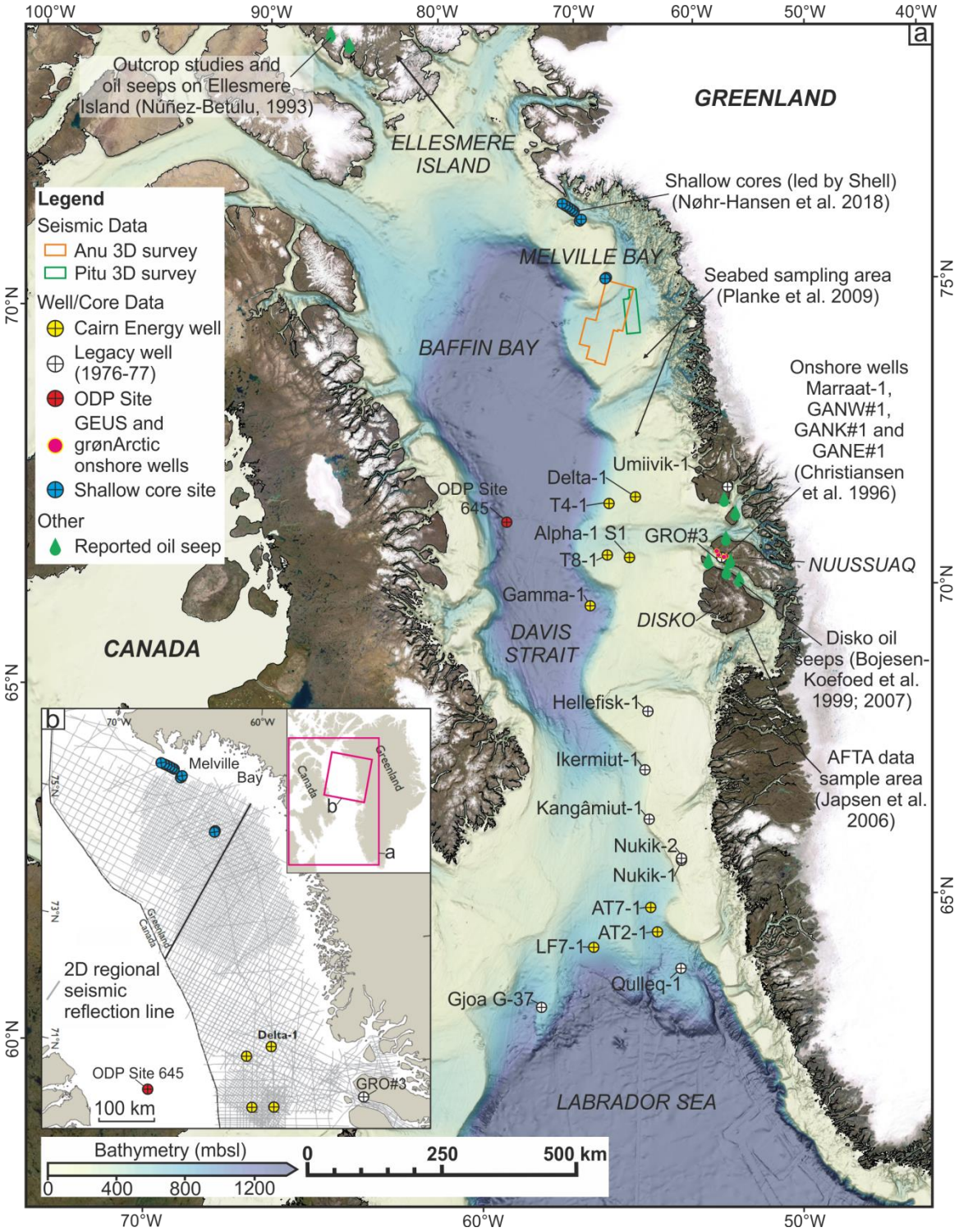

Figure 1.13. Regional data map | A map of West Greenland displaying the location of data used within this thesis (a), including 3D seismic volumes, well data and sampling studies. The bathymetry data shown is adapted from GEBCO Bathymetric Compilation Group 2020 (2020). A map of Baffin Bay is also shown (b), modified from Gregersen et al. (2017), displaying the 2D regional seismic survey (BBRE11), with the location of both a and b shown on the inset map.

Acquisition Parameter	Seismic Survey				
	Regional	Pitu	Pitu HR	Anu	LAKO UHR
Survey Type	**2D**	**3D**	**3D**	**3D**	**UHR 2D**
Date Acquired	2007-2010	2011	2013 Repro.	2013	2019
Area/Length Used	2,076 km	1,672 km^2	1,135.5 km^2	8700 km^2	306 km
No. of Vessels	1	1	-	2	1
Pop Interval	25 m	25 m (flip-flop)	-	25 m (flip-flop)	5-6 m
Source Depth	8 m	8 m	-	8 m	3 m
Source Separation	-	50 m	-	100 m	-
Streamer Length	6000 m	10 x 7050 m	-	6 x 7050 m	150 m
Streamer Separation	-	100 m	-	200 m	-
No. of Channels	480	564	-	564	40
Receiver Spacing	12.5 m	12.5 m	-	12.5 m	3.125 m
Sampling Rate	2 ms	4 ms	2 ms	2 ms	1 ms
Sail Line Separation	-	1 km	-	600 m	-
No. of 3D Sail Lines	-	93	-	118	-
Bin Spacing **Inline**	-	25 m	12.5 m	6.25 m	-
Bin Spacing **Crossline**	-	12.5 m	6.25 m	50 m	-
Fold	120	70	-	70	12.5
Domain	TWT	TWT / Depth	TWT	TWT	TWT
Provided Depth (down to)	9 s	6. 5 s/10 km	5 s	7.5 s	1.4 s
Depth of Given Resolution	1200 ms	1200 ms	1200 ms	1200 ms	900-1100 ms
Av. Dominant Frequency	40 Hz	55 Hz	90 Hz	45 Hz	120 Hz
Dominant Wavelength*	50 m	36 m	22 m	44 m	16.5 m
Vertical Resolution	12.5 m	9 m	6 m	11 m	4 m

***Calculated using an average velocity of 2000 metres per second (m/s).**

Table 1.1. Seismic data | A table displaying the acquisition parameters and survey statistics for the seismic data used within this thesis, from Cox et al. (2020a). The Pitu HR parameters can be read from the Pitu survey. Abbreviations used within the table include two-dimensional (2D), three-dimensional (3D), ultra-high-resolution (UHR), reprocessed (repro.), number (No.), average (Avg) and two-way time (TWT). Units used include metres (m), kilometres (km), milliseconds (ms), seconds (s) and hertz (Hz).

A summary of the acquisition parameters and survey statistics for each of the seismic surveys used within this thesis is provided on Table 1.1. The specific seismic survey(s) used within each study is stated within the data section of each research chapter within this thesis, along with a detailed description of the acquisition parameters and processing steps applied. All data used within this thesis were provided in SEG normal polarity with a downward increase in acoustic impedance represented by a red positive peak and a downward decrease in acoustic impedance represented by a blue negative trough. Data from a wide range of literature sources have also been utilized within Chapters 5 and 6 to create a 2D petroleum systems model, including Cairn Energy's offshore Greenland wells, legacy wells drilled by GEUS and grønArctic in the 1970s and 1990s respectively, shallow cores collected during the campaign led by Shell in 2012, seabed samples, apatite-fission-track data, oil seep samples and outcrop studies (Fig. 1.12).

1.3.5.2. Methods

Seismic interpretation workflows and 2D petroleum systems modelling comprise the key aspects of the research included within this thesis (Fig. 1.14). Several seminal works describe the process of interpreting seismic reflection data in order to gain an understanding of subsurface stratigraphy, structure and petroleum system character and how these elements have evolved through time, i.e. Badley (1985), Yilmaz (2001), Hilterman (2001), Avseth (2005), Posamentier (2004) and Posamentier et al. (2007). Schlumberger's Petrel software was used as the main seismic data interpretation platform. A description of the specific methodology used, along with critique analysis of these techniques, is provided within each research chapter, with a detailed summary of the seismic interpretation methods applied provided within Appendix C (Cox et al., 2020b). 2D petroleum system modelling was conducted using Schlumberger's PetroMod basin modelling software. A comprehensive background on basin modelling and the use of PetroMod is provided by Hantschel and Kauerauf (2009), with a detailed description of the model build process and uncertainties being provided within Chapters 5 and 6.

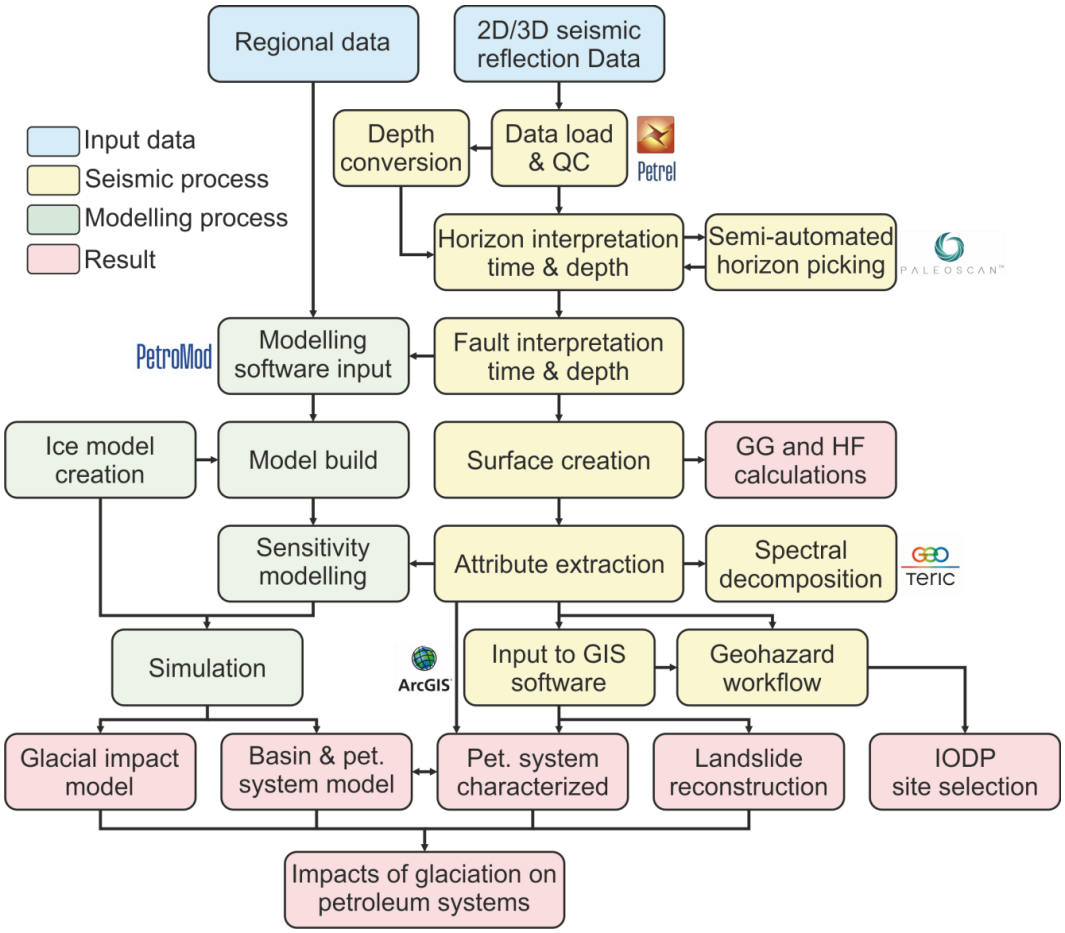

Figure 1.14. Methodology workflow | A flow diagram displaying the project workflow, including the seismic and modelling steps undertaken in an attempt to achieve the projects aims. Several software packages that were used are highlighted alongside processing steps including Schlumberger's Petrel and PetroMod, Eliis' Paleoscan, ffA's Geoteric and Esri's ArcGIS. The results displayed from this workflow comprise the research chapters within this thesis (Chapters 2-6).

References

Acton, G., 2012, Proceedings of the Baffin Bay Scientific Coring Program – Expedition 344S: Reporting by company consortium with eight companies led by Shell, p. 1-842.

Altenbernd, T., Jokat, W., Heyde, I., and Damm, V., 2015, Geophysical evidence for the extent of crustal types and the type of margin along a profile in the northeastern Baffin Bay: Journal of Geophysical Research: Solid Earth, v. 120, no. 11, p. 7337-7360.

Amantov, A., Plio-Pleistocene erosion of Fennoscandia and its implication for the Baltic Area, *in* Proceedings Proceedings of the 3rd Marine Geological Conference 'The Baltic', Warsaw, 1995, p. 47-56.

Amantov, A., Fjeldskaar, W., and Cathles, L., 2011, Glacial Erosion/Sedimentation of the Baltic Region and the Effect on the Postglacial Uplift, *in* Harff, J., Bjorck, S., and Hoth, P., eds., The Baltic Sea Basin: Berlin, Germany, Springer, p. 53-74.

Andreassen, K., Hubbard, A., Winsborrow, M., Patton, H., Vadakkepuliyambatta, S., Plaza-Faverola, A., Gudlaugsson, E., Serov, P., Deryabin, A., Mattingsdal, R., Mienert, J., and Bunz, S., 2017, Massive blow-out craters formed by hydrate-controlled methane expulsion from the Arctic seafloor: Science, v. 356, p. 948-953.

Andrews, J. T., 1970, Present and postglacial rates of uplift for glaciated northern and eastern North America derived from postglacial uplift curves: Canadian Journal of Earth Sciences, v. 7, no. 2, p. 703-715.

Avseth, P., 2005, Quantitative Seismic Interpretation: Applying rock physics tool to reduce interpretation risk, Cambridge, Cambridge University Press, 373 p.:

Aydin, A., 2000, Fractures, faults, and hydrocarbon entrapment, migration and flow: Marine and petroleum geology, v. 17, no. 7, p. 797-814.

Badley, M. E., 1985, Practical seismic interpretation, Prentice Hall, Englewood Cliffs, N.J, 1107 p.:

Batchelor, C. L., and Dowdeswell, J. A., 2014, The physiography of High Arctic cross-shelf troughs: Quaternary Science Reviews, v. 92, p. 68-96.

Batchelor, C. L., Margold, M., Krapp, M., Murton, D. K., Dalton, A. S., Gibbard, P. L., Stokes, C. R., Murton, J. B., and Manica, A., 2019, The configuration of Northern Hemisphere ice sheets through the Quaternary: Nature communications, v. 10, no. 1, p. 1-10.

Bechstadt, T., Jager, H., Spence, G., and Werner, G., 2009, Late Cryogenian (Neoproterozoic) glacial and post-glacial successions at the southern margin of the Congo Craton, northern Namibia: facies, palaeogeography and hydrocarbon perspective: Geological Society Special Publications, v. 326, p. 225-287.

Bell, J., and Campbell, G., 1990, Petroleum resources: Geology of the continental margin of eastern Canada: Geological Survey of Canada, Geology of Canada, no. 2, p. 677-720.

Benn, D. I., and Evans, D. J. A., 2010, Glaciers and Glaciation, London, Arnold.

Berg, R. R., 1975, Capillary Pressures in Stratigraphic Traps: AAPG Bulletin, v. 59, no. 6, p. 939-956.

Berndt, C., Bunz, S., and Mienert, J., 2003, Polygonal fault systems on the mid-Norwegian margin: a long term source for fluid flow, *in* Van Rensbergen, P., Hillis, R. R., Maltman, A. J., and Morley, C. K., eds., Subsurface sediment mobilization, Volume 216: London, Geological Society, p. 283-290.

Bintanja, R., and Van De Wal, R. S. W., 2008, North American ice-sheet dynamics and the onset of 100,000-year glacial cycles: Nature, v. 454, p. 869-872.

Bojesen-Koefoed, J. A., 2011, West Greenland Petroleum Systems – an Overview of Source Rocks and Oil Seepages and Their Implications for Offshore Petroleum Exploration: The Geological Survey of Denmark and Greenland.

Bojesen-Koefoed, J. A., Christiansen, F. G., Peter Nytoft, H., and Pedersen, A. K., 1999, Oil seepage onshore West Greenland: evidence of multiple source rocks and oil mixing: Petroleum Geology Conference Series, v. 5, p. 305-314.

Boote, D. R. D., Clark-Lowes, D. D., and Traut, M. W., 1998, Palaeozoic petroleum systems of North Africa: Geological Society Special Publications, v. 132, p. 7-68.

Boulton, G. S., 1979, Processes of glacier erosion on different substrata: Journal of glaciology, v. 23, no. 89, p. 15-38.

Buckley, F. A., 2012, An Early Pleistocene grounded ice sheet in the Central North Sea, *in* Huuse, M., Redfern, J., Le Heron, D. P., Dixon, R., Moscariello, A., and Craig, J., eds., Glaciogenic Reservoirs and Hydrocarbon Systems: London, Geological Society, p. 185-209.

Cartwright, J., Polygonal Faults and Seal Integrity, *in* Proceedings Sixth EAGE Shale Workshop, Bordeaux, France, 2019, Volume 2019, European Association of Geoscientists & Engineers, p. 1-4.

Cartwright, J. A., 1994, Episodic basin-wide hydrofracturing of overpressured Early Cenozoic mudrock sequences in the North Sea Basin: Marine and Petroleum Geology, v. 11, no. 5, p. 587-607.

Cartwright, J. A., Huuse, M., and Aplin, A., 2007, Seal Bypass Systems: AAPG Bulletin, v. 91, no. 8, p. 1141-1166.

Cartwright, J. A., James, D., and Bolton, A., 2003, The genesis of polygonal fault systems: a review: Geological Society Special Publications, v. 216, p. 223-243.

Cartwright, J. A., and Lonergan, L., 1996, Volumetric contraction during the compaction of mudrocks: a mechanism for the development of regional-scale polygonal fault systems: Basin Research, v. 8, no. 2, p. 183-193.

Cavanagh, A. J., Di Primio, R., Scheck-Wenderoth, M., and Horsfield, B., 2006, Severity and timing of Cenozoic exhumation in the southwestern Barents Sea: Journal of the Geological Society, v. 163, no. 5, p. 761-774.

Chalk, T. B., Hain, M. P., Foster, G. L., Rohling, E. J., Sexton, P. F., Badger, M. P., Cherry, S. G., Hasenfratz, A. P., Haug, G. H., and Jaccard, S. L., 2017, Causes of ice age intensification across the Mid-Pleistocene Transition: Proceedings of the National Academy of Sciences, v. 114, no. 50, p. 13114-13119.

Chand, S., Thorsnes, T., Rise, L., Brunstad, H., Stoddart, D., Boe, R., Lagstad, P., and Svolsbru, T., 2012, Multiple episodes of fluid flow in the SW Barents Sea (Loppa High) evidenced by gas flares, pockmarks and gas hydrate accumulation: Earth and Planetary Science Letters, v. 331-332, p. 305-314.

Christiansen, F. G., Bojesen-Koefoed, J., Dam, G., Nytoft, H.-P., Larsen, L. M., Pedersen, A. K., and Pulvertaft, T. C. R., 1996, The Marraat oil discovery on Nuussuaq, West Greenland: evidence for a latest Cretaceous–earliest Tertiary oil prone source rock in the Labrador Sea–Melville Bay region: Bulletin of Canadian Petroleum Geology, v. 44, no. 1, p. 39-54.

Clark, P. U., and Pollard, D., 1998, Origin of the middle Pleistocene transition by ice sheet erosion of regolith: Paleoceanography, v. 13, no. 1, p. 1-9.

Clayton, L., and Moran, S. R., 1982, A glacial process-form model, Glacial geomorphology, Springer, p. 89-119.

Collett, T. S., 1993, Natural gas hydrates of the Prudhoe Bay and Kuparuk River area, north slope, Alaska: AAPG bulletin, v. 77, no. 5, p. 793-812.

Conrad, C. P., 2013, The solid Earth's influence on sea level: Geological Society of America Bulletin, v. 125, no. 7-8, p. 1027-1052.

Corcoran, D., and Doré, A., 2002, Top seal assessment in exhumed basin settings—Some insights from Atlantic margin and borderland basins, Norwegian Petroleum Society Special Publications, Volume 11, Elsevier, p. 89-107.

Cox, D. R., Knutz, P. C., Campbell, D. C., Hopper, J. R., Newton, A. M. W., Huuse, M., and Gohl, K., 2020a, Geohazard detection using 3D seismic data to enhance offshore scientific drilling site selection: Scientific Drilling, v. 28, p. 1-27.

Cox, D. R., Newton, A. M. W., and Huuse, M., 2020b, An introduction to seismic reflection data: acquisition, processing and interpretation, *in* Scarselli, N., Adam, J., and Chiarella, D., eds., Regional Geology and Tectonics - Principles of Geologic Analysis: Amsterdam, Netherlands, Elsevier, p. 744.

Cramer, B., Braun, A., Poelchau, H. S., and Littke, R., 1997, Gas hydrates and permafrost in continental northern West Siberia; Gashydrate und Permafrost im kontinentalen noerdlichen Westsibirien, Conference on gas hydrates - noxious substances or resources: Clausthal-Zellerfeld, Germany, p. 27-36.

Dam, G., Pedersen, G. K., Sønderholm, M., Midtgaard, H. H., Larsen, L. M., Nøhr-Hansen, H., and Pedersen, A. K., 2009, Lithostratigraphy of the Cretaceous–Paleocene Nuussuaq Group, Nuussuaq Basin, West Greenland: Geological Survey of Denmark and Greenland (GEUS) Bulletin, v. 19, p. 1-171.

De Schepper, S., Gibbard, P. L., Salzmann, U., and Ehlers, J., 2014, A global synthesis of the marine and terrestrial evidence for glaciation during the Pliocene Epoch: Earth-Science Reviews, v. 135, p. 83-102.

Doré, A. G., Cartwright, J. A., Stoker, M. S., Turner, J. P., and White, N. J., 2002, Exhumation of the North Atlantic margin: introduction and background: Geological Society of London, Special Publication, v. 196, p. 1-12.

Doré, A. G., and Jensen, L. N., 1996, The impact of late Cenozoic uplift and erosion on hydrocarbon exploration: offshore Norway and some other uplifted basins: Global and Planetary Change, v. 12, no. 1-4, p. 415-436.

Fjeldskaar, W., 1994, The amplitude and decay of the glacial forebulge in Fennoscandia: Norsk Geologisk Tidsskrift, v. 74, p. 2-8.

Fjeldskaar, W., and Amantov, A., 2018, Effects of glaciations on sedimentary basins: Journal of Geodynamics, v. 118, p. 66-81.

Gaarenstroom, L., Tromp, R. A. J., De Jong, M. C., and Brandenburg, A. M., 1993, Overpressures in the Central North Sea: implications for trap integrity and drilling safety: Petroleum Geology Conference Series, v. 4, p. 1305-1313.

Gallagher, J. W., and Braaten, A. M., 1990, Shallow gas at Haltenbanken, Methane in Marine Sediments: Heriot Watt University, Edinburgh.

Gautier, D. L., Bird, K. J., Charpentier, R. R., Grantz, A., Houseknecht, D. W., Klett, T. R., Moore, T. E., Pitman, J. K., Schenk, C. J., Schuenemeyer, J. H., Sorensen, K., Tennyson, M. E., Valin, Z. C.,

and Wandrey, C. J., 2009, Assessment of undiscovered oil and gas in the Arctic: Science, v. 324, no. 5931, p. 1175-1179.

Gay, A., and Berndt, C., 2007, Cessation/reactivation of polygonal faulting and effects on fluid flow in the Vøring Basin, Norwegian Margin: Journal of the Geological Society, v. 164, p. 129-141.

Gildor, H., and Tziperman, E., 2000, Sea ice as the glacial cycles' climate switch: Role of seasonal and orbital forcing: Paleoceanography, v. 15, no. 6, p. 605-615.

Goffey, G., Attree, M., Curtis, P., Goodfellow, F., Lynch, J., Mackertich, D., Orife, T., and Tyrrell, W., 2016, New exploration discoveries in a mature basin: offshore Denmark, *in* Bowman, M., and Levell, B., eds., Petroleum Geology of NW Europe: 50 Years of Learning – Proceedings of the 8th Petroleum Geology Conference: London, Geological Society.

Grassmann, S., Cramer, B., Delisle, G., Hantschel, T., Messner, J., and Winsemann, J., 2010, pT-effects of Pleistocene glacial periods on permafrost, gas hydrate stability zones and reservoir of the Mittelplate oil field, northern Germany: Marine and petroleum geology, v. 27, no. 1, p. 298-306.

Gray, D. I., 1987, Troll, *in* Spencer, A. M., ed., Geology of the Norwegian Oil and Gas Fields: London, Graham and Trotman.

Gregersen, G., Knutz, P. C., Nøhr-Hansen, H., Sheldon, E., and Hopper, J. R., 2019, Tectonostratigraphy and evolution of the West Greenland continental margin: Bulletin of the Geological Society of Denmark, v. 67, p. 1-21.

Gregersen, U., 2008, The north-east Baffin Bay region, offshore Greenland–a new frontier petroleum exploration region: Geological Survey of Denmark and Greenland (GEUS) Bulletin, v. 15, p. 65-68.

Gregersen, U., Andersen, M. S., Nøhr-Hansen, H., Sheldon, E., Kokfelt, T. F., Olivarius, M., Knudsen, C., Jakobsen, K. G., and Adolfssen, J. S., 2018, New subsurface mapping offshore southern West Greenland using geophysical and geological data: Geological Survey of Denmark and Greenland Bulletin, p. 57-62.

Gregersen, U., Hopper, J. R., and Knutz, P. C., 2013, Basin seismic stratigraphy and aspects of prospectivity in the NE Baffin Bay, Northwest Greenland: Marine and Petroleum Geology, v. 46, p. 1-18.

Gregersen, U., Knutz, P. C., and Hopper, J. R., 2016, New geophysical and geological mapping of the eastern Baffin Bay region, offshore West Greenland: Geological Survey of Denmark and Greenland Bulletin, v. 35, p. 83-86.

Grollimund, B., and Zoback, M. D., 2003, Impact of glacially induced stress changes on fault-seal integrity offshore Norway: AAPG Bulletin, v. 87, p. 493-506.

Grollimund, B., Zoback, M. D., Wiprut, D., and Arnesen, L., 2001, Stress orientation, pore pressure and least principal stress in the Norwegian sector of the North Sea: Petroleum Geoscience, v. 7, p. 173-180.

Hantschel, T., and Kauerauf, A. I., 2009, Fundamentals of basin and petroleum systems modeling, Berlin, Heidelberg, Germany, Springer Science & Business Media, 476 p.:

Hao, F., Li, S., Dong, W., Hu, Z., and Huang, B., 1998, Abnormal organic-matter maturation in the Yinggehai Basin, South China Sea: implications for hydrocarbon expulsion and fluid migration from overpressured systems: Journal of Petroleum Geology, v. 21, no. 4, p. 427-444.

Henderson, G., Schiener, E., Risum, J., Croxton, C., and Andersen, B., 1981, The west Greenland basin.

Henriet, J. P., De Batist, M., and Verschuren, M., 1991, Early fracturing of Paleogene clays, southernmost North Sea: relevance to mechanisms of primary hydrocarbon migration, *in* Spencer, A. M., ed., Generation, Accumulation and Production of Europe's Hydrocarbons: Oxford, Oxford University Press, p. 217-227.

Henriksen, E., Bjørnseth, H., Hals, T., Heide, T., Kiryukhina, T., Kløvjan, O., Larssen, G., Ryseth, A., Rønning, K., and Sollid, K., 2011, Uplift and erosion of the greater Barents Sea: impact on prospectivity and petroleum systems: Geological Society, London, Memoirs, v. 35, no. 1, p. 271-281.

Henriksen, N., Higgins, A. K., Kalsbeek, F., Christopher, T., and Pulvertaft, R., 2009, Greenland from Archaean to Quaternary: Descriptive text to the 1995 Geological map of Greenland, 1:2500000: Geological Survey of Denmark and Greenland Bulletin, v. 18, p. 1-126.

Hermanrud, C., and Nordgard Bolas, H. M., 2002, Leakage from overpressured hydrocarbon reservoirs at Haltenbanken and in the northern North Sea, *in* Koestler, A. G., and Hunsdale, R., eds., Hydrocarbon Seal Quantification, Volume 11: Amsterdam, Elsevier Science, p. 221-231.

Hilterman, F. J., 2001, Seismic Amplitude Interpretation, Tulsa, OK, Society of Exploration Geophysicists, Distinguished Instructor Series No. 4, 244 p.:

Hirst, J. P. P., 2012, Ordovician proglacial sediments in Algeria: insights into the controls on hydrocarbon reservoirs in the In Amenas field, Illizi Basin, *in* Huuse, M., Redfern, J., Le Heron, D. P., Dixon, R., Moscariello, A., and Craig, J., eds., Glaciogenic Reservoirs and Hydrocarbon Systems, Volume 368: London, The Geological Society of London, p. 319-353.

Hunt, J. M., 1990, Generation and Migration of Petroleum from Abnormally Pressured Fluid Compartments: AAPG Bulletin, v. 74, no. 1, p. 1-12.

Huuse, M., Le Heron, D. P., Dixon, R., Redfern, J., Moscariello, A., and Craig, J., 2012, Glaciogenic reservoirs and hydrocarbon systems: an introduction: Geological Society Special Publications, v. 368, p. 1-28.

Huybers, P., 2011, Combined obliquity and precession pacing of late Pleistocene deglaciations: Nature, v. 480, no. 7376, p. 229-232.

Imbrie, J., Berger, A., Boyle, E., Clemens, S., Duffy, A., Howard, W., Kukla, G., Kutzbach, J., Martinson, D., and McIntyre, A., 1993, On the structure and origin of major glaciation cycles 2. The 100,000-year cycle: Paleoceanography, v. 8, no. 6, p. 699-735.

Japsen, P., Bonow, J. M., Green, P. F., Chalmers, J. A., and Lidmar-Bergstrom, K., 2006, Elevated, passive continental margins: Long-term highs or Neogene uplifts? New evidence from West Greenland: Earth and Planetary Science Letters, v. 248, no. 1-2, p. 330-339.

Jensen, L. N., and Schmidt, D. N., 1990, Late Tertiary uplift and erosion in the Skagerrak area : magnitude and consequences: Norsk Geologisk Tidsskrift, v. 72, no. 3, p. 275-279.

Johnston, A. C., 2000, The effect of large ice sheets on earthquake genesis, *in* Gregersen, S., and Basham, P., eds., Earthquakes at North Atlantic Passive Margins: Neotectonics and Postglacial Rebound, Volume 266, Mathematical and Physical Sciences, p. 581-599.

Karlsen, D., and Skeie, J., 2006, Petroleum migration, faults and overpressure, part I: calibrating basin modelling using petroleum in traps—a review: Journal of Petroleum Geology, v. 29, no. 3, p. 227-256.

Keen, C., Keen, M., Ross, D., and Lack, M., 1974, Baffin Bay: small ocean basin formed by sea-floor spreading: AAPG Bulletin, v. 58, no. 6, p. 1089-1108.

Kennett, J. P., Cannariato, K. G., Hendy, I. L., and Behl, R. J., 2003, Methane hydrates in quaternary climate change: The clathrate gun hypothesi: Methane hydrates in quaternary climate change: the clathrate gun hypothesis, v. 54, p. 1-9.

Kjemperud, A., and Fjeldskaar, W., 1992, Pleistocene glacial isostasy - implications for petroleum geology: NPF Special Publication, v. 1, p. 187-195.

Knutsen, S.-M., Arendt, N. P., Runge, M. K., Stilling, J., and Brandt, M. P., 2012, Structural provinces offshore West Greenland and key geological variations influencing play assessment: First Break, v. 30, no. 12.

Knutz, P. C., Gregersen, U., and Hopper, J. R., 2012, Late Paleogene Submarine Fans in Baffin Bay and North-West Greenland, 74th EAGE Conference and Exhibition incorporating EUROPEC 2012 Copenhagen, EAGE, p. 5.

Knutz, P. C., Harrison, C., Brent, T. A., Gregersen, G., and Hopper, J. R., submitted, Baffin Bay Tectono-Sedimentary Element, *in* Drachev, S., and Moore, T. E., eds., Arctic Sedimentary Basins, Volume Geological Society Memoir: London, Geological Society London.

Knutz, P. C., Hopper, J. R., Gregersen, U., Nielsen, T., and Japsen, P., 2015, A contourite drift system on the Baffin Bay–West Greenland margin linking Pliocene Arctic warming to poleward ocean circulation: Geology, v. 43, no. 10, p. 907-910.

Knutz, P. C., Newton, A. M. W., Hopper, J. R., Huuse, M., Gregersen, U., Sheldon, E., and Dybkjær, K., 2019, Eleven phases of Greenland Ice Sheet shelf-edge advance over the past 2.7 million years: Nature Geoscience, v. 12, p. 361-368.

Krey, V., Canadell, J. G., Nakicenovic, N., Abe, Y., Andruleir, H., Archer, D., Grubler, A., Hamilton, N. T. M., Johnson, A., Kostov, V., Lamarque, J., Langhorne, N., Nisbet, E. G., O'Neil, B., Riahi, K., Riedel, M., Wang, W., and Yakushev, V., 2009, Gas hydrates: entrance to a methane age or climate threat?: Environmental Research Letters, v. 4, p. 1-6.

Kvenvolden, K. A., 1993, A primer on gas hydrates, *in* Howell, D. G., Wiese, K., Fanelli, M., Zink, L. L., and Cole, F., eds., The Future of Energy Gases, Volume US Geological Survey Professional Paper 1570: Washington DC, USA, USGS, p. 279-291.

Le Meur, E., and Huybrechts, P., 1996, A comparison of different ways of dealing with isostasy: examples from modelling the Antarctic ice sheet during the last glacial cycle: Annals of Glaciology, v. 23, no. 1, p. 309-317.

Lerche, I., and Bagirov, E., 1998, Guide to gas hydrate stability in various geological settings: Marine and Petroleum Geology, v. 15, no. 5, p. 427-437.

Lisiecki, L. E., and Raymo, M. E., 2005, A Pliocene-Pleistocene stack of 57 globally distributed benthic δ18O records: Paleoceanography, v. 20, no. 1.

Løtveit, I. F., Fjeldskaar, W., and Sydnes, M., 2019, Tilting and flexural stresses in basins due to glaciations—An example from the Barents Sea: Geosciences, v. 9, no. 11, p. 474.

Lund, B., Schmidt, P., and Hieronymus, C., 2009, Stress evolution and fault stability during the Weichselian glacial cycle: Swedish Nuclear Fuel and Waste Management Co.

Luning, S., Craig, J., Loydell, D. K., Storch, P., and Fitches, B., 2000, Lower Silurian `hot shales' in North Africa and Arabia: regional distribution and depositional model: Earth Science Reviews, v. 49, no. 1-4, p. 121-200.

Maslin, M. A., and Ridgwell, A. J., 2005, Mid-Pleistocene revolution and the 'eccentricity myth': Geological Society, London, Special Publications, v. 247, no. 1, p. 19-34.

Medvedev, S., Hartz, E. H., Schmid, D. W., Zakariassen, E., and Varhaug, P., 2019, Influence of glaciations on North Sea petroleum systems: Geological Society, London, Special Publications, v. 494, p. SP494-2018-2183.

Mienert, J., Andreassen, K., Posewang, J., and Lukas, D., 2000, Changes of the hydrate stability zone of the Norwegian margin from glacial to interglacial times: Annals of the New York Academy of Sciences, v. 912, no. 1, p. 200-210.

Miller, K. G., Mountain, G. S., Wright, J. D., and Browning, J. V., 2011, A 180-million-year record of sea level and ice volume variations from continental margin and deep-sea isotopic records: Oceanography, v. 24, no. 2, p. 40-53.

Minshull, T. A., Marín-Moreno, H., Betlem, P., Bialas, J., Bünz, S., Burwicz, E., Cameselle, L., Cifci, G., Giustinaini, M., Hillman, J. I. T., Hölz, S., Hopper, J. R., Ion, G., León, R., Magalhaes, V., Makovsky, Y., Mata, M., Max, M. D., Nielsen, T., Okay, S., Ostrovsky, I., O'Neil, N., Pinheiro, L. M., Plaza-Faverola, A., Rey, D., Roy, S., Schwalenberg, K., Senger, K., Vadakkepuliyambatta, S., Vasilev, A., and Vázquez, J. T., 2020, Hydrate occurrence in Europe: A review of available evidence: Marine and Petroleum Geology, v. 111, p. 735-764.

Mudelsee, M., and Stattegger, K., 1997, Exploring the structure of the mid-Pleistocene revolution with advanced methods of time-series analysis: Geologische Rundschau, v. 86, no. 2, p. 499-511.

Newton, A., 2017, Seismic geomorphology of glaciated margins [PhD: University of Manchester.

Newton, A. M. W., Knutz, P. C., Huuse, M., Gannon, P., Brocklehurst, S. H., Clausen, O. R., and Gong, Y., 2017, Ice stream reorganization and glacial retreat on the northwest Greenland shelf: Geophysical Research Letters, v. 44, p. 7826-7835.

Nielsen, T., Andersen, C., Knutz, P. C., and Kuijpers, A., 2011, The Middle Miocene to Recent Davis Strait Drift Complex: implications for Arctic–Atlantic water exchange: Geo-Marine Letters, v. 31, no. 5-6, p. 419-426.

Nisbet, E. G., 1990, The end of the ice age: Canadian Journal of Earth Sciences, v. 27, no. 1, p. 148-157.

Nøhr-Hansen, H., Pedersen, G. K., Knutz, P. C., Bojesen-Koefoed, J. A., Sliwinska, K. K., and Hovikoski, J., 2018, Potential Cretaceous source-rocks from the north-east Baffin Bay, West Greenland, AAPG Europe Regional Conference - Global Analogues of the Atlantic Margin: Lisbon, p. 1.

Nordgard Bolas, H. M., Hermanrud, C., and Teige, G. M. G., 2005, Seal capacity estimation from subsurface pore pressures: Basin Research, v. 17, no. 4, p. 583-599.

Nottvedt, A., Berglung, T., Rasmussen, E., and Steel, R., 1988, Some aspects of Tertiary tectonics and sediments along the western Barents shelf, *in* Morton, A. C., and Parson, L. M., eds., Early Tertiary volcanism and the opening of the NE Atlantic, Volume 39: London, Geological Society of London, p. 421-425.

Núñez-Betelu, L. K., 1993, Rock-Eval/TOC pyrolysis data from the Kanguk Formation (Upper Cretaceous), Axel Heiberg and Ellesmere Islands, Canadian Arctic: Geological Survey of Canada.

Nyland, B., Jensen, L. N., Skagen, J. I., Skarpnes, O., and Vorren, T., 1992, Tertiary uplift and erosion in the Barents sea: magnitude, timing and consequences, *in* Larsen, R. M., Brekke, H., Larsen, B. T., and Talleraas, E., eds., Structural and Tectonic modelling and its application to petroleum geology: Amsterdam, Netherlands, Elsevier Science Publishers, p. 153-162.

Oakey, G. N., and Chalmers, J. A., 2012, A new model for the Paleogene motion of Greenland relative to North America: Plate reconstructions of the Davis Strait and Nares Strait regions between Canada and Greenland: Journal of Geophysical Research, v. 117, no. B10, p. 1-28.

Oakey, G. N., and Stephenson, R., 2008, Crustal structure of the Innuitian region of Arctic Canada and Greenland from gravity modelling: implications for the Palaeogene Eurekan orogen: Geophysical Journal International, v. 173, no. 3, p. 1039-1063.

Osborne, M. J., and Swarbrick, R. E., 1997, Mechanisms for Generating Overpressure in Sedimentary Basins: A Reevaluation: AAPG Bulletin, v. 81, no. 6, p. 1023-1041.

-, 1999, Diagenesis in North Sea HPHT clastic reservoirs - consequences for porosity and overpressure prediction: Marine and Petroleum Geology, v. 16, p. 337-353.

Ostanin, I., Anka, Z., and Di Primio, R., 2017a, Role of faults in Hydrocarbon Leakage in the Hammerfest Basin, SW Barents Sea: Insights from seismic data and numerical modelling: Geosciences, v. 7, no. 2, p. 28.

Ostanin, I., Anka, Z., Di Primo, R., and Bernal, A., 2012, Identification of a large Upper Cretaceous polygonal fault network in the Hammerfest basin: Implications on the reactivation of regional faulting and gas leakage dynamics, SW Barents Sea: Marine Geology, v. 332-334, p. 109-125.

Ostanin, I., Anka, Z., and Primio, R. D., 2017b, Role of faults in hydrocarbon leakage from Snohvit gas field, SW Barents Sea: insights from seismic data and numerical modelling.

Ottesen, D., Dowdeswell, J. A., Rise, L., and Bugge, T., 2012, Large-scale development of the Mid-Norwegian shelf over the last three million years and potential for hydrocarbon reservoirs in glacial sediments, *in* Huuse, M., Redfern, J., Le Heron, D. P., Dixon, R., Moscariello, A., and Craig, J., eds., Glaciogenic Reservoirs and Hydrocarbon Systems: London, Geological Society.

Page, A. A., Zalasiewicz, J. A., Williams, M., and Popov, L. E., 2007, Were transgressive black shales a negative feedback modulating glacioeustacy in the Early Palaeozoic icehouse?, *in* Williams, M.,

Haywood, A. M., Gregory, F. J., and Schmidt, D. N., eds., Deep- Time Perspectives on Climate Change: Marrying the Signal from Computer Models and Biological Proxies: London, Micropalaeontological Society, Geological Society, p. 123-156.

Peltier, W. R., 2004, Global Glacial Isostasy And The Surface Of The Ice-Age Earth: The ICE-5G (VM2) Model and Grace: Annual Review of Earth and Planetary Sciences, v. 32, no. 1, p. 111-149.

Portnov, A., Vadakkepuliyambatta, S., Mienert, J., and Hubbard, A., 2016, Ice-sheet-driven methane storage and release in the Arctic: Nature communications, v. 7, no. 1, p. 1-7.

Posamentier, H. W., 2004, Seismic Geomorphology: Imaging Elements of Depositional Systems from Shelf to Deep Basin Using 3D Seismic Data: Implications for Exploration and Development, *in* Davies, R. J., Cartwright, J. A., Stewart, S. A., Lappin, M., and Underhill, J. R., eds., 3D Seismic Technology: Application to the Exploration of Sedimentary Basins: London, Geological Society of London, p. 11-24.

Posamentier, H. W., Davies, R. J., Cartwright, J. A., and Wood, L., 2007, Seismic geomorphology- an overview, *in* Davies, R. J., Posamentier, H. W., Wood, L., and Cartwright, J. A., eds., Seismic Geomorphology: Applications to Hydrocarbon Exploration and Production: London, Geological Society of London, p. 1-14.

Raymo, M. E., 1997, The timing of major climate terminations: Paleoceanography, v. 12, no. 4, p. 577-585.

Reagan, M. T., and Moridis, G. J., 2007, Oceanic gas hydrate instability and dissociation under climate change scenarios: Geophysical Research Letters, v. 34, no. 22.

Riis, F., 1992, Dating and measuring erosion, uplift and subsidence in Norway and the Norwegian shelf in glacial periods. : Norsk Geologisk Tidsskrift, v. 72, p. 325-331.

Riis, F., and Fjeldskaar, W., 1992, On the magnitude of the Late Tertiary and Quaternary erosion and its significance for the uplift of Scandinavia and the Barents Sea: NPF Special Publication, v. 1, no. 163-185.

Rise, L., and Rokoengen, K., 1991, Regional Upper Cenozoic seismostratigraphy and soil properties in the Haltenbanken South area.

Rolle, F., 1985, Late Cretaceous–Tertiary sediments offshore central West Greenland: lithostratigraphy, sedimentary evolution, and petroleum potential: Canadian Journal of Earth Sciences, v. 22, no. 7, p. 1001-1019.

Rose, P., Byerley, G., Vaughan, O., Cater, J., and Rea, B. R., 2016, Aviat: a Lower Pleistocene shallow gas hazard developed as a fuel gas supply for the Forties Field, *in* Bowman, M., and Levell, B., eds., Petroleum Geology of NW Europe: 50 Years of Learning – Proceedings of the 8th Petroleum Geology Conference: London, Geological Society.

Rouchet, J. D., 1981, Stress Fields, A Key to Oil Migration: AAPG Bulletin, v. 65, no. 1, p. 74-85.

Ruppel, C. D., and Kessler, J. D., 2017, The interaction of climate change and methane hydrates: Reviews of Geophysics, v. 55, no. 1, p. 126-168.

Schenk, C. J., 2011, Geology and petroleum potential of the West Greenland–East Canada Province: Geological Society, London, Memoirs, v. 35, no. 1, p. 627-645.

Sclater, J. G., and Christie, P. A. F., 1980, Continental stretching: an explanation of the post-mid-cretaceous subsidence of the central north sea: Journal of Geophysical Research, v. 85, no. B7, p. 3711-3739.

Shackleton, N. J., and Opdyke, N. D., 1976, Oxygen-isotope and paleomagnetic stratigraphy of Pacific core V28-239 late Pliocene to latest Pleistocene.

Skaarup, N., and Pulvertaft, C., 2007, Aspects of the structure on the coast of the West Greenland volcanic province revealed in seismic data: Bulletin of the Geological Society of Denmark, v. 55, p. 65-80.

Skagen, J. I., 1993, Effects on hydrocarbon potential caused by Tertiary uplift and erosion in the Barents Sea: Norwegian Petroleum Society Special Publications, v. 2, p. 711-719.

Sloan, E. D., and Koh, C. A., 1990, Clathrate hydrates of natural gases: New York, New York, Marcel Drekker, Marcel Drekker, 1-641 p.:

Solheim, A., and Elverhoi, A., 1993, Gas-related seafloor craters in the Barents Sea: Geo-marine Letters, v. 21, p. 12-19.

Solheim, A., and Kristofferson, Y., 1984, Western Barents Sea; thickness, seismic stratigraphy and outline of the glacial history: Nor. Polarinst. Skr., v. 179 B, p. 26.

Solheim, A., Riis, F., Elverhoi, A., Faleide, J. I., Jensen, L. N., and Cloetingh, S., 1996, Impact of glaciations on basin evolution: data and models from the Norwegian Margin and adjacent areas: Global and Planetary Change, v. 12, no. 1-4, p. 1-9.

Stephenson, M. A., Guargena, C. G., Fjeldskaar, W., and Michelsen, J. K., 1995, Integrated basin modelling for maturity predictions in the Bjørnøyrenna Fault Complex: Norwegian Petroleum Society Special Publications, v. 4, p. 287-304.

Stewart, I. S., Sauber, J., and Rose, J., 2000, Glacio-seismotectonics: ice sheets, crustal deformation and seismicity: Quaternary Science Reviews, v. 19, no. 14-15, p. 1367-1389.

Sweeney, J. J., and Burnham, A. K., 1990, Evaluation of a simple model of vitrinite reflectance based on chemical kinetics: AAPG bulletin, v. 74, no. 10, p. 1559-1570.

Tasianas, A., Bünz, S., Bellwald, B., Hammer, Ø., Planke, S., Lebedeva-Ivanova, N., and Krassakis, P., 2018, High-resolution 3D seismic study of pockmarks and shallow fluid flow systems at the Snøhvit hydrocarbon field in the SW Barents Sea: Marine Geology, v. 403, p. 247-261.

Tasianas, A., Martens, I., Bünz, S., and Mienert, J., 2016, Mechanisms initiating fluid migration at Snøhvit and Albatross fields, Barents Sea: arktos, v. 2, no. 1.

Tziperman, T., and Gildor, H., 2003, On the mid-Pleistocene transition to 100-kyr glacial cycles and the asymmetry between glaciation and deglaciation times: Paleoceanography, v. 18, no. 1, p. 1-8.

Vagnes, E., Faleide, J. I., and Gudlaugsson, S. T., 1992, Glacial erosion and tectonic uplift in the barents sea: Norsk Geologisk Tidsskrift, v. 72, p. 333-338.

Van den Berg, J., Van de Wal, R., Milne, G., and Oerlemans, J., 2008, Effect of isostasy on dynamical ice sheet modeling: A case study for Eurasia: Journal of Geophysical Research: Solid Earth, v. 113, no. B5.

Verschuren, M., 1992, An integrated approach to clay tectonic deformation, and development of a new 3D surface modeling method [PhD: University of Ghent, 359 p.

Vorren, T. O., and Laberg, J. S., 1997, Trough mouth fans—palaeoclimate and ice-sheet monitors: Quaternary Science Reviews, v. 16, no. 8, p. 865-881.

Walderhaug, O., 1992, Magnitude of uplift of the Sto and Nordmela Formations in the Hammerfest Basin - a diagenetic approach: Norsk Geologisk Tidsskrift, v. 72, p. 321-323.

Watts, A. B., 2001, Isostacy and flexure of the lithosphere Cambridge, Cambridge University Press.

Weaver, P. P., Wynn, R. B., Kenyon, N. H., and Evans, J., 2000, Continental margin sedimentation, with special reference to the north-east Atlantic margin: Sedimentology, v. 47, p. 239-256.

Welford, K., Peace, A., Geng, M., and Dickie, K., 2018, Crustal structure of Baffin Bay from constrained 3-D gravity inversion and deformable plate tectonic models: Geophysical Journal International, v. 214, no. 2, p. 1281-1300.

Whittaker, R. C., Hamann, R. E., and Pulvertaft, T. C. R., 1997, A New Frontier Province Offshore Northwest Greenland: Structure, Basin Development, and Petroleum Potential of the Melville Bay Area: AAPG Bulletin, v. 81, no. 6, p. 978-998.

Winsborrow, M. C., Andreassen, K., Corner, G. D., and Laberg, J. S., 2010, Deglaciation of a marine-based ice sheet: Late Weichselian palaeo-ice dynamics and retreat in the southern Barents Sea reconstructed from onshore and offshore glacial geomorphology: Quaternary Science Reviews, v. 29, no. 3-4, p. 424-442.

Wiprut, D., and Zoback, M. D., 2002, Fault reactivation, leakage potential, and hydrocarbon column heights in the northern north sea: Norwegian Petroleum Society Special Publications, v. 11, p. 203-219.

Xu, W., Lowell, R. P., and Peltzer, E. T., 2001, Effect of seafloor temperature and pressure variations on methane flux from a gas hydrate layer: Comparison between current and late Paleocene climate conditions: Journal of Geophysical Research, v. 106, no. B11, p. 26413-26423.

Yilmaz, O., 2001, Seismic Data Analysis: Processing, Inversion, and Interpretation of Seismic Data¨, Tulsa, OK, USA, Society of Exploration Geophysics, Investigations in Geophysics.

Zachos, J., Pagani, M., Sloan, L., Thomas, E., and Billups, K., 2001, Trends, Rhythms, and Aberrations in Global Climate 65 Ma to Present: Science, v. 292, no. 5517, p. 686-693.

Zieba, K. J., and Grover, A., 2016, Isostatic response to glacial erosion, deposition and ice loading. Impact on hydrocarbon traps of the southwestern Barents Sea: Marine and Petroleum Geology, v. 78, p. 168-183.

2

Melville Bay Petroleum Systems: A Giant Gas Reservoir

Preamble

DRC interpreted the data, wrote the manuscript and drafted the figures presented in this chapter. MH gave input into interpretations, the method of analysis and the final manuscript. AMWN gave input into the landslide reconstruction process and the final manuscript. Both PG and JC assisted with initial interpretations and discussions, as well as reviewing the final manuscript.

This manuscript has been published in the journal *AAPG Bulletin*:

Cox, D. R., Huuse, M., Newton, A. M. W., Gannon, P., and Clayburn, J., 2020, Slip sliding away: enigma of large sandy blocks within a gas bearing mass transport deposit, offshore NW Greenland: AAPG Bulletin, v. 104, no. 5, pp. 1011-1043.

Slip Sliding Away: Enigma of Large Sandy Blocks Within a Gas-bearing Mass transport Deposit, Offshore Northwestern Greenland

David R. Cox[1], Mads Huuse[1], Andrew M. W. Newton[1],

Paul Gannon[2] and John Clayburn[2]

[1]Department of Earth and Environmental Sciences, The University of Manchester

[2]Cairn Energy PLC, Clydesdale Bank Plaza, Exchange Plaza, Lothian Rd, Edinburgh EH3 9BY

Abstract

The northwestern Greenland margin contains several underexplored sedimentary basins formed by Cretaceous rifting and Cenozoic post-rift sedimentation. The basins are thought to contain significant hydrocarbon reserves, although no exploration wells have been drilled to date. This paper reports the discovery of a gas-charged submarine landslide mass transport deposit (MTD) covering 420 km^2 (162mi^2) above the Melville Bay ridge (MBR) rift structure. The sedimentary succession that deformed into the MTD was likely deposited within a shallow-marine spit complex developed along the ridge axis extension during the Eocene. The MTD displays landslide characteristics with distinct blocks up to 1 km (3281 ft) wide and 80 m (262 ft) thick that geometrically fit together like a jigsaw puzzle. Clear direct hydrocarbon indicators and velocity estimations suggest the mass transport blocks are composed of highly porous, gas-charged sands intercalated with shale layers and overlain by post-slide pelagic mudstones. The reconstruction of all 499 MTD blocks suggests emplacement by bidirectional sliding, triggered by rejuvenation and a southward tilt of the MBR. Sliding most likely occurred slowly along a low-angle decollement surface, with the blocks remaining intact despite not being confined within a typical slide mass. Instead, coherency was likely aided by lithological layering and diagenesis. Gravitational shedding of the steep block margins has created interblock sand accumulations, which may enhance connectivity. This study provides an important analogue for significant reservoir occurrence in large MTD blocks and provides constraints on the basin development and petroleum prospectivity of northeast Baffin Bay.

2.1. Introduction

Sediments deposited by gravitational and mass-wasting processes are commonplace in deep water settings (Butler and Turner, 2010; Hampton et al., 1996; Prior et al., 1984). These processes can create seismic-scale deposits consisting of chaotic facies that can commonly host rotated and translated slide blocks within the matrix of the flow. These blocks commonly consist of meter- to kilometre-scale packages of undeformed strata that have remained coherent and intact throughout the sliding process (Alves, 2015; Huvenne et al., 2002; Jackson, 2011; Weimer and Shipp, 2004). In the rock record, these deposits are referred to as mass transport complexes or mass transport deposits (MTDs) (Weimer and Shipp, 2004).

On the northwestern Greenland shelf, a well-preserved MTD covering 420 km^2 (162 mi^2) above the Melville Bay ridge (MBR) rift structure has been interpreted using three dimensional (3-D) seismic data. The main objectives of this paper are to document the occurrence, architecture, and lithology of enigmatic, jigsaw-like blocks within this potentially gas-charged MTD, while also unravelling the complex depositional and deformational history that led to its emplacement. The paper concludes by assessing reservoir connectivity and the potential for exploration and development.

The discovery of this MTD reservoir was achieved because of renewed exploration interest in the Arctic caused in part by increasing oil prices from 2002 to 2008 and a prediction that the Arctic contains some 30% and 13% of the world's undiscovered gas and oil, respectively (Gautier et al., 2009). A significant proportion of this interest was focused offshore West Greenland because of its favourable fiscal terms and unexplored, thick sedimentary rift sequences (Henriksen et al., 2009). This interest prompted hydrocarbon exploration license rounds from 2007 to 2008 and 2010, when five licenses were awarded in northeast Baffin Bay alone (Fig. 2.1). This led to the acquisition of extensive two-dimensional (2-D) seismic data sets that cover much of the wider Baffin Bay area, offshore northwestern Greenland.

Pitu, one of the five awarded blocks within Melville Bay, contains a 3-D seismic survey covering an area of 1672 km^2 (646 mi^2) over part of the MBR and the western flank of the Melville Bay graben (MBG) (Fig. 2.1). The nearest well calibration is more than 300 km (>186.5 mi) to the south and is used to provide a chronostratigraphic framework for the shallow stratigraphy where key horizons can be tied southward above large areas of volcanic deposits to Ocean Drilling Program (ODP) site 645 (Fig. 2.1) (Gregersen et al., 2016; Knutz et al., 2015). Approximate constraints on the likely ages of older stratigraphy are inferred from their stratigraphic relationship to tied mega-unit boundaries, an

understanding of the regional geology (Gregersen et al., 2013) and data from seabed sampling (Gregersen et al., 2016) (which was not available for use in this study).

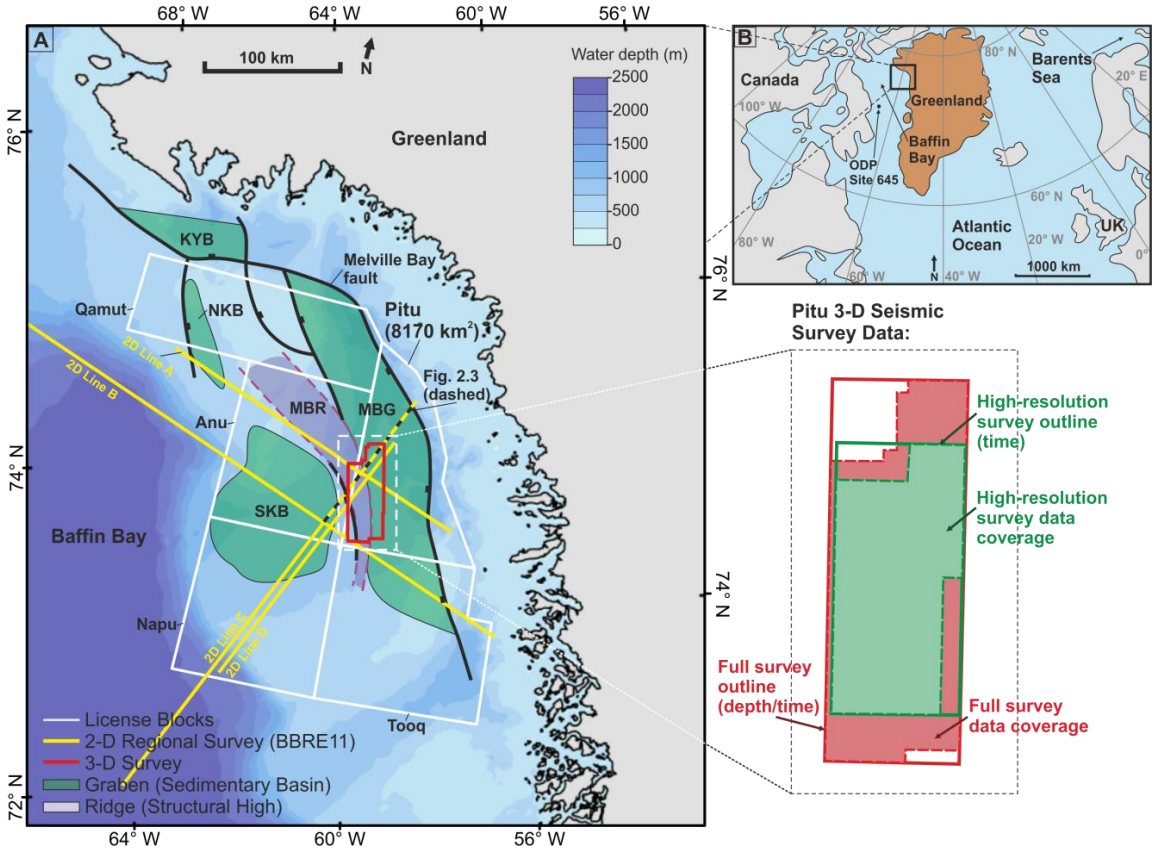

Figure 2.1. Study area and data location | A) Bathymetry of the Melville Bay area from Jakobsson et al. (2012) annotated with exploration license blocks, major faults, sedimentary basins, and structural ridges. Two-dimensional (2-D) and three-dimensional (3-D) seismic reflection data coverage is also shown within the map and on the adjacent enlargement. The 2-D line C represents the location of Fig. 2.3. B) A cartoon map of the Arctic region surrounding Greenland, showing the location of map A and Ocean Drilling Program (ODP) site 645. Abbreviations used include Baffin Bay 2-D regional seismic survey (BBRE11), Kap York Basin (KYB), Melville Bay Graben (MGB), Melville Bay Ridge (MBR), North Kivioq Basin (NKB), South Kivioq Basin (SKB) and United Kingdom (UK).

2.2. Geological and Tectonic Setting

The initial onset of rifting between Greenland and Canada began in the Late Jurassic, evidenced by volcanism and intruded dykes to the south of the Pitu (Larsen et al., 2009; Umpleby, 1979). This was triggered by northward propagation of North Atlantic spreading into the Arctic basins, leading to the creation of oceanic crust in central Baffin Bay during the Paleocene and Eocene (Gregersen et al., 2013; Oakey and Chalmers, 2012). Rifting was focused during the Cretaceous and created a series of northwest-southeast trending sedimentary basins, separated by elongate structural ridge-like highs (Whittaker et al., 1997) (Figs. 2.1, 2.2).

These basins and extensive ridges dominated the topography of the Melville Bay area throughout the Paleogene and into the Neogene. The largest of these basins is the 35–90

km (22–56 mi) wide MBG that is bounded to the east by the Melville Bay Fault (which shows a maximum heave of >30 km [>18.6 mi]) and is separated from the Kap York Basin to the north and the Kivioq Basin to the west by the MBR (Whittaker et al., 1997)) (Fig. 2.1). The MBR developed as an elongated syn-rift tilted fault block that has subsequently experienced post-rift reactivation (Gregersen et al., 2013) (Fig. 2.1). This ridge likely existed as a small emergent island extending from the Greenland mainland to the north during much of the Paleogene and Neogene (Fig. 2.2). This would have partially separated the deeper waters of the MBG from the rest of Baffin Bay to the west, creating an embayment (Gregersen et al., 2013; 2016).

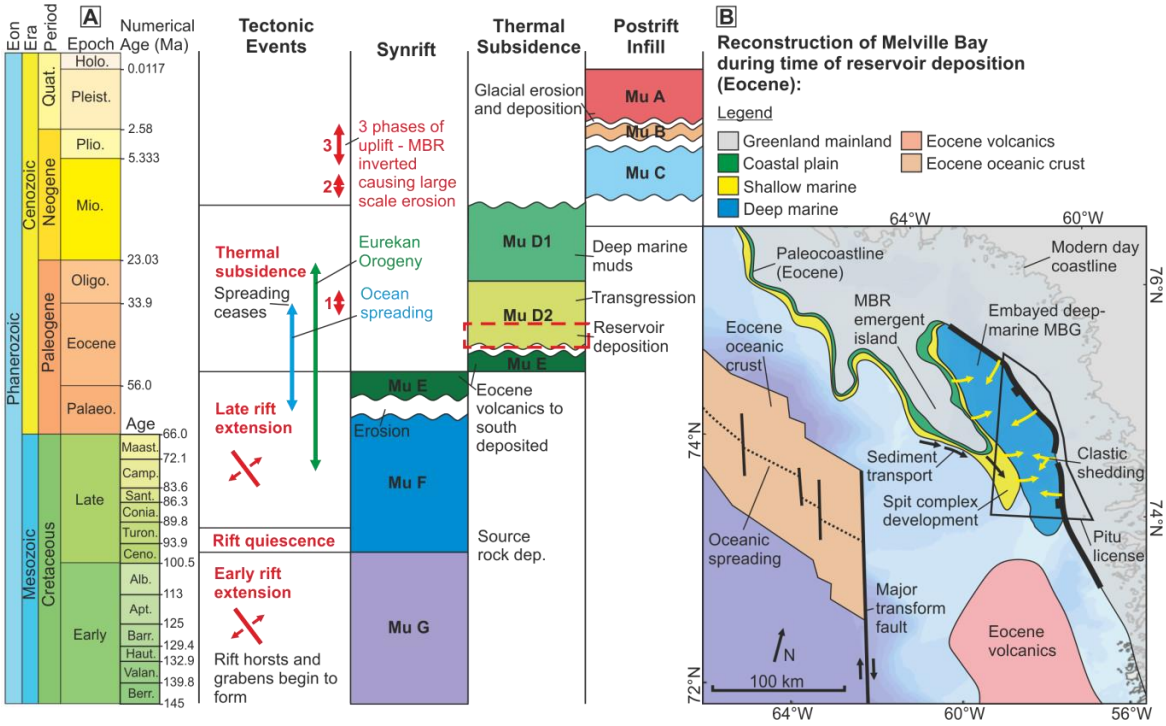

Figure 2.2. Tectono-stratigraphic development of the Melville Bay region | A) Stratigraphic age and the associated rift stages for the interpreted mega-units (Mu) G–A within the Pitu license block. The chart also shows predicted periods of erosion, rifting, and tectonic events associated with basin formation and adjustments as well as the timing of reservoir deposition (dep.) (compiled from Whittaker et al. (1997); Japsen et al. (2006); Oakey and Chalmers (2012); Gregersen et al. (2013) and Knutz et al. (2015). B) A reconstruction of Melville Bay during the time of reservoir deposition showing the embayment of the Melville Bay Graben (MBG) via the Melville Bay Ridge (MBR) emergent island as well as sediment transport and deposition and the location of sea-floor spreading. Oceanic crust and spreading locations have been modified from Welford et al. (2018). Alb. = Albian; Apt. = Aptian; Barr. = Barremian; Berr. = Berriasian; Camp. = Campanian; Ceno. = Cenomanian; Conia. = Coniacian; Haut. = Hauterivian; Holo. = Holocene; Maast. = Maastrichtian; Mio. = Miocene; Oligo. = Oligocene; Paleo. = Paleocene; Pleist. = Pleistocene; Plio. = Pliocene; Quat. = Quaternary; Sant. = Santonian; Turon. = Turonian; Valan. = Valanginian.

The restricted basin was infilled by Cretaceous– Paleogene sedimentary successions that contain mainly marine mudstones with inter-fingering coarse sands sourced from both the Greenland craton to the east and the uplifted MBR to the west (Gregersen et al., 2013). These successions can reach thicknesses up to approximately 13 km (~8 mi) and include

likely source rock deposition during the Late Cretaceous (Cenomanian–Turonian) (Bojesen-Koefoed et al., 1999; Gregersen et al., 2013; Planke et al., 2009; Whittaker et al., 1997) (Fig. 2.2). Accommodation upon the MBR was preserved during periods of uplift quiescence, allowing sediments to accumulate and create a thick (<80 m [<262 ft]) package of prograding sands, which constitute the potential reservoir studied here (Gregersen et al., 2013; 2016; Oakey and Chalmers, 2012).

Major extension and seafloor spreading ceased during the late Eocene–Oligocene (Oakey and Chalmers, 2012; Welford et al., 2018), with thermal subsidence driving the drowning of the emerged MBR and causing the transgression of clastic systems within Melville Bay as well as a widespread transition into a deep marine environment (Fig. 2.2) (Gregersen et al., 2013; Whittaker et al., 1997). The margin subsequently underwent several episodes of uplift and exhumation (up to 2 km [1.2 mi] over three time phases: 36–30 Ma, 11–10 Ma, and 7–2 Ma), evidenced by apatite fission-track modelling, vitrinite reflectance analysis, and seismic studies (Japsen et al., 2006; Knutz et al., 2015; Oakey, 2005) (Fig. 2.2). This led to the creation of significant inversion structures as well as the reactivation of several structural ridges within eastern Baffin Bay, including the MBR (Gregersen et al., 2013). The remnant rift topography of the MBR, along with continued phases of uplift during the late Paleogene and Neogene has caused sediment packages to thin over the high and for the deposition to be concentrated within the deeper basin, leading to the wedge-like geometry of post-rift packages (Fig. 2.3) (Gregersen et al., 2013; 2016; Japsen et al., 2006; Whittaker et al., 1997). This effect is increased by sand input from the Greenland craton to the east, depositing within the deeper basin before reaching the MBR slope (Knutz et al., 2012; 2015).

The late Pliocene and Pleistocene cycles of glacial advance and retreat of the Greenland Ice Sheet have caused the adjacent northwestern Greenland continental shelf to be extensively reworked (Aksu and Piper, 1987). This is evidenced by several erosional surfaces and several significant glacial sedimentary wedges overlying much of the deeper rift sequence within Baffin Bay (Knutz et al., 2015; 2019; Newton et al., 2017) (Fig. 2.3).

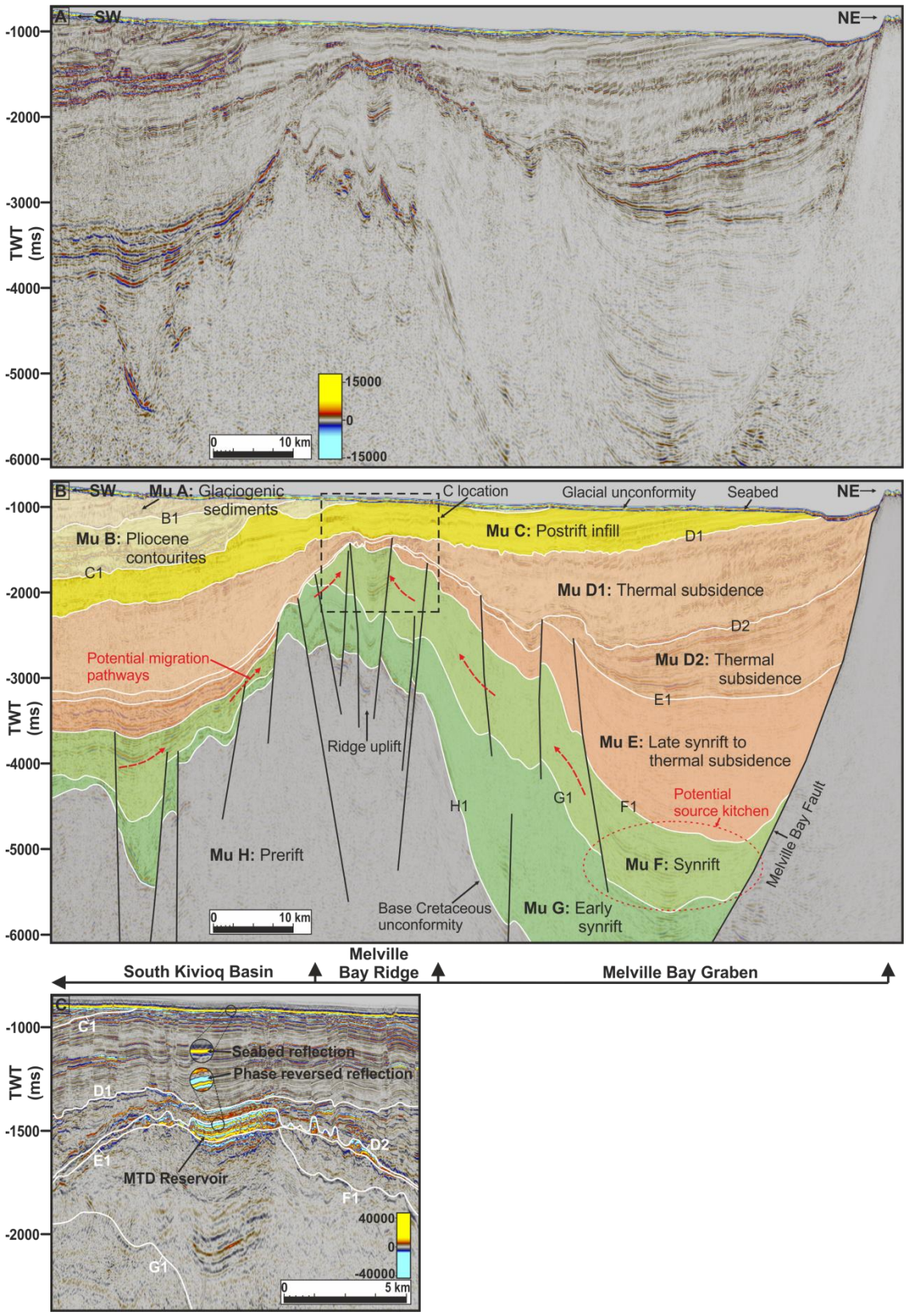

Figure 2.3. Regional basin development and structure | An uninterpreted regional two-dimensional (2-D) seismic reflection line (A) showing the basin and ridge structure across the study area. B) An interpreted regional 2-D seismic reflection line (2-D line A) showing nine mega-unit (Mu) horizons that have been modified from Gregersen et al. (2019); (2013; 2016) as well as rift stage interpretations. Also shown are interpretations of possible source rock kitchens and up-dip migration pathways within the Cretaceous Mu F. C) A seismic reflection intersection from the high-resolution three-dimensional survey along the 2-D line trajectory (location shown in (B)) to show the location of the main mass transport deposit (MTD) reservoir studied as well as the polarity comparison of the top reservoir and seabed. The 2-D seismic line location is shown in Fig. 2.1. TWT = two-way time.

The differentiation between basin and ridge rift structures and the thick sedimentary succession within the MBG is clearly evident on seismic data across the Pitu license block (Fig. 2.3). The 2-D and 3-D seismic data used within this study have been interpreted, resulting in nine seismic stratigraphic (mega-unit) horizons that define the sedimentary infill of the basin (Figs. 2.2, 2.3). These regional interpretations follow the work completed by Gregersen et al. (2019); (2013; 2016). This work defines the main rift-related sediments within the MBG as mega-units G–D1, which are overlain by post-rift infill as well as glacigenic sediments (mega-units C–A). The reservoir that this study focuses on exists within the base of mega-unit D2 (Figs. 2.2, 2.3). These sediments are underlain by early rift sediments that thin onto the high and are overlaid by polygonally faulted infill muds of mega-unit D1 (Fig. 2.3).

2.3. Data and Methods

The main data set used within this study consisted of a 3-D seismic reflection survey that was acquired by Cairn Energy PLC, in 2011 that consists of 93 3-D acquisition lines using a bin size of 25 x 12.5 m (82 x 41 ft) and 1 km (0.62 mi) separation between sail lines (Fig. 2.1). The shotpoint interval used was 25 m (82 ft) (flip-flop) with a source separation of 50 m (164 ft), leading to a common midpoint fold of 70 m (230 ft). The total survey area is 1672 km^2 (646 mi^2) with 12.6% data infill and is provided in two-way time (TWT) down to 6.5 s. Processing steps included signal noise attenuation and corrections and velocity analysis using Kirchhoff prestack time migration (PSTM). The frequency ranges between 5 and 75 Hz, with a dominant frequency within the target interval of 28 Hz producing a dominant wavelength of 71 m (233 ft) (using an average velocity of 2.0 km/s [6562 ft/s]) and a vertical resolution of 18 m (59 ft). Prestack depth migration was completed using a Kirchhoff algorithm down to 10,000 m (32,808 ft).

The survey was reprocessed in 2013, which included a more detailed poststack depth migration study using a Kirchhoff algorithm and attempted to remove several unwanted features such as a residual bubble oscillation, strong seabed multiples, and wave diffractions caused by glacial seabed scours. A subset high-resolution 3-D seismic survey in TWT was also produced that covers an area of 1135.5 km^2 (438 mi^2) down to 5 s, with a frequency range of 5–150 Hz and a dominant frequency across the target interval of 45 Hz producing a dominant wavelength of 44 m (144 ft) (using an average velocity of 2.0 km/s [6562 ft/s]) and an increased vertical resolution of 11 m (36 ft). The spatial resolution was also increased to 12.5 m (inline) x 6.25 m (crossline) (41 x 20.5 ft) (Fig. 2.1).

The data used in this study also include four regional 2-D seismic reflection lines (Fig. 2.1) that form part of the Baffin Bay 2-D regional seismic survey data set (BBRE11),

provided by TGS, that was acquired between 2007 and 2009, covering 5226.5 km (3248 mi) across Melville Bay. This survey was acquired using a 2000 psi source with a 25 m (82 ft) interval and 8 m (26 ft) gun depth. Data were recorded by a single 6000 m (19,685 ft) streamer with 480 channels spaced at 12.5 m (41 ft) intervals, using a sample interval of 2 ms. The survey was reprocessed in 2011, which involved bubble-pulse attenuation, diffraction multiple attenuation, low frequency enhancement, and Kirchhoff PSTM.

All seismic data were provided in Society of Exploration Geophysicists normal polarity, with positive peaks (red) representing a downward increase in acoustic impedance and negative troughs (blue) representing a downward decrease in acoustic impedance (Fig. 2.3C).

Converting the TWT thickness of blocks interpreted within the high-resolution seismic survey to depth was completed using an estimated average interval velocity of 1.69 km/s (5545 ft/s), which was calculated from the velocity pushdown effect observed beneath the reservoir blocks in seismic data (see the Seismic Observations section). This method was used instead of directly measuring the thicknesses on the depth-converted seismic survey. This was because of the increased vertical resolution within the high-resolution survey allowing more accurate imaging and interpretation of the blocks, leading to a more accurate thickness estimate. Seismic observations and interpretations were made within Schlumberger's Petrel software using industry standard seismic interpretation techniques (Cox et al., 2020; Posamentier, 2004; Posamentier et al., 2007). Spectral decomposition was completed and interpreted using Geoteric, which allowed for noise cancellation, seismic frequency selection, and colour blend cube creation (Castagna and Sun, 2006). Surface extractions were then taken from colour blend cubes for interpretation (Wright et al., 2018).

The landslide reconstruction process was carried out in ArcMap, in which the blocks were iteratively returned to their likely source location by comparing the following.

1. Geometrical fit: Because of block coherency, the shape and structure of the reservoir blocks in map view remains visible and allows for a geometrical reconstruction, much like jigsaw pieces, in which the pieces are slid back together. This process considered mass wasting and erosion at the block edges, giving a slightly blurry fit, and block translation and rotation.

2. Block thickness: Blocks that were once connected laterally adjacent to each other would likely be of similar thickness. Thickness trends across multiple blocks were used to constrain the reconstruction.

3. Internal reflections: Matching internal reflections from seismic profiles showed continuous depositional style and constituents across originally adjacent blocks.

4. Dip and azimuth of decollement surface: Because the uplift of the MBR is the most likely trigger of slide movement, the decollement surface structure was used as a guide to the possible flow paths and the direction of sliding along which the blocks can be repositioned in their original location.

The process only considered reservoir blocks that were thicker than 30 ms (~25 m [~82 ft]) in thickness. This allowed for a clear definition between reservoir blocks and interblock areas and defined a total of 499 individual blocks for use in the reconstruction. The assumption was made that the large main reservoir block existing on the MBR platform remains in its original location of deposition, allowing for the remaining blocks to be reconstructed back to this centre. The pre-slide location for each of the reservoir blocks was decided using the four guiding characteristics of either the blocks themselves or the underlying decollement surface outlined above. If the four considerations matched, then the blocks were moved into laterally adjacent positions. Each block was restored separately, according to the guiding characteristics, but the final fit of each block depended on the fit of previously reconstructed blocks.

The most likely direction of block sliding (flow line) was determined by comparing the pre- and post-slide location and orientation of individual blocks. Additionally, this process considered the pathway for all surrounding blocks, as deformational trends likely occurred across multiple block sections, with the crossing of individual slide paths being unlikely. This allowed an iterative assessment of block flow lines working outward from the main reservoir block, creating trends that agreed across multiple blocks as well as connecting individual pre- and post-slide block locations. Direct evidence of flow direction, such as erosional structures on the decollement surface, is not observed. This is possibly either because of a lack of beneath-block erosion occurring during sliding or existing features not being imaged within the seismic data. This may be because of limited vertical seismic resolution or beneath-block velocity pushdown significantly affecting the imaging and structure of the decollement surface.

2.4. Seismic Observations

A package of bright amplitudes and potential direct hydrocarbon indicators (DHIs) that exist on the crest and eastern flank of the MBR have been investigated using the Pitu high-resolution 3-D seismic survey. This package exists at the base of mega-unit D2, which consists of Paleogene sediments (Gregersen et al., 2013), with the top D1 horizon having

been interpreted as middle Miocene via a long-distance tie to ODP site 645 (Knutz et al., 2012; 2015) (Fig. 2.3). The package is likely Eocene in age because of the correlation of the base package horizon (top mega-unit E) into Eocene volcanics to the south of Melville Bay (Gregersen et al., 2013).

2.4.1. Mass Transport Deposit Characteristics

Seismic interpretation of the uppermost soft reflection revealed that this was associated with an extensive deposit that covers an area of 420 km^2 (162 mi^2) (Fig. 2.4). The strong negative amplitudes are observed across much of the crest and eastern flank of the MBR, with the highest negative amplitudes existing on the platform-like section of the MBR in the north. The response is observed to extend southeast along the strike of the MBR but becomes less continuous to the south and east (Fig. 2.5). Bright amplitudes are, however, observed to the south of 3-D seismic coverage on 2-D regional line B (Fig. 2.1) on the boundary of the Pitu and Tooq license blocks. This may suggest the package extends beyond the southern limit of the 3-D survey.

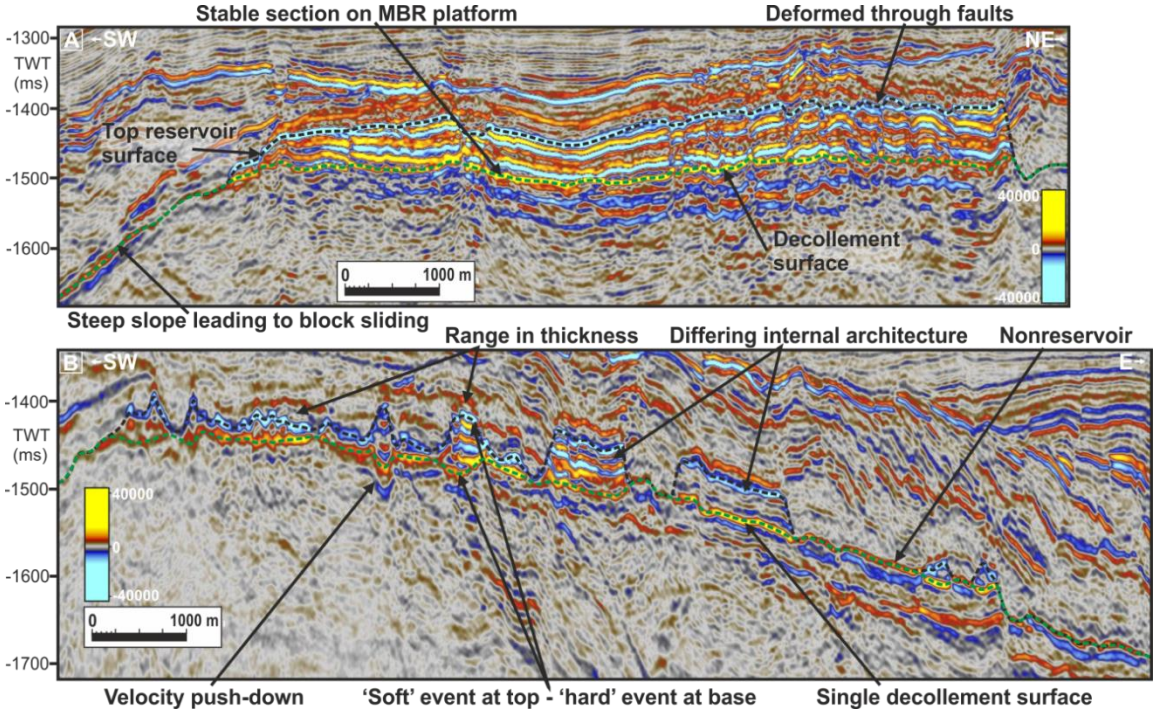

Figure 2.4. Reservoir description | A) Seismic section showing the seismic response from the reservoir on top of the Melville Bay Ridge (MBR) platform. B) Seismic section showing the seismic response of distributed reservoir blocks along the eastern ridge slope decollement surface. Line locations are shown in Fig. 2.5. TWT = two-way time.

The discontinuous soft response indicates that the package of reflections has broken up into several angular blocks that become smaller and further spaced apart to the south and east (Fig. 2.4B) before becoming no longer observed further downslope (having likely

disintegrated) (Fig. 2.5). The angular blocks range in sizes up to 1 km (3281 ft) wide and 80 m (262 ft) thick (maximum TWT of 95 ms at 1.69 km/s [1.05 mi/s]), with block thickness increasing toward the northwest (Fig. 2.5). The entire deposit sits on a single decollement surface (Fig. 2.4) that is consistent with the elongated dome structure created by the uplifted MBR. The deposit is observed to still be intact (with a continuous soft reflection) across much of the platform-like section of this decollement above the MBR to the north (Figs. 2.4A, 2.5). However, away from the central axis of the MBR where the decollement dip increases, the blocks show evidence of movement, with dominant sliding directions to the south in the dip direction along strike of the MBR and also to the east toward the deeper graben (Fig. 2.5).

On the western flank of the MBR, some extensive elongate ridge-like blocks have dislodged from the headscarp but have not disintegrated into smaller isolated blocks such as observed on the eastern flank (Fig. 2.5). The high amplitude response is not observed further down the steeply dipping western slope or on regional 2-D seismic lines that extend beyond the 3-D seismic survey limits to the west.

2.4.2. Direct Hydrocarbon Indicators

The seismic expression of the blocks shows clear DHIs with bright soft and hard events at the top and base of the package, respectively, with internal architectures that range from multiple continuous layers of varying acoustic impedance to more homogenous blocks with dim discontinuous internal reflections (Fig. 2.4). The deposit appears to have slid along a single decollement surface that displays as a positive amplitude response with reflection amplitudes increasing beneath the blocks. The approximately plane-parallel decollement surface also shows variable TWT between areas beneath and adjacent to the blocks. This is most likely caused by velocity pushdown because of anomalous fluids such as gas or oil within the package (Fig. 2.4).

The velocity pushdown effect observed beneath the blocks has been used to estimate the primary wave velocity within the package in an attempt to understand its potential lithology and fluid content and to specifically test whether the DHIs observed could be caused by porous, gas-bearing sands. This estimation uses the difference in TWT depth of the decollement surface in areas beneath and adjacent to the blocks (in areas in which the DHI response is not observed) (Fig. 2.6). In reality, the decollement surface is continuous in depth between the two areas, but slower velocities within the package are causing the apparent shift and are likely created by either a different lithology or pore fluid compared to the surrounding overburden (Fig. 2.6B, 2.C). The extent of the velocity reduction will provide evidence to what lithology and pore fluid the package may consist of.

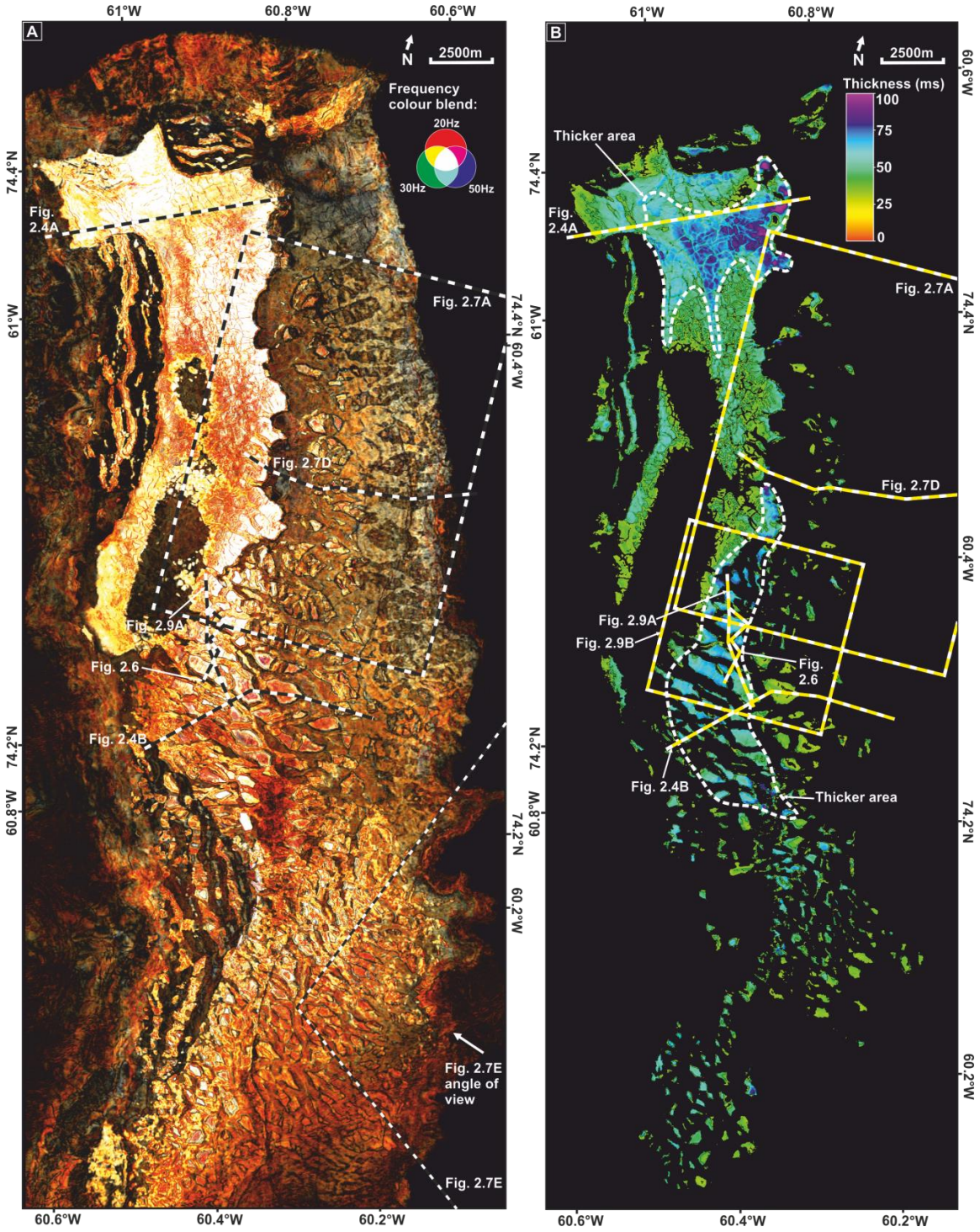

Figure 2.5. Reservoir distribution and character | A) Spectral decomposition red, green, and blue (RGB) extraction on the top reservoir surface across the Pitu high-resolution seismic survey. The RGB blend is composed of 20-Hz (red), 30-Hz (green), and 50-Hz (blue) frequency band volumes, created and visualized within Geoteric. B) A thickness map between the top reservoir and decollement surfaces (filtered to only show thicknesses >30 ms). Two areas of thicker reservoir are highlighted. The locations of Figs. 2.4A, B; 2.6; 2.7A, D, E; and 2.9A-B are shown.

A typical reservoir block was selected for this estimation, with a section from the top of the package to the decollement surface adjacent to the block (without the push down) (TWT_{norm}) being used to calculate the block height (H) (equation 1). This assumes an

average velocity for the overburden sediments ($V_{overburden}$) of 2.0 km/s (6562 ft/s). This gives a block height of 70 m (230 ft). The average velocity for within the block was then calculated using this block height along with the TWT value for the block and the pushdown (TWT_{slow}), measured from the top reflection to the decollement surface beneath the block (equation 2). This gives an estimated average velocity through the block (V_{block}) of 1.69 km/s (5545 ft/s), with this value being used for block thickness conversions from the TWT to depth. Additionally, if the overburden velocity is assumed at 2.2 km/s (7218 ft/s) instead, the block velocity is then estimated at 1.85 km/s (6070 ft/s).

1. $Block\ Height\ (H) = \frac{TWT_{norm}}{2} * V_{overburden}$ $\qquad 70\ m = \frac{70}{2} * 2.0$

2. $Average\ Block\ Velocity\ (V_{block}) = \frac{H * 2}{TWT_{slow}}$ $\qquad 1.69\ km/s = \frac{70 * 2}{83}$

This estimation, however, only considers the block to consist of 100% sand, where it is far more likely to contain several muddy layers, as evidenced by internal seismic reflections (Figs. 2.4 & 6). Considering the amount of internal layers within the typical block, it is estimated that mud could comprise up to 1/3 of the total block thickness (Fig. 2.6). Therefore, the mud must be considered in the velocity estimation as these low porosity layers will retain the overburden velocity (2.0 km/s [6562 ft/s]) and not create the velocity push down observed. The slower velocities causing the push-down effect will likely be confined to the higher porosity sand layers within the block.

3. $Sand\ Velocity\ (V_{sand}) = \frac{\frac{2}{3}H * 2}{TWT_{slow} - \frac{1}{3}TWT_{norm}}$ $\qquad 1.56\ km/s = \frac{46.6 * 2}{83 - 23.3}$

The estimation of V_{sand} (equation 3) only considers the two-thirds of the block height that is sand and removes the TWT of the mud layer (0.33 TWT_{norm}) from TWT_{slow}. This gives an estimated velocity for the sand layers within the package of 1.56 km/s (5118 ft/s), which is significantly lower than that of typical sandstones with 30%–40% porosity at this depth (commonly 2–2.5 km/s [6562–8202 ft/s]) (Rider and Kennedy, 2011). This velocity reduction is, therefore, most likely caused by the pore fluid within the sands and suggests that the package consists of gas-charged highly porous sands.

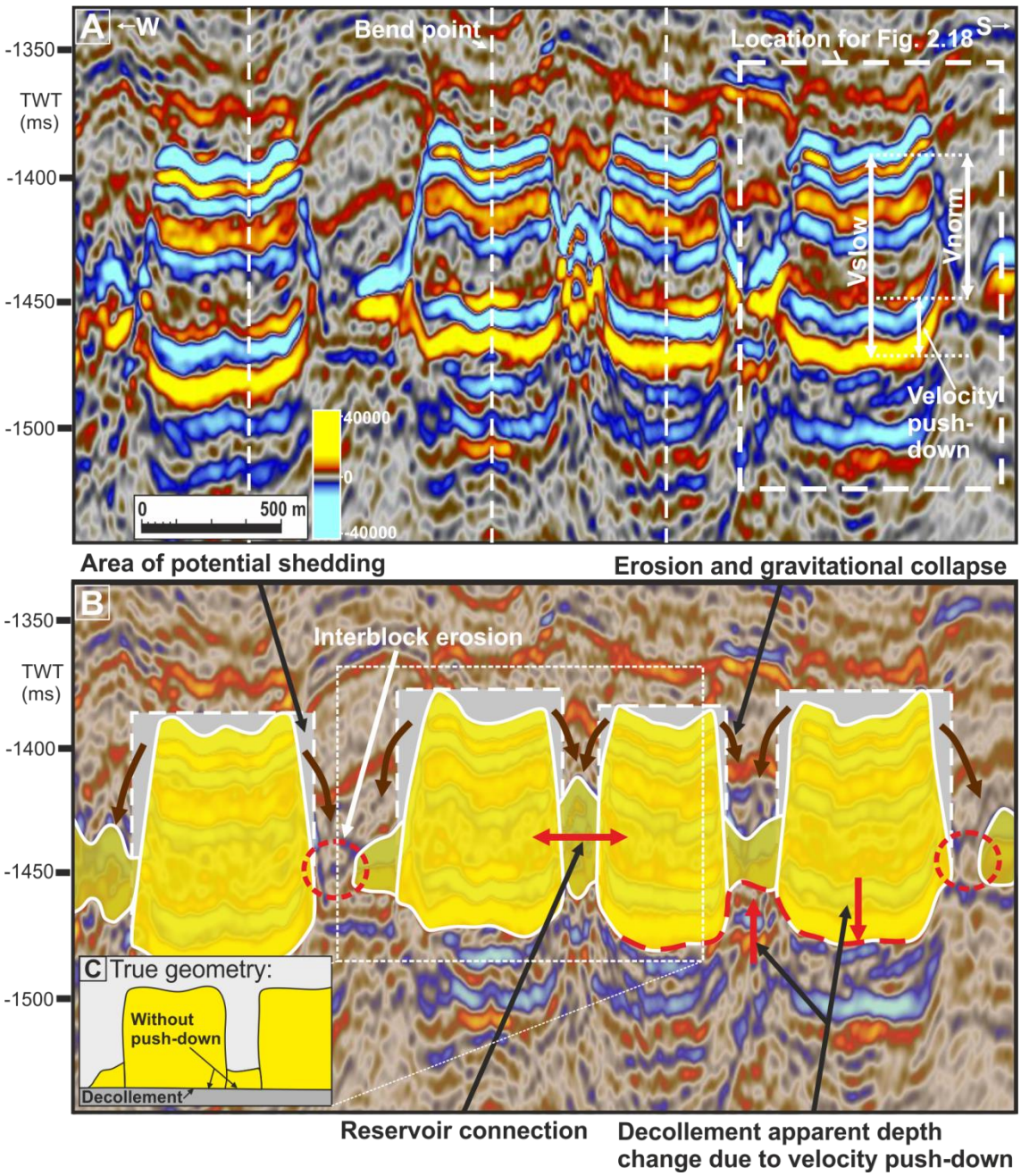

Figure 2.6. Block erosion and interblock sediment deposition | A) Uninterpreted seismic section showing four separated reservoir blocks along a single decollement surface. Location of seismic image used within Fig. 2.18 is shown. B) Interpreted seismic section highlighting reservoir blocks, gravitational shedding, and interblock sediment deposition. The location of the seismic line is shown in Fig. 2.5. TWT = two- way time; V_{norm} = average velocity adjacent to the block (without pushdown); V_{slow} = average velocity within the block (with pushdown).

A spectral decomposition colour blend of 10 (red), 20 (green), and 50 Hz (blue) (equivalent to a tuning thicknesses of 42, 21, and 8.5 m [138, 69, and 28 ft] at 1.69 km/s [5545 ft/s]) was created using the high-resolution 3-D seismic survey. An extraction along the top reservoir horizon clearly depicts a dominant bright white frequency response over much of the reservoir area (Fig. 2.5). This represents high saturations from all three blended frequencies and is a response typical for a relatively shallow (550 ms [550 m; 1804

ft] using an average velocity of 2.0 km/s [6562 ft/s]) below the seabed) gas sand reservoir (Wright et al., 2018). Other areas of the reservoir and surrounding decollement surface show dominance toward the low-frequency (red) response. The image also highlights the breakup of the deposit into a large number of separated blocks, with the thickest and most laterally extensive reservoir sections existing on the MBR platform in the north and the increased breakup and movement of smaller blocks mainly to the south and east (Fig. 2.5A). The reservoir is shown to thicken in two areas within the deposit, with reservoir thickness up to 80 m (262 ft) (Fig. 2.5B).

Spectral decomposition also highlights the same bright, multiple-frequency response seen for the reservoir blocks within certain interblock areas surrounding the large separated blocks south of the main reservoir section (Fig. 2.5A). This signature was also noted in the seismic extraction on the top reservoir surface and in the seismic cross section where interblock areas show similar soft and hard kicks to that of the main reservoir blocks (Fig. 2.6). The seismic sections show that the separated reservoir blocks narrow upward as well as the hummocky and erosive nature of the top reservoir reflections. The cross section shows that the high-amplitude response from the interblock area is absent in places. This can also be observed in Fig. 2.5A in which dark areas between the interblock bright responses represent areas of absence. This absence of response is more prevalent deeper into the graben on the eastern flank and between the smaller blocks within the far south-eastern section.

2.4.3. Deformation

The spectral decomposition image (Fig. 2.5) also highlights a series of east-west elongate and/or oblong features on the top reservoir surface that vary in frequency response and terminate at a similar depth on the slope (~-1600 ms) (Fig. 2.7A) at their western edge. To the east of this termination, no bright amplitude reservoir blocks are observed. Seismic amplitude extractions across these features display a dim, negative amplitude response (Fig. 2.7A). The onset of these features up-dip commonly occurs at the location of ridge-parallel extensional faults, with the feature existing on the downthrown, slightly steeper part of the slope (Fig. 2.7). Similarly, the features commonly terminate downslope at fault locations. Within each of the features exists numerous linear, low-amplitude zones that are perpendicular to their east-west orientation (Fig. 2.7B). These zones represent the location of small extensional faults (Fig. 2.7B, C). In the east, and downslope of the termination of these features, several deep, valley-like erosional depressions that trend basinward are observed on the decollement surface. High positive (hard kick) seismic amplitude responses are observed to be confined within these

depressions that extend downslope and likely beyond the eastern edge of the seismic survey (Fig. 2.7E).

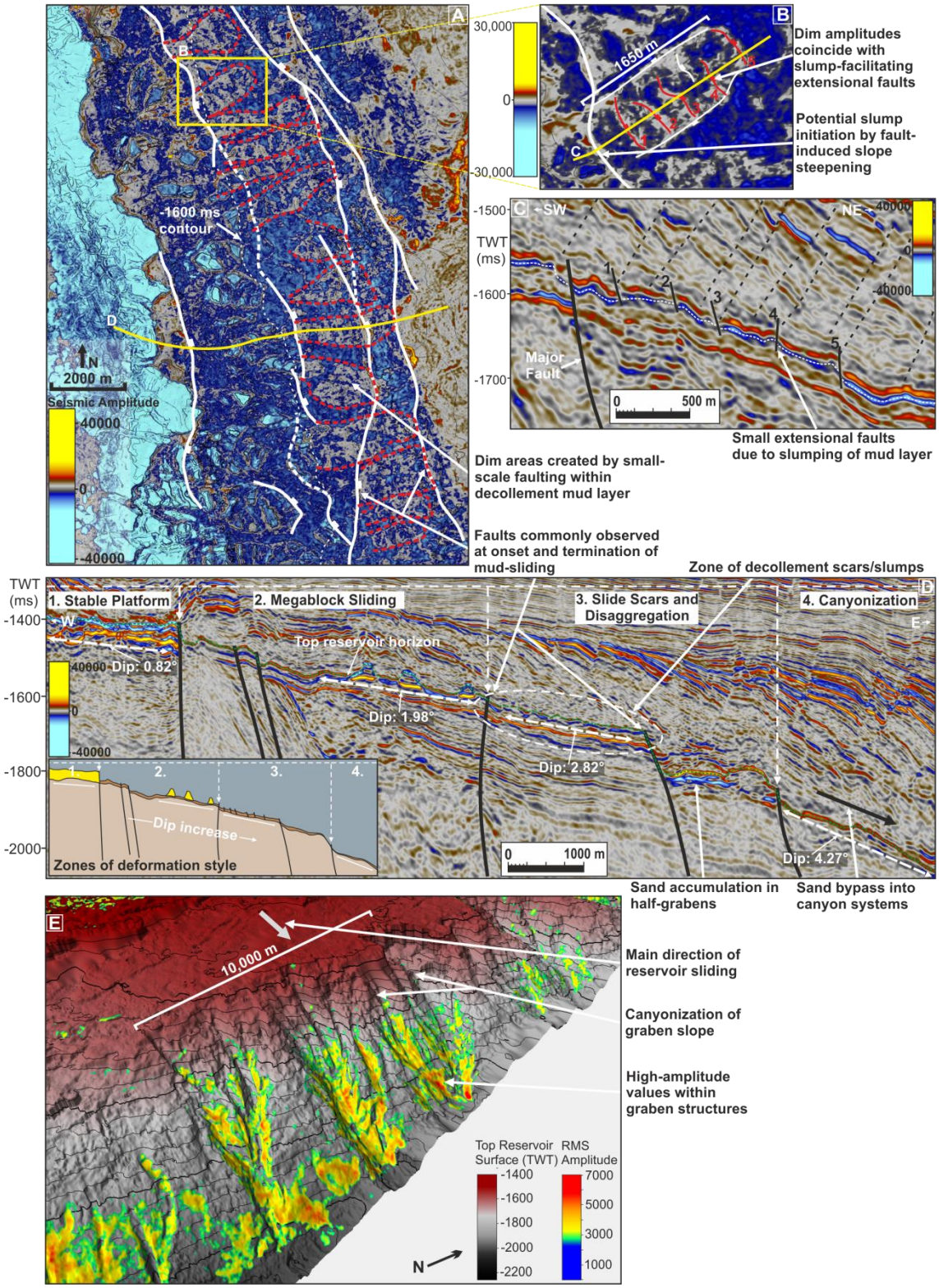

Figure 2.7. Seismic character transition and zones of deformation style | A) A two-dimensional (2-D) aerial view of a top reservoir seismic extraction surface showing the location of low-amplitude anomalous zones and their relationship to the interpreted fault network. B) A close-up 2-D aerial view of the top reservoir (decollement because reservoir is not present) extraction surface showing interpreted extensional faults within a low-amplitude feature. C) A seismic section through the feature shown in B, showing the location of small extensional faults that allow deformation of the decollement surface. D) A seismic section showing four zones of deformation style across the reservoir and decollement surface area. The insert shows

the four zones in schematic style. E) A top reservoir two-way time (TWT)–structural surface showing slope canyonization on the eastern flank of the Melville Bay ridge. Topographically controlled shed reservoir sediment is depicted deposited within the canyons as a filtered root-mean- square (RMS) amplitude surface. The locations as seen in A and E are shown in Fig. 2.5.

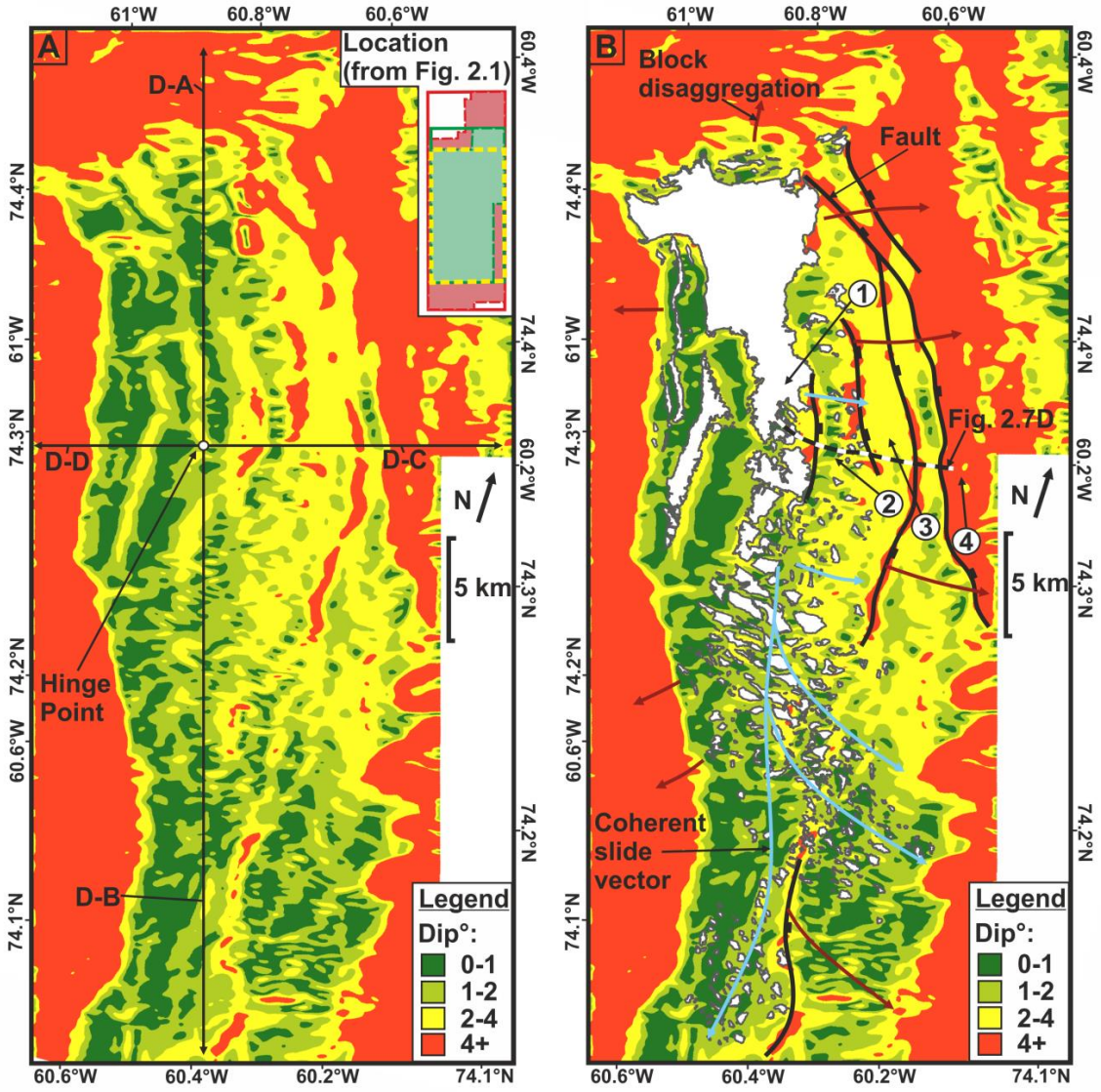

Figure 2.8. Decollement surface dip and its control on deformation and block sliding | A) An uninterpreted dip map of the modern-day reservoir decollement surface (shown in Fig. 2.4) that shows dip increasing away from the relatively flat central axis of the Melville Bay ridge. Four dip transects are shown extending from a central hinge point location on top of the ridge with average dip measurements of 1.6° (D-A), 0.41° (D-B), 3.3° (D-C), and 2.6° (D-D). B) An interpreted dip map of the modern-day reservoir decollement surface, overlaid by the modern-day distribution of reservoir blocks. The increase in dip downslope (eastward) is shown to coincide with a transition of deformational styles, with areas separated by zones of increased dip created by faults. These zones are numbered on the map and defined as (1) stable platform crest, (2) mega-block sliding, (3) slide scars and disaggregation, and (4) canyonization. The control of the dip on sliding is shown by coherent sliding vectors for visible reservoir blocks (blue arrows) remaining within areas of low dip, whereas areas of steeper dip highlight where the reservoir blocks are not visible with the sand likely having disaggregated and shed downslope (shown by sediment shedding vectors [red arrows]).

All of the reservoir features observed sit on a single decollement surface (Fig. 2.4). To ascertain controls on the slide block distribution, the present day dip of the decollement

has been estimated (Fig. 2.8). Because subsequent deformation has augmented the paleotopography, the present day angles are likely much greater than the original decollement dip at the time of slide emplacement. The dip of the decollement increases away from the MBR axis with a flatter, platform-like area on top of the ridge and along strike (Fig. 2.8). The majority of the reservoir blocks exist within the green low dip areas (0°–2°), with blocks becoming increasingly broken up into areas of increasing dip (1°–4°) and completely absent in areas of high dip (‡4°) shown in Fig. 2.8. The variations in reservoir signature across areas of increasing dip are commonly separated by linear areas of high dip (‡4°) that represent fault locations (Figs. 2.7D, 2.8). Blocks are commonly observed adjacent to these features up-dip but are not observed in the down-dip section (Figs. 2.7D, 2.8).

The dip of the decollement also highlights a hinge point on top of the ridge where spreading occurred radially from this high point. This coincides with the onset of block separation and sliding to the south away from the main reservoir block in the north. The higher-average slope angles shown by transects D-A (1.6°), D-C (3.3°), and D-D (2.6°) (Fig. 2.8A), highlight areas in which the slope angle dramatically increases away from the ridge hinge point, coinciding with shorter sliding vectors and a lack of observed reservoir blocks. Transect D-B, along strike of the MBR, shows the most gradual dip, with an average dip angle of 0.4°. In this direction, the majority of reservoir blocks are still observed intact, having slid further distances downslope (Fig. 2.8).

2.4.4. Controls on Fault Development

Reservoir blocks are flanked at their edges by normal faults that extend sub-vertically through the overburden and into the base of mega-unit D1 (Fig. 2.9A). Mega-unit D1 is characterized by numerous small horst and graben packages of discontinuous horizons that are offset and separated by thin, linear, sub-vertical low-amplitude zones (Figs. 2.3, 2.9A). Coherency and variance attribute time slices from within mega-unit D1 (Fig. 2.9B) show how these zones commonly connect to create networks, a typical characteristic of polygonal faults (Cartwright et al., 2003). These faults are mostly layer bound within the deep water muds of mega-unit D1 but show occasional fault extensions into mega-unit C and can reach close to the seabed. Many of these polygonal faults are shown to nucleate at the vertical extent of the block, bounding normal faults with the orientation of extension commonly following the directional trend set out by the underlying faults and block-edge orientations (Fig. 2.9A, C). Additionally, a small number of the block-edge normal faults seem to extend directly through mega-units D1 and C and are likely tectonic faults rather

than polygonal. These faults show larger degrees of offset with a continuous orientation of extension that is still determined by the location of the block edge.

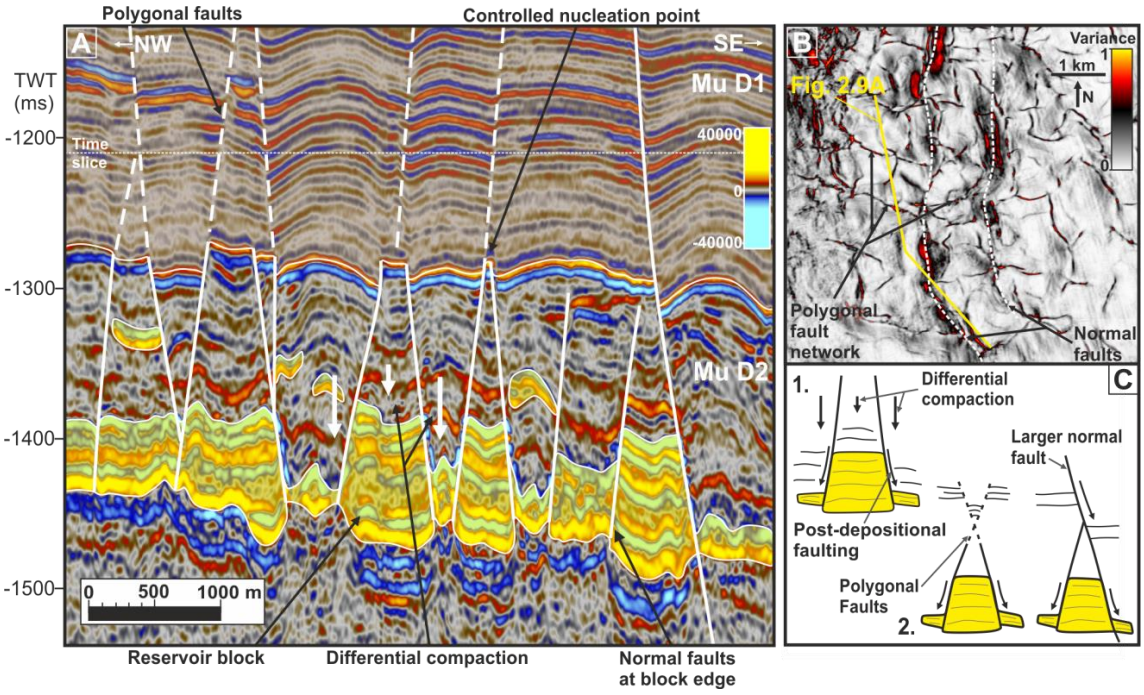

Figure 2.9. Reservoir block control on polygonal fault development | A) Interpreted seismic section showing separated reservoir blocks flanked by normal faults that coincide with the nucleation point of polygonal faults within the overlying mega-unit (Mu) D1. The location is shown in Fig. 2.5. B) Variance time slice at -1210 ms two-way time (TWT) showing the network of polygonal faults that have formed within Mu D1. The location is shown in Fig. 2.5B. C) Schematic diagram depicting the influence of reservoir block location on the development of polygonal faults and larger offset normal faults.

2.4.5. Landslide Reconstruction

The reconstruction of the 499 landslide blocks to their pre-slide configuration was facilitated by the high quality of imaging in the high-resolution 3-D survey used and the unique dispersal pattern and angular edges of the reservoir slide blocks. The reconstruction aids the understanding of the triggers and mechanisms of sliding as well as the uplift history of the MBR.

The comparison maps (Fig. 2.10) show the reconstructed location of the blocks that remain within the study area, along with large sections of exposed decollement, which likely represent areas in which once-deposited reservoir has now been shed from the high. This implies the significant transport of sandy sediments into the deeper parts of the basin in which data quality, acoustic characteristics, and data availability do not allow mapping of the equivalent deposit. Thickness trends and internal reflections across multiple blocks, along with interconnecting block shapes, indicate that the reservoir was deposited along the MBR and adjacent to the large undeformed section of the reservoir in the north (see the Data and Methods section). The blocks show a general trend of having been deposited

close to the central axis of the northwest-southeast–trending MBR. The reconstructed reservoir map in Fig. 2.10B is colour coded by distance travelled caused by sliding. This highlights an increased distance of sliding in the southern section of the reservoir, along the strike of the MBR in the least dipping direction of the decollement surface (Figs. 2.8, 2.10).

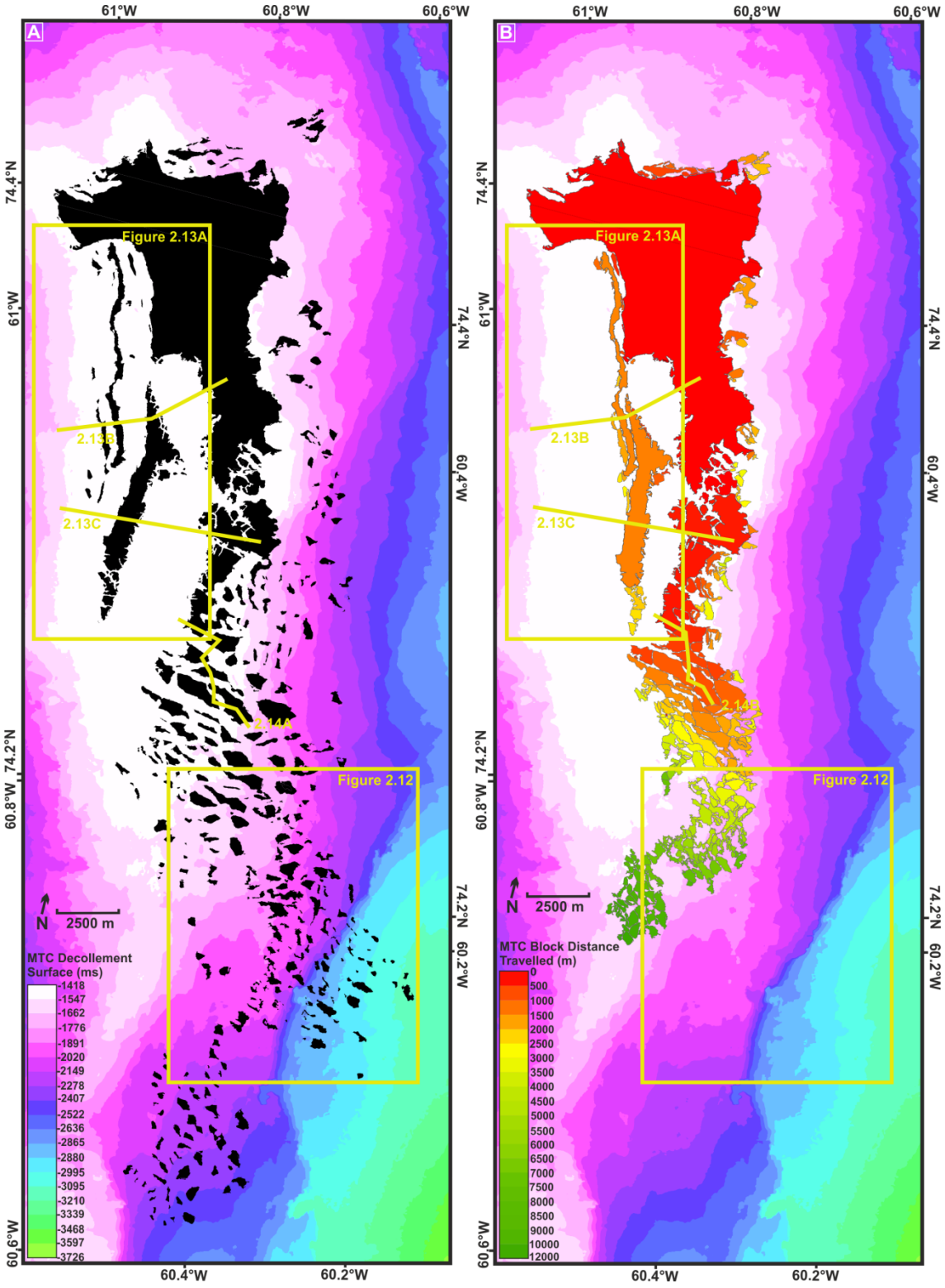

Figure 2.10. Landslide reconstruction | A) A two-way time–structure map of the decollement surface overlaid by black polygons representing the modern-day location of individual reservoir blocks that are in excess of 30 ms (~25 m [~82 ft]) thickness. The locations for Figs. 2.12; 2.13A–C; and 2.14A are shown. B) A two-way time–structure map of the decollement surface (legend within A) overlaid by polygons

representing the reconstructed location of individual reservoir blocks in their presecondary sliding location. Each polygon is coloured by the total distance travelled according to reconstruction. The locations for Figs. 2.12; 2.13A–C; and 2.14B are shown. Abbreviations used include mass transport deposit (MTD).

The maximum distance of block sliding was shown to be 11,825 m (38,795 ft) with an average slide distance of 3500 m (11,483 ft) (Fig. 2.11). The dominance of the 0–500 m (0–1640 ft) travel distance (78 blocks) is caused by small blocks that closely surround the large central reservoir block and are still within the flatter, platform-like area of the MBR. This causes the average travel distance to be reduced. Additional observations include two data spikes that are observed at 2000–2500 m (6562– 8202 ft) and 6500–7000 m (21,325–22,965 ft) ranges. All of the blocks that travelled a distance over 10,000 m (>32,808 ft) are observed within the southernmost section of the reservoir, which may be because of a gentler slope gradient in this direction (axis of MBR) (causing the blocks not to disaggregate) (Fig. 2.8) but could also, to some extent, be biased by the distribution of the available data set. It is possible that blocks exist outside of the data set, but is more likely that any blocks transported beyond the survey edge will have disintegrated because of an increased slope gradient (Fig. 2.8) away from the MBR central axis and been redeposited as gravity flows in the deeper basin, as seen on the eastern flank (Fig. 2.7).

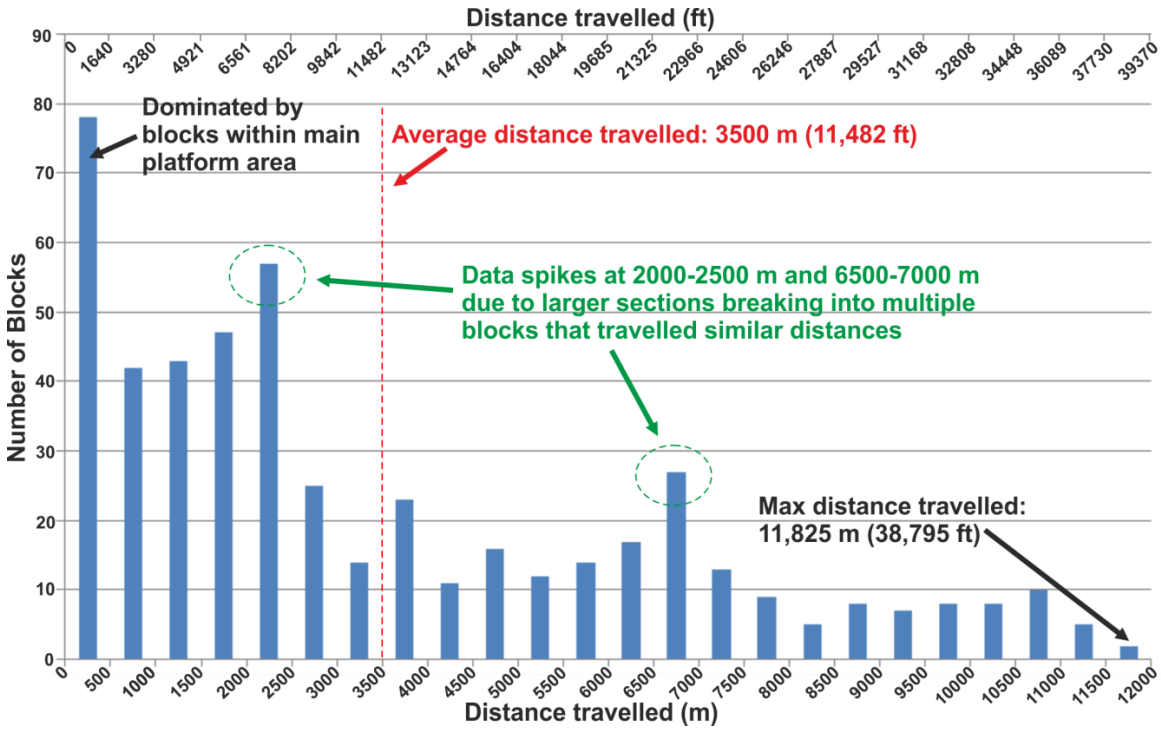

Figure 2.11. Block sliding | A histogram showing the distribution of block sliding distances calculated during the landslide reconstruction process. Abbreviations used include maximum (max).

Further analysis of the reconstruction over an area on the eastern flank depicts the flow directions for each of the reconstructed blocks (Fig. 2.12). This process highlights two trends of motion. First, the areas of the reservoir directly above the MBR trend toward the southeast along strike of the dipping ridge. The blocks then move in a secondary trend as they reach the eastern edge of a narrowing MBR and slide eastward and down into the deeper MBG. It is unknown whether sliding in the two directions was separated by a period of no movement or a smooth continuation. Within the southern section of the main reservoir block, two large areas do not show frequency or DHI responses and most likely do not contain reservoir (Figs. 2.5, 2.10, 2.13). This is also suggested by an opposite amplitude response (hard event) across these sections compared to that of the reservoir blocks and by the absence of the velocity pushdown effect likely created by gas in the reservoir. The two sections are underlain by localized high areas that suggest increased elevation and perhaps non-deposition on the decollement surface during original reservoir deposition. The location of these high areas coincides with the crests of tilted fault blocks that exist beneath the MBR and consist of pre-rift stratigraphy (mega-unit H) (Fig. 2.3) (Gregersen et al., 2013).

The surrounding internal reflections within the reservoir are shown to thin and onlap onto the flanks of the localized highs (Fig. 2.13). Comparison of the two adjacent non-reservoir areas shows a differing relationship with the elongated reservoir block to the west (Fig. 2.13). Within the southern section, the block looks to have slid away from the flank of the high, whereas the northern section of the elongated block is still directly adjacent to the high. This suggests that the whole block has not simply slid westward but has rotated clockwise by approximately 23°. Blocks are also shown to only exist above areas where the decollement is relatively flat, with no further blocks observed on the steeply dipping western flank of the MBR beyond the elongated reservoir blocks (Fig. 2.13).

2.4.6. Internal Stratigraphy of Landslide Blocks

Completing the geometric landslide reconstruction process allows the pre-sliding seismic characteristics of the reservoir to be assessed. This assessment removes the interblock areas along a seismic cross section (extracted along an MTD slide vector), juxtaposing the sections of the blocks, which were once laterally adjacent (Fig. 2.14). This provides a view of the original depositional structure of the reservoir pre-sliding, highlighting continuing internal stratification. The process can also help to highlight stratigraphic features that occur across multiple blocks, which may not be readily visible because of their present separation. The example highlights a central package within the reservoir response that are of lower amplitude to the under- and overlying sections. This

package only exists within the two thicker reservoir areas shown in Fig. 2.5B. Within this reconstructed package, several steeply dipping, oblique-sigmoidal reflections are observed that resemble clinoform features dipping toward the southeast (Fig. 2.14).

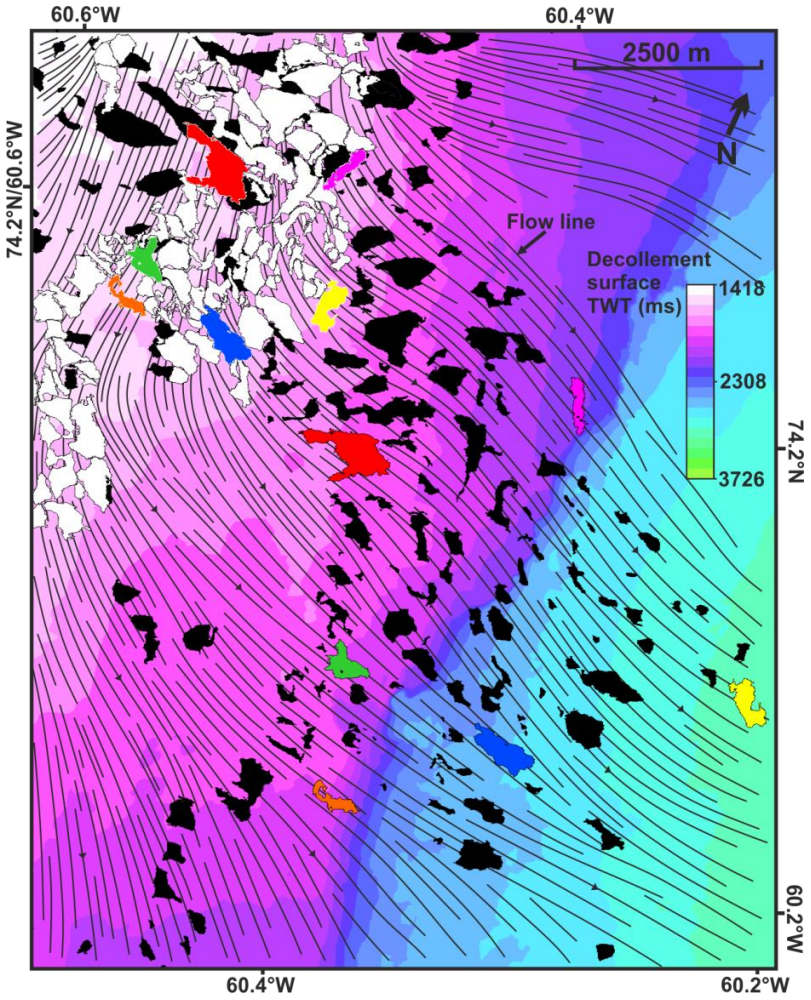

Figure 2.12. Sliding vectors | A two-way time (TWT)–structure map of the decollement surface overlaid by polygons representing the modern day location (black) and reconstructed location (white) of the reservoir blocks. Certain polygon pairs have been coloured for comparison. Flow lines are shown between block polygon pair locations that represent the direction of movement and highlight a bidirectional trend during sliding. The map location and decollement surface legend are shown in Fig. 2.10.

2.5. Discussion

MTDs have a significant impact on the hydrocarbon industry by commonly serving as hydrocarbon seals (Alves et al., 2014; Sun et al., 2017) and by forming major reservoirs for several fields in the North Sea and Gulf of Mexico alone (Meckel, 2010). With less than 10% of MTDs worldwide being sandy, it is often difficult to differentiate between sand-prone and shale-prone MTDs in seismic data, and it is often only after drilling a target that a sand-prone MTD interpretation can be made (Meckel, 2010). Here, seismic observations have identified the presence of a sandy MTD consisting of gas-charged, highly porous blocks on the crest and eastern flank of the MBR (Figs. 2.3, 2.4) that are of landslide origin

having experienced post-depositional breakup and sliding. The package is clearly defined by high amplitudes and exists at the base of mega-unit D2 above a single decollement surface (the top reflection of mega-unit E [E1]) (Fig. 2.3). Clear DHIs, frequency analysis via spectral decomposition, and estimations for velocity within the package all suggest a reservoir composed of highly porous sand that is likely gas charged, suggesting a working petroleum system within this area (Figs. 2.4, 2.5).

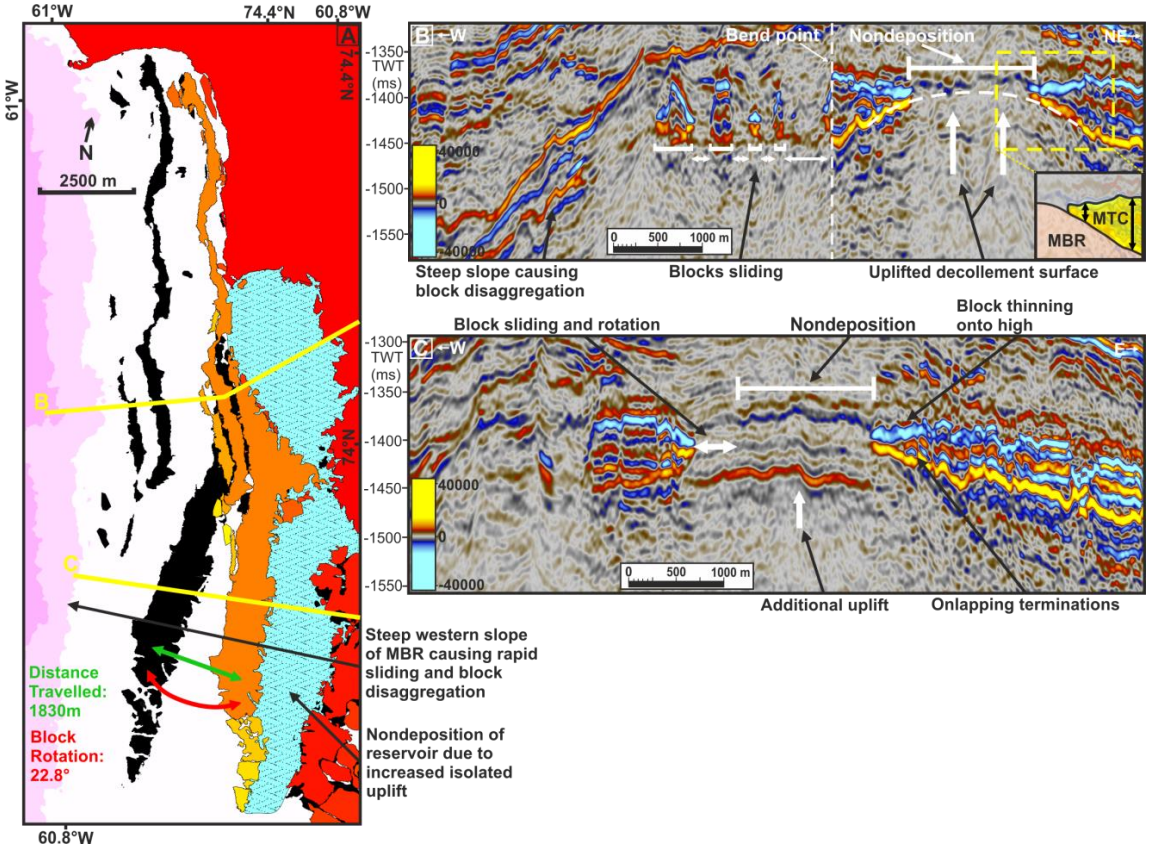

Figure 2.13. Areas of reservoir non-deposition | A) A comparison of modern day (black) and reconstructed (coloured) reservoir block locations, shown on top of a two-way time (TWT)–structure map of the decollement surface. Areas of reservoir non-deposition are highlighted in blue. The map location and decollement surface legend are shown in Fig. 2.10. B) A seismic section showing the location of an uplifted platform on the decollement surface on which reservoir deposition did not occur. The schematic insert depicts the thinning of the reservoir against this uplifted high. C) A seismic section showing non-deposition and subsequent sliding of a reservoir block to suggest block rotation. The line locations of B and C are shown on Fig. 2.10. Abbreviations used include Melville Bay Ridge (MBR) and mass transport deposit (MTD).

2.5.1. Reservoir Deposition and Deformation

The basin and ridge topography, created by Cretaceous rifting, existed throughout the Paleogene and into the Neogene in the Melville Bay area (Gregersen et al., 2013; Whittaker et al., 1997). The MBR was likely a small, elongated emergent island extending from the northwestern Greenland mainland southward, creating a deep water embayment above the MBG (Figs. 2.2, 2.15). This is evidenced by onlap terminations of thick syn-rift deposits on the flank of the high as well as the increasing ridge height to the north (Fig. 2.15). During

periods of ridge uplift, no deposition occurred on the high and any sediment input would have bypassed into the deeper graben via gravity driven processes (Gregersen et al., 2013) (Fig. 2.16).

A period of net subsidence of the MBR allowed for the deposition of reservoir sands upon the ridge (Gregersen et al., 2016) (Fig. 2.16). This likely occurred during the Eocene based on correlation of the base sand reflection (mega-unit E) on regional 2-D seismic data, with Eocene volcanics further south (Gregersen et al., 2013). The reservoir surrounds areas of non-deposition that exist above elevated areas on the ridge crest created by deep-seated tilted fault blocks (Figs. 2.13, 2.15). This suggests sand deposition in a very shallow marine environment, where restriction of deposition on these slightly more elevated areas is likely a result of being above the wave base.

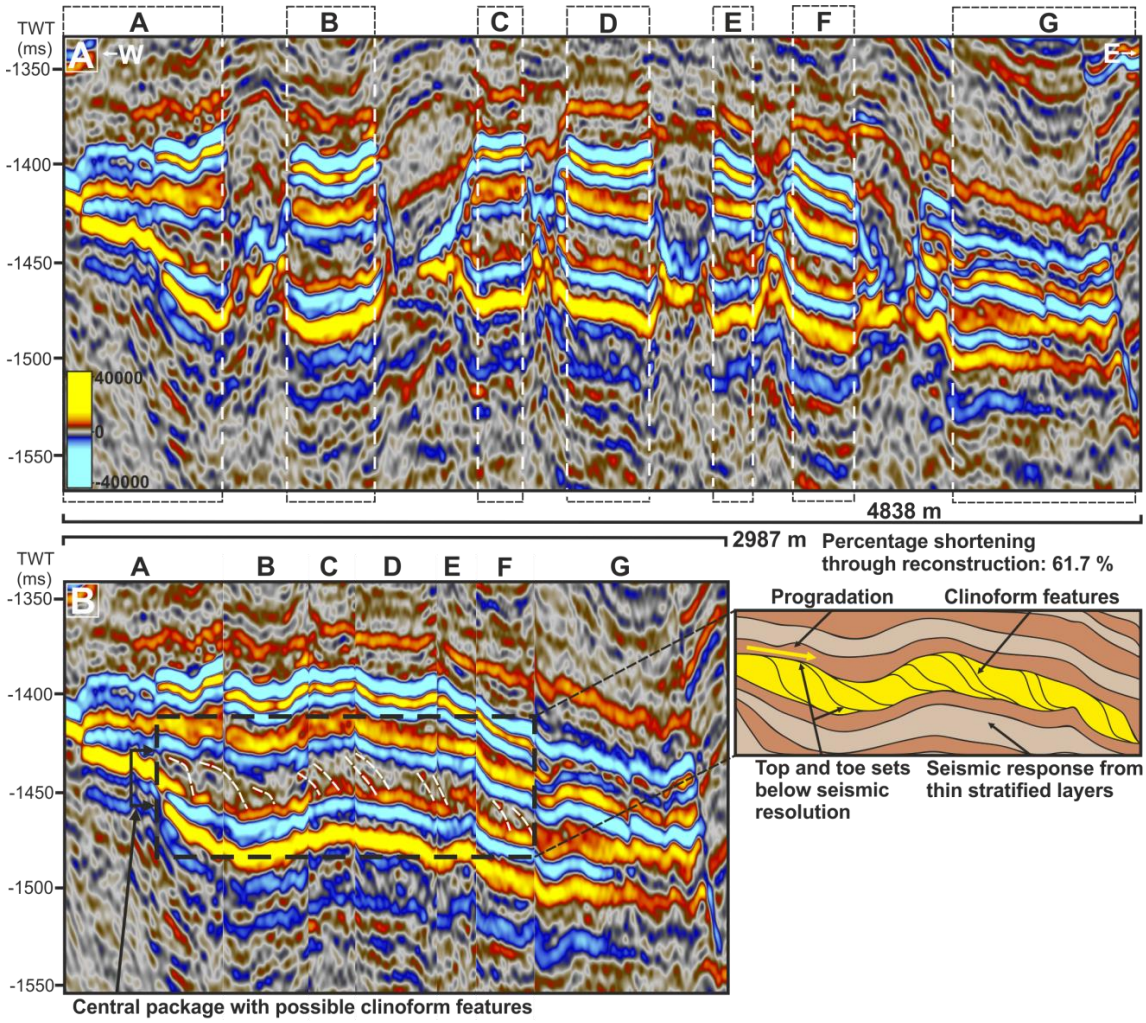

Figure 2.14. Reconstructed internal stratigraphy of mass transport deposit blocks | A) A seismic section showing reservoir blocks that have been separated through sliding. The areas of the section selected for the reconstruction are shown. The location of the seismic line is shown in Fig. 2.10A. B) A reconstructed seismic section that shows the laterally consistent reservoir in its pre-deformation state. An internal section of the reservoir is highlighted and shown to contain clinoforms. These clinoform features are shown in the adjacent schematic diagram. The location of the seismic line is shown in Fig. 2.10B. Abbreviations used include two-way time (TWT).

Additional accommodation, possibly caused by localized faulting of the ridge, allowed the deposition of a localized thicker package within the reservoir that is observed during seismic reconstruction (Fig. 2.14). This package is notably restricted to two areas on the ridge top platform (thicker areas of reservoir in Fig. 2.5B) and is seen to contain possible southeastwardly prograding clinoform foresets. These observations, along with the southeast sediment transport direction along the MBR axis extension, suggest the development of a spit-like complex that is restricted to the shallow waters on the ridge top (Fig. 2.15). Sediment transport may have been driven by near-surface ocean currents in the wider Baffin Bay, moving sediment southeastward along the paleo-coastline before eventual progradation along the submerged MBR southerly nose. The thickness and preservation of the sands upon the ridge suggest a high sediment supply (Swift, 1968) and would have likely led to the bypass and transport of excess sand into deeper waters via gravity driven processes (Fig. 2.15) (Raynal et al., 2009).

Candidate deposits that may contain these sediments have been observed by Knutz et al. (2012) and Gregersen et al. (2013) as submarine fans at the base of mega-unit D2 with sand transport down slope being the likely cause of canyon development at this horizon on the eastern flank of the MBR (Fig. 2.7E). However, deep marine clastics in the graben were still dominantly sourced from the Greenland mainland to the east, creating large packages of onlapping sediments that are observed at the basin centre (Gregersen et al., 2016). The focal point for sediment input may have been a relay ramp between fault sections of the MBG boundary fault (Fig. 2.15).

Major extension ended in Baffin Bay during the late Eocene–Oligocene (Oakey and Chalmers, 2012), and Melville Bay experienced thermal subsidence and deepening waters leading to the preservation of the reservoir sands. Relative sea level rise forced a southeast–northwest transgression of the spit complex system (Figs. 2.15, 2.16), leading to increased reservoir thicknesses to the northwest before a transition of the environment to deep marine mud deposition (Figs. 2.3, 2.4, 2.5B).

Soon after reservoir deposition and before the overlying muds were in place, the reservoir sands underwent significant deformation, leading to the mass redistribution of sediment from the ridge top to its upper flanks, resulting in the modern day reservoir structure, characterized by a large number of intact, separated MTD blocks along with a larger stable reservoir section to the north (Figs. 2.4, 2.16). The breakup and sliding of reservoir blocks was likely triggered by a southward tilt of the MBR, evidenced by the reconstructed flow directions (Fig. 2.12). This tilt was either caused by renewed heterogeneous uplift along strike of the MBR (with a relative increased degree of uplift to

the north) or increased subsidence to the south (Fig. 2.16). This is also supported by the increased quantity and travel distance (some >10 km [>6.2 mi]) of blocks southward (Fig. 2.10). However, the southern slope represents the least dipping direction because it is along the southerly nose of the MBR (Fig. 2.8). Therefore, the increased number of intact blocks may be because of preservation bias, with blocks down the steeper eastern and western ridge flanks having disintegrated.

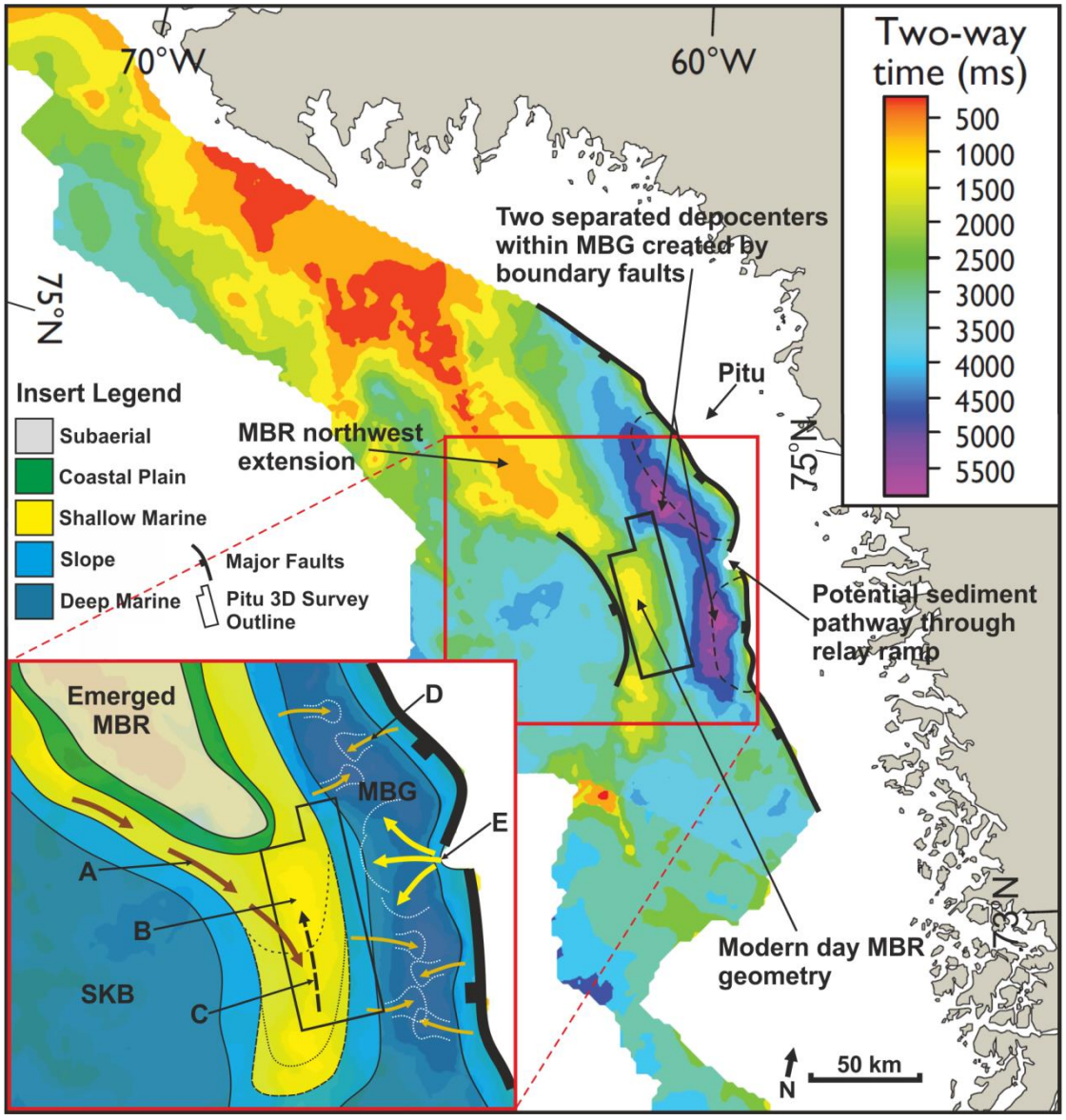

Figure 2.15. Reservoir deposition | A two-way time–depth structure map down to horizon F1 (top reflection of mega-unit F) showing the distribution of basin depocentres and structural ridges (modified from Gregersen et al., 2016). Major bounding faults and the location of the Pitu seismic survey are shown. The enlarged insert map shows an interpretation of the gross depositional environments during reservoir deposition upon the ridge. The lettered labels are as follows: A, coast parallel sediment input; B, shallow marine spit complex development along ridge axis; C, transgression of shallow marine system; D, gravity flow deposition into deeper marine environment; and E, major sediment input into the graben centre. Abbreviations used include three-dimensional (3-D), Melville Bay Graben (MBG), Melville Bay Ridge (MBR) and South Kivioq Basin (SKB).

The east-west-trending, low-amplitude features observed on the eastern flank of the MBR (Figs. 2.5, 2.7) are likely to represent decollement surface deformation and extensional slumping, controlled by the location of faults (Fig. 2.7). Low-amplitude zones within these features represent small extensional faults that facilitate deformation of the decollement surface (Fig. 2.7B, C). The deformational features seem to mimic the shape of the sliding reservoir blocks seen along strike and were possibly caused by beneath-block deformation of decollement muds during sliding. It is possible that these features represent resting places for the blocks, thus creating an imprint or slide scar on the decollement surface before sliding further down the steepening slope and disaggregating (since the blocks themselves are not observed). This disaggregation caused much of the sliding reservoir sand to be redeposited by graben floor gravity flows (Gregersen et al., 2013; Knutz et al., 2012) or to be trapped in topographically controlled depocentres on the ridge slopes in features such as half grabens and canyons (Figs. 2.7D, E; 2.16). The large volume of sediment shed from the high will have aided the development of the deep linear canyons that are observed trending into the MBG to the east (Fig. 2.7E). Within these canyons, high positive seismic amplitudes (Fig. 2.7E) likely represent redistributed reservoir sands.

The deformational features observed all suggest that reservoir deformation and preservation are controlled by the slope angle of the decollement (Fig. 2.8). This angle is likely controlled by the uplift and resultant structure of the MBR along with the location of faults. Based on this, the system can be subdivided into four zones of deformation style that define the distribution and character of the reservoir sands (Figs. 2.7D, 2.8).

1. Stable platform crest: post-depositional deformation and sliding not observed, likely bald high areas with reservoir onlap.
2. Mega-block sliding: shallow slope-induced breakup into blocks and sliding along a muddy decollement layer.
3. Slide scars and disaggregation: sliding reservoir blocks caused deformation of the underlying decollement muds before the disaggregation of sand blocks because of slope steepening (possibly controlled by fault locations).
4. Canyonization: erosional canyonization of the decollement surface caused by the continued downslope shedding of sediment; disaggregated sands deposit within canyon features.

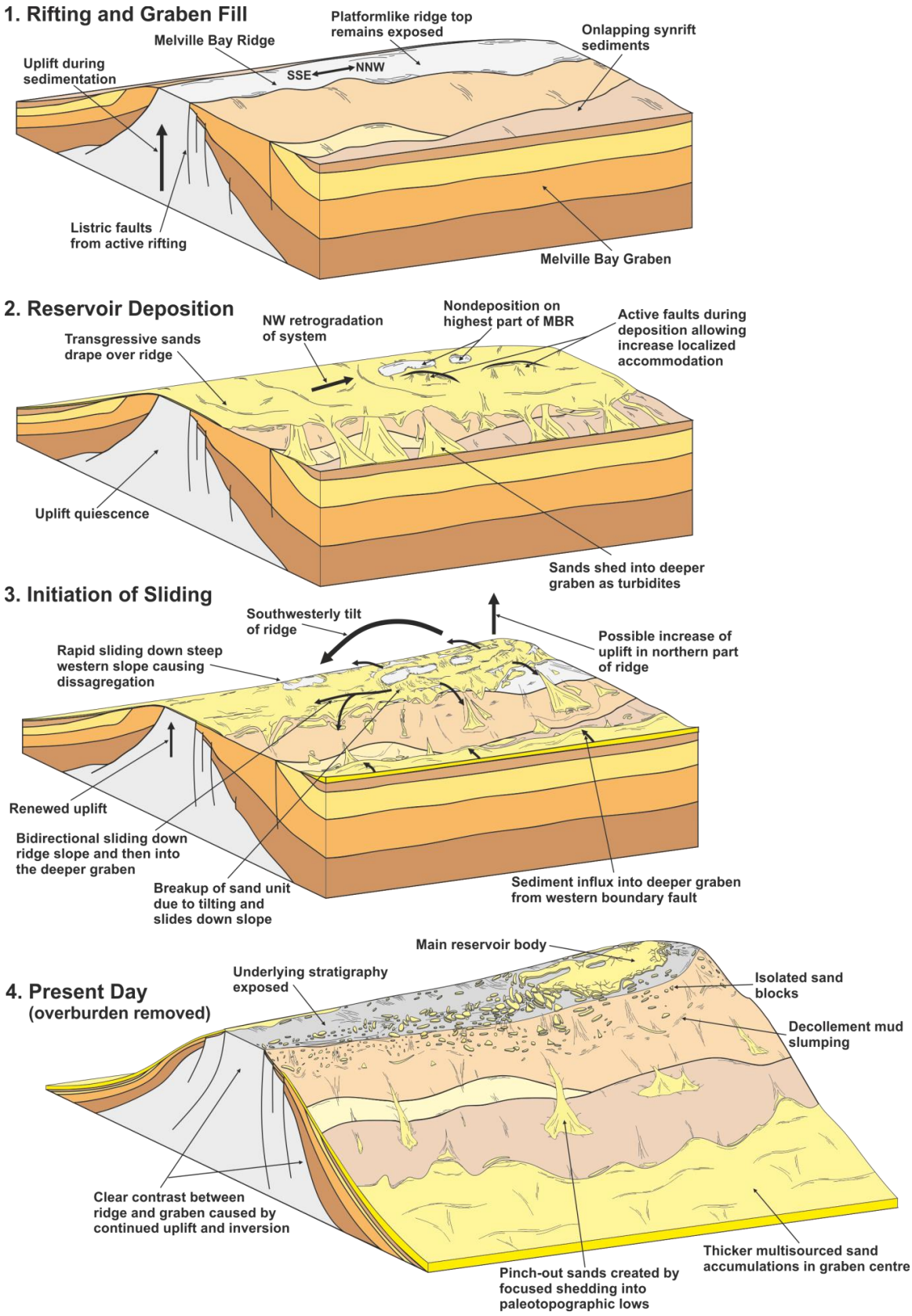

Figure 2.16. The stages of reservoir deposition and deformation | A series of schematic models that represent the depositional and structural development of the reservoir on the seabed above the uplifted Melville Bay ridge (MBR) and adjacent Melville Bay graben (models 1–3). Model 4 represents the modern day reservoir distribution with the overburden removed. The models are not drawn to scale.

These four deformational styles transition across areas of different dip angles seen across the modern day decollement surface. However, it is the paleo-dip of the decollement surface during the period of deformation (Eocene) that would have had the controlling effect on the modern day reservoir distribution. It is difficult to estimate paleo-dip in an area dominated by deep water hemipelagic sedimentation, a clastic supply dominantly from the east (Gregersen et al., 2013), and significant sediment erosion caused by recent glaciations (Figs. 2.2, 2.3). Still, paleo-dip was likely similar or less than that observed today because uplift of the MBR is expected to have continued into the Neogene, increasing the slope angle post-sliding (Japsen et al., 2006; Knutz et al., 2015; Oakey, 2005). Additionally, the main sliding vector toward the southeast aligning with the direction of lowest average dip at 0.41° suggests that breakup and sliding of the reservoir commenced at a very low dip angle (<0.5°).

After the deformation of the reservoir sands and the full transition to a deep marine setting during the late Eocene, a thick sequence of mud deposition occurred over both the basin and ridge. Mud deposition infilled between the separated reservoir blocks (evidenced by low-amplitude, flat-reflection geometries between blocks), suggesting deposition post-reservoir deformation. These muds make up the lower section of the thick, polygonally faulted mega-unit D1 (Figs. 2.3, 2.9).

The observed coincidence between faults extending sub-vertically from the block edge and the lower tips of polygonal faults (Fig. 2.9) suggests that the reservoir blocks were a major factor in the development of the polygonal fault network above the MTD deposit. This occurred because of differences in compaction behaviour between the sand blocks and infilled interblock muddy areas, which created a series of normal faults at the block edge (Fig. 2.9). The compactional differences between mud and sandy block areas likely created subtle stress perturbations, which controlled the nucleation of polygonal faults into the overburden. This process potentially created a vertical fluid pathway constrained at the block edge from the reservoir to shallower stratigraphy, potentially representing a significant exploration risk, although polygonal fault planes are only thought to conduct fluids when actively forming, and polygonal faulted claystones are extremely effective seals in much of the North Sea Basin (Cartwright et al., 2007; Goulty, 2012).

2.5.2. Mechanisms of Sliding

The deposition of MTDs commonly results in a deformed mass of partly disaggregated sediment, which may lack coherent primary depositional structures, and is typically characterized by chaotic internal seismic reflections (Shipp et al., 2011). These gravitational deposits, however, are capable of transporting large clasts or blocks within the flow, which

often maintain their primary structure and internal stratification (Alves, 2015; Jackson, 2011).

The phenomenon of relatively undeformed siliciclastic "mega-blocks" within a submarine slide deposit has been observed in different parts of the world (Table 2.1); examples include the northern Hikurangi Margin, New Zealand, where internally bedded slide blocks have been transported for greater than 40 km (>24.9 mi) (Collot et al., 2001); the Hopedale–Makkovik failure complex, southwest Labrador Sea, which contains angular blocks up to 6 km (3.7 mi) across with well-preserved internal stratification (Deptuck et al., 2007); and the internally undeformed slide blocks of the lower conglomerate sandstone that reach thicknesses of 30 m (98 ft) and widths up to 100 m (328 ft), found within basal canyon fill of the Upper Cretaceous Rosario Formation, Mexico (Morris and Busby-Spera, 1988).

#	Location	Lithology	Max. block width (m (ft))	Max. block height (m (ft))	Run out distance (km (mi))	Reference
1	Melville Bay, NW Greenland	Sand + Mud	1000 (3280)	80 (262)	12 (7.5)	This Study
2	Hikurangi Margin, New Zealand	Mud	18,000 (59,040)	1200 (3936)	40 (24.9)	Collot et al., 2001
3	San Carlos, Mexico	Sand	100 (328)	30 (98)	~<1 (0.6)	Morris & Busby Spera, 1988
4	SE Crete	Carbonate	100 (328)	64.5 (212)	~2.5 (1.6)	Alves, 2015 - Alves and Lourenco, 2010
5	SW Labrador Sea	Sand + Mud	6000 (19,680)	300 (984)	~50 (31.2)	Deptuck et al., 2007
6	Central North Sea	Carbonate	1000 (3280)	170 (558)	200 (124.6)	Soutter et al., 2018
7	Espirito Santo Basin, Brazil	Sand	2400 (7872)	250 (820)	10 (6.2)	Omosanya & Alves 2013 - Gamboa et al., 2011
8	Taranaki Basin, New Zealand	Sand + Mud	1000 (3280)	200 (656)	15 (9.3)	Rusconi et al., 2018
9	Niger Delta, Nigeria	Sand + Mud	250 (820)	10 (33)	12 (7.5)	Nissen et al., 1999
10	Offshore Morocco	Sand + Mud	4000 (13,120)	150 (492)	~>50 (31.2)	Lee et al., 2004
11	Santos Basin, Brazil	Mud	5000 (16,400)	350 (1148)	95 (59.2)	Jackson, 2011
12	Faeroe-Shetland Channel	Sand + Mud	70 (230)	18 (59)	25 (15.6)	Kuijpers et al., 2001
13	Gela Basin, Italy	Sand + Mud	800 (2624)	10 (33)	9.1 (5.7)	Minisini et al., 2007

Table 2.1. Analogous mass transport deposits | Summary table of the location, lithology, maximum block width, maximum block height, and run-out distance for this study and several analogous mass transport deposits. The reference for each example is shown in the table. Abbreviations used include maximum (max).

The enigma of the MTD studied here is the apparent lack of transporting flow, with blocks sliding downslope as independent rafts of sediment, not confined or hosted within a more typical debris flow as seen in the majority of other block-containing MTDs (Table 2.1) (Alves, 2015; Deptuck et al., 2007; Jackson, 2011). This is evidenced by areas between blocks being infilled by hemipelagic sedimentation post-sliding (Fig. 2.4). Despite this, the blocks have still managed to maintain their gross depositional structure throughout the processes of breakup and sliding up to and greater than distances of 10 km (>6.2 mi). This is evidenced by the large, angular, sandy reservoir blocks along with the apparently unaffected internal stratification of the blocks post-sliding at least on a seismic scale (Figs. 2.4, 2.5). This suggests that slide momentum and block cohesion during sliding can occur independently and without containment in a typical cohesive debris flow. Although the more typical confining flow is not observed, the similarities in block size, distribution, and run-out length to other MTD analogues (Fig. 2.17; Table 2.1) supports the conclusion that similar gravitational processes, including the downslope coherent sliding of reservoir facies, led to the modern day structure and distribution of the MTD studied here.

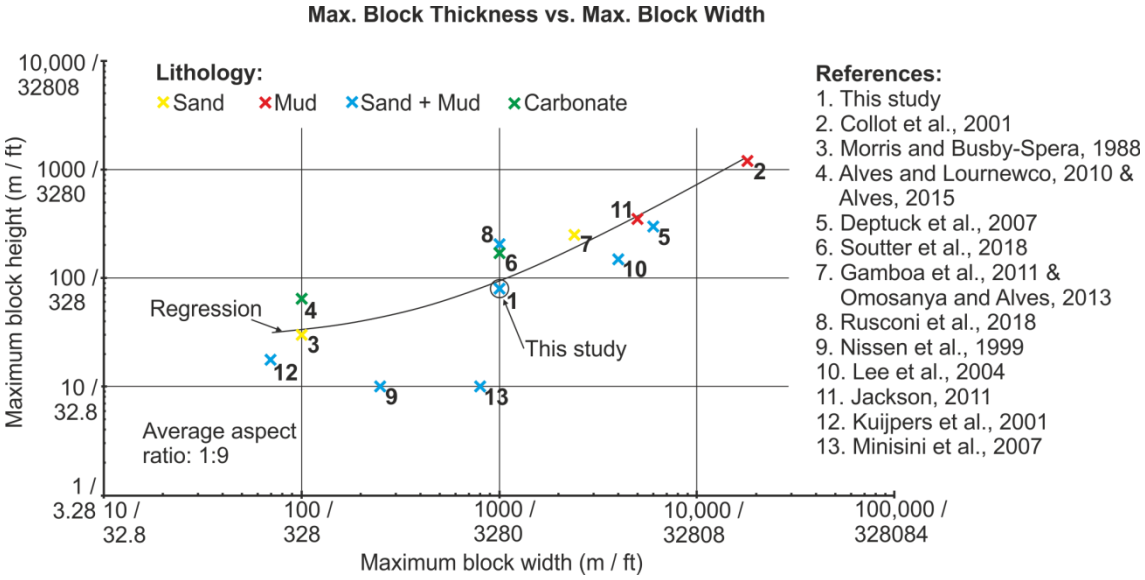

Figure 2.17. Block height versus width | A graph showing the relationship between the maximum (max.) block height and the maximum block width for this study and mass transport deposit (MTD) blocks observed within analogue MTDs. These data are shown in Table 2.1, and references are shown in the figure.

The similarity of this MTD to other analogues is highlighted by its maximum block size (maximum block width vs. maximum block height) plotting within a data trend that strongly suggests that increased block width commonly coincides with increased block

height within MTDs (Fig. 2.17). The blocks from this MTD plot within the centre of the distribution; therefore, it could be argued that blocks observed here represent a somewhat average example with regard to block size in MTDs.

Without the surrounding coherency and sliding lubrication provided by confinement within a larger debris flow, coherency of the blocks within this MTD was likely maintained and impacted by differing factors. First, the decollement surface itself would have provided a lubricated and smooth surface for the blocks to slide along (most likely a muddy horizon). This surface represents an unconformity above the underlying mega-units E and F (Fig. 2.3), which are interpreted to be dominated by fine-grained claystones (Fig. 2.18) (Gregersen et al., 2013). This weak, high–water-content lithology may have led to the development of a thin, sub-seismic veneer of mud slurry or a low-viscosity water layer (Prior et al., 1984) upon the decollement surface. In that scenario, a basal lubricating layer will reduce basal drag during sliding, increasing both block coherency and run-out distance while maintaining momentum. The underlying lubricating layer may also have caused blocks to hydroplane and decouple from the underlying surface during sliding; however, the probable slow speed of sliding makes hydroplaning less likely (Harbitz et al., 2003; Mohrig et al., 1998).

Slow, creep-like sliding would have reduced the attrition of the layered sediments, leading to a maintained primary depositional structure (Masson et al., 1996). The rate of sliding is most likely controlled by the decollement angle (Kehle, 1970) (Fig. 2.8). This may be the reason why no reservoir blocks are observed beyond the platform edge in areas where the decollement slope dip angle increases significantly (>4°) (Fig. 2.8). Increasing slope angle away from the ridge axis, or at fault locations, would promote faster sliding, disaggregation, and shedding of sediments into the deeper basin (Figs. 2.7, 2.8, 2.16). Along the ridge axis, however, the slide-triggering tilt of the MBR caused either by differential uplift or subsidence along strike (northwest-southeast) (Gregersen et al., 2013), would have likely only created a decollement surface tilt of less than 0.5° (Figs. 2.8, 2.18). This low angle is commonly thought to be enough to facilitate sliding of marine sediments (Harbitz et al., 2003; Kvalstad et al., 2005) but remains low enough to maintain a slow sliding speed. Furthermore, the large scale of the blocks may provide protection to internal strata from disaggregation at the block edges (Alves, 2015; Morris and Busby-Spera, 1988). This protection may have occurred as larger slide blocks broke away from the main platform section and slid as one before subsequently breaking up into smaller blocks, as seen in Collot et al. (2001) (Fig. 2.11).

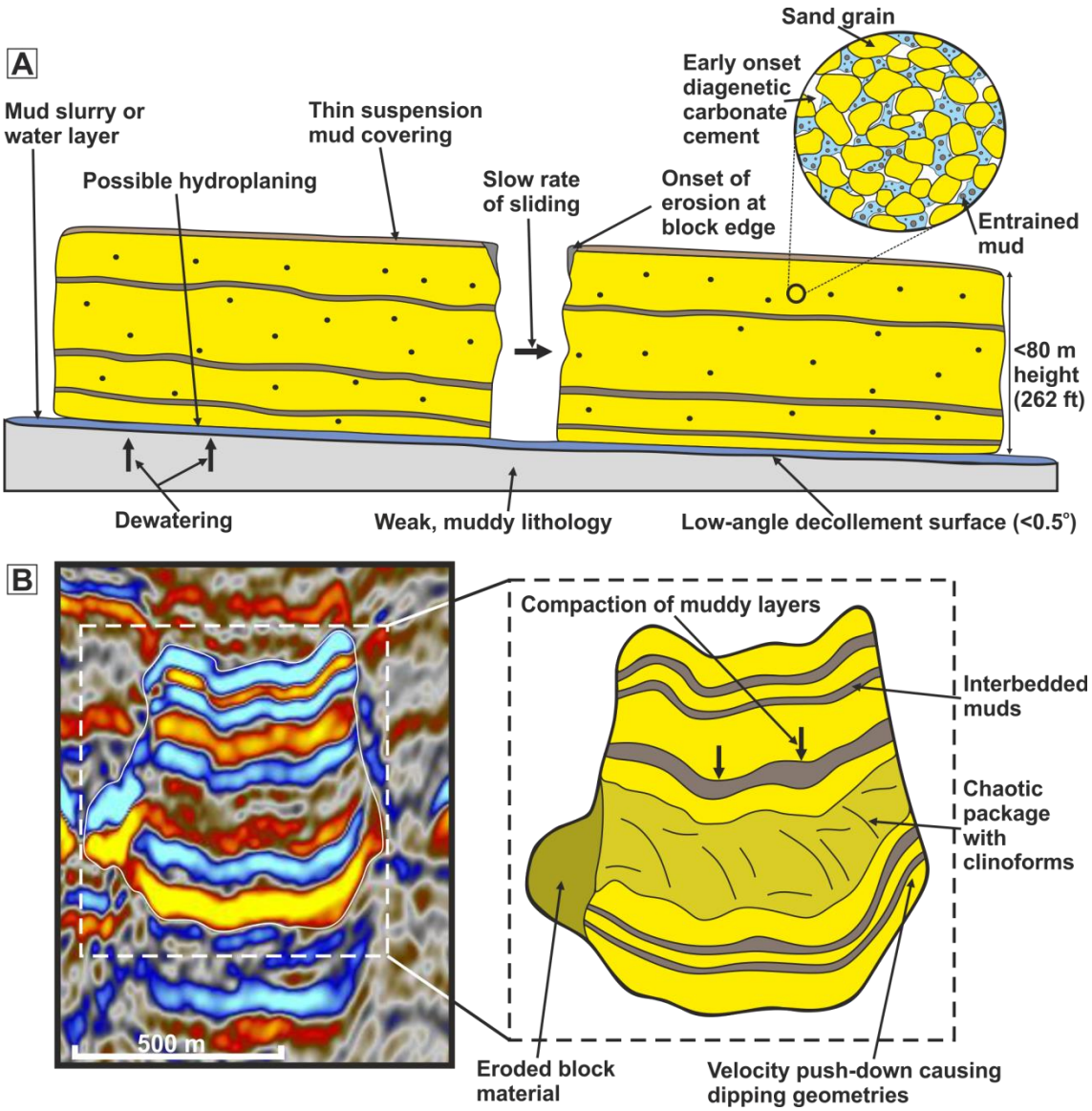

Figure 2.18. Mechanisms of sliding and internal reservoir stratification | A) A schematic diagram showing the potential factors that led to coherent sliding of reservoir sands along the decollement surface. B) A schematic interpretation of the internal stratigraphy within a separated reservoir block (shown on seismic section). The location of the seismic section is shown in Fig. 2.6.

Block coherency may have also been promoted by the internal stratification of the reservoir, evidenced by bright seismic reflections within the reservoir package (Figs. 2.4, 2.18). This heterogeneity suggests that the reservoir contains muddy layers that will have experienced a degree of compaction and dewatering because of the thickness of the reservoir (Fig. 2.18). This compaction would have increased the shear strength of these mud layers, which in turn would increase the stability of the reservoir block. Additionally, these mud layers, along with mud entrained into the reservoir sands, would have caused the sediment to become more cohesive and may also have helped block stability during sliding (Fig. 2.18) (Le Hir et al., 2011). Furthermore, the environment transition into a deep marine setting during the time of sliding may have caused slight burial of the reservoir by a

hemipelagic mud drape. The covering of sand beds with thin layers of muddy sediment has been proven to enhance the coherency of the beds. This is because of silt grains plugging the pore space of sand beds and reducing the inflow in the bed, leading to a reduction in erosion and increased bed stability (Bartzke et al., 2013). However, any burial would have been minimal because of the short time between deposition and sliding, evidenced by the lack of slide-related deformation of the overburden.

Finally, early-onset carbonate cementation may have occurred within the reservoir because of the potential deposition of shelly carbonate material within the reservoir sands (Fig. 2.18). Grain cementation would likely reduce the porosity of the sands but increase the shear strength of the sediment package, causing it to become more stable and resist collapse during sliding (Dyke and Dobereiner, 1991). Any cementation would however be slight because the fluid effect is strong, implying low acoustic rigidity.

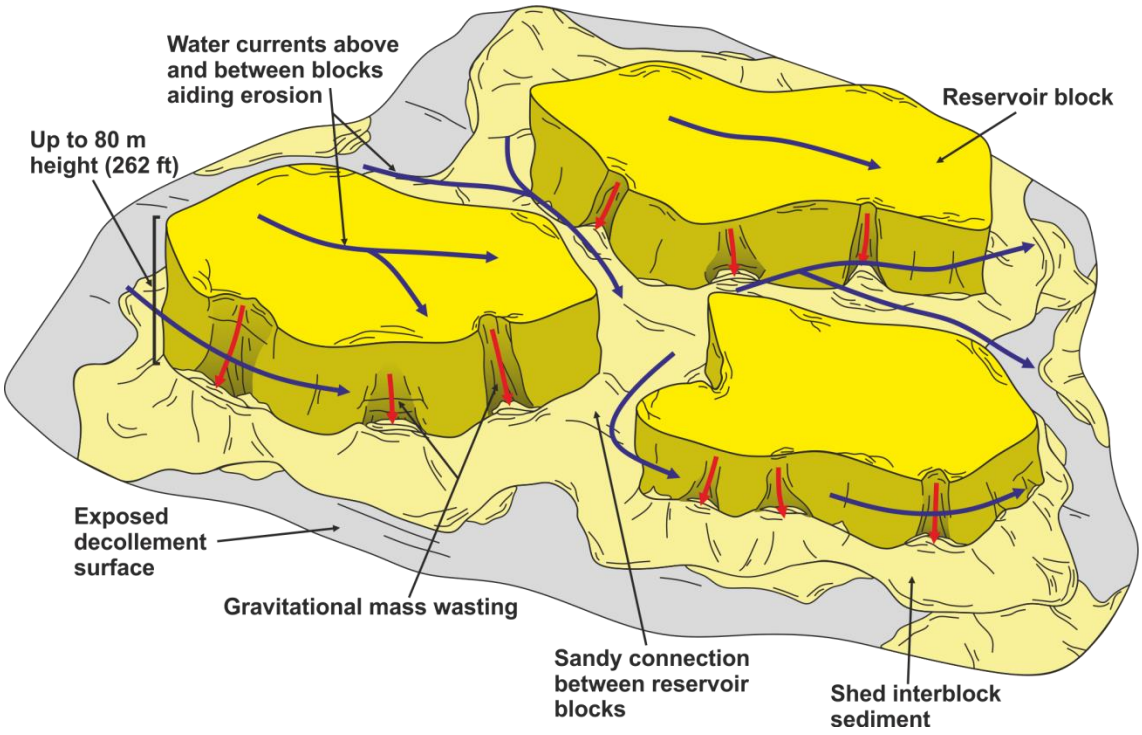

Figure 2.19. Block erosion and interblock sediment deposition | A schematic three-dimensional diagram showing water current and gravity driven erosional collapse of sediment from the edges of angular reservoir blocks exposed on the seabed. This eroded sediment possibly creates sandy connections between separated reservoir blocks.

2.5.3. Implications for Reservoir Connectivity

Post-depositional breakup and sliding has caused much of the reservoir to exist as distributed MTD blocks. The potential disconnection between these blocks may have a major impact on hydrocarbon extraction efforts, causing much of the reservoir to be uneconomic. However, the distribution of DHIs across all observed MTD blocks and

within the interblock areas (Figs. 2.4, 2.5, 2.6) suggest that gas has reached all parts of the reservoir. Because gas charging is thought to have occurred after the deformation and burial of the reservoir (to allow the seal to be in place), this may suggest that the isolated reservoir blocks are connected to allow migration.

However, source rocks within the Melville Bay area are likely to exist within Upper Cretaceous (Cenomanian and Turonian) stratigraphy (mega-unit F) (Gregersen et al., 2013; Planke et al., 2009; Whittaker et al., 1997), the sediments that directly underlie the majority of the reservoir, up-dip from potential deeper source kitchens in the MBG and South Kivioq Basin to the east and west, respectively (Fig. 2.3). This connection between source rocks and the overlying reservoir would allow for up-dip migration into the MBR and subsequent upward migration and charging of all overlying reservoir sands. Therefore, a connection between distributed MTD blocks is likely not required to create the distribution of gas observed. It is more likely that any connectivity between MTD blocks is restricted to areas containing interblock sediments that have been mapped (Figs. 2.5, 2.6). This sediment shows similar frequency and DHI responses on seismic data to the thicker reservoir blocks and likely represents gas-charged sands (Figs. 2.5, 2.6). It was most likely deposited because of syn- and post-slide block exposure at the seabed before seal coverage and gas charging. The edges of the reservoir sections would have resembled up to 80 m (262 ft)-tall cliffs with vast, deep areas between the blocks. This varied seabed topography, along with poorly consolidated sediment, would have promoted cliff edge erosion and gravitational collapse that was likely aided by current flow. This block-edge erosion is evidenced by the seismic geometry of the reservoir blocks (Fig. 2.6) and is also depicted in schematic form in Fig. 2.19, showing the erosional collapse of sediment from the cliff edge caused by exposure. However, because of the angular nature of reservoir blocks (Fig. 2.10), erosion over much of the reservoir is likely to be minimal or below seismic resolution, with more significant erosion confined to blocks within areas defined by reservoir zones in Fig. 2.20. Within these zones, eroded block sediment was deposited adjacent to the block edge, upon the exposed decollement surface (Figs. 2.6, 2.19), most likely during and after sliding, allowing for deposition to be relatively widespread around the block edges. This led to the creation of a sandy connection between separated reservoir blocks, which may provide widespread reservoir communication.

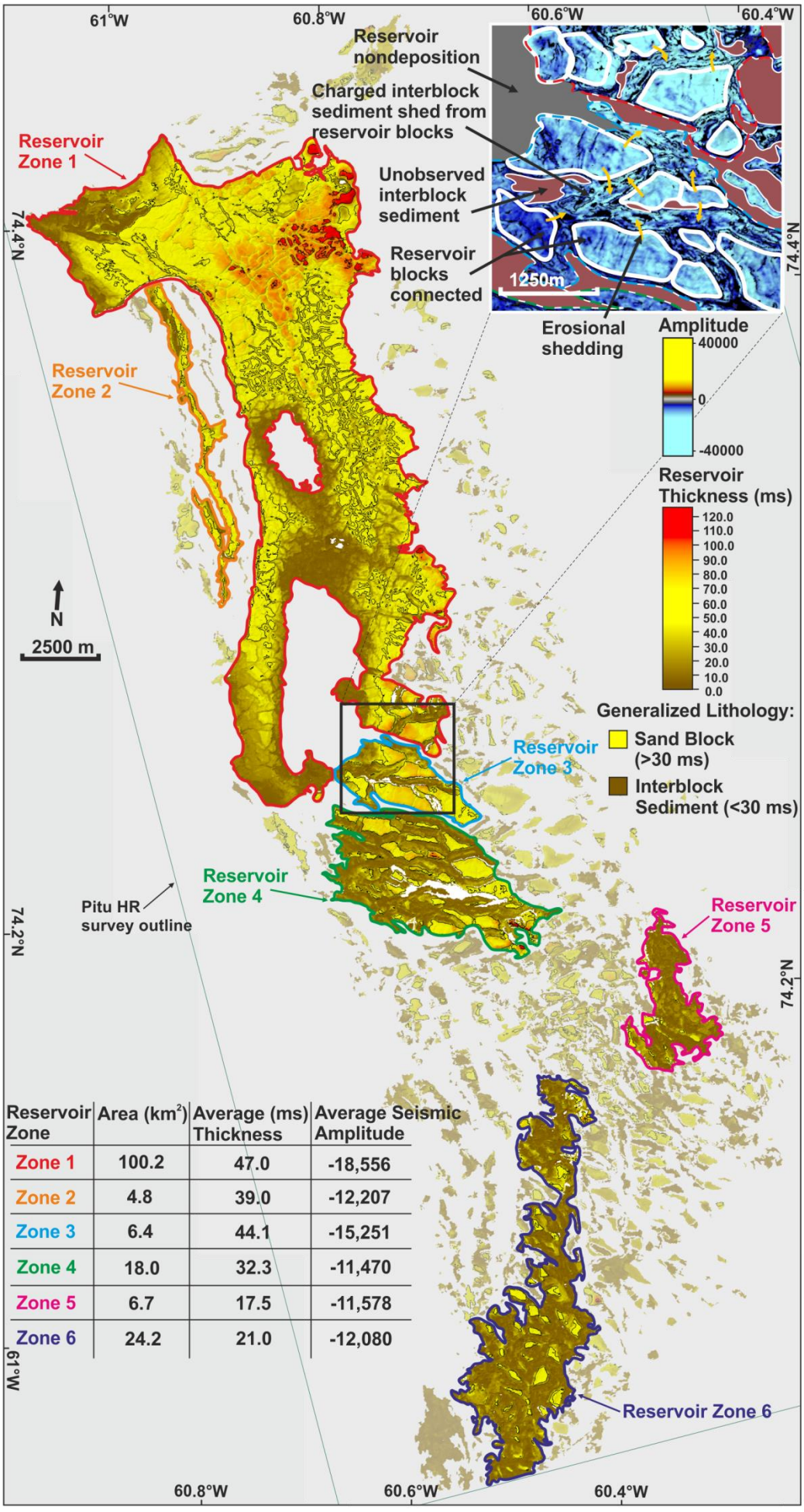

Reservoir Zone	Area (km²)	Average (ms) Thickness	Average Seismic Amplitude
Zone 1	100.2	47.0	-18,556
Zone 2	4.8	39.0	-12,207
Zone 3	6.4	44.1	-15,251
Zone 4	18.0	32.3	-11,470
Zone 5	6.7	17.5	-11,578
Zone 6	24.2	21.0	-12,080

Figure 2.20. Interconnected reservoir zones | Interpreted zones suitable for exploration targeting because of potential cross-block communication provided by interblock sediment. The insert map shows a seismic amplitude extraction on the top reservoir surface that depicts the similar seismic amplitude of both the reservoir blocks and the interblock sediment that may create these cross-block connections. The map also indicates areas of interblock sediment non-deposition or erosion. The table inset within the figure shows the area (square kilometres), average thickness (milliseconds), and average seismic amplitude for each of the six highlighted reservoir zones.

However, this sandy connection and potential reservoir communication may only exist within the identified reservoir zones (Fig. 2.20) because charged interblock sediment is not observed in other areas (Figs. 2.5-6, 2.19-20). This absence may be caused by sediment shedding occurring only in certain areas or caused by post-depositional erosion of the interblock sediment. Also, because of the slow rate of sliding as well as the transition of the system into a deeper marine environment, fine-grained hemipelagic sediment may have become entrained into the interblock sands. This would reduce reservoir quality and potentially restrict both hydrocarbon charge and the fluid amplitude response. Overall, the sporadic absence of the reservoir-connecting sediment suggests that significant areas of the reservoir will remain disconnected.

Nevertheless, large areas of the reservoir do contain interblock sediment and are potentially in pressure communication. These areas have been divided into separate zones that are most suitable for exploration targeting (Fig. 2.20). The six most connected zones cover an area of 160.3 km^2 (62 mi^2) with an average thickness of 33.5 ms (28 m [92 ft]). The remaining unknowns regarding interblock infill creating block connection increase exploration risk significantly. However, a large part of the selected reservoir zone area exists within zone 1, which is the main reservoir block in its original depositional location. This block covers an area of 100.2 km^2 (39 mi^2) with an average thickness of 47 ms (40 m [131 ft]) and may provide fewer production issues than the other selected surrounding zones.

2.6. Conclusions

Seismic investigations show an MTD prospect that displays acoustic and velocity characteristics consistent with thick gas-charged sands intercalated with mudstone layers. Reservoir structure shows landslide characteristics with much of the reservoir consisting of intact MTD blocks, which have slid downslope as independent rafts of sediment, not confined or hosted within a more typical debris flow. Sliding is interpreted to have occurred slowly and soon after deposition, with sediment coherency during sliding likely being aided by lithological and diagenetic characteristics as well as lubrication along a mud slurry or water layer upon the decollement surface. The reconstruction of 499 reservoir

blocks provided evidence for basin development and post-rift tectonic adjustments. The process identified a bidirectional sliding motion that suggests rejuvenation and a southward tilt of the MBR, which was likely the trigger of reservoir breakup and sliding. The process also provided evidence for the source of reservoir sands from the northwest, which were likely deposited within a shallow-marine transgressional spit complex at the southern end of an elongated emergent island created by the uplifted MBR during the Eocene.

The mechanisms of sliding along a low-angled decollement, along with the maintained sediment coherency during deformation, provide a high-quality analogue of post-depositional breakup and sliding of reservoir facies. Furthermore, clear DHIs and velocity pushdown effects serve to calibrate MTD lithology and fluid content and are evidence of a working petroleum system. Overall, the reservoir has significant exploration potential focused around the large 100.2 km^2 (39 mi^2) main reservoir block (zone 1). However, any exploration considerations of the wider reservoir area must consider substantial development challenges linked to the separation and isolation of reservoir sections, as well as the additional uncertainty of interblock sediment connectivity.

Acknowledgments

The authors would like to thank Cairn Energy, PLC, for access to seismic data from the Pitu area and for permission to publish images and results herein. The results and opinions expressed within this work are those of the authors and are not a representation of Cairn Energy, PLC. We would also like to thank TGS for the provision of the Baffin Bay two-dimensional regional seismic survey (BBRE11). Finally, we are grateful for software provisions to The University of Manchester that were used within this work from Schlumberger (Petrel), Esri (ArcMap), and Foster Findlay Associates, Ltd. (Geoteric).

References

Aksu, A. E., and Piper, J. W., 1987, Late Quaternary sedimentation in Baffin Bay: Canadian Journal of Earth Sciences, v. 24, no. 9, p. 1833-1846.

Alves, T. M., 2015, Submarine slide blocks and associated soft-sediment deformation in deep-water basins: A review: Marine and Petroleum Geology, v. 67, p. 262-285.

Alves, T. M., Kurtev, K., Moore, G. F., and Strasser, M., 2014, Assessing the internal character, reservoir potential, and seal competence of mass-transport deposits using seismic texture: A geophysical and petrophysical approach: AAPG Bulletin, v. 98, no. 4, p. 793-824.

Alves, T. M., and Lourenço, S. D. N., 2010, Geomorphologic features related to gravitational collapse: Submarine landsliding to lateral spreading on a Late Miocene–Quaternary slope (SE Crete, eastern Mediterranean): Geomorphology, v. 123, p. 13-33.

Bartzke, G., Bryan, K. R., Pilditch, C. A., and Huhn, K., 2013, On the Stabilizing Influence of Silt On Sand Beds: Journal of Sedimentary Research, v. 83, no. 8, p. 691-703.

Bojesen-Koefoed, J. A., Christiansen, F. G., Peter Nytoft, H., and Pedersen, A. K., 1999, Oil seepage onshore West Greenland: evidence of multiple source rocks and oil mixing: Petroleum Geology Conference Series, v. 5, p. 305-314.

Butler, R. W. H., and Turner, J. P., 2010, Gravitational collapse at continental margins: products and processes; an introduction: Journal of the Geological Society, v. 167, p. 569-570.

Cartwright, J. A., Huuse, M., and Aplin, A., 2007, Seal Bypass Systems: AAPG Bulletin, v. 91, no. 8, p. 1141-1166.

Cartwright, J. A., James, D., and Bolton, A., 2003, The genesis of polygonal fault systems: a review: Geological Society Special Publications, v. 216, p. 223-243.

Castagna, J. P., and Sun, S., 2006, Comparison of spectral decomposition methods: First Break, v. 24, no. 3.

Collot, J., Lewis, K., Lamarche, G., and Lallemand, S., 2001, The giant Ruatoria debris avalanche on the northern Hikurangi margin, New Zealand: Result of oblique seamount subduction: Journal of Geophysical Research, v. 106, no. B9, p. 19271-19297.

Cox, D. R., Newton, A. M. W., and Huuse, M., 2020, An introduction to seismic reflection data: acquisition, processing and interpretation, *in* Scarselli, N., Adam, J., and Chiarella, D., eds., Regional Geology and Tectonics - Principles of Geologic Analysis: Amsterdam, Netherlands, Elsevier, p. 744.

Deptuck, M. E., Mosher, D. C., Campbell, D. C., Hughes-Clarke, J. E., and Noseworthy, D., 2007, Along Slope Variations In Mass Failures And Relationships To Major Plio-Pleistocene Morphological Elements, Sw Labrador Sea, *in* Lykousis, V., Sakellariou, D., and Locat, J., eds., Submarine Mass Movements and Their Consequences: Dordrecht, The Netherlands, Springer, p. 37-45.

Dyke, C. G., and Dobereiner, L., 1991, Evaluating the strength and deformability of sandstones: Quarterly Journal of Engineering Geology and Hydrogeology, v. 24, p. 123-134.

Gamboa, D., Alves, T. M., and Cartwright, J. A., 2011, Distribution and characterization of failed (mega)blocks along salt ridges, southeast Brazil: Implications for vertical fluid flow on continental margins: Journal of Geophysical Research, v. 116 B08103, no. B08103, p. 1-20.

Gautier, D. L., Bird, K. J., Charpentier, R. R., Grantz, A., Houseknecht, D. W., Klett, T. R., Moore, T. E., Pitman, J. K., Schenk, C. J., Schuenemeyer, J. H., Sorensen, K., Tennyson, M. E., Valin, Z. C., and Wandrey, C. J., 2009, Assessment of undiscovered oil and gas in the Arctic: Science, v. 324, no. 5931, p. 1175-1179.

Goulty, N. R., 2012, Properties of Polygonal Fault Systems - Fluid Flow, Aligned Arrays and Simple Shear, 74th EAGE Conference and Exhibition incorporating EUROPEC 2012: Copenhagen, EAGE.

Gregersen, G., Knutz, P. C., Nøhr-Hansen, H., Sheldon, E., and Hopper, J. R., 2019, Tectonostratigraphy and evolution of the West Greenland continental margin: Bulletin of the Geological Society of Denmark, v. 67, p. 1-21.

Gregersen, U., Hopper, J. R., and Knutz, P. C., 2013, Basin seismic stratigraphy and aspects of prospectivity in the NE Baffin Bay, Northwest Greenland: Marine and Petroleum Geology, v. 46, p. 1-18.

Gregersen, U., Knutz, P. C., and Hopper, J. R., 2016, New geophysical and geological mapping of the eastern Baffin Bay region, offshore West Greenland: Geological Survey of Denmark and Greenland Bulletin, v. 35, p. 83-86.

Hampton, M. A., Lee, H. J., and Locat, J., 1996, Submarine Landslides: Reviews of Geophysics, v. 34, no. 1, p. 33-59.

Harbitz, C. B., Parker, G., Elverhoi, A., Marr, J. G., Mohrig, D., and Harff, P. A., 2003, Hydroplaning of subaqueous debris flows and glide blocks: Analytical solutions and discussion: Journal of Geophysical Research, v. 108, no. B7, p. 2349.

Henriksen, N., Higgins, A. K., Kalsbeek, F., Christopher, T., and Pulvertaft, R., 2009, Greenland from Archaean to Quaternary: Descriptive text to the 1995 Geological map of Greenland, 1:2500000: Geological Survey of Denmark and Greenland Bulletin, v. 18, p. 1-126.

Huvenne, V. A., Croker, P. F., and Henriet, J. P., 2002, A refreshing 3D view of an ancient sediment collapse and slope failure: Terra Nova, v. 14, no. 1, p. 33-40.

Jackson, C. A.-L., 2011, Three-dimensional seismic analysis of megaclast deformation within a mass transport deposit; implications for debris fl ow kinematics: Geology, v. 39, no. 3, p. 203-206.

Jakobsson, M., Mayer, L., Coakley, B., Dowdswell, J. A., Forbes, S., Fridman, B., Hodnesdal, H., Noormets, R., Pedersen, R., Rebesco, M., Schenke, H. W., Zarayskaya, Y., Accettella, D., Armstrong, A., Anderson, R. M., Beinhoff, P., Camerlenghi, A., Church, I., Edwards, M., Gardner, J. V., Hall, J. K., Hell, B., Hestvik, O., Kristoffersen, Y., Marcussen, C., Mohammad, R., Mosher, D. C., Nghiem, S. V., Pedrosa, M. T., Travaglini, P. G., and Weatherall, P., 2012, The International Bathymetric Chart of the Arctic Ocean (IBCAO) Version 3.0: Geophysical Research Letters, v. 39, p. 1-6.

Japsen, P., Bonow, J. M., Green, P. F., Chalmers, J. A., and Lidmar-Bergstrom, K., 2006, Elevated, passive continental margins: Long-term highs or Neogene uplifts? New evidence from West Greenland: Earth and Planetary Science Letters, v. 248, no. 1-2, p. 330-339.

Kehle, R. O., 1970, Analysis of Gravity Sliding and Orogenic Translation: GSA Bulletin, v. 81, no. 6, p. 1641-1664.

Knutz, P. C., Gregersen, U., and Hopper, J. R., 2012, Late Paleogene Submarine Fans in Baffin Bay and North-West Greenland, 74th EAGE Conference and Exhibition incorporating EUROPEC 2012 Copenhagen, EAGE, p. 5.

Knutz, P. C., Hopper, J. R., Gregersen, U., Nielsen, T., and Japsen, P., 2015, A contourite drift system on the Baffin Bay–West Greenland margin linking Pliocene Arctic warming to poleward ocean circulation: Geology, v. 43, no. 10, p. 907-910.

Knutz, P. C., Newton, A. M. W., Hopper, J. R., Huuse, M., Gregersen, U., Sheldon, E., and Dybkjær, K., 2019, Eleven phases of Greenland Ice Sheet shelf-edge advance over the past 2.7 million years: Nature Geoscience, v. 12, p. 361-368.

Kuijpers, A., Dalhoff, F., Brandt, M., Hümbs, P., Schott, T., and Zotova, A., 2007, Giant iceberg plow marks at more than 1 km water depth offshore West Greenland: Marine Geology, v. 246, no. 1, p. 60-64.

Kvalstad, T. J., Andresen, L., Forsberg, C. F., Berg, K., Bryn, P., and Wangen, M., 2005, The Storegga slide: evaluation of triggering sources and slide mechanic: Ormen Lange–an Integrated Study for Safe Field Development in the Storegga Submarine Area, p. 245-256.

Larsen, L. M., Heaman, L. M., Creaser, R. A., Frei, R., and Hutchinson, M., 2009, Tectonomagmatic events during stretching and basin formation in the Labrador Sea and the Davis Strait: evidence from age and composition of Mesozoic to Palaeogene dyke swarms in West Greenland: Journal of the Geological Society, v. 166, p. 999-1012.

Le Hir, P., Cayocca, F., and Waeles, B., 2011, Dynamics of sand and mud mixtures: A multiprocess-based modelling strategy: Continental Shelf Research, v. 31, no. 10, p. 135-149.

Lee, C., Nott, J. A., and Keller, F. B., 2004, Seismic Expression of the Cenozoic Mass Transport Complexes, Deepwater Tarfaya-Agadir Basin, Offshore Morocco, Offshore Technology Conference: Houston, Texas, USA.

Masson, D. G., Kenyon, N. H., and Weaver, P. P. E., 1996, Slides, debris flows, and turbidity currents, *in* Summerhayes, C. P., and Thorpe, S. A., eds., Oceanography: an illustrated guide: Boca Raton, Florida, CRC Press.

Meckel, T., 2010, Classifying and Characterizing Sand-Prone Submarine Mass-Transport Deposits: Search and Discovery Article #50270, no. 50270.

Minisini, D., Trincardi, F., Asioli, A., Canu, M., and Foglini, F., 2007, Morphologic variability of exposedmass-transport deposits on the eastern slope of Gela Basin (Sicily channel): Basin Research, v. 19, p. 217-240.

Mohrig, D., Ellis, C., Parker, G., Whipple, K. X., and Hondzo, M., 1998, Hydroplaning of subaqueous debris flows: GSA Bulletin, v. 110, no. 3, p. 387-394.

Morris, W. R., and Busby-Spera, C. J., 1988, Sedimentologic Evolution of a Submarine Canyon in a Forearc Basin, Upper Cretaceous Rosario Formation, San Carlos, Mexico: AAPG Bulletin, v. 72, no. 6, p. 717-737.

Newton, A. M. W., Knutz, P. C., Huuse, M., Gannon, P., Brocklehurst, S. H., Clausen, O. R., and Gong, Y., 2017, Ice stream reorganization and glacial retreat on the northwest Greenland shelf: Geophysical Research Letters, v. 44, p. 7826-7835.

Nissen, S. E., Haskell, N. L., Steiner, C. T., and Coterill, K. L., 1999, Debris flow outrunner blocks, glide tracks, and pressure ridges identified on the Nigerian continental slope using 3-D seismic coherency: The Leading Edge, v. 18, no. 5, p. 595-599.

Oakey, G. N., 2005, Cenozoic Evolution and Lithosphere Dynamics of the Baffin Bay - Nares Strait Region of Arctic Canada and Greenland [PhD: Vrije Universiteit Amsterdam, 233 p.

Oakey, G. N., and Chalmers, J. A., 2012, A new model for the Paleogene motion of Greenland relative to North America: Plate reconstructions of the Davis Strait and Nares Strait regions between Canada and Greenland: Journal of Geophysical Research, v. 117, no. B10, p. 1-28.

Omosanya, K. O., and Alves, T. M., 2013, A 3-dimensional seismic method to assess the provenance of Mass-Transport Deposits (MTDs) on salt-rich continental slopes (Espírito Santo Basin, SE Brazil): Marine and Petroleum Geology, v. 44, p. 223-239.

Planke, S., Symonds, P. A., Alvestad, E., and Skogseis, J., 2009, Mid-Cretaceous source rock subcropping in the Baffin Bay: GEO ExPro, v. 6, p. 1-8.

Posamentier, H. W., 2004, Seismic Geomorphology: Imaging Elements of Depositional Systems from Shelf to Deep Basin Using 3D Seismic Data: Implications for Exploration and Development, *in* Davies, R. J., Cartwright, J. A., Stewart, S. A., Lappin, M., and Underhill, J. R., eds., 3D Seismic Technology: Application to the Exploration of Sedimentary Basins: London, Geological Society of London, p. 11-24.

Posamentier, H. W., Davies, R. J., Cartwright, J. A., and Wood, L., 2007, Seismic geomorphology- an overview, *in* Davies, R. J., Posamentier, H. W., Wood, L., and Cartwright, J. A., eds., Seismic Geomorphology: Applications to Hydrocarbon Exploration and Production: London, Geological Society of London, p. 1-14.

Prior, D. B., Bornhold, B. D., and Johns, M. W., 1984, Depositional Characteristics of a Submarine Debris Flow: The Journal of Geology, v. 92, no. 6, p. 707-727.

Raynal, O., Bouchette, F., Certain, R., Seranna, M., Dezileau, L., Sabatier, P., Lofi, J., Bui Xuan Hy, A., Briqueu, L., Pezard, P., and Tessier, B., 2009, Control of alongshore-oriented sand spits on the

dynamics of a wave-dominated coastal system (Holocene deposits, northern Gulf of Lions, France): Marine Geology, v. 264, no. 3-4, p. 242-257.

Rider, M., and Kennedy, M., 2011, The geological interpretation of well logs, Edinburgh, Rider-French Consulting Ltd., 432 p.:

Rusconi, F. J., McGilvery, T. A., and Liner, C. L., 2018, Tracks, Outrunner Blocks, and Barrier Scours: 3-D Seismic Interpretation of a Mass Transport Deposit in the Deepwater Taranaki Basin of New Zealand, ACE 2018 Annual Convention & Exhinition: Salt Lake City, Utah, USA.

Shipp, R. C., Weimer, P., and Posamentier, H. W., 2011, Mass transport deposits in deepwater settings: an introduction, *in* Shipp, R. C., Weimer, P., and Posamentier, H. W., eds., Mass transport deposits in deepwater settings: Darlington, Society of Sedimentary Geology.

Soutter, E. L., Kane, I. A., and Huuse, M., 2018, Giant submarine landslide triggered by Paleocene mantle plume activity in the North Atlantic: Geology, v. 46, no. 6, p. 511-514.

Sun, Q., Alves, T. M., Xie, X., He, J., Li, W., and Ni, X., 2017, Free gas accumulations in basal shear zones of mass-transport deposits (Pearl River Mouth Basin, South China Sea): An important geohazard on continental slope basins: Marine and Petroleum Geology, v. 81, p. 17-32.

Swift, D. J. P., 1968, Coastal Erosion and Transgressive Stratigraphy: The Journal of Geology, v. 76, no. 4, p. 444-456.

Umpleby, D., 1979, Geology of the Labrador shelf: Geological Survey of Canada, v. 79-13, p. 1-41.

Weimer, P., and Shipp, C., 2004, Mass Transport Complex: Musing on Past Uses and Suggestions for Future Directions Offshore Technology Conference: Houston, Offshore Technology Conference.

Welford, K., Peace, A., Geng, M., and Dickie, K., 2018, Crustal structure of Baffin Bay from constrained 3-D gravity inversion and deformable plate tectonic models: Geophysical Journal International, v. 214, no. 2, p. 1281-1300.

Whittaker, R. C., Hamann, R. E., and Pulvertaft, T. C. R., 1997, A New Frontier Province Offshore Northwest Greenland: Structure, Basin Development, and Petroleum Potential of the Melville Bay Area: AAPG Bulletin, v. 81, no. 6, p. 978-998.

Wright, K., Nice, R., Tazzi, M., Purnell, K., and Penasse, V., 2018, Spectral decomposition: an aid in characterizing field architectures of the Laggan and Tormore fields, Faroe–Shetland Basin: Geological Society, London, Petroleum Geology Conference series, v. 8, no. 1, p. 525-535.

3

Melville Bay Petroleum Systems: Shallow Gas and Gas Hydrates

Preamble

DRC interpreted the data, wrote the manuscript and drafted the figures presented in this chapter. MH and AMWN gave input into interpretations, the development of analytical methods, as well as the final manuscript. ADS provided input towards conducting geothermal gradient and heat flow estimations and writing those sections of the manuscript. PKN gave input and advice towards interpretations as well as providing a detailed review of the final manuscript.

This manuscript is published in the journal *Marine Geology*:

Cox, D. R., Huuse, M., Newton, A. M.W., Sarkar, A. D., and Knutz, P. C., 2021, Shallow gas and gas hydrate occurrences on the northwest Greenland shelf margin, Marine Geology, v. 432, pp. 1-21.

Shallow Gas and Gas Hydrate Occurrences on the Northwest Greenland Shelf Margin

David R. Cox[1], Mads Huuse[1], Andrew M. W. Newton[1, 2],

Arka D. Sarkar[1] and Paul C. Knutz[3]

[1]Department of Earth and Environmental Sciences, The University of Manchester

[2]School of Natural and Built Environment, Elmwood Building, Queens University Belfast, University Road, UK, BT7 1NN

[3]Geophysics Department, Geological Survey of Denmark and Greenland, Øster Voldgade 10, DK-1350 Copenhagen K, Denmark

Abstract

Industrial 3D seismic data are used to investigate the contemporary hydrocarbon distribution and historical fluid migration in Melville Bay offshore northwest Greenland. Gas-related amplitude anomalies and an extensive bottom simulating reflector (BSR) were mapped within the uppermost 1-2 km of stratigraphy to define the first inventory of shallow gas and gas hydrate along this part of the Greenland margin. The shallow gas anomalies vary in seismic character and have been subdivided into four categories that represent (I) isolated shallow gas, (II) free gas trapped at the base of the gas hydrate stability zone (GHSZ), (III) gas charged glacial clinoforms and (IV) a giant mass transport deposit gas reservoir. Gas hydrate deposits have been identified across an area of 537 km^2 via the identification of a discontinuous BSR that marks the base of the GHSZ. The BSR has been used to estimate a geothermal gradient of 49 °C/km across the GHSZ and a heat flow of 70-90 mW/m^2, providing the first publically available heat flow estimates offshore western Greenland. The contemporary hydrocarbon distribution and historical fluid migration is influenced by the underlying paleo-rift topography and multiple shelf edge glaciations since ~2.7 Ma. Continued uplift of the Melville Bay Ridge, as well as glacial-sediment redistribution and basinward margin tilting from isostatic compensation, have led to a concentration of hydrocarbons within the Cenozoic stratigraphy above the ridge. Furthermore, repeated variations in subsurface conditions during glacial-interglacial cycles

likely promoted fluid re-migration, and possibly contributed to reservoir leakage and increased fluid migration through faults. The top of the gas hydrate occurrence at 650 m water depth is well below the hydrate-free gas phase boundary (~350 m) for the present bottom-water temperature of 1.5 °C, suggesting this hydrate province mainly adjusted to glacial-interglacial changes by expansion and dissociation at its base and is relatively inert to current levels of global warming. This glacial-related dissociation may have significantly contributed to the numerous free gas accumulations observed below the GHSZ at present day.

3.1. Introduction

Gas-rich sediments have been documented on most continental shelf margins worldwide (Fleischer et al., 2001), with these accumulations predominantly representing thermogenically or biogenically generated shallow gas or gas hydrate deposits (Floodgate and Judd, 1992; Kvenvolden, 1993; Minshull et al., 2020; Schoell, 1988; Stopler et al., 2014). These deposits have attracted considerable interest over the last few decades as they: (1) represent potential drilling hazards (McConnell et al., 2012; Merey, 2016; Prince, 1990); (2) can impact the stability of seafloor sediments (Brown et al., 2006; Yang et al., 2018); (3) have been considered as a future lower-carbon energy source (Collett et al., 2009; Demirbas, 2010; McGlade and Ekins, 2015); (4) can be used to indirectly estimate shallow geothermal gradient and heat flow through identified bottom simulating reflectors (BSRs) (Dickens and Quinby-Hunt, 1994; Grevemeyer and Villinger, 2001); and (5), since methane is a powerful greenhouse gas, hydrate dissociation may pose a positive feedback mechanism for global climate warming, especially when found in relatively shallow water depths (Karisiddaiah and Veerayya, 1994; Krey et al., 2009; Ruppel and Kessler, 2017; Zhao et al., 2017).

For these reasons, it is important to document and understand the distribution of shallow gas and gas hydrates, especially within high latitude environments sensitive to environmental change (Portnov et al., 2016). Understanding high latitude hydrocarbon systems can be difficult, however, as glaciations during the Pliocene-Pleistocene may have significantly influenced fluid migration (Goffey et al., 2016; Medvedev et al., 2019). The redistribution of sediment across glaciated margins, along with repeated ice loading and unloading on the shelf through glacial-interglacial cycles, can cause substantial structural changes, isostatic compensation, and significant variations in subsurface conditions (Fjeldskaar and Amantov, 2018; Zieba and Grover, 2016). These changes often promote the re-migration of hydrocarbons, through processes such as fault reactivation, trap spill and seal breach, potentially leading to expulsion at the seabed into the water column

(Goffey et al., 2016; Kjemperud and Fjeldskaar, 1992; Ostanin et al., 2017). Gas hydrate stability is also affected by variations in subsurface temperature and pressure (Kvenvolden, 1993), such as those related to glacial (un)loading, and can possibly lead to dissociation of hydrate at the seabed (Andreassen et al., 2017; Grassmann et al., 2010). Attempting to understand this cryosphere-methane interaction may reveal the sensitivity of gas hydrate deposits to environmental change; providing critical insight into how these deposits may respond to future oceanic warming (Biastoch et al., 2011; Krey et al., 2009; Ruppel and Kessler, 2017).

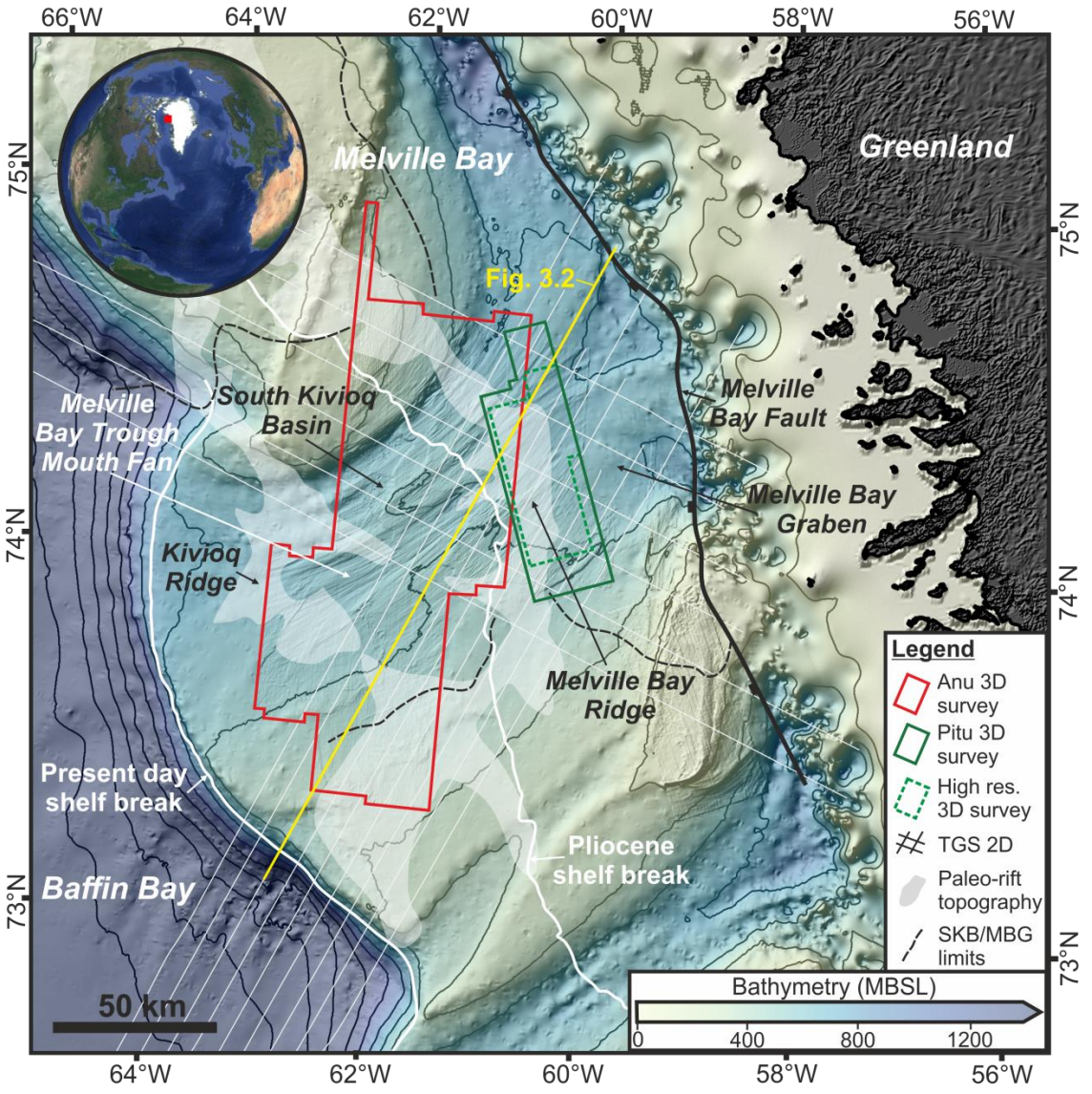

Figure 3.1. Location Map | Bathymetric map from Newton et al. (2017) of the Melville Bay region offshore northwest Greenland (see insert map), displaying the location of seismic data as well as the influence of repeated glaciations on margin architecture. Black labels indicate the location of paleo-rift topography and deep rift basins across the shelf. SKB = South Kivioq Basin. MBG = Melville Bay Graben.

The Melville Bay continental margin, offshore northwest Greenland, has experienced multiple episodes of ice sheet advance and retreat across the shelf since ~2.7 Ma, with

sediment redistribution contributing to ~100 km of shelf edge progradation (Figs. 3.1 and 3.2) (Knutz et al., 2019; Newton et al., 2020; 2017). The region is thought to contain hydrocarbon systems (Bojesen-Koefoed, 2011; Gregersen et al., 2013; Whittaker et al., 1997) that were likely impacted by these glaciations. Here, extensive 3D seismic reflection data acquired for petroleum exploration are used to document the structure, stratigraphy and hydrocarbon occurrence across the glaciated margin of Melville Bay. The data coverage and mapping provides the most widespread and high-resolution imaging of the subsurface and hydrocarbon anomalies along the west coast of Greenland, as well as the most northerly documentation of gas hydrates in Baffin Bay (Minshull et al., 2020; Nielsen et al., 2014). The primary objectives were to address: (1) Have hydrocarbons accumulated within shallow, post-rift sediments on the Melville Bay shelf; (2) What does the seismic character and distribution of observed hydrocarbon occurrences tell us about migration history; and (3) How have these accumulations been affected by recent glaciations? In addition to answering these questions, the analysis contributes to the wider understanding of Arctic gas hydrates, the West Greenland subsurface thermal regime and shallow subsurface drilling hazards for the upcoming IODP Leg (909) (Knutz et al., 2018).

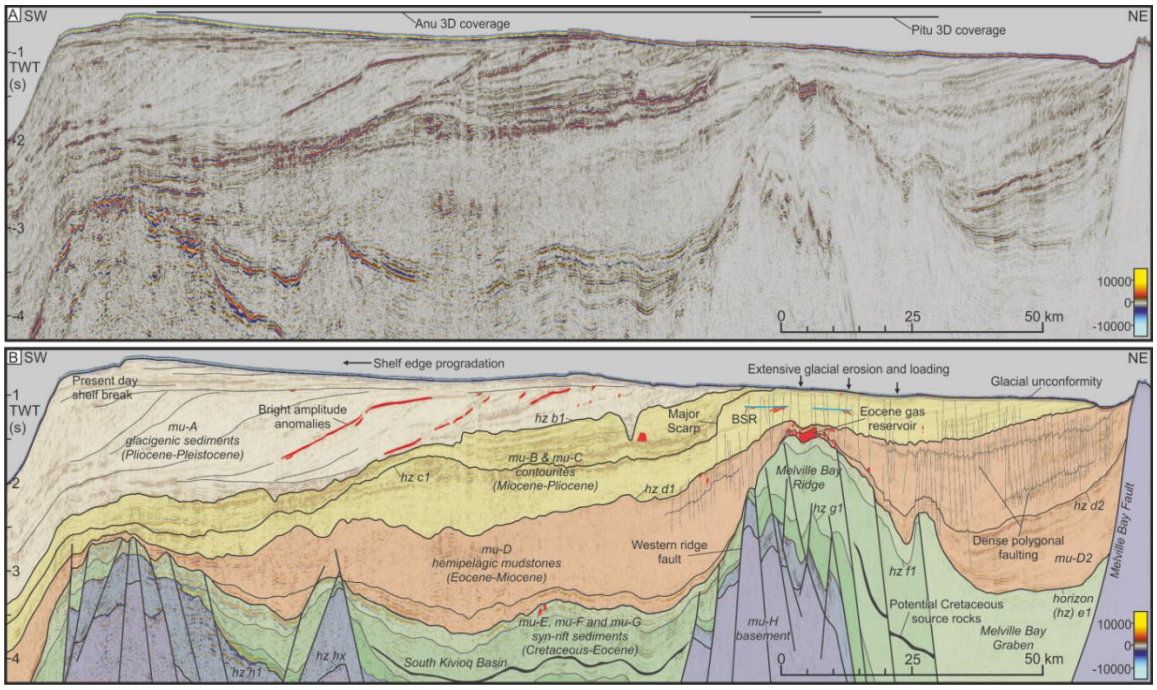

Figure 3.2. Regional stratigraphy | (A) Uninterpreted regional 2D seismic reflection line in two-way-time, displaying the stratigraphy across the Melville Bay continental shelf. (B) An interpreted version of (A) defining the character of the regional stratigraphy including deep rift basins, the prominent Melville Bay Ridge and the thick package of glacigenic sediments. Nine seismic mega-units (mu-H to -A) as well as top unit horizons (horizon hx to b1) are defined, based on Gregersen (2013; 2017) and Knutz et al. (2015). The occurrence of potential seismic fluid anomalies, faults and possible organic rich Cretaceous strata are also shown. The location of the seismic line is shown on Fig. 3.1.

3.2. Regional Setting

Baffin Bay represents a large marginal sea between Greenland and Canada that formed during the early phase (Paleocene-Eocene) of North Atlantic opening (Gregersen et al., 2013; Oakey and Chalmers, 2012). Melville Bay is located in northeast Baffin Bay and overlies large areas of the northwest Greenland rifted continental margin (Fig. 3.1). The shelf area of Melville Bay is characterised by deep sedimentary basins, with thicknesses >10 km, separated by extensive elongate ridges (Gregersen et al., 2019; Whittaker et al., 1997), with this complex paleo-rift topography overlain by a thick (1-3 km) Cenozoic post-rift succession (Fig. 3.2) (Gregersen et al., 2013; Knutz et al., 2012; 2015; 2019).

3.2.1. Stratigraphic Framework

The rift and post-rift succession of the northwest Greenland continental margin has been mapped extensively and subdivided into seven seismic mega-units (mu) (A-G) bounded by regional horizons with up-dip unconformable expressions (Gregersen et al., 2013; 2016; Knutz et al., 2015) (Fig. 3.2). This regional seismic-stratigraphic framework for West Greenland has been adopted as a basis for a detailed 3D seismic analysis of the uppermost (1-2 km) stratigraphic packages.

Proterozoic aged basement (mu-H) underlies Early Cretaceous-early Paleocene syn-rift sedimentary rocks that make up mu-G and –F (Cox et al., 2020a; Gregersen et al., 2019; 2013). These sediments likely consist of marine mudstones intercalated with sandy deposits, as well as possible organic shales (source rocks) within mu-F, which may have been deposited during a period of rift quiescence during the Cenomanian-Turonian (Bojesen-Koefoed et al., 1999; Cox et al., 2020a; Nohr-Hansen et al., 2018; Planke et al., 2009).

The oldest section of the post-rift succession is represented by mu-E and consists mainly of hemipelagic marine mudstones intercalated with submarine fan deposits (Knutz et al., submitted). The mu-E succession was deposited during the seafloor spreading phase of Baffin Bay (syn-drift), followed by mu-D, of likely late Eocene to early-middle Miocene age. The lower part of mu-D consists of asymmetric wedges of submarine fans that possibly formed as a result of inversion as Greenland and North America converged and spreading in Baffin Bay ceased (Knutz et al., 2012; submitted). The upper part of mu-D displays a hemipelagic infill character, presumably with a high clay content facilitating the development of polygonal fault networks (Goulty and Swarbrick, 2005). Mu-D thins significantly above the crest of the Melville Bay Ridge (MBR) and is top bounded by a regional unconformity (horizon d1) (Fig. 3.2) (Cox et al., 2020a; Gregersen et al., 2019; Knutz et al., 2012). This thinning package represents the seal for a gas-charged mass

transport deposit covering 420 km^2 of the MBR crest (within mu-D2) (Fig. 3.2). The reservoir displays seismic characteristics interpreted as direct hydrocarbon indicators and was likely deposited as a shallow marine spit complex along the ridge axis during the Eocene (Cox et al., 2020a). Reservoir deformation and transport occurred along a muddy décollement layer that represents horizon e1; an important unconformity that marks the top of the MBR structure and the transition from syn- to post-rift sedimentation (Gregersen et al., 2019).

On the inner shelf, the uppermost post-rift succession consists of extensive, thick marine sediment packages that were deposited during the late Miocene and Pliocene (mu-C and mu-B) (Knutz et al., 2015) (Fig. 3.2), and have been heavily truncated by glacial erosion. Mu-C, which buried the MBR, is interpreted as a deep shelf drift accumulation influenced by northward flowing ocean currents (Knutz et al., 2015; 2019). Mu-B is considered mainly Pliocene in age and displays mounded and wavy depositional features that preferentially infilled erosional scarps where large parts of mu-C had been removed (Fig. 3.2). Basinward, the contourite accumulations and their correlative downslope mass transport deposits are buried progressively deeper by the thick glacigenic packages of mu-A corresponding to the Melville Bay Trough Mouth Fan (Knutz et al., 2019) (Fig. 3.2). The progradational succession of mu-A has been subdivided into 11 units reflecting deposition by migrating ice-streams since the late Pliocene (Knutz et al., 2019; Newton et al., 2020).

3.2.2. Structural Framework

The paleo-rift topography consists of northwest-southeast trending elongate ridges formed during Early Cretaceous to early Paleogene syn-rift phases (Figs. 3.2 and 3.3) (Gregersen et al., 2013; 2016; Larsen et al., 2009; Whittaker et al., 1997). The Kivioq Ridge, located beneath the present outer shelf margin, and the MBR, separate the main depocentres of the Melville Bay Graben and South Kivioq Basin (Figs. 3.2 and 3.3) (Cox et al., 2020a; Gregersen et al., 2013; 2016; Knutz et al., 2015). The ~200 km long MBR has continued as a positive relief feature into the Neogene, long after rifting ceased in the late Eocene/early Oligocene (Oakey and Chalmers, 2012; Welford et al., 2018). Consequently, the flanks of the MBR are onlapped and in parts draped by both syn- and post-rift sedimentary successions (Fig. 3.2) with potential implications for regional fluid migration.

The MBR and Kivioq Ridge are characterised by numerous internal and ridge bounding deep tectonic normal faults generally oriented parallel to the ridge strike (Figs. 3.2 and 3.3) (Gregersen et al., 2019). The MBR formed as an elongate tilted fault block, with large offsets and disconnected syn-rift stratigraphy on its western flank adjoining the ‘western

ridge fault' (Figs. 3.2 and 3.3). This is contrasted by a steeply dipping stratigraphy to the east that continues into the Melville Bay Graben (Figs. 3.2 and 3.3).

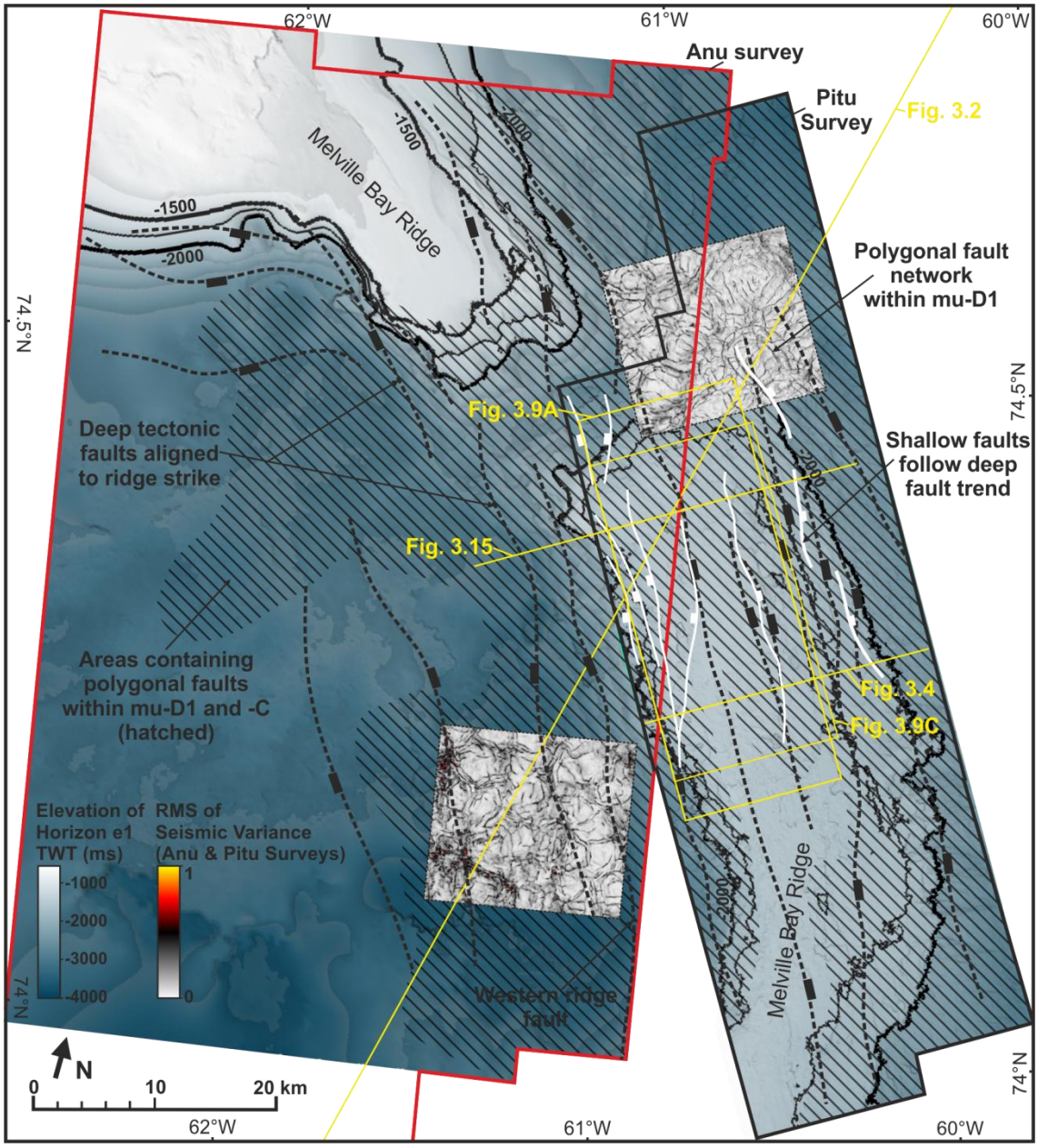

Figure 3.3. Structural Framework | A two-way-time structure map of horizon e1 has been used to define the location of the Melville Bay Ridge. The location of deep tectonic faults (black) (including the western ridge fault) and post-rift faults (white) are shown, with the faults observed to strike parallel to ridge strike. Two windows (to scale) displaying seismic variance time slices from depths of 1600 ms TWT (Pitu) and 2230 ms TWT (Anu), display a network of thin, curvilinear high amplitude features that represent the polygonal fault network that exists within mu-D and -C, with the location of these faults across the area shown by the diagonal hatch. The location of Figs. 3.4, 3.9A, 3.9C, 3.15 and a section of 3.2 are shown.

The deep pre- and syn-rift tectonic faults extend vertically to the horizon e1 unconformity marking the MBR apex (Fig. 3.2) (Gregersen et al., 2019). This horizon acts as a boundary between the deeper faults and a dense fault network within the post-rift stratigraphy (above horizon d2; Fig. 3.2). As well as tectonic faults, the 3D seismic mapping

revealed that a large proportion of post-rift faults, especially within the grabens, exist as closely spaced, short offset faults that likely represent an intra-formational polygonal fault network formed by compactional processes, e.g. shale dewatering and diagenesis, (Figs. 3.2 and 3.3) (Cartwright and Dewhurst, 1998; Cox et al., 2020a). A neo-tectonic influence on the ridge complex is suggested by the observation that faults intersecting mu-D and -C over the ridge flanks often extend from deeper structural features (Fig. 3.2).

3.3. Material and Methods

3.3.1. Seismic and Velocity Data

The main database for this study consists of two 3D seismic reflection datasets and one regional 2D seismic reflection grid that covers much of the continental shelf in Melville Bay (Fig. 3.1). The first 3D seismic reflection survey (Pitu) was acquired by Cairn Energy in 2011 and covers an area of 1,672 km^2. It is provided in two-way time (TWT) down to 6.5 seconds and was acquired using 93 3D acquisition lines with 25 x 12.5 m bin spacing and a line separation of 1 km. A 25 m shot point interval (flip flop) was used with a 50 m source separation creating a common-mid-point fold of 70. Ten 7050 m long streamers were used, each with 564 channels and towed at a depth of 20 m. The dominant frequency varies with depth but is 28 Hz at approximately 1500 ms TWT, producing a dominant wavelength of 71 m (using an average velocity of 2.0 km/s) and a vertical resolution of 18 m. The reprocessing of this survey in 2013 provided a sub-set high resolution 3D seismic survey in TWT (Pitu HR survey) that covers an area of 1,135.5 km^2 down to 5 seconds TWT. The resolution of the data has been improved to a spatial resolution of 12.5 m (inline) x 6.25 m (crossline) and a vertical resolution of 11 m at the same stratigraphic interval (~1500 ms TWT) due to a dominant frequency of 45 Hz and a dominant wavelength of 44 m.

The processing of the Pitu survey involved noise attenuation and filtering, 3D deconvolution, Pre-Stack Depth Migration (PSDM), post-migration velocity analysis and a parabolic radon de-multiple process. An understanding of the velocity field was gained during the PSDM of the full survey, which involved an iterative velocity investigation including multi-layer tomography to minimise residual move-out, stack scanning to help flatten irregular unconformities and finally Kirchhoff pre-stack Tilted Transverse Isotropy (TTI) depth migration, creating a depth domain volume which was subsequently converted into the time domain. This process produced an interval velocity cube based solely on seismic velocities (Fig. 3.4) as well as a depth domain seismic volume down to 10 km. An assessment of the accuracy of both the depth conversion and interval velocity cube is not possible as no calibration data (such as boreholes) exist in the area for comparison.

However, interval velocity variations show a good correlation to both regional 2D stacking velocities and the location of regional unconformities (where rapid increase in velocity may be expected), such as at the top of the MBR (horizon e1) (Fig. 3.4).

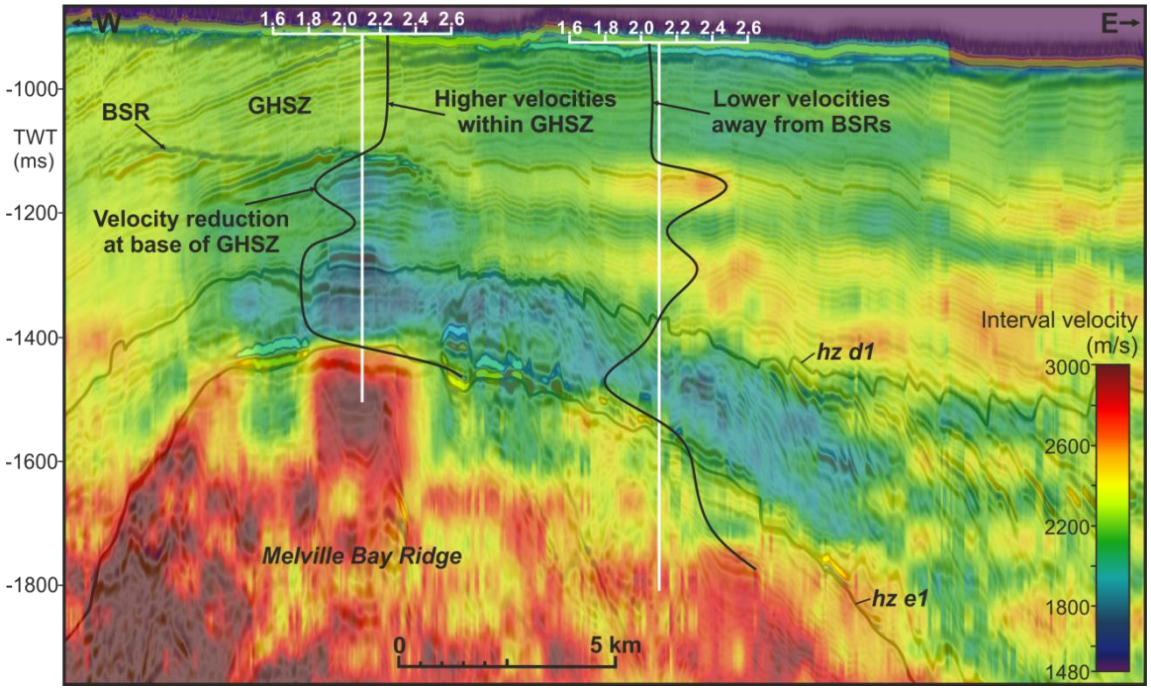

Figure 3.4. Interval velocity | Seismic cross section from the Pitu HR survey demonstrating the relationship between seismic stratigraphy, interval velocity and potential gas hydrate deposits. The seismic amplitudes are overlain by a semi-transparent cross section displaying the corresponding interval velocity. Key seismic horizons and a bottom simulating reflector (BSR), marking the base of the gas hydrate stability zone (GHSZ), are indicated. 1D interval velocity profiles display the variation of velocity through the GHSZ and the adjacent stratigraphy. The cross section location is shown on Fig. 3.3.

The second 3D seismic reflection survey (Anu) was acquired by Shell in 2013 over an area of 8700 km^2 (Fig. 3.1). It is provided in TWT down to 7.5 seconds and was acquired using 118 sail lines with a 50 m (cross-line) x 6.25 m (inline) bin spacing and a line separation of 600 m. The acquisition used a dual vessel set-up with six, 7050 m long streamers (each with 564 channels) that were separated by 200 m and towed at a depth of 10 (front end) to 15 m (tail end). Two sources were separated by 100 m at a depth of 8 m and were fired using a shot point interval (flip flop) of 25 m, producing a nominal fold coverage of 70. The processing workflow included noise and acquisition footprint attenuation processes, multiple removal using both 3D surface related multiple reflection (SRME) and 2D model-based water-layer de-multiple (MWD) modelling, a 1 km migration velocity analysis and a final isotropic Kirchhoff pre-stack time migration (PSTM). This produced a volume with a dominant frequency of 30 Hz at approximately 1500 ms TWT, a dominant wavelength of 67 m (using an average velocity of 2.0 km/s) and a vertical resolution of 17 m.

The 15 lines of 2D seismic reflection data used were acquired by TGS between 2007 and 2009 and form part of the Baffin Bay 2D (BBRE11) regional dataset (Fig. 3.1). The lines used here cover 5,038 km and were acquired using a single 6000 m streamer with 480 channels, 12.5 m intervals and a sampling rate of 2 ms, as well as a 2000 psi source with a 25 m interval at a gun depth of 8 m, yielding a 120-fold stack. The survey was reprocessed in 2011 to boost low frequencies and enhance resolution, specifically targeting multiple and bubble pulse attenuation. The processing sequence involved a 2 km Kirchhoff pre-stack curved ray time migration and velocity analysis within this process produced stacking velocity data for each 2D line.

All data used were provided in SEG normal polarity with a downward increase in acoustic impedance (such as at the seabed) represented by a red positive peak and a downward decrease in acoustic impedance represented by a blue negative trough (Fig. 3.5). No well data were available within the area of interest.

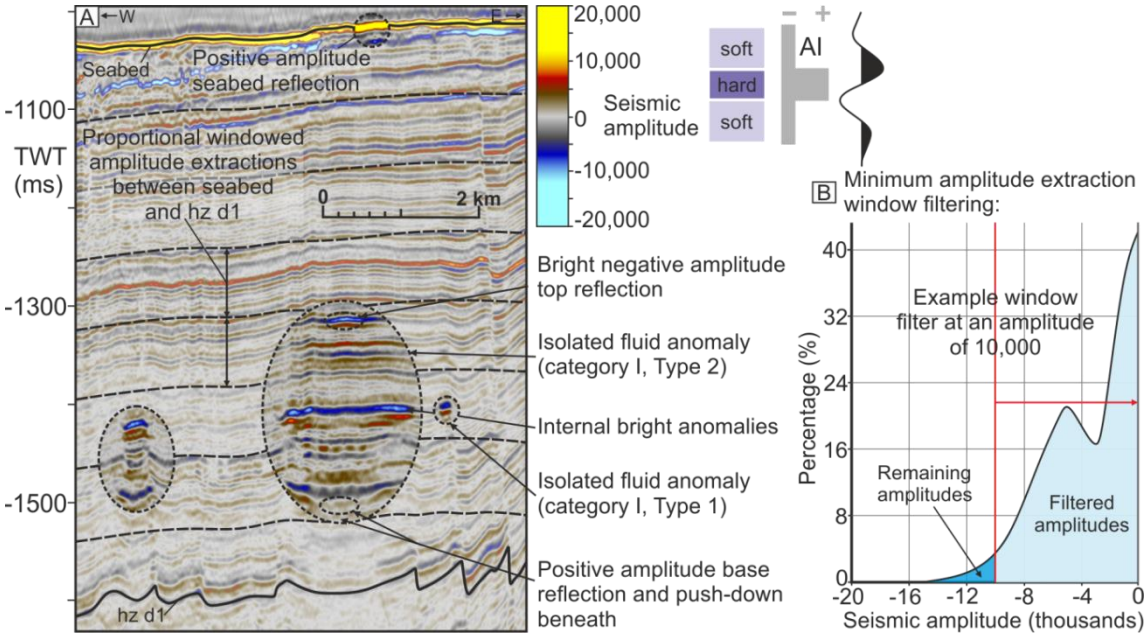

Figure 3.5. Anomaly detection | A seismic cross section (A) illustrating the method of using proportional minimum amplitude extraction windows to identify shallow gas anomalies. Examples of isolated anomalies are shown (category I). The polarity of seismic data used in this study is shown with an increase in acoustic impedance at the seabed representing a positive amplitude brown-red-yellow peak. The location of the line is shown on Fig. 3.7. (B) Histogram of the amplitude distribution from an extracted minimum amplitude window, demonstrating the filtering process for isolating the seismic signal most likely representing shallow gas occurrences.

3.3.2. Interpretation Methods

The regional structural and stratigraphic framework (Gregersen et al., 2013; 2016; Knutz et al., 2015) was propagated through the 3D seismic data using Schlumberger's

Petrel software and standard 3D seismic interpretation techniques (Cox et al., 2020c; Posamentier, 2004; Posamentier et al., 2007). This study focused on the mapping of features such as seismic discontinuities and amplitude anomalies that could be linked with fluid migration and hydrocarbon accumulations (Hilterman, 2001). Analysis of such features found that likely gas-related anomalies often displayed seismic amplitudes larger than -10,000 (Fig. 3.5), although dimmer anomalies may also comprise shallow gas accumulations associated with saturations of less than 10%, poorer reservoir quality or thin-bed effects (Hilterman, 2001), and this was considered when filtering results. Using this understanding of anomaly amplitude, automated anomaly detection and filtering was applied to the 3D data via the method described in Cox et al. (2020b) (Fig. 3.5). The individual scrutiny of each anomaly within the filtered results was then conducted to determine whether that anomaly was in fact fluid-related or created by another feature.

Non-fluid-related bright 'soft' amplitude anomalies may represent features such as high porosity, low density and low velocity (i.e. low acoustic impedance) stratigraphic layers such as diatomaceous ooze or coal beds, organic-rich claystones, and data acquisition footprint (stronger near the seabed) (Cox et al., 2020b). Distinguishing between fluid-related and lithology-related anomalies, for example those created by low density oozes which may create similar amplitudes, is sometimes difficult, but can usually be distinguished based on context as lithological variations are more often stratigraphically restricted and more widespread, e.g. Batchelor et al. (2017). This evaluation is therefore somewhat subjective, increasing uncertainty, and this should be considered in the final result. Additionally, high saturation gas anomalies have likely been detected efficiently through this process, but the number of fluid-related anomalies may be underestimated, as very thin (few metres) or very low saturation gas pockets (<<5%), causing only low amplitude seismic anomalies, may have been omitted.

3.3.3. Geothermal Gradient and Heat Flow Calculations

Near surface geothermal gradient and heat flow were estimated across part of the Pitu 3D seismic survey area using an identified BSR that is thought to represent the base of the gas hydrate stability zone (GHSZ) (Dickens and Quinby-Hunt, 1994; Grevemeyer and Villinger, 2001). Gas hydrate stability is influenced by fluid composition, pressure and temperature conditions (Kvenvolden, 1993), and the estimation requires key parameters including temperature at the seabed and BSR, as well as the thermal conductivity of the shallow gas hydrate hosting sediments (Grevemeyer and Villinger, 2001; Minshull and Keddie, 2010). These parameters are often provided by seabed and downhole temperature probes and logging data. However, no such data exist in northeast Baffin Bay, so these

essential parameters have to be either extracted from interpolated global databases or from published gas hydrate stability models and empirical relationships using the constraints provided by the seismic data (TWT and depth of seabed and BSR, interval velocity of the GHSZ).

Estimating parameters in such ways creates uncertainty - e.g. estimating heat flow without direct temperature data is thought to cause an error of 20% or above, whilst the estimation of thermal conductivity through empirical relationships instead of seabed measurements, can cause errors of 5-30% (Grevemeyer and Villinger, 2001; Minshull, 2011). Other uncertainties arise from seismic interpretation errors, velocity model creation and depth conversion and uncertainty of the true phase boundary depth, due to an unknown composition of pore water and hydrate (other gases such as hydrogen sulphide or higher order hydrocarbons can affect the phase boundary) (Grevemeyer and Villinger, 2001; Minshull, 2011; Minshull and Keddie, 2010). Error resulting from these uncertainties is often over 10%, with the compound uncertainty being potentially large (e.g. > 50% cf. Grevemeyer and Villinger 2001), but in areas where no data exist, an estimate with recognised uncertainty is better than no information at all. The geothermal gradient and heat flow were estimated using the procedure described by several authors (Dickens and Quinby-Hunt, 1994; Grevemeyer and Villinger, 2001; Yamano et al., 1982) and used within a number of similar studies (Calves et al., 2010; Minshull and Keddie, 2010; Serié et al., 2017; Shankar et al., 2010).

It was assumed that hydrate gas is pure methane and the pore water exhibits normal sea-water salinity – this is the most commonly observed scenario and thus a typical assumption when no borehole data are available (Dickens and Quinby-Hunt, 1994; Shankar et al., 2010). There is a chance of higher order hydrocarbons, with the hydrate forming gas potentially sourced from Cretaceous marine source rocks (Cox et al., 2020a; Nohr-Hansen et al., 2018), however, no 'double-BSR' is observed that may suggest the presence of three fluid phases (Andreassen et al., 2000; Geletti and Busetti, 2011). The first step was to interpret the seabed and the BSR on the Pitu depth domain seismic. The pressure (ϱ) at the BSR was then calculated using Equation 1, which represents a standard hydrostatic pressure equation (Dickens and Quinby-Hunt, 1994). This used an estimated seawater density of 1034 kg/m^3 for relatively deep, saline and cold ocean bottom waters on the Melville Bay shelf provided by Tang et al. (2004). The pressure equation assumes hydrostatic pressure at the BSR depth and therefore depth is measured from mean sea level.

Equation 1: $\text{BSR Pressure } (\rho) = (1034 * 9.81 * \text{BSR Depth})/-1000000$

Units: Seawater density = 1034 kg/m^3 Gravity = 9.81 m/s^2
Megapascals (MPa) conversion = 1000000

The temperature at the BSR was estimated from the calculated pressure using Equation 2. This equation is based on an empirical relationship between pressure and dissociation temperature, defined by experimental data for various methane hydrate stability conditions, with a regression showing a Chi-squared of >0.99 (Dickens and Quinby-Hunt, 1994). Equation 2 represents this empirical relationship rearranged to find the dissociation temperature for any pressure between 2.5-10 MPa. The only variable in the equation is pressure, with the values 0.00379 and 0.000283 representing constants derived from the original empirical relationship.

Equation 2: $\text{BSR Temperature} = (1/((0.00379) - (0.000283 * \text{Log}(\text{BSR Pressure})))) - 273$

Units: BSR Pressure (ρ) = MPa °C conversion = -273

The temperature change across the GHSZ was then calculated by subtracting the seabed temperature which was estimated from the world ocean temperature database (Locarnini et al., 2013), showing an annual mean temperature of ~1.5 °C for ocean bottom waters at this depth (~650 m) across Melville Bay. The seabed elevation varies in depth by ~100 m across the BSR area and therefore, this temperature may vary slightly (less than 0.5 °C), translating to a BSR temperature error of < +/- 0.2 °C. The temperature difference across the GHSZ was then divided by the thickness (in metres) (Equation 3) to calculate the Geothermal Gradient (Dickens and Quinby-Hunt, 1994; Grevemeyer and Villinger, 2001).

Equation 3: $\text{Geothermal Gradient} = \frac{(\text{BSR Temperature} - \text{Seabed Temperature})}{(\text{BSR Depth} - \text{Seabed Depth})}$

Units: BSR/Seabed Temperature = °C BSR/Seabed Depth = m

Heat flow across the same zone was then derived from the estimated geothermal gradient. This requires an understanding of the thermal conductivity structure of the GHSZ. In the absence of borehole control, an empirical relationship between interval velocities and thermal conductivity (k) is used, that was derived from a number of experimental datasets (filtered to only include wet samples to represent subsurface fluid saturation) that include P-wave velocity, thermal conductivity and porosity measurements across a wide range of lithologies, e.g. Grevemeyer and Villinger (2001), Boulanouar et al. (2013) and Esteban et al. (2015). This relationship was used to estimate the thermal conductivity of the shallow sediments as a function of the seismically-defined interval velocities of the GHSZ (Equation 4). The empirical relationship is represented by 0.5071 in

equation 4, which is the intercept of the regression equation through the selected experimental data points. Within equation 4, the interval velocities are multiplied by 0.001 to convert from m/s to km/s to ensure the thermal conductivity units match those of geothermal gradient and heat flow.

Equation 4: $\text{Thermal Conductivity (k)} = (\text{Interval Velocity} * 0.001) - 0.5071$

Units: $k = W/m^{-1}/K^{-1}$ $\text{Interval Velocity} = m/s$

The final step was to use the thermal conductivity and the geothermal gradient to calculate heat flow (Q) through the GHSZ using Fourier's Law (Equation 5). It should be noted, as acknowledged above, that the compound uncertainties may be as much as 50-60 % on the final heat flow estimates (Grevemeyer and Villinger, 2001).

Equation 5: $\text{Heat Flow (Q)} = \text{Geothermal Gradient} * \text{Thermal Conductivity (k)}$

Units: $Q = mWm^{-2}$ $GTG = °C/m$ $k = W/m^{-1}/K^{-1}$

3.4. Results

3.4.1. Shallow Gas

Numerous, scattered seismic anomalies are observed within the Cenozoic sedimentary succession covering the rift basins of Melville Bay (Figs. 3.6 and 3.7) and potentially represent the presence of free gas or gas-rich pore fluids. The identified acoustic anomalies often exhibit a bright, negative amplitude top reflection against a generally lower amplitude background response (Fig. 3.5). The anomalies vary in their seismic character and have been subdivided into four categories:

3.4.1.1. Category I: Isolated Anomalies

The majority of seismic anomalies observed across the study area occur as isolated, negative amplitude anomalies within a background of subtle or low amplitudes (Figs. 3.6-8). These isolated (category I) anomalies still vary in seismic character and therefore have been subdivided into four key types (Figs. 3.5 and 3.7B-D; Type 1-4). The vast majority of category I anomalies display a small, bright event, characterized by a single loop trough-peak response (Type 1) (Fig. 3.5). These anomalies are limited in the horizontal (< ~150 m) and vertical (< ~20 m) plane but tend to occur at various stratigraphic levels (Figs. 3.5, 3.7B and 3.8). Polarity reversals are occasionally observed at the edge of the anomaly, dependent on the seismic properties of the host sediments.

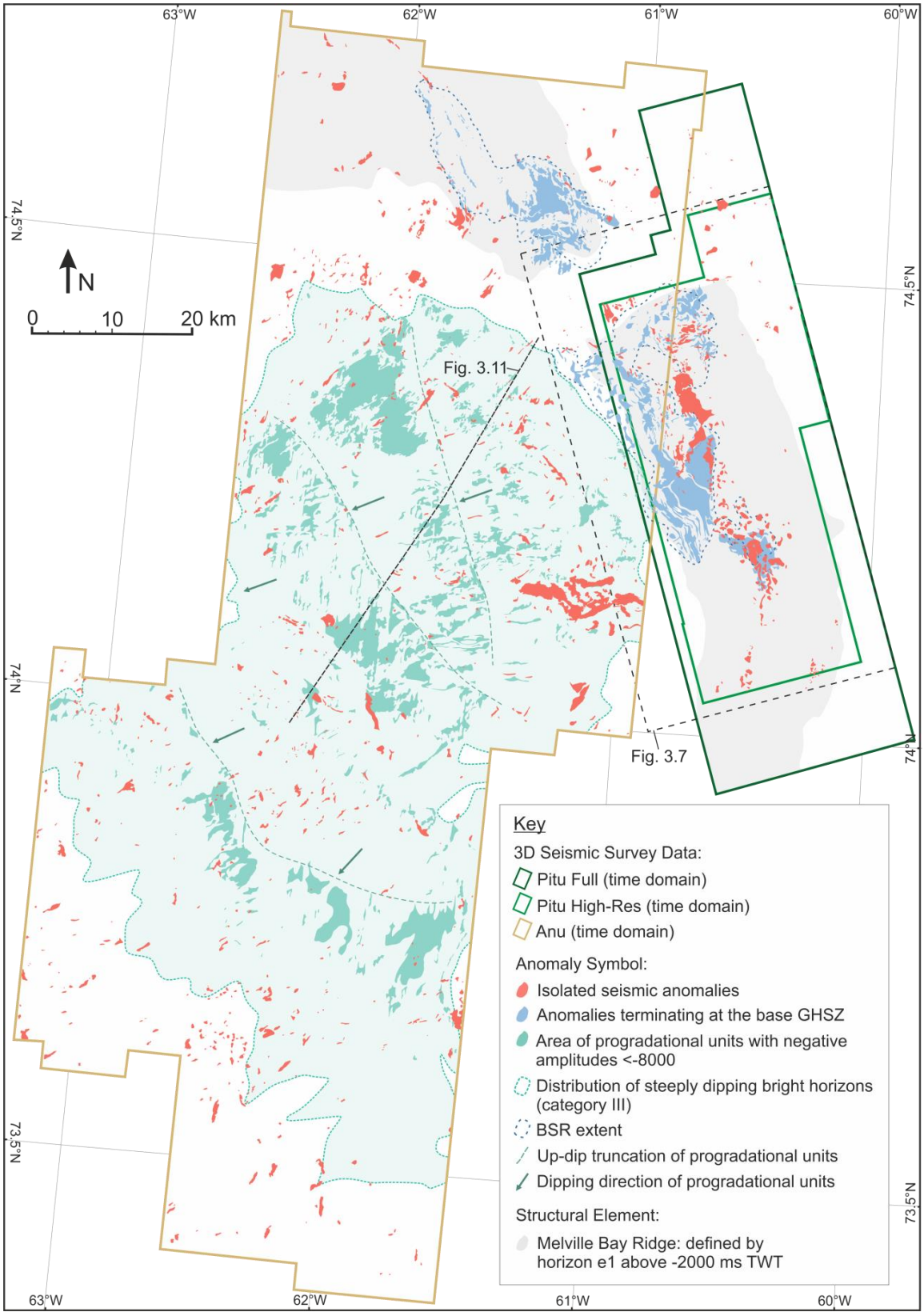

Figure 3.6. Regional anomaly map | A regional map of the area covered by 3D seismic data, displaying all seismic anomalies that were identified and interpreted to represent shallow hydrocarbon occurrences, the location of paleo-rift topography and the direction of glacial unit progradation. Location of Figs. 3.7 and 3.11 are shown.

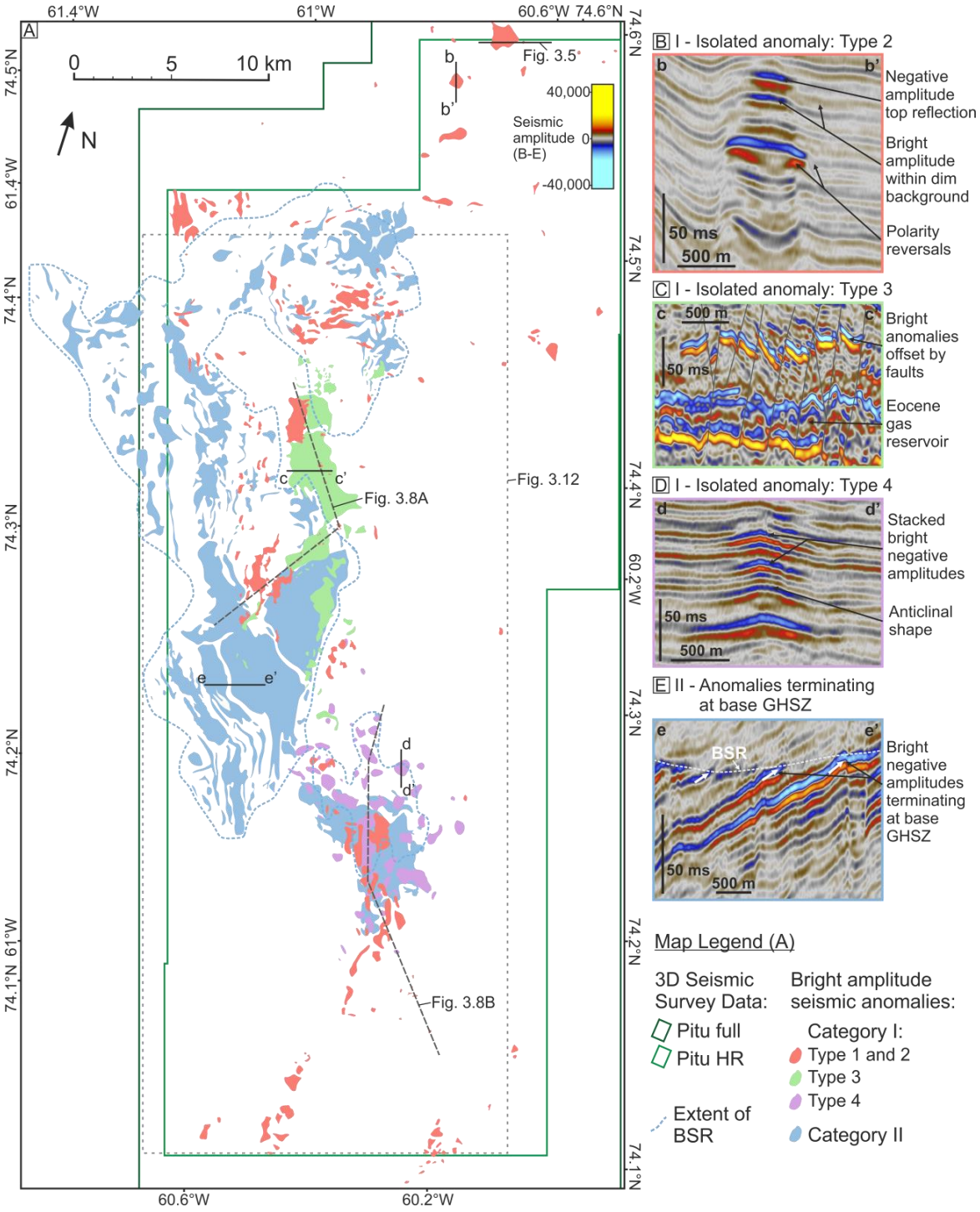

Figure 3.7. Anomaly map of the Pitu area | Enlarged section of the Pitu area shown in Fig. 3.6 (A), displaying the seismic anomalies interpreted as shallow hydrocarbon occurrences from categories I and II. Category I anomalies are colour coded to match the key types of isolated anomalies shown within the adjacent seismic boxes (B, C and D). An example of category II anomalies, corresponding to the blue polygons in (A), is shown in box E. Seismic line locations of key examples (B-E) and Figs. 3.5, 3.8A-B, and 3.12 are shown on the map (A).

Isolated anomalies also occur as larger features observed across multiple stratigraphic layers (horizontal/vertical extent of >2 km/>200 m) characterised by bright negative amplitude top reflections and a positive amplitude base (Type 2) (Figs. 3.5 and 3.7A). Internal reflections exhibiting bright amplitudes, as well as polarity reversals at the edge of the stacked anomalies, suggests a variable pore fluid as the main cause for the lower seismic velocities (Fig. 3.5).

Within mu-D1, above the southern extension of the MBR, a concentration of category I anomalies occurs (Type 3). These anomalies differ from the more typical Type 1, as they appear restricted to a single stratigraphic horizon, with the anomalies and the surrounding stratigraphy being offset by closely spaced, near vertical linear features characterised by dim amplitudes (Figs. 3.7 and 3.8A). These offsets are interpreted as small faults that extend downwards to the base of the Eocene gas reservoir (see category IV). A seismic variance attribute extraction through the stratigraphy at this depth shows a dense network of these faults (Fig. 3.9A-B). The bright anomalies occur in between the faults suggesting entrapment of hydrocarbon fluids focussed within the Miocene interval directly above the MBR (Figs. 3.8 and 3.9A-B).

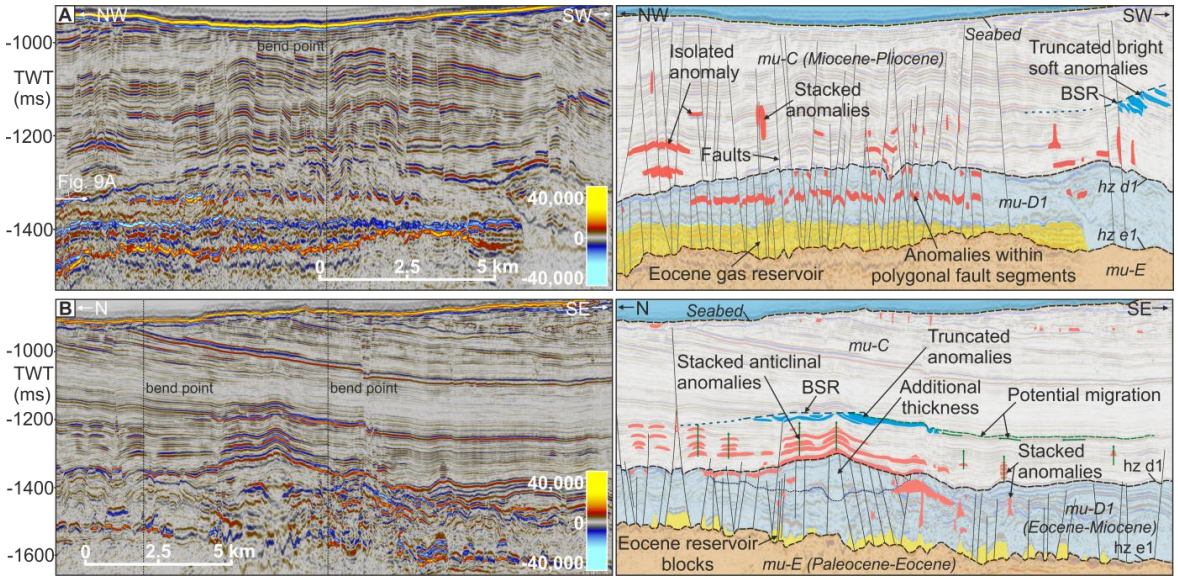

Figure 3.8. Seismic anomaly character | Seismic cross sections, un-interpreted (left) and with interpretations (right), showing identified shallow seismic anomalies. (A) Seismic cross sections illustrating category I, II and IV seismic anomalies observed within the Pitu survey area. Dense faulting and hydrocarbon occurrences are shown throughout the sealing unit (mu-D1) of the Eocene reservoir. (B) Seismic cross sections highlighting category I anomalies within anticlinal folds. Category II (blue) and IV (yellow) anomalies are present in both profiles along with the gas hydrate stability zone (GHSZ) (blue dashed line), with the wide and thin dash representing high and low amplitude sections of the bottom simulating reflector (BSR) respectively. Seismic line locations are shown in Fig. 3.7.

Several, more laterally continuous faults are also observed on the variance extraction (Fig. 3.9), with some containing small, bright amplitude seismic anomalies within or

truncating against the low amplitude linear zone between the offset horizons, a zone likely representing the fault plane (Figs. 3.8 and 3.9D).

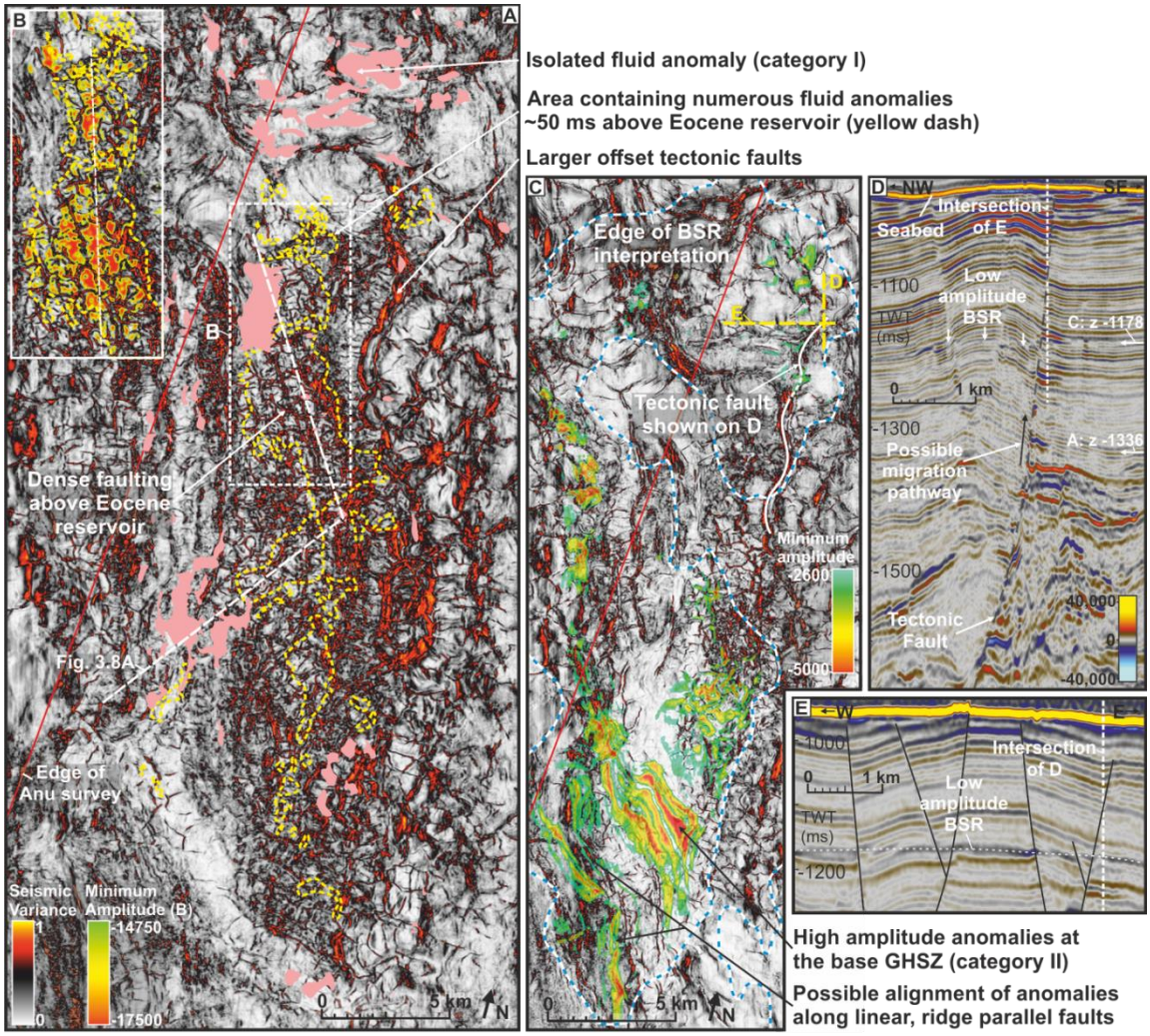

Figure 3.9. Faults and fluids | Seismic data illustrating the relationship between faults and hydrocarbon fluid signatures. (A) Time slice surface of seismic variance from the Pitu 3D survey (depth of 1336 TWT corresponding to mu-D1), displaying a concentrated network of small, high amplitude (variance) faults on the crest of the Melville Bay Ridge. The relationship between the location of small fluid anomalies observed within mu-D1 (yellow dashed areas) and the network of faults is shown. A minimum amplitude extraction displaying the location of the individual anomalies across a section of (A) is shown on (B), highlighting this relationship further. C) A time slice of seismic variance from the Pitu 3D survey at a depth of -1178 TWT, showing the difference in the fault network at this shallower depth (compared to A). The location of the observed BSR and a minimum amplitude extraction displaying the location of fluid anomalies trapped beneath the GHSZ (category II) are shown. The locations of A and C are shown on Fig. 3.3. D) A seismic cross section in two-way-time from the Pitu 3D survey displaying potential fluid anomalies trapped within and truncated against a vertically extensive tectonic fault. This fault is observed to cross cut a low amplitude section of the bottom simulating reflector (BSR), which is also shown on (E). The location of both (D) and (E) is shown on (C).

Numerous category I anomalies are observed at the base of mu-C in a limited area in the southern part of the Pitu HR survey (Fig. 3.7A – purple polygons). These anomalies, referred to as Type 4, occur as vertically stacked, negative amplitude narrow anticlines across several layers of stratigraphy. The anticlinal anomalies follow the structure of the

host stratigraphy, and often gradually diminishing upwards suggesting drape across an underlying structure (Figs. 3.7D and 3.8B). In the lower section of mu-C (Fig. 3.8B), the anomalies occur in between fault locations within the underlying and more chaotic section of mu-D. They also become more widespread (~2 km) above a local unit of enhanced thickness within mu-D1 (Fig. 3.8B), which causes the overlying anomalies and the surrounding stratigraphy to dip more steeply around its crest.

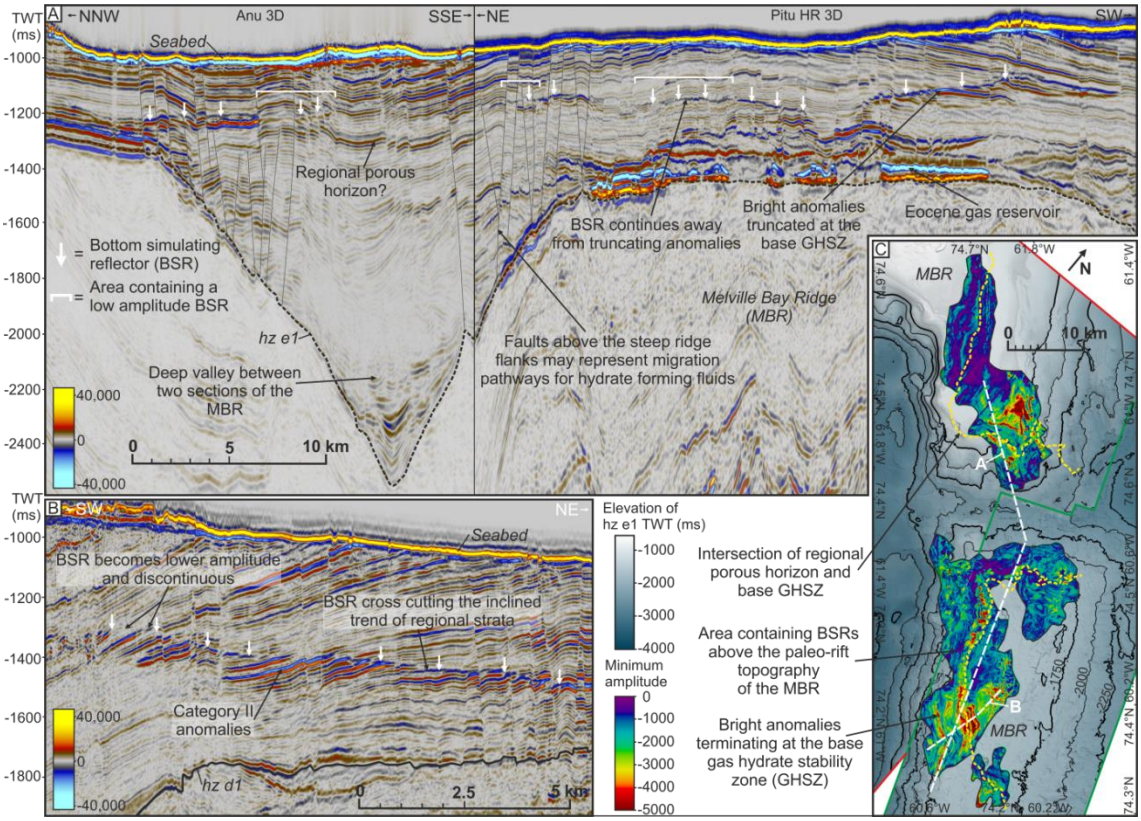

Figure 3.10. Bottom simulating reflectors (BSRs) and gas hydrates | A) A composite seismic cross section from the Anu and Pitu 3D seismic surveys along part of the northern and southern extensions of the Melville Bay Ridge as well as the deep valley between the two extensions. A discontinuous BSR can be observed above much of the paleo-rift structure, but is not observed above the majority of the valley area. The BSR varies in amplitude between areas containing terminating bright anomalies at the base gas hydrate stability zone (GHSZ) and areas without these anomalies where it displays as a low amplitude reflection (highlighted by white brackets). B) A seismic cross section in two-way-time from the Pitu HR 3D survey showing a clear cross-cutting BSR, as well as numerous bright anomalies terminating at the base of the GHSZ (category II). The location of both (A) and (B) are shown on (C). C) A minimum amplitude extraction for a 20 ms two-way-time window across the mapped BSR horizon that highlights the location of bright amplitude anomalies that terminate at the base of the GHSZ (category II). The relationship of the hydrate deposits to the underlying Melville Bay Ridge is also shown, via the underlying two-way-time structure map of horizon e1 defining the ridge topography. The intersection of a regional potentially porous horizon (identified on A) with the base GHSZ is also shown (yellow dashed line), with the intersection location coinciding with numerous terminating fluid anomalies.

3.4.1.2. Category II: Anomalies terminating at the base GHSZ

This category refers to bright, negative amplitude anomalies observed within dipping strata packages that terminate at a level corresponding to a BSR (Figs. 3.7 and 3.10). The BSR appears as a cross-cutting negative amplitude reflection, interpreted as the base of the

GHSZ (see section 3.4.2) (Fig. 3.10). These anomalies exist within multiple layers of tilted stratigraphy with the bright negative response existing for ~50 ms below the BSR (Fig. 3.8C). The brightest terminating anomalies exist within linear zones that trend northwest-southeast (Figs. 3.9C and 3.10C) and represent the location where the base GHSZ cross-cuts the host layers. These host layers maintain a bright reflection down-dip from the truncated anomaly, but switch to a positive amplitude response that continues regionally across the study area (Fig. 3.10A). The category II anomalies are most clearly expressed above laterally and vertically extensive faults that extend from the top horizon (e1) of the western flank of the MBR, to a near-seabed position (Figs. 3.2-3, 3.9C and 3.10).

3.4.1.3. Category III: Steeply Dipping Bright Horizons

This anomaly category is observed within the progradational units of mu-A, forming part of the Melville Bay Trough Mouth Fan (Figs. 3.1-2, 3.6 and 3.11) (Knutz et al., 2019). It is characterized by anomalously bright, negative amplitude top reflections, that display top set erosion and are interpreted as glacial clinoform packages (Fig. 11) (Newton et al., 2020). The clinoforms covered by the Anu 3D seismic survey display west to south-westerly dips (Figs. 3.6 and 3.11). The category III anomalies are distributed throughout much of the shallow stratigraphy (uppermost 1 second TWT) within the Anu 3D survey (light green area; Fig. 3.6), but with the highest amplitudes observed below the truncated top-sets, representing paleo-shelf breaks of the prograding wedge (dark green areas; Fig. 3.6). Towards the northwest within the survey area, corresponding to the oldest prograding units, dipping bright horizons terminate abruptly up-dip against a major glacigenic unconformity (Fig. 3.11). Down-dip, the category III anomalies continue along semi-continuous, seismic-stratigraphic horizons but with variable and generally fading amplitudes (Fig. 3.11).

3.4.1.4. Category IV: Eocene Gas Reservoir

An extensive, potential gas reservoir has been mapped at the base of the Cenozoic succession (mu-D2) overlying the MBR (Fig. 3.8) (Cox et al., 2020a). The reservoir is likely of Eocene age and interpreted as laterally continuous sand deposits on the northern parts of the ridge crest while towards the south and east, the unit appears fragmented due to mass transport (Figs. 3.8 and 3.12). Thus, large sections of the reservoir exist as separated blocks above a likely muddy decollement surface (represented by horizon e1) (Figs. 3.2 and 3.8). The reservoir package displays very bright amplitudes on seismic data including a bright negative amplitude top reflection and a bright positive amplitude base (Fig. 3.8a).

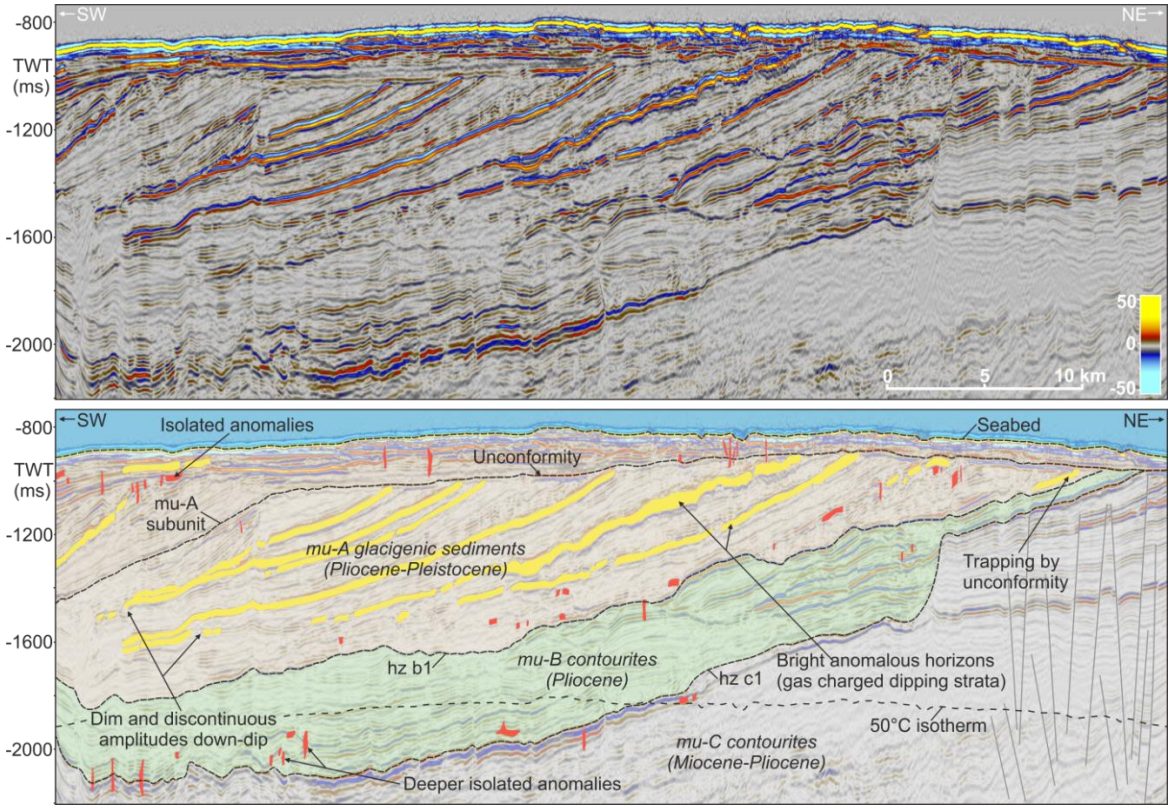

Figure 3.11. Glacial clinoforms | Uninterpreted and interpreted seismic cross section in two-way-time from the Anu 3D survey, highlighting steeply dipping bright horizons (category III) (yellow) from within the glacigenic stratigraphy of mu-A. Isolated shallow gas anomalies (category I) are also shown (red). The distribution of the category III anomalies and the location of the seismic intersection are shown on Fig. 3.6.

The thin overlying sealing stratigraphy of mu-D1 is characterised by a dense network of closely spaced small offset faults that often appear aligned to the edge of the reservoir blocks (Figs. 3.8 and 3.9A-B). These faults, hosting isolated bright anomalies (category I), commonly extend between the base of the reservoir (horizon e1) and horizon d1, with some extending upwards towards the seabed. Hence, there is a clear spatial relationship between the regional distribution of the reservoir blocks on the MBR crest and the isolated anomalies throughout the shallow stratigraphy (mu-D1 and -C) (Figs. 3.6 and 3.12).

3.4.2. Gas Hydrates

A discontinuous BSR has been observed across an area of 537 km^2 above the central axis and western flank of the MBR (Figs. 3.6-7 and 10). This feature exists approximately 200 m below the seafloor, in water depths of 625–720 m and marks the base of the GHSZ. The BSR is observed as a negative amplitude reflection with variable intensity that cross-cuts the stratigraphy. It is best defined in areas with tilted stratigraphy where bright anomalies terminate at the BSR and the base of the GHSZ (category II) (Figs. 3.7E and 3.10B). Away from these anomalies, and especially in areas where the stratigraphic dip is

similar to the seabed the BSR amplitude is reduced to a dimmer response, but can still be observed (Figs. 3.8, 3.9D-E and 3.10).

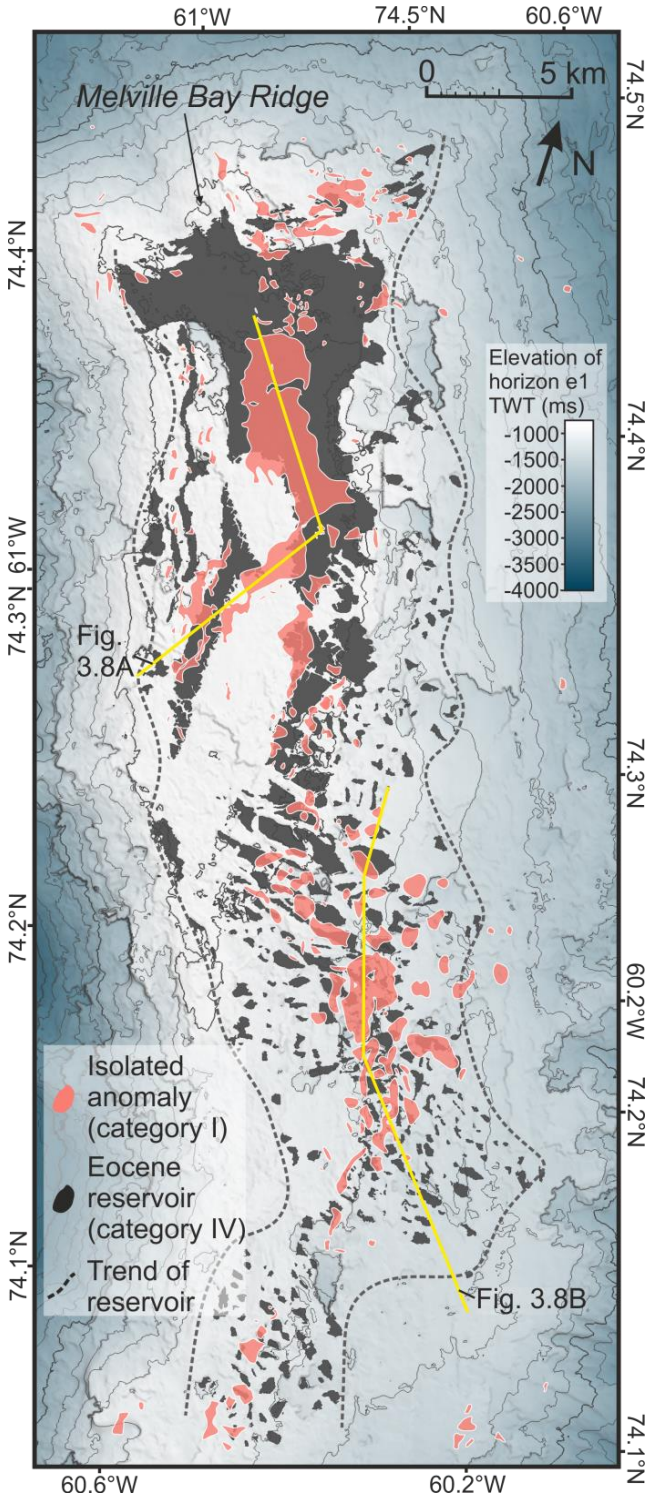

Figure 3.12. Anomalies above the deeper reservoir | A two-way-time structure map of horizon e1 that represents the top of the Melville Bay Ridge overlaid by the distribution of the Eocene gas reservoir (category IV) across the ridge crest (black polygons) (Cox et al., 2020). The location of Isolated anomalies (category I) (red polygons), interpreted to represent shallow gas, are shown with their distribution following the trend of the underlying reservoir. This spatial relationship may suggest that the deeper reservoir is leaking hydrocarbons into the overlying stratigraphy.

The seafloor topography across the region contains several erosional and depositional features related to glaciation (Figs. 3.1 and 3.14). The BSR is observed to mirror this seafloor topography, deepening and shallowing in areas of erosion and deposition, respectively – e.g. such as the glacial wedge (Figs. 3.10A and 3.13G-H). The thickness of the GHSZ varies, generally in relation to seabed depth – e.g. with the GHSZ thinning or thickening in areas of shallower or deeper water, respectively. An exception to this trend is observed in the northern and eastern parts of the BSR, where the GHSZ thins in areas where water depth increases (Fig. 3.13C and E). The increased water depths are a result of seabed glacial erosion (Fig. 3.14) (Newton et al., 2017).

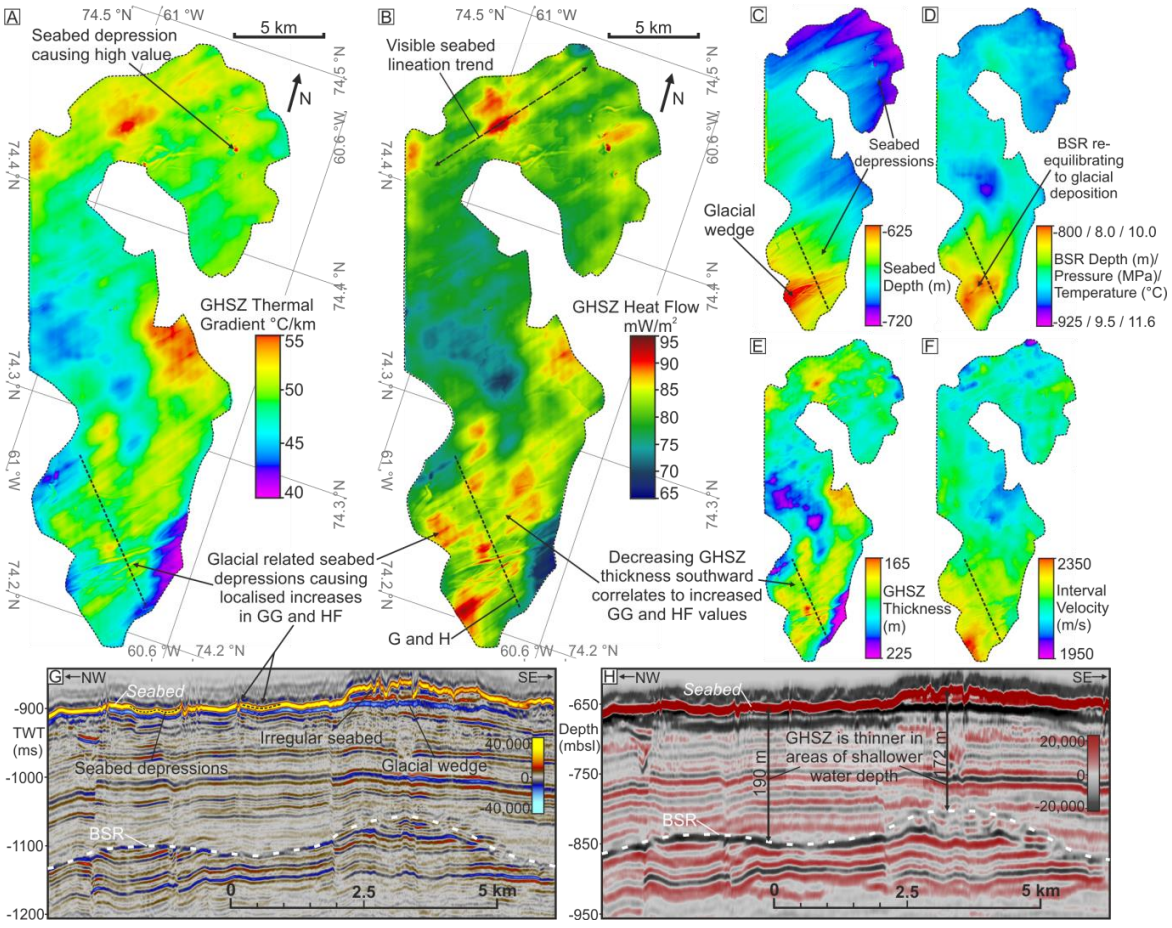

Figure 3.13. Geothermal gradient and heat flow estimations | Maps showing the calculated average geothermal gradient (A) and average heat flow (B) through the gas hydrate stability zone (GHSZ) interval for the area containing the observed bottom simulating reflector (BSR) within the Pitu depth survey limits. Maps used within this calculation are shown including seabed depth (C), BSR depth, pressure and temperature (D), GHSZ thickness (E) and average interval velocity through the GHSZ (F). Seismic cross sections in two-way-time (G) and depth (H) are shown across a section within the south of the BSR distribution highlighting the irregular seabed topography, and the likely post-glacial re-equilibration of the hydrate phase boundary beneath a depositional glacial wedge.

Interval velocities increase by ~200 m/s within the stratigraphy above the BSR (e.g. GHSZ), when compared with areas outside the BSR (Fig. 3.4). Below the BSR, seismic velocities at the GHSZ base are reduced from ~2200 m/s within the GHSZ to ~1800-

1900 m/s beneath. Conversely, a velocity increase is observed at a corresponding depth level away from the BSR (Fig. 3.4).

Despite its discontinuous appearance, the distribution of the BSR suggests a relationship to the paleo-rift topography and the MBR. The BSR is observed in most areas along the western flank of the MBR, but disappears above a deep valley between the northern and southern extensions of the ridge (Fig. 3.10A). In the vicinity of the valley system, the amplitude strength of the BSR reduces, and disappears completely above the central parts of the valley. Within the buried valley zone, several of the regional horizons that host the bright category II anomalies are located at depths well below the depth of the base GHSZ. The lack of cross-cutting between the host strata and the GHSZ within this area is a likely reducing factor for the seismic imaging of the BSR (Fig. 3.10A and C). In areas containing extensive faults that extend from the top ridge horizon (horizon e1) and through the post-rift stratigraphy, the BSR retains a strong amplitude response within the host strata (Figs. 3.2-3, 3.9C and 3.10).

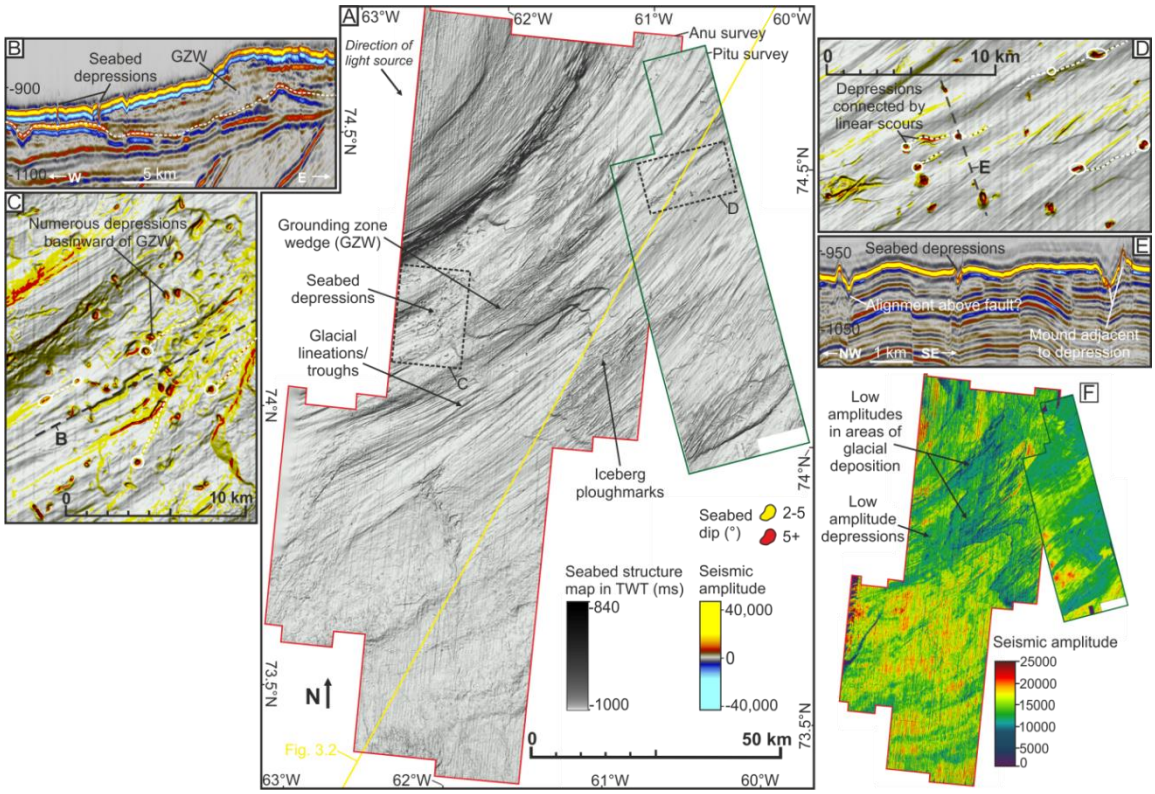

Figure 3.14. Seabed mapping | A) A two-way-time structure map of the seabed horizon across the area of 3D seismic coverage, highlighting the widespread distribution of glacial-erosional and depositional features. Numerous curvilinear and concentric seabed depressions are observed on both a seismic cross section in two-way-time (B) and the seabed surface (C), basinward of a grounding zone wedge (GZW) (Newton et al., 2017). The dashed white line on (B) represents the base of the GZW. Similar features are observed within the Pitu survey area on both the seabed surface (D) and in seismic cross section (E). (F) An amplitude map of the seabed horizon across the 3D seismic coverage that displays the relationship between glacial erosion and depositional features on the seabed and seismic amplitude.

3.4.3. Evidence for Seabed Fluid Escape

The seafloor located in the northern part of the study area represents a major glacial trough, characterised by numerous features of glacial erosion and deposition, such as lineations, ridges, iceberg scours and grounding zone wedges (GZW) (Figs. 3.2 and 3.13-14) (Newton et al., 2017). Within the trough area, semi-circular seafloor depressions are commonly observed, with lateral dimensions up to 500 m and depths up to 50 m (Fig. 3.14D-B). Small mounds of sediment often occur on the seabed next to the depression. These mounds are not evenly distributed but tend to be skewed to one side of the depression (Fig. 3.14D).

The depressions seem to be unrelated to the underlying stratigraphy, as no seismic features are observed consistently beneath their locations, such as faults, pipes or anomalous brightening (although on occasion a fault will occur beneath the depression, e.g. Fig. 3.14E). On the seabed structure map, curvilinear scours are often observed connecting the circular depressions, commonly extending towards the northeast, trending similar to glacial lineations (Fig. 3.14B and D). In the western part of the study area (Anu survey), numerous seabed depressions occur towards the southwest, lee-side of a depositional feature interpreted as a GZW (Newton et al., 2017). Several semi-circular depressions are also observed on the base horizon of the GZW, which represents a paleo-seabed surface (white dashed line on Fig. 3.14C). Both the seabed depressions and GZW deposits coincide with lower seismic amplitudes of the seabed horizon (Fig. 3.14E). Based on seabed geomorphology and the distribution of glacial features, the semi-circular depressions are interpreted as having been formed by glacial erosion, and most likely represent iceberg pit-marks (e.g. Brown et al., 2017) as opposed to gas-hydrate explosion craters (e.g. Andreassen et al., 2017).

3.4.4. Geothermal Gradient

The geothermal gradient has been estimated using the GHSZ thickness inferred from the BSR distribution covered by the Pitu 3D survey (depth domain) and known P-T phase relationships for gas hydrates (Fig. 3.13; section 3.3.3). Accordingly, pressure and temperature at the BSR depth, range between 8.0 - 9.5 MPa (average 8.9), and 10.0 - 11.6 °C (average 10.9) respectively (Fig. 3.13D). As both the pressure and temperature estimations are dependent on BSR depth, the two parameters show identical lateral variation. Hence, shallowing of the BSR coinciding with a shallowing seabed depth, as seen in the southern part of the Pitu survey (in the area of glacigenic deposition), causes a reduction in both pressure and temperature (Fig. 3.13). A differing trend to that of the seabed depth is seen in the northern section and along the eastern edge where the seabed

deepens, at the same locations where the relationship between seabed depth and GHSZ thickness diverts (section 3.4.2).

The calculated geothermal gradient across the thickness of the GHSZ ranges from 40 - 59 °C/km with an average of 49 °C/km (Fig. 3.13). The trend of the estimated geothermal gradient matches that of the GHSZ thickness, with the geothermal gradient increasing in areas of a thinner stability zone and vice versa. However, superimposed on this trend, are a number of localised high values that are either concentric or linear in shape. These anomalous values occur in the same location as similar features observed on both the GHSZ thickness (Fig. 3.13E) and the seabed depth maps (Fig. 3.13C).

The interval velocities through the GHSZ range between 1950-2350 m/s (Fig. 13F) and are observed to increase towards the south within an area coinciding with glacigenic deposition at the seabed (Fig. 3.14 C, and F-H). The conversion of these velocities to thermal conductivity yields a range from 1.45 to 1.85 $W/m^{-1}/K^{-1}$. The thermal conductivity estimates, in combination with the geothermal gradient model values, produces a heat flow across the thickness of the GHSZ, ranging from 58 - 100 mW/m^2 with an average of 81 mW/m^2 (Fig. 3.13B). Again, several concentric or linear anomalies are observed on the heat flow map (Fig. 3.13B), which coincide with areas of high geothermal gradient, a thin GHSZ and high interval velocities.

3.5. Discussion

3.5.1. Hydrocarbon Occurrence

The detailed analysis of the shallow Cenozoic stratigraphy in Melville Bay yielded numerous seismic amplitude anomalies which have been interpreted to represent the most northerly occurrence of shallow gas and gas hydrates offshore western Greenland (Figs, 3.6-8 and 3.11). The gas anomalies were categorised by seismic character and mainly represent the different trapping mechanisms observed across the region (categories I-IV), with the majority of hydrocarbon occurrences existing as isolated pockets of gas (category I), with variable seismic character (Type 1-4) (Figs. 3.5-9).

Free gas was observed trapped against the base of the GHSZ (category II) (Figs. 6-10), a boundary recognised by a discontinuous BSR (Berndt et al., 2004; Hillman et al., 2017), hosted within tilted, likely porous horizons, with the termination of the fluid response down dip (Fig. 3.10B), suggesting a maximum gas column of ~50 m. Dimming of the BSR (Figs. 3.8-10) occurs in areas away from these terminating free gas anomalies, as the acoustic impedance contrast at the base GHSZ is lowered (Hilterman, 2001). The free gas may be absent due to a lack of migration, lack of reservoir at the base GHSZ, and due to all

available gas having been converted to hydrate. The dimming may suggest low saturation of gas hydrate in areas without a BSR (Spence et al., 1995). It is also possible that dim or absent BSRs could be a result of recent glaciations having caused variations in the temperature field which still persist today, if the hydrate system has not fully re-equilibrated post-glaciation (Crémière et al., 2016; Grassmann et al., 2010; Mienert et al., 2000). Overall, the abrupt alternations between BSR and no BSR seen in Fig. 3.10 are probably due to a combination of stratigraphic occurrence of reservoir porosity and permeability and availability of methane around the base of the GHSZ.

Furthermore, the gas interpreted to exist within glacigenic, progradational units of mu-A (category III) (Knutz et al., 2019), is observed trapped up-dip against horizontal and unconformable muddy strata of the overlying glacial sequence (Fig. 3.11). The brightest fluid-related amplitudes coincide with truncated top-sets at the paleo-shelf break positions of the prograding wedge; possibly representing increased gas concentrations or greater porosities (Hilterman, 2001). The rotating alignment of these fluid anomalies southward, as well as the variable dip of glacigenic stratigraphy (Fig. 3.6), reflects the variable pathways of ice streams and shelf break progradation (Knutz et al., 2019; Newton et al., 2020; 2017).

3.5.2. Fluid Migration

Although the seismic evidence provided only offers a static view of contemporary hydrocarbon occurrences, and features such as chimneys, pipes and pockmarks are not observed at present day (Chand et al., 2012; Huuse et al., 2010), several relationships between structural and stratigraphic elements and the distribution and character of the hydrocarbons observed, provides evidence towards understanding the migration history of fluids within this area.

3.5.2.1. Paleo-rift Topography and Tectonic Faults

A significant concentration of free gas anomalies, as well as all identified gas hydrate deposits, exist directly above or along the western flank of the underlying MBR (Figs. 3.6-7, 3.9-10 and 3.12), with the deposits only becoming discontinuous above a large buried valley separating the ridge's north and south extensions (Figs. 3.6 and 3.10). This relationship suggests that the underlying paleo-rift topography is influencing upward fluid migration. Post-rift depositional units either onlap onto the ridge flanks, or extend and thin above its crest, forming a broad anticline structure throughout mu-D and -C (Fig. 3.2) (Gregersen et al., 2019; 2013). This causes the post-rift stratigraphy within the adjacent grabens to tilt towards the ridge structure, likely facilitating the up-dip migration of fluids into areas above the MBR.

Potential Cretaceous source rock intervals within mu-F (Nohr-Hansen et al., 2018; Planke et al., 2009), are interpreted to extend from the Melville Bay Graben up-dip into the MBR structure on the eastern flank; a factor which likely led to the charging of the Eocene reservoir (category IV) (Cox et al., 2020a). On the western flank the syn-rift stratigraphy terminates against deep tectonic faults (Figs. 3.2-3 and 3.15), with disconnection of this strata occurring at the western ridge fault. This termination and offset likely restricts fluid migration from the South Kivioq Basin, and instead, fluids are forced upward through a number of post-rift fault conduits that are observed to extend from the tips of deeper faults and the top ridge horizon (horizon e1), to close to the seabed (Figs. 3.2-3, 3.9 and 3.15). Above these faults on the western ridge flank, gas hydrate deposits (Figs. 3.6, 3.9-10) suggest the location of these migration pathways have influenced gas hydrate formation.

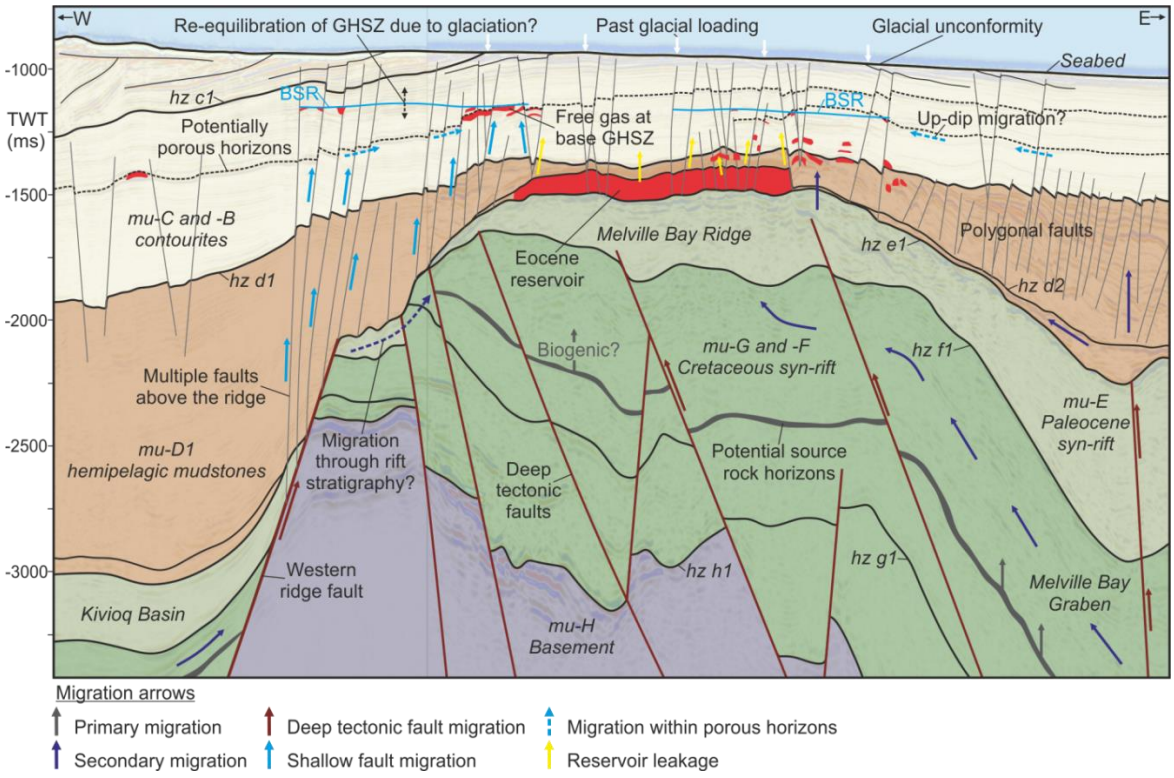

Figure 3.15. Fluid migration | A composite seismic cross section in two-way-time across the Anu and Pitu 3D seismic surveys, overlain by an interpretation of the structure, stratigraphy and complex fluid migration history that likely characterises the study area. Fluid migration into the Cenozoic stratigraphy is observed via syn-rift carrier beds and tectonic faults from both within the ridge and above its western flank. The location of shallow gas accumulations, the Eocene gas reservoir and gas hydrate deposits, along with the potential migration pathways for these fluids is shown, along with possible effects of glaciation on hydrocarbon re-migration. The location of the seismic line is shown on Fig. 3.3.

Furthermore, free gas trapped beneath the hydrate deposits (category II) is also observed above these fault locations (Fig. 3.9C), although this distribution may instead be influenced by the intersection of the host strata (regional, potentially porous and permeable horizons), that have been uplifted and tilted by the MBR structure, with the base GHSZ

along the western flank of the ridge (Figs. 3.9C, 3.10 and 3.15). Still, no free gas is observed within the GHSZ above the fault locations (Figs. 3.10 and 3.15) and no seabed expulsion features are observed directly above the fault tips (Figs. 3.10 and 3.14-15). Therefore, any fluids migrating upward through the faults, post hydrate formation, either became trapped within the fault plane at the base GHSZ (Fig. 3.15), or migrated stratigraphically up-dip once reaching the potentially porous carrier bed horizons until again becoming trapped at the base GHSZ (Figs. 3.10 and 3.15).

3.5.2.2. Reservoir Leakage

Above the crest of the MBR, a clear relationship is observed between the location of isolated gas anomalies (category I) and the trend of the Eocene gas reservoir (category IV) (Figs. 3.6, 3.8 and 3.12). The sealing unit (mu-D1) is at its thinnest above the reservoir (due to depositional thinning above the ridge and erosion) (Cox et al., 2020a; Gregersen et al., 2013), and is observed to contain a dense network of short offset, near vertical faults, extending from the base of the reservoir (horizon e1) to the top of the sealing unit (horizon d1) (Cox et al., 2020a). Several fluid anomalies are observed trapped within this dense network of faults (Figs. 3.8A and 3.9A-B), with their occurrence, as well as overlying anomalies in the lower section of mu-C (Figs. 3.8A, 3.10A and 3.12), suggesting that the underlying reservoir is leaking hydrocarbons upwards through these fault conduits (Figs. 3.8-9, 3.12 and 3.15) (Cartwright et al., 2007; Ingram and Urai, 1999).

These faults occur in a dense, polygonal network (Figs. 3.3 and 3.8-9) and are geometrically similar to sets of polygonal faults within the same stratigraphy above the grabens (Figs. 3.2 and 3.15) (Cartwright and Dewhurst, 1998; Cox et al., 2020a). However, their exact origin is uncertain and fault growth in certain areas may instead be controlled by the presence of the underlying deformed reservoir (Figs. 3.8B and 3.12), with normal faults forming along the flanks of reservoir blocks, likely due to differential compaction above the blocks and adjacent areas (Fig. 3.8) (Cox et al., 2020a). Polygonal faults are then thought to nucleate at the tip of these faults (at horizon d1) and extend vertically into mu-C. A similar scenario may have occurred above the ridge crest, where the gas anomalies are observed (Figs. 3.8-9). Here, the underlying reservoir is more laterally continuous, but faults may still be influenced by reservoir structure as they coincide with irregular offsets between narrow sections of the reservoir (Fig. 3.8A), although this offset may instead be caused by the faults themselves. Therefore, if fault genesis is not typically polygonal (Cartwright et al., 2003), then gas leakage through these faults is more likely as polygonally faulted muds are known to create excellent sealing formations (Cartwright, 2019; Goulty,

2008). If leaking did occur, then this may be providing at least part of the methane constituent of the overlying hydrate deposits (Figs. 3.7-10).

3.5.2.3. Glacial Clinoforms

The source and likely migration pathway of the gas interpreted to exist within glacial clinoform units of mu-A (category III) (Figs. 3.2 and 3.11) is uncertain, due to the disconnection of this stratigraphy from potential source rock horizons in the deeper basins (Fig. 3.2) (Cox et al., 2020a; Nohr-Hansen et al., 2018) via thick packages of likely sealing formations including hemipelagic muds (mu-D) and contourites (mu-C and –B) (Gregersen et al., 2013; Knutz et al., 2015). No deep tectonic fault connections are observed, and the paleo-rift topography close to the shelf edge (Figs. 3.1-2) is likely too far away to focus fluids into sediments that were only deposited since ~2.7 Ma (Knutz et al., 2019). Shallow source rocks may exist, although sufficient burial and time for maturation is unlikely when considering burial only increased after ~2.7 Ma (Knutz et al., 2019; Wilson, 1975). Instead, the gas could be biogenically generated, either in situ as the clinoforms may contain organic material - as suggested for other glacial related clinoforms, e.g. Verweij et al. (2012); Muller et al. (2018) – or more likely, from organic horizons within the contourite succession, e.g. Knapp et al. (2019); Rebesco et al. (2014). The contourites (mu-C and -B) are estimated to exist at temperatures around 40-50 °C at present day (Fig. 3.11), the theoretical peak temperature of biogenic generation (Stopler et al., 2014), based on the estimated shallow geothermal gradient from this study (49 °C/km) (Fig. 3.13).

3.5.2.4. Seabed Expulsion

Attempts were made to document fluid expulsion features at the seabed (e.g. chimneys, pipes and pockmarks) which may represent the existence of cold hydrocarbon seeps into the water column (Andreassen et al., 2017; Chand et al., 2012), similar to those observed ~500 km to the south near Disko Island (Nielsen et al., 2014). The seafloor across the study area, however, represents a time-transgressive glacial unconformity that has experienced significant erosion since ~2.7 Ma (Figs. 3.2 and 3.14) (Bennett et al., 2014; Knutz et al., 2019; Newton et al., 2020). This erosion has removed large amounts of sediment from the inner shelf and likely removed any seabed expulsion features that may have formed prior to glaciation (Fig. 3.14). Further towards the shelf edge, horizons interpreted as pre-glacial paleo-seabeds are now buried beneath a thick unit of glacigenic sedimentation (Fig. 3.2), and seismic resolution is likely insufficient to distinctly image any potential buried features. Additionally, much of the area above the MBR, where upward fluid migration is focussed, contains gas hydrates (Figs. 3.2, 3.6-7, 3.10 and 3.15), which may restrict upward fluid migration and expulsion to the surface (through both

conventional trapping - such as the free gas anomalies observed - and transformation to hydrate) (Grauls, 2001; White, 1979).

Several erosional depressions are however, observed on the present day seabed within two distinct regions of the 3D data (Fig. 3.14). These features could represent fluid escape locations at the seabed (Andreassen et al., 2017; Chand et al., 2012), but no direct evidence for fluid flow is observed, although features such as gas chimneys would likely have had time to dissipate if formed during the early stages of glaciation (Huuse et al., 2010). Evidence such as their geometry, the asymmetrical sediment berms and their occurrence within seabed scours (Fig. 3.14), instead suggests that the depressions are more likely associated with glacial erosion of the seabed, and are interpreted as iceberg pit-marks (Brown et al., 2017). Such pits form by the impact of an iceberg keel with the seabed (Newton et al., 2018; Woodworth-Lynas et al., 1985), with the adjacent asymmetrical berms of sediment (Fig. 3.14E) likely having been excavated and deposited to one side by the iceberg upon impact. The connection of several of the depressions by curvilinear scours (Fig. 3.14B and D), marking the iceberg pathway across the seafloor in between low tides, strongly supports genesis by iceberg grounding (Brown et al., 2017; Newton et al., 2016). Furthermore, the depressions within the Anu survey were observed basinward of a major grounding zone wedge (Fig. 3.14B and C), marking a potential ice sheet calving margin (Newton et al., 2020; 2017). Icebergs reworking the seafloor have been observed in water depths up to, and occasionally exceeding, 1 km offshore Greenland, e.g. Kuijpers et al. (2007), meaning that icebergs impacting the seafloor in the observed water depths of ~650 m is not uncommon.

3.5.3. Geothermal Gradient and Heat Flow

Geothermal gradient and heat flow estimations from this study provide the only data points across the entire continental shelf of western Greenland (Lucazeau, 2019). An average shallow geothermal gradient of 49 °C/km and heat flow of 70-90 mW/m^2 was estimated (Fig. 3.13), with these values being comparatively high when compared to the closest available (~225 km away from the study area) temperature probe data from within the centre of Baffin Bay (but only for the top <~2 m of sediment), which recorded five geothermal gradient values between 26-48 °C/km and heat flow values between 54-64 mW/m^2 (Lucazeau, 2019; Pye and Hyndman, 1972). The heat flow estimate is also slightly greater than the nearest points (64-75 mW/m^2) in the global heat flow model by Davies (2013), albeit at the edge of its interpolated coverage.

Several factors may have resulted in higher geothermal gradient and heat flow estimations (Fig. 3.13). This could be associated with uncertainty in both the BSR based

estimation method (up to ~50-60%; Grevemeyer and Villinger, (2001); see section 3.3.3) and the temperature probe measurements of which the data are compared (Pye and Hyndman, 1972). An increase in heat flow is expected however, in areas of focussed fluid flow (Ganguly et al., 2000; Minshull and Keddie, 2010), such as above the MBR, and also due to the advection of heat towards underlying paleo-rift topography (the MBR) (Serié et al., 2017). Hydrocarbon leakage from the underlying Eocene gas reservoir may also add to this effect (Figs. 3.8-9 and 3.12). Heat flow may have been over estimated however, due to the use of seismic interval velocities to derive thermal conductivity (see section 3.3.3). The velocity within the GHSZ has likely been elevated by the presence of gas hydrate (Fig. 3.4) (Shankar and Riedel, 2011; Stoll et al., 1971), as such rapid lateral variations in velocity are unlikely to be geological. The thermal conductivity of methane hydrate is approximately equal to the pore water (<10% difference) (Ruppel, 2000; Waite et al., 2009), so elevated velocity would cause an over estimation of both thermal conductivity and heat flow, and the results may in fact be closer to those estimated previously (Lucazeau, 2019; Pye and Hyndman, 1972). Additionally, heat flow may not be in a steady state, due to the impact of recent glaciations on the temperature regime (Johansen et al., 1996), such as is observed on the Norwegian margin (Jung and Vogt, 2004; Mienert et al., 2000). Therefore, the hydrate system may not yet have fully re-equilibrated post-glaciation, affecting the BSR depth and heat flow estimates (see section 3.5.4).

Several localised, high geothermal gradient and heat flow anomalies are observed across the BSR area (Fig. 3.13), but no seismic features, that may suggest focussed fluid flow pathways (e.g. pipes or faults), are observed beneath (Ganguly et al., 2000; Minshull and Keddie, 2010). Instead, many of the anomalies coincide with either positive, likely depositional, or negative, erosional seabed features that likely formed during the last glaciation (Figs. 3.13-14) (Newton et al., 2020; 2017). These include multiple concentric and linear anomalies that represent iceberg pit-marks, glacial lineations and shallow seabed depressions (Fig. 3.13). These erosional features have caused localised deepening of the seabed, which is not reflected at the BSR depth (or at least is not visible given the seismic resolution), causing a thinner GHSZ, and increased apparent geothermal gradients (Fig. 3.13A and E).

3.5.4. Possible Impacts of Glaciation

Melville Bay has experienced multiple cycles of ice sheet advance and retreat across the shelf since ~2.7 Ma (Knutz et al., 2019), resulting in the removal of vast amounts of sediment from the inner shelf and the re-deposition of this sediment to the shelf edge, as part of the Melville Bay Trough Mouth Fan (mu-A) (Figs. 3.1-2, 3.11 and 3.15) (Knutz et

al., 2019; Newton et al., 2020). These processes have transformed the structural position of the stratigraphy across the shelf (Fig. 3.2), with structural changes likely exacerbated by isostatic compensation resulting from load redistribution (Fjeldskaar and Amantov, 2018; Zieba and Grover, 2016). The combination of erosion from the inner shelf and the increased burial (and compaction) of post-rift sediments beneath the glacigenic wedge on the outer shelf (Fig. 3.2), as well as isostatic compensation, has led to the Melville Bay margin tilting basinward west of the MBR. Tilting of the stratigraphy has likely effected fluid migration by focussing fluids up-dip towards the inner shelf and above the MBR, possibly contributing to increased hydrocarbon occurrences in this area (Figs. 3.2, 3.6-7 and 3.15).

Long-term sediment redistribution and tilting likely occurred alongside repeated cycles of glacial loading on the shelf, impacting both isostasy and subsurface conditions (Cavanagh et al., 2006; Medvedev et al., 2019; Ostanin et al., 2017). Cyclic fluctuations in subsurface pressure and temperature during glacial-interglacial cycles, may have promoted fluid re-migration (Fig. 3.15) (Goffey et al., 2016; Plaza-Faverola et al., 2011), with increased pore pressure beneath the ice load, potentially causing the fracturing of hydrocarbon seals and leakage (Hermanrud and Nordgard Bolas, 2002; Tasianas et al., 2018). This process may explain the dense network of fractures and gas pockets observed within the Eocene gas reservoir seal (mu-D1) and the overlying stratigraphy (Figs. 3.8-9). Furthermore, faults may reactivate, increasing fault permeability during deglaciation and load removal (Løtveit et al., 2011; Ostanin et al., 2017), possibly promoting leakage through the mu-D1 fractures, and increasing fluid migration through larger syn- and post-rift faults parallel to the MBR. This may have contributed to the increase in hydrocarbon occurrences (Figs. 3.6-8 and 3.12) and the formation of gas hydrates (Figs. 3.10 and 3.15) above the western flank of the MBR.

Glacial-related variations in subsurface conditions can also affect the stability of gas hydrate (Portnov et al., 2016). The relatively large water depths in the study area (~650 m) mean the seabed is well within the stable region of the gas hydrate phase diagram (Fig. 3.16) and can thus be considered relatively stable, with hydrate dissociation at the seabed only likely to occur in response to glacial erosion (unlike that seen at shallower water depths in the Barents Sea, e.g. Andreassen et al., 2017). These variations are more likely to have affected hydrate formation and dissociation at the phase boundary at the base of the GHSZ (Fig. 3.16) (Ruppel and Kessler, 2017; Serov et al., 2017). Ice loading and erosion during glacial periods likely cooled the underlying sediments and increased pore pressure, allowing increased hydrate stability and a deeper phase boundary than during ice-free

periods (Fig. 3.16) (Grassmann et al., 2010; Ostanin et al., 2017). This suggests gas hydrate may have expanded downwards during glacial periods and once deglaciation and load removal began, would have experienced hydrate dissociation at the base of the stability zone (Portnov et al., 2016; Serov et al., 2017). This process may have contributed to the numerous free gas accumulations that are observed trapped at the base of the present day GHSZ (Figs. 3.6-10).

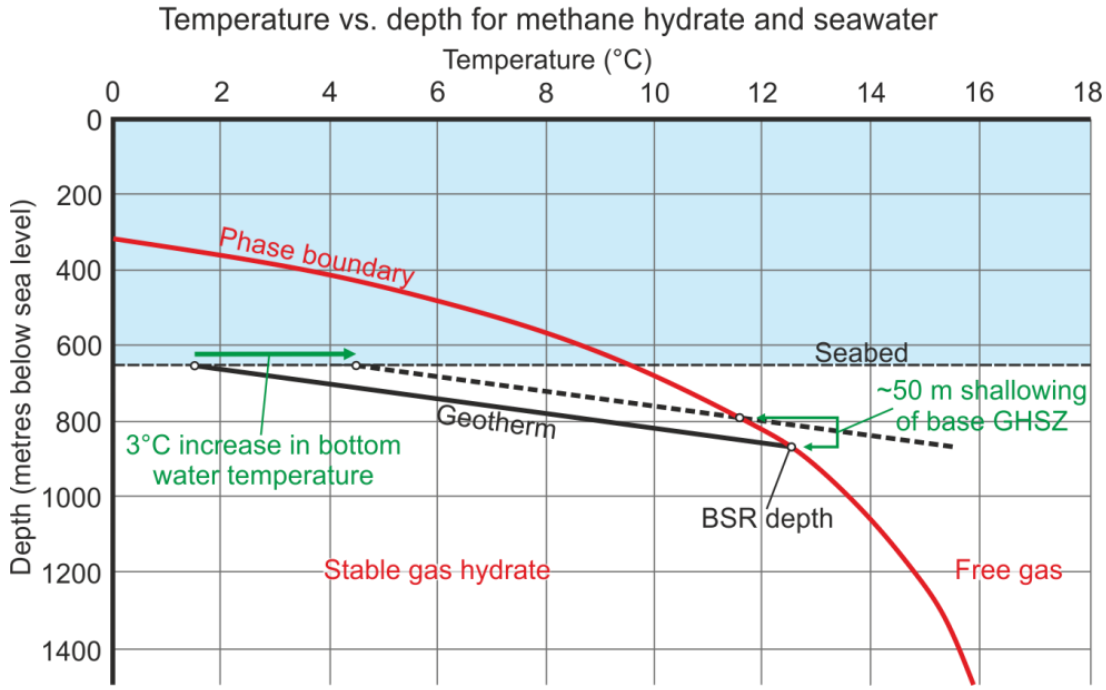

Figure 3.16. Temperature pressure conditions and methane hydrate stability | The phase boundary represents the transition of stable gas hydrate to free gas via dissociation and is based on the empirical relationship between pressure and dissociation temperature from Dickens and Quinby-Hunt (1994). Present day hydrate stability is shown at a seabed depth of 650 m and the present water temperature of 1.5 °C, with the estimated geothermal gradient through the gas hydrate stability zone (GHSZ) indicating the depth of the phase boundary and the observed bottom simulating reflector (BSR). Gas hydrate stability at the seabed is also shown to be less sensitive to future climate warming scenarios (3 °C increase in water bottom temperature in Baffin Bay) due to the relatively large water depths.

Post-glacial re-equilibration and shallowing of the phase boundary is evidenced beneath a glacigenic wedge (Figs. 3.10A and 3.13), where the BSR has shallowed significantly and mirrors the post-glacial seabed topography. However, evidence for the phase boundary not yet having re-equilibrated post-glaciation is observed below an area of recent glacial-related seabed erosion (evidenced by glacial lineations) (Fig. 3.13C and 3.14) (Milkov and Sassen, 2000; Wang et al., 2006). This is causing an un-expectedly thin GHSZ in an area of deeper water (Fig. 3.13C and E) and has likely increased geothermal gradient and heat flow estimates (Fig. 3.13).

The sensitivity of the gas hydrate deposits to future climate warming is an important consideration, especially within the Arctic, which is an area sensitive to the amplification of

temperature increases compared to lower latitudes (Serreze et al., 2000; Serreze and Barry, 2011). Bottom water temperatures in Baffin Bay are estimated to increase by 0.2 to 3 °C by 2100 in a response to global warming (Stocker et al., 2014). However, due to the hydrate stability imparted by the relatively deep, and cold waters in Melville Bay, the gas hydrate deposits documented here are, at least in the short-term, likely less sensitive to projected future warming scenarios than hydrates in shallower waters, such as the Barents Sea (Andreassen et al., 2017). Even at the maximum of the estimated warming (3 °C warmer ocean bottom temperatures), hydrate at the seabed is likely to remain stable (Fig. 3.16). This scenario would cause the hydrate phase boundary to shallow by ~50 m causing further dissociation at the base GHSZ. But for gas hydrate to dissociate at the seabed and be released into the atmosphere, ocean bottom water temperature would likely need to increase by ~8 °C, a scenario that is currently unlikely.

3.6. Conclusions

Numerous fluid related anomalies have been identified and mapped throughout the Cenozoic sedimentary succession of the Melville Bay continental shelf margin, using extensive 3D seismic data coverage. These data provide the most widespread and high-resolution imaging of the subsurface along the west coast of Greenland and the identified fluid anomalies represent the most northerly recorded occurrence of shallow gas and gas hydrates in Baffin Bay. Shallow gas anomalies have been categorized by different trapping styles, with free gas occurring in isolated pockets (category I), trapped at the base of the gas hydrate stability zone (GHSZ) (II), within laterally extensive glacial clinoforms (III) and finally within an Eocene aged, giant mass transport deposit reservoir (IV). Extensive gas hydrate deposits have been identified across an area of 537 km^2 via the identification of a discontinuous bottom simulating reflector (BSR) that represents the base of the GHSZ. The BSR was used to estimate a near surface geothermal gradient of 49 °C/km across the GHSZ and a heat flow of 70-90 mW/m^2, providing the first geothermal gradient and heat flow data points on the entire west Greenland margin.

Paleo-rift topography is predicted to have influenced fluid migration and the thermal regime, with increased concentrations of gas and all gas hydrate deposits occurring above the centre and western flank of the Melville Bay Ridge (MBR). Regional post-rift stratigraphy onlaps and is tilted towards the ridge, promoting fluid migration towards the ridge crest. Related sets of faults along the ridge flanks have likely provided fluid migration pathways from potential deeply buried Cretaceous source rocks towards the overlying Cenozoic stratigraphy. Leakage from the Eocene reservoir is also likely, evidenced by condensed gas anomalies both within and above the densely faulted overlying seal.

Multiple cycles of glaciation since ~2.7 Ma have likely affected the contemporary distribution of hydrocarbons and the fluid migration history. Extensive sediment redistribution from the inner to outer shelf, along with the resulting isostatic compensation, has caused a regional tilt of the margin basinward, focussing fluids up-dip towards the inner shelf and above the ridge. Variations in subsurface conditions due to repeated cycles of glacial (un)loading, have likely promoted fluid flow, potentially causing seal breach and leakage from the Eocene reservoir due to increased pore pressures, as well as increased migration through ridge flanking faults due to fault reactivation. Finally, variations in pressure and temperature likely led to the expansion of gas hydrate deposits during glacial periods, and subsequent hydrate dissociation at the phase boundary during deglaciation; a process which may have contributed to the numerous free gas accumulations observed at the base GHSZ at present day. The relatively large water depths in this gas hydrate province would probably ensure continued stability of the top of the GHSZ both during de-glaciation in the past and during most future warming scenarios over the next several decades.

Acknowledgments

We thank Cairn Energy PLC (Pitu Survey), Shell (Anu Survey) and TGS (2D Regional Survey (BBRE11) for providing the data used within this study and for the permission to publish the images and results herein. The results shown and opinions made are those solely of the authors and are not a representation of Cairn Energy PLC, Shell or TGS. The data were analysed using Petrel software kindly provided under academic license to The University of Manchester by Schlumberger.

References

Andreassen, K., Hubbard, A., Winsborrow, M., Patton, H., Vadakkepuliyambatta, S., Plaza-Faverola, A., Gudlaugsson, E., Serov, P., Deryabin, A., Mattingsdal, R., Mienert, J., and Bunz, S., 2017, Massive blow-out craters formed by hydrate-controlled methane expulsion from the Arctic seafloor: Science, v. 356, p. 948-953.

Andreassen, K., Mienert, J., Bryn, P., and Singh, S. C., 2000, A double gas-hydrate related bottom simulating reflector at the Norwegian continental margin: Annals of the New York Academy of Sciences, v. 912, no. 1, p. 126-135.

Batchelor, C. L., Ottesen, D., and Dowdeswell, J. A., 2017, Quaternary evolution of the northern North Sea margin through glacigenic debris-flow and contourite deposition: Journal of Quaternary Science, v. 32, no. 3, p. 416-426.

Bennett, R., Campbell, D. C., Furze, M. F., and Haggart, J. W., 2014, The shallow stratigraphy and geohazards of the Northeast Baffin Shelf and Lancaster Sound: Bulletin of Canadian Petroleum Geology, v. 62, no. 4, p. 217-231.

Berndt, C., Bunz, S., Clayton, T., Mienert, J., and Saunders, M., 2004, Seismic character of bottom simulating reflectors: examples from the mid-Norwegian margin: Marine and Petroleum Geology, v. 21, p. 723-733.

Biastoch, A., Treude, T., Rüpke, L. H., Riebesell, U., Roth, C., Burwicz, E. B., Park, W., Latif, M., Böning, C. W., Madec, G., and Wallmann, K., 2011, Rising Arctic Ocean temperatures cause gas hydrate destabilization and ocean acidification: Geophysical Research Letters, v. 38, no. L08602, p. 1-5.

Bojesen-Koefoed, J. A., 2011, West Greenland Petroleum Systems – an Overview of Source Rocks and Oil Seepages and Their Implications for Offshore Petroleum Exploration: The Geological Survey of Denmark and Greenland.

Bojesen-Koefoed, J. A., Christiansen, F. G., Peter Nytoft, H., and Pedersen, A. K., 1999, Oil seepage onshore West Greenland: evidence of multiple source rocks and oil mixing: Petroleum Geology Conference Series, v. 5, p. 305-314.

Boulanouar, A., Rahmouni, A., Boukalouch, M., Samaouali, A., Géraud, Y., Harnafi, M., and Sebbani, J., 2013, Determination of Thermal Conductivity and Porosity of Building Stone from Ultrasonic Velocity Measurements: Geomaterials, v. 03, no. 04, p. 138-144.

Brown, C. S., Newton, A. M., Huuse, M., and Buckley, F., 2017, Iceberg scours, pits, and pockmarks in the North Falkland Basin: Marine Geology, v. 386, p. 140-152.

Brown, H. E., Holbrook, W. S., Hornbach, M. J., and Nealon, J., 2006, Slide structure and role of gas hydrate at the northern boundary of the Storegga Slide, offshore Norway: Marine Geology, v. 229, p. 179-186.

Calves, G., Schwab, A. M., Huuse, M., Clift, P. D., and Inam, A., 2010, Thermal regime of the northwest Indian rifted margin e Comparison with predictions: Marine and Petroleum Geology, v. 27, p. 1133-1147.

Cartwright, J., Polygonal Faults and Seal Integrity, *in* Proceedings Sixth EAGE Shale Workshop, Bordeaux, France, 2019, Volume 2019, European Association of Geoscientists & Engineers, p. 1-4.

Cartwright, J. A., and Dewhurst, D. N., 1998, Layer-bound compaction faults in fine-grained sediments: GSA Bulletin, v. 110, no. 10, p. 1242-1257.

Cartwright, J. A., Huuse, M., and Aplin, A., 2007, Seal Bypass Systems: AAPG Bulletin, v. 91, no. 8, p. 1141-1166.

Cartwright, J. A., James, D., and Bolton, A., 2003, The genesis of polygonal fault systems: a review: Geological Society Special Publications, v. 216, p. 223-243.

Cavanagh, A. J., Di Primio, R., Scheck-Wenderoth, M., and Horsfield, B., 2006, Severity and timing of Cenozoic exhumation in the southwestern Barents Sea: Journal of the Geological Society, v. 163, no. 5, p. 761-774.

Chand, S., Thorsnes, T., Rise, L., Brunstad, H., Stoddart, D., Boe, R., Lagstad, P., and Svolsbru, T., 2012, Multiple episodes of fluid flow in the SW Barents Sea (Loppa High) evidenced by gas flares, pockmarks and gas hydrate accumulation: Earth and Planetary Science Letters, v. 331-332, p. 305-314.

Collett, T. S., Johnson, A., Knapp, C., and Boswell, R., 2009, Natural gas hydrates: a review, *in* Collett, T. S., Johnson, A., Knapp, C., and Boswell, R., eds., Natural gas hydrates - Energy resource potential and associated geologic hazards, American Association of Petroleum Geologists Memoir, p. 89.

Cox, D. R., Huuse, M., Newton, A. M. W., Gannon, P., and Clayburn, J., 2020a, Slip Sliding Away: Enigma of Large Sandy Blocks within a Gas Bearing Mass Transport Deposit, Offshore NW Greenland: AAPG Bulletin, v. 104, no. 5, p. 1011-1043.

Cox, D. R., Knutz, P. C., Campbell, D. C., Hopper, J. R., Newton, A. M. W., Huuse, M., and Gohl, K., 2020b, Geohazard detection using 3D seismic data to enhance offshore scientific drilling site selection: Scientific Drilling, v. 28, p. 1-27.

Cox, D. R., Newton, A. M. W., and Huuse, M., 2020c, An introduction to seismic reflection data: acquisition, processing and interpretation, *in* Scarselli, N., Adam, J., and Chiarella, D., eds., Regional Geology and Tectonics - Principles of Geologic Analysis: Amsterdam, Netherlands, Elsevier, p. 744.

Crémière, A., Lepland, A., Chand, S., Sahy, D., Condon, D. J., Noble, S. R., Martma, T., Thorsnes, T., Sauer, S., and Brunstad, H., 2016, Timescales of methane seepage on the Norwegian margin following collapse of the Scandinavian Ice Sheet: Nature communications, v. 7, no. 1, p. 1-10.

Davies, J. H., 2013, Global map of solid Earth surface heat flow: Geochemistry Geophysics Geosystems v. 14, no. 10, p. 1525-2027.

Demirbas, A., 2010, Methane hydrates as potential energy resource: Part 1 – Importance, resource and recovery facilities: Energy Conversion and Management, v. 51, no. 7, p. 1547-1561.

Dickens, G. R., and Quinby-Hunt, M. S., 1994, Methane hydrate stability in seawater: Geophysical Research Letters, v. 21, no. 19, p. 2115-2118.

Esteban, L., Pimienta, L., Sarout, J., Delle Piane, C., Haffen, S., Geraud, Y., and Timms, N. E., 2015, Study cases of thermal conductivity prediction from P-wave velocity and porosity: Geothermics, v. 53, p. 255-269.

Fjeldskaar, W., and Amantov, A., 2018, Effects of glaciations on sedimentary basins: Journal of Geodynamics, v. 118, p. 66-81.

Fleischer, P., Orsi, T. H., Richardson, M. D., and Anderson, A. L., 2001, Distribution of free gas in marine sediments: a global overview: Geo-marine Letters, v. 21, p. 103-122.

Floodgate, G. D., and Judd, A. G., 1992, The origins of shallow gas: Continental Shelf Research, v. 12, no. 10, p. 1145-1156.

Ganguly, N., Spence, G., Chapman, N., and Hyndman, R., 2000, Heat flow variations from bottom simulating reflectors on the Cascadia margin: Marine geology, v. 164, no. 1-2, p. 53-68.

Geletti, R., and Busetti, M., 2011, A double bottom simulating reflector in the western Ross Sea, Antarctica: Journal of Geophysical Research: Solid Earth, v. 116, no. B4.

Goffey, G., Attree, M., Curtis, P., Goodfellow, F., Lynch, J., Mackertich, D., Orife, T., and Tyrrell, W., 2016, New exploration discoveries in a mature basin: offshore Denmark, *in* Bowman, M., and Levell, B., eds., Petroleum Geology of NW Europe: 50 Years of Learning – Proceedings of the 8th Petroleum Geology Conference: London, Geological Society.

Goulty, N., 2008, Geomechanics of polygonal fault systems: a review: Petroleum Geoscience, v. 14, no. 4, p. 389-397.

Goulty, N., and Swarbrick, R., 2005, Development of polygonal fault systems: a test of hypotheses: Journal of the Geological Society, v. 162, no. 4, p. 587-590.

Grassmann, S., Cramer, B., Delisle, G., Hantschel, T., Messner, J., and Winsemann, J., 2010, pT-effects of Pleistocene glacial periods on permafrost, gas hydrate stability zones and reservoir of the

Mittelplate oil field, northern Germany: Marine and petroleum geology, v. 27, no. 1, p. 298-306.

Grauls, D., 2001, Gas hydrates: importance and applications in petroleum exploration: Marine and Petroleum Geology, v. 18, p. 519-523.

Gregersen, G., Knutz, P. C., Nøhr-Hansen, H., Sheldon, E., and Hopper, J. R., 2019, Tectonostratigraphy and evolution of the West Greenland continental margin: Bulletin of the Geological Society of Denmark, v. 67, p. 1-21.

Gregersen, U., Hopper, J. R., and Knutz, P. C., 2013, Basin seismic stratigraphy and aspects of prospectivity in the NE Baffin Bay, Northwest Greenland: Marine and Petroleum Geology, v. 46, p. 1-18.

Gregersen, U., Knutz, P. C., and Hopper, J. R., 2016, New geophysical and geological mapping of the eastern Baffin Bay region, offshore West Greenland: Geological Survey of Denmark and Greenland Bulletin, v. 35, p. 83-86.

Grevemeyer, I., and Villinger, H., 2001, Gas hydrate stability and the assessment of heat flow through continental margins: Geophysics, v. 145, p. 647-660.

Hermanrud, C., and Nordgard Bolas, H. M., 2002, Leakage from overpressured hydrocarbon reservoirs at Haltenbanken and in the northern North Sea, *in* Koestler, A. G., and Hunsdale, R., eds., Hydrocarbon Seal Quantification, Volume 11: Amsterdam, Elsevier Science, p. 221-231.

Hillman, J. I. T., Cook, A. E., Sawyer, D. E., Küçük, H. M., and Goldberg, D. S., 2017, The character and amplitude of 'discontinuous' bottom-simulating reflections in marine seismic data: Earth and Planetary Science Letters, v. 459, p. 157-169.

Hilterman, F. J., 2001, Seismic Amplitude Interpretation, Tulsa, OK, Society of Exploration Geophysicists, Distinguished Instructor Series No. 4, 244 p.:

Huuse, M., Jackson, C. A.-L., Rensbergen, P. V., Davies, R. J., Flemings, P. B., and Dixon, R. J., 2010, Subsurface sediment remobilization and fluid flow in sedimentary basins: an overview: Basin Research, v. 22, no. 4, p. 342-360.

Ingram, G. M., and Urai, J. L., 1999, Top-seal leakage through faults and fractures: the role of mudrock properties: Geological Society, London, Special Publications, v. 158, no. 1, p. 125-135.

Johansen, H., Fjeldskaar, W., and Mykkeltveit, J., 1996, The influence of glaciation on the basin temperature regime: Global and Planetary Change, v. 12, no. 1-4, p. 437-448.

Jung, W. Y., and Vogt, P. R., 2004, Effects of bottom water warming and sea level rise on Holocene hydrate dissociation and mass wasting along the Norwegian-Barents Continental Margin: Journal of Geophysical Research: Solid Earth, v. 109, no. B6.

Karisiddaiah, S. M., and Veerayya, M., 1994, Methane-bearing shallow gas-charged sediments in the eastern Arabian Sea: a probable source for greenhouse gas: Continental Shelf Research, v. 14, no. 12, p. 1361-1370.

Kjemperud, A., and Fjeldskaar, W., 1992, Pleistocene glacial isostasy - implications for petroleum geology: NPF Special Publication, v. 1, p. 187-195.

Knapp, L. J., Harris, N. B., and McMillan, J. M., 2019, A sequence stratigraphic model for the organic-rich Upper Devonian Duvernay Formation, Alberta, Canada: Sedimentary Geology, v. 387, p. 152-181.

Knutz, P. C., Campbell, D. C., Bierman, P. R., de Vernal, A., Huuse, M., Jennings, A., Cox, D. R., DeConto, R., Gohl, K., Hogan, K., Hopper, J. R., Keisling, B., Newton, A. M. W., Perez, L., Rebschläger, J., Sliwinska, K. K., Thomas, E., Willerslev, E., Xuan, C., and Stoner, J., 2018, Cenozoic

evolution of the northern Greenland Ice Sheet exposed by transect drilling in northeast Baffin Bay (CENICE): International Ocean Discovery Program.

Knutz, P. C., Gregersen, U., and Hopper, J. R., 2012, Late Paleogene Submarine Fans in Baffin Bay and North-West Greenland, 74th EAGE Conference and Exhibition incorporating EUROPEC 2012 Copenhagen, EAGE, p. 5.

Knutz, P. C., Harrison, C., Brent, T. A., Gregersen, G., and Hopper, J. R., submitted, Baffin Bay Tectono-Sedimentary Element, *in* Drachev, S., and Moore, T. E., eds., Arctic Sedimentary Basins, Volume Geological Society Memoir: London, Geological Society London.

Knutz, P. C., Hopper, J. R., Gregersen, U., Nielsen, T., and Japsen, P., 2015, A contourite drift system on the Baffin Bay–West Greenland margin linking Pliocene Arctic warming to poleward ocean circulation: Geology, v. 43, no. 10, p. 907-910.

Knutz, P. C., Newton, A. M. W., Hopper, J. R., Huuse, M., Gregersen, U., Sheldon, E., and Dybkjær, K., 2019, Eleven phases of Greenland Ice Sheet shelf-edge advance over the past 2.7 million years: Nature Geoscience, v. 12, p. 361-368.

Krey, V., Canadell, J. G., Nakicenovic, N., Abe, Y., Andruleir, H., Archer, D., Grubler, A., Hamilton, N. T. M., Johnson, A., Kostov, V., Lamarque, J., Langhorne, N., Nisbet, E. G., O'Neil, B., Riahi, K., Riedel, M., Wang, W., and Yakushev, V., 2009, Gas hydrates: entrance to a methane age or climate threat?: Environmental Research Letters, v. 4, p. 1-6.

Kuijpers, A., Dalhoff, F., Brandt, M., Hümbs, P., Schott, T., and Zotova, A., 2007, Giant iceberg plow marks at more than 1 km water depth offshore West Greenland: Marine Geology, v. 246, no. 1, p. 60-64.

Kvenvolden, K. A., 1993, A primer on gas hydrates, *in* Howell, D. G., Wiese, K., Fanelli, M., Zink, L. L., and Cole, F., eds., The Future of Energy Gases, Volume US Geological Survey Professional Paper 1570: Washington DC, USA, USGS, p. 279-291.

Larsen, L. M., Heaman, L. M., Creaser, R. A., Frei, R., and Hutchinson, M., 2009, Tectonomagmatic events during stretching and basin formation in the Labrador Sea and the Davis Strait: evidence from age and composition of Mesozoic to Palaeogene dyke swarms in West Greenland: Journal of the Geological Society, v. 166, p. 999-1012.

Locarnini, R. A., Mishonov, A. V., Antonov, J. I., Boyer, T. P., Garcia, H. E., Baranova, O. K., Zweng, M. M., Paver, C. R., Reagan, J. R., Johnson, D. R., Hamilton, M., and Seidov, D., 2013, World Ocean Atlas 2013, *in* Levitus, S., and Mishonov, A., eds., Technical Ed.; NOAA Atlas NESDIS, Volume 73, p. 39.

Løtveit, I. F., Gudmundsson, A., and Fjeldskaar, W., 2011, Effects of stress changes due to glacial erosion on reservoir excess pressure and fault-zone reactivation: EGU Gen. Assem.

Lucazeau, F., 2019, Analysis and mapping of an updated terrestrial heat flow data set: Geochemistry, Geophysics, Geosystems, v. 20, no. 8, p. 4001-4024.

McConnell, D. R., Zhang, Z., and Boswell, R., 2012, Review of progress in evaluating gas hydrate drilling hazards: Marine and Petroleum Geology, v. 34, no. 1, p. 209-223.

McGlade, C., and Ekins, P., 2015, The geographical distribution of fossil fuels unused when limiting global warming to 2 °C: Nature, v. 517, p. 187-190.

Medvedev, S., Hartz, E. H., Schmid, D. W., Zakariassen, E., and Varhaug, P., 2019, Influence of glaciations on North Sea petroleum systems: Geological Society, London, Special Publications, v. 494, p. SP494-2018-2183.

Merey, S., 2016, Drilling of gas hydrate reservoirs: Journal of Natural Gas Science and Engineering, v. 35, p. 1167-1179.

Mienert, J., Andreassen, K., Posewang, J., and Lukas, D., 2000, Changes of the hydrate stability zone of the Norwegian margin from glacial to interglacial times: Annals of the New York Academy of Sciences, v. 912, no. 1, p. 200-210.

Milkov, A. V., and Sassen, R., 2000, Thickness of the gas hydrate stability zone, Gulf of Mexico continental slope: Marine and Petroleum Geology, v. 17, p. 981-991.

Minshull, T. A., Some comments on the estimation of geothermal gradients from depths of bottom simulating reflectors, *in* Proceedings Proceedings of the 7th international conference on gas hydrates (ICGH 2011), Edinburgh, UK, 17-21 July 2011 2011, p. 1-8.

Minshull, T. A., and Keddie, A., 2010, Measuring the geotherm with gas hydrate bottom-simulating reflectors: a novel approach using three-dimensional seismic data from the eastern Black Sea: Terra Nova, v. 22, no. 2, p. 131-136.

Minshull, T. A., Marín-Moreno, H., Betlem, P., Bialas, J., Bünz, S., Burwicz, E., Cameselle, L., Cifci, G., Giustinaini, M., Hillman, J. I. T., Hölz, S., Hopper, J. R., Ion, G., León, R., Magalhaes, V., Makovsky, Y., Mata, M., Max, M. D., Nielsen, T., Okay, S., Ostrovsky, I., O'Neil, N., Pinheiro, L. M., Plaza-Faverola, A., Rey, D., Roy, S., Schwalenberg, K., Senger, K., Vadakkepuliyambatta, S., Vasilev, A., and Vázquez, J. T., 2020, Hydrate occurrence in Europe: A review of available evidence: Marine and Petroleum Geology, v. 111, p. 735-764.

Muller, S., Reinhardt, L., Franke, D., Gaedicke, C., and Winsemann, J., 2018, Shallow gas accumulations in the German North Sea: Marine and Petroleum Geology, v. 91, p. 139-151.

Newton, A. M., Huuse, M., and Brocklehurst, S. H., 2016, Buried iceberg scours reveal reduced North Atlantic Current during the stage 12 deglacial: Nature communications, v. 7, no. 1, p. 1-7.

Newton, A. M. W., Huuse, M., and Brocklehurst, S. H., 2018, A persistent Norwegian Atlantic Current through the Pleistocene glaciations: Geophysical Research Letters, v. 45, no. 11, p. 5599-5608.

Newton, A. M. W., Huuse, M., Knutz, P. C., Cox, D. R., and Brocklehurst, S. H., 2020, Repeated ice streaming on the northwest Greenland shelf since the onset of the Middle Pleistocene Transition: The Cryosphere Discuss., v. 2019, p. 1-18.

Newton, A. M. W., Knutz, P. C., Huuse, M., Gannon, P., Brocklehurst, S. H., Clausen, O. R., and Gong, Y., 2017, Ice stream reorganization and glacial retreat on the northwest Greenland shelf: Geophysical Research Letters, v. 44, p. 7826-7835.

Nielsen, T., Laier, T., Kuijpers, A., Rasmussen, T. L., Mikkelsen, N. E., and Nørgård-Pedersen, N., 2014, Fluid flow and methane occurrences in the Disko Bugt area offshore West Greenland: indications for gas hydrates?: Geo-Marine Letters, v. 34, no. 6, p. 511-523.

Nohr-Hansen, H., Pedersen, G. K., Knutz, P. C., Bojesen-Koefoed, J. A., Sliwinska, K. K., and Hovikoski, J., 2018, Potential Cretaceous source-rocks from the north-east Baffin Bay, West Greenland, AAPG Europe Regional Conference, Global Analogues of the Atlantic Margin: Lisbon, AAPG.

Oakey, G. N., and Chalmers, J. A., 2012, A new model for the Paleogene motion of Greenland relative to North America: Plate reconstructions of the Davis Strait and Nares Strait regions between Canada and Greenland: Journal of Geophysical Research, v. 117, no. B10, p. 1-28.

Ostanin, I., Anka, Z., and Di Primio, R., 2017, Role of faults in Hydrocarbon Leakage in the Hammerfest Basin, SW Barents Sea: Insights from seismic data and numerical modelling: Geosciences, v. 7, no. 2, p. 28.

Planke, S., Symonds, P. A., Alvestad, E., and Skogseis, J., 2009, Mid-Cretaceous source rock subcropping in the Baffin Bay: GEO ExPro, v. 6, p. 1-8.

Plaza-Faverola, A., Bünz, S., and Mienert, J., 2011, Repeated fluid expulsion through sub-seabed chimneys offshore Norway in response to glacial cycles: Earth and Planetary Science Letters, v. 305, no. 3-4, p. 297-308.

Portnov, A., Vadakkepuliyambatta, S., Mienert, J., and Hubbard, A., 2016, Ice-sheet-driven methane storage and release in the Arctic: Nature communications, v. 7, no. 1, p. 1-7.

Posamentier, H. W., 2004, Seismic Geomorphology: Imaging Elements of Depositional Systems from Shelf to Deep Basin Using 3D Seismic Data: Implications for Exploration and Development, *in* Davies, R. J., Cartwright, J. A., Stewart, S. A., Lappin, M., and Underhill, J. R., eds., 3D Seismic Technology: Application to the Exploration of Sedimentary Basins: London, Geological Society of London, p. 11-24.

Posamentier, H. W., Davies, R. J., Cartwright, J. A., and Wood, L., 2007, Seismic geomorphology- an overview, *in* Davies, R. J., Posamentier, H. W., Wood, L., and Cartwright, J. A., eds., Seismic Geomorphology: Applications to Hydrocarbon Exploration and Production: London, Geological Society of London, p. 1-14.

Prince, P. K., 1990, Current drilling practices and the occurrence of shallow gas, *in* Ardus, D. A., and Green, C. D., eds., Safety in offshore drilling: Dordrecht, Springer, p. 3-25.

Pye, G. D., and Hyndman, R. D., 1972, Heat-flow measurements in Baffin Bay and the Labrador Sea: Journal of Geophysical Research, v. 77, no. 5, p. 938-944.

Rebesco, M., Hernández-Molina, F. J., Van Rooij, D., and Wåhlin, A., 2014, Contourites and associated sediments controlled by deep-water circulation processes: state-of-the-art and future considerations: Marine Geology, v. 352, p. 111-154.

Ruppel, C., 2000, Thermal state of the gas hydrate reservoir, *in* Max, M. D., ed., Natural Gas Hydrate: In Oceanic and Permafrost Environments: Dordrecht, The Netherlands, Springer, p. 29-42.

Ruppel, C. D., and Kessler, J. D., 2017, The interaction of climate change and methane hydrates: Reviews of Geophysics, v. 55, no. 1, p. 126-168.

Schoell, M., 1988, Multiple origins of methane in the earth: Chemical Geology, v. 71, p. 1-10.

Serié, C., Huuse, M., Schødt, N. H., Brooks, J. M., and Williams, A., 2017, Subsurface fluid flow in the deep-water Kwanza Basin: Basin Research, v. 29, no. 2, p. 149-179.

Serov, P., Vadakkepuliyambatta, S., Mienert, J., Patton, H., Portnov, A., Silyakova, A., Panieri, G., Carroll, M. L., Carroll, J., and Andreassen, K., 2017, Postglacial response of Arctic Ocean gas hydrates to climatic amelioration: Proceedings of the National Academy of Sciences, v. 114, no. 24, p. 6215-6220.

Serreze, M., Walsh, J., Chapin, F. S., Osterkamp, T., Dyurgerov, M., Romanovsky, V., Oechel, W., Morison, J., Zhang, T., and Barry, R., 2000, Observational evidence of recent change in the northern high-latitude environment: Climatic change, v. 46, no. 1-2, p. 159-207.

Serreze, M. C., and Barry, R. G., 2011, Processes and impacts of Arctic amplification: A research synthesis: Global and planetary change, v. 77, no. 1-2, p. 85-96.

Shankar, U., and Riedel, M., 2011, Gas hydrate saturation in the Krishna–Godavari basin from P-wave velocity and electrical resistivity logs: Marine and Petroleum Geology, v. 28, no. 10, p. 1768-1778.

Shankar, U., Riedel, M., and Sathe, A. V., 2010, Geothermal modeling of the gas hydrate stability zone along the Krishna Godavari Basin: Marine Geophysical Researches, v. 31, no. 1-2, p. 17-28.

Spence, G. D., Minshull, T. A., and Fink, C., Seismic studies of methane gas hydrate, offshore Vancouver Island, *in* Proceedings PROCEEDINGS-OCEAN DRILLING PROGRAM SCIENTIFIC RESULTS1995, National Science Foundation, p. 163-174.

Stocker, T. F., Qin, D., Plattner, G.-K., Tignor, M. M., Allen, S. K., Boschung, J., Nauels, A., Xia, Y., Bex, V., and Midgley, P. M., 2014, Climate Change 2013: The physical science basis. contribution of working group I to the fifth assessment report of IPCC the intergovernmental panel on climate change: Cambridge, UK, Cambridge University Press, p. 1-29.

Stoll, R. D., Ewing, J., and Bryan, G. M., 1971, Anomalous wave velocities in sediments containing gas hydrates: Journal of Geophysical Research, v. 76, no. 8, p. 2090-2094.

Stopler, D. A., Lawson, M., Davis, C. L., Ferreira, A. A., Santos Neto, E. V., Ellis, G. S., Lewan, M. D., Martini, A. M., Tang, Y., Schoell, M., Sessions, A. L., and Eiler, J. M., 2014, Formation temperatures of thermogenic and biogenic methane: Science, v. 344, no. 6191, p. 1500-1503.

Tang, C. C. L., Ross, C. K., Yao, T., Petrie, B., DeTracey, B. M., and Dunlap, E., 2004, The circulation, water masses and sea-ice of Baffin Bay: Progress in Oceanography, v. 63, p. 183-228.

Tasianas, A., Bünz, S., Bellwalkd, B., Hammer, Ø., Planke, S., Lebedeva-Ivanova, N., and Krassakis, P., 2018, High-resolution 3D seismic study of pockmarks and shallow fluid flow systems at the Snøhvit hydrocarbon field in the SW Barents Sea: Marine Geology, v. 403, p. 247-261.

Verweij, J. M., Ten Veen, J. H., De Bruin, G., Nelskamp, S. N., Donders, T., Kunakbayeva, G., and Geel, K., 2012, Shallow Gas Migration and Trapping in the Cenozoic Eridanos Delta Deposits, Dutch Offshore, 74th EAGE Conference and Exhibition incorporating EUROPEC 2012: Copenhagen.

Waite, W. F., Santamarina, J. C., Cortes, D. D., Dugan, B., Espinoza, D., Germaine, J., Jang, J., Jung, J., Kneafsey, T. J., and Shin, H., 2009, Physical properties of hydrate-bearing sediments: Reviews of geophysics, v. 47, no. 4.

Wang, S., Wen, Y., and Song, H., 2006, Mapping the thickness of the gas hydrate stability zone in the South China Sea: TAO: Terrestrial, Atmospheric and Oceanic Sciences, v. 17, no. 4, p. 815.

Welford, K., Peace, A., Geng, M., and Dickie, K., 2018, Crustal structure of Baffin Bay from constrained 3-D gravity inversion and deformable plate tectonic models: Geophysical Journal International, v. 214, no. 2, p. 1281-1300.

White, R. S., 1979, Gas hydrate layers trapping free gas in the gulf of oman: Earth and Planetary Science Letters, v. 42, p. 114-120.

Whittaker, R. C., Hamann, R. E., and Pulvertaft, T. C. R., 1997, A New Frontier Province Offshore Northwest Greenland: Structure, Basin Development, and Petroleum Potential of the Melville Bay Area: AAPG Bulletin, v. 81, no. 6, p. 978-998.

Wilson, H., 1975, Time of hydrocarbon expulsion, paradox for geologists and geochemists: AAPG Bulletin, v. 59, no. 1, p. 69-84.

Woodworth-Lynas, C., Simms, A., and Rendell, C., 1985, Iceberg grounding and scouring on the Labrador Continental Shelf: Cold Regions Science and Technology, v. 10, no. 2, p. 163-186.

Yamano, M., Uyeda, S., Aoki, Y., and Shipley, T. H., 1982, Estimates of heat flow derived from gas hydrates: Geology, v. 10, no. 7, p. 339-343.

Yang, S., Choi, J. C., Vanneste, M., and Kvalstad, T. J., 2018, Effects of gas hydrates dissociation on clays and submarine slope stability: Bulletin of Engineering Geology and the Environment, v. 77, no. 3, p. 941-952.

Zhao, J., Song, Y., Lim, X., and Lam, W., 2017, Opportunities and challenges of gas hydrate policies with consideration of environmental impacts: Renewable and Sustainable Energy Reviews, v. 70, p. 875-885.

Zieba, K. J., and Grover, A., 2016, Isostatic response to glacial erosion, deposition and ice loading. Impact on hydrocarbon traps of the southwestern Barents Sea: Marine and Petroleum Geology, v. 78, p. 168-183.

4

Geohazard Assessment for Scientific Drilling Site Selection

Preamble

DRC interpreted the data, wrote the manuscript and drafted the figures presented in this chapter. PCK and DCC are lead proponent and data lead on IODP Proposal 909 respectively, and assisted this work by leading the selection of stratigraphic targets (Targets I–VII), conducting depth conversions and, in collaboration with DRC, selecting drill site locations. JRH was the lead on LAKO UHR data acquisition and processing. AMWN assisted DRC with the geohazard assessment and figure creation. All the authors were part of the Proposal 909 seismic team and assisted with initial stratigraphic target and site selections, along with conducting co-author reviews on the manuscript and figures.

This manuscript is published in the journal *Scientific Drilling*:

Cox, D. R., Knutz, P. C., Campbell, D. C., Hopper, J. R., Newton, A. M. W., Huuse, M., and Gohl, K., 2020, Geohazard detection using 3D seismic data to enhance offshore scientific drilling site selection, Scientific Drilling, v. 28, pp. 1-27.

Geohazard Detection Using 3D Seismic Data to Enhance Offshore Scientific Drilling Site Selection

David R. Cox[1], Paul C. Knutz[2], D. Calvin Campbell[3], John R. Hopper[2],

Andrew M. W. Newton[1, 4], Mads Huuse[1] and Karsten Gohl[5]

[1]Department of Earth and Environmental Sciences, The University of Manchester

[2]Geophysics Department, Geological Survey of Denmark and Greenland, Øster Voldgade 10, DK-1350 Copenhagen K, Denmark

[3]Geological Survey of Canada (Atlantic), Natural Resources Canada, Dartmouth, Nova Scotia B2Y 4A2, Canada

[4]School of Natural and Built Environment, Elmwood Building, Queens University Belfast, University Road, UK, BT7 1NN

[5]Alfred-Wegener-Institut Helmholtz-Zentrum für Polar- und Meeresforschung, Bremerhaven, Germany

Abstract

A geohazard assessment workflow is presented that maximises the use of 3D seismic reflection data to improve the safety and success of offshore scientific drilling. This workflow has been implemented for International Ocean Discovery Program (IODP) Proposal 909 that aims to core seven sites with targets between 300-1000 m below seabed across the northwest Greenland continental shelf. This glaciated margin is a frontier petroleum province containing potential drilling hazards that must be avoided during drilling. Modern seismic interpretation techniques are used to identify, map and spatially analyse seismic features that may represent subsurface drilling hazards, such as seabed structures, faults, fluids and challenging lithologies. These hazards are compared against the spatial distribution of stratigraphic targets to guide site selection and minimize risk. The 3D seismic geohazard assessment specifically advanced the proposal by providing a more detailed and spatially extensive understanding of hazard distribution that was used to confidently select 8 new site locations, abandon 4 others and fine-tune sites originally selected using 2D seismic data. Had several of the more challenging areas targeted by this

proposal only been covered by 2D seismic data, it is likely that they would have been abandoned, restricting access to stratigraphic targets. The results informed the targeted location of an ultra-high-resolution 2D seismic survey by minimising acquisition in unnecessary areas, saving valuable resources. With future IODP missions targeting similarly challenging frontier environments where 3D seismic data are available, this workflow provides a template for geohazard assessments that will enhance the success of future scientific drilling.

4.1. Introduction

When planning an offshore drilling campaign, one of the primary technical concerns that governs site selection is safety (Jeanjean et al., 2005; Mearns and Flin, 1995). The subsurface can be hazardous and is full of unknowns; therefore, it requires the full interrogation of all available data to reduce risks during drilling. Common subsurface geohazards include phenomena related to excess pore pressure such as shallow hydrocarbons, shallow water flows, faulting to shallow depths, mud volcanoes, and pockmarks; all of which can lead to incompetent sediments and seabed instability (Aird, 2010; Jensen and Cauquil, 2013; West and West, 2005; Wood and Hamilton, 2002). Identifying these hazards prior to drilling allows for decisions to be made during site selection to either avoid the hazard completely, mitigate it or to select the lowest risk option (Aird, 2010; Jensen and Cauquil, 2013). This process, often termed a geohazard assessment, is integral to drilling success and safety, with its effectiveness often relying on the availability of high quality data coverage such as seismic reflection, bathymetry and well data.

The importance of geohazard identification is amplified in environments such as deep water, high pressure/high temperature, glaciated margins and frontier petroleum provinces where there is little prior drilling experience (Galavazi et al., 2006; Moore et al., 2007; Weimer and Pettingill, 2007). Within these locations, the frequency and significance of geohazards is often increased, as well as the consequences of accidents (Eriksen et al., 2014; Li et al., 2016). Furthermore, it is often these locations where data coverage and quality are poorest, resulting in a limited subsurface understanding and higher risk to drilling. In the last few decades, exploration for subsurface resources has expanded into more challenging environments due to increased global demand for petroleum products (Mitchell et al., 2012; Poppel, 2018; Suicmez, 2016). This has led to the acquisition of extensive 2D and 3D seismic reflection datasets and industry drilling in frontier areas. The expansion, especially with regards to new 3D seismic reflection data coverage, provides an opportunity to use these data for reasons beyond their original commercial purpose. This includes regional

geological mapping and geohazard assessments allowing site identification and de-risking for scientific boreholes (Dutta et al., 2010; Hovland et al., 1998; Selvage et al., 2012).

Leg/Proposal Number	Location	Ocean	Status
308	Ursa Basin, Gulf of Mexico	Atlantic	Completed
311	Cascadia Margin, OR, USA	Pacific	Completed
322	Nankai Trough, Japan	Pacific	Completed
372A	Hikurangi Margin, New Zealand	Pacific	Completed
P537A	Costa Rica	Pacific	Proposal
P603CDP	Nankai Trough, Japan	Pacific	Proposal
P857C	Balearic Promontory	Mediterranean	Proposal
P859	Amazon Fan, Brazil	Atlantic	Proposal
P908	Costa Rica	Pacific	Proposal
P909	Melville Bay, Greenland	Arctic	Proposal
P935	The Fram Strait	Arctic	Proposal
P943	West Iberian Margin	Atlantic	Proposal

Table 4.1. IODP expeditions and proposals with seismic data

A geohazard assessment involves the geospatial quantification of drilling hazards, ideally through the use of densely sampled 2D or 3D reflection seismic data (Aird, 2010; Heggland et al., 1996; Khan et al., 2018; Selvage et al., 2012). In the past, the required resolution to detect small, but potentially hazardous features, could only be provided through dedicated high-resolution site surveys across potential drill sites using such tools as sub-bottom profilers, small volume airguns, or sparker reflection systems (Jensen and Cauquil, 2013; Parkinson, 2000). Today, the acquisition of large-scale 3D seismic reflection datasets in frontier basins provides spatial coverage that far exceeds most conventional site surveys (Games and Self, 2017). The processing of these datasets have improved sufficiently to provide vertical resolution that approaches that of a traditional site survey, and often provides a horizontal resolution exceeding that of even closely spaced 2D seismic site surveys (Games and Self, 2017; Oukili et al., 2019). 3D seismic surveys thus minimise the need for additional data, except for particularly complicated areas (Hill, 1996; Roberts et al., 1996; Selvage et al., 2012; Sharp and Badalini, 2013; Williams and Andresen, 1996).

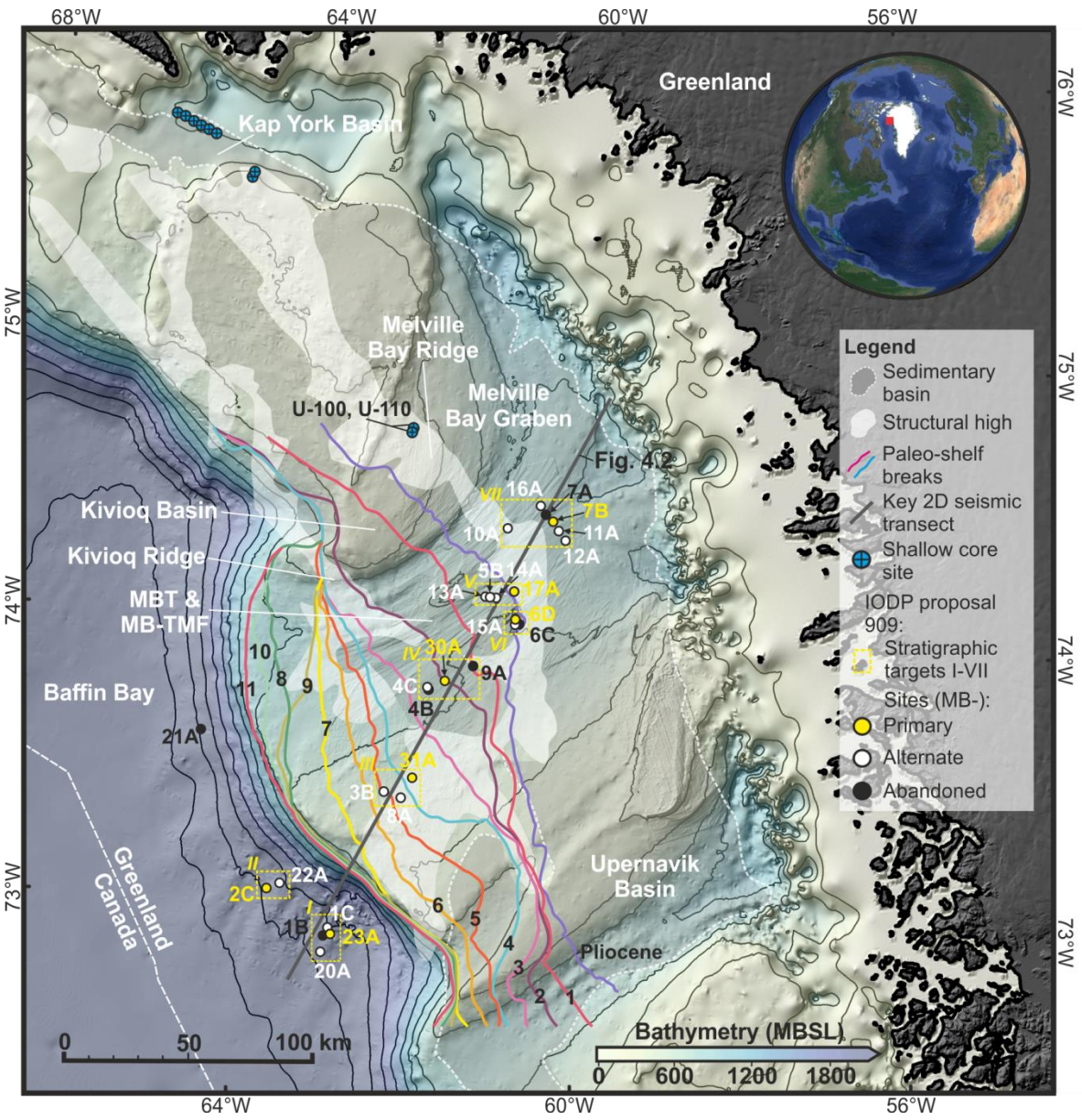

Figure 4.1. Location map | A bathymetric map of the Melville Bay area in northwest Greenland from (Newton et al., 2017), showing the extensive influence of glaciation on the seabed including the Melville Bay Trough (MBT) and Melville Bay Trough Mouth Fan (MB-TMF). The red square on the inset map shows the global location of the bathymetry. Annotations on the map include the distribution of regional rift elements including sedimentary basins and structural ridges, as well as the location of paleo-shelf break positions of glacigenic prograding units from (Knutz et al., 2019). IODP Proposal 909 site locations are shown as well as the associated stratigraphic Targets of each site (I-VII). Shallow cores that were drilled by a consortium led by Shell that provide stratigraphic information used within the proposal are also shown (Acton, 2012; Nøhr-Hansen et al., 2018). The location of the key regional 2D seismic transect used for original site selection is also shown and represents the location of Fig. 4.2.

The increased availability of 3D seismic volumes in continental shelf areas often coincides with areas targeted by scientific drilling programs. These include the International Ocean Discovery Program (IODP) that operates the drilling vessels *Joides Resolution* and *Chikyu* but also national facilities such as the Meeresboden-Bohrgerat (MeBO) of the Alfred Wegener Institute (AWI) and the British Geological Survey (BGS) Rock Drill. For this study, we present data from an Arctic frontier basin that supports site selection for a

proposed scientific drilling leg under the IODP. IODP has an excellent safety record, achieved through review of proposed sites by panels of international experts, and has drilled within frontier petroleum provinces in the past, with examples such as the early passive margin drilling along the western Atlantic margin (e.g. DSDP Legs 11 and 41 (Ewing and Hollister, 1972; Lancelot and Seibold, 1977) and more recently in areas such as the Demerara Rise, offshore Suriname (Leg 207) and the Great Australian Bight (Leg 182) (National Research National Research Council, 2011). Several completed and proposed IODP expeditions report the availability of 3D seismic data within the study area and it is possible that several others had undocumented access (Table 1). As commercial 3D seismic reflection datasets become more widely available for academic research, there is an opportunity to optimize both the scientific benefits and safety of proposed drilling sites by conducting more comprehensive geological and geohazard assessments. This study, whilst focussed on the hazards associated with IODP Proposal 909 within the northwest Greenland glaciated margin (Fig. 4.1), provides a geohazard assessment workflow that optimises drill site selection through the use of 3D seismic data and serves as a template for the improved safety and success of future scientific drilling campaigns using 3D seismic data in frontier areas.

4.2. IODP Proposal 909

4.2.1. Setting

IODP Proposal 909 aims to drill a transect of seven sites across Melville Bay offshore northwest Greenland, in water depths ranging from 0.5-1.9 km (Fig. 4.1). Here, a thick (>2 km) Cenozoic sedimentary succession overlies a rift basin topography that formed during several stages of Early Cretaceous to early Paleogene rifting between Greenland and Canada (Altenbernd et al., 2015; Gregersen et al., 2013; 2016; Oakey and Chalmers, 2012). This includes the extensive, elongate inversion structures of the Melville Bay and Kivioq Ridges. These ridges separate the deep sedimentary basins of the Melville Bay Graben and Kivioq Basin, and contain up to 9 km thick successions of syn-rift (seismic mega-units (mu) mu-G, -F and the lowermost -E) and post-rift (mu-E, -D, -C, -B and -A) sediments (Figs. 4.1 and 4.2) (Altenbernd et al., 2015; Gregersen et al., 2013; 2016; Knutz et al., 2015; Whittaker et al., 1997). Mu-E is attributed to the continental drift phase as seafloor spreading commenced in Baffin Bay. The lower part of mu-D is considered to have formed during the final syn-drift stage influenced by compressional tectonics as a consequence of Greenland converging with the North American plate (Knutz et al., submitted). Deposition of the upper part of mu-D, representing a hemipelagic succession, was presumably deposited during a phase of post-drift tectonic relaxation. The mega-units are separated by

seismic horizons (hz) e1, d1, c1 and b1 that are generally expressed as regional unconformities.

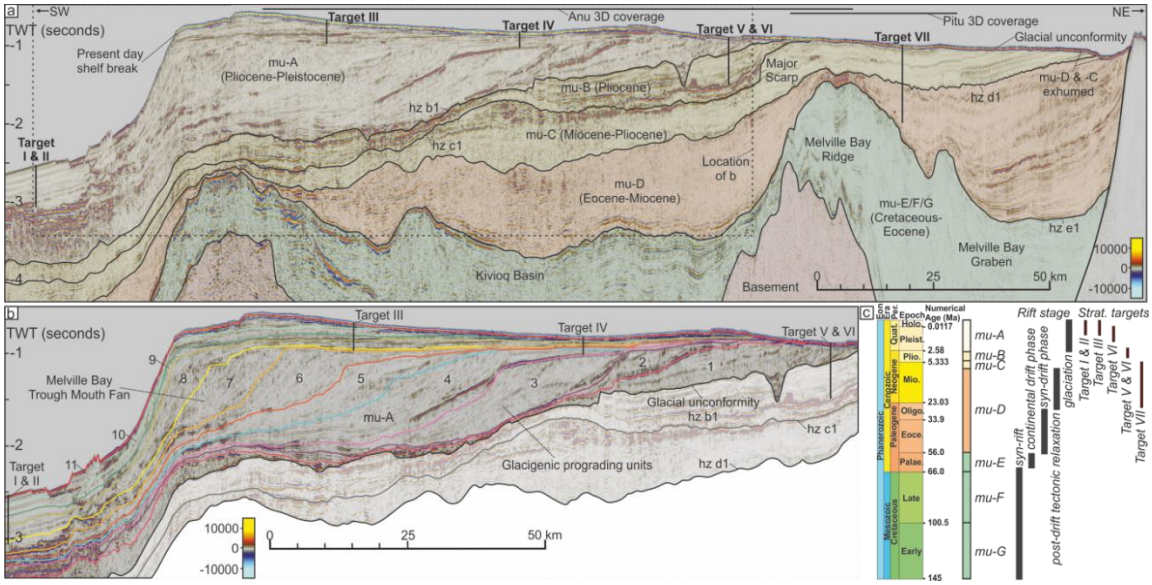

Figure 4.2. Regional Geology | A 2D regional seismic reflection line showing the stratigraphy and structure across the shelf. Regionally mapped seismic mega-unit interpretations from (Gregersen et al., 2013; 2016) and (Knutz et al., 2015) are shown as well as the projected locations of the seven IODP Proposal 909 stratigraphic Targets and the comparative coverage of 3D seismic data. b) An enlarged section of the seismic line from (a) that focusses on the glacigenic wedge that represents the Melville Bay Trough Mouth Fan system, showing the 11 interpreted sub-units of mega unit (mu)-A from (Knutz et al., 2019) as well as the projected location and depth of the IODP Proposal 909 sites. The location of the seismic line is shown on Fig. 4.1.c) A stratigraphic column displaying seven seismic mega-units and their associated rift stages, as well as the expected age of the stratigraphy that comprises each of the stratigraphic Targets (I-VII).

On the inner shelf margin, thick late Miocene and Pliocene (mu-C and mu-B) marine sediments constitute the uppermost post-rift sequence (Knutz et al., 2015). This includes widespread, late Neogene contourites and their correlative mass transport deposits, down-slope from a major erosional scarp above the Melville Bay Ridge (Fig. 4.1 and 4.2). The Neogene sediments are exposed at the seabed on the inner shelf and are progressively buried towards the basin by thick glacigenic packages forming part of mu-A (Fig. 4.2) (Knutz et al., 2019). The exposure and burial of the Neogene marine successions occurred due to multiple phases of ice sheet expansion since the late Pliocene. Through these glaciations, material was eroded and redistributed, leading to over ~100 km of shelf edge progradation and accumulation of the Melville Bay Trough Mouth Fan (MB-TMF) (Figs. 4.1 and 4.2) (Knutz et al., 2019; Newton et al., 2017). These glacigenic progradational units likely consist of highly variable sediment lithologies and grain size compositions (Christ et al., 2020; Knutz et al., 2019). The prograding units are separated by unconformities that generate distinct unconformable seismic reflections that express detailed morphologies formed by sub-glacial erosion and deposition, similar to the features observed on the present seabed (Newton et al., 2020; 2017).

The glacigenic succession (mu-A) has been subdivided into progradational units that suggest a minimum of 11 major phases of ice advance and retreat across the shelf since ~2.7 Ma. These sub-units (1-11), proposed by (Knutz et al., 2019), are used throughout this study (Fig. 4.2b). Furthermore, the regional stratigraphic framework consisting of seven seismic mega-unit subdivisions (mu-G to –A) (Fig. 4.2), was proposed after extensive regional mapping of the northwest Greenland continental margin by (Gregersen et al., 2013; 2016) and (Knutz et al., 2015).

4.2.2. Scientific Drilling Objectives

IODP Proposal 909 aims to illuminate the late Cenozoic history of the northern Greenland Ice Sheet (GrIS) and specifically to ascertain the paleo-ice sheet dynamics during past warm climates (Knutz et al., 2018). This will be achieved by recovering drill cores at seven sites along a transect crossing the northwest Greenland margin (Figs. 4.1 and 4.2), each recovering key stratigraphic targets (Targets I-VII) to obtain a composite stratigraphic succession from Oligocene/early Miocene to Holocene (Fig. 4.2). The overall objective is to examine the range of feedback and forcing mechanisms (oceanic, atmospheric, orbital, tectonic) impacting the GrIS through time – addressing several current themes of the IODP Science Plan (Bickle et al., 2011).

4.2.3. Site Selection Requirements

The seven stratigraphic targets (Targets I-VII) were selected along the southwest-northeast trending regional 2D seismic transect (Figs. 4.1 and 4.2) and represent high-accumulation rate deposits within the hemipelagic sequence of mu-D, contourite drifts of mu-B and -C, as well as potential interglacial and proximal shelf deposits within the trough mouth fan system of mu-A (Fig. 4.2). Once stratigraphic targets were defined, specific drill sites were selected. The strategy for site selection was to maximise both the chance of reaching the stratigraphic target and the chance of good core recovery, whilst avoiding all identified potential drilling hazards. Additionally, the selection of several alternate sites was required in preparation for unexpected drilling issues or iceberg mitigation management.

4.2.4. Regional Geohazard Considerations

The northwest Greenland margin is a frontier petroleum province with potential Cretaceous source rocks identified across the region in shallow cores and outcrop (Fig. 4.1) (Acton, 2012; Bojesen-Koefoed et al., 2004; Nøhr-Hansen et al., 2018; Núñez-Betelu, 1993), as well as deep un-explored sedimentary rift basins (Henriksen et al., 2009). The area experienced a surge in oil and gas exploration activity between 2007-2014, resulting in five exploration licenses being awarded within Melville Bay and the acquisition of extensive 2D

and 3D seismic data sets. A shallow coring program was carried out in 2012 but no exploration wells have been drilled. Since then, the identification of a large potential gas reservoir (Cox et al., 2020a) and widespread evidence for shallow gas and gas hydrates (Cox et al., 2021) further support an active petroleum system, thus underscoring the need for a geohazard assessment study prior to drilling.

Today, marine-terminating glacial outlets do not expand much beyond the coastline, and Melville Bay is generally free of sea ice cover during the summer, allowing access to industry and research vessels (Saini et al., 2020). However, Arctic weather conditions and the potential for icebergs carried northward by the West Greenland coastal current presents a challenge to any logistical operations in the area. The environmental factors, considered alongside the possibility of shallow hydrocarbon occurrence and coarse-grained Quaternary sediments indurated by ice loading, makes drilling complicated and highly reliant on site survey data. To evaluate and select coring sites for Proposal 909, available 2D and 3D seismic reflection data were used to conduct a comprehensive geohazard assessment that maximised the chance of safe drilling and successful core recovery.

4.3. Data

The seismic data used within this study includes four separate surveys that were acquired between 2007 and 2019 (Table 2). All data used were provided in SEG normal polarity with a downward increase in acoustic impedance represented by a red positive peak and a downward decrease in acoustic impedance represented by a blue negative trough (Fig. 4.2). The regional 2D data used in this study, form part of four surveys that were acquired by the geophysical company TGS (2007-2010) as part of the Baffin Bay 2D regional dataset. The dataset was used to help understand the regional geology and map the spatial distribution of stratigraphic packages that represent drilling targets (full extent of regional 2D survey shown by (Gregersen et al., 2019) - Fig. 4.1). From the TGS 2D data, a subset of 7 lines crossing the Melville Bay shelf were used directly within the site selection process (Fig. 4.3) (Table 2).

Two 3D seismic surveys represent the principal data used for geohazard detection within this study (Fig. 4.3). The first is the Pitu survey that was acquired by Cairn Energy PLC in 2011 (Table 2). This survey was also provided as a pre-stack depth migration (PSDM) volume. The survey was reprocessed by CGG in 2013 to provide the Pitu HR (high-resolution) survey, which is a subset of the full volume with increased spatial and vertical resolution (Table 4.2). The second 3D survey, the Anu survey, provides extensive 3D coverage towards the shelf edge and was acquired by Shell in 2013 (Fig. 4.3). In 2019, a new ultra-high-resolution (UHR) survey, the LAKO UHR survey (LAKO is an acronym

for the research vessel *HDMS Lauge Koch*), was acquired across several preliminary site locations through collaboration between the Geological Survey of Denmark and Greenland and Aarhus University (Pearce et al., 2019) (Table 4.2 and Fig. 4.3). The aim was to provide UHR imaging of the upper 500 ms below the seabed in order to supplement the existing industry seismic data within the pre-defined target areas. In addition, several longer transects were obtained that could provide additional seismic-stratigraphic information and add to the reconnaissance of additional sites. Eight lines from the UHR survey were used to characterize drill sites located within the areas of 3D seismic coverage (Fig. 4.3).

Acquisition Parameter	**Seismic Survey**				
	Regional	**Pitu**	**Pitu HR**	**Anu**	**LAKO UHR**
Survey Type	**2D**	**3D**	**3D**	**3D**	**UHR 2D**
Date Acquired	2007-2010	2011	2013 Repro.	2013	2019
Area/Length Used	2,076 km	1,672 km^2	1,135.5 km^2	8700 km^2	306 km
No. of Vessels	1	1	-	2	1
Pop Interval	25 m	25 m (flip-flop)	-	25 m (flip-flop)	5-6 m
Source Depth	8 m	8 m	-	8 m	3 m
Source Separation	-	50 m	-	100 m	-
Streamer Length	6000 m	10 x 7050 m	-	6 x 7050 m	150 m
Streamer Separation	-	100 m	-	200 m	-
No. of Channels	480	564	-	564	40
Receiver Spacing	12.5 m	12.5 m	-	12.5 m	3.125 m
Sampling Rate	2 ms	4 ms	2 ms	2 ms	1 ms
Sail Line Separation	-	1 km	-	600 m	-
No. of 3D Sail Lines	-	93	-	118	-
Bin Spacing Inline	-	25 m	12.5 m	6.25 m	-
Bin Spacing Crossline	-	12.5 m	6.25 m	50 m	-
Fold	120	70	-	70	12.5
Domain	TWT	TWT / Depth	TWT	TWT	TWT
Provided Depth (down to)	9 s	6. 5 s/10 km	5 s	7.5 s	1.4 s
Depth of Given Resolution	1200 ms	1200 ms	1200 ms	1200 ms	900-1100 ms
Av. Dominant Frequency	40 Hz	55 Hz	90 Hz	45 Hz	120 Hz
Dominant Wavelength*	50 m	36 m	22 m	44 m	16.5 m
Vertical Resolution	12.5 m	9 m	6 m	11 m	4 m

***Calculated using an average velocity of 2000 metres per second (m/s).**

Table 4.2. Acquisition parameters and survey statistics for seismic surveys used in this study | A dash (-) represents a parameter that is not applicable for that survey. The Pitu HR parameters can be read from the Pitu survey. Abbreviations used within the table include: two-dimensional (2D), three-dimensional (3D), ultra-high-resolution (UHR), reprocessed (Repro), number (No), average (Av) and two-way-time (TWT). Units used include: metres (m), kilometres (km), milliseconds (ms), seconds (s) and hertz (Hz).

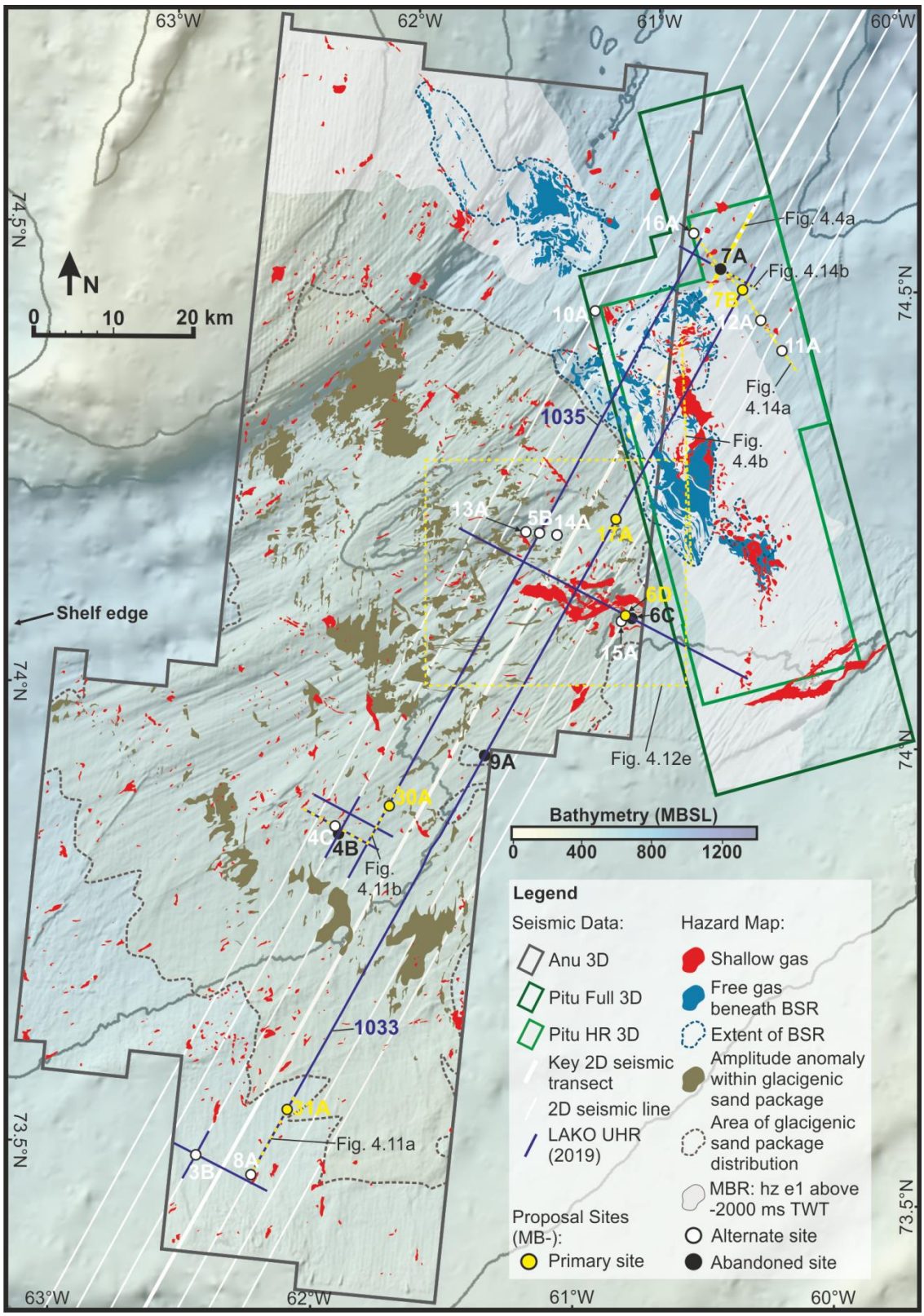

Figure 4.3. Fluid hazard and data map | A map displaying seismic fluid anomalies identified within the study area, the regional bathymetry from (Newton et al., 2017) and the location of all seismic data used within the Proposal 909 study. The location of potential fluid anomalies were identified and mapped via the shallow gas detection process within the geohazard assessment workflow. Active and abandoned IODP Proposal 909 sites that exist within the 3D seismic extent are shown as well as the location of the Melville Bay Ridge (MBR) and Figs. 4.4a-b, 4.11a-b, 4.12e, and 4.14a-b.

4.3.1. Depth Conversion

Depth conversion was required to provide accurate estimates of seismically-defined drill target depths in metres. Velocity information was provided from industry wells drilled by Cairn Energy PLC >~300 km south of the transect (location shown in (Gregersen et al., 2019) – Fig. 4.1), shallow core sites U0100/110 (Fig. 4.1) and from an interval velocity cube that was provided over the Pitu survey area (Figs. 4.3 and 4.4). The interval velocity cube was created from seismic velocities during seismic processing, through the application of a Kirchhoff Pre-Stack TTI Depth Migration (PSDM) that used a bin size of 12.5 x 25 m and a migration half aperture of 4500 m (Fig. 4.4). This process produced a depth converted version of the Pitu 3D survey. The interval velocities, and the depth cube however, have not been calibrated to measured depth data, due to large distances to the closest well (>~300 km), and likely contain some error.

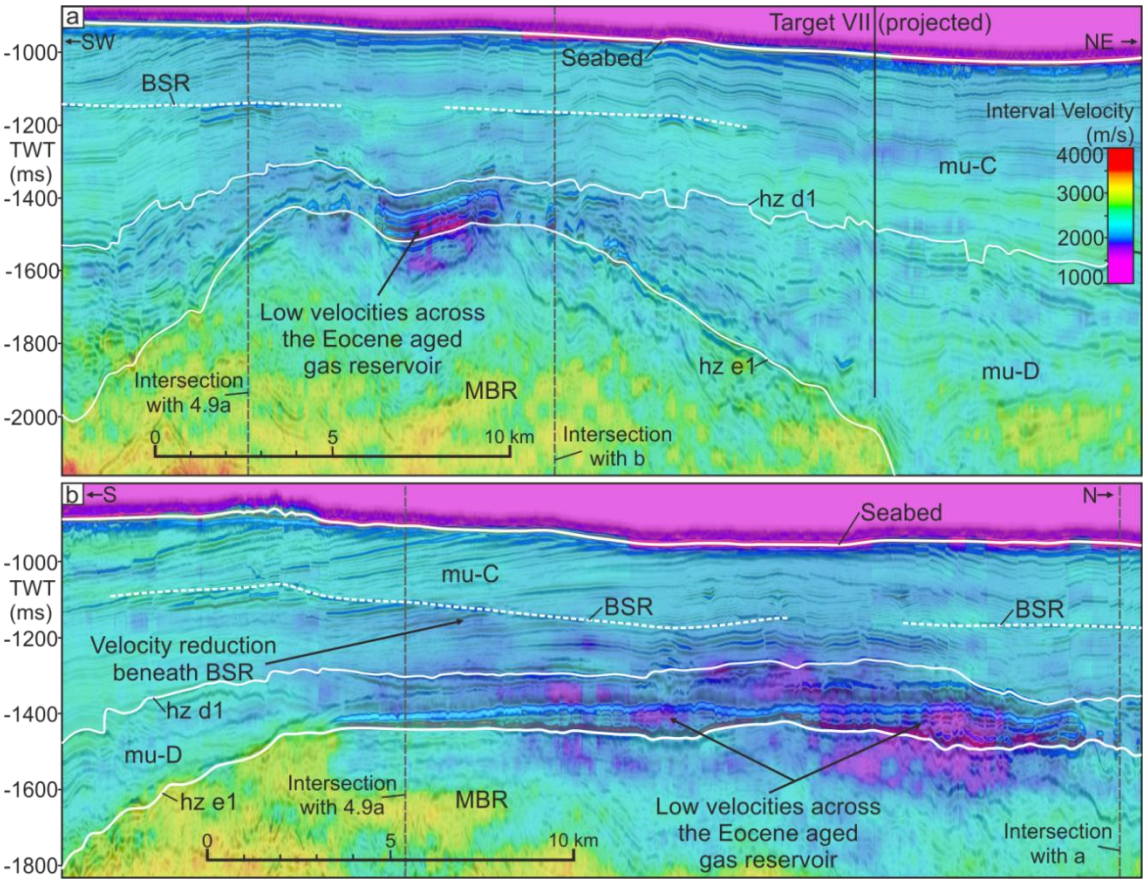

Figure 4.4. Interval velocities | Interval Velocities created through Kirchhoff Pre-Stack TTI Depth Migration (PSDM) for the Pitu survey overlaid on seismic reflection dip (a) and strike lines (b) in two-way-time across the Melville Bay Ridge structure. Velocity reduction likely due to the presence of gas can be observed in the location of the Eocene aged reservoir on top of the ridge, as well as beneath a bottom simulating reflector (BSR) within the free gas zone. The locations of a and b are shown on Fig. 4.3.

Therefore, average velocities were determined using all of the velocity data available (mentioned above) and were then extrapolated across the study area using a comparison of

the potential lithology and depositional setting of the sediments as well as their general depth. Linear time-depth equations were also generated for sites within the glacigenic wedge to consider elevated compaction and velocity due to ice loading. Velocities from this linear trend were then compared against the original estimated average velocities and interval velocities from the velocity cube to calculate the potential error (often ~100 m). This error was used to adjust the final metric depth targets to minimize overestimation and avoid drilling into deeper, potentially hazardous intervals.

4.4. Geohazard Assessment Workflow

The following geohazard assessment workflow was used to select drill sites that represent the lowest possible risk whilst meeting the scientific objectives (Fig. 4.5). The workflow considers the increasing availability of data that is typical through a projects progression, starting with regional 2D seismic data to understand the regional geology and pick initial stratigraphic targets and sites. 3D seismic data is then used to conduct a more detailed interrogation of the subsurface in order to delimit geohazards within the proposal area, guide site selection and minimize risk. Finally, additional data, in this case 2D UHR seismic data, is used in collaboration with the 3D seismic to fine tune the selected sites to ensure they represent the most suitable and safest locations possible.

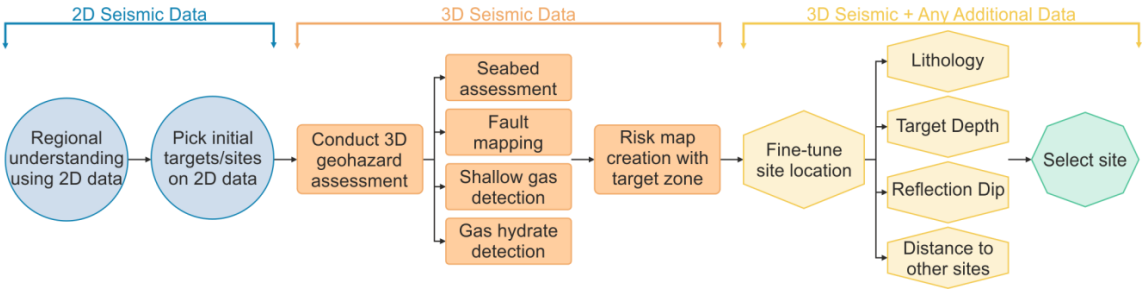

Figure 4.5. Geohazard assessment workflow | A workflow diagram that outlines both the steps conducted within the geohazard assessment leading to site selection and how the differing seismic data types were used throughout the process. This workflow should be used as a guide for future geohazard assessments using 3D seismic data but is not fully exhaustive and can be amended to fit different data sets and locations through the addition of extra steps that fulfil the requirements of future projects.

4.4.1. Seabed

The first step of the 3D seismic geohazard assessment is to map the strong, positive amplitude event that represents the seabed across the area of 3D coverage (Fig. 4.6). This provided the seabed depth, firstly in TWT and subsequently in metric depth, after a conversion using a typical seawater velocity of 1480 m/s (based on the Pitu interval velocity cube) (Fig. 4.6a). A bathymetric compilation from Newton et al. (2017) provided an additional high-resolution image of the seabed morphology. The mapping, supported by

the bathymetry data, identified a wide range of seabed features that have been interpreted as being of glacial origin, created by recent shelf glaciations, including lineations, ridges, iceberg scours and near-circular depressions interpreted as iceberg pits (Fig. 4.6) (Newton et al., 2017). These features can create localized areas of high-dip and highly compacted sediment, and should be avoided to prevent instability of the coring equipment on the seabed (Bennett et al., 2014).

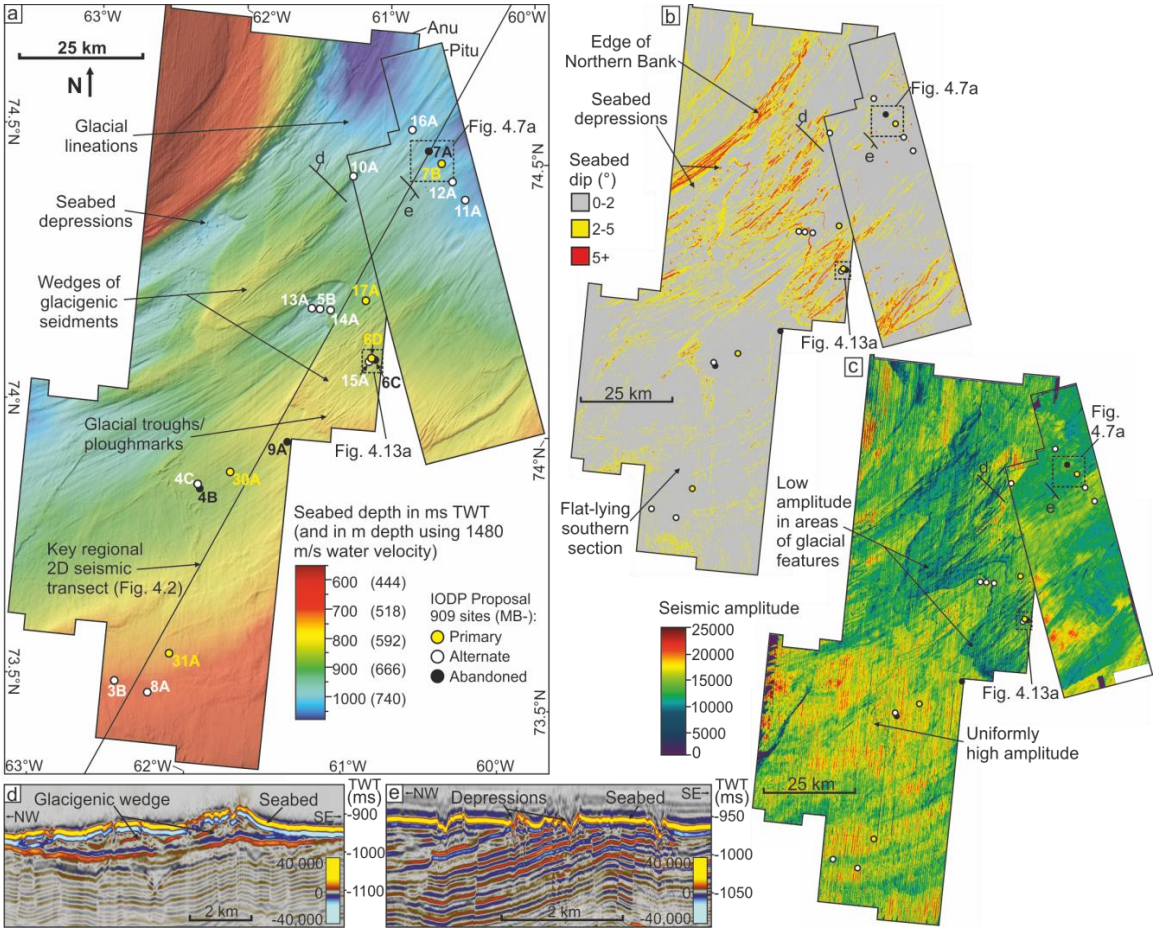

Figure 4.6. Seabed mapping | a) A seabed structure map across the 3D seismic coverage shown in both two-way-time and converted metric depth, with the bathymetry data from Newton et al. (2017) shown beneath. b) A dip attribute map across the 3D seismic coverage that has been filtered to display features by dip severity, with colours amber and red relating to moderate (2-5°) and high (5+°) risk respectively. c) An amplitude attribute extraction map at the seabed surface across the 3D seismic extent showing the variation in amplitude between areas dominated by or free from glacigenic features. The locations of both active and abandoned IODP Proposal 909 sites are shown on a-c along with the locations of d, e, Fig. 4.7a and 4.13a. d) A seismic cross section from the Anu survey showing an example of a glacigenic wedge which is topped by glacial lineations. e) A seismic cross section from the Pitu HR survey showing the unconformable nature of the seabed as well as seabed depressions that likely represent iceberg pit-marks (cf: (Brown et al., 2017)).

A structural dip attribute was extracted onto the mapped seabed surface to identify areas of high seabed dip (Fig. 4.6b). Filtering of the attribute allowed the severity of dip to be separated into areas of low (0-2°), medium (2-5°) and high (5°+) dip, which relates to areas of low, medium and high risk, respectively. The seabed dip-risk cut-offs are used here primarily to help avoid glacial geomorphological features on the seabed, but this technique

is applied in commercial geohazard assessments to consider the effect of the seabed structure on the critical failure of slope sediments as well as seafloor infrastructure tension and strength (Dan et al., 2014; Vanneste et al., 2014). The cut-offs selected are relatively low compared to other studies (e.g. (Haneberg et al., 2015)), but these were chosen to remain cautious and decrease potential risk, as much of the study area is relatively flat lying, and therefore, remains classified as low risk (Fig. 4.6b). Applying a cautious approach allows for steeper-dipping sections to be documented for further analysis should the underlying stratigraphy be potentially suitable for drilling – e.g. steep dip does not necessarily preclude drilling, but these bins allow for areas requiring greater consideration to be highlighted. Seismic amplitudes were also extracted onto the seabed surface (Fig. 4.6c). Extreme high or low amplitudes were shown to coincide with either glacial depositional features (such as Fig. 4.6d) (low amplitudes) or iceberg pit-marks/depressions (high amplitudes) (Fig. 4.6e), supporting the inferred composition of elements represented by areas of high dip. Away from these features, the seabed amplitude is relatively uniform.

4.4.2. Faults

Fault mapping within the 3D survey area involved the use of the variance seismic volume attribute (coherency within other software packages) to image discontinuities, viewed mainly through time-slice intersections (z-slice) (Fig. 4.7). Faults in the immediate area of the drill sites were manually mapped, including small faults belonging to a dense polygonal fault system within the post-rift stratigraphy of mu-D and -C (mainly within the Pitu area) (Cox et al., 2020a). Several deep-seated faults are observed extending close to the seabed (Fig. 4.7b), potentially connecting deeper fluid pressures to the shallow stratigraphy, which would represent a significant drilling hazard. Therefore, in areas close to a proposed site, fault characteristics were assessed based on their vertical extents, offsets and possible connections to deeper seismic anomalies (as shown on Fig. 4.7). High risks were associated with faults displaying connections to deeper anomalies, however, it was recommended to avoid all fault penetrations where possible to maximise the chance of good and stratigraphically continuous core recovery.

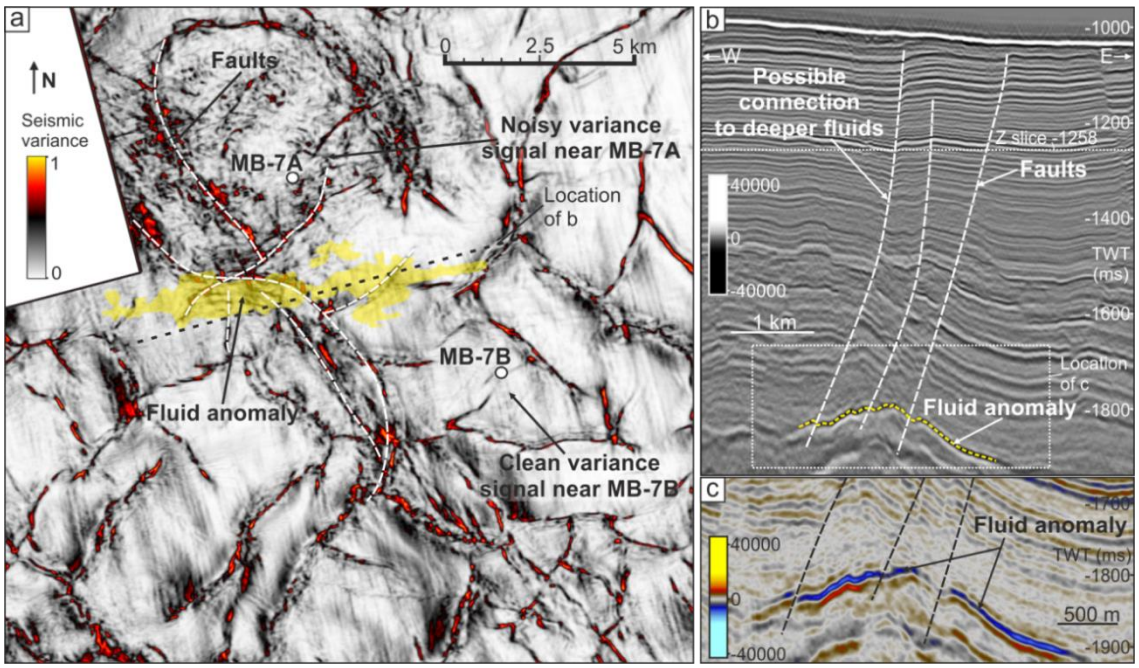

Figure 4.7. Fault mapping | a) A time slice intersection (z-slice) through the Pitu HR survey displaying the variance structural attribute to highlight fault locations at a depth of -1258 ms two-way-time. Interpreted fault planes (white dashed lines) are shown as well as the spatial distribution of a potential hydrocarbon fluid anomaly that may be in pressure communication to shallower depths due to the intersection with fault planes. IODP Proposal 909 sites MB-7A (abandoned) and MB-7B (primary) are also shown as well as the location of b. The location of a is shown on Fig. 4.6a. b) A seismic cross section from the Pitu HR survey in black and white to emphasize faults, which displays interpreted fault planes and the location of a deeper fluid anomaly as well as the location of c. c) An enlarged seismic cross section from the Pitu HR survey that shows the seismic character of the deeper fluid anomaly.

4.4.3. Shallow Gas Detection

Gas-related seismic anomalies are expected to display 'bright', anomalously high negative amplitudes due to gas fluids causing a reduction of the bulk modulus (due to the extremely low density of gas) causing a significantly negative acoustic impedance contrast across the boundary at the top of the gas-bearing reservoir (Cox et al., 2020b; Hilterman, 2001; Nanda, 2016). A positive seismic amplitude, often of comparable amplitude, is often associated with the gas/oil/water contact or the base of the reservoir if it contains anomalous fluids across its entire vertical extent. For thin reservoirs filled with gas, the response is often a highly asymmetric high negative to high positive doublet (Cox et al., 2020b; Raef et al., 2017). The presence of oil can cause a similar but often much reduced seismic anomaly. Due to these phenomena, the 3D seismic data were investigated to understand the seismic character of fluid-related anomalies within the study area. This included the physical character of anomalies, which were often isolated bright spots or brightening along single horizons (Fig. 4.8), as well as their spatial and stratigraphic distribution, which was widespread within all levels of the post-rift stratigraphy (mu-D-A) and focussed around the Melville Bay Ridge (Cox et al., 2021). The seismic amplitude range

of the bright anomalies was also analysed to aid amplitude extractions. The analysis identified that an amplitude of negative (-) 10,000 or above, likely represented a fluid anomaly, although some dim anomalies can occur beneath this limit and this was considered during the filtering of results (Fig. 4.8c). Dimmer anomalies can be attributed to poorer reservoir quality or thin bed tuning effects, whereas amplitude is expected to be insensitive to gas saturation when this exceeds 10% of the pore volume (e.g. (Hilterman, 2001)).

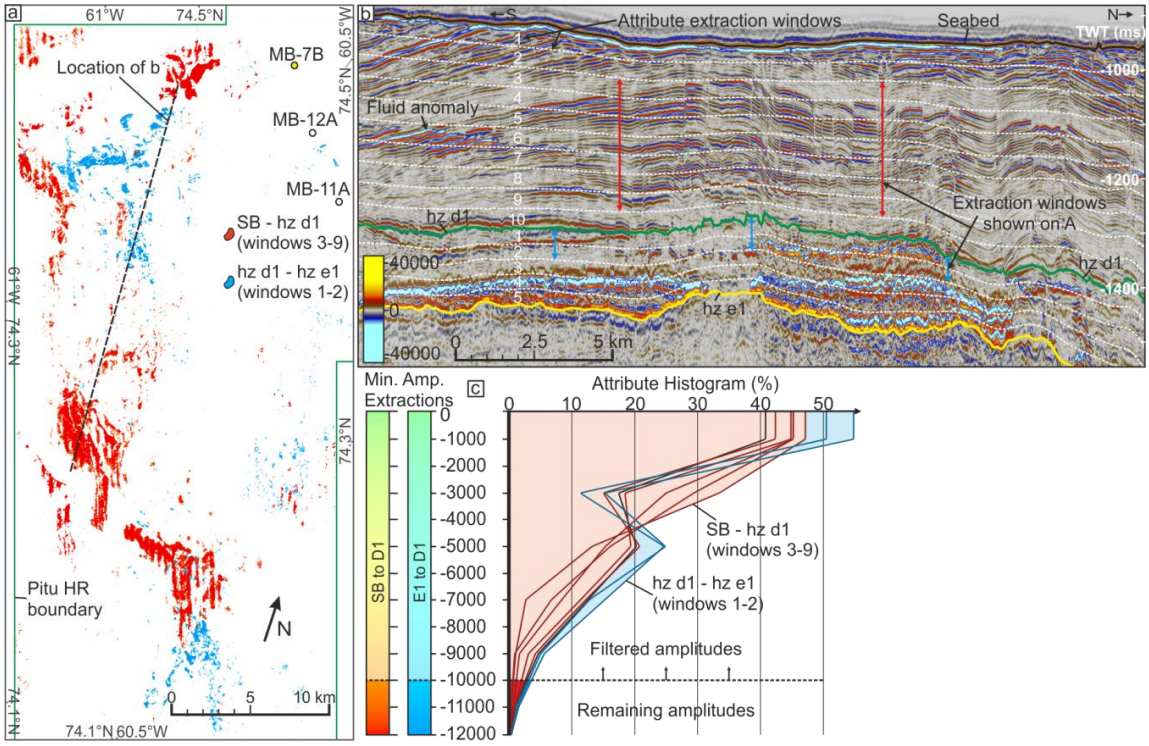

Figure 4.8. Shallow gas detection | a) A 2D map view of several overlaid windowed minimum amplitude extractions from the Pitu HR survey that have been filtered to only display amplitudes that are greater than -10,000 and likely represent fluid anomalies. The extracted amplitudes have been colour coded to distinguish between windows from different mega unit packages, giving a sense of anomaly depth; a technique which can also be applied to individual windows. The windows displayed are shown on both panels (a) and (b). The IODP Proposal 909 sites in this area are also shown in locations that avoid the potential fluid anomalies as well as the location of the seismic line used in b. b) A seismic cross section from the Pitu HR survey that highlights the main horizons used to create the proportionally distributed extraction windows. Several seismic anomalies that will be identified within the extractions are also shown along with the specific windows displayed on a. c) A histogram that shows the distribution of amplitudes from the selected extraction windows shown on a and b. The histogram and the colour bars show how the amplitudes have been filtered to only show the extreme values which are more likely to represent fluid anomalies. These amplitude cut-offs can be altered for specific windows to either display or hide certain amplitude ranges.

Once this initial analysis was complete, the information was used to automatically extract amplitude anomalies from the 3D seismic data above the defined threshold that likely represents hydrocarbon occurrences. This process used a series of minimum amplitude extraction windows that cut proportionally through the stratigraphy extracting the most negative amplitude at every seismic trace (Fig. 4.8). The amplitude extraction

result was then filtered to remove the majority of data and highlight just the most negative amplitudes (those that likely represent fluid anomalies) (Fig. 4.8c).

The stratigraphy was split into two units for the extractions. The first between the seabed and seismic horizon (hz) d1 with 10 proportional extraction windows (each ~50 ms TWT thick) and the second between hz d1 and hz e1 with 5 windows (each ~35 ms TWT thick) (Fig 4.8). Using relatively narrow windows provided some depth control for each anomaly, which can be displayed through colour coding (Fig. 4.8a), instead of having a wide depth estimate that is as thick as the seismic mega-unit. This was important when selecting a shallow drill site where many of the deeper anomalies well below the target are less relevant. It also allowed the windows to be displayed separately – i.e. just for a particular depth zone. Furthermore, the resulting amplitudes for each window were often filtered differently (often using opacity rendering), in an attempt to highlight the anomalies at that level and also to try and remove unwanted amplitudes that may mask fluid events, such as naturally bright horizons, data acquisition footprints (near the seabed) and amplitudes interpreted to not represent fluid anomalies.

Once the data had been filtered, the individual scrutiny of each anomaly was conducted to determine whether that anomaly was in fact fluid related, or whether the anomalous amplitude may instead represent something else (such as the high amplitude causing features mentioned above). This evaluation is subjective to some degree and this should be considered in the final result. Nonetheless, this evaluation was important as it stops potentially credible locations from being ruled out due to non-fluid related anomalies and may also highlight other dimmer amplitude anomalies that were missed. This whole process was iterative and involved returning to the attribute extraction or filtering stage to adjust the parameters when required to ensure all potential anomalies were considered.

Once the result was finalised, the locations of the remaining amplitudes were used both within the interpretation software directly and within GIS software for spatial analysis. The remaining amplitudes were either converted into 2D automatic boundary polygons or extracted as 3D geobodies to allow efficient visualization and to aid the creation of multi-layer hazard maps used within the site selection process (Fig. 4.3).

4.4.4. Gas Hydrate Detection

Bright fluid anomalies were identified hosted within inclined, likely sandy, strata that terminate abruptly at a certain depth beneath the seabed (Fig. 4.9) (Cox et al., 2021). This level, characterised by a dim, negative amplitude reflection that cuts across the stratigraphic layering in a manner that mirrors the seabed topography, represents a bottom simulating

reflector (BSR). Such cross-cutting features have been interpreted as representing the base of a zone containing stable gas hydrates, below which free gas can become trapped resulting in a bright negative crosscutting reflection that may be discontinuous or continuous depending on the degree of porosity and permeability variations of the host strata (Fig. 4.9) (Berndt et al., 2004; Kvenvolden, 1993).

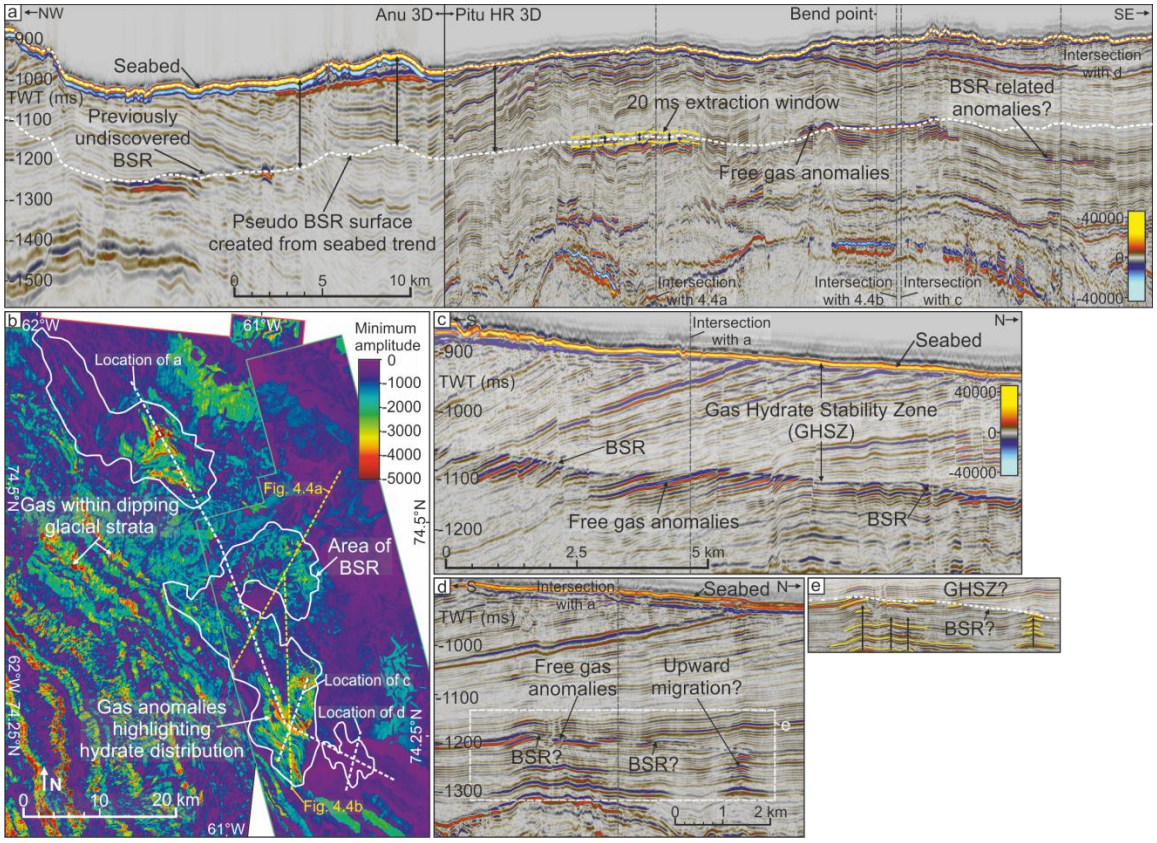

Figure 4.9. Gas hydrate detection | a) A composite seismic cross section through the Anu and Pitu HR surveys showing the distribution and seismic character of the identified bottom simulating reflector (BSR) in the study area. The white dashed line (ca 200 ms below seabed) at the BSR represents the pseudo BSR surface. b) A 2D map view of a minimum amplitude extraction across the pseudo BSR surface showing the distribution of bright negative amplitudes that likely represent trapped free gas. The mapped area of the BSR is shown as well as the locations of the seismic lines used in a, c, d and Fig. 4.4a-b. c) A seismic cross section from the Pitu HR survey confirming the presence of the BSR, along with multiple free gas anomalies trapped beneath it. d) A seismic cross section from the Pitu HR survey across the area containing a potential deeper BSR (ca 300 ms below seabed). The location of e is also shown. e) A zoom in of a section of d showing the location of fluid anomalies (yellow lines) beneath the potential deeper BSR and much thicker gas hydrate stability zone (GHSZ).

BSR features were mapped within the 3D seismic surveys to identify an area of 537 km^2 that likely contains gas hydrates (Fig. 4.3 and 4.9). Bright, negative amplitude free gas anomalies are observed trapped beneath the BSR boundary and suggest a free gas column of up to 50 m thick (Fig. 4.9c). However, away from the bright free gas anomalies, mapping of the BSR became difficult due to an intermittent and dim BSR reflection. Therefore, due to the relationship between the BSR and the seabed, a pseudo BSR surface was created to aid the identification of this boundary in other areas of the survey (Fig. 4.9). This pseudo

surface was based on empirical evidence from obvious BSRs in the data (Fig. 4.9c) and was created by cross plotting the thickness of the GHSZ in areas containing these BSRs against the seabed depth. The best fit line between these two data was then used to create a surface at the expected BSR depth across the entire 3D survey extent; a surface that tolerates variations in stability zone thickness in response to changes in seabed depth.

This guide surface was used to focus BSR reconnaissance throughout the 3D seismic data. It was also used to identify additional areas of free gas (a much higher risk) that may be trapped at the base of the gas hydrates (Figs. 4.3 and 4.9). This involved combining the extensive pseudo surface with the BSR map and producing a minimum amplitude extraction for a 20 ms window across this surface (Fig. 4.9b). This technique, along with the manual reconnaissance of the seismic character at the pseudo surface depth, resulted in the identification of a previously undiscovered BSR as well as trapped free gas in the north of the Anu Survey (Fig. 4.9a and b).

Within the south of the Pitu survey, a cross-cutting negative amplitude reflection also has been interpreted to potentially represent a BSR; however this feature exists ~100 ms TWT deeper than the guide surface (Fig. 4.9a, d and e). This potential BSR is not as obvious as in other areas, but multiple stacked bright anticlinal anomalies exist within the underlying stratigraphy that may represent the upward flow of hydrocarbon fluids that are subsequently trapped beneath the BSR boundary (Fig. 4.9d and e). Rapid changes in BSR depth over short distances can occur and have been observed in other areas, e.g. the Lower Congo Basin (Andresen et al., 2011). However, as the seabed depth and shallow sediments are relatively consistent to the main BSR area a short distance away (<5 km) (Fig. 4.9a), a significant variation in the phase boundary depth is unlikely. Therefore, these deeper anomalies could instead represent more traditionally trapped gas unrelated to hydrates (Fig. 4.9d and e).

4.4.5. Risking

Once the main geohazards described above were analysed, the individual results were combined to create a composite hazard map that was used directly for site selection (often known as a common risk segment (CRS) map (Hill et al., 2015) (Fig. 4.10). The hazards considered within this process (seabed features, shallow gas and gas hydrates) were rated as either moderate risk, such as low dip glacial seabed features or areas containing gas hydrate (without free gas) or as high risk such as seabed depressions or shallow gas occurrences. These features were then colour coded using a traffic light system, with red representing high risk, amber representing moderate risk, and green representing low risk. After initial

site locations were proposed, significant faults were mapped in more detail around the site and subsequently added to the map to assess whether alterations were required.

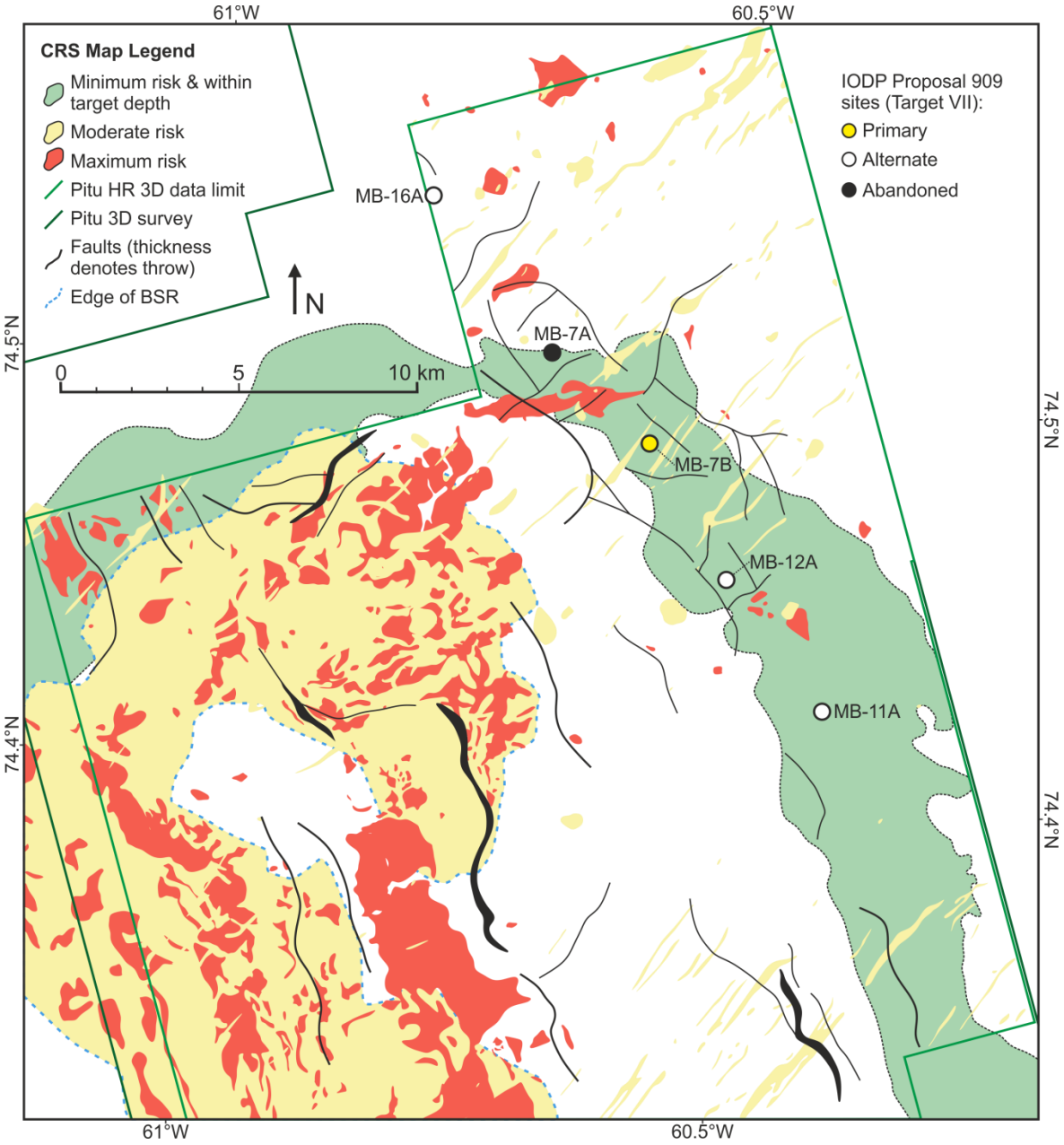

Figure 4.10. Common risk segment (CRS) map | A summary hazard map for Target VII displaying the green, minimum risk, depth target zone where sites can be located safely whilst meeting the stratigraphic objectives. This CRS map was used to guide the site selection and abandonment of the shown Target VII sites. Similar CRS maps were also created to guide site selection and abandonment for the other stratigraphic targets within 3D seismic coverage (Targets III-VI).

All areas surrounding the moderate and high risk features could be considered as minimum risk (green) but an attempt was made to maintain a minimum radius from each site location of 500 m to the nearest identified hazard. For each stratigraphic target (I-VII), a target seismic horizon and the maximum tolerable drilling depth to reach that horizon were defined, creating a more localized target zone where the site had to be located. These

target zones were overlaid on the CRS maps to create the green, minimum risk zone, which highlighted the area that could be drilled safely and still reach the desired stratigraphic target within the tolerated depth (Fig. 4.10).

4.4.6. Site Selection: Geohazards and Lithology

The geohazard assessment and CRS map creation provided a minimum risk target zone to guide safe site selection. However, several other logistical and geological factors had to then be considered whilst fine tuning the final location of each site.

This included an assessment and interpretation of the seismic character to give an idea of the potential lithology of the sediments (following work by several authors on lithology interpretations from seismic data, e.g. Badley (1985); Frey-Martínez (2010); Hilterman (2001); Sangree and Widmier (1979); Stewart and Stoker (1990)). An attempt was made to avoid certain seismic features, such as (1) chaotic packages of reflections, often down-slope from erosional scarps, that likely represent mass transport deposits; (2) structureless to chaotic, near surface packages that may represent boulder prone glacigenic tills or debris flows; (3) high, positive amplitude reflections at the top of glacigenic progradational units, that may represent paleo-seabeds that have been indurated due to ice loading during the following glacial period; and (4) relatively high, negative amplitude reflections that are often wavy (within mu-B or –C) or laterally continuous within mu-D, that may represent the top of sand packages. These seismically inferred lithologies were considered risks and avoided due to the likelihood of poor core recovery and the possibility of the coring equipment becoming stuck in the hole.

The stratigraphic dip (on seismic) was also considered in an attempt to try and target flat horizons to maximise the chance of good core recovery. Finally, the site priority (either primary or alternate) had an influence on location, as alternate sites attempting to reach the same stratigraphic target as the primary, were required to be sited a minimum of 5-10 km away from the next nearest site (primary or alternate) if possible to manage the iceberg risk. After considering these additional factors within the low risk zone provided by the CRS map, a suitable drilling location was selected.

4.5. Assessment Results – Proposal 909 Sites

Seven primary and fifteen alternate sites have been identified for the 909-Full2 proposal (Figs. 4.1 and 4.3) (Knutz et al., 2018). These sites cover the seven stratigraphic targets (Targets I-VII) that have been identified in order to meet the scientific objectives of the drilling proposal (Figs. 4.1 and 4.2). The selection of these sites was based on multiple data that have become available as the proposal developed since its inception in 2016. Initially,

the regional 2D seismic data represented the principal source of information for identifying drilling targets along the key seismic transect (Fig. 4.2). Since then, the majority of site selections were refined based on industry 3D seismic volumes and the LAKO UHR seismic data that was collected in 2019 (Table 2). In the final iteration of the proposal, none of the proposed sites exist in an area only covered by regional 2D seismic reflection data (Table 3). The final review resulted in several site alterations and additions as part of Proposal 909-Full2 to accommodate alternate site requirements for iceberg-prone waters. This version was subsequently accepted by the Scientific Evaluation Panel and by the Environmental Protection and Survey Panel of IODP.

Tar-get	Strat. Target	Site (MB-)	Prio-rity	Sb Depth (mbss)	Target Depth (mbsf)	Seismic Data Coverage			Result of GHA	Notes
						2D	3D	UHR		
I	Mu-A	**23A**	**Prim.**	**1821**	**422**			✓	**-**	Primary due to reflection continuity
	(su. 9-11)	1C	Alt.	1809	473	✓		✓	-	
		20A	Alt.	1928	450	✓		✓	-	
		1B	Ab.	-	-	✓		✓	-	Ab. to avoid amplitude anomaly at TD
II	Mu-A	**2C**	**Prim.**	**1957**	**522**	✓		✓	**-**	
	(su. 8)	22A	Alt.	1850	611	✓		✓	-	Ab. considered due to lith. concerns
		21A	Ab.	-	-	✓			-	Ab. due to location on lower fan wedge
III	Mu-A	**31A**	**Prim.**	**531**	**282**	✓	✓	✓	**Confirm**	
	(su. 6-8)	8A	Alt.	503	370	✓	✓	✓	Confirm	
		3B	Alt	497	375	✓	✓	✓	Confirm	
IV	Mu-A	**30A**	**Prim.**	**618**	**303**	✓	✓	✓	**Confirm**	
	(su. 4-6)	4C	Alt.	628	305		✓	✓	Confirm	
		4B	Ab.	-	-	✓	✓	✓	Abandon	Ab. due to amendment to MB-30A
		9A	Ab.	-	-	✓	✓	✓	Abandon	Ab. due to noisy seismic
V	Mu-A	**17A (1)**	**Prim.**	**655**	**224**	✓	✓	✓	**Select**	
	(su. 1) and -B	5B	Alt.	704	520	✓	✓	✓	Confirm	
		13A	Alt.	707	540		✓		Select	
		14A	Alt.	663	510		✓		Select	
VI	Mu-B	**6D**	**Prim.**	**614**	**561**	✓	✓	✓	**Amend**	Plan to drill before Target V
	and -C	17A (2)	Alt.	655	411	✓	✓	✓	Select	Additional depth to Target V primary
		15A	Alt.	605	648		✓		Select	
		6C	Ab.	-	-		✓	✓	Abandon	Ab. due to potential gas anomalies
VII	Mu-C	**7B**	**Prim.**	**736**	**978**	✓	✓	✓	**Amend**	
	and -D	16A	Alt.	734	1089		✓		Select	
		11A	Alt.	747	1200		✓		Select	
		12A	Alt.	739	1186		✓		Select	
		10A	Alt.	698	1288	✓	✓		Confirm	
		7A	Ab.	-	-	✓	✓	✓	Abandon	Ab. (reasons in main text)

Table 4.3. Site information table for the active and abandoned sites of IODP Proposal 909 | The ticks indicate the seismic data coverage at each site while the red coloured ticks denote which data was used primarily for initial site selection. The result of the geohazard assessment column signifies the impact the assessment had on that site and includes: confirm (site approved after being initially selected on a form of 2D seismic data), amended (site was moved to this location from an abandoned site), select (site was chosen as an initial location) and abandon (site was deemed an unfit location). Abbreviations used include stratigraphy (Strat), sub-unit (su), primary (Prim), alternate (Alt), abandoned (Ab), seabed (sb), metres below sea-surface

(mbss), metres below seafloor (mbsf), ultra-high resolution (UHR), geohazard assessment (GHA), lithology (lith) and total depth (TD). All site locations are shown on Fig. 4.1.

The coverage of the three seismic data types (2D, 3D and UHR) varies across the sites and their availability restricts which data can be used within the site selection process (e.g. Targets I and II sites which are outside of 3D seismic coverage (Fig. 4.1 and Table 4.3)). However, for all sites located within the 3D seismic extent, this data and the geohazard assessment were considered the principal data that either guided the selection of new sites or was used to amend and confirm the suitability of locations that were previously selected on 2D data (Table 4.3). This led to several sites being abandoned (Figs. 4.1, 4.3 and Table 4.3). In cases where the UHR seismic data were used to select a new site (such as MB-17A or MB-7B), the spatial analysis of drill targets and hazards from the 3D seismic reflection data was still the primary method used for final site approval.

4.5.1. Targets I and II

The deep water sites for Targets I and II (c. 1950-1800 m water depth) are located beyond the present day shelf break and aim to recover a paleoceanographic record of a Pleistocene drift system associated with the MB-TMF (Fig. 4.1 and Table 4.3). Target I represents mu-A subunits 9, 10 and 11 with Target II comprising an expanded section of the stratigraphically underlying subunit 8 (Fig. 4.2). These two sites were initially selected using regional 2D seismic data with the majority having been subsequently refined by LAKO UHR data, apart from site MB-23A which was selected directly on the LAKO UHR data. For the remaining sites, an assessment for potential drilling hazards was conducted using the 2D data sets (regional and UHR) which confirmed their suitability, but as these sites exist outside of the 3D seismic coverage, the full geohazard assessment could not be applied during the site selection process.

4.5.2. Targets III and IV

Target III sites on the southern flank of the Melville Bay Trough (c. 500 m water depth) aim to recover potential glacial and interglacial intervals expected to be of Early-Middle Pleistocene age within top-set strata of the MB-TMF that onlap onto glacial unconformities within mu-A subunits 6, 7 and 8 (Figs. 4.1, 4.2, 4.11 and Table 4.3). Target IV sites in the southern central part of the Melville Bay Trough (MBT) (c. 600 m water depth) focus on similar top-set strata covering a stratigraphic interval of likely Early Pleistocene age, corresponding to mu-A subunits 3-6.

Three of the sites, including both primaries, have been selected predominantly using the LAKO UHR seismic, with the remaining two alternate sites using the regional 2D

survey (Table 3). During this selection, potential hazards observed on the 2D surveys, including amplitude anomalies, were identified and avoided. All of the selected sites, however, exist within the 3D seismic coverage (Fig. 4.3) and therefore, have been analysed as part of the geohazard assessment. Each site location and the depth of the target seismic horizon were assessed against each step of the geohazard assessment workflow through the process of CRS map creation. In this case, no site alterations were required and all sites selected existed within the green, low risk zone (Fig. 4.10), avoiding all identified hazards, for example the potential fluid anomalies shown on Fig. 4.11, by an acceptable radius (usually >500 m).

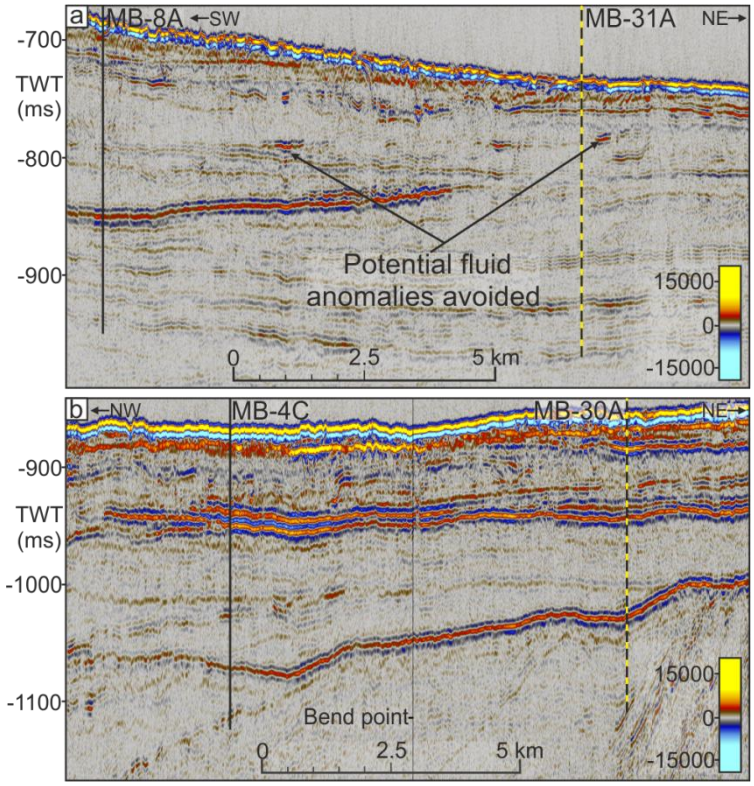

Figure 4.11. Target III and IV | Seismic cross sections from the LAKO UHR survey, that highlight the glacigenic stratigraphy of Targets III (a) and IV (b) as well as the location of potential fluid anomalies and sites MB-31A (primary), MB-8A, MB-30A (primary) and MB-4C (alternate). The location of both a and b are shown on Fig. 4.3.

4.5.3. Targets V and VI

Target V and VI sites, located in the central MBT (c. 600-700 m water depth), aim to recover pre-glacial Neogene contourite drifts, of presumed early Pliocene age (Figs. 4.2, 4.3 and 4.12), and a limited portion of the overlying prograding sediments, which may reflect the earliest marine-based glaciations in northwest Greenland (mu-A subunit 1).

Analysis of both the new LAKO UHR data and the geohazard assessment from the 3D seismic reflection data, led to the selection of a new primary site (MB-17A) that compared

favourably to the originally proposed site (MB-5B). Site MB-17A fulfils the Target V criteria whilst avoiding several potential fluid anomalies and minimizes drilling through potentially boulder-prone glacial debris flow sediments (Fig. 4.12d). The new site also allows operational flexibility, providing an alternate site for Target VI by sampling both Target V and VI sediments (e.g. Option 1 and Option 2) (Fig. 4.12 and Table 4.3). The recovery of the youngest drift sediments has been optimized through targeting a sequence of evenly layered strata that are located less than ~60 m below the seabed (Fig. 4.12a).

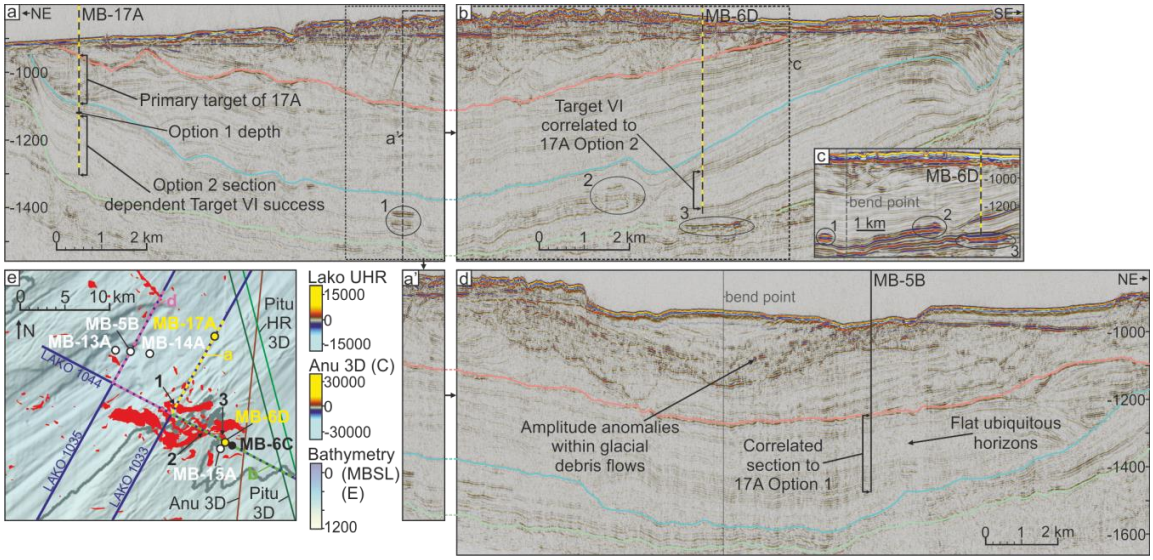

Figure 4.12. Target V | a) A seismic cross section from the LAKO UHR survey showing the location of the primary site MB-17A. Both depth options for this site are shown along with horizon interpretations (coloured) that were mapped throughout the area to allow the correlation of target stratigraphy to the other sites. The section of seismic that represents (a') is also shown, with a' displayed beneath, next to (d), to show how both the seismic lines on b and d are connected to the seismic line of (a). b) A LAKO UHR seismic cross section displaying the stratigraphic correlation between sites MB-17A and MB-6D. c) A seismic cross-section from the Anu survey shown for comparison between the two surveys. Fluid anomalies are shown and numbered and their appearance can be compared with the associated anomalies displayed on the LAKO UHR survey on both a and b. The location of c is also shown on both a and b. d) A LAKO UHR seismic cross section displaying the stratigraphic correlation between sites MB-17A and MB-5B. e) A location map for the seismic lines used on a, b and d that represents an enlarged section of Fig. 4.3 displaying the regional bathymetry from (Newton et al., 2017) as well as the location of seismic data and mapped seismic fluid anomalies (red). The locations of the seismic anomalies that are highlighted and numbered on c are also shown. The location of e is shown on Fig. 4.3.

Target VI sites aim to recover the oldest stratigraphic section of the Neogene contourite drift within mu-B. For Target VI, in combination with Target V, the overall strategy is to obtain a composite, high-resolution record containing the early Pliocene warm phase to the late Pliocene cooling (Table 3). The main drilling target is an expanded section of the wavy-mounded contourite drift that accumulated over an underlying erosional unconformity (hz c1) (Figs. 4.2, 4.12 and 4.13). Both the primary and alternate sites were picked directly on the 3D seismic data using the geohazard assessment as a guide. Primary

site MB-6D is also covered by LAKO UHR data which was used to confirm the site (Table 3).

Initially, the primary for Target VI was selected using regional 2D data but was located in an area just beyond the limit of the 3D seismic coverage (between the Anu and Pitu surveys – Fig. 4.3). Therefore, it was decided to relocate the site to within the 3D seismic extent to allow a more detailed site analysis using the geohazard assessment (to MB-6C – Fig. 4.13). The shallow gas detection analysis (Fig. 4.8) identified two bright spots at the edges of the mounded contourite target package that may represent tuning effects between the negative amplitude reflection at the target top and a short-extent, possibly cross-cutting, positive amplitude event beneath it, but could also (in a less likely worst case scenario) represent pockets of gas charged sand at the target top (Fig. 4.13b and c). MB-6C however, targeted the central part of the mound that looked evenly stratified and free of bright events (Fig. 4.13b), but after further considerations of the amplitude distributions and target dip, the site was moved to a new position (MB-6D) where it would penetrate the potential gas hosting sandy horizon further down dip. This was a cautious effort to reduce the chance of encountering gas that have migrated up-dip (Fig. 4.13).

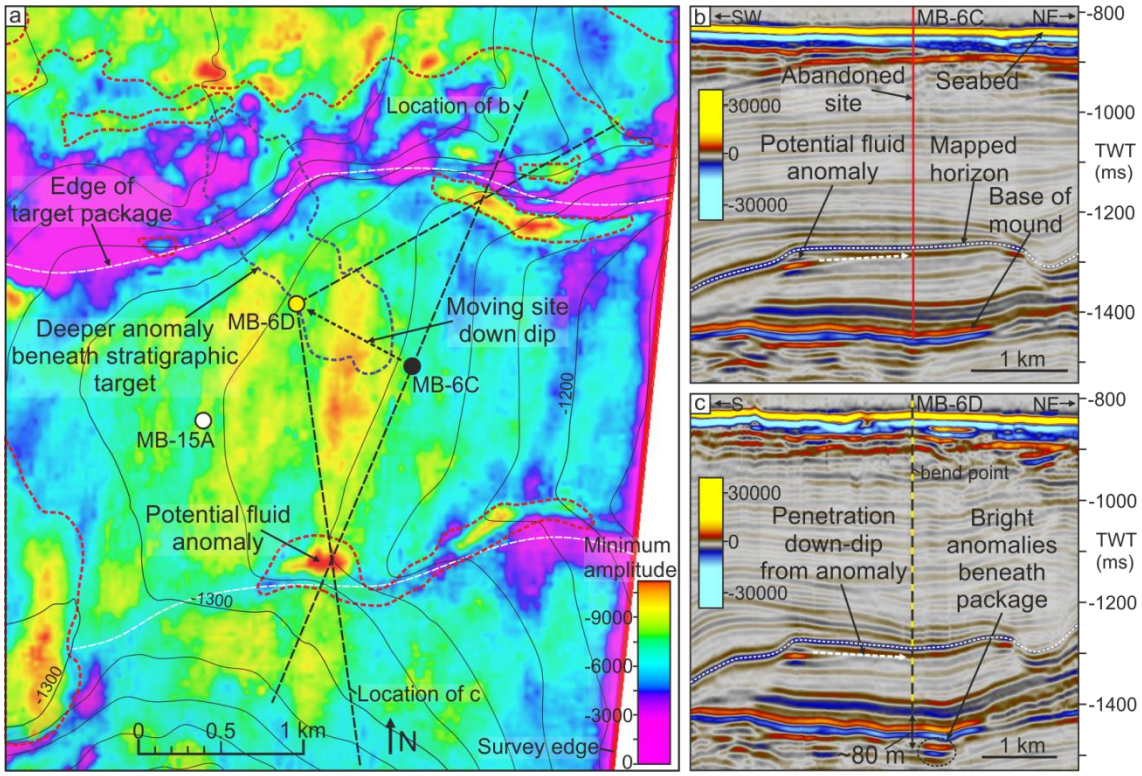

Figure 4.13. Target VI | a) A minimum amplitude attribute extraction along a mapped horizon representing the top of the contourite mound package that constitutes Target VI (horizon shown on b and c). The attribute extraction highlights bright amplitudes that may represent either tuning or fluid anomalies. The spatial relationship between these bright anomalies and fluid anomalies extracted through the shallow gas detection process (red dashed polygons) (displayed on Fig. 4.3) is highlighted. The Target VI site locations are shown as well as the locations of b and c. The location of a is shown on Fig. 4.6. b) A seismic cross section from the Anu survey showing the contourite mound that comprises Target VI. The occurrence of the potential fluid anomalies are also displayed along with the location of abandoned site MB-6C. c) A seismic

cross section from the Anu survey showing the location of the Target VI primary site MB-6D. The site location is shown to penetrate the top mound horizon down-dip from the potential fluid anomalies on the packages flanks.

The geohazard assessment also highlighted a potential fluid anomaly (bright spot) directly in the area where MB-6D is located (~180 m to the N/NE), but ~50 m beneath the base of the targeted drift package (Figs. 4.3 and 4.13). Due to this feature, a conservatively shallow target depth was selected that maintains a depth stand-off of ~80 m, minimizing the chance of drilling too deep and reaching the underlying anomaly (Figs. 4.12 and 4.13).

4.5.4. Target VII

Target VII sites are located in the inner central part of the MBT (c. 750 m water depth) within the area covered by the Pitu 3D (and Pitu HR) seismic survey and comprise the deepest planned sites within the proposal (Fig. 4.1 and Table 4.3). Target VII represents an apparently continuous Miocene succession (including a middle Miocene unconformity - hz d1) that has been exhumed on the inner shelf (Figs. 4.3 and 4.14), down to the top of a sedimentary wedge of likely Oligocene age (the target horizon) (Figs. 4.10 and 4.14a) (Gregersen et al., 2019; 2013). All of the Target VII sites have been selected using the geohazard assessment (Fig. 4.10 and Table 4.3).

The previous primary site, MB-7A, had been selected on the key transect of regional 2D seismic (Figs. 4.2 and 4.14). However, the geohazard assessment, in combination with the LAKO UHR seismic, identified a number of issues with the original site location that were not identified using the regional 2D seismic:

1. Narrow, vertical sections of acoustic blanking were identified on both the 3D and LAKO UHR seismic that have been interpreted to possibly represent fluid-flow pipes (cf. (Cartwright et al., 2007)) or gas streaking (Fig. 4.14). Although site MB-7A did not intersect these features they were within close proximity (<500 m).
2. The MB-7A location was within close proximity to a deep-seated fault that potentially could create pressure communication between the shallow subsurface and a deeper, anticlinal anomaly that may represent trapped hydrocarbon fluids (Fig. 4.7).
3. The seismic signal is locally disturbed around the MB-7A site on both the 3D and LAKO UHR seismic (Figs. 4.5a and 4.7). This is likely caused by an overlying chaotic package of sediments directly beneath the seabed, affecting the signal

beneath and possibly containing heterogeneities that would affect drilling, but may also suggest a higher sand content at the target interval.

4. Potential thick mass transport deposit (MTD) sand packages were identified in the lowermost section of the MB-7A site, both beneath the highlighted target horizon, and onlapping onto it (Fig. 4.14). These sediments would likely cause poor core recovery and could contain high fluid pressures due to their structural dip and proximity to the ridge flanks (Figs. 4.1 and 4.14). The top of the MTD sand package was used as the target seismic horizon within the geohazard assessment and the site selection strategy was to avoid drilling into these sands, maintaining realistic maximum drill depths and include as much of the overlying Miocene section as possible (Figs. 4.10 and 4.14).

These issues led to site MB-7A being abandoned and relocated to the new primary site MB-7B which targets an area of flat-lying strata within a 1-1.5 km wide fault block (with no fault intersections) that is bounded by a combination of northwest-southeast trending deep-seated faults and the polygonal fault system (Figs. 4.7, 4.10 and 4.14).

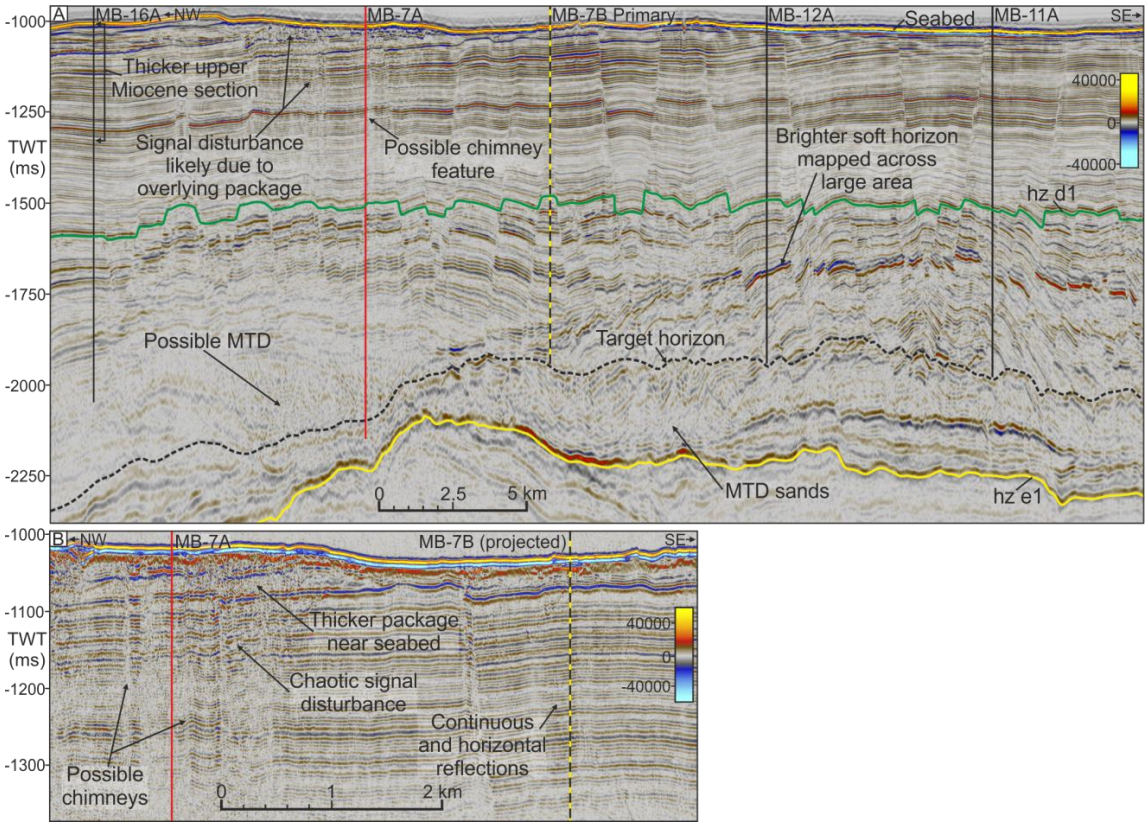

Figure 4.14. Target VII | a) A seismic cross section from the Pitu HR survey that displays the location of primary site MB-7B, the alternate sites MB-16A, MB-12A and MB-11A and the abandoned site MB-7A. Regional seismic mega-unit interpretations are shown as well as the target seismic horizon used to define the depth target used within the CRS Map on Figure 10 that represents the top of a potentially sandy MTD package. b) A seismic cross section from the LAKO UHR seismic that shows potentially hazardous seismic features near site MB-7A that are also observed on the Pitu HR survey (shown on a) and ultimately led to the abandonment of that site. A projection of primary site MB-7B is also shown penetrating a section containing continuous and horizontal seismic reflections. The locations of a and b are shown on Figure 3.

4.6. Discussion

A geohazard assessment is conducted prior to drilling in an attempt to restrict unnecessary delays, reduce costs, avoid poor data collection and most importantly reduce the likelihood of dangerous drilling events (Aird, 2010; Nadim and Kvalstad, 2007). The assessment allows the selection of sites that represent the lowest possible risk, whilst also achieving the scientific objectives. This requires a detailed spatial analysis of all potential risks and the consideration of additional viable target areas, both regionally and stratigraphically (Selvage et al., 2012). For IODP Proposal 909, the sensitive environment associated with high-latitude continental shelves, as well as the likelihood of hydrocarbon occurrences, made a robust risk analysis increasingly important (Hasle et al., 2009; Li et al., 2016; Nadim and Kvalstad, 2007). The geohazard assessment was conducted in line with commercial site safety analyses (Jensen and Cauquil, 2013) whilst focussing on hazards that commonly create risks to drilling operations within both deep water continental margin settings (hydrocarbon occurrences, gas hydrates, near surface faults etc. (Aird, 2010; Jensen and Cauquil, 2013; Minshull et al., 2020; West and West, 2005)), and glaciated margins (glacial seabed features, problematic lithologies, indurated horizons etc. (Bennett et al., 2014; Newton et al., 2017)).

The assessment identified a pervasive distribution of hydrocarbon related anomalies across the 3D seismic coverage which exist within all levels of the post-rift stratigraphy (mu-D to –A) (Figs. 4.3, 4.8-10). The majority of these anomalies exist within the shallow subsurface (top 1 km of sediment) and most likely represent pockets of trapped gas or gas hydrates (Hilterman, 2001; Nanda, 2016). It was imperative to identify and avoid the shallow fluid anomalies prior to drilling as unexpected pressure kicks caused by low density hydrocarbons can often lead to shut-ins, site abandonment and in a worst case scenario can cause blow-outs to occur (Holland, 1997; Prince, 1990). Gas hydrates, however, can be drilled through successfully and have even been the focus of several recent coring campaigns (Khabibullin et al., 2011; Ruppel et al., 2008; Ruppel, 2018; Wei et al., 2019). Though the hydrate deposits in this area, are underlain by a free gas column that is up to 50 m thick (Fig. 4.9) (Cox et al., 2021), and although overpressure beneath the hydrates is unlikely (thought to be at hydrostatic pressure (Dickens and Quinby-Hunt, 1994)), the free gas content may create significant buoyancy pressure which could be catastrophic if drilled (Holland, 1997; Minshull et al., 2020). Therefore, all potential hydrocarbon fluid anomalies were classified as 'maximum risk' and avoided as a priority (Fig. 4.10).

A dense network of both tectonic and polygonal faults was also identified within the study area (Figs. 4.2, 4.7 and 4.10). Avoiding fault intersections while drilling is important

as deep-seated near surface tectonic faults can pass high fluid pressures and hydrocarbons along the fault plane, and if not controlled, can lead to a loss of borehole control (Fig. 4.7) (Frydman et al., 2017; Jensen and Cauquil, 2013). Fault zones also have a much lower fracture gradient than non-faulted zones which may lead to sediments breaking up during drilling and poor core recovery. Polygonal faults however, are thought to be sealing under non-extreme pressure conditions (caused by factors such as glacial loading) and exist within many effective petroleum system seals worldwide, therefore, negating the risk of fluid flow along the fault plane (Cartwright, 2019). Still, densely polygonally faulted successions close to the seabed can hold significant fluid pressures, although it is likely that the shallow fluid system here would have been depressurized during repeated glacial loading and unloading cycles (Fjeldskaar and Amantov, 2018; Goulty, 2008; Ostanin et al., 2017) that occurred from 2.7 Ma (Knutz et al., 2019). Polygonally faulted clays with high smectite content can be problematic however, as they can cause drill pipes to become stuck due to the clays swelling when in contact with borehole fluids (Anderson et al., 2010).

Lithology variations were identified during the fine tuning of site locations in an attempt to avoid problematic lithologies such as glacial debris flow deposits which may contain boulders (potentially damaging coring equipment), hard indurated horizons or mass transport deposits which affect the continuous chronostratigraphic nature of successions due to sediment re-deposition (Bennett et al., 2014; Jensen and Cauquil, 2013). An attempt was also made to avoid sandy horizons that were identified through certain acoustic impedance contrasts (often semi-bright, negative amplitude events denote a top sand horizon) or through a chaotic seismic facies (e.g. Fig. 4.14). These uncompacted horizons would likely cause poor core recovery, possibly exacerbated by high fluid pressures within the sands which would further promote sediment collapse (shallow water flow) (West and West, 2005). Uncompacted coarse sand could even lead to the coring equipment getting stuck, such as was experienced on ODP Leg 174A (Austin et al., 1998).

Once a potential hazard was identified, the primary concern was to eliminate any drilling through or near to the potential hazard more so than on unravelling the detailed nature of the feature observed. However, the detailed results provided by the geohazard assessment coupled with a desire to understand the complex geological and fluid migration history of the area, did allow a closer assessment of the identified hazards, with the most notable conclusions being discussed below.

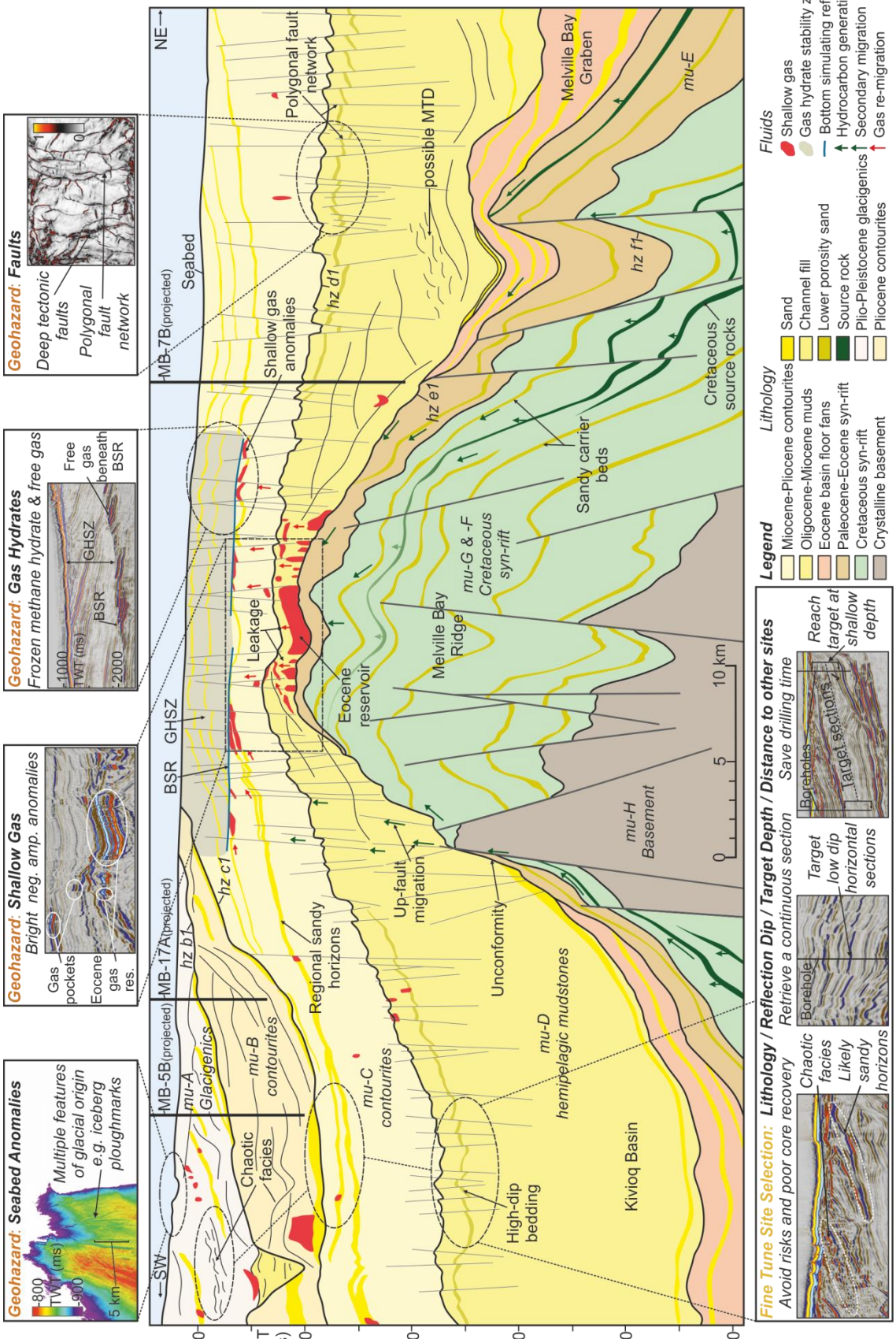
Geohazard: Seabed Anomalies
Multiple features of glacial origin e.g. iceberg ploughmarks
TWT (ms)
800
900
5 km
Geohazard: Shallow Gas
Bright neg. amp. anomalies
Gas pockets
Eocene gas res.
Geohazard: Gas Hydrates
Frozen methane hydrate & free gas
Free gas beneath BSR
GHSZ
BSR
1000
2000
TWT (ms)
Geohazard: Faults
Deep tectonic faults
Polygonal fault network
1
0
SW
NE
MB-5B(projected)
MB-17A(projected)
MB-7B(projected)
Seabed
BSR
GHSZ
mu-A
Glacigenics
mu-B
contourites
mu-C
contourites
hz b1
hz c1
Leakage
Chaotic facies
Regional sandy horizons
Up-fault migration
Unconformity
mu-D
hemipelagic mudstones
High-dip bedding
Kivioq Basin
Eocene reservoir
Melville Bay Ridge
mu-G & -F
Cretaceous
syn-rift
mu-H
Basement
Shallow gas anomalies
Polygonal fault network
hz d1
hz e1
hz f1
possible MTD
Sandy carrier beds
Cretaceous source rocks
Melville Bay Graben
mu-E
0
5
10 km
-1000
-1500
-2000
-2500
-3000
-3500
TWT (ms)
Legend
Lithology
Miocene-Pliocene contourites
Oligocene-Miocene muds
Eocene basin floor fans
Paleocene-Eocene syn-rift
Cretaceous syn-rift
Crystalline basement
Sand
Channel fill
Lower porosity sand
Source rock
Plio-Pleistocene glacigenics
Pliocene contourites
Fluids
Shallow gas
Gas hydrate stability zone
Bottom simulating reflector
Hydrocarbon generation
Secondary migration
Gas re-migration
Fine Tune Site Selection: Lithology / Reflection Dip / Target Depth / Distance to other sites
Avoid risks and poor core recovery
Retrieve a continuous section
Save drilling time
Chaotic facies
Likely sandy horizons
Borehole
Target low dip horizontal sections
Boreholes
Target sections
Reach target at shallow depth

Figure 4.15. Schematic summary | A schematic summary of the structure, stratigraphy, geohazards and fluid flow history that has been analysed and used within the process of site selection for IODP Proposal 909. Key features related to the elements of the geohazard assessment workflow are shown including the location of hydrocarbon fluids, sandy lithologies, faults and the location of potential source rock horizons and possible fluid migration pathways. The surrounding thumbnails show how these features were analysed and considered within the geohazard assessment workflow. Highlighting the distribution of these features across the schematic aims to provide context on how these features fit together and interact within the subsurface. The understanding of this system, along with the distribution of potential geohazards was crucial in the identification of viable stratigraphic targets and safe drill sites.

Firstly, the varying seismic character of the identified fluid anomalies (Figs. 4.3 and 4.8) along with their relationship to stratigraphic and structural elements (Fig. 4.15) suggests various styles of trapping mechanisms along with a complex fluid migration history (Figs. 4.2, 4.8-9 and 4.15) (Cox et al., 2021). The distribution of fluid anomalies shows a concentration above the Melville Bay Ridge, suggesting that this positive relief feature focussed the upward migration of hydrocarbons in this area (Figs. 4.2-3 and 4.15). This conclusion is further evidenced by the discovery of an extensive, likely gas charged, Eocene aged reservoir on the crest of the ridge (Figs. 4.8 and 4.15) (Cox et al., 2020a). Cretaceous source rocks are expected to exist within the buried syn-rift stratigraphy of the Melville Bay Graben and Kivioq Basin (Bojesen-Koefoed, 2011; Gregersen et al., 2019; Planke et al., 2009) which onlap onto the ridge high, thus providing the potential for hydrocarbon migration along sandy carrier beds or fault planes either up towards the ridge crest (charging the Eocene Reservoir) or into the shallower post-rift stratigraphy (Figs. 4.2 and 4.15). Furthermore, the stratigraphy directly above the Eocene reservoir displays evidence for gas leakage which is likely linked to the onset of multiple cycles of glacial loading and unloading of the crust and the mass-redistribution of sediment associated with the development of the MB-TMF (Cox et al., 2020a; Cox et al., 2021; Knutz et al., 2019; Newton et al., 2017). These processes likely caused episodic variations in subsurface conditions and structural tilt that may have promoted pulses of fluid leakage (Figs. 4.1-2 and 4.15) (Fjeldskaar and Amantov, 2018).

These processes also contributed to the concentration of hydrocarbons within the stratigraphy directly overlying the Melville Bay Ridge, causing the majority of this zone to be unsuitable for scientific drilling (Fig. 4.3). Moreover, expected fluid migration pathways from the deep basins and leakage from the Eocene reservoir are likely connected to the presence of gas hydrates, again within areas directly overlying the Melville Bay Ridge (Figs 4.2-3, 4.9 and 4.15). It is likely that the hydrate-forming fluids followed similar migration pathways to that of the identified gas anomalies, with free gas anomalies observed trapped at the base of the GHSZ at present day, suggesting continued hydrocarbon migration and post-hydrate formation (Figs. 4.9 and 4.15) (Cox et al., 2021). A portion of these fluids are

possibly sourced from the leaking Eocene reservoir, but the presence of free gas anomalies within regional sandy horizons suggests that upward migration of these fluids may have occurred away from the ridge, before entering these horizons and migrating laterally up-dip into areas uplifted above the ridge structure (Figs. 4.9 and 4.15). Numerous fluid anomalies also exist in areas away from the ridge (Fig. 4.3) suggesting a more complex regional migration history which is likely characterised by the trapping and subsequent re-migration of fluids in areas above the deeper basins (Cox et al., 2021; Grecula et al., 2018). In addition, biogenic gas production, possibly from organic horizons within the contourite succession (mu-B and –C), may represent the source of gas observed within glacigenic progradational sands (mu-A) (Figs. 4.3 and 4.9b) (Muller et al., 2018; Rebesco et al., 2014). Anomalies away from the ridge however, are more sporadic, and there are no identified gas hydrates or deeper gas reservoirs within the section investigated (Fig. 4.15).

Although aside to the principal task of identifying geohazards to minimize risk, the conclusions drawn from the more detailed assessment into the nature of the geohazard features identified, provided a greater understanding of fluid distribution and an enhanced prediction of what identified seismic features may represent. This knowledge ultimately informed the assessment of risk and actively affected site selection decisions and stratigraphic target amendments by avoiding areas characterised as representing focussed pathways for historical fluid migration (Fig. 4.15).

4.6.1. Influence on IODP Proposal 909

On the northwest Greenland continental margin, the geohazard assessment workflow was used to identify and document a wide range of potential drilling risks (Figs. 4.3, 4.5-10 and 4.15), which were considered on par with the scientific objectives and expedition logistics (number of drilling days available), when defining the final site localities. This process led to an efficient and informed selection of the primary and alternate sites, and the added detail and understanding provided through the assessment positively influenced the progression of the proposal through several stages of review and was integral to its success when considering its location within such a challenging region.

The influence of the assessment on minimizing risk is highlighted through a re-assessment of several original sites that were selected using regional 2D seismic data against the spatial distribution of geohazards identified through the 3D seismic assessment (Figs. 4.10, 4.13-15 and Table 4.3). An attempt was already made to avoid potential drilling risks when selecting sites on the 2D data, but the restricted spatial coverage and lower seismic resolution led to a number of features remaining unseen in the 2D assessment, such as close-proximity out of plane fluid anomalies and faults (Figs. 4.3 and 4.7), or variations in

seismic character suggesting sandy lithologies (Figs. 4.12 and 4.14). These types of geohazards were identified through the 3D assessment (and augmented by the LAKO UHR survey), leading to the alteration of these original sites to new and likely safer locations (Figs. 4.12-14 and Table 4.3). These alterations highlight the benefit of using 3D seismic analysis to identify safer areas outside of the 2D seismic lines whilst achieving the same or more optimal target parameters. Most importantly, the geohazard analysis enabled refined site selection within the Target VII area, which would have likely been abandoned if only covered by 2D seismic due to the deep drilling target, shallow gas distribution and a dense polygonal fault network, coupled with deeper faults and deeper gas sands (Figs. 4.2, 4.7, 4.10 and 4.14-15).

The results of the 3D geohazard assessment workflow (along with the location of the regional 2D seismic) also significantly influenced the acquisition plan for the 2D UHR seismic survey. This survey was acquired in 2019 to complement the 3D assessment by providing a higher resolution image of the top ~500 ms below the seabed (Figs. 4.3, 4.11-12, 4.14 and Table 4.2). These additional data both confirmed features observed on 3D seismic data and highlighted additional, more subtle features (such as potential lithology changes) which prompted several site amendments. Importantly, tailoring the acquisition using the 3D assessment results allowed the UHR survey to be focussed over areas that contained either the selected sites (to confirm location), more complex geology or a concentration of geohazards, and also for target areas outside of the existing 3D seismic coverage (Targets I and II – Fig. 4.1). This allowed a more efficient integration of the two data types, whilst minimizing acquisition within unnecessary areas, saving valuable expedition time.

4.6.2. Benefits to Future Projects

The geohazard assessment workflow provides a blueprint that maintains the high level of safety assessment associated with IODP drilling by incorporating modern 3D seismic data manipulation and interpretation techniques to take full advantage of the available data (e.g. Heggland et al. (1996); Sharp and Samuel (2004); Sharp and Badalini (2013)) (Fig. 4.5 and Table 4.1). This helps improve both safety and the chance of success of future scientific drilling. Improved 3D seismic acquisition and processing workflows have led to significant improvements in 3D resolution and a reduced reliance on dedicated site surveys (Games and Self, 2017; Oukili et al., 2019). Comparison of the 3D seismic volumes as pseudo site surveys within Proposal 909, against the recently acquired 2D UHR site survey lines, shows that the quality and resolution of imaging is mostly consistent across the two data types, confirming its suitability (comparison on Figs. 4.12, 4.14 and Table 4.2). The

main differences observed included subtle seismic variations, possibly due to lithology differences noted on the UHR seismic, as well as some additional brightening observed on the Anu 3D survey, possibly caused by tuning effects from thin beds that are thicker than the resolution threshold on the UHR seismic and therefore do not display as brightly (seismic survey vertical resolution shown on Table 2) (Fig. 4.12b and c) (Francis, 2015; Marzec and Pietsch, 2012). The 3D seismic volumes also meet the minimum acceptability criteria set out by the International Association of Oil & Gas Producers (IOGP) for using exploration 3D seismic data for site survey studies (Jensen and Cauquil, 2013).

Still, many projects never gain access to 3D seismic data, but the techniques defined within the workflow are still applicable in the 2D sense, especially if instead using high resolution and closely spaced 2D site survey data. Therefore, the seismic interpretation techniques presented could help maximise the use of available data whilst increasing interpretation quality and efficiency for a wide range of future projects (Selvage et al., 2012; Smith et al., 2019). These methods include using amplitude extraction windows to quickly identify potential fluid anomalies (Fig. 4.8), using pseudo BSR surfaces created using the BSR-seabed relationship to expand and guide BSR interpretations (Fig. 4.9) or using stratigraphic depth target zones within CRS maps to collate all identified hazards while focussing site selection within an appropriate, low risk area (Figs. 4.10 and 4.14).

The workflow also outlines how the increasing availability of seismic data through a projects progression can be combined to further assess potential geohazards and provide increased confidence in the chosen sites (Fig. 4.5). Importantly, the workflow addresses the key hazards that are likely considered within all site selection safety assessments (Figs. 4.5 and 4.15), though the list is not fully exhaustive and several other geohazards or geophysical techniques could be included dependent on context and whether additional data are available. Additional datasets could include acoustic or elastic impedance volumes and derivative rock property estimations (e.g. (Dutta, 2002); (Huuse and Feary, 2005)), 'fluid' volumes, electromagnetic-derived resistivity volumes (e.g. (Weitemeyer et al., 2006)), angle stacks for use in amplitude versus offset/angle (AVO/AVA) studies (Castagna and Swan, 1997) etc.

Examples of additional or modified techniques include using stratigraphical (instead of proportional) attribute extraction windows to follow reflection dip and remove interference from bright amplitude regional reflections and also predicting the BSR depth from the water depth in areas conducive for gas hydrate formation but where no obvious BSR is observed (Field and Kvenvolden, 1985; Gehrmann et al., 2009; Kvenvolden et al., 1993). Alterations to selected cut-offs (such as seabed dip and amplitude filters (Figs. 4.6 and 4.8))

and other parameters used to define the site location (such as the minimum radius to the nearest hazard) within the geohazard assessment workflow can also be made. If required, this may even include expanding the area where a specific site can be drilled, as seen used in regions even more prone to sea ice and icebergs, such as for IODP Exp. 379 (Amundsen Sea) (Gohl et al., 2019), where the safety radius (in this case along the 2D seismic line) defined around each site locality as being free of hazards, was used as a zone of which last minute borehole adjustments could be made in response to the predicted ice trajectory.

The (Gohl et al., 2019) study provides an example in which the subsurface or geohazard related requirements of a particular location would have influenced the techniques and processes considered within the workflow presented here. Other location specific requirements include areas containing deep and active fault zones (e.g. the Nankai Trough, Japan) or hydrocarbon fluid venting and extensive gas hydrate deposits (e.g. the Cascadia Margin, offshore Oregon, USA). Drilling safely within such locations with specific geohazard requirements may only be possible when 3D seismic data are available for the assessment of geohazards and drill site selection. This is why IODP legs targeting such areas (Legs 322 and 311 (Table 1)) have been supported by dedicated, research council funded, 3D seismic acquisition and processing (Bangs et al., 2009; Scherwath et al., 2006). This again, demonstrates the importance of 3D seismic data analysis on the future of scientific drilling.

4.7. Conclusions

IODP Proposal 909 aims to drill a transect of seven sites across the northwest Greenland continental margin that represents an area that is both a frontier petroleum province and a glaciated margin. A geohazard assessment was conducted that was optimized by the use of high-resolution 3D seismic data to accurately extract, document and spatially analyse potential geohazard evidence and select drill sites that represent the lowest risk possible whilst meeting the scientific objectives in terms of realistic drill depths, section age, completeness and thickness. The workflow undertaken for this assessment used 3D seismic analytical techniques to identify geohazards such as seabed features, fluid anomalies, faults and certain lithologies. The mapped geohazards were combined to create common risk segment maps for each of the primary site groups, using a restricted (green) zone defined by the depth to the stratigraphic target to focus site selection. This process led to the alteration or abandonment of several sites that were originally sited on regional 2D seismic data to more optimal locations within the 3D seismic coverage. The workflow and results were also used to tailor the acquisition of an ultra-high resolution site survey

which optimized acquisition and overall expedition planning. This survey was then used in combination with 3D seismic to verify site locations and identify more subtle shallow features such as potential lithology changes. Ultimately, the full geohazard assessment workflow was used to support 7 primary and 15 alternate sites for the scientific drilling proposal.

The detailed, accurate and comprehensive results provided by the 3D geohazard assessment, as well as its influence on the success of IODP Proposal 909, highlight the importance and benefit of maximising the use of all available data during the planning of a drilling campaign within a challenging environment. With both past and future IODP campaigns targeting areas such as frontier petroleum provinces or glaciated margins, whilst having access to 3D seismic data, the detailed consideration of geohazards outlined by this workflow provides a template for future projects. Incorporation of 3D seismic data analysis in site selection and hazard evaluation will help allow a more comprehensive safety assessment that could enable scientific drilling in areas otherwise considered too risky whilst maintaining the high safety standards required by the IODP.

Acknowledgments

The authors would like to thank the IODP and the members of the Science Evaluation Panel as well as all of the proponents who contributed to Proposal 909. We would also like to thank Cairn Energy PLC (Pitu Survey), Shell (Anu Survey), TGS (2D Regional Survey) and both the Geological Survey of Denmark and Greenland and Aarhus University (LAKO UHR) for the provision of seismic data and the permission to publish the images and results. Acquisition of the LAKO UHR data was possible through grants to PKN and JRH from the Danish Center for Marine Research and the Carlsberg Foundation and we would like to thank the scientific party involved with the acquisition during the LAKO 2019 expedition. The results and opinions expressed within this work are solely of the authors and not a representation of the companies or institutions. Finally we would like to thank both Schlumberger (Petrel) and Esri (ArcGIS) for providing the software packages used to complete the analysis within this work.

References

Acton, G., 2012, Proceedings of the Baffin Bay Scientific Coring Program – Expedition 344S: Reporting by company consortium with eight companies led by Shell, p. 1-842.

Aird, P., 2010, Assessing geo-hazards: BP Norge AS.

Altenbernd, T., Jokat, W., Heyde, I., and Damm, V., 2015, Geophysical evidence for the extent of crustal types and the type of margin along a profile in the northeastern Baffin Bay: Journal of Geophysical Research: Solid Earth, v. 120, no. 11, p. 7337-7360.

Anderson, R., Ratcliffe, I., Greenwell, H., Williams, P., Cliffe, S., and Coveney, P., 2010, Clay swelling—a challenge in the oilfield: Earth-Science Reviews, v. 98, no. 3-4, p. 201-216.

Andresen, K. J., Huuse, M., Schødt, N. H., Clausen, L. F., and Seidler, L., 2011, Hydrocarbon plumbing systems of salt minibasins offshore Angola revealed by three-dimensional seismic analysis: AAPG bulletin, v. 95, no. 6, p. 1039-1065.

Austin, J. A., Jr., Christie-Blick, N., and Malone, M. J., 1998, Leg 174A Preliminary Report - Continuing the New Jersey Mid-Atlantic sea-level transect: Ocean Drilling Program.

Badley, M. E., 1985, Practical seismic interpretation, Prentice Hall, Englewood Cliffs, N.J, 1107 p.:

Bangs, N., Moore, G., Gulick, S., Pangborn, E., Tobin, H., Kuramoto, S., and Taira, A., 2009, Broad, weak regions of the Nankai Megathrust and implications for shallow coseismic slip: Earth and Planetary Science Letters, v. 284, no. 1-2, p. 44-49.

Bennett, R., Campbell, D. C., Furze, M. F., and Haggart, J. W., 2014, The shallow stratigraphy and geohazards of the Northeast Baffin Shelf and Lancaster Sound: Bulletin of Canadian Petroleum Geology, v. 62, no. 4, p. 217-231.

Berndt, C., Bunz, S., Clayton, T., Mienert, J., and Saunders, M., 2004, Seismic character of bottom simulating reflectors: examples from the mid-Norwegian margin: Marine and Petroleum Geology, v. 21, p. 723-733.

Bickle, M., Arculus, R., Barrett, P., DeConto, R., Camoin, G., Edwards, K., Fisher, F., Inagaki, F., Kodaira, S., and Ohkouchi, N., 2011, Illuminating Earth's Past, Present and Future The Science Plan for the International Ocean Discovery Program 2013-2023: International Ocean Discovery Program.

Bojesen-Koefoed, J. A., 2011, West Greenland Petroleum Systems – an Overview of Source Rocks and Oil Seepages and Their Implications for Offshore Petroleum Exploration: The Geological Survey of Denmark and Greenland.

Bojesen-Koefoed, J. A., Nytoft, H. P., and Christiansen, F. G., 2004, Age of oils in West Greenland: Was there a Mesozoic seaway between Greenland and Canada: Geological Survey of Denmark and Greenland Bulletin, v. 4, p. 49-52.

Cartwright, J., Polygonal Faults and Seal Integrity, *in* Proceedings Sixth EAGE Shale Workshop, Bordeaux, France, 2019, Volume 2019, European Association of Geoscientists & Engineers, p. 1-4.

Cartwright, J. A., Huuse, M., and Aplin, A., 2007, Seal Bypass Systems: AAPG Bulletin, v. 91, no. 8, p. 1141-1166.

Castagna, J. P., and Swan, H. W., 1997, Principles of AVO crossplotting: The Leading Edge, v. 16, no. 4, p. 337-344.

Christ, A. J., Bierman, P. R., Knutz, P. C., Corbett, L. B., Fosdick, J. C., Thomas, E. K., Cowling, O. C., Hidy, A. J., and Caffee, M. W., 2020, The northwestern Greenland Ice Sheet during the Early Pleistocene was similar to today: Geophysical Research Letters, v. 47, no. 1.

Cox, D. R., Huuse, M., Newton, A. M. W., Gannon, P., and Clayburn, J., 2020a, Slip Sliding Away: Enigma of Large Sandy Blocks within a Gas Bearing Mass Transport Deposit, Offshore NW Greenland: AAPG Bulletin, v. 104, no. 5, p. 1011-1043.

Cox, D. R., Huuse, M., Newton, A. M. W., Sarkar, A. D., and Knutz, P. C., 2021, Shallow gas and gas hydrate occurrences on the northwest Greenland shelf margin: Marine Geology, v. 432, p. 1-21.

Cox, D. R., Newton, A. M. W., and Huuse, M., 2020b, An introduction to seismic reflection data: acquisition, processing and interpretation, *in* Scarselli, N., Adam, J., and Chiarella, D., eds., Regional Geology and Tectonics - Principles of Geologic Analysis: Amsterdam, Netherlands, Elsevier, p. 744.

Dan, G., Cauquil, E., and Bouroullec, J.-L., 3D seismic and AUV data integration for deepwater geohazard assessment: Application to offshore northwest Borneo, Brunei, *in* Proceedings Offshore Technology Conference-Asia2014, Offshore Technology Conference, p. 1-9.

Dickens, G. R., and Quinby-Hunt, M. S., 1994, Methane hydrate stability in seawater: Geophysical Research Letters, v. 21, no. 19, p. 2115-2118.

Dutta, N. C., 2002, Deepwater geohazard prediction using prestack inversion of large offset P-wave data and rock model: The Leading Edge, v. 21, no. 2, p. 193-198.

Dutta, N. C., Utech, R. W., and Shelander, D., 2010, Role of 3D seismic for quantitative shallow hazard assessment in deepwater sediments: The Leading Edge, v. 29, no. 8, p. 930-942.

Eriksen, F. N., Assad, M., Eriksen, O. K., Stokke, H. H., and Planke, S., HiRes P-Cable 3D data for shallow reservoir mapping and geohazard predictions–case examples from the Barents Sea, *in* Proceedings Near Surface Geoscience 2014-20th European Meeting of Environmental and Engineering Geophysics, Athens, Greece, 2014, Volume 2014, European Association of Geoscientists & Engineers, p. 1-5.

Ewing, J. I., and Hollister, C. H., 1972, Regional aspects of deep sea drilling in the western North Atlantic: Deep sea drilling project intial reports, v. 11, p. 951-973.

Field, M. E., and Kvenvolden, K. A., 1985, Gas hydrates on the northern California continental margin: Geology, v. 13, no. 7, p. 517-520.

Fjeldskaar, W., and Amantov, A., 2018, Effects of glaciations on sedimentary basins: Journal of Geodynamics, v. 118, p. 66-81.

Francis, A., 2015, A simple guide to seismic amplitudes and detuning: GEO ExPro, v. 12, no. 5, p. 68-72.

Frey-Martínez, J., 2010, 3D seismic interpretation of mass transport deposits: Implications for basin analysis and geohazard evaluation, *in* Mosher, D. C., Moscardelli, L., Shipp, R. C., Chaytor, J. D., Baxter, C. D. P., Lee, H. J., and Urgeles, R., eds., Submarine mass movements and their consequences: Dordrecht, Netherlands, Springer, p. 553-568.

Frydman, M., Holzberg, B., Pastor, J., Salies, J., and Pedroso, C., Reducing Fault Reactivation Risk on Deepwater Drilling, *in* Proceedings SPE Latin America and Caribbean Petroleum Engineering Conference, 1-15, 2017, Society of Petroleum Engineers.

Galavazi, M., Moore, R., Lee, M., Brunsden, D., and Austin, B., Quantifying the impact of deepwater geohazards, *in* Proceedings Offshore Technology Conference, Houston, Texas, USA, 2006, Offshore Technology Conference, p. 1-5.

Games, K. P., and Self, E., 2017, HRS 3D data—a fundamental change in site survey geohazard interpretation: First Break, v. 35, no. 3, p. 39-47.

Gehrmann, R., Müller, C., Schikowsky, P., Henke, T., Schnabel, M., and Bönnemann, C., 2009, Model-based identification of the base of the Gas hydrate stability zone in multichannel reflection seismic data, Offshore Costa Rica: International Journal of Geophysics, v. 2009, p. 12.

Gohl, K., Wellner, J. S., and Klaus, A., 2019, Expedition 379 Preliminary Report: Amundsen Sea West Antarctic Ice Sheet History: International Ocean Discovery Program.

Goulty, N., 2008, Geomechanics of polygonal fault systems: a review: Petroleum Geoscience, v. 14, no. 4, p. 389-397.

Grecula, M., Wadsworth, S., Maloney, D., Lauferts, H., Cooke, G., Jones, A., and Stevanovic, S., Baffin Bay Elusive Plays: Geological Surprises of an Arctic Exploration Campaign, *in* Proceedings American Association of Petroleum Geology International Conference and Exhibition (ICE), London, UK, 2018, Volume 30548, p. 1-20.

Gregersen, G., Knutz, P. C., Nøhr-Hansen, H., Sheldon, E., and Hopper, J. R., 2019, Tectonostratigraphy and evolution of the West Greenland continental margin: Bulletin of the Geological Society of Denmark, v. 67, p. 1-21.

Gregersen, U., Hopper, J. R., and Knutz, P. C., 2013, Basin seismic stratigraphy and aspects of prospectivity in the NE Baffin Bay, Northwest Greenland: Marine and Petroleum Geology, v. 46, p. 1-18.

Gregersen, U., Knutz, P. C., and Hopper, J. R., 2016, New geophysical and geological mapping of the eastern Baffin Bay region, offshore West Greenland: Geological Survey of Denmark and Greenland Bulletin, v. 35, p. 83-86.

Haneberg, W. C., Kelly, J. T., Graves, H. L., and Dan, G., 2015, A GIS-based decision-support approach to deepwater drilling-hazard maps: The Leading Edge, v. 34, no. 4, p. 398-404.

Hasle, J. R., Kjellén, U., and Haugerud, O., 2009, Decision on oil and gas exploration in an Arctic area: case study from the Norwegian Barents Sea: Safety science, v. 47, no. 6, p. 832-842.

Heggland, R., Nygaard, E. t., and Gallagher, J., Techniques and experiences using exploration 3D seismic data to map drilling hazards, *in* Proceedings Offshore Technology Conference, Houston, Texas, USA, 1996, Offshore Technology Conference.

Henriksen, N., Higgins, A. K., Kalsbeek, F., Christopher, T., and Pulvertaft, R., 2009, Greenland from Archaean to Quaternary: Descriptive text to the 1995 Geological map of Greenland, 1:2500000: Geological Survey of Denmark and Greenland Bulletin, v. 18, p. 1-126.

Hill, A. W., The use of exploration 3D data in geohazard assessment: where does the future lie?, *in* Proceedings Offshore Technology Conference, Houston, Texas, USA, 1996, Offshore Technology Conference.

Hill, A. W., Hampson, K. M., Hill, A. J., Golightly, C., Wood, G. A., Sweeney, M., and Smith, M. M., ACG field geohazards management: unwinding the past, securing the future, *in* Proceedings Offshore Technology Conference2015, Offshore Technology Conference.

Hilterman, F. J., 2001, Seismic Amplitude Interpretation, Tulsa, OK, Society of Exploration Geophysicists, Distinguished Instructor Series No. 4, 244 p.:

Holland, P., 1997, Offshore blowouts: causes and control, Houston, Texas, USA, Gulf Publishing Company.

Hovland, M., Francis, T. J. G., Claypool, G. E., and Ball, M. M., 1998, Strategy for scientific drilling of marine gas hydrates: JOIDES journal, v. 25, no. 1, p. 20-24.

Huuse, M., and Feary, D. A., 2005, Seismic inversion for acoustic impedance and porosity of Cenozoic cool-water carbonates on the upper continental slope of the Great Australian Bight: Marine Geology, v. 215, no. 3-4, p. 123-134.

Jeanjean, P., Liedtke, E., Clukey, E. C., Hampson, K., and Evans, T., An operator's perspective on offshore risk assessment and geotechnical design in geohazard-prone areas, *in* Proceedings Frontiers in Offshore Geotechnics: Proceedings of the International Symposium on Frontiers in Offshore Geotechnics (IS-FOG 2005), Perth, WA, Australia, 2005, CRC Press, p. 115.

Jensen, P. J., and Cauquil, E., 2013, Guidelines for the conduct of offshore drilling hazard site surveys: International Association of Oil & Gas Producers.

Khabibullin, T., Falcone, G., and Teodoriu, C., 2011, Drilling through gas-hydrate sediments: Managing wellbore-stability risks: SPE drilling & completion, v. 26, no. 02, p. 287-294.

Khan, F. A., Zohdi, S. B. M., Beng, Q. K., Mohamed, H. B., and Yahya, M. A. M., High-resolution pseudo 3D seismic data for shallow marine exploration and geohazard assessment in Offshore Malaysia, *in* Proceedings 80th EAGE Conference and Exhibition 2018, Copenhagen, Denmark, 2018, Volume 2018, European Association of Geoscientists & Engineers, p. 1-5.

Knutz, P. C., Campbell, D. C., Bierman, P. R., de Vernal, A., Huuse, M., Jennings, A., Cox, D. R., DeConto, R., Gohl, K., Hogan, K., Hopper, J. R., Keisling, B., Newton, A. M. W., Perez, L., Rebschläger, J., Sliwinska, K. K., Thomas, E., Willerslev, E., Xuan, C., and Stoner, J., 2018, Cenozoic evolution of the northern Greenland Ice Sheet exposed by transect drilling in northeast Baffin Bay (CENICE): International Ocean Discovery Program.

Knutz, P. C., Harrison, C., Brent, T. A., Gregersen, G., and Hopper, J. R., submitted, Baffin Bay Tectono-Sedimentary Element, *in* Drachev, S., and Moore, T. E., eds., Arctic Sedimentary Basins, Volume Geological Society Memoir: London, Geological Society London.

Knutz, P. C., Hopper, J. R., Gregersen, U., Nielsen, T., and Japsen, P., 2015, A contourite drift system on the Baffin Bay–West Greenland margin linking Pliocene Arctic warming to poleward ocean circulation: Geology, v. 43, no. 10, p. 907-910.

Knutz, P. C., Newton, A. M. W., Hopper, J. R., Huuse, M., Gregersen, U., Sheldon, E., and Dybkjær, K., 2019, Eleven phases of Greenland Ice Sheet shelf-edge advance over the past 2.7 million years: Nature Geoscience, v. 12, p. 361-368.

Kvenvolden, K. A., 1993, A primer on gas hydrates, *in* Howell, D. G., Wiese, K., Fanelli, M., Zink, L. L., and Cole, F., eds., The Future of Energy Gases, Volume US Geological Survey Professional Paper 1570: Washington DC, USA, USGS, p. 279-291.

Kvenvolden, K. A., Ginsburg, G. D., and Soloviev, V. A., 1993, Worldwide distirbution of subaquatic gas hydrates: Geo-Marine Letters, v. 13, p. 32-40.

Lancelot, Y., and Seibold, E., 1977, The evolution of the central Northeastern Atlantic - Summary of results of DSDP Leg 41, *in* Lancelot, Y., Seibold, E., and Gardner, J. V., eds., Initial reports of the DSDP, Volume 41: Washington, U.S. Government Printing Office, p. 1215-1245.

Li, P., Cai, Q., Lin, W., Chen, B., and Zhang, B., 2016, Offshore oil spill response practices and emerging challenges: Marine Pollution Bulletin, v. 110, no. 1, p. 6-27.

Marzec, P., and Pietsch, K. M., 2012, Thin-bedded strata and tuning effect as causes of seismic data anomalies in the top part of the Cenomanian sandstone in the Grobla–Rajsko–Rylowa area (Carpathian foreland, Poland): Geological Quarterly, v. 56, no. 4, p. 690-710.

Mearns, K., and Flin, R., 1995, Risk perception and attitudes to safety by personnel in the offshore oil and gas industry: a review: Journal of loss prevention in the process industries, v. 8, no. 5, p. 299-305.

Minshull, T. A., Marín-Moreno, H., Betlem, P., Bialas, J., Bünz, S., Burwicz, E., Cameselle, L., Cifci, G., Giustinaini, M., Hillman, J. I. T., Hölz, S., Hopper, J. R., Ion, G., León, R., Magalhaes, V., Makovsky, Y., Mata, M., Max, M. D., Nielsen, T., Okay, S., Ostrovsky, I., O'Neil, N., Pinheiro, L. M., Plaza-Faverola, A., Rey, D., Roy, S., Schwalenberg, K., Senger, K., Vadakkepuliyambatta, S., Vasilev, A., and Vázquez, J. T., 2020, Hydrate occurrence in Europe: A review of available evidence: Marine and Petroleum Geology, v. 111, p. 735-764.

Mitchell, J., Marcel, V., and Mitchell, B., 2012, What next for the oil and gas industry?: Chatham House.

Moore, R., Ushet, N., and Evans, T., Integrated multidisciplinary assessment and mitigation of West Nile Delta geohazards, *in* Proceedings Offshore Site Investigation and Geotechnics, Confronting New Challenges and Sharing Knowledge, London, UK, 2007, Society of Underwater Technology, p. 1-10.

Muller, S., Reinhardt, L., Franke, D., Gaedicke, C., and Winsemann, J., 2018, Shallow gas accumulations in the German North Sea: Marine and Petroleum Geology, v. 91, p. 139-151.

Nadim, F., and Kvalstad, T. J., Risk assessment and management for offshore geohazards, *in* Proceedings Proceedings of the ISGSR, Shanghai, China, October 2007 2007, p. 159-173.

Nanda, N. C., 2016, Direct Hydrocarbon Indicators (DHI), Seismic Data Interpretation and Evaluation for Hydrocarbon Exploration and Production: Cham, Switzerland, Springer, p. 103-113.

National Research Council, 2011, Scientific ocean drilling: accomplishments and challenges, Washington, DC, USA, The National Academies Press, 1-158 p.:

Newton, A. M. W., Huuse, M., Knutz, P. C., Cox, D. R., and Brocklehurst, S. H., 2020, Repeated ice streaming on the northwest Greenland shelf since the onset of the Middle Pleistocene Transition: The Cryosphere Discuss., v. 2019, p. 1-18.

Newton, A. M. W., Knutz, P. C., Huuse, M., Gannon, P., Brocklehurst, S. H., Clausen, O. R., and Gong, Y., 2017, Ice stream reorganization and glacial retreat on the northwest Greenland shelf: Geophysical Research Letters, v. 44, p. 7826-7835.

Nøhr-Hansen, H., Pedersen, G. K., Knutz, P. C., Bojesen-Koefoed, J. A., Sliwinska, K. K., and Hovikoski, J., 2018, Potential Cretaceous source-rocks from the north-east Baffin Bay, West Greenland, AAPG Europe Regional Conference - Global Analogues of the Atlantic Margin: Lisbon, p. 1.

Núñez-Betelu, L. K., 1993, Rock-Eval/TOC pyrolysis data from the Kanguk Formation (Upper Cretaceous), Axel Heiberg and Ellesmere Islands, Canadian Arctic: Geological Survey of Canada.

Oakey, G. N., and Chalmers, J. A., 2012, A new model for the Paleogene motion of Greenland relative to North America: Plate reconstructions of the Davis Strait and Nares Strait regions between Canada and Greenland: Journal of Geophysical Research, v. 117, no. B10, p. 1-28.

Ostanin, I., Anka, Z., and Di Primio, R., 2017, Role of faults in Hydrocarbon Leakage in the Hammerfest Basin, SW Barents Sea: Insights from seismic data and numerical modelling: Geosciences, v. 7, no. 2, p. 28.

Oukili, J., Gruffeille, J.-P., Otterbein, C., and Loidl, B., 2019, Can high-resolution reprocessed data replace the traditional 2D high-resolution seismic data acquired for site surveys?: First Break, v. 37, no. 8, p. 49-54.

Parkinson, R., 2000, High-resolution site surveys, London, CRC Press.

Pearce, C., Knutz, P. C., and Party, S. S., 2019, Baffin Bay Ice-Ocean-Sediment Interactions (BIOS) cruise report.

Planke, S., Symonds, P. A., Alvestad, E., and Skogseis, J., 2009, Mid-Cretaceous source rock subcropping in the Baffin Bay: GEO ExPro, v. 6, p. 1-8.

Poppel, B., 2018, Arctic Oil & Gas Development: The Case of Greenland: Arctic Yearbook 2018, p. 328.

Prince, P. K., 1990, Current drilling practices and the occurrence of shallow gas, *in* Ardus, D. A., and Green, C. D., eds., Safety in offshore drilling: Dordrecht, Springer, p. 3-25.

Raef, A., Totten, M., Vohs, A., and Linares, A., 2017, 3D Seismic Reflection Amplitude and Instantaneous Frequency Attributes in Mapping Thin Hydrocarbon Reservoir Lithofacies: Morrison NE Field and Morrison Field, Clark County, KS: Pure and Applied Geophysics, v. 174, no. 12, p. 4379-4394.

Rebesco, M., Hernández-Molina, F. J., Van Rooij, D., and Wåhlin, A., 2014, Contourites and associated sediments controlled by deep-water circulation processes: state-of-the-art and future considerations: Marine Geology, v. 352, p. 111-154.

Roberts, H. H., Doyle, E. H., Booth, J. R., Clark, B. J., Kaluza, M. J., and Hartsook, A., 3D-Seismic Amplitude Analysis of the Sea Flooc An Important Interpretive Method for Improved Geohazards Evaluations, *in* Proceedings Offshore Technology Conference, Houston, Texas, USA, 1996, Offshore Technology Conference.

Ruppel, C., Boswell, R., and Jones, E., 2008, Scientific results from Gulf of Mexico gas hydrates Joint Industry Project Leg 1 drilling: introduction and overview: Marine and Petroleum Geology, v. 25, no. 9, p. 819-829.

Ruppel, C. D., 2018, The US Geological Survey's Gas Hydrates Project: US Geological Survey, 2327-6932.

Saini, J., Stein, R., Fahl, K., Weiser, J., Hebbeln, D., Hillaire-Marcel, C., and de Vernal, A., 2020, Holocene variability in sea ice and primary productivity in the northeastern Baffin Bay: Arktos, p. 1-19.

Sangree, J. B., and Widmier, J. M., 1979, Interpretation of depositional facies from seismic data: Geophysics, v. 44, no. 2, p. 131-160.

Scherwath, M., Riedel, M., Spence, G., and Hyndman, R., 2006, Data report: seismic structure beneath the north Cascadia drilling transect of IODP Expedition 311: Proceedings of the Integrated Ocean Drilling Program: Scientific Results, v. 311, p. 1-25.

Selvage, J., Jones, C., and Edgar, J., 2012, Maximizing the value of 3D seismic data for shallow geohazard identification: First Break, v. 30, no. 8.

Sharp, A., and Badalini, G., 2013, Using 3D seismic data to map shallow-marine geohazards: a case study from the Santos Basin, Brazil: Petroleum Geoscience, v. 19, no. 2, p. 157-167.

Sharp, A., and Samuel, A., 2004, An example study using conventional 3D seismic data to delineate shallow gas drilling hazards from the West Delta Deep Marine Concession, offshore Nile Delta, Egypt: Petroleum Geoscience, v. 10, no. 2, p. 121-129.

Smith, P., Milne, R., Vey, G., Apeland, G., and Way, S., Can Shallow Hazard 3D Seismic Cubes Enable Leaner Exploration Workflows?, *in* Proceedings 81st EAGE Conference and Exhibition2019, Volume 2019, European Association of Geoscientists & Engineers, p. 1-5.

Stewart, F. S., and Stoker, M. S., 1990, Problems associated with seismic facies analysis of diamicton-dominated, shelf glacigenic sequences: Geo-Marine Letters, v. 10, no. 3, p. 151-156.

Suicmez, V. S., 2016, Future Direction in Oil and Gas Exploration and Production, *in* Riazi, M., ed., Exploration and Production of Petroleum and Natural Gas: West Conshohocken, PA, USA, ASTM International, p. 693-710.

Vanneste, M., Sultan, N., Garziglia, S., Forsberg, C. F., and L'Heureux, J.-S., 2014, Seafloor instabilities and sediment deformation processes: The need for integrated, multi-disciplinary investigations: Marine Geology, v. 352, p. 183-214.

Wei, J., Liang, J., Lu, J., Zhang, W., and He, Y., 2019, Characteristics and dynamics of gas hydrate systems in the northwestern South China Sea-Results of the fifth gas hydrate drilling expedition: Marine and Petroleum Geology, v. 110, p. 287-298.

Weimer, P., and Pettingill, H. S., 2007, Deep-water exploration and production: A global overview, *in* Nilsen, T. H., Shew, R. D., Steffens, G. S., and Studlick, J. R. J., eds., Atlas of deep-water outcrops: AAPG Studies in Geology, Volume 56: CD-ROM, AAPG, p. 1-29.

Weitemeyer, K., Constable, S., and Key, K., 2006, Marine EM techniques for gas-hydrate detection and hazard mitigation: The Leading Edge, v. 25, no. 5, p. 629-632.

West, A. U., and West, C. L., 2005, Shallow water flow presents costly, challenging drilling hazard: Porosity loss within the sand, shale: Offshore, v. 65, no. 4, p. 1.

Whittaker, R. C., Hamann, R. E., and Pulvertaft, T. C. R., 1997, A New Frontier Province Offshore Northwest Greenland: Structure, Basin Development, and Petroleum Potential of the Melville Bay Area: AAPG Bulletin, v. 81, no. 6, p. 978-998.

Williams, J. P., and Andresen, P. C., Application of conventional 3D data to geohazard assessment, *in* Proceedings Offshore Technology Conference, Houston, Texas, USA, 1996, Offshore Technology Conference, p. 1-7.

Wood, G. A., and Hamilton, I. W., Current geohazard problems and their geophysical interpretation-An international overview, *in* Proceedings Offshore Technology Conference, Houston, Texas, USA, 2002, Offshore Technology Conference, p. 1-9.

5

Petroleum Systems Modelling

Preamble

DRC built the PetroMod model, interpreted the data, wrote the manuscript and drafted the figures presented in this chapter. SS and AB assisted with model creation, simulation and refinement, and reviewed the final manuscript. AMWN and MH assisted with figure creation and manuscript reviewing.

Modelling Basin Evolution and Petroleum Systems Along a 2D Seismic Section Offshore Northwest Greenland

David R. Cox[1], Simone Salazar[2], Attila Bartha[2], Andrew M. W. Newton[1, 3] and Mads Huuse[1, 2]

[1]Department of Earth and Environmental Sciences, The University of Manchester

[2]Schlumberger GmbH, Aachen Technology Centre, Ritterstraße 23, 52072 Aachen, Germany.

[3]School of Natural and Built Environment, Elmwood Building, Queens University Belfast, University Road, UK, BT7 1NN

Abstract

Petroleum systems modelling has been conducted across a ~225 km cross section of the Melville Bay continental shelf, offshore northwest Greenland. This model improves our understanding of the geological evolution and the nature of hydrocarbons through time. This provides important constraints within one of the last remaining frontier areas that contains little calibration data. For this reason, analogue data from across the West Greenland region have been used in combination with detailed analyses from seismic reflection data to inform model creation. Sensitivity analysis, testing the impact of several parameters through time, was used to identify the most likely scenarios for paleo-conditions such as; heat flow history, variations in fault permeability and the potential lithological characteristics of sealing formations. The model predicts a viable petroleum system fed by Cretaceous and Paleocene source rocks. The maturation of these source rocks is significantly influenced by variable subsidence rates across the margin, with much greater prospectivity suggested for the Melville Bay Graben compared to the South Kivioq Basin. Hydrocarbon expulsion likely began in the latest Paleogene, with migration significantly influenced by extensional faults and fault blocks and the presence of the Melville Bay Ridge inversion structure. However, the trapping and accumulation of hydrocarbons did not begin until the development of the regional seal horizon (mu-D1) in

the mid-Miocene. Several hydrocarbon accumulations are predicted to currently exist, with one of the largest being contained within an extensive mass transport complex on the crest of the Melville Bay Ridge, which most likely contains methane gas. Long standing biogenic hydrocarbon generation from organic shale-rich post-rift sediments, is also a probable scenario across much of the Melville Bay shelf, and may represent the only reasonable method of creating the gas accumulations suggested by seismic amplitude anomalies within glacigenic sediments overlying the South Kivioq Basin.

5.1. Introduction

The northwest Greenland continental margin represents an under-studied geological setting that has experienced a complicated past of rifting and deep subsidence, multiple episodes of uplift and ridge formation (Cox et al., 2020a; Gregersen et al., 2019; Oakey and Chalmers, 2012; Whittaker et al., 1997), as well as large scale erosion and sediment redistribution associated with repeated shelf edge glaciations during the Plio-Pleistocene (Knutz et al., 2019; Newton et al., 2017). Throughout this evolution, petroleum systems are thought to have developed (Gregersen, 2008; Gregersen et al., 2013), with mature source rocks expected to exist within the deep basins (Nøhr-Hansen et al., 2018) and a number of potential hydrocarbon accumulations existing within the post-rift stratigraphy (Cox et al., 2020a; 2021). Understanding the contemporary character of these hydrocarbons, and the influence of basin evolution on hydrocarbon generation, migration, accumulation and preservation is important for the natural resource potential of the Arctic frontier (Gregersen, 2008; Henriksen et al., 2009; Whittaker et al., 1997). Additionally, due to the sensitivity of Arctic environments, any hydrocarbon leakage or the dissociation of near surface hydrocarbons, such as gas hydrates, in response to geological or oceanographic change, could act as a strong feedback mechanism for climate change (Karisiddaiah and Veerayya, 1994; Krey et al., 2009; Ruppel and Kessler, 2017).

The subsurface offshore northwest Greenland is imaged by a large database of 2D and 3D seismic reflection data that were acquired as a result of exploration interest in Baffin Bay between 2007-2014 (Cox et al., 2021; Gregersen et al., 2019). This has led to a number of seismic-based studies detailing the seismic stratigraphy and geomorphology of Melville Bay (Gregersen et al., 2013; 2016; Knutz et al., 2015), as well as the contemporary distribution of hydrocarbons (Cox et al., 2020a; 2021). However, calibration of this hydrocarbon system is lacking due to the closest well data being more than 300 km to the south (Fig. 5.1). This restricts our understanding of several fundamental aspects of the hydrocarbon system such as petroleum system elements (source rocks, migration pathways,

reservoirs, traps and seals), fluid content, saturations, and subsurface pressure and temperature (Hantschel and Kauerauf, 2009). Without the availability of direct calibration data, this study aims to utilise all the available data from across northwest West Greenland (Fig. 5.1), to create a regional 2D petroleum systems model that can predict the most likely nature of the hydrocarbon system at present day and how this system has evolved through time. This will assess a wide range of elements across the Melville Bay margin, from source rock burial and maturity, to reservoir accumulation and surface leakage, whilst sensitivity analysis of parameters through time aims to reveal probable scenarios for heat flow history, fault permeability, seal development and the likely contribution from both thermogenic and biogenic source rocks. The study will give particular focus to the evolution and contemporary nature of the hydrocarbons that are thought to have accumulated within an extensive, 420 km^2 Eocene aged mass transport complex on the crest of the Melville Bay Ridge (Fig. 5.2) (Cox et al., 2020a).

5.2. Regional Setting

5.2.1. Tectonic History and Structural Framework

The northwest Greenland margin is characterised by deep sedimentary basins and elongate structural ridges that developed as a result of rifting and seafloor spreading between Greenland and Canada during the Cretaceous to Paleogene (Altenbernd et al., 2015; Gregersen et al., 2013; 2016; Oakey and Chalmers, 2012). The sedimentary basins of the Melville Bay Graben (MBG) and South Kivioq Basin (SKB) contain both syn- and post-rift sediments that can reach thickness of over 10 km (Fig. 5.2) (Whittaker et al., 1997), and developed during two phases of rifting; the first during the Early Cretaceous (145.5-99.6 Ma) and the second during the Campanian-Danian (83.6-61.6 Ma) after a period of rift quiescence (Cox et al., 2020a; Gregersen et al., 2019; Oakey and Chalmers, 2012). The Melville Bay Ridge (MBR) and the Kivioq Ridge, which separate these basins, represent northwest-southeast trending elongate inversion structures that likely formed during the second phase of rifting through the Late Cretaceous. The structures also experienced a renewal of uplift associated with a change in spreading direction during the latest Paleocene and Eocene, which resulted in compressional tectonics as Greenland drifted northward and converged with the North American Plate (the Eurekan Orogeny) (Cox et al., 2020b; Knutz et al., submitted; Oakey and Stephenson, 2008). These movements created a regional unconformity in the Eocene that marks the top of the ridge structures and the transition from syn- to post-rift deposition (Balkwill, 1987; Gregersen et al., 2019). Today, syn-rift stratigraphy within the ridge structures has been significantly

offset by extensive tectonic faults that occur parallel to the ridge strike and have likely played a major controlling factor in regional fluid migration (Cox et al., 2021).

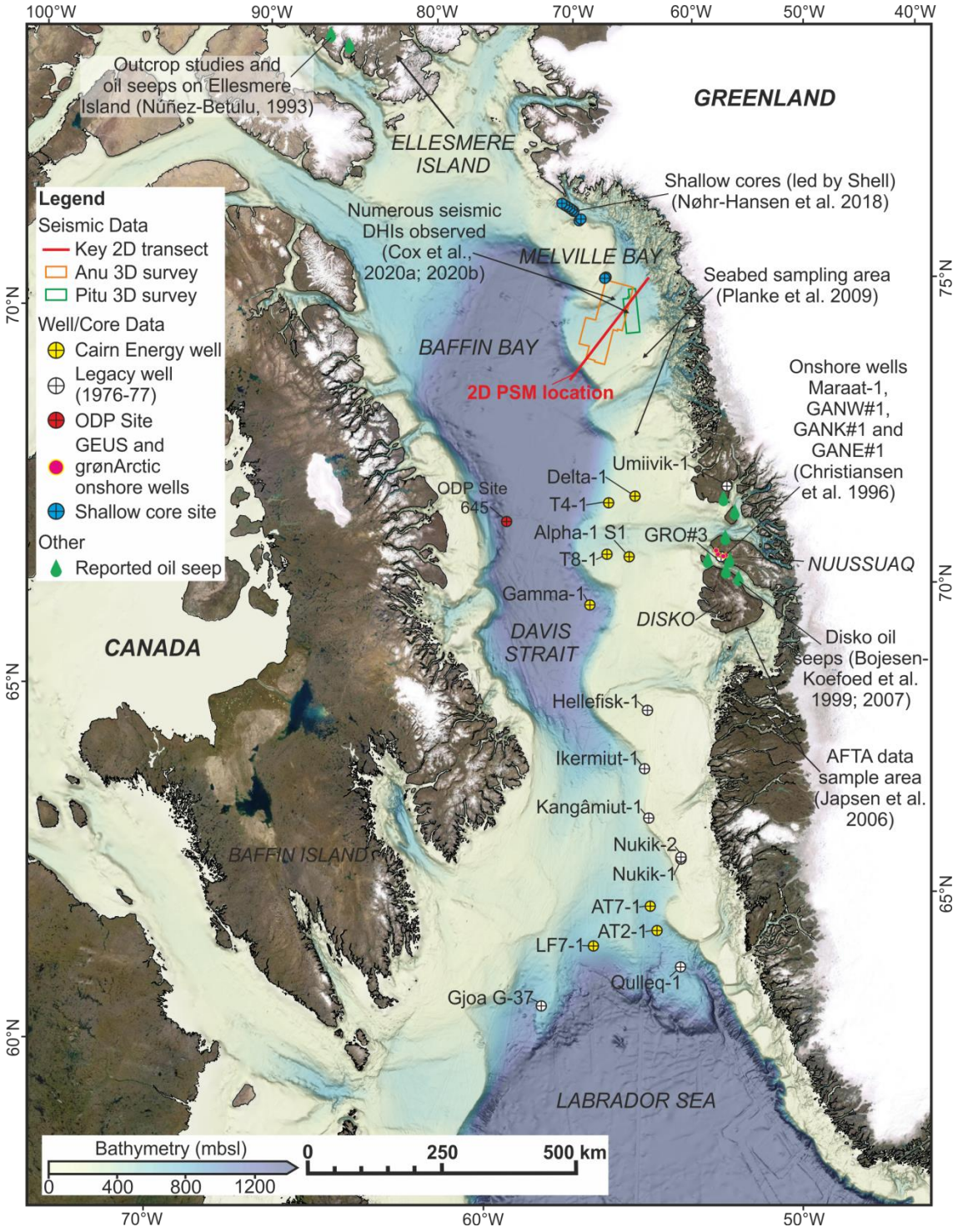

Figure 5.1. Regional data map | A map of West Greenland displaying the location of the 2D seismic cross section used to create the 2D petroleum systems model (PSM), along with the location of seismic studies, wells, outcrops, seeps and sample sites that provided analogue data used to inform model creation. More information on these data can be found via the references given on the map. The bathymetry data shown is adapted from GEBCO Bathymetric Compilation Group 2020 (2020).

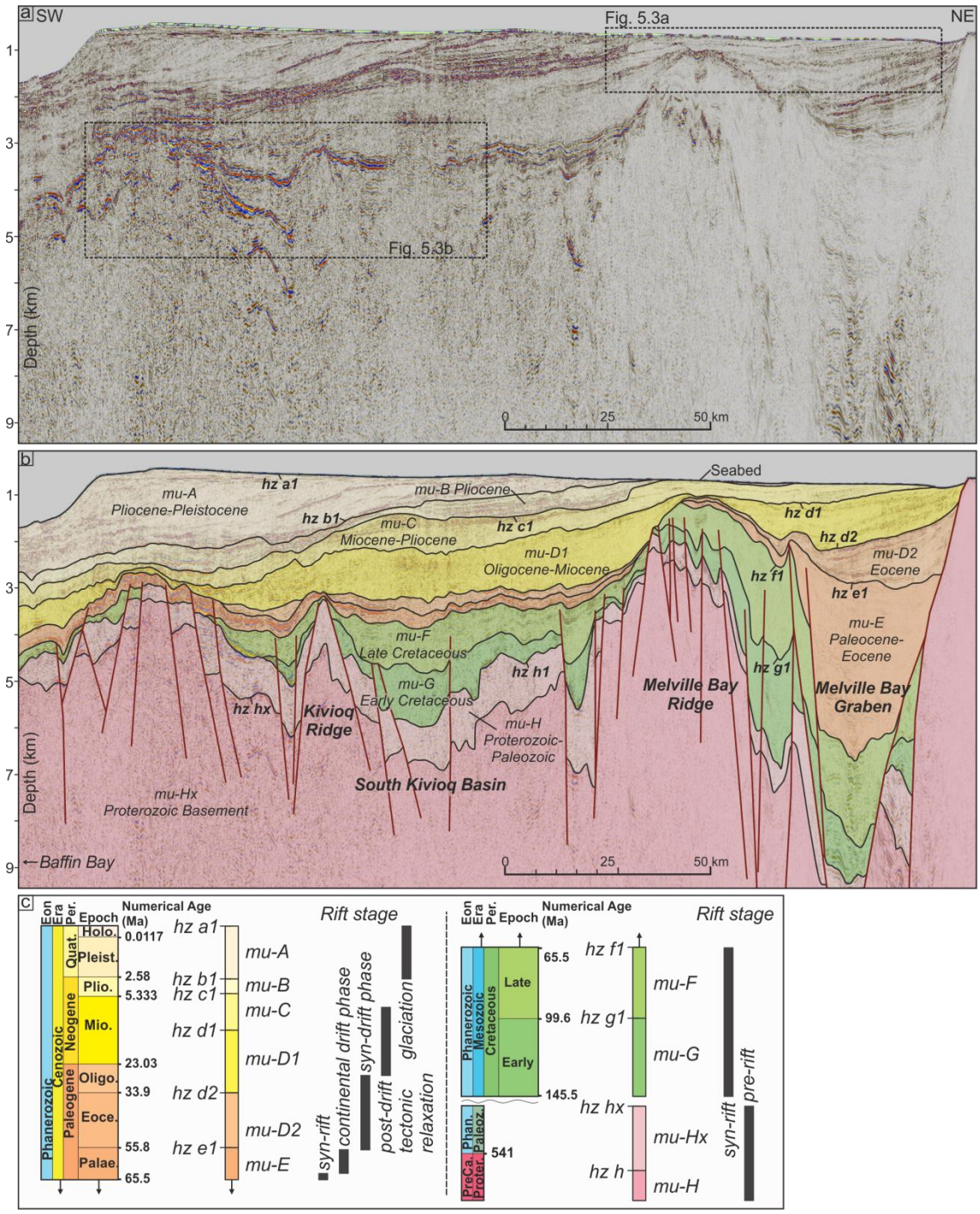

Figure 5.2. Regional stratigraphic and structural framework | An uninterpreted (a) and interpreted (b) depth converted 2D seismic cross section, displaying the structure and stratigraphy of the Melville Bay continental margin as well as interpretations of the regional seismo-stratigraphic framework (c). This seismic line, and the horizons and faults interpreted on it, were used to create the present day geometry of the 2D petroleum systems model. The location of the seismic line is shown on Fig. 5.1. The chronology of the depositional mega-units (mu-) and bounding horizons (hz), as well as the stages of rift margin evolution are shown on (c).

Seafloor spreading in Baffin Bay ceased during the late Eocene-Oligocene (Oakey and Chalmers, 2012; Welford et al., 2018) and post-rift basin infill occurred during and after a phase of post-drift tectonic relaxation (Knutz et al., submitted). Several phases of renewed

uplift likely affected the region throughout the Neogene, evidenced by paleo-topographic and apatite-fission-tracking analysis (Japsen et al., 2006) (Fig. 5.1). These movements led to the development of post-rift unconformities (e.g. the middle Miocene unconformity (Knutz et al., 2012; 2015)) as well as phases of localised uplift that affected the MBR (Cox et al., 2020a; Japsen et al., 2006). These periods of ridge uplift caused the MBR to remain a prominent positive relief feature throughout post-rift sedimentation, forcing deposited sediments to onlap onto the ridge flanks and drape across the crest (Fig. 5.2). The renewed uplift, along with increased sediment thickness and compaction within the adjacent basins, likely caused the formation of vertically extensive, post-rift faults that often exist parallel to ridge strike and occur much more frequently in areas above the ridge flanks (Cox et al., 2021). Since ~2.7 Ma, the Melville Bay shelf area has been transformed by multiple shelf edge glaciations that caused the removal of hundreds of meters (thickness) of sediment on the inner shelf, as well as ~100 km of shelf edge progradation associated with the development of the Melville Bay Trough Mouth Fan (Knutz et al., 2019; Newton et al., 2021; 2017).

5.2.2. Stratigraphic Framework

The syn- and post-rift successions of northwest Greenland have been extensively mapped, with the seismic-stratigraphy nomenclature of Gregersen et al. (2013, 2017) and Knutz et al. (2015) used in this study (Fig. 5.2). This work divides the stratigraphy into ten seismic mega-units (mu-) (Hx-A, from oldest to youngest) which are bounded by regional unconformities (horizons (hz) hx-b1, from oldest to youngest) (Fig. 5.2b-c).

The basement (mu-Hx) represents Proterozoic aged crystalline rocks that are likely of granitic composition, as sampled in well AT-7 (Fig. 5.1), which displayed U-Pb zircon ages of 3190-2730 Ma (Gregersen et al., 2018). Overlying the true acoustic basement, are Proterozoic-Paleozoic aged metamorphosed sediments (mu-H) that include sandstones interbedded with carbonates and muds that likely correspond to the youngest strata of the Thule Supergroup that were recovered in several shallow cores (Acton, 2012; Gregersen et al., 2019; Nøhr-Hansen et al., 2018). The syn-rift sedimentation is represented by mu-G and -F, which were deposited within the Early and Late Cretaceous, respectively (Fig. 5.2). Mu-G contains well lithified metamorphosed sediments that are possibly deltaic in origin, including sandstones, mudstones and thin coal beds that were recovered in shallow cores in the north of Melville Bay (Fig. 5.1) (Nøhr-Hansen et al., 2018). Several thicker (~100 m) sandstone units may exist that are equivalent to the syn-rift, Albian aged Kome and Slibestensfjeldet Formations that are observed exposed to the south within the Nuussuaq Basin (Dam et al., 2009). Mu-F has been sampled in several wells (Gregersen et al., 2019)

and contains marine mudstones, sandstones and local conglomerates; sediments which are equivalent to the Upper Cretaceous Kangeq sequence which includes the Ikermiut Formation sands (Chalmers et al., 1995; Gregersen et al., 2019). The unit is also expected to contain organic rich shale horizons deposited during a period of uplift quiescence during the Cenomanian and Turonian (Cox et al., 2020a; Gregersen et al., 2013), which have been observed in seabed samples to the north (Planke et al., 2009). Hz f1 (Fig. 5.2) represents a regional unconformity spanning millions of years, where up to 1.3 km of uplift caused erosion to occur west of the MBR, possibly removing early Paleogene and latest Cretaceous sediments (Fig. 5.3) (Dam et al., 1998).

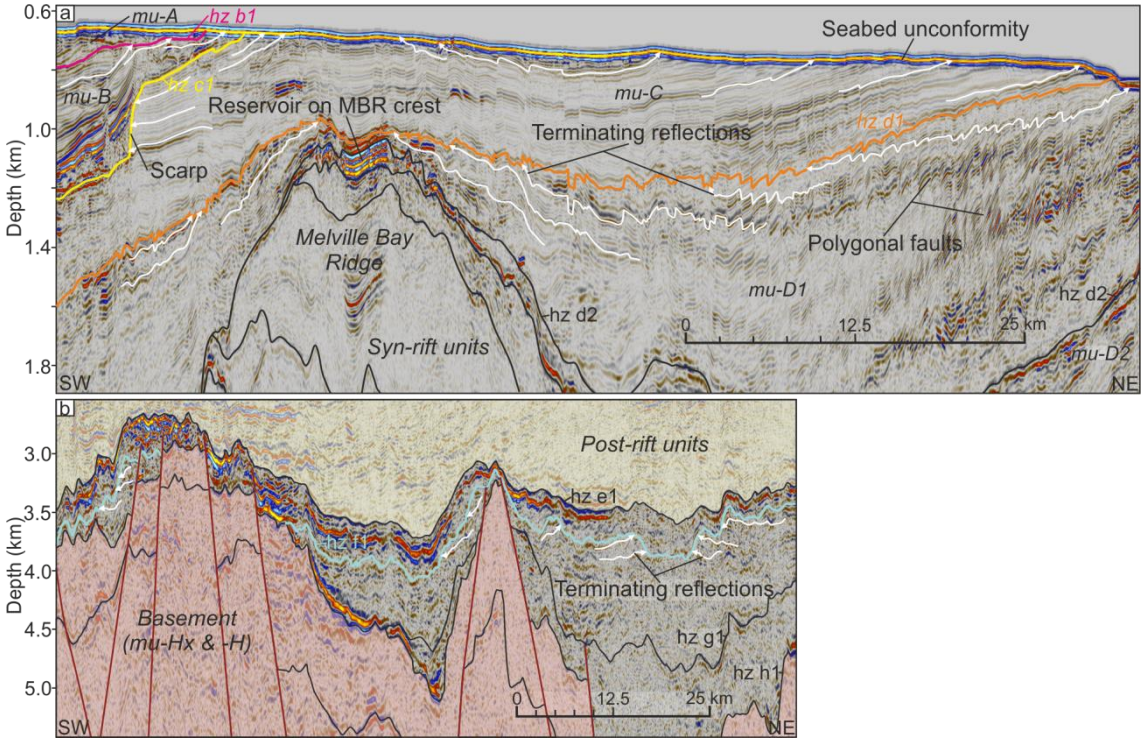

Figure 5.3. Estimates of erosion | Enlarged sections of the depth converted 2D seismic cross section on Fig. 5.2, that highlight reflection terminations that are used to identify unconformities formed by past erosion events. These events are included within the evolution of the petroleum systems model (see Appendix 5A). Glacial erosion of mu-B and -C is shown on (a), as well as terminations indicating up to ~400 m of erosion at the hz d1 unconformity. Several terminations at the hz f1 unconformity are also shown in areas west of the Melville Bay Ridge on (b). The location of these cross sections is shown on Fig. 5.2.

The transition between syn- and post-rift stratigraphy is represented by mu-E (Fig. 5.2), which was deposited during the transition of margin evolution to the drift phase (Fig. 5.2c) during the late Paleocene-mid Eocene (Cox et al., 2021; Knutz et al., submitted). Mu-E consists of mainly marine mudstones with inter-fingering coarse clastics. Several thicker sands may also be present equivalent to the Hellefisk, Nukik and Kangamiut sandstones (Gregersen et al., 2019). The top of this package, hz e1, is bounded by a regional unconformity associated with the Eurekan Orogeny, that marks the top of the MBR

structure (Cox et al., 2020a; 2021; Gregersen et al., 2019). The overlying post-rift unit, mu-D, which is likely of Eocene to mid-Miocene age, consists of thick packages of sediment in the grabens that thin significantly over the crest of the MBR. The unconformable top horizon of this package has been interpreted as a middle Miocene unconformity via a long-distance tie to ODP site 645 (Figs. 5.1 and 5.3) (Knutz et al., 2012; 2015). The unit is split into two, with the lower section (mu-D2) consisting of an asymmetric wedge of sand rich, basin floor fans, possibly linked to episodes of inversion related to the Eurekan Orogeny during the Eocene (Cox et al., 2021; Gregersen et al., 2019; Knutz et al., 2012). Within the section of mu-D2 on the crest of the MBR, exists an extensive package of likely shallow marine sands that were deposited along the ridge extension during a period of uplift quiescence and increased accommodation (Cox et al., 2020a). These sands are now likely gas charged and represent a 420 km^2 mass transport complex reservoir that has experienced post-depositional deformation and sliding along a muddy decollement layer represented by hz e1.

The upper part of mu-D (mu-D1), displays a hemipelagic infill character and likely consists of predominantly fine grained sediments, presumable with a high clay content which has facilitated the development of layer bound polygonal fault networks (Cox et al., 2021; Goulty and Swarbrick, 2005; Knutz et al., 2015). These muds display some seismic heterogeneity and likely contain occasional layers of thin, inter-fingering submarine fan clastics. Above the mid-Miocene unconformity is Mu-C and -B, which consist of kilometre thick muddy contourite deposits which continued to infill the basin during the mid-Miocene-Pliocene (Fig. 5.2) (Knutz et al., 2015; Nielsen et al., 2011). These deposits represent the uppermost post-rift stratigraphy on the inner shelf, with the majority of mu-B and parts of mu-C having been eroded during several cycles of shelf edge glaciation since ~2.7 Ma (Figs. 5.2 and 5.3) (Cox et al., 2021; Knutz et al., 2019; Newton et al., 2017). Towards the outer shelf, mu-C and -B are buried progressively deeper beneath mu-A, which represents the Melville Bay Trough Mouth Fan. This accumulation of glacigenic sediments are deposited within thick, mainly progradational clinoform packages and likely contain highly variable sediment lithologies and grain sizes (Christ et al., 2020; Knutz et al., 2019).

5.2.3. Source Rocks

The existence of organic-rich source rocks in Melville Bay is suggested by several studies based on data from across the entire region of West Greenland (Fig. 5.1). This includes several outcrop and oil seep studies that show the existence of regional Cretaceous and Paleocene source rocks (Bojesen-Koefoed et al., 2007; 1999; Núñez-Betelu, 1993), wet

gas or oil being sampled within legacy wells Umiivik-1 and Kangamuit-1, hydrocarbon indications in several of Cairn Energy's wells (Cairn Energy PLC, 2011) as well as the results of a shallow coring campaign led by Shell, that targeted inverted stratigraphy close to the seabed in the north of Melville Bay that cored several potential source rock horizons (Grecula et al., 2018; Nøhr-Hansen et al., 2018). Through these studies, four source rocks were selected to be included in the petroleum systems model.

The oldest and deepest source rock interval (SR1) is of Early Cretaceous, possibly Albian (112-99.6 Ma) age and exists within mu-G. The source rock horizon was sampled during the shallow coring campaign (Nøhr-Hansen et al., 2018) and is possibly related to oil seeps found on Ellesmere Island (Núñez-Betelu, 1993). The source rock is likely non-marine, type III-IV and gas prone, containing terrestrial organic material that has minor potential for generation and expulsion (Grecula et al., 2018; Nøhr-Hansen et al., 2018).

Within the Late Cretaceous (mu-F), two source rock intervals may exist. The first includes a Cenomanian-Turonian (99.6-88.6 Ma) source rock (SR2) that was sampled by the shallow coring campaign (Fig. 5.1) (Nøhr-Hansen et al., 2018), and is also possibly related to younger oil seeps on Ellesmere Island (Núñez-Betelu, 1993) and also 'Ittilli type' oil that was sampled on Disko Island (Bojesen-Koefoed, 2011; Bojesen-Koefoed et al., 2007; 1999). These source rocks consist of black marine mudstones that contain amorphous organic material and dinocycts that were likely deposited in an anoxic, outer shelf, pro-delta environment. The 335 m of source rock that was cored, contained a total organic content (TOC) of 3-6% and a hydrogen index (HI) of 200-350 mg HC/g TOC, and is likely type II-III, oil and gas prone (Nøhr-Hansen et al., 2018). The second Late Cretaceous source rock is of Campanian (83.5-70.6 Ma) age (SR3) and was sampled on Disko Island (Bojesen-Koefoed et al., 1999) and has a close biological marker correlation to solvents extracted from similar aged samples that were taken from the GANT#1 onshore well (Fig. 5.1) (Christiansen et al., 1996). The source rocks are likely type II-III, marine mudstones and contain high proportions of terrigenous organic matter and a HI of ~300 mg HC/g TOC.

The shallowest and youngest source rock is of Paleocene age (SR4) and is inferred from 'Maraat type' oils that have been sampled within seeps on Disko Island and near Maraat (Fig. 5.1) (Bojesen-Koefoed, 2011; Bojesen-Koefoed et al., 2007), as well as from vesicles within lava cores from the onshore wells Marraat-1, GANW#1, GANK#1 and GANE#1 (Bojesen-Koefoed, 2011; Christiansen et al., 1996; 1994; Philp, 1994). The source rock sediments are thought to be of deltaic origin and contain abundant terrigenous organic debris causing them to likely be gas prone (Bojesen-Koefoed et al., 1999).

Additionally, biogenic gas was discovered by Cairn Energy's T8-1 well (Fig. 5.1) (Cairn Energy PLC, 2011), suggesting a potential for biogenic generation further north in Melville Bay. Organic-rich source rock horizons will often produce biogenic methane - created via decomposition of organic material by anaerobic micro-organisms - during shallow burial, before switching to thermogenic generation as burial continues and temperatures increase (Rice, 1993; Rice and Claypool, 1981). This can create significant volumes of hydrocarbons at shallow burial depths (peak biogenic generation occurs at 50°C (Stopler et al., 2014)), and can also reduce the thermogenic potential of those source rock horizons. Biogenic gas generation is more likely focused within source rock horizons, but the lack of geochemical data in Melville Bay means it is unknown whether other potentially organic rich lithologies, such as shale rich packages (mu-F, -E and -D) and contourite successions (mu-C and -B), also have the potential for biogenic gas generation (Bertassoli Jr et al., 2016; Rebesco et al., 2014). Thus, biogenic generation from both the regional source rocks and shale rich packages is possible in Melville Bay and should be considered alongside thermogenic generation from source rocks.

5.3. Data

The main input used within this study is a 2D regional seismic line (Fig. 5.1) that represents part of the Baffin Bay 2D (BBRE11) regional seismic dataset that was acquired by the geophysical company TGS between 2007-2010. The full coverage of this dataset is shown by Gregersen et al. (2019) and the selected line is dip-oriented from the southwest to northeast, extending from within Baffin Bay across much of the shelf (Fig. 5.1). The survey was acquired using a single 6 km streamer hosting 480 channels spaced at 12.5 m and recorded at a sampling rate of 2 ms. The 2000 psi source was fired every 25 m at a depth of 8 m, producing a 120-fold stack. The survey was reprocessed in 2011 using a workflow that aimed to boost low frequencies and enhance the resolution, specifically by targeting attenuation of multiples and the bubble pulse. This process involved a 2 km Kirchhoff pre-stack curved ray time migration and velocity analysis which produced stacking velocity data for each line. These stacking velocities were used to depth convert the 2D seismic line to provide regional interpretations in depth, which is a requirement of building a petroleum systems model (see section 5.4).

Additional seismic data from the study area includes three 3D seismic surveys, the Anu 3D survey, the Pitu 3D survey, and the high-resolution (HR), reprocessed 3D volume, the Pitu HR survey (Fig. 5.1). The 3D volumes were used to calibrate 2D regional interpretations with higher resolution 3D interpretations published by Cox et al., (2020a;

2020b and accepted). The acquisition and processing parameters for the 3D data can be found in those papers.

Data from a wide range of literature sources were used within this study to inform and create a model that best represents our current understanding of Melville Bay's tectonic history, basin evolution, stratigraphy (including petroleum system elements) and structure (see section 5.2). A summary of these data is shown on Fig. 5.1, and includes: Cairn Energy's offshore Greenland wells, legacy wells drilled by GEUS and grønArctic in the 1970s and 1990s respectively, shallow cores collected during the campaign led by Shell (2012), seabed samples, apatite-fission-track data, oil seep sampling and outcrop studies. More information on all these contributing data can be found within the references provided in Fig. 5.1.

5.4. Methods: Building the Petroleum Systems Model

The 2D petroleum systems model was created using Schlumberger's basin modelling software PetroMod (version 2019.1). Model building required the definition of present day input data such as the basin geometry (depth horizons and faults) and properties that define the basin infill and processes modelled (lithology properties, fluid properties and chemical kinetics). Input data through geological time are also required, such as age assignments for geological events, such as deposition, non-deposition and erosion, as well as for thermal boundary conditions (basal heat flow and sediment water interface temperatures) and paleo water depths. The PetroMod software performs a dynamic forward modelling of geological processes through time that includes structural and stratigraphic restoration, pore pressure and compaction calculations, heat flow and temperature analysis and the modelling of hydrocarbon generation, adsorption, expulsion, migration, accumulation and preservation (see Hantschel and Kauerauf (2009); Fig. 1.1). Fluid migration was modelled using high-resolution Darcy flow and Invasion Percolation within low and high permeability cells respectively. The inputs selected for the basin model within this study are described below, and have been provided by seismic data, literature and a range of regional analogue data (Figs. 5.1 and 5.2) (see section 5.2). More information on the numerical simulation performed by PetroMod and increased detail into how each input parameter effects the calculation, can be found in Hantschel and Kauerauf (2009).

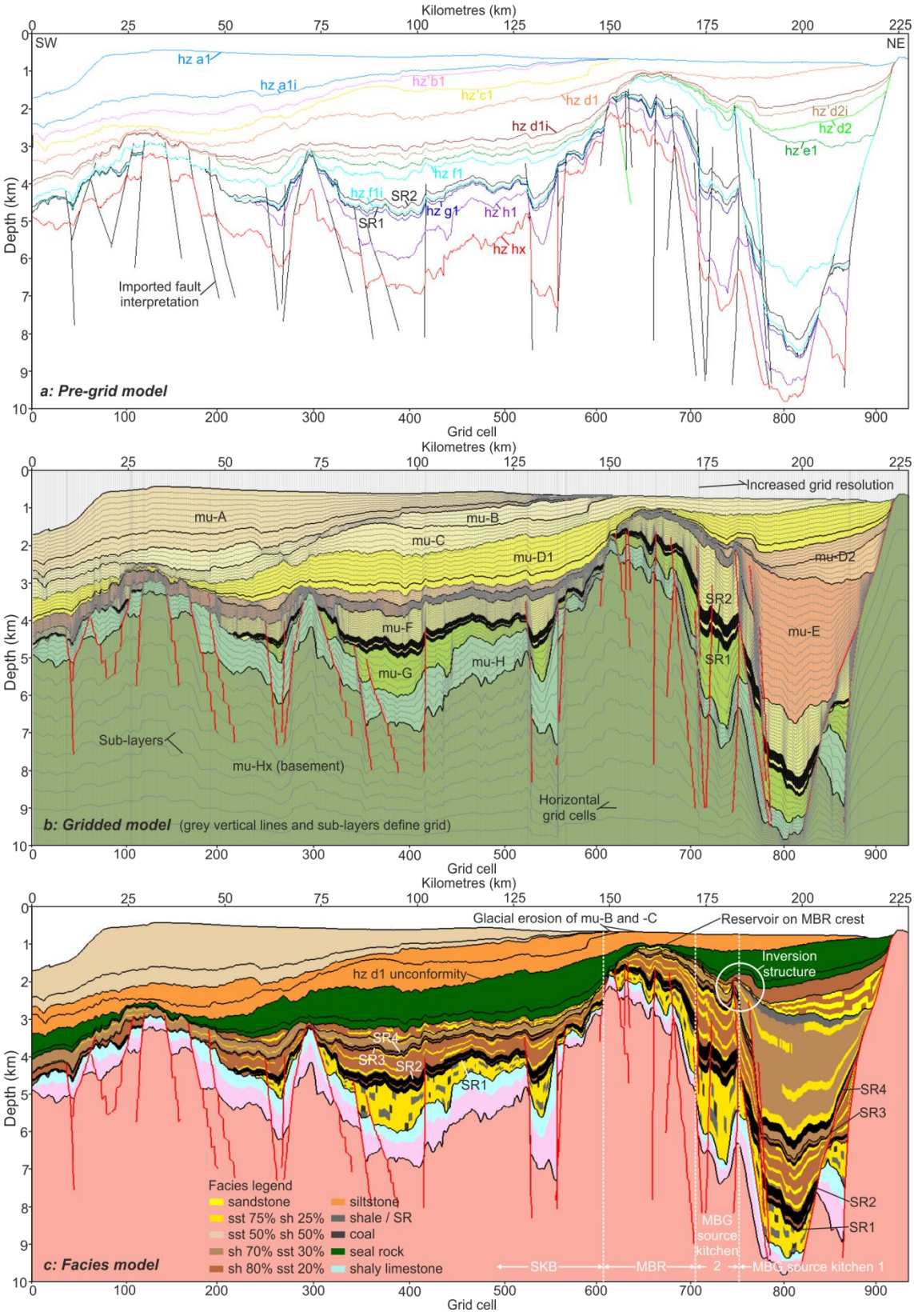

Figure 5.4. Petroleum systems model | The present day geometry of the petroleum systems model in PetroMod, displaying horizons and faults that were imported from seismic data interpretations (a), the model after horizontal and vertical gridding is applied (b) and the model once populated with facies (c). On (c), the model is divided into four zones used to describe variations in source rock maturity across the margin (Melville Bay Graben (MBG) source kitchen (SK) 1, MBG SK2, Melville Bay Ridge (MBR) and South Kivioq Basin (SKB); see Section 5.5.2).

5.4.1. Input Data

5.4.1.1. Present Day Model

The input geometry of the present day model was provided by the key 2D seismic transect (Figs. 5.1 and 5.2). This ~225 km long seismic line has been depth converted using seismic stacking velocities (see section 5.3) and extends down to ~9 km depth. Stratigraphic and structural interpretations were made within Schlumberger's Petrel software following the regional seismic stratigraphic framework defined by Gregersen et al. (2013, 2017) and Knutz et al. (2015, 2019). Depth interpretations were imported into PetroMod and digitised, with seismic horizons defining the present day geometry of the stratigraphic packages within the model (Fig. 5.4a). Fault interpretations were also imported and digitised. The model was then gridded; a process that defines the resolution of the model and the number of volumetric cells within the simulation (Fig. 5.4b). 934 vertical grid points (GPs) were defined, with an increased number of cells around stratigraphic pinch-outs and the intersections between horizons and faults to improve the accuracy of the model geometry. Stratigraphic layers were then further subdivided (henceforth referred to as sub-layers), proportional to their thickness, to define the vertical cell size (Fig. 5.4b). The number of sub-layers defined is relative to the thickness of the unit as well as the desired heterogeneity of the input facies.

The lithology for each stratigraphic unit was defined by selecting certain facies, which determine the physical properties such as thermal conductivity, porosity and permeability (Table 5.1), that broadly reflect the type of depositional environments inferred from the seismic data (Gregersen et al., 2013; 2016; Knutz et al., 2015; Newton et al., 2021; 2020) or observed from comparable outcrop/borehole data elsewhere (Fig. 5.1). The facies distribution within each stratigraphic package (Table 5.1), was defined using a facies map for every sub-layer within that package (Fig. 5.4c), with the assigned facies either being continuous across the entire layer or varied between cells. The presence of source rock intervals were also inferred from regional data (Fig. 5.1; Section 5.2.3) and were applied to certain (sub-) layers within the model (Fig. 5.4c and Table 5.1).

Two different source rock scenarios were tested, a purely thermogenic scenario and a scenario that considered both biogenic and thermogenic generation (Table 5.2). The assigned geochemical input data for the thermogenic model was provided by a range of regional data (see Section 5.2.3), resulting in a four component, type III kinetic model being selected for the transformation of kerogen into hydrocarbons. Using four components gives more information on the hydrocarbon type, and allows the separation of the pure methane component which is important when considering gas hydrate formation.

Furthermore, an adsorption rate of 75% was used which determines the rate in which inert kerogen will adsorb hydrocarbons (Hantschel and Kauerauf, 2009). For the biogenic scenario model, source rock intervals will generate both thermogenic and biogenic hydrocarbons and are assigned kinetic models for both reactions. The biogenic reaction is also assigned to certain potentially organic shale rich layers (Table 5.2). The thermogenic kinetic model applied to the source rocks is the same as the thermogenic scenario, with the only modification being the TOC, which is reduced by half (as a result of sensitivity analysis (see Section 5.4.2.4)). The single component (bio-methane) biogenic kinetic model was selected after sensitivity analysis, and uses several parameters that define a generation rate distribution around a peak temperature (Table 5.2). A Gaussian distribution of 10 standard deviations was selected around a peak temperature of 50 °C (Stopler et al., 2014); if the source rocks enter this temperature window, organic matter will transform into bio-methane. Using this distribution however, simplifies the process of biogenic generation and is therefore associated with uncertainty that should be considered when analysing results.

5.4.1.2. Age Assignment

The age assignment table (Appendix 5A) defines the geological age of the deposition and erosion of each stratigraphic unit (or layer) defined within the present day model. These ages were selected following the regional seismic stratigraphic framework as well as information regarding basin evolution (Altenbernd et al., 2015; Gregersen et al., 2019; 2013; 2016; Knutz et al., submitted; 2015; 2019; Oakey and Chalmers, 2012).

5.4.1.3. Paleo-geometry Data

The model geometry reflects interpretations from seismic reflection data (Fig. 5.4). But how this geometry varied through geological time is controlled by a number of paleo-geometry inputs, including paleo-water depth, erosion and paleo-thickness maps. This requires the use of information relating to regional geology, tectonics and basin evolution and is often associated with uncertainty, e.g. identifying the exact thickness of sediment that was removed during an erosion event.

Water depth maps, along with erosion maps, control the subsidence and uplift of the basin through time. In this model, paleo-water depths reflect the interpreted environment of deposition for the various stratigraphic packages within the model, as well as the likely structure of the basin and paleo-accommodation, inferred through seismic reflection terminations (e.g. onlap of reflections onto the MBR suggests water depth was shallower above the crest) (Fig. 5.3). Erosion maps are often related to changes in the paleo-water depth, with uplift events defined by shallowing that corresponds with sediment removal. Erosion events are included in the model at: (1) hz f1, associated with up to 1.3 km of

uplift affecting areas west of the MBR (Dam et al., 1998); (2) hz d1, associated with ~400 m of erosion suggested by the truncation of seismic reflections beneath hz d1 (the Middle Miocene Unconformity) (Fig. 5.3) (Gregersen et al., 2013), likely in response to Neogene uplift (Cox et al., 2020a; Japsen et al., 2006); and (3) hz b1, which considers the glacial erosion of mu-B and -C since ~2.7 Ma (Cox et al., 2021; Knutz et al., 2019), with erosion estimates based on comparisons to the thickness of the non-eroded sections of these packages.

Lithology properties

Mu-	No. of sub-layers	Brief description	Facies selected	Compaction and permeability models
A	11	Variable sediment lithologies and grain sizes	50% sand and 50% shale	
B	4	Muddy contourite deposits	Siltstone (organic rich)	
C	5	Muddy contourite deposits	Siltstone (organic rich)	
D1	D1: 10 D1i: 1	Hemipelagic, fine grained sediments with high clay content	Custom seal lithology (see section 3.2)	
D2	D2i:5	D2i: Transition of submarine fans to hemipelagic mud	D2i: 80% shale and 20% sand	
	D2:5	D2: Sand rich basin floor fans with shallow marine sands on ridge crest	D2: variable facies = sandstone; 80% shale and 20% sand	
E	15 (sub-layer 14 = SR4)	Mainly marine mudstones with inter-fingering coarse clastics. Muddy layer beneath unconformity.	Variable facies = shale; 70% shale and 30% sand; 75% sand and 25% shale	
F	F: 15 (sub-layer 2 = SR3)	Marine mudstones, local conglomerates and sandstone formations.	Variable facies = 80% shale and 20% sand;	
	SR2: 1		Sandstone;	
	Fi: 1		75% sand and 25% shale	
G	SR1: 1	Sandstones, mudstones and thin coal beds.	Variable facies = shale;	
	G: 5		75% sand and 25% shale	
			Silty coal	
H	5	Sandstones interbedded with carbonates and muds.	Shaly limestone; Quartzite	
Hx	10	Crystalline rocks of granitic composition.	Granite	

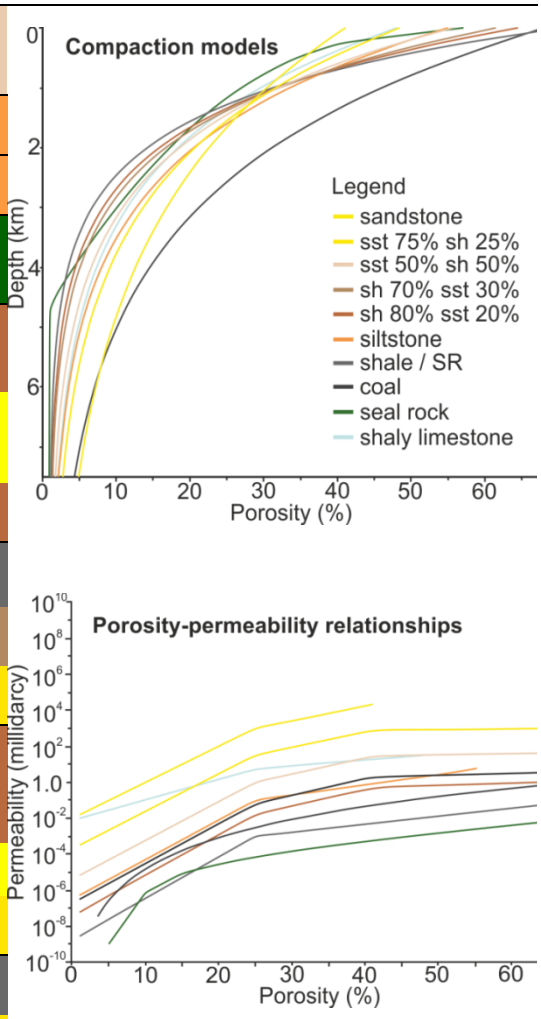

Table 5.1. Lithology properties | The table displays the facies and lithological parameters (compaction models and porosity-permeability relationships) selected for each of the depositional units included within the model (mega unit (mu) -Hx to -A). The information was provided by a range of studies and analogue data

from across West Greenland (section 5.2.2; Fig. 5.1). The distribution of the facies within the model is shown on Fig. 5.4c. Abbreviations used include sandstone (sst), shale (sh) and source rock (SR).

Finally, paleo-thickness maps are used to correct the propagation of unrealistic geometries across multiple time steps that are often created by an irregular present day geometry affecting the back-stripping process. Paleo-thickness maps were used in this model to control the inversion of certain faults, in particular a large fault to the east of the MBR that causes a significant anticlinal structure to form above the fault tip (Fig. 5.4c); a structure that likely affects fluid migration. This feature was propagating back across several time steps, so paleo-thickness maps were used to delay its formation until the late Paleocene, where Eurekan orogeny related compression likely led to the formation of these inversion structures (Knutz et al., submitted).

Thermogenic Scenario Model

Source rock	Geological Age	Layer/sub-layer	TOC	HI (mg HC/g TOC)	Max. Thickness	Thermogenic Kinetic model		
						No. of components	Kerogen Type	Adsorption rate
SR 4	Paleocene	mu-E / SL14	2%	300	200 m	4	III	75%
SR 3	Campanian	mu-F / SL2	1	150	100			
SR 2	Cenomanian-Turonian	SR2	2	300	200			
SR 1	Albian	SR1	2	300	200			

Biogenic Scenario Model

Source rock	Geological Age	Layer/sub-layer	TOC	HI (mg HC/g TOC)	Biogenic Kinetic model			
					Component	Distribution	Mean Temp.	Standard deviation
SR 4	Paleocene	mu-E / SL14	1%	300	Biomethane	Gaussian	50 °C	10
SR 3	Campanian	mu-F / SL2	0.5	150				
SR 2	Cenomanian-Turonian	SR2	1	300				
SR 1	Albian	SR1	1	300				
Custom seal	-	mu-D1	0.1	50				
Shale	-	mu-G; mu-E	0.3	50				
80% sh. 20% sa.	-	mu-F; mu-D2	0.2	50				
70% sh. 30% sa.	-	mu-E	0.1	50				
Siltstone	-	mu-C; mu-B	0.1	50				

Table 5.2 Geochemical input data | The table displays the geochemical input data that was inferred from regional data (section 5.2.3) and assigned to source rock facies within both the thermogenic and biogenic scenario models. Thermogenic kinetics are also used within the biogenic scenario for source rock horizons which will generate both biogenic and thermogenic hydrocarbons. Abbreviations used include total organic carbon (TOC), hydrogen index (HI), temperature (temp), source rock (SR), sub-layer (SL), sand (sa), shale (sh), maximum (max) and number (no).

5.4.1.4. Boundary Conditions

Boundary conditions influence the calculation of heat, pressure and fluid migration and are required inputs for simulation of the model. The boundary conditions used here include the sediment-water-interface temperature (SWIT) which controls upper temperature boundary condition, as well as the basal heat-flow assigned at the model base. The SWIT was defined using PetroMod's Auto-SWIT tool (Hantschel and Kauerauf, 2009; Wygrala, 1989), which determines paleo-SWIT as a function of paleo-water depths and paleo-latitudes of the study area through geologic time (with a latitude value of 74° N assigned to present-day). After sensitivity analysis (section 5.2.2), basal heat flow through geological time was assigned using theoretical values of heat flow for the different rift stages of a tectonic margin from Allen and Allen (2013). Present day heat flow was assigned at the low end of bottom simulating reflector (BSR) derived heat flow within the area (65 mW/m^2) (Cox et al., 2021). The boundary conditions for pressure and fluid flow assumed an open boundary at the water-sediment interface and closed boundaries at the model base and sides.

5.4.1.5. Uncertainties

2D petroleum systems modelling within a frontier area containing little or no direct calibration data, is often associated with high degrees of uncertainty (Hantschel and Kauerauf, 2009). For example, many of the input data and aspects of the model build in this study, such as lithology properties, source rock kinetics, thermal boundary conditions and paleo-water depths, are either based on interpretations of seismic reflection data or determined from regional analogue data, some of which exists hundreds of kilometres away. Even the present day geometry of the model can be uncertain, as it is affected by seismic interpretation error, seismic resolution limitations and uncertainty associated with velocity model creation and depth conversion; factors that could, for example, affect source rock maturity significantly. Due to the high level of uncertainty, this study aims to analyse the range of possibilities and outcomes that could be expected through sensitivity analysis and testing several scenarios for paleo-parameters and conditions, before analysing whether the modelled result is reasonable and probable, according to our current understanding of the Melville Bay region and the petroleum system in place (see Section 5.4.2). The most likely scenarios (thermogenic and biogenic) are then selected to be analysed further (even though other scenarios could be just as likely). These attempts will reduce some uncertainty, but until direct calibration (such as source rock sampling) from the study area is available, the results will remain highly uncertain and represent a high level frontier assessment; therefore, no specific values of hydrocarbon volumes, mass or

saturations are provided and any estimations of these elements shown are purely for comparative reasons, having been calculated in the 2D approach (extending the 2D plane by 0.5 km both sides).

5.4.2. Sensitivity Analysis

5.4.2.1. Mu-D1 Seal Lithology

After initial simulations, the base case lithology properties assigned to mu-D1 were deemed unrepresentative, as the permeability of the unit remained too high throughout the simulation to act as an effective barrier to fluid flow. This was likely occurring due to mu-D1's shallow burial and small thickness (~50 m at its thinnest point); especially above the MBR crest (Fig. 5.2). Mu-D1 is assumed to be a somewhat effective seal however, due to strong direct hydrocarbon indicators (DHIs) observed on seismic data indicating the likely existence of a gas reservoir trapped beneath the mu-D1 seal on the crest of the MBR (Cox et al., 2020a). For this reason, sensitivity analysis was conducted in an attempt to understand the range of possible lithological parameters that could be representative of mu-D1 and create a working seal (Appendix 5B); before selecting the most probable scenario for both the thermogenic and biogenic scenario models.

Sensitivity analysis involved testing several parameters of the mu-D1 lithology against the base case model, such as the compaction model (Test 1), the porosity-permeability relationship (Test 2), and the amount of additional burial that the unit experienced before the additional thickness was removed by erosion at the top boundary of mu-D1 (Test 3) (hz d1) (Fig. 5.3; Appendix 5B). Within each of these tests, several key parameters were varied to analyse the sensitivity of that parameter on the porosity, permeability and density of the mu-D1 seal. Several of the varied parameters resulted in a tighter seal, and were more likely a better representation of the mu-D1 lithology than the base case.

However, as no calibration data was available for the mu-D1 lithology, except for the knowledge that gas is currently trapped beneath the seal, selecting values that simply forced the model to work was avoided, even if they were potentially more likely than the base case. Instead, an analogue dataset was used to help select more representative lithology parameters for mu-D1 that would be based on potentially similar sealing rocks. The dataset consists of porosity and permeability measurements from 303 marine sediment samples with varying clay contents (Yang and Aplin, 2004, 2010). The porosity-permeability relationship from this dataset for various clay fractions (40-70%) was tested to analyse the impact it had on the sealing potential of mu-D1 (Test 4; Appendix 5B). All three scenarios created seal parameters that allowed mu-D1 to trap hydrocarbons at the MBR ridge crest,

however, a slightly lower clay fraction is more likely for mu-D1, due to continued seismic reflectivity throughout the unit, possibly indicating a heterogeneous lithology, as well as polygonal faults being layer bound (Fig. 5.3). Therefore analogue samples containing the lower clay content (40-50%) were used. To select the final compaction model and porosity-permeability relationship for mu-D1 in PetroMod, the 40-50% analogue samples were compared with the earlier tested models (Tests 1-2) (Fig. 5.5; Appendix 5B), with this comparison showing that a mudstone compaction model with 40% clay fraction (the model created from the same analogue dataset (Yang and Aplin, 2004)) and the Kozeny-Carman porosity-permeability relationship, had the best correlation with the analogue data and were therefore selected as the mu-D1 lithology properties for both the thermogenic and biogenic scenario models.

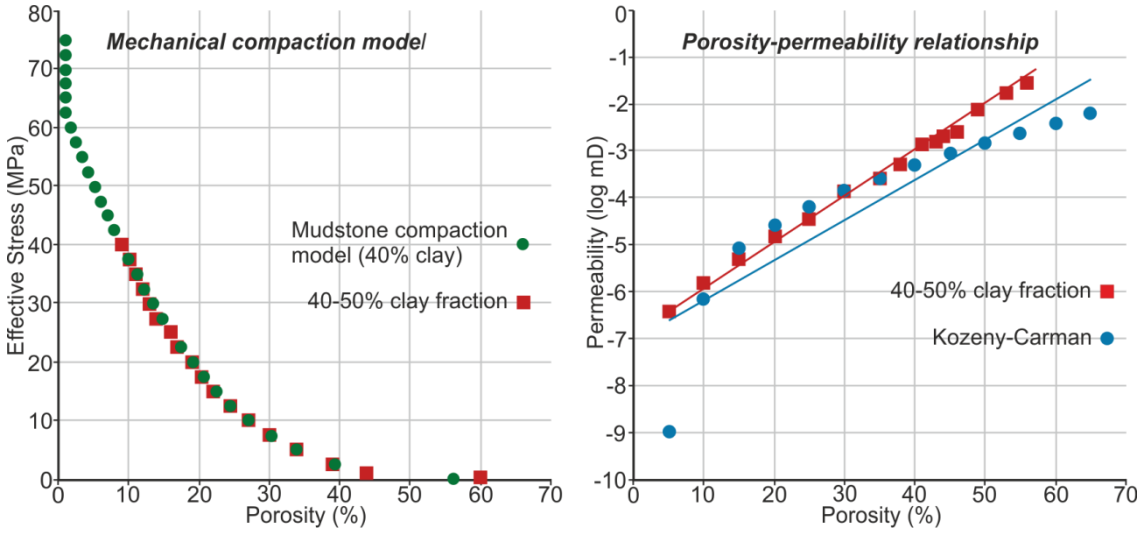

Figure 5.5. Lithology properties of the mu-D1 seal | A comparison between the mechanical compaction model and porosity-permeability relationship selected for mu-D1 after sensitivity analysis and those from Yang and Aplin, (2004), derived from analogue data samples containing a 40-50% clay fraction.

5.4.2.2. Heat Flow

The impact of varying the basal heat flow boundary condition on source rock maturation and HC generation and expulsion was analysed. The base model used a default constant heat flow of 65 mW/m^2, a value at the low end of estimated present day heat flow for the area (Cox et al., 2021). This scenario was compared against four heat flow models that were based on theoretical values for different rift stages (Allen and Allen, 2013), reflecting the tectonic history of the Melville Bay margin (Appendix 5C). The four models included: (1) a scenario based entirely on theoretical values; (2) a hotter scenario; (3) a cooler scenario; and (4) a scenario which experiences quicker cooling after rifting. Scenarios 3 and 4 were shown to significantly restrict source rock maturation within the MBG source kitchen 2 area (see section 5.2; Fig. 5.4c; Appendix 5B). Scenarios 1 and 2, enhanced source

rock maturation when compared to the base model, with the hotter scenario (2), causing a negligible difference when compared to scenario 1. Therefore, as increased heat flow was not required for maturation to occur, and other calibration data were not available to suggest a different heat flow history, theoretical heat flow values (scenario 1) were selected for the model.

5.4.2.3. Fault Properties

The resistance to fluid flow along the fault plane is assigned to each fault in the model through geological time, and can vary between being impermeable, permeable or somewhere in between the two end members, according to the fault capillary pressure and permeability parameters assigned (Hantschel and Kauerauf, 2009). Several fault permeability scenarios were tested to create a range of possible outcomes that could help us understand how sensitive fluid migration is to fault permeability within the model, and to help define the most reasonable and likely scenario that could lead to a hydrocarbon distribution somewhat similar to our interpretation of the present day framework (Appendix 5D and 5E).

Fault properties were assigned to the base model that reflected the tectonic history of the basin (such as Cretaceous rifting and Neogene uplifts), but included several fault property variations that did not align with the timing of erosion and uplift events included in the model. The fault scenarios compared against this base model included: (1) no consideration of faults; (2) impermeable faults; (3) permeable faults; (4) a scenario of fault permeability based on the timing of tectonic events considered in the model; and (5) a modified version of scenario 4, which contains increased fault permeability after 13.82 Ma. The analysis of these scenarios involved comparing predicted hydrocarbon accumulations, with a specific focus on the reservoir on the MBR crest, as well as an analysis of hydrocarbon migration pathways, surface leakage events and timings. In summary, these tests showed that scenario 5 produced the most reasonable hydrocarbon distribution scenario, which was similar to our present day understanding, thus these parameters were assigned within the final model. Scenario 5 also represents a geologically more realistic scenario, with fault parameters reflecting the tectonic events considered in the model, whilst allowing migration into the main reservoir via carrier beds in mu-F; a pathway that represents a previously proposed (Cox et al., 2021) method of hydrocarbon migration towards the ridge crest.

5.4.2.4. Biogenic Methane Production

Parameters controlling biogenic gas generation in both source rock horizons and shale rich packages were tested (Appendix 5F), providing a range of possible model outcomes

that were analysed to help select input values that generated a geologically possible and, according to our analysis, most likely hydrocarbon distribution scenario at present day. Variations in TOC, HI and parameters controlling the generation rate distribution (mean temperature and standard deviation), were tested against default values to understand the effect of these variables on source rock maturation, hydrocarbon generation and charging of the reservoir on the MBR crest. The results of these tests suggested that TOC values between 0.1–0.3% and HI values of 50 mg HC/g TOC represent the most appropriate inputs for the various shale rich packages, along with a 50% reduction in TOC for the regional source rock horizons compared to the thermogenic study (Appendix 5F and Table 5.2).

5.5. Results and Discussion

5.5.1. Basin Evolution

Using input data defined by seismic interpretations, regional data and sensitivity testing, a most likely scenario for the geological evolution of the Melville Bay margin has been predicted by back-stripping the present day geometry and correcting for decompaction and erosion (Fig. 6) (Hantschel and Kauerauf, 2009). Rift-related subsidence is variable across the margin, with the inner shelf and the MBG experiencing significantly higher rates of subsidence, thicker depositional packages and deeper burial (Figs. 5.6 and 5.7). This increased subsidence likely began by the Late Cretaceous. By the mid-Eocene, syn-rift sediments had already reached ~7 km in thickness, whilst in the SKB, the comparable packages were only ~3 km thick (Fig. 5.6). These two distinct subsidence regimes, separated by the MBR, have caused the basin sediments to experience a contrasting burial, and therefore thermal history, which has likely significantly impacted the potential for hydrocarbon generation across the two basins (Fig. 5.6 and 5.7).

The MBR had begun formation by the Late Cretaceous (Gregersen et al., 2013; Whittaker et al., 1997), and has affected accommodation, sediment deposition and erosion since. The separation of the MBG and SKB had begun by the earliest Paleogene (Fig. 5.6), with the MBR remaining as a barrier between the separately evolving basins until post-rift infill drowned the ridge in the mid-Miocene (Fig. 5.6). Inversion of ridge-related tectonic faults, which possibly occurred in response to regional compressional stresses (Knutz et al., submitted; Oakey and Stephenson, 2008) since the Eocene, has caused the formation of inversion anticlines (Fig. 5.4c), which likely influence regional fluid migration.

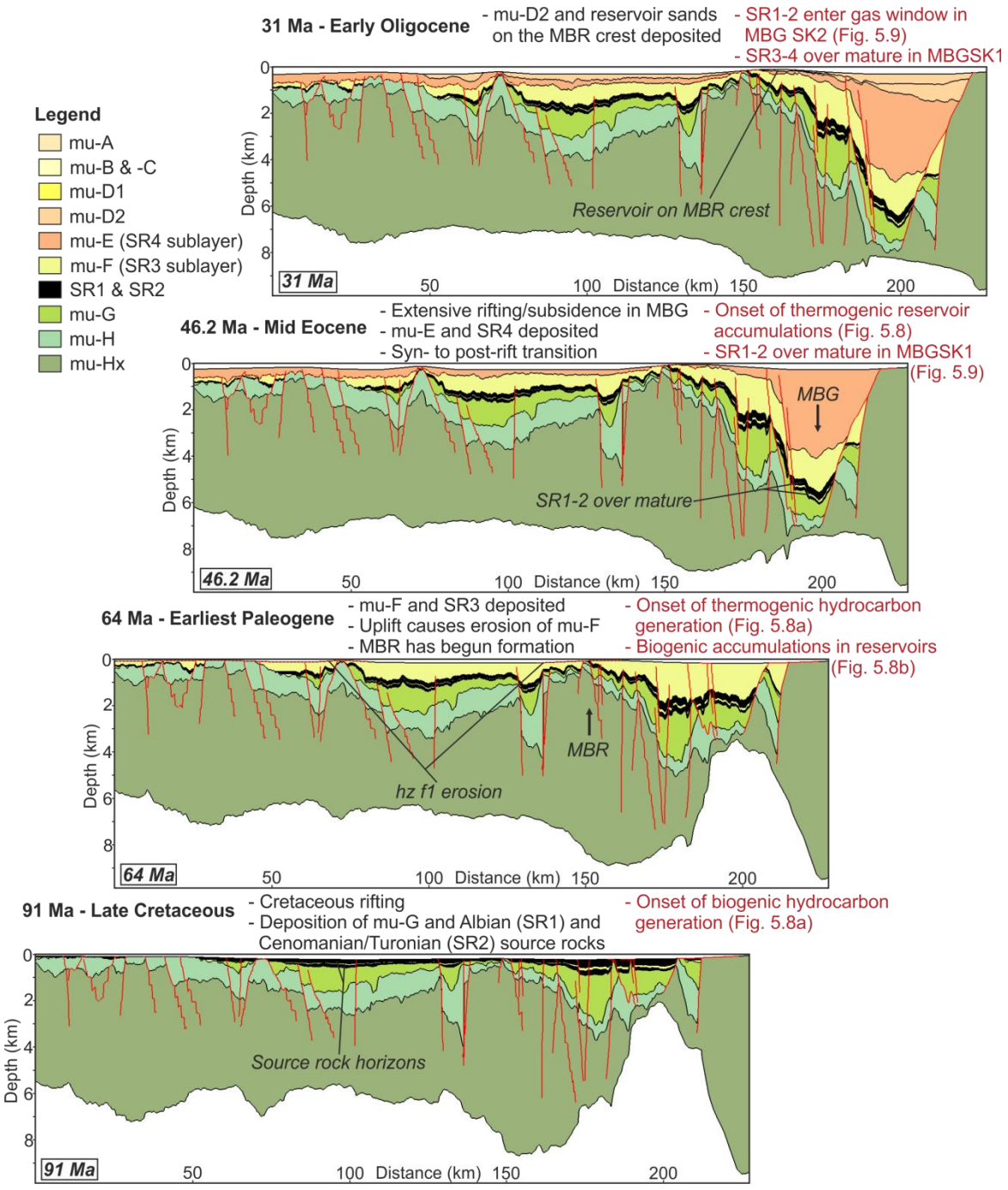

Figure 5.6. Basin evolution | A timeline of the stratigraphic, structural and petroleum system evolution of the Melville Bay continental shelf margin from 91 Ma to present day (also overleaf). Eight paleo cross sections at individual time steps display variable subsidence histories between the South Kivioq Basin (SKB) and the Melville Bay Graben (MBG) as well as the formation of the Melville Bay Ridge (MBR) and the influence the ridge structure has on sediment deposition. Uplift and erosion events are shown, as well as the paleo-water depth through time. Key events in the evolution of the petroleum system, found in this study, are shown in red text.

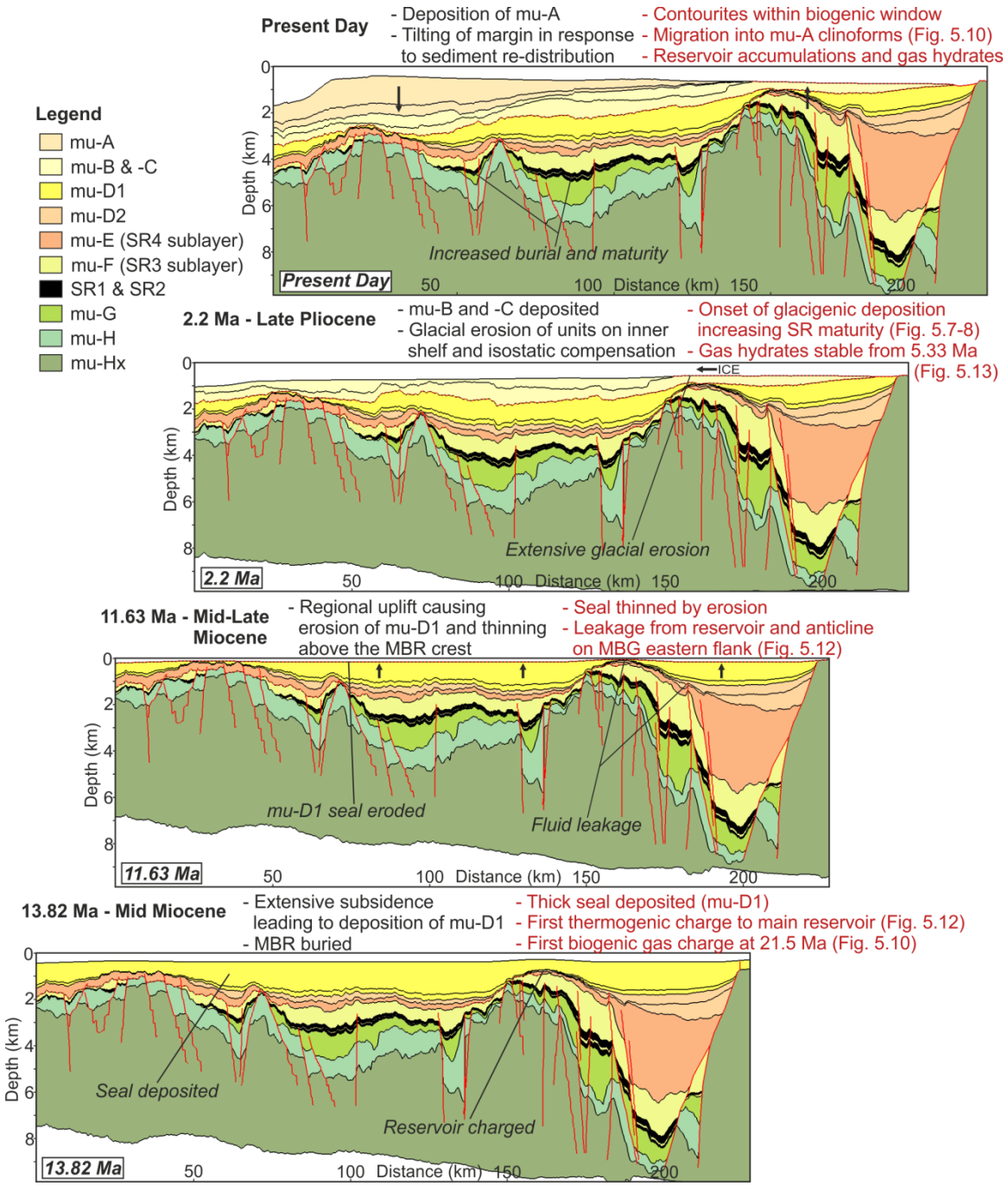

Sensitivity analysis to determine input parameters for mu-D1 (see section 5.4.2), suggested up to 400 m of additional burial in the vicinity of the MBR, prior to the regional uplift (and erosion) that created the middle-Miocene Unconformity (MMU) (Knutz et al., 2012). Similar burial and erosion has been inferred elsewhere in West Greenland around this time (Japsen et al., 2006; Nøhr-Hansen, 2003), but this is the first estimation of the eroded sediment thickness at the MMU in Melville Bay. The erosion is evidenced through seismic analyses (Fig. 5.3), but the inclusion of this degree of burial was found to be crucial

in providing the required compaction to allow mu-D1 to develop as an effective seal above the MBR ridge crest (see section 5.4.2); a scenario which is a reasonable assumption due to the existence of direct hydrocarbon indicators (DHIs) within reservoir sands beneath the seal (Cox et al., 2020a). This increased estimation of erosion may be relatively local however, as erosion above the ridge was probably greater than in the adjacent basins, due to the structure's prominence through time (Fig. 5.6), and sensitivity to uplifting forces (Cox et al., 2020a; 2021; Gregersen et al., 2013).

Since ~2.7 Ma, glacial erosion has removed a significant sediment thickness (~400-500 m) (Fig. 5.3) from the inner shelf (mu-B and –C) and this sediment has been redeposited as part of the Melville Bay Trough Mouth Fan (deposition of mu-A) (Fig. 5.4 and 5.6). Sediment removal on the inner shelf likely caused isostatic compensation in response to load removal (Cavanagh et al., 2006; Fjeldskaar and Amantov, 2018), whilst simultaneously, the outer shelf and the SKB experienced increased burial and subsidence in response to the deposition of ~2 km thick package of glacigenic sediments (Figs. 5.2 and 5.6) (Cox et al., 2021). These opposing actions have caused the Melville Bay margin to tilt towards the southwest (basinward) (Fig. 5.6), causing sediment packages containing potential permeable carrier beds west of the MBR, to dip more steeply; a factor that is likely focussing fluid migration upwards toward the MBR (Cox et al., 2021).

5.5.2. Source Rock Maturation and Hydrocarbon Generation

The four source rock intervals included in the model (SR1-4; Table 5.1) have been buried sufficiently to generate and expel hydrocarbons (Fig. 5.8), with their current depth representing the maximum burial depth. Source rock maturation and the thermogenic generation and expulsion of hydrocarbons began in the earliest Paleogene (Fig. 5.8a), with increased generation until the mid-Eocene likely related to the rapid and deep subsidence in the MBG (Fig. 5.7) (Gregersen et al., 2013; Whittaker et al., 1997). Subsequently, during post-rift sedimentation, hydrocarbon generation increased more steadily until another period of increased generation rate in the Pliocene and Pleistocene, likely in response to glacigenic deposition causing deeper burial and enhanced source rock maturation within the SKB (Fig. 5.7) (Knutz et al., 2019; Medvedev et al., 2019). Over half of the generated hydrocarbons within the model represent methane gas (Fig. 5.8e), with the majority of the remaining mass representing short chained hydrocarbons (C2-5). This is a function of the selected source rock kinetics (based on regional data – section 5.3), but the result correlates well with seismic observations indicating numerous gas accumulations across the margin (Cox et al., 2020a; 2021). Almost three quarters of the generated mass in the model is

attributed to SR1 (Albian) and SR2 (Cenomanian-Turonian), with SR3 (Campanian) only generating and expelling very minor amounts.

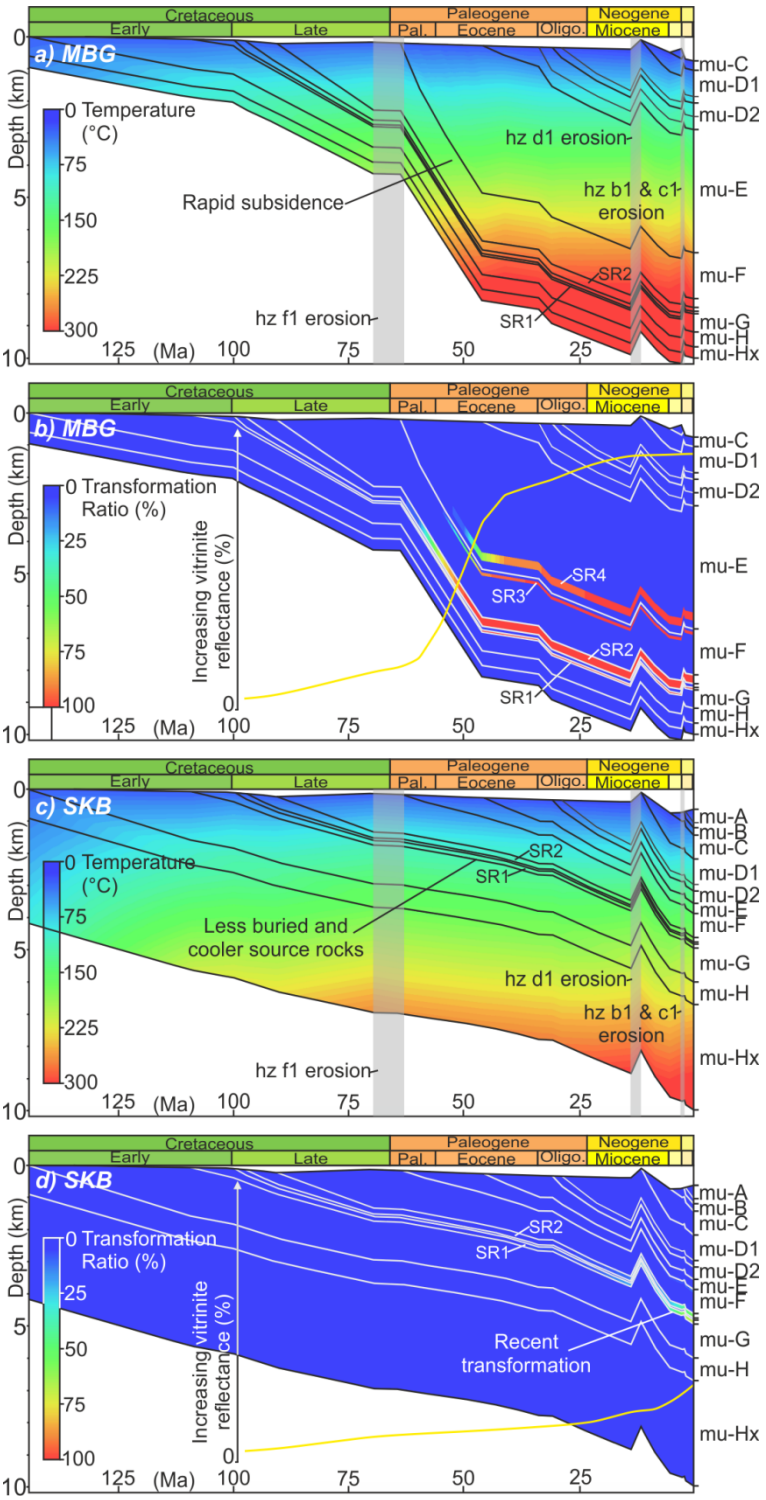

Figure 5.7. Burial history and source rock transformation | 1D burial history extractions from the Melville Bay Graben (MBG) (a) and South Kivioq Basin (SKB (c) display the contrasting subsidence rate experienced between the two basins, as well as the temperatures experienced by deposited units through time. The timing of uplift and erosion events are also shown. An overlay on top of the burial history, displaying source rock transformation ratio in both the MBG (b) and SKB (d) is also shown, which highlights the early onset of hydrocarbon generation in the MBG compared to in the SKB which only begins during the Miocene. This difference in maturity is also shown by the theoretical curves of vitrinite reflectance that are shown for source rock (SR) 2 and based on Sweeney and Burnham, (1990). The locations of the two 1D extractions from within the SKB and MBG source kitchen 1 are shown on Fig. 5.9.

Over half of the generated hydrocarbons were expelled (Fig. 5.8a) (a proportion of generated hydrocarbons are adsorbed by unreacted kerogen and coke in the source rocks and are not expelled (Hantschel and Kauerauf, 2009)), with the majority of the expelled mass deriving from SR1-2 (Fig. 5.8e). However, the variable contemporary structure and thermal histories of the source rock intervals, means that hydrocarbon generation and expulsion has likely varied significantly across the different geological domains of the margin (e.g. SKB, MBR and MBG). For this reason, the model has been split into four zones (below; Figs. 5.4c and 5.9a) in an attempt to understand how variations in the geological and thermal history has affected source rock maturation and hydrocarbon generation and expulsion.

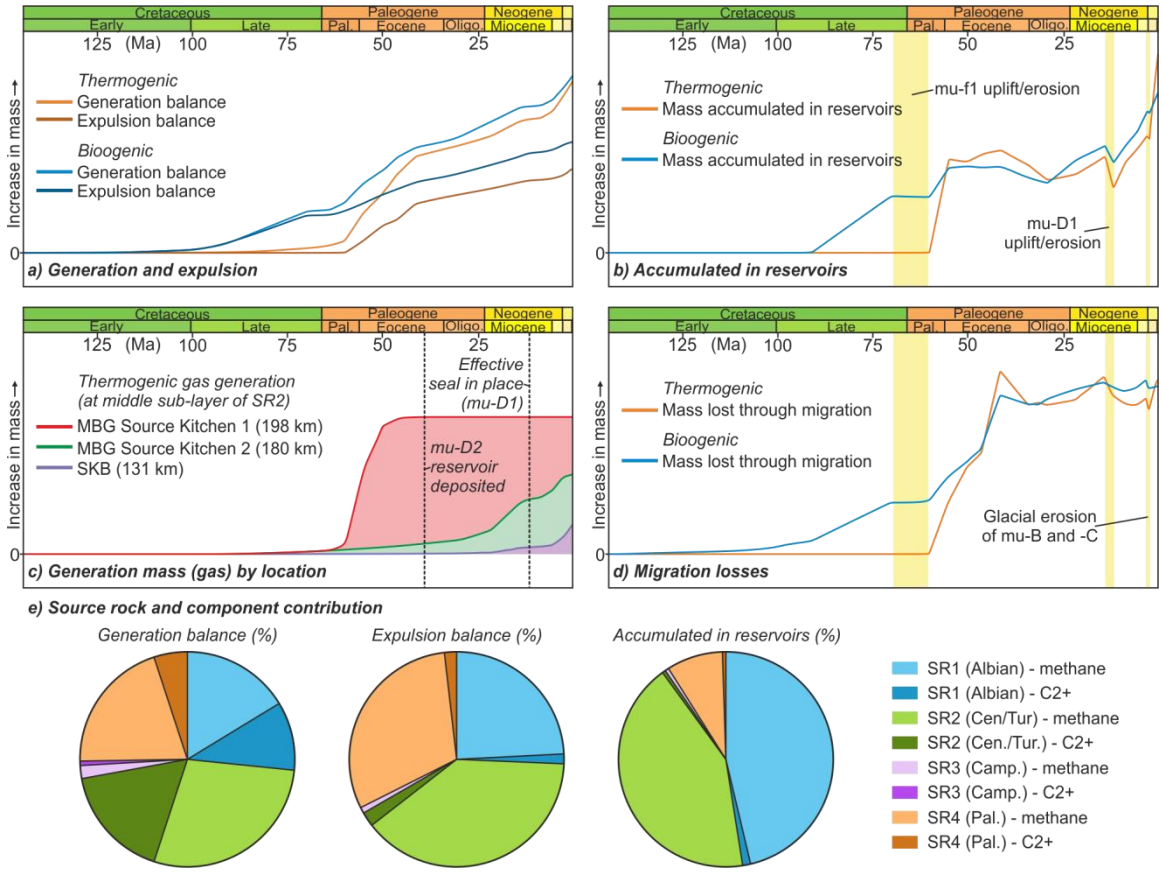

Figure 5.8. Hydrocarbon generation, migration and accumulation | The modelled variations in mass through time for the generation and expulsion of hydrocarbons (a), the accumulation of hydrocarbons in reservoirs (b) and the loss of hydrocarbons through migration to the sediment-water interface (c) are shown, including comparisons for both the thermogenic and biogenic scenario models. A comparison of the generation mass (gas) between three different localities (shown on Fig. 5.9) is shown on (c). The pie charts on (e) represent fluids within the entire model and display the proportion of hydrocarbon generation, expulsion and accumulation in reservoirs, sourced from each source rock (SR) interval, as well as an estimation of what hydrocarbon component those fluids represent.

5.5.2.1. MBG Source Kitchen 1

The MBG has experienced more rapid subsidence and deeper burial than the SKB, and all four source rock intervals at present day are buried at temperatures >250 °C in the centre of the graben, and are, therefore, over mature (Figs. 5.7 and 5.9). Due to rapid subsidence, the generation of hydrocarbons began during the early Paleogene (Fig. 7), with expulsion from these source rocks beginning prior to the deposition of the key reservoir package of interest in this study (mu-D2) as well as the regional seal (mu-D1) (Fig. 5.9c), meaning much of this early expulsion likely migrated and were lost at the surface (Fig. 5.8d). The transformation ratios for the source intervals reach ~100% in the Eocene for SR1-2 and the Oligocene for SR3-4 (Fig. 5.7b and 5.8c), meaning the majority of hydrocarbon generation from these source rocks had already occurred prior to the development of mu-D1 as an effective seal.

5.5.2.2. MBG Source Kitchen 2

The thick package of syn-rift stratigraphy within the MBG source kitchen 2 (Fig. 5.9a) exists along much of the eastern flank of the MBR (Gregersen et al., 2019; 2016), and is offset from the deeper sediments within the MBG centre via a vertically extensive (and possibly inverted) tectonic fault (Fig. 5.4 and 5.9). This area has experienced comparably less subsidence than the graben centre, with SR1-2 at present day existing within the gas window at temperatures between ~150-200 °C and SR3-4 experiencing temperatures <~100 °C and being immature (Fig. 5.9). Due to the rapid subsidence during rifting (Fig. 5.7), these source rocks likely reached close to their present day burial depth during the early Oligocene (Fig. 5.9d), and therefore SR1-2 have existed within the gas window for a significant amount of time (since ~30 Ma). Still, the onset of expulsion from these source rocks only occurred between 25-10 Ma (Fig. 5.9c), much later than the deeper graben (Fig. 5.8c), with expulsion continuing into the period after reservoir deposition and the sufficient burial of mu-D1, creating the regional seal. This means that SR1-2 in this area are much more likely to have generated the gas now trapped within the reservoir on the MBR crest (Cox et al., 2020a) than their counterparts within the deeper MBG.

5.5.2.3. Melville Bay Ridge

Thinner syn-rift sediment packages within the MBR suggest that by the Late Cretaceous the ridge was already restricting accommodation, and that potential source rock horizons (SR2-4) may have been deposited in shallower waters (with a greater clastic input) than the adjacent basins (Fig. 5.6), potentially decreasing their hydrocarbon generation potential (Schwarzkopf, 1993). Additionally, due to the continued prominence of the MBR as a positive relief feature (Cox et al., 2021; Gregersen et al., 2013), and multiple episodes of

uplift since its formation (Cox et al., 2020a; Japsen et al., 2006), the syn-rift stratigraphy within the ridge (including the source rocks) has not experienced significant burial, and at present day exists at ~2 km depth, experiencing temperatures <~70 °C (Fig. 5.9). These low temperatures mean that all four source rock intervals remain thermogenically immature.

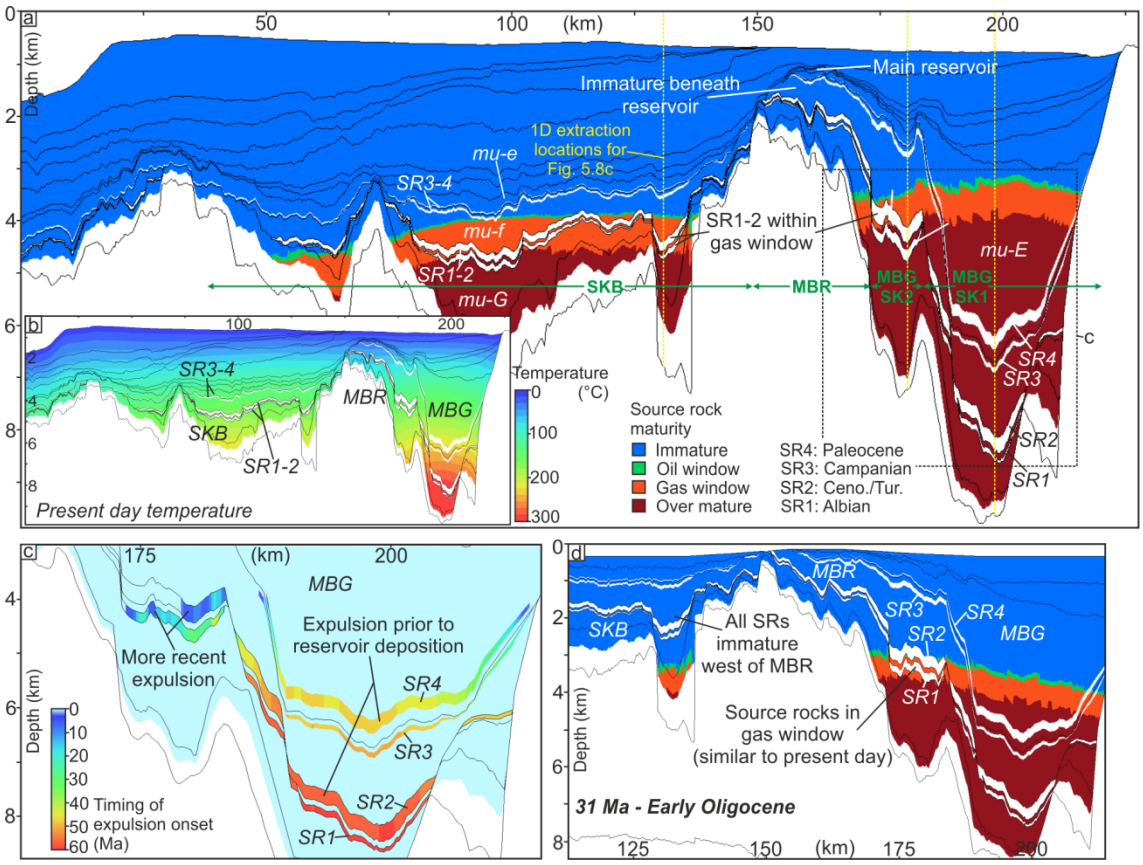

Figure 5.9. Source rock maturity | Present day hydrocarbon maturity zones, defined by the selected source rock kinetics, are shown on (a), highlighting the variation in maturity for the source rock intervals within the Melville Bay Graben (MBG), South Kivioq Basin (SKB) and Melville Bay Ridge (MBR). The four zones used for describing the variability of source rock (SR) maturity across the margin are shown (green text and arrows), which include the MBG source kitchen (SK) 1, MBG SK2, MBR and SKB. The locations of 1D extractions used on Figs. 5.7 and 5.8 are also shown. The predicted present day temperature across the model is shown on (b). The timing of expulsion onset for the MBG is shown on (c), with (d) displaying the hydrocarbon maturity zones at 31 Ma, which suggests that SR1-2 on the eastern flank of the MBR have been within the gas window since that time.

5.5.2.4. South Kivioq Ridge

The >~100 km wide SKB has experienced a less rapid subsidence history when compared to the MBG (Figs. 5.6 and 5.7), with source rock intervals remaining at much shallower depths and therefore cooler temperatures. SR3-4 have not been buried sufficiently to generate hydrocarbons and at present day they remain immature, experiencing temperatures of <~140 °C (Fig. 5.7 and 5.9). SR1-2 however, exist within the gas window at present day (temperatures of 160-170 °C), with hydrocarbon generation

beginning at the start of the Miocene (Fig. 5.8c), although only very slowly, as the transformation ratio of SR1-2 only reach ~20% at 2.2 Ma and are still only 30% at present day (Fig. 5.7d). Additionally, the generated mass (gas) is comparably much lower than what is produced in the MBG (Fig. 5.8c). This late onset of maturation is likely in response to the additional burial experienced in the SKB, due to deposition of glacigenic sediments since ~2.7 Ma (Figs. 5.6, 5.7d, and 5.8c) (Cox et al., 2021; Fjeldskaar and Amantov, 2018; Medvedev et al., 2019). Due to hydrocarbon generation (and even more so expulsion) only occurring relatively recently (mainly since the Pliocene; Fig. 5.8c), it is unlikely that thermogenic generation within the SKB contributes to much of the seismically defined distribution of hydrocarbons across the shallow stratigraphy of the Melville Bay margin (Cox et al., 2020a; 2021), and instead this gas is more likely sourced from the MBG or through biogenic generation (see section 5.1.5).

5.5.2.5. Biogenic Scenario

The key difference observed for the biogenic scenario, compared to the thermogenic case, was the timing of the onset of generation and expulsion. Biogenic gas is produced at much lower temperatures, and therefore much shallower burial (Stopler et al., 2014). Biogenic generation from the source rock intervals and syn-rift shale horizons began during the Early Cretaceous (Fig. 5.8a), and by the Paleogene a large majority of the biogenic potential had already been exploited. By this point, all of the biogenic hydrocarbons generated had also been expelled and likely lost at the surface due to shallow burial and the lack of sealing lithologies (Figs. 5.6 and 5.8a). Since the Paleogene, thermogenic generation commences and the trend of hydrocarbon generation is similar to the thermogenic scenario (Fig. 5.8a), with only minor amounts of biogenic hydrocarbons being generated from the younger, and much lower TOC, post-rift sediments (Fig. 5.10b). By present day, the contribution to generated hydrocarbons from thermogenic and biogenic reactions is roughly equal (Fig. 5.10a), but a much higher proportion of biogenically generated hydrocarbons have also been expelled.

Within the MBG (source kitchen 1 and 2), larger volumes of biogenic gas have been generated than compared to both the SKB and shallow post-rift sediments (Fig. 5.10a). However, these volumes are minor in comparison to thermogenically generated hydrocarbons from the source rock intervals. Also, the biogenic generation and expulsion likely occurred >50 Myr ago, therefore it is very unlikely any of those hydrocarbons remain preserved at present day (Fig. 5.10). The biogenic and thermogenic scenarios differ significantly within the SKB and MBR however, with much greater hydrocarbon generation occurring when considering biogenic generation. In this scenario, the slower and shallower

burial means that biogenic generation has been occurring almost consistently through the Paleogene and Neogene (Fig. 5.10), with shallow sediments of mu-D1 and –C existing within the biogenic window at present day. This may have a significant effect on the distribution of present day hydrocarbons, as generation would have occurred in close proximity to buried post-rift reservoirs (such as within the ridge crest beneath the mu-D2 reservoir sands (Fig. 5.10a)).

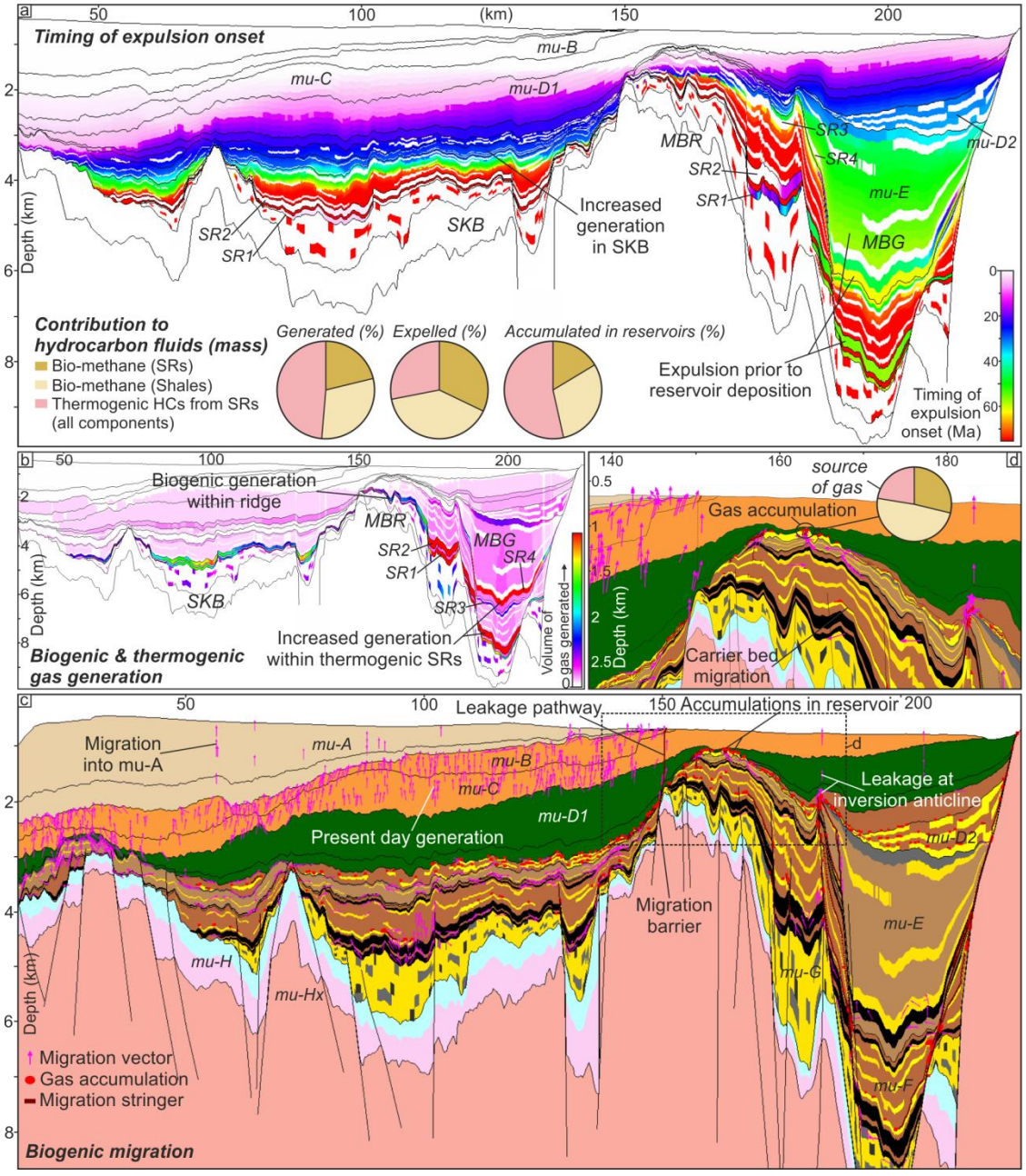

Figure 5.10. Biogenic generation, migration and accumulation | The timing of expulsion onset for the biogenic scenario is shown on (a), highlighting that expulsion began within the Melville Bay Graben (MBG) and South Kivioq Basin (SKB) at ~80 Ma, as well as recent expulsion within the shallow stratigraphy and the Melville Bay Ridge (MBR). The contribution to fluids in the model from different source rocks is shown on the pie charts. Gas generation volume from the various source rocks is shown on (b). The predicted accumulation of present day hydrocarbons, as well as likely migration pathways is shown on (c), with numerous accumulations existing beneath the mu-D1 seal. The enlarged section of the model (d) highlights biogenic gas within the reservoir sands on the MBR crest, as well as the diversion of migrating hydrocarbons from the SKB into the post-rift stratigraphy via an extensive fault on the western flank of the MBR.

5.5.3. Hydrocarbon Migration and Accumulation

5.5.3.1. Migration and Leakage

The present day porosity and permeability output for the most likely scenario modelled (Fig. 5.11), predicts that multiple sand rich horizons that exist within mu-G, -F, -E and -D2, remain permeable and have potentially acted as carrier beds for hydrocarbon migration. As previously discussed, the majority of hydrocarbon generation and expulsion occurred within two areas of the MBG (Figs. 5.7, 5.8c and 5.9). Carrier beds extending up-dip, south-westward from the deeper MBG (source kitchen 1) and into the MBR, are offset by two vertically extensive faults (Fig. 5.11 and 5.12) that act as barriers to secondary migration within these permeable layers. Instead, the fluids are focussed upwards along the fault planes and either migrate to the surface, or become trapped, either against the fault plane or within a large anticline that has developed above the more western fault (Figs. 5.11 and 5.12). These faults play an integral role in the distribution of present day hydrocarbons, as nearly all hydrocarbons generated within the deeper MBG do not migrate into the ridge crest area that contains the main reservoir. Only a minor volume of fluid does reach the crest from this area, which migrated beneath the seal horizon at 13.82 Ma (Fig. 5.12e), before the erosion of mu-D1 occurred. On the eastern side of the MBG, migration is focussed upward at the graben bounding fault, where multiple sands pinch-out (Fig. 5.12a). This feature likely caused extensive leakage of fluids to the surface since the onset of expulsion.

Hydrocarbons generated during the Paleogene and Neogene within the MBG source kitchen 2 (Figs. 5.7-9) are shown to migrate up-dip into the MBR structure, and, importantly, reach the reservoir sands on the ridge crest. Secondary migration occurs via carrier beds within mu-F, before the fluids migrate vertically to the base of the mu-D1 seal (Fig. 5.12). Hydrocarbon fluids first reach the reservoir sands at 13.82 Ma (Fig. 5.12e), and this charge system remains in place up to present day, along with multiple periods of leakage from the reservoir, through the thin mu-D1 seal above the ridge crest, to the surface (Fig. 5.12). The MBG source kitchen 2 area, therefore provides the most likely source of the gas that exists within the reservoir on the MBR crest at present day (Cox et al., 2020a). Additionally, fluid migration through the seal suggests the permeability of mu-D1 above the ridge (Fig. 5.11b) is only sufficient to trap smaller accumulations of hydrocarbons, increasing the likelihood of the trapping system being sensitive to small pressure fluctuations which may have been experienced throughout cycles of glacial loading since ~2.7 Ma (Knutz et al., 2019; Medvedev et al., 2019); fluctuations which may have promoted episodic fluid leakage from the reservoir (Cox et al., 2021). Furthermore, within

the SKB, due to the late burial and recent expulsion of hydrocarbons, migration is relatively restricted across the basin and fluids remain within carrier beds that exist in close proximity to source rocks (Fig. 5.12a).

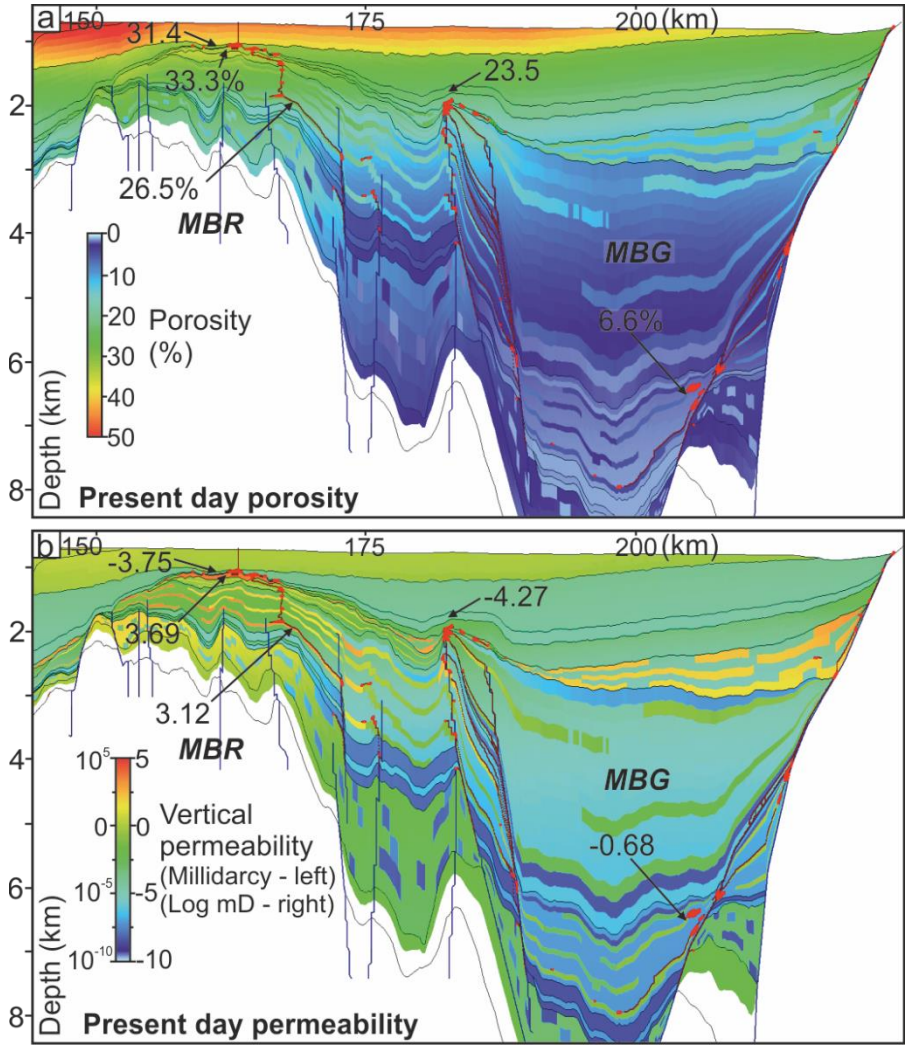

Figure 5.11. Porosity and permeability | A modelled outcome of the present day porosity (a) and permeability (b) across the Melville Bay Ridge (MBR) and Melville Bay Graben (MBG). The arrows show porosity-permeability comparisons for key locations and facies within the model. Several high porosity and permeability layers exist within the model, post-burial, which may represent carrier beds or reservoirs. The seal horizons also display low permeability values which will likely allow effective trapping of hydrocarbons.

The majority of the expelled hydrocarbons within the model have migrated to the surface (Fig. 5.8), with the main pathways of leakage occurring above the eastern flank of the MBR and above the faults that flank both sides of the deeper MBG (Fig. 5.11). The majority of this leakage, however, occurred prior to the Eocene and the development of the principal reservoir and seal formations in this study, with surface losses reducing considerably since (Fig. 5.8d). Spikes in migration losses coincide with uplift and erosion events during the Miocene as the mu-D1 seal lithology is thinned significantly, and during

the Pliocene, where a significant volume of sediment is removed due to glacial erosion on the inner shelf (Cox et al., 2021; Knutz et al., 2019; Newton et al., 2017).

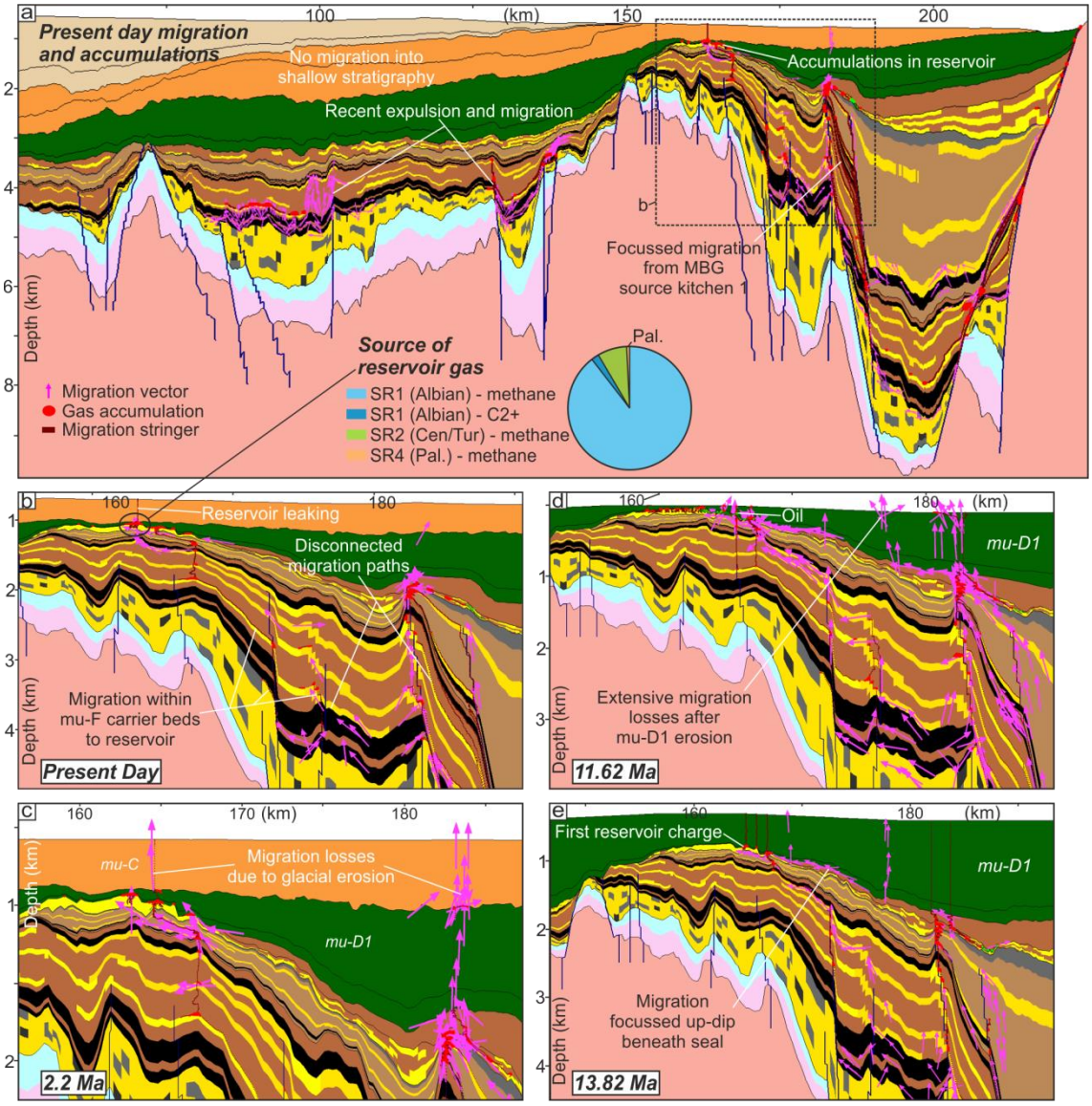

Figure 5.12. Migration and accumulation of thermogenic hydrocarbons | The predicted occurrence of reservoir accumulations at present day is shown on (a) as well as likely migration pathways and fluid leakage to the surface. The enlargement (b), shows a predicted hydrocarbon accumulation within the reservoir sands on the crest of the Melville Bay Ridge, with the pie chart on (a) displaying the predicted contribution of these fluids from the various source rock (SR) intervals. Extensive hydrocarbon leakage to the surface is shown in two locations on (c), at 2.2 Ma, in response to glacial erosion at the seabed. Similar losses occur after the erosion of mu-D1 at 11.62 Ma (d), as well as significant migration of hydrocarbons through carrier beds in mu-F towards the Melville Bay Ridge (MBR) crest. The onset of reservoir charge is shown at 13.82 Ma (e), with these fluids sourced mainly from the Melville Bay Graben (MBG) source kitchen 2 (see Fig. 5.9).

5.5.3.2. Reservoir Accumulations

Hydrocarbons are predicted to have begun accumulating in reservoirs during the early Eocene, at the same time as the rapid onset of gas generation from the deep MBG and the increase in migration losses at the surface (Fig. 5.8b-d). The volume of trapped hydrocarbons remained relatively stable throughout much of the Paleogene and Neogene,

with rapid decreases occurring in response to erosion events (Fig. 5.8b). A rapid increase in preservation occurs close to present day and likely represents the onset of expulsion into reservoir sands within the SKB (Figs. 5.8b and 5.12a). Only a small percentage of expelled hydrocarbons within the model remain trapped within reservoirs at present day. The source of these accumulations is dominated by SR1 and SR2 (Fig. 5.8e), with almost all of the persevered hydrocarbons predicted to represent methane gas. The dominance of SR1-2 generating the accumulated hydrocarbons can be attributed to enhanced maturation, and SR3-4 only being mature within the deeper MBG, where expelled hydrocarbons are rapidly lost to the surface through points of focussed upward fluid migration above faults (Fig. 5.12).

Hydrocarbon accumulations occur most frequently within the sandy horizons of mu-F, in a variety of locations including within localised anticlines on the flanks of the MBR, within pinch-out sands that exist against major faults and within sands directly overlying source rocks in the SKB (Fig. 5.12a). Hydrocarbons (including the only predicted presence of liquid hydrocarbons) have accumulated beneath the mu-D1 seal within the anticline on the eastern flank of the MBR (Fig. 5.12a-b). Finally, and most pertinent to this study, the most likely outcome modelled, predicts that hydrocarbons have accumulated within the reservoir sands on the MBR crest, with first charge occurring at 13.82 Ma. The majority of the fluids preserved in the reservoir are sourced from SR1 (Fig. 5.12a), and are primarily composed of methane, matching previous fluid content predictions that were made for this reservoir (Cox et al., 2020a).

5.5.3.3. Biogenic Scenario

The most likely modelled outcome for the biogenic scenario predicts that hydrocarbons began accumulating in reservoirs during the Late Cretaceous, at the same time as biogenic gas generation and expulsion began within both the MBG and SKB (Fig. 5.8). These fluids, however, were probably all lost to the surface due to the lack of effective seals being in place at this time. Since this early onset of expulsion, temporary trapping and subsequent leakage, biogenic and thermogenic hydrocarbon accumulations follow a similar trend to that modelled for the purely thermogenic scenario (Fig. 5.8b), with minor loss events associated with erosion events (Fig. 5.8d) and a late increase in accumulation, likely in response to additional burial in the SKB due to glacigenic sediment deposition (Figs. 5.6 and 5.8). Again, only a small proportion of expelled hydrocarbons remain preserved within present day reservoirs, with over half of the accumulated fluids representing thermogenic hydrocarbons (Fig. 5.10a). Thermogenic hydrocarbons within the biogenic scenario follow the same expulsion, migration and accumulation trends as described above for the

thermogenic case (comparison between Figs. 5.10c and 5.12a), despite the reduction in source rock parameters. This suggests that the contemporary distribution of hydrocarbons is also possible, especially with regards to gas sourced from SR1-2 in the MBG, even with lower quality source rocks (Table 5.1).

The generation and migration of biogenic gas occurs almost continuously since the Late Cretaceous, as progressive subsidence causes additional shale rich horizons to enter the biogenic generation window (peak generation at ~50 °C; Stopler et al., 2014) at each time step (Fig. 5.10a-b). By 21.5 Ma, and the deposition of the mu-D1 seal, biogenic gas generated within shale horizons in the MBR crest and the SKB, began to be preserved within reservoirs due to the seal presence. Within the MBR, biogenic generation and expulsion from shale horizons within mu-F and -E, occurred in close proximity to the reservoir sands on the ridge crest, with fluids first migrating into the reservoir at 21.5 Ma, ~7.5 Myr earlier than predicted in the thermogenic case. This biogenic charge, along with a contribution of thermogenic fluids, continued through to present day, with repeated increases in the reservoir accumulation, triggering multiple leakage events from the reservoir to the surface, possibly contributing to DHIs observed on seismic data within the overlying seal (Cox et al., 2021). At present day, the reservoir accumulation consists of both thermogenic (~1/4) and biogenic (~3/4) hydrocarbons (Fig. 5.10d), with half of the preserved fluids having been sourced from biogenic generation in shale horizons, likely from directly beneath the reservoir within the MBR structure.

In the SKB, the most likely biogenic scenario modelled, predicted a hydrocarbon distribution much different to what was predicted for the thermogenic case, with numerous gas accumulations within sediment packages beneath the mu-D1 seal, and migration occurring through post-rift stratigraphy westward of the MBR. Biogenic gas generated within the section of the SKB <50 km west of the MBR, is focussed up-dip towards the ridge structure, but importantly, does not enter the ridge crest (Fig. 5.10c-d). Instead, fluids migrate upwards at an extensive tectonic fault that flanks the ridge on its western edge, causing biogenic gas to migrate into the post-rift stratigraphy above this fault, with the fluids subsequently lost at the surface. This again suggests that fluids within the reservoir on the MBR crest are sourced solely from the MBG or the MBR itself. This diversion of fluids from the SKB into the post-rift stratigraphy has been previously predicted from the distribution of seismic DHI anomalies (Cox et al., 2021), and could represent an important pathway for gas hydrate forming fluids to reach the stability zone (see section 5.5.4). Additionally, since ~2.7 Ma, biogenic generation and upward migration are modelled to have occurred within potentially organic rich horizons within the contourite packages of

mu-B and -C (Fig. 5.10). This generation allows migration of biogenic hydrocarbons into the glacigenic sediments that have deposited since 2.7 Ma (Fig. 5.6) (Knutz et al., 2019). This is the most reasonable scenario of supplying the hydrocarbons interpreted to exist within gas charged glacial clinoforms throughout mu-A (Cox et al., 2021; Cox et al., 2020b). Since the clinoform-hosted reservoirs were deposited from 2.7 Ma migration from the deeper SKB is unlikely due to the short time period since deposition and migration most likely being restricted by the thick package of sealing muds (mu-D1).

5.5.4. Gas Hydrate Stability

A ~150 m thick, gas hydrate stability zone (GHSZ) has been predicted to exist across the majority of the margin at present day (Fig. 5.13), with the onset of hydrate stability occurring at 5.33 Ma (Fig. 5.13b). This estimation used the pressure temperature phase relationship provided by Sloan and Koh (1990), assuming an average sea water salinity of 35 parts per thousand (Hantschel and Kauerauf, 2009). The model results suggests that the margin contains the necessary pressure and temperature conditions for upwardly migrating fluids (shown within section 5.5.3) to have potentially formed gas hydrate deposits within the shallow sediments of mu-C, -B and -A. This may have significantly affected migration, gas accumulation and seabed leakage since the onset of stability (Chand et al., 2012; MIlkov et al., 2004). Additionally, if gas hydrates did form from 5.33 Ma, then they would likely have experienced large scale dissociation during the extensive erosion that occurred on the inner shelf during multiple shelf edge glaciations since 2.7 Ma (Knutz et al., 2019).

Extensive bottom simulating reflectors indicate the presence of gas hydrate deposits across large areas of the inner shelf (Cox et al., 2021; Cox et al., 2020b). These hydrate deposits are intersected by the 2D seismic line used in this study in areas above the MBR; the area where much of the hydrocarbons generated within the MBG source kitchen 2 area (Fig. 5.9) have migrated to and subsequently leaked upward into the shallow stratigraphy (Figs. 5.10-13). This suggests that hydrocarbons sourced from SR1-2 on the flank of the MBG are the most likely candidates for generating the methane that comprises the hydrocarbon constituent of gas hydrate forming fluids (Sloan and Koh, 1990). However, these fluids may also be sourced from the SKB if biogenic generation occurred within shale-rich, post-rift sediments, with migration to the shallow stratigraphy possible through an extensive fault conduit that flanks the western edge of the MBR (Fig. 5.10) (Cox et al., 2021).

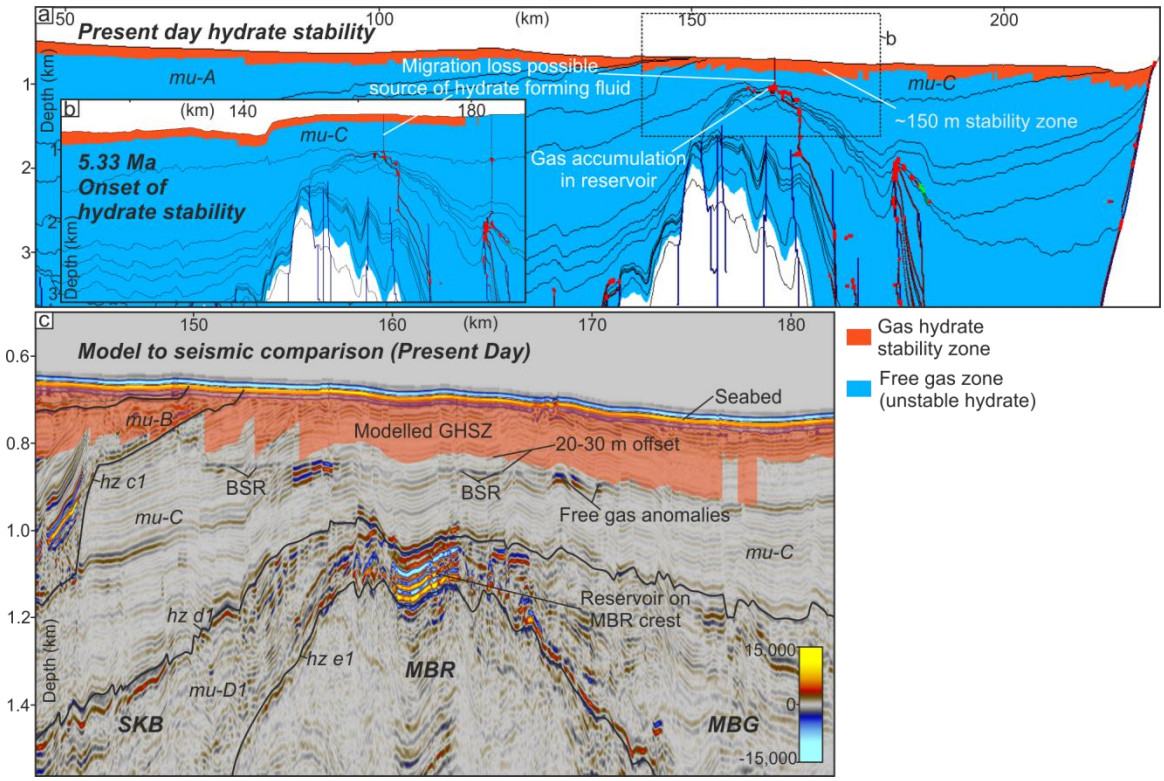

Figure 5.13. Gas hydrate stability | A ~150 m gas hydrate stability zone is predicted across the margin at present day (a). The onset of this stability is shown to occur at 5.33 Ma (b). At both time periods, hydrocarbon leakage from reservoir sands on the crest of the Melville Bay Ridge (MBR) may represent a source of gas hydrate forming fluids. A comparison of seismically identified bottom simulating reflectors (BSRs) on the depth converted 2D seismic cross section from Fig. 5.2, with the modelled base of the stability zone in areas above the MBR, and flanks of the Melville Bay Graben (MBG) and South Kivioq Basin (SKB) are shown on (c).

Comparisons of the BSR depth (the phase boundary mapped by Cox et al. (2021)), and the phase boundary predicted by the model (Fig. 5.13c), show a good correlation, with only a 20-30 m difference. This minor difference between the seismically observed and model predicted boundaries is likely due to the model resolution being restricted by the thickness of sub-layers, but could also be associated with slight variations in heat flow, thermal conductivity or hydrate and pore water composition than those that were assumed for the phase boundary during modelling (Grevemeyer and Villinger, 2001; Minshull and Keddie, 2010; Sloan and Koh, 1990). The correlation provides confidence in the predicted stability zone, which suggests that other areas of the margin may also contain ~150 m thick deposits of gas hydrates (or even thicker in deeper waters; c.f. Milkov and Sassen (2000)), if a source of upward hydrocarbon migration is in place to sustain hydrate formation. Limited or absent hydrocarbon flux to the shallow subsurface could be the reason why no seismic evidence for gas hydrate deposits is observed elsewhere along the 2D line (Cox et al., 2021). If gas hydrate deposits do exist elsewhere on the margin, they may pose an environmental risk due to the sensitivity of gas hydrate to rising ocean temperatures (Krey

et al., 2009; Ruppel and Kessler, 2017). Although, it is predicted that gas hydrate at the seabed in Melville Bay is relatively stable due to the large present day water depths whilst the base of the gas hydrate stability zone would be sensitive to sustained warming of bottom waters (Cox et al., 2021).

5.6. Conclusions

Petroleum systems modelling has been conducted on a ~225 km long section spanning the Melville Bay continental shelf, the deep, unexplored sedimentary basins of the Melville Bay Graben (MBG) and South Kivioq Basin (SKB), and the extensive rift-related inversion structure of the Melville Bay Ridge (MBR). Modelling included sensitivity analysis, testing the influence of several model parameters on the hydrocarbon systems throughout basin evolution, allowing an informed selection of the most likely paleo-parameters. This process provided a greater understanding of past and present subsurface conditions in Melville Bay, including reasonable estimations for the heat flow history, the most likely timings for variations in fault permeability, an understanding of the lithological parameters for the regional seal formation (mu-D1), as well as suitable source rock kinetics to allow biogenic gas generation to be modelled across the margin.

The most likely model outcome predicts that significant volumes of hydrocarbons, mainly methane, have likely been generated and expelled upward within the two basins, if the regionally predicted Cretaceous and Paleocene source rocks actually are present. This generation and expulsion likely began in the earliest Paleogene, with source rock maturation being significantly influenced by the variable rate of subsidence between the two basins. In the centre of the MBG, source rocks were over mature by the mid-Eocene, whereas in the SKB, source rock maturation only occurred since ~2.7 Ma, when glacigenic sediment deposition caused additional burial. Hydrocarbons began to accumulate in Paleogene reservoirs since the deposition and development of a regional seal formation (mu-D1) by the mid-Miocene, with fluid migration being influenced by extensive tectonic faults as well as the structure and presence of the MBR. Methane generated from Albian-aged source rocks on the flank of the MBG represents the most likely fluid composition of the hydrocarbons predicted to be contained within an extensive shallow marine reservoir reworked by mass transport that exists on the crest of the MBR.

Biogenic hydrocarbon generation was also shown to be a realistic scenario within Melville Bay; a factor that could have significant implications for hydrocarbon exploration. The most likely biogenic scenario model also predicted a present day distribution of hydrocarbons similar to what is interpreted on seismic data, but additionally, may represent the only realistic method of sourcing the gas that is predicted to be trapped within glacial

clinoforms that overlie the SKB. Furthermore, the model suggests that gas hydrates were stable from 5.33 Ma, with the predicted stability zone correlating well with interpretations of bottom simulating reflectors on seismic data. Over 500 km^2 of gas hydrate deposits have been identified on seismic data across Melville Bay, but the model suggests gas hydrates could also be stable elsewhere across the margin, representing an environmental consideration due to the sensitivity of gas hydrate to future ocean warming.

5.7. Recommendations for Future Work

Additional work is recommended to reduce the uncertainty associated with the results of this study. For example, examining uncertainty in the velocity model used for depth conversion could reduce error in the present day model geometry. The accuracy of paleo-geometries could also be improved through conducting a structural restoration study. Additionally, due to the availability of dense 2D and 3D seismic data, the model could be compared to another location on the Melville Bay margin, or modelled in 3D. Although, the main uncertainty in this study is the lack of direct calibration data; if such calibration data was provided however, for example through the detailed geochemical analysis of source rocks in the area (possible using shallow core data (Nøhr-Hansen et al., 2018), this would reduce uncertainty significantly, and may then warrant a more detailed 3D modelling study. Finally, a higher resolution model during the Pliocene-Pleistocene would allow the effects of extensive glaciations on the Melville Bay margin to be fully examined, something which may have had a considerable effect on the petroleum system.

References

Acton, G., 2012, Proceedings of the Baffin Bay Scientific Coring Program – Expedition 344S: Reporting by company consortium with eight companies led by Shell, p. 1-842.

Allen, P. A., and Allen, J. R., 2013, Basin Analysis: Principles and Application to Petroleum Play Assessment, Oxford, Wiley-Blackwell, 632 p.:

Altenbernd, T., Jokat, W., Heyde, I., and Damm, V., 2015, Geophysical evidence for the extent of crustal types and the type of margin along a profile in the northeastern Baffin Bay: Journal of Geophysical Research: Solid Earth, v. 120, no. 11, p. 7337-7360.

Balkwill, H. R., 1987, Labrador Basin: structural and stratigraphic style, *in* Beaumont, C., and Tankard, A. J., eds., Sedimentary Basins and Basin-forming Mechanisms. Memoir of the Canadian Society of Petroleum Geologists, Volume 12, p. 17-43.

Bertassoli Jr, D. J., Sawakuchi, H. O., Almeida, N. S., Castanheira, B., Alem, V. A. T., Camargo, M. G. P., Krusche, A. V., Brochsztain, S., and Sawakuchi, A. O., 2016, Biogenic methane and carbon dioxide generation in organic-rich shales from southeastern Brazil: International Journal of Coal Geology, v. 162, p. 1-13.

Bojesen-Koefoed, J. A., 2011, West Greenland Petroleum Systems – an Overview of Source Rocks and Oil Seepages and Their Implications for Offshore Petroleum Exploration: The Geological Survey of Denmark and Greenland.

Bojesen-Koefoed, J. A., Bidstup, T., Christiansen, F. G., Dalhoff, F., Gregersen, G., Nytoft, H. P., Nøhr-Hansen, H., Pedersen, A. K., and Sønderholm, m., 2007, Petroleum seepages at Asuk, Disko, West Greenland: implications for regional petroleum exploration: Journal of Petroleum Geology, v. 30, no. 3, p. 219-236.

Bojesen-Koefoed, J. A., Christiansen, F. G., Peter Nytoft, H., and Pedersen, A. K., 1999, Oil seepage onshore West Greenland: evidence of multiple source rocks and oil mixing: Petroleum Geology Conference Series, v. 5, p. 305-314.

Cairn Energy PLC, 2011, Greenland operational update [press release], p. 1-2.
Cavanagh, A. J., Di Primio, R., Scheck-Wenderoth, M., and Horsfield, B., 2006, Severity and timing of Cenozoic exhumation in the southwestern Barents Sea: Journal of the Geological Society, v. 163, no. 5, p. 761-774.
Chalmers, J. A., Dahl-Jensen, T., Bate, K. J., and Whittaker, R. C., 1995, Geology and petroleum prospectivity of the region offshore southern West Greenland–a summary.
Chand, S., Thorsnes, T., Rise, L., Brunstad, H., Stoddart, D., Boe, R., Lagstad, P., and Svolsbru, T., 2012, Multiple episodes of fluid flow in the SW Barents Sea (Loppa High) evidenced by gas flares, pockmarks and gas hydrate accumulation: Earth and Planetary Science Letters, v. 331-332, p. 305-314.
Christ, A. J., Bierman, P. R., Knutz, P. C., Corbett, L. B., Fosdick, J. C., Thomas, E. K., Cowling, O. C., Hidy, A. J., and Caffee, M. W., 2020, The northwestern Greenland Ice Sheet during the Early Pleistocene was similar to today: Geophysical Research Letters, v. 47, no. 1.
Christiansen, F. G., Bojesen-Koefoed, J., Dam, G., Nytoft, H.-P., Larsen, L. M., Pedersen, A. K., and Pulvertaft, T. C. R., 1996, The Marraat oil discovery on Nuussuaq, West Greenland: evidence for a latest Cretaceous–earliest Tertiary oil prone source rock in the Labrador Sea–Melville Bay region: Bulletin of Canadian Petroleum Geology, v. 44, no. 1, p. 39-54.
Christiansen, F. G., Bojesen-Koefoed, J. A., Dam, G., Nytoft, P., and Pedersen, A. K., 1994, Oil discovery onshore West Greenland: characterization of thermal history and depositional environment of an as yet untouched source rock, Western Canadian Internation Expertise: Calgary, Canadian Sciety of Petroleum Geologists.
Cox, D. R., Huuse, M., Newton, A. M. W., Gannon, P., and Clayburn, J., 2020a, Slip Sliding Away: Enigma of Large Sandy Blocks within a Gas Bearing Mass Transport Deposit, Offshore NW Greenland: AAPG Bulletin, v. 104, no. 5, p. 1011-1043.
Cox, D. R., Huuse, M., Newton, A. M. W., Sarkar, A. D., and Knutz, P. C., 2021, Shallow gas and gas hydrate occurrences on the northwest Greenland shelf margin: Marine Geology, v. 432, p. 1-21.
Cox, D. R., Knutz, P. C., Campbell, D. C., Hopper, J. R., Newton, A. M. W., Huuse, M., and Gohl, K., 2020b, Geohazard detection using 3D seismic data to enhance offshore scientific drilling site selection: Scientific Drilling, v. 28, p. 1-27.
Dam, G., Larsen, M., and Sønderholm, M., 1998, Sedimentary response to mantle plumes: Implications from Paleocene onshore successions, West and East Greenland: Geology, v. 26, no. 3, p. 207-210.
Dam, G., Pedersen, G. K., Sønderholm, M., Midtgaard, H. H., Larsen, L. M., Nøhr-Hansen, H., and Pedersen, A. K., 2009, Lithostratigraphy of the Cretaceous–Paleocene Nuussuaq Group, Nuussuaq Basin, West Greenland: Geological Survey of Denmark and Greenland (GEUS) Bulletin, v. 19, p. 1-171.
Fjeldskaar, W., and Amantov, A., 2018, Effects of glaciations on sedimentary basins: Journal of Geodynamics, v. 118, p. 66-81.
Goulty, N., and Swarbrick, R., 2005, Development of polygonal fault systems: a test of hypotheses: Journal of the Geological Society, v. 162, no. 4, p. 587-590.
Grecula, M., Wadsworth, S., Maloney, D., Lauferts, H., Cooke, G., Jones, A., and Stevanovic, S., Baffin Bay Elusive Plays: Geological Surprises of an Arctic Exploration Campaign, *in* Proceedings American Association of Petroleum Geology International Conference and Exhibition (ICE), London, UK, 2018, Volume 30548, p. 1-20.
Gregersen, G., Knutz, P. C., Nøhr-Hansen, H., Sheldon, E., and Hopper, J. R., 2019, Tectonostratigraphy and evolution of the West Greenland continental margin: Bulletin of the Geological Society of Denmark, v. 67, p. 1-21.
Gregersen, U., 2008, The north-east Baffin Bay region, offshore Greenland–a new frontier petroleum exploration region: Geological Survey of Denmark and Greenland (GEUS) Bulletin, v. 15, p. 65-68.
Gregersen, U., Andersen, M. S., Nøhr-Hansen, H., Sheldon, E., Kokfelt, T. F., Olivarius, M., Knudsen, C., Jakobsen, K. G., and Adolfssen, J. S., 2018, New subsurface mapping offshore southern West Greenland using geophysical and geological data: Geological Survey of Denmark and Greenland Bulletin, p. 57-62.
Gregersen, U., Hopper, J. R., and Knutz, P. C., 2013, Basin seismic stratigraphy and aspects of prospectivity in the NE Baffin Bay, Northwest Greenland: Marine and Petroleum Geology, v. 46, p. 1-18.
Gregersen, U., Knutz, P. C., and Hopper, J. R., 2016, New geophysical and geological mapping of the eastern Baffin Bay region, offshore West Greenland: Geological Survey of Denmark and Greenland Bulletin, v. 35, p. 83-86.
Grevemeyer, I., and Villinger, H., 2001, Gas hydrate stability and the assessment of heat flow through continental margins: Geophysics, v. 145, p. 647-660.
Hantschel, T., and Kauerauf, A. I., 2009, Fundamentals of basin and petroleum systems modeling, Berlin, Heidelberg, Germany, Springer Science & Business Media, 476 p.:

Henriksen, N., Higgins, A. K., Kalsbeek, F., Christopher, T., and Pulvertaft, R., 2009, Greenland from Archaean to Quaternary: Descriptive text to the 1995 Geological map of Greenland, 1:2500000: Geological Survey of Denmark and Greenland Bulletin, v. 18, p. 1-126.

Japsen, P., Bonow, J. M., Green, P. F., Chalmers, J. A., and Lidmar-Bergstrom, K., 2006, Elevated, passive continental margins: Long-term highs or Neogene uplifts? New evidence from West Greenland: Earth and Planetary Science Letters, v. 248, no. 1-2, p. 330-339.

Karisiddaiah, S. M., and Veerayya, M., 1994, Methane-bearing shallow gas-charged sediments in the eastern Arabian Sea: a probable source for greenhouse gas: Continental Shelf Research, v. 14, no. 12, p. 1361-1370.

Knutz, P. C., Gregersen, U., and Hopper, J. R., 2012, Late Paleogene Submarine Fans in Baffin Bay and North-West Greenland, 74th EAGE Conference and Exhibition incorporating EUROPEC 2012 Copenhagen, EAGE, p. 5.

Knutz, P. C., Harrison, C., Brent, T. A., Gregersen, G., and Hopper, J. R., submitted, Baffin Bay Tectono-Sedimentary Element, *in* Drachev, S., and Moore, T. E., eds., Arctic Sedimentary Basins, Volume Geological Society Memoir: London, Geological Society London.

Knutz, P. C., Hopper, J. R., Gregersen, U., Nielsen, T., and Japsen, P., 2015, A contourite drift system on the Baffin Bay–West Greenland margin linking Pliocene Arctic warming to poleward ocean circulation: Geology, v. 43, no. 10, p. 907-910.

Knutz, P. C., Newton, A. M. W., Hopper, J. R., Huuse, M., Gregersen, U., Sheldon, E., and Dybkjær, K., 2019, Eleven phases of Greenland Ice Sheet shelf-edge advance over the past 2.7 million years: Nature Geoscience, v. 12, p. 361-368.

Krey, V., Canadell, J. G., Nakicenovic, N., Abe, Y., Andruleir, H., Archer, D., Grubler, A., Hamilton, N. T. M., Johnson, A., Kostov, V., Lamarque, J., Langhorne, N., Nisbet, E. G., O'Neil, B., Riahi, K., Riedel, M., Wang, W., and Yakushev, V., 2009, Gas hydrates: entrance to a methane age or climate threat?: Environmental Research Letters, v. 4, p. 1-6.

Medvedev, S., Hartz, E. H., Schmid, D. W., Zakariassen, E., and Varhaug, P., 2019, Influence of glaciations on North Sea petroleum systems: Geological Society, London, Special Publications, v. 494, p. SP494-2018-2183.

MIlkov, A. V., Dickens, G. R., Claypool, G. E., Lee, Y., Borowski, W. S., Torres, M. E., Xu, W., Tomaru, H., Tre´hu, A. M., and Schultheiss, P., 2004, Co-existence of gas hydrate, free gas, and brine within the regional gas hydrate stability zone at Hydrate Ridge (Oregon margin): evidence from prolonged degassing of a pressurized core: Earth and Planetary Science Letters, v. 222, p. 829-243.

Milkov, A. V., and Sassen, R., 2000, Thickness of the gas hydrate stability zone, Gulf of Mexico continental slope: Marine and Petroleum Geology, v. 17, p. 981-991.

Minshull, T. A., and Keddie, A., 2010, Measuring the geotherm with gas hydrate bottom-simulating reflectors: a novel approach using three-dimensional seismic data from the eastern Black Sea: Terra Nova, v. 22, no. 2, p. 131-136.

Newton, A. M. W., Huuse, M., Cox, D. R., and Knutz, P. C., 2021, Seismic geomorphology and evolution of the Melville Bugt Trough Mouth Fan, northwest Greenland: Quaternary Science Reviews, v. 255, p. 1-23.

Newton, A. M. W., Huuse, M., Knutz, P. C., Cox, D. R., and Brocklehurst, S. H., 2020, Repeated ice streaming on the northwest Greenland shelf since the onset of the Middle Pleistocene Transition: The Cryosphere Discuss., v. 2019, p. 1-18.

Newton, A. M. W., Knutz, P. C., Huuse, M., Gannon, P., Brocklehurst, S. H., Clausen, O. R., and Gong, Y., 2017, Ice stream reorganization and glacial retreat on the northwest Greenland shelf: Geophysical Research Letters, v. 44, p. 7826-7835.

Nielsen, T., Andersen, C., Knutz, P. C., and Kuijpers, A., 2011, The Middle Miocene to Recent Davis Strait Drift Complex: implications for Arctic–Atlantic water exchange: Geo-Marine Letters, v. 31, no. 5-6, p. 419-426.

Nøhr-Hansen, H., 2003, Dinoflagellate cyst stratigraphy of the Palaeogene strata from the Hellefisk-1, Ikermiut-1, Kangâmiut-1, Nukik-1, Nukik-2 and Qulleq-1 wells, offshore West Greenland: Marine and Petroleum Geology, v. 20, no. 9, p. 987-1016.

Nøhr-Hansen, H., Pedersen, G. K., Knutz, P. C., Bojesen-Koefoed, J. A., Sliwinska, K. K., and Hovikoski, J., 2018, Potential Cretaceous source-rocks from the north-east Baffin Bay, West Greenland, AAPG Europe Regional Conference - Global Analogues of the Atlantic Margin: Lisbon, p. 1.

Núñez-Betelu, L. K., 1993, Rock-Eval/TOC pyrolysis data from the Kanguk Formation (Upper Cretaceous), Axel Heiberg and Ellesmere Islands, Canadian Arctic: Geological Survey of Canada.

Oakey, G. N., and Chalmers, J. A., 2012, A new model for the Paleogene motion of Greenland relative to North America: Plate reconstructions of the Davis Strait and Nares Strait regions between Canada and Greenland: Journal of Geophysical Research, v. 117, no. B10, p. 1-28.

Oakey, G. N., and Stephenson, R., 2008, Crustal structure of the Innuitian region of Arctic Canada and Greenland from gravity modelling: implications for the Palaeogene Eurekan orogen: Geophysical Journal International, v. 173, no. 3, p. 1039-1063.

Philp, R., 1994, Geochemical characteristics of oils derived predominantly from terrigenous source materials, *in* Scott, A. C., and Fleet, A. J., eds., Coal-bearing strata as oil-prone source rocks?, Volume 77, Geological Society, London, Special Publications, p. 71-91.

Planke, S., Symonds, P. A., Alvestad, E., and Skogseis, J., 2009, Mid-Cretaceous source rock subcropping in the Baffin Bay: GEO ExPro, v. 6, p. 1-8.

Rebesco, M., Hernández-Molina, F. J., Van Rooij, D., and Wåhlin, A., 2014, Contourites and associated sediments controlled by deep-water circulation processes: state-of-the-art and future considerations: Marine Geology, v. 352, p. 111-154.

Rice, D. D., 1993, Biogenic gas: controls, habitats, and resource potential, *in* Howell, D. G., ed., The future of energy gases, Volume 1570: Washington, USA, United States Government Printing Office, p. 583-606.

Rice, D. D., and Claypool, G. E., 1981, Generation, accumulation, and resource potential of biogenic gas: AAPG bulletin, v. 65, no. 1, p. 5-25.

Ruppel, C. D., and Kessler, J. D., 2017, The interaction of climate change and methane hydrates: Reviews of Geophysics, v. 55, no. 1, p. 126-168.

Schwarzkopf, T. A., 1993, Model for prediction of organic carbon content in possible source rocks: Marine and petroleum geology, v. 10, no. 5, p. 478-492.

Sloan, E. D., and Koh, C. A., 1990, Clathrate hydrates of natural gases: New York, New York, Marcel Drekker, Marcel Drekker, 1-641 p.:

Stopler, D. A., Lawson, M., Davis, C. L., Ferreira, A. A., Santos Neto, E. V., Ellis, G. S., Lewan, M. D., Martini, A. M., Tang, Y., Schoell, M., Sessions, A. L., and Eiler, J. M., 2014, Formation temperatures of thermogenic and biogenic methane: Science, v. 344, no. 6191, p. 1500-1503.

Welford, K., Peace, A., Geng, M., and Dickie, K., 2018, Crustal structure of Baffin Bay from constrained 3-D gravity inversion and deformable plate tectonic models: Geophysical Journal International, v. 214, no. 2, p. 1281-1300.

Whittaker, R. C., Hamann, R. E., and Pulvertaft, T. C. R., 1997, A New Frontier Province Offshore Northwest Greenland: Structure, Basin Development, and Petroleum Potential of the Melville Bay Area: AAPG Bulletin, v. 81, no. 6, p. 978-998.

Wygrala, B., P., 1989, Integrated study of an oil field in the southern Po Basin, Northern Italy [PhD: University of Cologne, 328 p.

Yang, Y., and Aplin, A. C., 2004, Definition and practical application of mudstone porosity–effective stress relationships: Petroleum Geoscience, v. 10, no. 2, p. 153-162.

-, 2010, A permeability–porosity relationship for mudstones: Marine and Petroleum Geology, v. 27, no. 8, p. 1692-1697.

Chapter 5 Appendix

Age Assignment Table						
Age (Ma)	*Horizon*	*Layer*	*Principal Facies*	*Event Type*	*Erosion Event*	*No. of Sublayers*
0.0	**hz a1**					
		mu-A	50% sand and 50% shale	Deposition		8
1.9	**hz a1i**					
		mu-A1	50% sand and 50% shale	Deposition		3
2.2				Erosion	Glacial erosion	
2.7	**hz b1**					
		mu-B	Siltstone	Deposition		4
5.33	**hz c1**					
		mu-C	Siltstone	Deposition		5
11.63				Erosion	MMU erosion	
13.82	**hz d1**					
		mu-D1	Custom seal lithology	Deposition		10
29.0	**hz d1i**					
		mu-D1i	Custom seal lithology	Deposition		1
31.0	**hz d2i**					
		mu-D2i	D2i: 80% shale and 20% sand	Deposition		5
33.9	**hz d2**					
		mu-D2	80% shale and 20% sand	Deposition		5
46.2	**hz e1**					
		mu-E	70% shale and 30% sand	Deposition		15
64.0				Erosion	f1 erosion	
70.0	**hz f1**					
		mu-F	80% shale and 20%	Deposition		15
91.0	**SR2**					
		SR2	Organic rich shale	Deposition		1
98.0	**hz f1i**					
		mu-F1	80% shale and 20% sand	Deposition		1
100.5	**SR1**					
		SR1	Organic rich shale	Deposition		1
110.0	**hz g1**					
		mu-G	75% sand and 25% shale	Deposition		5
145.5				Hiatus	Hiatus	
443.8	**hz h1**					
		mu-H	Quartzite	Deposition		5
541.0	**hz hx**					
		mu-Hx	Granite	Deposition		10
550.0	**base model**					

Appendix 5A. Age assignment | The age assignment table used to define geological events within the model. The horizons, layers, sub-layers and facies defined here can be observed on Fig. 5.4c.

Base Model – shale lithology (with initial porosity of 60%)			
Model variable	*Porosity (%)*	*Density (g/cc)*	*Vertical Permeability (log mD)*
Typical shale	47.0	1.92	-2.0
Test 1 – Compaction model tests (with initial porosity of 60%)			
Model type and variable	*Change in Porosity (%) (to Base Model)*	*Change in Density (g/cc)*	*Change in Vertical Permeability (log mD)*
Athy's Law, k = 1	- 6.9	+ 0.11	- 0.3
Athy's Law, k = 2	- 17.7	+ 0.29	- 0.8
Mudstone, 15% clay	- 24.4	+ 0.40	- 1.6
Mudstone, 45% clay	- 7.3	+ 0.12	- 0.4
Test 2 – Porosity-permeability relationship test (Kozeny-Carman (K-C) model used)			
Model type and variable	*Change in Porosity (%) (to Base Model)*	*Change in Density (g/cc)*	*Change in Vertical Permeability (log mD)*
Athy's Law, k = 1	- 6.9	+ 0.11	- 1.3
Athy's Law, k = 2	- 17.7	+ 0.29	- 1.9
Mudstone, 15% clay	- 24.4	+ 0.4	- 2.3
Mudstone, 45% clay	- 7.3	+ 0.12	- 1.3
Test 3 – Additional burial of mu-D1			
Model variable	*Change in Porosity (%) (to Base Model)*	*Change in Density (g/cc)*	*Change in Vertical Permeability (log mD)*
300 m erosion = scenario used for base model and Tests 1 and 2			
400 m erosion			
Athy's Law, k = 2, K-C.	- 17.2	+ 0.29	- 1.8
Mudstone, 45% clay, K-C.	- 23.9	+ 0.4	- 2.3
Mudstone, 15% clay, K-C.	- 7.3	+ 0.12	- 1.3
500 m erosion			
Athy's Law, k = 2, K-C.	- 19.4	+ 0.32	- 2.0
Mudstone, 45% clay, K-C.	- 23.8	+ 0.4	- 2.3
Mudstone, 15% clay, K-C.	- 9.1	+ 0.15	- 1.4
Test 4 – Permeability model from Yang and Aplin (2010), using a mudstone compaction model with 45% clay			
Model variable	*Change in Porosity (%) (to Base Model)*	*Change in Density (g/cc)*	*Change in Vertical Permeability (log mD)*
40-50% clay	- 9.6	+ 0.16	- 1.4
50-60% clay	- 8.5	+ 0.14	- 1.7
60-70% clay	- 6.6	+ 0.11	- 2.3

Appendix 5B. Mu-D1 seal property test | A table displaying the results of sensitivity analysis testing the lithology properties of the mu-D1 seal formation. Four tests were conducted, with the results compared to the base model, including different compaction models (Test 1), the same compaction models but using a different porosity-permeability relationship (Test 2), the effect of additional burial at the hz d1 unconformity (Test 3) and finally, a comparison of results when using three porosity-permeability relationships defined by analogue data from Yang and Aplin (2004).

Heat flow comparisons (default = constant 65 mW/m²)					
Scenario	*Temperature at MBG SK2 (°C)*	*Surface HF above MBR crest (mW/m²)*	*Generation mass potential at MBG SK2 for SR1 (mgHC/gTOC)*	*Depth of gas window (Sweeney & Burnham, 1990) (mbsl)*	*Top of gas generation window (HC zones from HI)*
Default	159	69.6	69.5	4128	3616 m
RP 1	+1	0.0	+4.5	-63	-38
RP 2 (hot)	+1	+0.4	+16.4	-125	-138
RP 3 (cool)	-33	-13.2	-65.8	+738	+737
RP 4	-33	-13.2	-65.6	+725	+712

Heat flow scenarios:

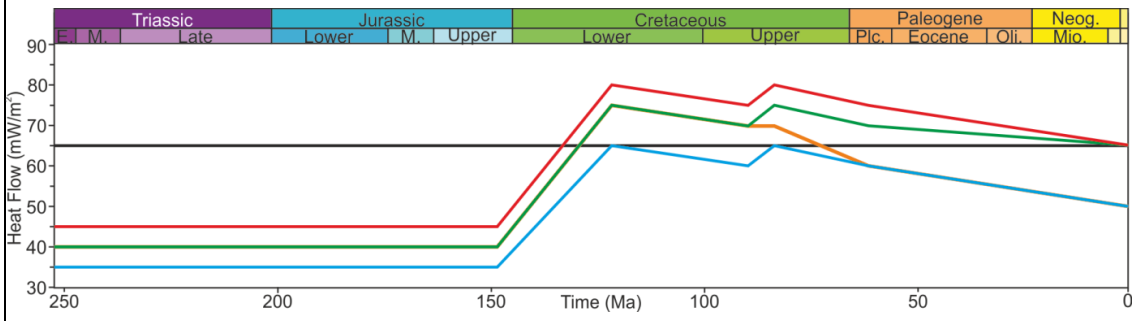

Appendix 5C. Heat flow | A table displaying the results of sensitivity analysis that tested the heat flow history used in the model, with various basal heat flow scenarios compared against the base model. The RP1 model was shown to be the most likely and realistic scenario and was selected. The colours shown on the table for each scenario are related to the graph below. Abbreviations used include Melville Bay Graben (MBG), Melville Bay Ridge (MBR), source kitchen (SK), source rock (SR), hydrocarbon (HC), hydrogen index (HI) and meters below sea level (mbsl).

Fault property scenarios – Input parameters								
Fault parameters used: - 'Permeable': FCP = 3.5 MPa & Perm = -1.8 log mD								
- 'Semi-permeable': FCP = 6 MPa & Perm = -5.05 log mD								
- 'Semi-impermeable.': FCP = 11 MPa & Perm = -6.14 log mD								
- 'impermeable.': FCP = 21 MPa & Perm = -7.3 log mD								
Scenario								
Base Model	*Fault number*	*Fault parameter assigned at certain ages (Ma)*						
	8, 12, 18, 21, 22, 23, 24, 25, 27, 28, 40	145 – 61.6 permeable	61.6 - 0 imperm.	-	-	-	-	-
	1, 2, 3, 4, 5, 16, 17, 19, 20, 27, 36, 37, 38, 39, 41	145 – 46.2 permeable	46.2 - 0 impermeable	-	-	-	-	-
	6, 9, 10, 11, 13, 14	145 - 36 closed	36 – 30 perm-eable	30 – 11 imperm.	11 – 10 perm-eable	10 – 7 imperm.	7 – 2 perm-eable	2 - 0 imperm.
	7, 26, 29, 42	Turned off						
1) Off	No faults considered							
2) Imper-meable	All faults imperm.							
3) Perm-eable	All faults permeable							
4) Model Events	*Fault number*	*Fault parameter assigned at certain ages (Ma)*						
	3, 4, 5, 12, 16, 17, 18, 20, 21, 22, 23, 27, 28, 36, 37, 38, 39, 41	145 – 61.6 permeable	61.6 - 0 imperm.	-	-	-		
	1, 2, 8, 10, 11, 13, 14, 24, 25	145 – 61.6 permeable	61.6 – 46.2 semi-imperm.	46.2 – 13.82 imperm.	13.82 – 11.63 semi-imperm.	11.63 - 0 imperm.		
	6, 7, 9, 19	145 – 46.2 permeable	- -	46.2 – 13.82 imperm.	13.82 – 11.63 semi-imperm.	11.63 - 0 imperm.		
	7, 26, 29, 42	Turned off						
5) Model Events Edit	*Fault number*	*Fault parameter assigned at certain ages (Ma)*						
	3, 4, 5, 12, 16, 17, 18, 20, 21, 22, 23, 27, 28, 36, 37, 38, 39, 41	145 – 61.6 permeable	61.6 - 0 imperm.	-	-	-		
	1, 2, 8, 10, 11, 13, 14, 24, 25	145 – 61.6 permeable	61.6 – 46.2 semi-imperm.	46.2 – 13.82 imperm.	13.82 – 0 permeable	11.63 - 0 semi-perm.		
	6, 7, 9, 19	145 – 46.2 permeable	- -	46.2 – 13.82 imperm.	13.82 – 0 permeable	11.63 - 0 semi-perm.		
	7, 26, 29, 42	Turned off						

Numbers assigned to modelled faults:

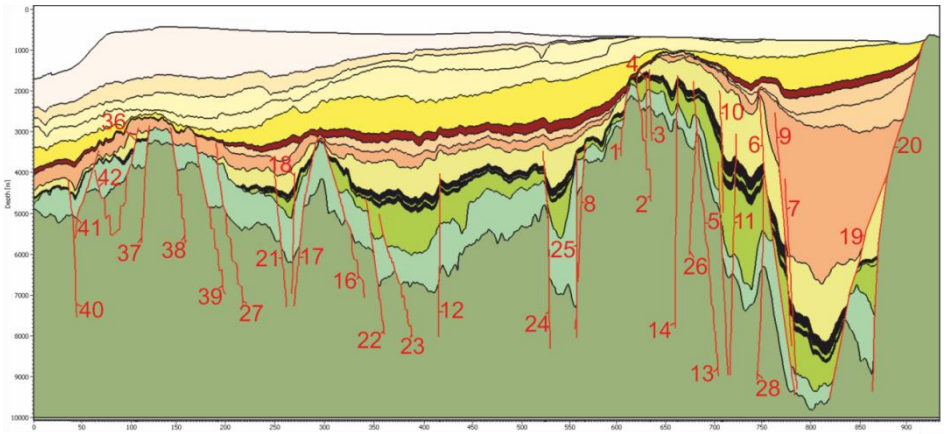

Appendix 5D. Fault permeability input parameters | A table defining the range of input parameters used for sensitivity analysis to test fault permeability through time (previous page). Five scenarios and the base model parameters are shown, as well as the number assignment of faults throughout the model, which relates to the numbers used within the table. Abbreviations used include fault capillary pressure (FCP), fault permeability (Perm), semi-impermeable (semi-imperm) and impermeable (imperm).

Fault property scenarios – result comparisons						
Scenario	***Accumulated in reservoirs (%)***	***Migrated and lost at surface (%)***	***Max. accum. column height in reservoir (m)***	***Max. accum. volume in reservoir (Mm^3)***	***Age of first migration to reservoir***	***Notes***
Base Model	3.1%	95.9%	10.2	0.92	7.5 Ma	*Extensive losses through faults 6 and 9 at anticline.*
1) Off	↓1.0	↑1.0	0	↓0.04	31 Ma	*Migration to MBR crest prior to seal deposition*
2) Imperm-eable	↑0.3	↓0.3	↓10.2 (no charge)	↓0.92	N/A	*Faults restrict carrier bed migration with fluids only reaching near the ridge crest at present day*
3) Perm-eable	↓0.4	↑0.4	↑2.0	↑3.80	31 Ma	*Continued migration post-seal deposition via carrier beds in mu-F & -E*
4) Model Events	↑0.2	↓0.2	↓10.2 (no charge)	↓0.92	N/A	*Carrier bed migration restricted by faults 10 and 11 – need to be open for migration to ridge crest*
5) Model Events Edit	↑0.8	↓0.8	↑14.5	↑1.38	11.63 Ma	*Majority of accumulation from mu-F carrier bed, with 90% sourced from SR1 in MBG SK2*

Appendix 5E. Fault permeability test results| A table displaying the results of sensitivity modelling for fault permeability through time (above). The input data for the base model and five tested scenarios are shown on Appendix D. The results are displayed as change from the base model, with green and red representing a either positive or negative change respectively, with regards to the similarity of the modelled result to our interpretation of the present day distribution of hydrocarbons from seismic data analyses. Abbreviations used include maximum (max.), accumulation (accum), source rock (SR) and Melville Bay Graben source kitchen 2 (MBG SK2).

Appendix 5F. Biogenic kinetics test | A table displaying both the input parameters and results of sensitivity analysis aimed at testing the range of parameters that define the biogenic kinetic model used in the conversion of kerogen to biogenic methane within the biogenic scenario model (overleaf). A range of results were analysed related to source rock maturity and hydrocarbon generation, including an assessment of how geologically reasonable the results were, whilst considering our understanding of the present day hydrocarbon distribution interpreted from seismic data. Nine scenarios were compared against the base model, with a further three scenarios that also included biogenic generation within potentially organic rich shale horizons.

Biogenic generation tests – Input parameters				
Variable	*Hydrogen Index (HI)* (mg HC/g TOC)	*Total Organic Carbon (TOC) (%)*	*Mean Temperature (°C)*	*Standard Deviation*
Source rock horizons only				
Default	50	0.5	50	10
TOC (0.25)	50	**0.25**	50	10
TOC (0.75)	50	**0.75**	50	10
TOC (1.0)	50	**1.0**	50	10
HI (25)	**25**	0.5	50	10
HI (75)	**75**	0.5	50	10
Mean temperature (60)	50	0.5	**60**	10
Mean temperature (40)	50	0.5	**40**	10
Standard deviation (15)	50	0.5	50	**15**
Standard deviation (20)	50	0.5	50	**20**
Source rock and shale rich horizons				
TOC (shales)	50	Shale: 0.25 80% Shale: 0.2	50	10
TOC (shales - Low)	50	Shale: 0.15 80% Shale: 0.1	50	10
TOC (shales – High)	50	Shale: 0.4 80% Shale: 0.3	50	10

Test Results	***Green = measurement taken at SR1 below Melville Bay Ridge (MBR) crest***						***Blue = measurement taken at SR3 below MBR crest***			
Variable	*TOC reduction (%)*	*TOC reduction (%)*	*Transformation ratio (TR) (%)*	*Transformation ratio (TR) (%)*	*Generation mass (tonne)*	*Generation mass (tonne)*	*Maximum generation age (Ma)*	*Maximum generation age (Ma)*	*TR at shallowest part of SR4 (%)*	*Ma. column height in reservoir*
Source rock horizons only										
Default	0.02	0.01	14.8	18.6	19350	4200	70	5.33-2.7	6.9	9.7 m
TOC .25	-0.01	0	-0.4	0.0	-9680	-2101	70	5.33-2.7	0	-3
TOC .75	+0.01	+0.01	-0.4	+0.0	+9662	+2104	70	5.33-2.7	0	+1
TOC 1	+0.02	0	-0.7	-14.1	+15992	-2426	70	5.33-2.7	-6	-5
HI 25	+0.01	0	+4.9	-12.9	+7688	-2870	22.5-13.8	4	-6	-2
HI 75	-0.01	-0.01	-7.2	-16.0	-10334	-3770	22.5-13.8	4.0-2.7	-7	-5
Temp 60	0	-0.01	-2.4	-18.0	-3414	-4064	22.5-13.8	2.7	-7	-5
Temp 40	0	0	-0.5	-5.2	-1029	-1591	22.5-13.8	2.7	-3	-6
SD 15	0	-0.01	-0.9	-12.0	-2454	-2868	22.5	2.7	-5	-3
SD 20	0	0	9.2	-9.6	-847	-692	22.5-13.8	2.7	0	+1

Variable	***Green = measurement taken from the shale overlying SR1 below MBR crest***					***Blue = measurement from the shale overlying SR3 below the MBR crest***		
	TOC reduction (%)	*TOC reduction (%)*	*Transformation ratio (TR) (%)*	*Transformation ratio (TR) (%)*	*Generation mass (tonne)*	*Generation mass (tonne)*	*Main gen. window for mu-F shales in ridge crest*	*Reservoir column height (Bio-methane)*
Shale rich horizons								
TOC (shales)	0	0	99.8	68	644	335	70 & 2.7 Ma	9.2 m
TOC Low (shales)	0	0	99.8	68	1289	670	70 & 2.7 Ma	10.2
TOC High (shales)	0	0	99.8	68	128	67	70 & 2.7 Ma	10.2

6

The Impacts of Glaciation

Preamble

DRC built the PetroMod model, interpreted the data, wrote the manuscript and drafted the figures presented in this chapter. SS, AB and OS assisted with model creation, simulation and refinement, and reviewed the final manuscript. AMWN, MH and PKN provided assistance in selecting input data for the model, assisted with figure creation and manuscript reviewing.

The Impacts of Glaciation on Arctic Petroleum Systems Offshore Northwest Greenland

David R. Cox[1], Simone Salazar[2], Attila Bartha[2], Oliver Schenk[2],

Andrew M. W. Newton[1, 3] and Mads Huuse[1, 2]

[1]Department of Earth and Environmental Sciences, The University of Manchester

[2]Schlumberger GmbH, Aachen Technology Centre, Ritterstraße 23, 52072 Aachen, Germany.

[3]School of Natural and Built Environment, Elmwood Building, Queens University Belfast, University Road, UK, BT7 1NN

Abstract

Melville Bay, offshore northwest Greenland, has experienced multiple episodes of cross-shelf advance and retreat of the Greenland Ice Sheet since ~2.7 Ma. The impacts of these shelf-edge glaciations on the petroleum systems observed in this area have been assessed through the creation of a 2D petroleum systems model that simulates the effects of glacial erosion, sediment re-deposition and six cycles of ice loading. The model predicts that glacial processes have caused substantial variations in subsurface pressure, temperature and sediment compaction since ~2.7 Ma, with these variations significantly impacting hydrocarbon generation, migration and accumulation. Pressure and temperature on the inner shelf has reduced significantly in response to glacial erosion, whilst contrastingly increasing on the outer shelf due to additional burial from sediment re-deposition. Ice loading during glacial advance across the shelf is predicted to have caused repeated cycles of increased pore pressure (~5 MPa) and decreased temperature (5-6 °C) beneath the ice, with temperatures not fully re-equilibrating during interglacials, leading to a ~3 °C reduction at ~350 m burial depth throughout the last 2.7 Myr. In response to these changes, thermogenic hydrocarbon generation was shown to increase beneath the ice load, but biogenic gas generation dramatically decreases due to rapid, near surface temperature reductions. Hydrocarbon re-migration is observed to increase during deglacial periods, with leakage from the main reservoir predicted to occur in response to deglacial pressure variations which potentially caused top seal fracturing and breach. Reservoir quality is

reduced through mechanical compaction under the ice load, and accumulations are shown to have experienced cyclic episodes of gas expansion and contraction. Temperature reductions on the inner shelf have also increased hydrate stability, deepening the phase boundary by ~150 m, with no dissociation predicted at the seabed other than during glacial erosion. The gas hydrate stability zone is modelled to have repeatedly expanded by several hundred meters beneath the ice load, leading to extensive dissociation at the phase boundary during deglaciation. This expansion included a conventional gas reservoir, potentially causing methane accumulations to repeatedly convert to gas hydrate; a process that would cause vast volumes of water to be sucked into the reservoir during hydrate formation, which may reduce reservoir quality, hydrocarbon volumes and gas saturation.

6.1. Introduction

Glaciated margins have experienced multiple episodes of glacial advance and retreat during the Quaternary (last 2.6 million years) (Fjeldskaar and Amantov, 2018), with thick, grounded ice sheets regularly advancing across many high latitude continental shelves (Cavanagh et al., 2006; Knutz et al., 2019; Winsborrow et al., 2010). This has led to the geometry of many of these margins being dramatically transformed by extensive glacial erosion and sediment re-deposition (Doré and Jensen, 1996; Fjeldskaar and Amantov, 2018), with the redistributed load causing significant isostatic adjustments (Van den Berg et al., 2008; Zieba and Grover, 2016). These adjustments, along with repeated cycles of ice loading on the shelf, cause considerable impacts on subsurface conditions, including cyclic variations in pressure and temperature and increased sediment compaction; elements that have an influence on underlying petroleum systems (Cavanagh et al., 2006; Grassmann et al., 2010; Zieba and Grover, 2016). Variable pressure and temperature between glacial and interglacial periods can significantly influence factors such as hydrocarbon generation and expulsion, zones of overpressure, and along with variations in trap geometry and tilt in response to differential isostatic adjustments (Kjemperud and Fjeldskaar, 1992; Løtveit et al., 2019), can often lead to increased hydrocarbon migration and spillage from reservoirs (Lerche et al., 1997; Medvedev et al., 2019; Zieba and Grover, 2016). Gas hydrate deposits commonly occur on high latitude, glaciated margins (Kvenvolden et al., 1993; Minshull et al., 2020), with the stability of these deposits controlled by pressure and temperature conditions (Sloan and Koh, 1990). Therefore, variations in these conditions can shift the depth of phase boundaries through time (Collett et al., 2009; Grassmann et al., 2010), potentially leading to extensive hydrate dissociation and the release of methane, a powerful greenhouse gas, at the seabed into the water column, a process that may pose a positive

feedback mechanism for global climate warming (Krey et al., 2009; Ruppel and Kessler, 2017).

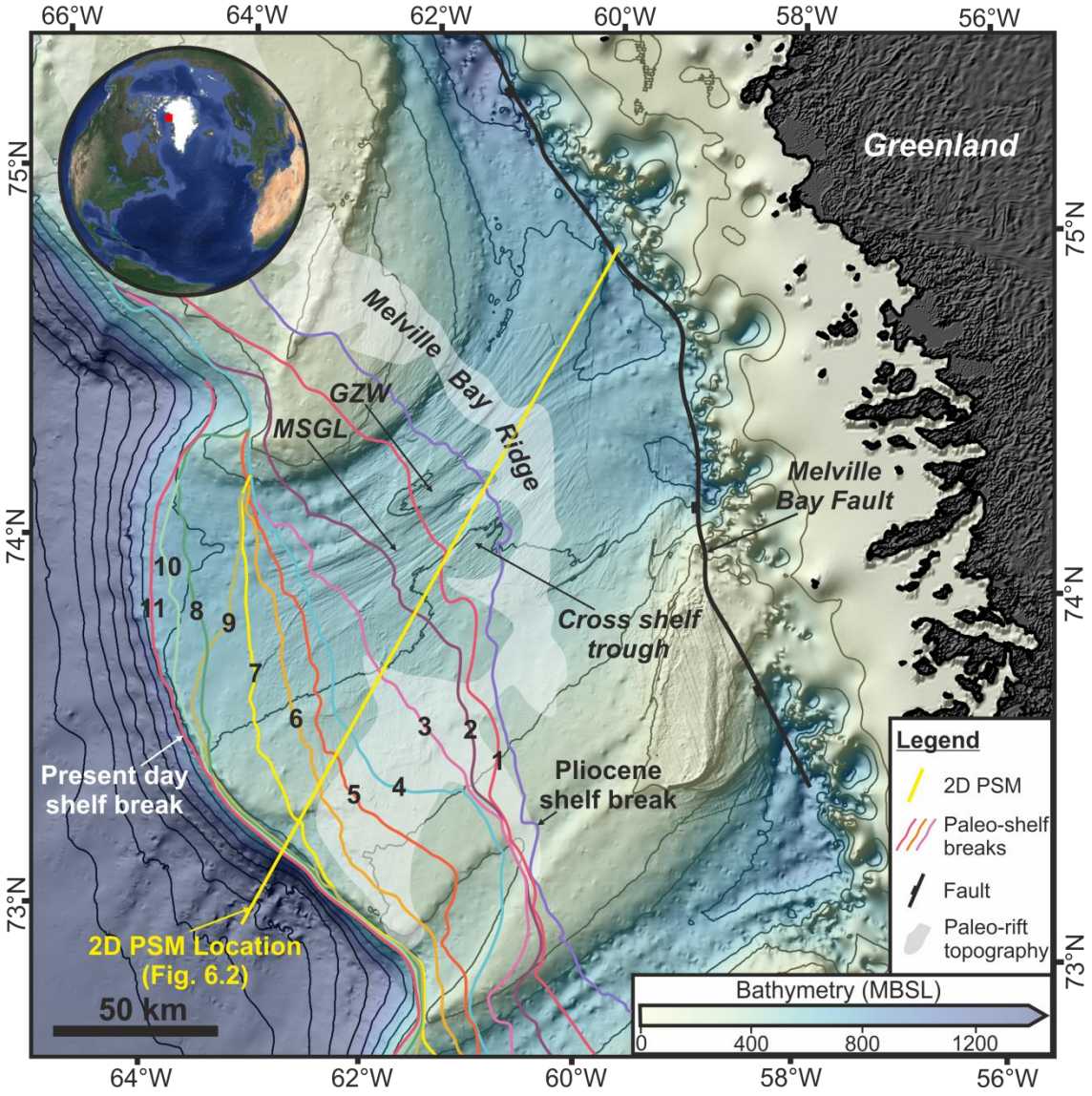

Figure 6.1. Location map | A bathymetric map of the Melville Bay area from Newton et al. (2017), showing the influence of Pliocene-Pleistocene glaciations on margin architecture, including cross-shelf trough development and up to 100 km of shelf edge progradation. Glacial geomorphological features are also shown on the seabed including a grounding zone wedge (GWZ) and mega-scale glacial lineations (MSGL). The red square on the inset map shows the global location of the bathymetry. 11 paleo-shelf break positions for the progradational sub-units of the Melville Bay Trough Mouth Fan are shown from Knutz et al. (2019), as well as the location of the underlying ridge topography of the Melville Bay Ridge. A 225 km cross section intersecting the Melville Bay margin is also shown, which represents the location of the 2D petroleum systems model used in this study as well as Fig. 6.2.

In Melville Bay, offshore northwest Greenland, it is likely that the petroleum systems underlying the extensive shelf margin have experienced such effects throughout the period of glaciation. Since ~2.7 Ma, the Melville Bay margin has been transformed by at least 11 cycles of shelf edge glaciations, causing extensive erosion on the inner shelf and the re-deposition of this sediment at the (paleo-) shelf edge, contributing to over ~100 km of

shelf edge progradation (Fig. 6.1) (Knutz et al., 2019; Newton et al., 2021; 2020; 2017). The petroleum system is thought to exist within deep Cretaceous syn-rift basins and thick post-rift sediments across the margin (Fig. 6.2), with the potential for both thermogenic and biogenic hydrocarbon generation (Bojesen-Koefoed, 2011; Cairn Energy PLC, 2011; Cox et al., 2020a; 2021; Gregersen et al., 2013). Although still to be proven due to the underexplored nature of this area, gas has been interpreted to exist across much of the post-rift stratigraphy, with fluid migration being focussed above the extensive, elongate inversion structure of the Melville Bay Ridge (Cox et al., 2021; 2020b). The largest potential reservoir identified, exists on the crest of this ridge structure, and represents a 420 km^2, sand-rich mass transport deposit that is likely gas charged (Fig. 6.2c) (Cox et al., 2020a). Furthermore, extensive gas hydrate deposits have been discovered across an areas of >500 km^2 above the ridge, via the identification of bottom simulating reflectors (BSRs) on seismic data (Cox et al., 2021).

A 2D basin model was created to study the petroleum systems along a 225 km cross section of the Melville Bay glaciated margin (Figs. 6.1 and 6.2) (Chapter 5). The model predicted that both conventional hydrocarbon and gas hydrate accumulations are likely to have formed prior to the onset of glaciation at ~2.7 Ma. The aim of this study is to incorporate glacial erosion, sediment redistribution and the repeated cycles of glacial advance and retreat across the shelf since ~2.7 Ma, to assess the impacts of glaciation on subsurface pressures, temperatures, and how these processes influence the modelled petroleum system. This will allow us to answer three key questions: (1) how have glaciations impacted both thermogenic and biogenic hydrocarbon generation and expulsion; (2) has glaciation influenced fluid migration and caused reservoir leakage; and (3) how has gas hydrate stability varied during the period of glaciation and has this variation caused hydrate dissociation.

6.2. Regional Setting

6.2.1. Glacial History

The Melville Bay continental margin has experienced multiple phases of shelf edge glaciation since ~2.7 Ma (Knutz et al., 2019), causing significant truncation by glacial erosion on the inner shelf, in areas above the Melville Bay Ridge (MBR) and Melville Bay Graben (MBG) (Figs. 6.1 and 6.2) (Cox et al., 2021; Knutz et al., 2019; Newton et al., 2021). This erosion has contributed to extensive sediment redistribution across the margin, with sediment from the inner shelf and coastal mainland, being re-deposited at the outer shelf during the formation of the Melville Bay Trough Mouth Fan (MB-TMF) (Fig. 6.2)

(Newton et al., 2021). These processes have transformed the continental shelf in Melville Bay, with cross-shelf trough development causing over-deepening and a widespread glacial unconformity on the inner shelf, whilst trough mouth fan deposition has caused over ~100 km of shelf edge progradation (Figs. 6.1 and 6.2) (Knutz et al., 2019; Newton et al., 2017). Alongside glacial erosion and truncation of post-rift sediments, other geomorphological features suggest the extensive grounding of ice across the shelf throughout glaciation, including mega-scale glacial lineations (MSGL), grounding zone wedges (GZWs) and gullies that were most likely formed by hyperpycnal glacial meltwater flows (Newton et al., 2021; 2020; 2017).

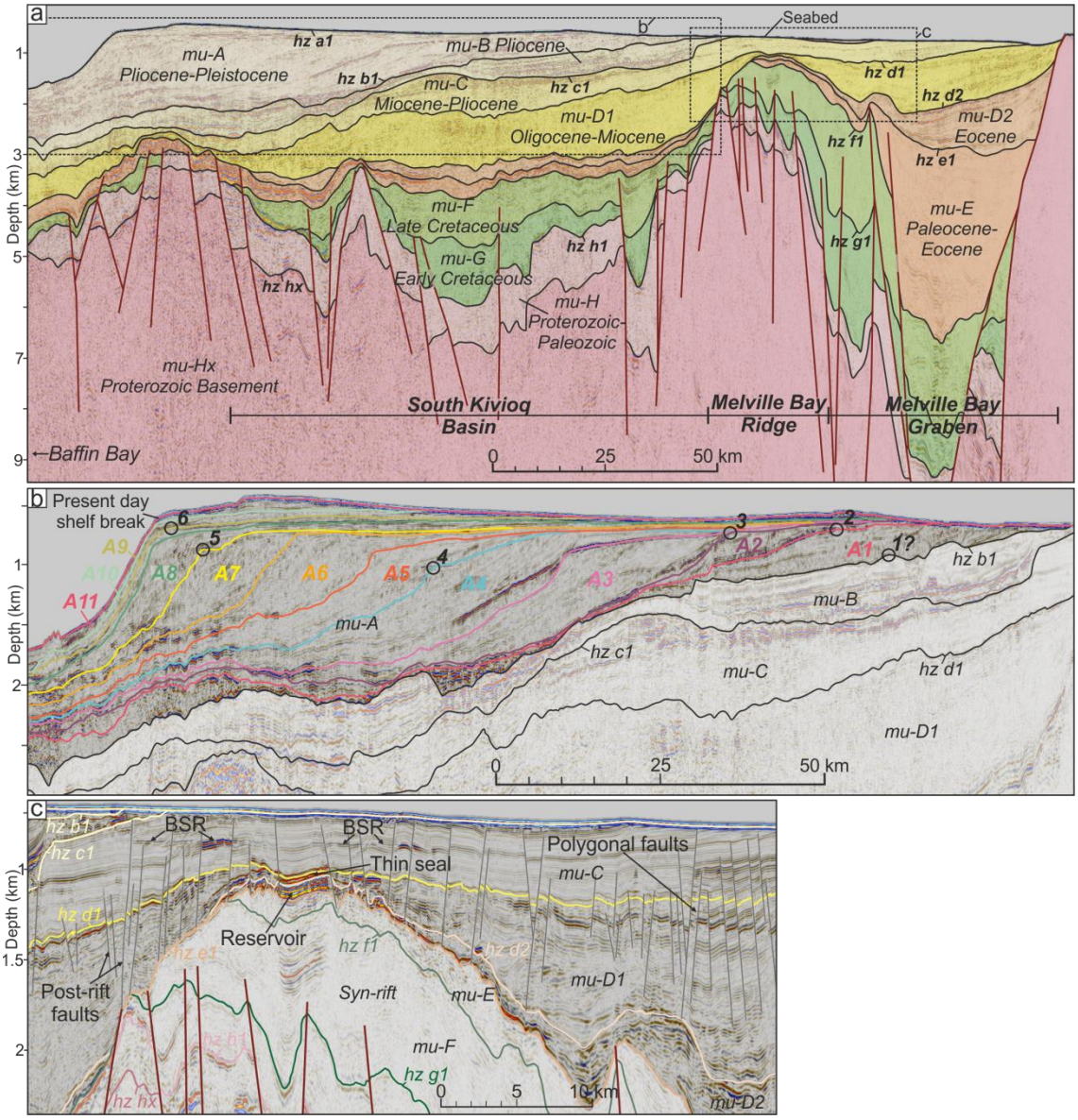

Figure 6.2. Regional structure and stratigraphy | a) A 2D regional seismic reflection line in depth (modified from Chapter 5), showing the structure and stratigraphy of the Melville Bay margin. The stratigraphy has been divided into 10 seismic mega-units (mu) following the regional framework defined by Gregersen et al. (2013); (2016) and Knutz et al. (2015). The horizon and fault interpretations shown, have been imported into PetroMod and form the present day geometry of the 2D petroleum systems model. b) an enlarged section of the seismic line from (a) focussing on mu-A which represents the Melville Bay Trough Mouth Fan. 11 progradational sub-units from Knutz et al. (2019) are shown, along with paleo-shelf break

interpretations for the 6 depositional packages related to each of the 6 glacial cycles included within the model. c) An enlarged section of the seismic line from (a) focussing on the stratigraphy, structure and petroleum systems elements within the Melville Bay Ridge area. The location of a gas reservoir on the crest of the ridge is shown, as well as bottom simulating reflectors (BSRs) marking the base of the gas hydrate stability zone. A series of tectonic and polygonal post-rift faults are also shown which may influence fluid migration.

The MB-TMF consists of thick glacigenic, mainly progradational sediment packages that are separated by unconformities and likely consist of highly variable sediment lithologies and grain sizes (Fig. 6.2) (Christ et al., 2020; Knutz et al., 2019; Newton et al., 2020). The glacigenic succession has been subdivided into progradational units that represent a minimum of 11 major phases of glacial expansion and retreat across the shelf since ~2.7 Ma. The sub-units (mu-A units 1-11; Fig. 6.2), are proposed by Knutz et al. (2019), and have been correlated with regional and global climate proxies to give an approximate age of deposition, and therefore an approximate timing of each phase (Fig. 6.3).

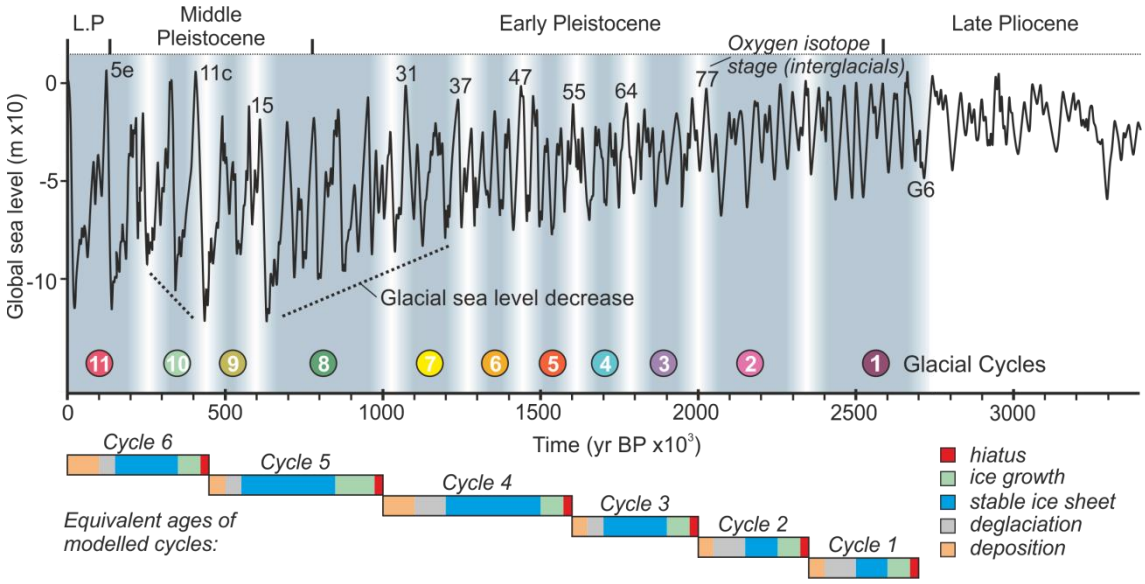

Figure 6.3. Glaciation age correlations | A correlation of the 11 progradational units of the Melville Bay Trough Mouth Fan (mu-A) from Knutz et al. (2019), to the global sea level curve relative to present (Miller et al., 2011) providing an approximate age for each of the shelf edge glaciations. These 11 events have been combined into 6 glacial cycles for modelling purposes, with the modelled cycles age, duration and the division into different glacial stages being shown.

6.2.2. Structural and Stratigraphic Framework

Rifting and the opening of Baffin Bay during the Cretaceous to Paleogene (Altenbernd et al., 2015; Oakey and Chalmers, 2012; Welford et al., 2018), led to the development of deep sedimentary basins separated by extensive elongate inversion ridges (Fig. 6.1) (Gregersen et al., 2013; Whittaker et al., 1997). The South Kivioq Basin (SKB) and MBG, contain syn- and post-rift sediment packages that can reach thicknesses of >10 km, and are

separated by the MBR inversion structure, that likely had developed by the Late Cretaceous (Gregersen et al., 2019; Whittaker et al., 1997) (Chapter 5). The ridge experienced several episodes of renewed uplift (Cox et al., 2020a; Japsen et al., 2006; Knutz et al., submitted) and remained a prominent positive relief feature throughout the Paleogene and Neogene, significantly affecting post-rift deposition and fluid migration (Cox et al., 2021). During ridge development, numerous tectonic faults formed that are vertically extensive and often parallel to the ridge (Fig. 6.2). These faults disconnect the syn-rift stratigraphy on the western flank of the MBR, whilst causing large offsets and anticlinal geometries on the eastern flank (Fig. 6.2) (Cox et al., 2021; Gregersen et al., 2019). Faults also exist throughout the post-rift stratigraphy, often extending from deeper structural features and are more common in areas above the ridge flanks (Fig. 6.2c). A dense network of layer bound polygonal faults also exists within muddy post-rift lithologies within both of the basins (within mu-D1 and -C) (Cox et al., 2020a; 2021).

The syn- and post-rift stratigraphy in Melville Bay has been subdivided into ten seismic mega-units (mu) (Hx – A) that are separated by regional unconformable horizons (hz) (hx-a1) and follow the regional framework defined by Gregersen et al. (2013); (2016) and Knutz et al. (2015). Proterozoic-Paleozoic aged basement (mu-Hx and -H) (Acton, 2012; Gregersen et al., 2018), underlies thick Cretaceous-Paleocene syn-rift packages (mu-G, -F and -E) that contain a range of clastic lithologies (Chalmers et al., 1995; Dam et al., 2009; Gregersen et al., 2019), and are thought to include four source rock (SR) intervals within Albian (SR1), Cenomanian-Turonian (SR2), Campanian (SR3) and Paleocene (SR4) aged stratigraphy (Fig. 6.4) (Grecula et al., 2018; Gregersen et al., 2013; Nøhr-Hansen et al., 2018). Mu-E represents the transition between syn- and post-rift stratigraphy (Cox et al., 2021; Knutz et al., submitted), with the top of this package, hz e1, representing the top of the MBR structure.

The overlying post-rift sedimentation contains thick packages of Eocene-Miocene aged basin floor fans (mu-D2) and hemipelagic muds (mu-D1) in the grabens (Gregersen et al., 2013; Knutz et al., 2012), but these packages onlap onto the MBR, and thin significantly over the crest (Fig. 6.2). The thinned mu-D1 package above the MBR, contains a dense network of short offset vertical faults (Cox et al., 2021), and represents the seal for an extensive, likely gas-charged, mass transport complex reservoir that exists within mu-D2 on the ridge crest (Fig. 6.2) (Cox et al., 2020a). The top of mu-D1, hz d1, represents the middle Miocene unconformity (Knutz et al., 2012; 2015) and >400 m (thickness) of eroded sediment due to regional uplift (Chapter 5). Above this, mu-C and -B are comprised of thick, Miocene-Pliocene aged muddy contourite successions, which have been significantly

truncated by glacial erosion on the inner shelf (Fig. 6.2) (Cox et al., 2021; Knutz et al., 2015), and are buried progressively deeper by glacigenic sediments towards the shelf edge (Fig. 6.2). Mu-C represents the host formation for extensive gas hydrate deposits that have been identified within the area via the interpretation of bottom simulating reflectors (BSRs) on seismic data (Fig. 6.2c) (Cox et al., 2021). The glacigenic sediments of mu-A, represent the MB-TMF and consist of thick progradational clinoform packages (Knutz et al., 2019).

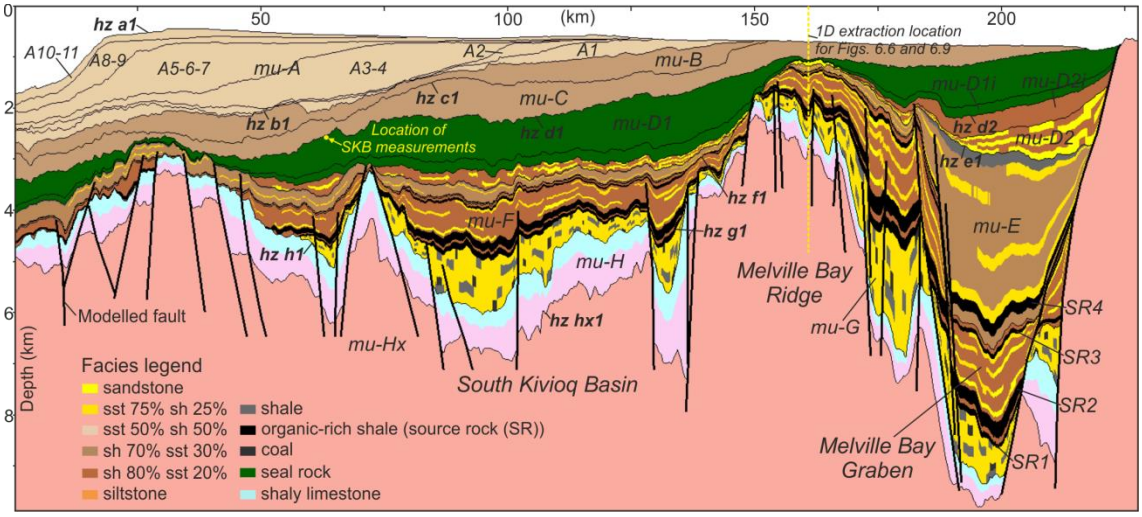

Figure 6.4. Present day model | Present day geometry of the 2D petroleum systems model, displaying the horizons and faults converted from seismic depth interpretations as well as all assigned facies. Note the division of mu-A into 6 progradational packages related to each of the 6 modelled glacial cycles. The location of the 1D extraction used in both Figs. 6.6 and 6.9 is also shown, as well as the location that pore pressure and temperature was measured within the South Kivioq Basin (SKB). A margin tilt of 0.5° throughout the last 2.7 Myr was calculated between these two locations for the top of mu-D1.

6.3. Data

The principal data used for this study is a ~225 km long 2D regional seismic line (Figs. 6.1 and 6.2) which defines the present day stratigraphic and structural geometry used to create the petroleum systems model. This 2D line is part of the Baffin Bay 2D (BBRE11) regional seismic dataset that was acquired by the geophysical company TGS between 2007-2010. The seismic line has been depth converted to provide regional interpretations in depth using seismic stacking velocities. Full details of the acquisition and processing of this survey can be found within section 5.3 of Chapter 5.

Model events and stratigraphy						
Mega-unit	**Sub-units**	**No. of sublayers**	**Facies**	**Top horizon (hz)**	**Event type**	**Age (Ma)**
mu-A	A10-11 A8-9 A5-6-7 A3-4 A2		50% sand and 50% shale	hz a1	Deposition	0 0.45 1 1.6 2
Glacial erosion					Erosion	2.05
mu-A	A1		50% sand and 50% shale			2.35
Glacial erosion					Erosion	2.4
mu-B		4	Siltstone	hz b1	Deposition	2.7
mu-C		5	Siltstone	hz c1	Deposition	5.33
MMU erosion					Erosion	11.63
mu-D1	D1 D1i	10 1	Custom seal lithology	hz d1	Deposition	13.82 29
mu-D2	D2i D2	5 5	D2i: 80% shale and 20% sand D2: sandstone; 80% shale and 20% sand	hz d2	Deposition	31 33.9
mu-E	SR4 (SL 14)	15	Shale; 70% shale and 30% sand; 75% sand and 25% shale	hz e1	Deposition	46.2
f1 erosion					Erosion	64
mu-F	F: 15 SR3 (SL 2) SR2 Fi	15 1 1	80% shale and 20% sand; Sandstone; 75% sand and 25% shale	hz f1	Deposition	70 91 98
mu-G	SR1 G	1 5	Shale; 75% sand and 25% shale Silty coal	hz g1	Deposition	100.5 110
hiatus					Hiatus	145.5
mu-H		5	Shaly limestone; Quartzite	hz h1	Deposition	443.8
mu-Hx		10	Granite	hz hx	Deposition	541

Table 6.1. Base model parameters | A table displaying the event age assignment and key model parameters for the base model (Chapter 5). Only parameters after 2.7 Ma have been modified within this study to simulate the effects of glaciation.

The petroleum systems model, that represents the template for the tests conducted within this study, was created to generate possible scenarios to help predict the present day condition and evolution of the hydrocarbon system across the Melville Bay margin, and test the likelihood of certain paleo-conditions related to basin evolution and lithology (Chapter 5). The model was created using a wide range of regional analogue data to inform model events and parameters, including legacy wells, shallow core data, seabed samples, oil seep sampling and outcrop studies (Bojesen-Koefoed et al., 2007; Christiansen et al., 1996; Gregersen et al., 2019; Nøhr-Hansen et al., 2018; Planke et al., 2009). Full details of these data and how they were used in combination with seismic interpretations to create the base model can be found in Chapter 5, but a summary of the key geometry, lithology, event type and age assignment parameters are provided (Table 6.1). Additionally, the base model tests

two separate scenarios; firstly, the 'thermogenic scenario', which models purely thermogenic hydrocarbon generation within 4 source rock intervals and secondly, the 'biogenic scenario', which models a combination of thermogenic (within source rocks) and biogenic (within source rocks and shale-rich layers) hydrocarbon generation. Both scenarios use the same thermogenic kinetic model for the source rock intervals (Table 6.2), with only the assigned total organic carbon (TOC) varying between the two. For the biogenic scenario, the source rock intervals and potentially organic shale rich lithologies are also assigned a biogenic kinetic model using a single component (bio-methane) Gaussian distribution around a central peak generation temperature of 50°C (Table 6.2; Chapter 5).

Thermogenic Scenario Model

Source rock	Geological Age	Layer/sub-layer	TOC	HI (mg HC/g TOC)	Max. Thickness	Thermogenic Kinetic model		
						No. of components	Kerogen Type	Adsorption rate
SR 4	Paleocene	mu-E / SL14	2%	300	200 m	4	III	75%
SR 3	Campanian	mu-F / SL2	1	150	100			
SR 2	Cenomanian-Turonian	SR2	2	300	200			
SR 1	Albian	SR1	2	300	200			

Biogenic Scenario Model

Source rock	Geological Age	Layer/sub-layer	TOC	HI (mg HC/g TOC)	Biogenic Kinetic model			
					Component	Distribution	Mean Temp.	Standard deviation
SR 4	Paleocene	mu-E / SL14	1%	300	Bio-methane	Gaussian	50 °C	10
SR 3	Campanian	mu-F / SL2	0.5	150				
SR 2	Cenomanian-Turonian	SR2	1	300				
SR 1	Albian	SR1	1	300				
Custom seal	-	mu-D1	0.1	50				
Shale	-	mu-G; mu-E	0.3	50				
80% sh. 20% sa.	-	mu-F; mu-D2	0.2	50				
70% sh. 30% sa.	-	mu-E	0.1	50				
Siltstone	-	mu-C; mu-B	0.1	50				

Table 6.2. Geochemical input data | A table from Chapter 5, displaying the geochemical input data used for both the thermogenic and biogenic scenario models. The biogenic scenario tests a combination of thermogenic and biogenic hydrocarbon generation, with the thermogenic kinetics shown also used within the biogenic scenario for source rock horizons which will generate both biogenic and thermogenic hydrocarbons. Abbreviations used include total organic carbon (TOC), hydrogen index (HI), temperature (temp), source rock (SR), sub-layer (SL), sand (sa), shale (sh), maximum (max) and number (no).

6.4. Building the Petroleum Systems Model

The 2D Petroleum systems model was created using Schlumberger's basin modelling software PetroMod (version 2019.1) (Fig. 6.4). Several aspects of the base model (Chapter 5) have been modified to create scenarios that can help predict the effect of glaciation on subsurface conditions and how these changes may have influenced hydrocarbon generation, expulsion, migration, accumulation and preservation, including the stability of gas hydrates. These modifications are applied to both the thermogenic and biogenic scenario models (Table 6.1 and 6.2; Chapter 5).

6.4.1. Ice Load Model

Ice load modelling requires the understanding and selection of several parameters related to ice sheet dynamics. As our understanding of past glaciations in Melville Bay is limited, especially beyond the last glacial maximum, several local parameters were estimated based on theoretical or contemporary analogues to ensure the model represents a realistic scenario. As a result of the uncertainty raised by these estimations, as well as those highlighted in chapter 5, results from the 2D modelling exercise aim to answer the key questions previously defined and provide basin scale, high level estimations of the impact of geological and glacial processes on the evolution of the Melville Bay petroleum systems. The parameters that define the glacial dynamics within the model include:

1. The number of glacial cycles: 11 seismic packages of glacigenic progradational sediments have been identified within the MB-TMF (mu-A) that have been correlated with regional and global climate proxies to give an approximate age of deposition (Knutz et al., 2019). These packages suggest a minimum of 11 major phases of ice advance to, and retreat from, the shelf edge occurred on the Melville Bay margin since ~2.7 Ma. To reduce model complexity and simulation time, the 11 glacigenic progradational seismic units, and corresponding glacial cycles, have been combined into six cycles. The cycles were combined based on the seismic geomorphological character of the progradational units (units that could be joined into larger progradational packages were often combined) (Fig. 6.3), the age and duration of the associated glacial cycle (so that they cover broadly equivalent time intervals), and the amplitude of sea level change based on the Miller curve (so glacial cycles of similar magnitude are grouped together) (Fig. 6.3) (Miller et al., 2011) (grouped cycles: 1, 2, 3-4, 5-7, 8-9 and 10-11).
2. Timing: The progradational units have been correlated against the global sea level curve (Miller et al., 2020) in an attempt to determine the age of each cycle (Fig. 6.3)

(Knutz et al., 2019). These data were used to estimate the duration of ice sheet growth, the period of ice sheet stability and retreat (Fig. 6.2 and Appendix 6A).

3. Ice Thickness: Ice sheet grounding is evidenced by seismic geomorphological interpretations across the Melville Bay shelf (Newton et al., 2020; 2017). Based on estimations that consider contemporary water depths (Fig. 6.1), expected water level drops during glacial stages (Miller et al., 2011), isostatic depression (Fleming and Lambeck, 2004; Lecavalier et al., 2014) and an estimation of minimum ice sheet thickness to prevent floatation using Archimedes' principle (Archimedes, ca. 220 BC; Noerdlinger and Brower, 2007), the minimum ice sheet thickness on the shelf would likely have needed to be at least 1000-1500 m in order to remain sufficiently grounded to produce the observed landform records.
4. Isostatic adjustments: Within the model, airy-type isostatic subsidence and rebound occurs in response to the ice load, with tilting occurring near the ice margin between ice covered and non-ice covered areas. Isostatic depression will not, however, affect subsurface temperature, pressure and compaction beneath the ice sheet, as this is controlled by the ice thickness and boundary conditions. Ice loading can cause isostatic depression of the Earth's crust up to one third of the ice sheet thickness (Van den Berg et al., 2008). This likely represents a maximum case scenario, with an adjustment of 500 m beneath the maximum ice thickness; a value similar to other estimates of glacial rebound after the last glacial cycles in the Barents Sea and on the mid-Norwegian Shelf (400-600 m) (Fjeldskaar and Amantov, 2018), as well in areas of the North Sea (up to 400 m) (Kjemperud and Fjeldskaar, 1992).
5. Base ice temperature: Glaciers on the Melville Bay shelf were most likely warm based, due to ice thickness and ice streaming, as is evidenced by glacial landforms indicative of fast ice flow (Newton et al., 2021). Therefore, it was assumed the base of the ice was at the pressure melting point (Andreassen et al., 2017; Benn and Evans, 2010) and a temperature of -1 °C was used.
6. Paleo-water depth at ice: ~2/3 of the ice was assumed to be below sea level, similar to what has been observed for contemporary ice streams of comparable size in Antarctica. These estimates have been derived from Bedmap2 data capturing ice thickness, bedrock depth and sea level (Fretwell et al., 2013).
7. Ice sheet advance distance: Paleo-shelf breaks were identified for the 11 progradational units representing the 11 cycles of ice sheet advance and retreat (Fig. 6.2b) (Knutz et al., 2019). These paleo-shelf breaks are used to determine the limit of grounded ice during each glacial cycle.

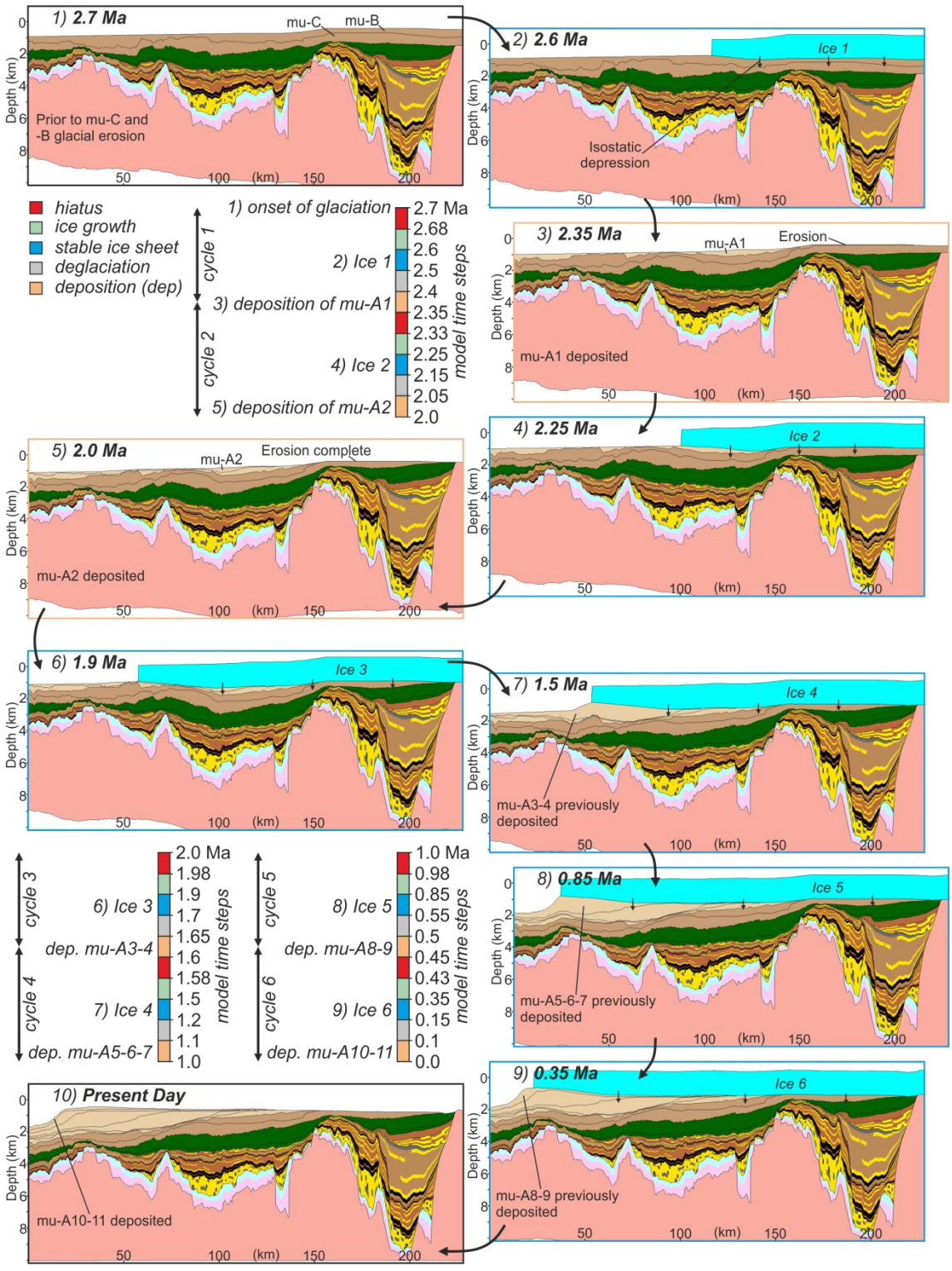

Figure 6.5. Ice sheet model evolution from 2.7 Ma to present day | 10 model cross sections at individual time steps display the 6 cycles of ice advance and retreat across the shelf, as well as glacial erosion on the inner shelf during the first two glacial cycles and the re-deposition of sediment to the outer shelf creating mu-A and the Melville Bay Trough Mouth Fan, prograding the shelf edge by ~100 km. Individual time steps applied within the model for each stage of the 6 glacial cycles are shown.

Ice within PetroMod is considered as another lithology which has the density of frozen water, zero porosity and is considered impermeable and incompressible (Cavanagh et al., 2006; Hantschel and Kauerauf, 2009). The distribution of ice across the model is controlled by erosion and paleo-water depth 2D maps, which are used to simulate the effect of ice growth, stability and retreat, before the deposition of glacigenic sediments related to that glacial cycle (Figs. 6.3, 6.5 and Appendix 6A). Adding the ice load to the model, required the base model to be modified (Table 6.1 and Appendix 6A; Chapter 5), affecting periods after the onset of glaciation at ~2.7 Ma (Knutz et al., 2019). The first step was to divide the mu-A stratigraphy into sediment packages that were deposited within each of the six glacial cycles chosen to be modelled (Figs. 6.2 and 6.4-5). Seismic depth interpretations of these progradational unit boundaries were imported into the model and were added to the existing present day geometry (Fig. 6.4). Higher resolution modelling (0.02-0.3 Myr time steps; Fig. 6.5) was used from 2.7 Ma, with a time step inserted for every stage (hiatus, growth, stability, deglaciation, deposition) of the six glacial cycles (Figs. 6.3, 6.5 and Appendix 6A). This increased model complexity and simulation time significantly, with 29 time steps being modelled between 2.7 Ma and present day (instead of just two at 2.2 and 1.9 Ma for the base model; Chapter 5) (Appendix 6A).

Ice thickness is controlled by a 2D erosion map (a thickness value is defined at every vertical grid point (GPs) within the model) (Hantschel and Kauerauf, 2009) at each of the glacial time steps, which is then removed at the deglaciation step (Fig. 6.3 and Appendix 6A). Paleo-water depth maps are also inserted at each of these time steps to control both the depth of the ice (2/3 submerged) and the degree of isostatic depression beneath the ice (Fig. 6.5). Paleo-water depth maps assigned at interglacial events define the morphology of the paleo-margin, including the shelf break position, prior to the next cycle of glaciation advance across the defined paleo-shelf. Erosion and paleo-water depth maps are created for each of the six glacial cycles, with the ice extending further offshore during each cycle, according to seismically identified paleo-shelf break positions for the preceding interglacial (Fig. 6.2b) (Knutz et al., 2019). The ice thickness changes from 1000 m at the ice margin to 1500 m over a distance of 160 km (Fig. 6.5). This represents an estimation of the paleo-ice thickness that has been based on the downstream thickness variations of several analogous ice streams in Antarctica (Fretwell et al., 2013).

Importantly, within PetroMod, sub-glacial erosion cannot be simulated simultaneously with deposition at one single grid point. Therefore, as the ice thickness is controlled by an erosion map, all glacigenic deposition for each cycle (mu-A sub-units), must occur after the ice has been removed (an unlikely scenario in reality), and is the reason that deposition is

assigned to a period of 0.05-0.1 Myr after deglaciation (Appendix 6A). The final step is to assign the temperature at the sediment-water (or -air if above sea level) interface, in order to control the temperature at the base of the ice. As the ice is seen as a lithology, the sediment-water (or air) interface is assumed to be the top of the ice package and not the base, therefore, a temperature needs to be selected that will increase through the ice package, relative to the ice thickness and thermal gradient, resulting in a temperature of -1 °C at the ice-sediment interface.

Model simulation in PetroMod can then be conducted, which involves the reconstruction of geometries and the forward modelling of several geological processes and parameters through time, including pressure and compaction calculations, temperature and heat flow analysis as well as the modelling of the hydrocarbon system (Hantschel and Kauerauf, 2009). Fluid migration was modelled using high-resolution Darcy flow and Invasion Percolation within low and high permeability cells respectively (Hantschel and Kauerauf, 2009). Within both the thermogenic and biogenic scenario models, only results after 2.7 Ma have been modified compared to the base model (Chapter 5).

6.4.2. Gas Hydrate Stability

The calculation of pressure and temperature conditions within the model allows for gas hydrate stability and the depth of the phase boundary (the transition between gas hydrate and free gas) to be predicted for every time step. This estimation uses the pressure temperature phase relationship provided by Sloan and Koh (1990), and assumes pure methane and an average sea water salinity of 35 parts per thousand (Hantschel and Kauerauf, 2009). The resolution of the predicted phase boundary depth is limited by the cell size determined by the number of sub-layers defined for the formations within the gas hydrate stability zone (GHSZ). A single model cell can only be defined as either stable (for gas hydrate) or unstable. Therefore, the number of sub-layers were increased for gas hydrate stability simulations to allow for a more accurate prediction (mu-B: 10, mu-C: 25, mu-D: 20 – original layering on Table 6.1).

6.5. Results and Discussion

Six cycles of glaciation across the Melville Bay continental shelf have been modelled to help predict the possible impacts of glaciation on subsurface temperature, pressure and sediment compaction. The model considers both glacial erosion and sediment redistribution across multiple glaciations, as well as the effect of shorter duration glacial loading and unloading cycles (Fig. 6.5). It is the predicted impact of these processes on subsurface conditions and the petroleum systems that will be unravelled within this section,

with particular focus on hydrocarbon generation and expulsion, fluid migration and gas hydrate stability.

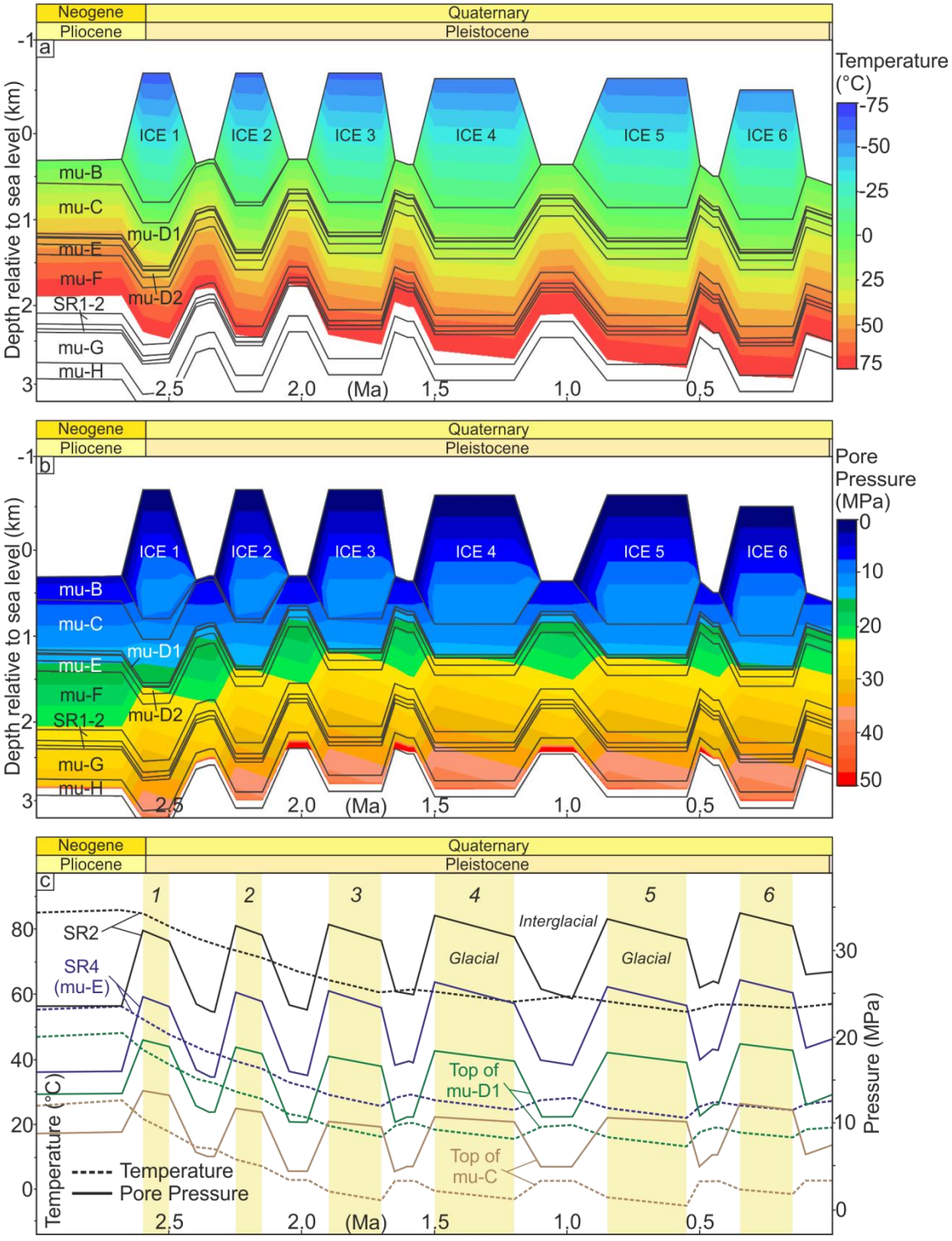

Figure 6.6. Burial history, temperature and pressure | A 1D burial history extraction at the Melville Bay Ridge since 3.0 Ma, with unit burial depths overlaid by subsurface temperature (a) and pore pressure (b). The location of the extraction is shown on Fig. 6.4. The graphs display the impact of glacial erosion throughout the first two glacial cycles, decreasing subsurface temperatures and pore pressures, as well as repeated fluctuations in subsurface conditions beneath the ice load. c) A time series graph from the same location, displaying the average variation in pore pressure and temperature since 3.0 Ma, within key stratigraphic packages (SR2, SR4 and the top of mu-D1 and -C). Note how temperature and pressure increases upwards on (c), opposite to (a) and (b) to ease comparison.

6.5.1. Glacial Erosion and Sediment Redistribution

Extensive glacial erosion and the redistribution of sediment to the outer shelf, has caused a dramatic transformation of the margin, including over ~100 km of shelf edge progradation since 2.7 Ma (Fig. 6.5) (Knutz et al., 2019; Newton et al., 2021; 2017). On the inner shelf, above the MBR and MBG, up to ~500 m of post-rift sediments have been eroded due to over deepening and incision of the shelf during the gradual development of the cross shelf trough by ice stream erosion (Figs. 6.1-2 and 6.5; Chapter 5) (Cox et al., 2021; Freire et al., 2015; Newton et al., 2021; Slabon et al., 2016). The eroded sediments represent muddy contourite successions of mu-B and -C (Knutz et al., 2015), which due to recent deposition and lack of burial, represented soft, uncompacted sediments that would have been easily eroded by glacial action (Amantov et al., 2011). For this reason, it is likely that the majority of erosion experienced on the inner shelf, occurred during the first few glacial cycles (erosion was split between cycles 1 and 2; Fig. 6.5) (Knutz et al., 2019).

These eroded sediments have been re-deposited along with large quantities of sediment from onshore Greenland as part of the Melville Bay Trough Mouth Fan (mu-A) (Gregersen et al., 2019; Knutz et al., 2019; Newton et al., 2021). The deposition of the thick progradational units has caused significant burial and compaction of the underlying sediments on the outer shelf and has effectively caused the entire margin west of the MBR, to tilt in a basinward direction (Figs. 6.2 and 6.4-5) (Cox et al., 2021; Gregersen et al., 2019). This tilt of ~0.5° (over the ~100 km section between the two extraction points shown on Fig. 6.4), is likely intensified by isostatic adjustments that have occurred in response to the load redistribution from the hinterland and from inner to outer shelf (Fjeldskaar and Amantov, 2018; Riis and Fjeldskaar, 1992; Zieba and Grover, 2016), and likely has influenced regional fluid migration since 2.7 Ma (Cox et al., 2021).

The load redistribution also is predicted to have affected subsurface pressure and temperature across the margin. Pressure is a 3D concept however, and within a 2D model, stratigraphic packages and the dissipation of pressure are not extended away from the 2D plane. These limitations cause pressure (and fluid volume) calculations within the model to represent high level estimations, and this should be considered when analysing the results. The model predicts that sediment removal on the inner shelf during the first 2 glacial cycles causes a reduction of both pore pressure by ~5 MPa and temperature by ~25 °C at the top of the mu-D1 package above the MBR (Fig. 6.6). In general, the impact of erosion on temperature and pressure on the inner shelf is greatest in the shallow section, meaning deeply buried source rocks are less affected (Fig. 6.6c). In contrast, within the outer section of the SKB (Fig. 6.4), additional burial beneath the glacigenic sediment wedge (mu-A) has

caused the top of the mu-D1 package to experience increased pore pressures by ~6.5 MPa and a temperature increase of ~15 °C. Variations in pressure and temperature across the shelf have likely impacted the hydrocarbon system, influencing processes such as fluid migration and source rock maturity (e.g. Medvedev et al. (2019), with the potential for biogenic gas generation within shallow sediments being particularly influenced by the considerable (~-25 to +16 °C) temperature variations since 2.7 Ma (Cox et al., 2021; Stopler et al., 2014) (Chapter 5). Additionally, the increase in pressure and temperature on the outer shelf during this period is the probable cause for increased hydrocarbon generation and expulsion that is predicted to have occurred within the SKB since 2.7 Ma (Chapter 5).

6.5.2. Ice Loading Cycles

The impact of relatively short duration glacial loading and unloading cycles are superimposed on the prolonged effects of glacial erosion and deposition. The ice during glaciation is assumed to have been grounded on the seabed, evidenced by numerous examples of buried subglacial landforms (Newton et al., 2021; 2020), causing the ice to directly impact subsurface temperature, pressure and sediment compaction, as well as causing isostatic subsidence and rebound (Fjeldskaar and Amantov, 2018). Ice sheet basal temperatures are defined as ~-1 °C (Fig. 6.6) (see section 6.4.1), and these temperatures influence the subsurface temperature field throughout the periods of ice growth, stability and deglaciation. Beyond the ice margin, PetroMod's auto-SWIT temperatures (re-calculated considering paleo-water depth) were used at the sediment-water boundary (Hantschel and Kauerauf, 2009; Wygrala, 1989).

Subsurface temperatures are estimated to be significantly affected by the ice cover, with underlying sediments being cooled by ~5-6 °C between the onset of ice growth and deglaciation (Fig. 6.6a), before returning to temperatures close to the preceding interglacial once the ice is removed. This estimation of glacial cooling correlates well with similar studies conducted by Grassmann et al. (2010) and Johansen et al. (1996) who estimated glacial cooling rates of 7 °C in the Mittelplate area of northern Germany and in the Norwegian North Sea, respectively. The temperature change observed does not occur instantaneously; instead, the cooling permeates downwards through the sediments during the period of ice sheet stability, to an amount dependant on the duration of each glacial cycle, before warming begins at the onset of deglaciation (Fig. 6.6a). The temperature does not fully re-equilibrate during each relatively short interglacial period (0.7-1.2 Myr), and therefore, subsurface temperature cumulatively decreases across the period of glaciation. Over the last 2.7 Myr, the model predicts that subsurface temperature has been cooled by

~28 °C on the inner shelf (at ~350 m present day burial depth (Fig. 6.6)); however, ~25 °C of this cooling occurs during the first two glacial cycles in response to glacial erosion.

The oscillating ice load is similarly predicted to have a significant effect on subsurface pressure. The addition of the ice lithology effectively increases the lithostatic column, with the weight of the ice being supported by subsurface pore waters (Cavanagh et al., 2006; Grassmann et al., 2010), causing a dramatic increase in pore pressure beneath the ice load (Fig. 6.6b) (Thorson, 2000). Pore pressure within the post-rift stratigraphy beneath the ice (Fig. 6.6b), is repeatedly increased by ~5 MPa during glacial periods (at the top of mu-D1). The pore pressure increase is instantaneous with loading, but partly dissipates throughout the period of ice sheet stability (Fig. 6.6b-c), likely due to the excess pore pressure pushing or draining fluids out of the sediments (Strout and Tjelta, 2005; Urlaub et al., 2020), before returning to normal pressures when the load is removed. Pore pressure may have increased by ~3 MPa since the end of glacial erosion at 2.05 Ma, but this is attributed to increased subsidence and water depth during this period (Figs. 6.5 and 6.6).

The repeated excursions in both temperature and pressure in response to ice loading, has almost certainly impacted the underlying hydrocarbon system, affecting processes such as thermogenic and biogenic maturation, fluid migration, gas hydrate stability and possibly the phase behaviour of existing accumulations if the liquid phase is present (Doré and Jensen, 1996; Grassmann et al., 2010; Medvedev et al., 2019; Zieba and Grover, 2016). Variations in pressure (burial) have significantly influenced sediment compaction, leading to variations in reservoir quality and seal strength (see section 6.5.4) (Doré et al., 2002b; Fjeldskaar and Amantov, 2018). For example, the porosity of sands within mu-D2 (the reservoir on the MBR crest) has decreased in the range of ~1.5% (from 32.5% to 31%) since the onset of glaciation, with the majority of the compaction occurring during the first glacial loading cycle (see section 6.5.4). Additionally, the ice loading cycles will have caused differential isostatic adjustments in response to the variable load, as the ice sheet advanced and retreated across the shelf (Fjeldskaar and Amantov, 2018; Kjemperud and Fjeldskaar, 1992; Zieba and Grover, 2016). This process will have tilted the underlying stratigraphy, creating see-saw motion between glacial-interglacial cycles, and would have likely affected hydrocarbon trapping, potentially causing spillage and leakage to the subsurface. However, the complexities of isostatic adjustments were not modelled in this study.

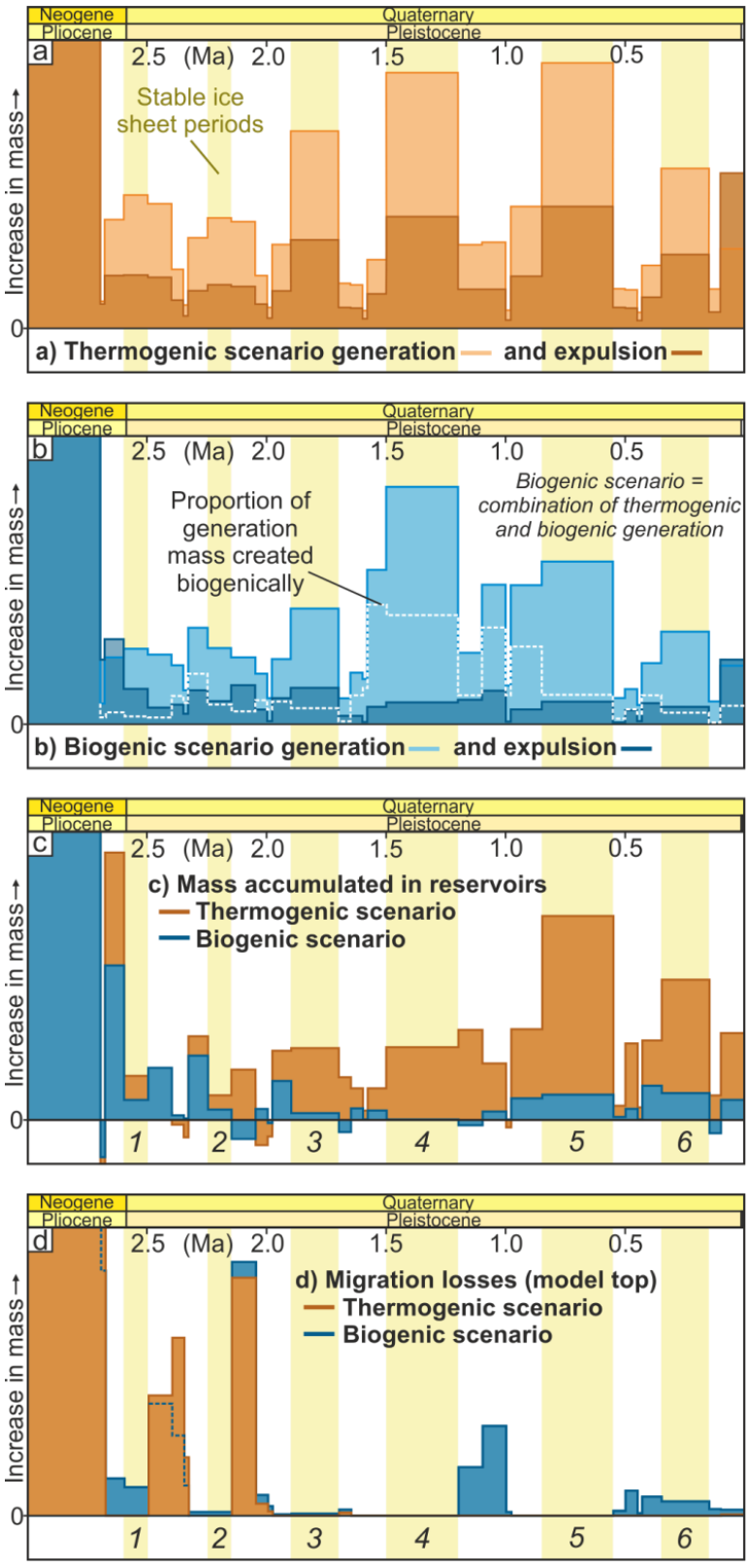

Figure 6.7. Hydrocarbon generation, accumulation and losses | Graphs depicting the relationship between the 6 modelled glacial events (stable ice sheet periods shown in yellow) and variations in hydrocarbon generation and expulsion for the thermogenic (a) and biogenic (combination) (b) scenario models, accumulated reservoir mass (c) and migration losses through the top boundary of the model (d). The vertical scales on a-d are not directly comparable. In (c), a reservoir is considered as any model cell that has permeability above a defined threshold (2.01 log mD), causing migration in that cell to be modelled by the Invasion Percolation migration method during simulation (Hantschel and Kauerauf, 2009). On each graph, the data is displayed for the entire model, per individual time step event.

6.5.3. Hydrocarbon Generation and Expulsion

Sediment redistribution and the cyclic loading and unloading of the Melville Bay shelf, has caused considerable variation in subsurface pressure and temperature over the last 2.7 Ma (Fig. 6.6). These conditions control the thermal maturity of source rock horizons (McCarthy et al., 2011), thus the model predicts that glaciation has impacted hydrocarbon generation and expulsion significantly across the whole modelled section (Fig. 6.7). Thermogenic hydrocarbon generation and expulsion from syn-rift source rock intervals is shown to repeatedly increase during glacial periods (Fig. 7a). This increase is likely caused by the additional burial experienced beneath the ice load, especially above the SKB, elevating pressure and importantly, temperature, at the source rock depths. The change in pressure during glacial periods, however, outweighs only very minor temperature variations that occur at the depth of the source rock horizons (Fig. 6.6). This is due to pressure affecting the subsurface instantaneously beneath the load (Thorson, 2000), but transient temperature permeating slowly to greater depths (Johansen et al., 1996). On the inner shelf, across the first two glacial cycles, hydrocarbon generation and expulsion within the model decreases in response to glacial erosion (Fig. 6.7a). The significant reduction in pressure (~5 MPa) and temperature (~25 °C) as a result of erosion (Fig. 6.6), has considerably reduced the potential for hydrocarbon generation within the MBR and MBG area (Fig. 6.7a); a process that is thought to have affected other basins in the Barents Sea and Norwegian Shelf (Doré et al., 2002b; Henriksen et al., 2011; Nyland et al., 1992). The increase in generation across cycles 3-5 reflects the progressive advance of the ice sheet across the SKB, with more of the basin experiencing additional burial beneath the ice load during each cycle, enhancing the maturity of Cretaceous source rock intervals (Fig. 6.7) (Chapter 5).

At the onset of glaciation at ~2.7 Ma, biogenic hydrocarbon generation may have been occurring within shallow post-rift sediments (the upper part of mu-D1 and mu-C) across the shelf (Cox et al., 2020b) (Chapter 5). As biogenic generation occurs at relatively shallow depths (peak generation at 50°C Stopler et al. 2014), it is likely more sensitive to pressure and, in particular, temperature changes caused by ice loading. For the biogenic scenario model (Fig. 6.7b), the majority of the increase in the generation of hydrocarbons observed during glacial periods, is attributed to thermogenic source rocks within the SKB (Figs. 6.7b and 6.8). Biogenic generation is instead, significantly reduced beneath the ice load during the first 3 glacial cycles (Figs. 6.7b and 6.8b) as a result of reduced temperatures from glacial erosion on the inner shelf (~25 °C; Fig. 6.6) and sediment cooling beneath the ice load (Figs. 6.6-8). Reduced temperatures cause the biogenic maturity zone to deepen into

formations that have already exhausted their biogenic potential whilst buried at shallower depths in the past (Stopler et al., 2014) (Chapter 5). This effect is apparent during the first glacial cycle (Fig. 6.8b), where biogenic generation beneath the ice dramatically decreases, but is maintained beyond the ice margin (Fig. 6.8a-b). The temperature change from repeated ice loads and glacial erosion on the inner shelf, cause biogenic generation in areas above the MBR to cease at 2.6 Ma. This may have implications for gas hydrate formation above the MBR (see section 6.5.5), as continued biogenic gas generation has been suggested as a mechanism of supplementing gas hydrate deposits that have dissociated in response to glacially induced variations in the thickness of the gas hydrate stability zone (GHSZ) (Cox et al., 2021; Grassmann et al., 2010; Ker et al., 2019).

By the fourth glacial cycle, the thick package of mu-A3-4 has been deposited (Figs. 6.4-5 and 8d), and this additional thickness, as well as the ice load of cycle 4, causes a large section of mu-C and -B to enter the biogenic generation window, increasing hydrocarbon generation and expulsion (Figs. 6.7-8). Similarly, thermogenic generation within deeper source rocks in the SKB is also predicted to increase beneath the additional sediment load at this time (Figs. 6.7b and 6.8d-e). After glacial cycle 4, biogenic generation continues to occur within mu-C and -B beneath the area of glacial deposition up to present day but is observed to decrease during glacial periods in response to lowered subsurface temperatures (Figs. 6.7b and 6.8). This continued generation on the outer and mid-shelf, represents the most likely source of the gas that has been interpreted to exist within glacial clinoforms of mu-A (Cox et al., 2021; Cox et al., 2020b) (Chapter 5).

6.5.4. Fluid Migration and Reservoir Leakage

Glacial erosion, sediment re-deposition and the loading and melting of ice on the shelf since 2.7 Ma, is predicted to have significantly influenced hydrocarbon migration and trapping. The mass of trapped thermogenic and biogenic hydrocarbons within the model decreases over the first two glacial cycles in response to erosion (Fig. 6.7c), before increasing during cycles 3-5 due to enhanced generation and accumulation within the SKB (Figs. 6.7-8). Significant reductions in accumulated reservoir hydrocarbon masses are predicted to occur immediately at the onset of ice load removal (deglaciation) (Fig. 6.7c), and this correlates with significant increases in migration losses at the top of the model during the same interglacial periods (Fig. 6.7d). The same effect is observed for the reservoir on top of the MBR crest (Figs. 6.2c, 6.4 and 6.9), where a significant reduction in the trapped hydrocarbon mass is experienced at the onset of load removal during glacial cycle 1 (Fig. 6.9b).

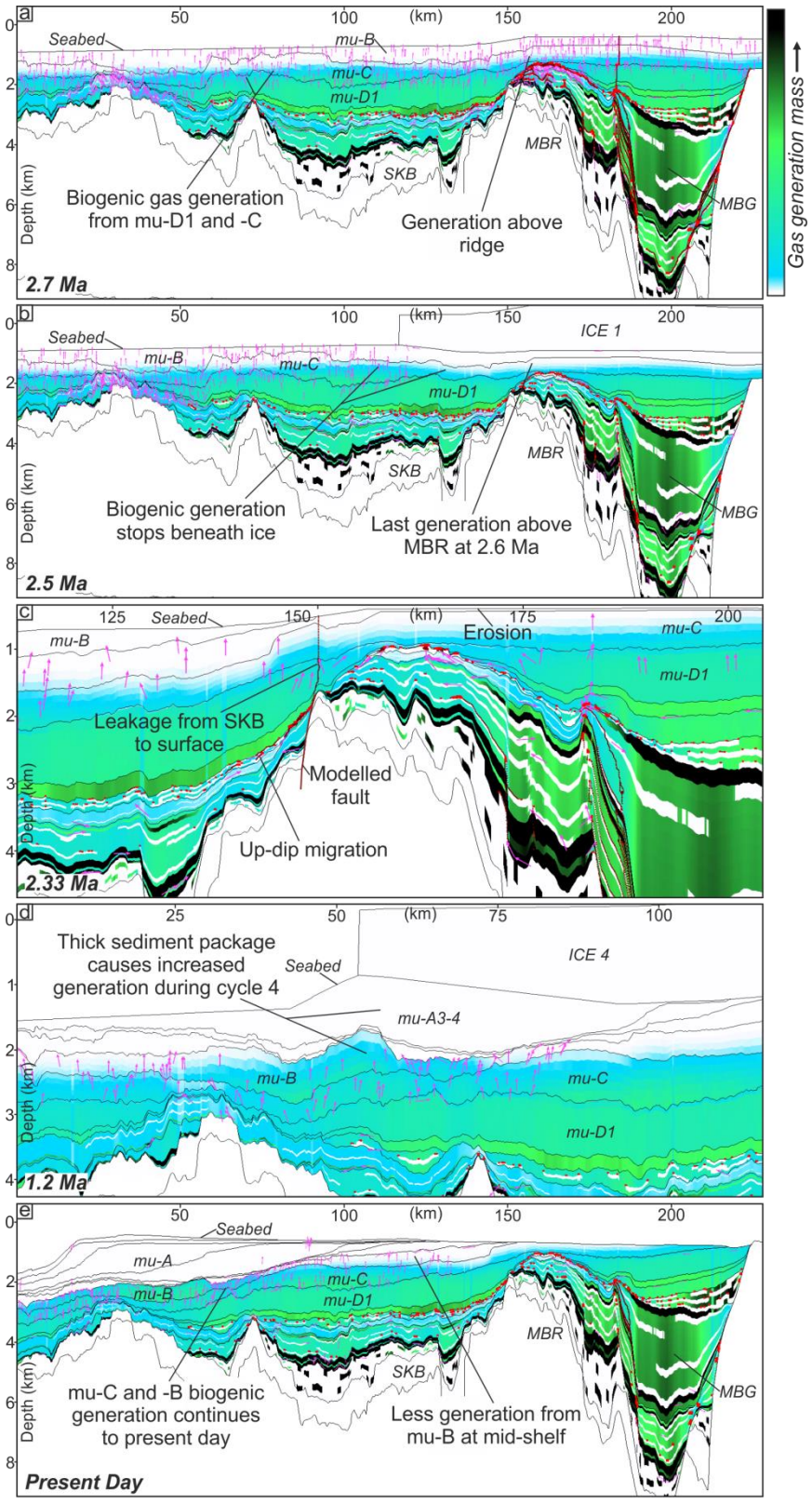

Figure 6.8. The impact of glaciation on biogenic gas generation, expulsion and migration | Five cross sections of the biogenic scenario model are displayed (a-e) at individual time steps, displaying an overlay (gas generation mass), that depicts the cumulative mass of gas generated within each cell of the model (both biogenic and thermogenic). Note the different horizontal scales of sections at different times defined by the distance scale. Hydrocarbon migration within the biogenic scenario model is shown via purple vectors. Biogenic generation and migration is shown to significantly reduce beneath the ice load, but increase beneath re-deposited sediment packages at the outer shelf. Migration and seal bypass through fault conduits into the shallow subsurface is predicted to occur, as well as the continuation of biogenic generation and migration up to present day on the mid and outer shelf. Abbreviations used include Melville Bay Ridge (MBR), Melville Bay Graben (MBG) and South Kivioq Basin (SKB).

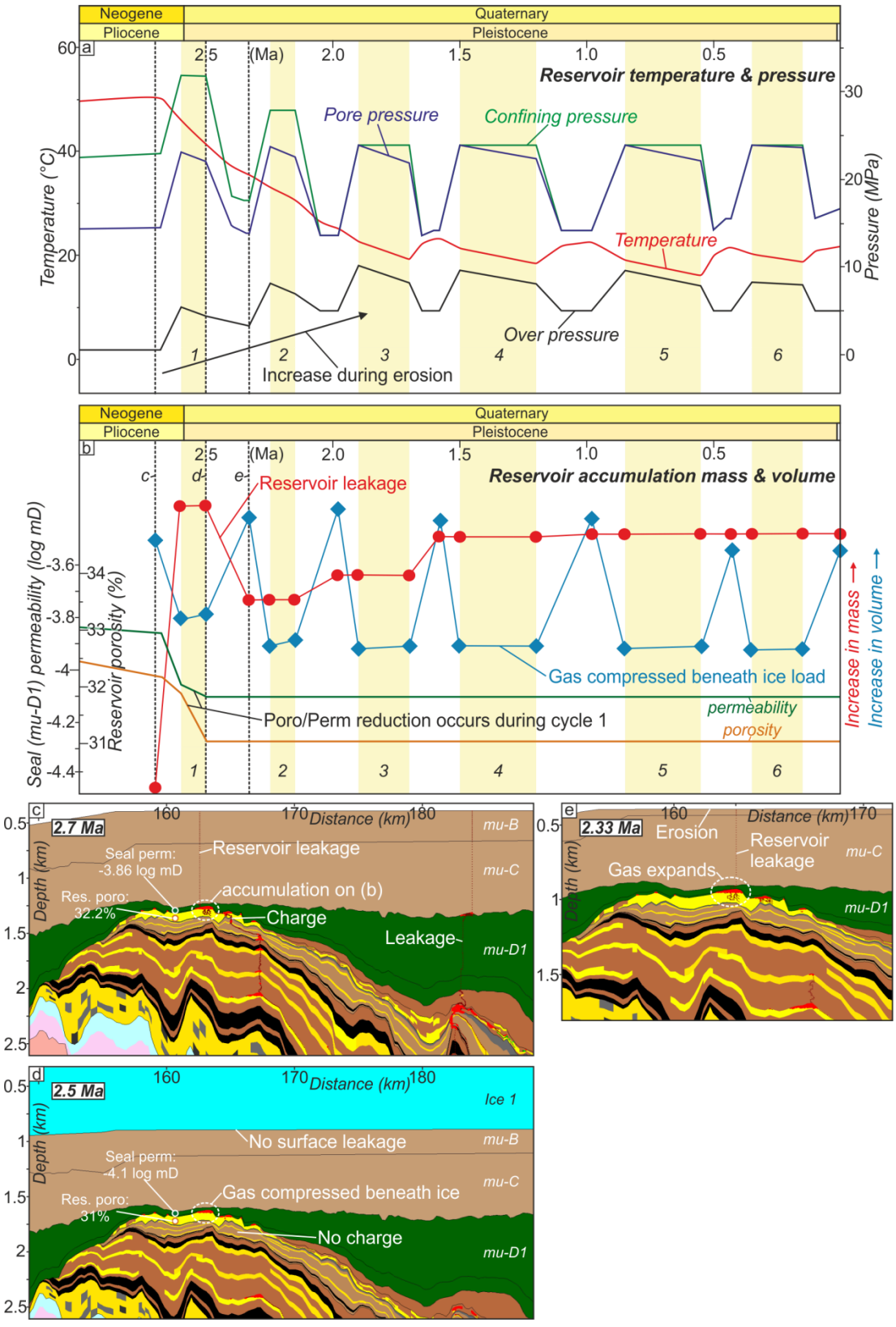

Figure 6.9. Variations in reservoir conditions, leakage and accumulation volumes and masses | a) a graph displaying the influence of ice loading on pressure and temperature conditions within the reservoir on the Melville Bay Ridge crest (mu-D2). b) a graph depicting the variation in volume and mass of a vapour phase (methane) accumulation within the reservoir on the MBR crest throughout the period of glaciation, as well as the impact of glacial loading on reservoir porosity and overlying seal (mu-D1) permeability. The gas accumulation volume is shown to repeatedly expand and contract due to pressure changes associated with ice loading. c-e) Three model cross sections at individual time steps highlighting the impact of glacial loading and erosion on reservoir conditions and leakage, as well as gas expansion. The specific gas accumulation described on b is shown on c.

During periods of ice loading, pore pressure within the reservoir on the crest of the MBR is estimated to increase by ~8.5-10 MPa (Fig. 6.9a). Additionally, the reservoir has experienced overpressures of ~10 MPa throughout glaciation (since 2.7 Ma) and remains overpressured (~5 MPa) at present day. This may be due to increased sediment compaction through ice loading restricting fluid outflow (Goffey et al., 2016). Overpressure repeatedly increased in the range of ~5 MPa in response to ice loading, before returning to interglacial, but still elevated pressures (Fig. 6.9). Whilst the ice load is in place, reservoir fluids remain stable and no re-migration or leakage occurs, likely due to the increased stress state of the subsurface effectively locking the fluids in place (Goffey et al., 2016; Johnston, 2000). Major pressure changes (Fig. 6.9) occur during deglaciation however, as the lithostatic load is removed (Fjeldskaar and Amantov, 2018; Lund et al., 2009), with overburden erosion exacerbating these changes. The resulting reduction in confining pressure may occur before elevated fluid pressures have had time to re-equilibrate (Corcoran and Doré, 2002), promoting rock failure and fluid leakage (Fig. 6.9). Although modelling processes such as fracturing were not attempted in this study, these elevated reservoir pressures could have resulted in the creation of tensile fractures within the top seal (mu-D1) via Coulomb failure (Hubbert and Rubey, 1959; Petrie et al., 2014), something that can lead to the loss of pre-existing hydrocarbons (Corcoran and Doré, 2002; Hermanrud and Nordgard Bolas, 2002; Karlsen and Skeie, 2006). This process may represent the genesis of the dense network of near-vertical fractures that are observed on seismic data within the top seal, inter-connected by small pockets of potentially leaked gas (Cox et al., 2021). Reservoir leakage is predicted to end by the onset of glacial cycle 2 at 2.25 Ma (Figs. 6.6 and 6.9b), with the accumulation never again reaching the same mass as experienced during the first glacial loading period (Fig. 6.9a). This may suggest this process has decreased the seal capacity (Corcoran and Doré, 2002; Nordgard Bolas et al., 2005), and the accumulation mass reached at 1.6 Ma (which remains constant to present day), represents the maximum trap capacity in the most recent events.

Furthermore, sediment compaction beneath the first cycle of ice loading impacted reservoir porosity (on the ridge crest) (reduced by ~1.5%) and top seal (mu-D1) permeability (decreased by ~0.25 log mD) (Fig. 6.9b). This may have also influenced factors such as hydrocarbon volumes (due to reduced pore space), overpressure creation, as well as the potential for fluid leakage, with decreased seal permeability possibly contributing to why the reservoir is not predicted to leak after 2.25 Ma (Fig. 6.9) (Ingram and Urai, 1999). Within the SKB, reduced seal permeability is thought to also impact upward fluid migration, with seal (mu-D1) bypass ending at the onset of glacial cycle 2. A pulse of fluid migration does occur through a fault on the western edge of the MBR (Fig.

6.8c) at the onset of deglaciation during glacial cycle 1, but this again ends at 2.25 Ma, either due to the more efficient seal or a lack of hydrocarbon migration from the deeper basin. This means that the last period of upward fluid migration via conventional mechanisms into the post-rift stratigraphy above the MBR, potentially occurred prior to 2.25 Ma. This may explain why no recently created fluid escape features are observed at the seabed (Cox et al., 2021), as any feature formed by fluid escape prior to 2.25 Ma, would have most likely since been removed by glacial erosion. Contrastingly however, the substantial excursions in subsurface pressure between glacial and interglacial periods predicted within the model (Figs. 6.6 and 6.9), are of sufficient magnitude to potentially cause the reactivation of faults, promoting seal bypass (Goffey et al., 2016; Grollimund and Zoback, 2003; Ostanin et al., 2017). This may have affected both syn- and post-rift faults (Cox et al., 2021), including the fault on the western flank of the MBR (Fig. 6.8c), possibly allowing pulses of fluid leakage to occur during the latter glacial cycles, most likely during periods of deglaciation (Ostanin et al., 2017). Still, it is possible that these fluids were either converted into or trapped beneath the extensive gas hydrate deposits that are predicted to have been stable since 5.33 Ma (see section 6.5.5; Chapter 5; Cox et al., 2020b), again potentially restricting fluid migration to the seabed (Chand and Minshull, 2003; Grassmann et al., 2010).

Cyclic reservoir pressure variations are predicted to have caused gas compression and expansion during glacial and interglacial periods, respectively, causing the volume of reservoir accumulations to vary dramatically (Fig. 6.9) (Ostanin et al., 2017). The accumulation of vapour phase hydrocarbons (mainly methane) predicted to exist within the MBR crest reservoir (Chapter 5), is compressed beneath the ice load, with the gas being more sensitive to these pressure changes when at a shallower burial depth (more compression after erosion) (Fig. 6.9b) (Fjeldskaar and Amantov, 2018). This cyclic process may have significant implications for reservoir leakage at the spill point, especially when considering this reservoir as a 3D structure in the real world which may be filled to spill (Cox et al., 2020a). During ice loading, a compressed volume may allow additional gas to migrate into the reservoir, which during deglaciation and gas expansion, will be pushed out of the reservoir at the spill point (Tasianas et al., 2016). This effect is not unique and has likely affected many reservoirs on glaciated margins worldwide (Doré et al., 2002a), such as the Snøhvit Field in the Barents Sea (Nyland et al., 1992; Tasianas et al., 2016) and also the Troll field in the Norwegian sector of the North Sea (Gray, 1987; Nyland et al., 1992).

Finally, temperature within the reservoir on the MBR crest is predicted to have reduced by ~30 °C since 2.7 Ma, with a large fraction of this cooling occurring during the periods

of erosion (Fig. 6.9a). Cooler temperatures may contribute to variable accumulation volumes, whilst also potentially influencing biodegradation of the hydrocarbons within the reservoir, something that is a particular risk due to shallow burial depth (Cox et al., 2020a; Wenger et al., 2002), especially if the reservoir contains wet gases or even an oil rim (Larter and di Primio, 2005).

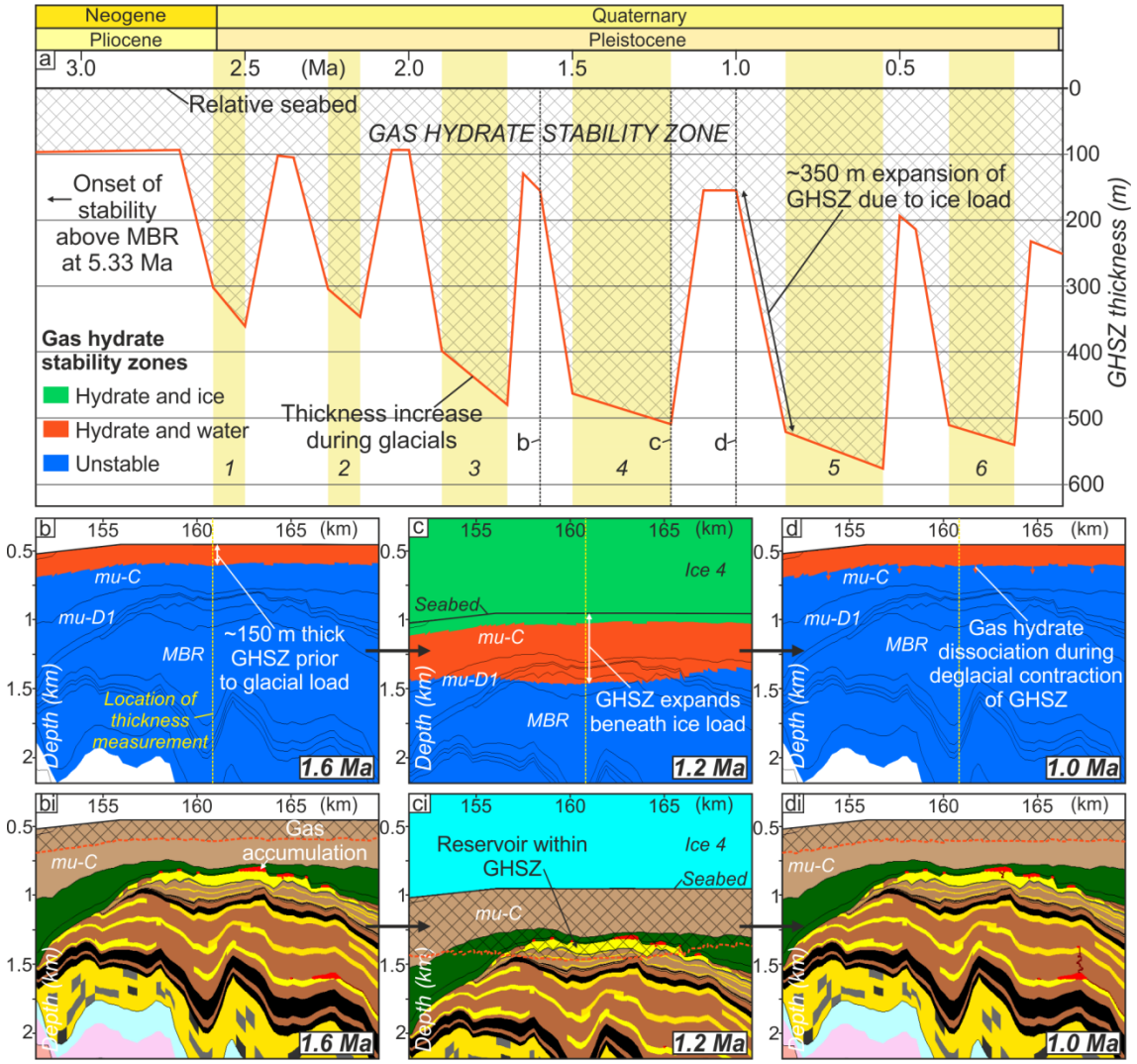

Figure 6.10. Gas hydrate stability zone variations during glaciations | a) a 1D time evolution graph displaying the predicted thickness of the gas hydrate stability zone (GHSZ) above the Melville Bay Ridge (MBR) since 3.0 Ma, and the repeated cycles of stability zone expansion and contraction in response to glacial loading cycles. b/bi-d/di) Three model cross sections at individual time steps displayed with an overlay of the predicted thickness of the hydrate stability zone (b, c and d), with the same stability zone shown on top of the facies model (bi, ci, di). GHSZ expansion during glacial loading is shown to capture the reservoir on the MBR crest. The key for the facies displayed can be found on Fig. 6.4.

6.5.5. Gas Hydrate Stability

The onset of gas hydrate stability across the Melville Bay shelf is predicted at 5.33 Ma (Chapter 5), with the predicted thickness of the GHSZ at present day correlating with identified BSRs on seismic data (Chapter 5) (Cox et al., 2021). Throughout the last 2.7 Myr,

repeated cross-shelf glaciations and extensive glacial erosion on the inner shelf, have cooled the underlying shallow sediments (by up to ~28 °C) (Figs. 6.6 and 6.8) and increased water depths (Figs. 6.1 and 6.5), leading to increased hydrate stability and a deeper phase boundary (between hydrate and free gas) by ~150 m (considering the resolution limited by cell thickness) – see section 6.4.2) (Fig. 6.10) (Grassmann et al., 2010; Kvenvolden, 1993). On top of this prolonged change, the GHSZ is predicted to have repeatedly expanded by several hundred meters during periods of ice loading, before contracting during deglaciation and load removal (Fig. 6.10a). These periods of dramatic expansion and contraction are caused by the cyclic temperature and pressure changes experienced beneath the ice (Figs. 6.6 and 6.9-10) (Grassmann et al., 2010; Tasianas et al., 2018). During glacial cycles 1 and 2, the stability zone expands by ~250 m, but this increases up to ~350 m of expansion during glacial cycles 3-6, with the additional 100 m likely in response to cooler subsurface temperatures after overburden removal (glacial erosion) and progressive cooling by grounded ice (Figs. 6.9 and 6.10) (Doré et al., 2002a; Lerche and Bagirov, 1998). The thickness of the hydrate stability zone also expands slightly (by ~50 m) during each stable ice sheet period, as lower temperatures permeate into the subsurface (Fig. 6.10a).

Within the MBR area, the phase boundary variation by ~350 m between glacial and interglacial periods (Fig. 6.10), suggests extensive hydrate dissociation at the base of the GHSZ during periods of deglaciation (Tasianas et al., 2018). For this dissociation to have occurred, however, significant volumes of gas hydrate forming fluids would need to have migrated into the shallow subsurface during glacial periods to allow additional gas hydrate to form within the expanded zone (Clennell et al., 2000). Although the model suggested hydrocarbon migration into the shallow stratigraphy above the MBR may have ended at 2.25 Ma (Figs. 6.9-10; section 6.5.4), the depth of the present day phase boundary (BSR) on seismic data (~200 m) is deeper than the predicted phase boundary depth during the interglacial periods following glacial cycles 1-4 (Fig. 6.10) (Chapter 5; Cox et al., 2020b). This alternatively suggests that additional hydrate forming fluids must have migrated into the shallow sediments during glacial cycles 5 and 6 (since 1.0 Ma), to expand the hydrate deposits to their present day depth (Clennell et al., 2000; Cox et al., 2021). The source of these fluids may be biogenic generation within organic horizons above the ridge (mu-D1 and -C), as this represents the simplest and shortest migration pathway (Fig. 6.8), or from within the mid and outer shelf (SKB) (Fig. 6.8d-e), with fluids migrating towards the inner shelf, possibly influenced by margin tilt (Fig. 6.5) (Cox et al., 2021). Alternatively, migration from deeper sources is possible, and may have occurred during periods of deglaciation and pressure variations (Figs. 6.7d and 6.9b) (Fjeldskaar and Amantov, 2018; Lund et al., 2009; Ostanin et al., 2017), possibly aided by periods of fault reactivation, promoting fluid

migration and seal bypass along fault planes (Fig. 6.8 and section 6.5.4), something that is already predicted at earlier time steps (Figs. 6.8 and 6.9) (Cox et al., 2021; Tasianas et al., 2016).

Additionally, the expansion of the stability zone possibly caused the reservoir on the MBR crest (Figs. 6.2c and 6.9-10) to enter the GHSZ several times throughout glaciation. This is predicted for glacial cycles 3-6, after glacial erosion on the inner shelf had shallowed the reservoir to less than 500 m burial depth (Figs. 6.5 and 6.10). Therefore, it is possible that methane gas predicted to exist within the reservoir (Chapter 5; Cox et al., 2020a), experienced repeated cycles of conversion to gas hydrate during glacial periods and deeper hydrate stability. This scenario is rare, but a similar process is thought to have converted conventional gas to gas hydrate in both the northern part of the West Siberia Basin (Cramer et al., 1997) and on the North Slope of Alaska (Collett, 1993), due to the expansion of the GHSZ in response to thicker permafrost. The difference here is that any methane converted to gas hydrate would have subsequently dissociated back into free gas during deglaciation (Fig. 6.10). This process may have affected the volume of hydrocarbon in the reservoir, as conversion to gas hydrate results in a volume reduction and greater gas storage capacity (Collett, 1993; Davidson, 1978; Rao and Knight, 2016; Stoll and Bryan, 1979). Additional volumes may have accumulated within the reservoir during glacial periods, before being pushed out due to hydrate dissociation during deglaciation. Gas hydrate conversion may also affect reservoir quality, potentially impacting the pore space and permeability (Lee et al., 2013; Seol and Kneafsey, 2011), as well as reservoir gas saturation, due to the vast amounts of water required for this conversion (Lei and Seol, 2019); water which may still remain in the reservoir today. Still, it is unlikely that the entire reservoir volume was converted to hydrate, due to the relatively short time period that the gas hydrate stability zone was expanded (shorter than the duration of cycles modelled – see section 6.4.1). Instead, it is possible that a hydrate gas cap formed at the top of the reservoir and below this, the reservoir and free methane gas remained unaffected.

Importantly, gas hydrate is predicted to be stable at the seabed throughout the period of glaciation (Fig. 6.10), potentially since 5.33 Ma (Chapter 5). This likely restricted seabed expulsion, with gas hydrates acting as a barrier to upward fluid flow (Chand and Minshull, 2003; Grassmann et al., 2010), possibly leading to free gas becoming trapped beneath the phase boundary; something that is observed on seismic data at present day (Cox et al., 2021). Furthermore, the predicted stability suggests that near-seabed gas hydrate deposits (upper ~100 m) remained relatively unaffected by the considerable variation in subsurface temperature and pressure experienced during glacial loading cycles, and that seabed

dissociation did not occur in response. This is likely due to the large water depths (~650 m) in Melville Bay (Fig. 6.1), causing gas hydrate to be relatively stable (Cox et al., 2021; Milkov and Sassen, 2000). A very different scenario to what is observed at shallower water depths, such as within the Barents Sea (Andreassen et al., 2017). Hydrate dissociation at the seabed likely did occur, however, during the removal of up to 500 m thickness of potential gas hydrate hosting sediments on the inner shelf due to glacial erosion (Fig. 6.5). This may have released a significant volume of gas hydrate into the water column and potentially the atmosphere, likely impacting the climate system (Krey et al., 2009; Reagan and Moridis, 2007; Ruppel and Kessler, 2017).

6.6. Conclusions

A petroleum systems model along a seismic section has been created to test the impact of glaciation on the petroleum systems in Melville Bay, offshore northwest Greenland. The Melville Bay margin has experienced multiple cross-shelf glaciations since ~2.7 Ma, which have caused extensive erosion on the inner shelf, the re-deposition of sediment to the shelf edge, and repeated periods of ice loading. The model simulates the progressive effect of sediment redistribution across the margin, as well as six cycles of ice growth, stability and deglaciation. Glacial processes are predicted to have significantly affected subsurface pressure and temperature conditions, causing considerable reductions (~5 MPa and ~25 °C at the top of mu-D1) and increases (~6.5 MPa and ~15 °C) on the inner and outer shelf, respectively, in response to erosion and sediment re-deposition. Ice loading is predicted to have caused repeated cycles of increased pore pressure (~5 MPa) and decreased temperature (5-6 °C) beneath the ice, with temperatures not fully re-equilibrating during interglacials, leading to a ~3 °C reduction (at ~350 m burial depth) across the entire glacial period.

These variations in subsurface conditions are predicted to have a substantial effect on the underlying hydrocarbon system. Hydrocarbon generation is shown to dramatically decrease due to erosion-related temperature reductions on the inner shelf, but contrastingly increase at the mid to outer shelf beneath the thick package of re-deposited glacigenic sediment. Repeated ice loading is also predicted to impact hydrocarbon generation, with thermogenic generation increasing during glacial loading due to additional burial, but biogenic generation significantly decreasing due to rapid, near surface temperature reductions. Fluid re-migration and reservoir leakage increases during periods of deglaciation and load removal, with the majority of fluid movement occurring during the first two deglaciations as the inner shelf is eroded. Part of this leakage may have occurred due to the removal of the lithostatic load during deglaciation before increased reservoir

pore pressure (8.5-10 MPa) and over-pressure has re-equilibrated, leading to seal fracturing and reservoir leakage. Reservoir porosity is also shown to decrease by 1.5% (32.5 to 31%) in response to sediment compaction beneath the ice and accumulated gas in the reservoir has likely experienced cyclic episodes of gas expansion and contraction throughout glacial and interglacial periods, which may have impacted both reservoir volumes and leakage.

Finally, the reduction in temperature on the inner shelf throughout glaciation is predicted to have increased gas hydrate stability, with the phase boundary depth increasing by ~150 m since 2.7 Ma. During this period however, ice loading and unloading cycles have caused the gas hydrate stability zone to repeatedly expand by 250-350 m during glacial periods, before contracting throughout deglaciation, with this contraction potentially causing extensive hydrate dissociation at the base of the stability zone. Additionally, this expansion possibly caused the gas reservoir on the crest of the Melville Bay Ridge, to enter the hydrate stability zone several times throughout glaciation. This may have caused reservoir gas to repeatedly convert into gas hydrate; a process that requires substantial ingress of water and may have reduced reservoir quality, hydrocarbon volumes and gas saturation. Throughout these considerable variations in the thickness of the hydrate stability zone during glaciation, gas hydrates are predicted to have been continuously stable at the seabed, with dissociation only likely occurring during glacial erosion of hydrate hosting sediments. This insensitivity to such substantial geological and oceanographic condition changes, suggests that near seabed gas hydrate deposits in the deep waters of northwest Greenland would remain stable throughout most scenarios for global warming for the next several decades.

6.7. Recommendations for Future Work

Due to several inputs for glacial dynamics being estimated in this study, the associated uncertainty could be reduced by creating several versions of this model, testing a range of glacial scenarios. Additionally, accurate modelling of the lithospheric flexure response to glacial loading (glacial isostasy), using a dedicated software package, would add to the understanding of paleo-geometries and -water depths. Both of these efforts would reduce uncertainty and may provide a better understanding of the range and severity of glacial impacts. Similarly, only one thermogenic and one biogenic (combination) scenario model were tested, models that represent our interpretation of the most likely case, but other (equally likely) scenarios could also be tested, in order to observe potentially different impacts on the hydrocarbon system. Furthermore, additional modelling methods could be used to reduce uncertainty and provide more dedicated testing of certain impacts to the petroleum systems. These methods, for example, may include testing different time

resolutions, conducting uncertainty analysis of gas hydrate parameters and considering fracturing and geomechanics during glacial-interglacial cycles. Finally, the value of this study would improve if a comparative study was available either within a different location on the Melville Bay margin, or across an analogously glaciated margin also containing a hydrocarbon system, such as the mid-Norwegian shelf or Barents Sea.

References

Acton, G., 2012, Proceedings of the Baffin Bay Scientific Coring Program – Expedition 344S: Reporting by company consortium with eight companies led by Shell, p. 1-842.

Altenbernd, T., Jokat, W., Heyde, I., and Damm, V., 2015, Geophysical evidence for the extent of crustal types and the type of margin along a profile in the northeastern Baffin Bay: Journal of Geophysical Research: Solid Earth, v. 120, no. 11, p. 7337-7360.

Amantov, A., Fjeldskaar, W., and Cathles, L., 2011, Glacial Erosion/Sedimentation of the Baltic Region and the Effect on the Postglacial Uplift, *in* Harff, J., Bjorck, S., and Hoth, P., eds., The Baltic Sea Basin: Berlin, Germany, Springer, p. 53-74.

Andreassen, K., Hubbard, A., Winsborrow, M., Patton, H., Vadakkepuliyambatta, S., Plaza-Faverola, A., Gudlaugsson, E., Serov, P., Deryabin, A., Mattingsdal, R., Mienert, J., and Bunz, S., 2017, Massive blow-out craters formed by hydrate-controlled methane expulsion from the Arctic seafloor: Science, v. 356, p. 948-953.

Archimedes, ca. 220 BC, On Floating Bodies.

Benn, D. I., and Evans, D. J. A., 2010, Glaciers and Glaciation, London, Arnold.

Bojesen-Koefoed, J. A., 2011, West Greenland Petroleum Systems – an Overview of Source Rocks and Oil Seepages and Their Implications for Offshore Petroleum Exploration: The Geological Survey of Denmark and Greenland.

Bojesen-Koefoed, J. A., Bidstup, T., Christiansen, F. G., Dalhoff, F., Gregersen, G., Nytoft, H. P., Nøhr-Hansen, H., Pedersen, A. K., and Sønderholm, m., 2007, Petroleum seepages at Asuk, Disko, West Greenland: implications for regional petroleum exploration: Journal of Petroleum Geology, v. 30, no. 3, p. 219-236.

Cairn Energy PLC, 2011, Greenland operational update [press release], p. 1-2.

Cavanagh, A. J., Di Primio, R., Scheck-Wenderoth, M., and Horsfield, B., 2006, Severity and timing of Cenozoic exhumation in the southwestern Barents Sea: Journal of the Geological Society, v. 163, no. 5, p. 761-774.

Chalmers, J. A., Dahl-Jensen, T., Bate, K. J., and Whittaker, R. C., 1995, Geology and petroleum prospectivity of the region offshore southern West Greenland–a summary.

Chand, S., and Minshull, T., 2003, Seismic constraints on the effects of gas hydrate on sediment physical properties and fluid flow: a review: Geofluids, v. 3, no. 4, p. 275-289.

Christ, A. J., Bierman, P. R., Knutz, P. C., Corbett, L. B., Fosdick, J. C., Thomas, E. K., Cowling, O. C., Hidy, A. J., and Caffee, M. W., 2020, The northwestern Greenland Ice Sheet during the Early Pleistocene was similar to today: Geophysical Research Letters, v. 47, no. 1.

Christiansen, F. G., Bojesen-Koefoed, J., Dam, G., Nytoft, H.-P., Larsen, L. M., Pedersen, A. K., and Pulvertaft, T. C. R., 1996, The Marraat oil discovery on Nuussuaq, West Greenland: evidence for a latest Cretaceous–earliest Tertiary oil prone source rock in the Labrador Sea–Melville Bay region: Bulletin of Canadian Petroleum Geology, v. 44, no. 1, p. 39-54.

Clennell, M. B., Judd, A., and Hovland, M., 2000, Movement and accumulation of methane in marine sediments: relation to gas hydrate systems, Natural gas hydrate, Springer, p. 105-122.

Collett, T. S., 1993, Natural gas hydrates of the Prudhoe Bay and Kuparuk River area, north slope, Alaska: AAPG bulletin, v. 77, no. 5, p. 793-812.

Collett, T. S., Johnson, A., Knapp, C., and Boswell, R., 2009, Natural gas hydrates: a review, *in* Collett, T. S., Johnson, A., Knapp, C., and Boswell, R., eds., Natural gas hydrates - Energy resource potential and associated geologic hazards, American Association of Petroleum Geologists Memoir, p. 89.

Corcoran, D., and Doré, A., 2002, Top seal assessment in exhumed basin settings—Some insights from Atlantic margin and borderland basins, Norwegian Petroleum Society Special Publications, Volume 11, Elsevier, p. 89-107.

Cox, D. R., Huuse, M., Newton, A. M. W., Gannon, P., and Clayburn, J., 2020a, Slip Sliding Away: Enigma of Large Sandy Blocks within a Gas Bearing Mass Transport Deposit, Offshore NW Greenland: AAPG Bulletin, v. 104, no. 5, p. 1011-1043.

Cox, D. R., Huuse, M., Newton, A. M. W., Sarkar, A. D., and Knutz, P. C., 2021, Shallow gas and gas hydrate occurrences on the northwest Greenland shelf margin: Marine Geology, v. 432, p. 1-21.

Cox, D. R., Knutz, P. C., Campbell, D. C., Hopper, J. R., Newton, A. M. W., Huuse, M., and Gohl, K., 2020b, Geohazard detection using 3D seismic data to enhance offshore scientific drilling site selection: Scientific Drilling, v. 28, p. 1-27.

Cramer, B., Braun, A., Poelchau, H. S., and Littke, R., 1997, Gas hydrates and permafrost in continental northern West Siberia; Gashydrate und Permafrost im kontinentalen noerdlichen Westsibirien, Conference on gas hydrates - noxious substances or resources: Clausthal-Zellerfeld, Germany, p. 27-36.

Dam, G., Pedersen, G. K., Sønderholm, M., Midtgaard, H. H., Larsen, L. M., Nøhr-Hansen, H., and Pedersen, A. K., 2009, Lithostratigraphy of the Cretaceous–Paleocene Nuussuaq Group, Nuussuaq Basin, West Greenland: Geological Survey of Denmark and Greenland (GEUS) Bulletin, v. 19, p. 1-171.

Davidson, D., Natural gas hydrates in northern Canada, *in* Proceedings Proc. 3rd Int. Conf. on Permafrost1978, Volume 1, National Research Council of Canada, p. 938-943.

Doré, A., Corcoran, D., and Scotchman, I., 2002a, Prediction of the hydrocarbon system in exhumed basins, and application to the NW European margin: Geological Society, London, Special Publications, v. 196, no. 1, p. 401-429.

Doré, A. G., Cartwright, J. A., Stoker, M. S., Turner, J. P., and White, N. J., 2002b, Exhumation of the North Atlantic margin: introduction and background: Geological Society of London, Special Publication, v. 196, p. 1-12.

Doré, A. G., and Jensen, L. N., 1996, The impact of late Cenozoic uplift and erosion on hydrocarbon exploration: offshore Norway and some other uplifted basins: Global and Planetary Change, v. 12, no. 1-4, p. 415-436.

Fjeldskaar, W., and Amantov, A., 2018, Effects of glaciations on sedimentary basins: Journal of Geodynamics, v. 118, p. 66-81.

Fleming, K., and Lambeck, K., 2004, Constraints on the Greenland Ice Sheet since the Last Glacial Maximum from sea-level observations and glacial-rebound models: Quaternary Science Reviews, v. 23, no. 9-10, p. 1053-1077.

Freire, F., Gyllencreutz, R., Greenwood, S. L., Mayer, L., Egilsson, A., Thorsteinsson, T., and Jakobsson, M., 2015, High resolution mapping of offshore and onshore glaciogenic features in metamorphic bedrock terrain, Melville Bay, northwestern Greenland: Geomorphology, v. 250, p. 29-40.

Fretwell, P., Pritchard, H. D., Vaughan, D. G., Bamber, J. L., Barrand, N. E., Bell, R., Bianchi, C., Bingham, R. G., Blankenship, D. D., and Casassa, G., 2013, Bedmap2: improved ice bed, surface and thickness datasets for Antarctica: The Cryosphere, v. 7, no. 1, p. 375-393.

Goffey, G., Attree, M., Curtis, P., Goodfellow, F., Lynch, J., Mackertich, D., Orife, T., and Tyrrell, W., 2016, New exploration discoveries in a mature basin: offshore Denmark, *in* Bowman, M., and Levell, B., eds., Petroleum Geology of NW Europe: 50 Years of Learning – Proceedings of the 8th Petroleum Geology Conference: London, Geological Society.

Grassmann, S., Cramer, B., Delisle, G., Hantschel, T., Messner, J., and Winsemann, J., 2010, pT-effects of Pleistocene glacial periods on permafrost, gas hydrate stability zones and reservoir of the Mittelplate oil field, northern Germany: Marine and petroleum geology, v. 27, no. 1, p. 298-306.

Gray, D. I., 1987, Troll, *in* Spencer, A. M., ed., Geology of the Norwegian Oil and Gas Fields: London, Graham and Trotman.

Grecula, M., Wadsworth, S., Maloney, D., Lauferts, H., Cooke, G., Jones, A., and Stevanovic, S., Baffin Bay Elusive Plays: Geological Surprises of an Arctic Exploration Campaign, *in* Proceedings American Association of Petroleum Geology International Conference and Exhibition (ICE), London, UK, 2018, Volume 30548, p. 1-20.

Gregersen, G., Knutz, P. C., Nøhr-Hansen, H., Sheldon, E., and Hopper, J. R., 2019, Tectonostratigraphy and evolution of the West Greenland continental margin: Bulletin of the Geological Society of Denmark, v. 67, p. 1-21.

Gregersen, U., Andersen, M. S., Nøhr-Hansen, H., Sheldon, E., Kokfelt, T. F., Olivarius, M., Knudsen, C., Jakobsen, K. G., and Adolfssen, J. S., 2018, New subsurface mapping offshore southern West Greenland using geophysical and geological data: Geological Survey of Denmark and Greenland Bulletin, p. 57-62.

Gregersen, U., Hopper, J. R., and Knutz, P. C., 2013, Basin seismic stratigraphy and aspects of prospectivity in the NE Baffin Bay, Northwest Greenland: Marine and Petroleum Geology, v. 46, p. 1-18.

Gregersen, U., Knutz, P. C., and Hopper, J. R., 2016, New geophysical and geological mapping of the eastern Baffin Bay region, offshore West Greenland: Geological Survey of Denmark and Greenland Bulletin, v. 35, p. 83-86.

Grollimund, B., and Zoback, M. D., 2003, Impact of glacially induced stress changes on fault-seal integrity offshore Norway: AAPG Bulletin, v. 87, p. 493-506.

Hantschel, T., and Kauerauf, A. I., 2009, Fundamentals of basin and petroleum systems modeling, Berlin, Heidelberg, Germany, Springer Science & Business Media, 476 p.:

Henriksen, E., Bjørnseth, H., Hals, T., Heide, T., Kiryukhina, T., Kløvjan, O., Larssen, G., Ryseth, A., Rønning, K., and Sollid, K., 2011, Uplift and erosion of the greater Barents Sea: impact on prospectivity and petroleum systems: Geological Society, London, Memoirs, v. 35, no. 1, p. 271-281.

Hermanrud, C., and Nordgard Bolas, H. M., 2002, Leakage from overpressured hydrocarbon reservoirs at Haltenbanken and in the northern North Sea, *in* Koestler, A. G., and Hunsdale, R., eds., Hydrocarbon Seal Quantification, Volume 11: Amsterdam, Elsevier Science, p. 221-231.

Hubbert, M. K., and Rubey, W. W., 1959, Role of fluid pressure in mechanics of overthrust faulting: I. Mechanics of fluid-filled porous solids and its application to overthrust faulting: Geological Society of America Bulletin, v. 70, no. 2, p. 115-166.

Ingram, G. M., and Urai, J. L., 1999, Top-seal leakage through faults and fractures: the role of mudrock properties: Geological Society, London, Special Publications, v. 158, no. 1, p. 125-135.

Japsen, P., Bonow, J. M., Green, P. F., Chalmers, J. A., and Lidmar-Bergstrom, K., 2006, Elevated, passive continental margins: Long-term highs or Neogene uplifts? New evidence from West Greenland: Earth and Planetary Science Letters, v. 248, no. 1-2, p. 330-339.

Johansen, H., Fjeldskaar, W., and Mykkeltveit, J., 1996, The influence of glaciation on the basin temperature regime: Global and Planetary Change, v. 12, no. 1-4, p. 437-448.

Johnston, A. C., 2000, The effect of large ice sheets on earthquake genesis, *in* Gregersen, S., and Basham, P., eds., Earthquakes at North Atlantic Passive Margins: Neotectonics and Postglacial Rebound, Volume 266, Mathematical and Physical Sciences, p. 581-599.

Karlsen, D., and Skeie, J., 2006, Petroleum migration, faults and overpressure, part I: calibrating basin modelling using petroleum in traps—a review: Journal of Petroleum Geology, v. 29, no. 3, p. 227-256.

Ker, S., Thomas, Y., Riboulot, V., Sultan, N., Bernard, C., Scalabrin, C., Ion, G., and Marsset, B., 2019, Anomalously deep BSR related to a transient state of the gas hydrate system in the western Black Sea: Geochemistry, Geophysics, Geosystems, v. 20, no. 1, p. 442-459.

Kjemperud, A., and Fjeldskaar, W., 1992, Pleistocene glacial isostasy - implications for petroleum geology: NPF Special Publication, v. 1, p. 187-195.

Knutz, P. C., Gregersen, U., and Hopper, J. R., 2012, Late Paleogene Submarine Fans in Baffin Bay and North-West Greenland, 74th EAGE Conference and Exhibition incorporating EUROPEC 2012 Copenhagen, EAGE, p. 5.

Knutz, P. C., Harrison, C., Brent, T. A., Gregersen, G., and Hopper, J. R., submitted, Baffin Bay Tectono-Sedimentary Element, *in* Drachev, S., and Moore, T. E., eds., Arctic Sedimentary Basins, Volume Geological Society Memoir: London, Geological Society London.

Knutz, P. C., Hopper, J. R., Gregersen, U., Nielsen, T., and Japsen, P., 2015, A contourite drift system on the Baffin Bay–West Greenland margin linking Pliocene Arctic warming to poleward ocean circulation: Geology, v. 43, no. 10, p. 907-910.

Knutz, P. C., Newton, A. M. W., Hopper, J. R., Huuse, M., Gregersen, U., Sheldon, E., and Dybkjær, K., 2019, Eleven phases of Greenland Ice Sheet shelf-edge advance over the past 2.7 million years: Nature Geoscience, v. 12, p. 361-368.

Krey, V., Canadell, J. G., Nakicenovic, N., Abe, Y., Andruleir, H., Archer, D., Grubler, A., Hamilton, N. T. M., Johnson, A., Kostov, V., Lamarque, J., Langhorne, N., Nisbet, E. G., O'Neil, B., Riahi, K., Riedel, M., Wang, W., and Yakushev, V., 2009, Gas hydrates: entrance to a methane age or climate threat?: Environmental Research Letters, v. 4, p. 1-6.

Kvenvolden, K. A., 1993, A primer on gas hydrates, *in* Howell, D. G., Wiese, K., Fanelli, M., Zink, L. L., and Cole, F., eds., The Future of Energy Gases, Volume US Geological Survey Professional Paper 1570: Washington DC, USA, USGS, p. 279-291.

Kvenvolden, K. A., Ginsburg, G. D., and Soloviev, V. A., 1993, Worldwide distirbution of subaquatic gas hydrates: Geo-Marine Letters, v. 13, p. 32-40.

Larter, S., and di Primio, R., 2005, Effects of biodegradation on oil and gas field PVT properties and the origin of oil rimmed gas accumulations: Organic Geochemistry, v. 36, no. 2, p. 299-310.

Lecavalier, B. S., Milne, G. A., Simpson, M. J. R., Wake, L., Huybrechts, P., Tarasov, L., Kjeldsen, K. K., Funder, S., Long, A. J., and Woodroffe, S., 2014, A model of Greenland ice sheet deglaciation constrained by observations of relative sea level and ice extent: Quaternary Science Reviews, v. 102, p. 54-84.

Lee, J., Jung, J., Lee, M., Bahk, J.-J., Choi, J., Ryu, B.-J., and Schultheiss, P., 2013, Pressure core based study of gas hydrates in the Ulleung Basin and implication for geomechanical controls on gas hydrate occurrence: Marine and Petroleum Geology, v. 47, p. 85-98.

Lei, L., and Seol, Y., 2019, High-Saturation Gas Hydrate Reservoirs—A Pore Scale Investigation of Their Formation From Free Gas and Dissociation in Sediments: Journal of Geophysical Research: Solid Earth, v. 124, no. 12, p. 12430-12444.

Lerche, I., and Bagirov, E., 1998, Guide to gas hydrate stability in various geological settings: Marine and Petroleum Geology, v. 15, no. 5, p. 427-437.

Lerche, I., Yu, Z., Tørudbakken, B., and Thomsen, R., 1997, Ice loading effects in sedimentary basins with reference to the Barents Sea: Marine and Petroleum Geology, v. 14, no. 3, p. 277-338.

Løtveit, I. F., Fjeldskaar, W., and Sydnes, M., 2019, Tilting and flexural stresses in basins due to glaciations—An example from the Barents Sea: Geosciences, v. 9, no. 11, p. 474.

Lund, B., Schmidt, P., and Hieronymus, C., 2009, Stress evolution and fault stability during the Weichselian glacial cycle: Swedish Nuclear Fuel and Waste Management Co.

McCarthy, K., Rojas, K., Niemann, M., Palmowski, D., Peters, K., and Stankiewicz, A., 2011, Basic petroleum geochemistry for source rock evaluation: Oilfield Review, v. 23, no. 2, p. 32-43.

Medvedev, S., Hartz, E. H., Schmid, D. W., Zakariassen, E., and Varhaug, P., 2019, Influence of glaciations on North Sea petroleum systems: Geological Society, London, Special Publications, v. 494, p. SP494-2018-2183.

Milkov, A. V., and Sassen, R., 2000, Thickness of the gas hydrate stability zone, Gulf of Mexico continental slope: Marine and Petroleum Geology, v. 17, p. 981-991.

Miller, K. G., Browning, J. V., Schmelz, W. J., Kopp, R. E., Mountain, G. S., and Wright, J. D., 2020, Cenozoic sea-level and cryospheric evolution from deep-sea geochemical and continental margin records: Science advances, v. 6, no. 20, p. eaaz1346.

Miller, K. G., Mountain, G. S., Wright, J. D., and Browning, J. V., 2011, A 180-million-year record of sea level and ice volume variations from continental margin and deep-sea isotopic records: Oceanography, v. 24, no. 2, p. 40-53.

Minshull, T. A., Marín-Moreno, H., Betlem, P., Bialas, J., Bünz, S., Burwicz, E., Cameselle, L., Cifci, G., Giustinaini, M., Hillman, J. I. T., Hölz, S., Hopper, J. R., Ion, G., León, R., Magalhaes, V., Makovsky, Y., Mata, M., Max, M. D., Nielsen, T., Okay, S., Ostrovsky, I., O'Neil, N., Pinheiro, L. M., Plaza-Faverola, A., Rey, D., Roy, S., Schwalenberg, K., Senger, K., Vadakkepuliyambatta, S., Vasilev, A., and Vázquez, J. T., 2020, Hydrate occurrence in Europe: A review of available evidence: Marine and Petroleum Geology, v. 111, p. 735-764.

Newton, A. M. W., Huuse, M., Cox, D. R., and Knutz, P. C., 2021, Seismic geomorphology and evolution of the Melville Bugt Trough Mouth Fan, northwest Greenland: Quaternary Science Reviews, v. 255, p. 1-23.

Newton, A. M. W., Huuse, M., Knutz, P. C., Cox, D. R., and Brocklehurst, S. H., 2020, Repeated ice streaming on the northwest Greenland shelf since the onset of the Middle Pleistocene Transition: The Cryosphere Discuss., v. 2019, p. 1-18.

Newton, A. M. W., Knutz, P. C., Huuse, M., Gannon, P., Brocklehurst, S. H., Clausen, O. R., and Gong, Y., 2017, Ice stream reorganization and glacial retreat on the northwest Greenland shelf: Geophysical Research Letters, v. 44, p. 7826-7835.

Noerdlinger, P. D., and Brower, K. R., 2007, The melting of floating ice raises the ocean level: Geophysical Journal International, v. 170, no. 1, p. 145-150.

Nøhr-Hansen, H., Pedersen, G. K., Knutz, P. C., Bojesen-Koefoed, J. A., Sliwinska, K. K., and Hovikoski, J., 2018, Potential Cretaceous source-rocks from the north-east Baffin Bay, West Greenland, AAPG Europe Regional Conference - Global Analogues of the Atlantic Margin: Lisbon, p. 1.

Nordgard Bolas, H. M., Hermanrud, C., and Teige, G. M. G., 2005, Seal capacity estimation from subsurface pore pressures: Basin Research, v. 17, no. 4, p. 583-599.

Nyland, B., Jensen, L. N., Skagen, J. I., Skarpnes, O., and Vorren, T., 1992, Tertiary uplift and erosion in the Barents sea: magnitude, timing and consequences, *in* Larsen, R. M., Brekke, H., Larsen, B. T., and Talleraas, E., eds., Structural and Tectonic modelling and its application to petroleum geology: Amsterdam, Netherlands, Elsevier Science Publishers, p. 153-162.

Oakey, G. N., and Chalmers, J. A., 2012, A new model for the Paleogene motion of Greenland relative to North America: Plate reconstructions of the Davis Strait and Nares Strait regions between Canada and Greenland: Journal of Geophysical Research, v. 117, no. B10, p. 1-28.

Ostanin, I., Anka, Z., and Di Primio, R., 2017, Role of faults in Hydrocarbon Leakage in the Hammerfest Basin, SW Barents Sea: Insights from seismic data and numerical modelling: Geosciences, v. 7, no. 2, p. 28.

Petrie, E. S., Evans, J. P., and Bauer, S., 2014, Failure of cap-rock seals as determined from mechanical stratigraphy, stress history, and tensile-failure analysis of exhumed analogsStress History and Tensile Failure Analysis of Exhumed Caprock Seal Analogs: AAPG Bulletin, v. 98, no. 11, p. 2365-2389.

Planke, S., Symonds, P. A., Alvestad, E., and Skogseis, J., 2009, Mid-Cretaceous source rock subcropping in the Baffin Bay: GEO ExPro, v. 6, p. 1-8.

Rao, V., and Knight, R., 2016, Sustainable Shale Oil and Gas: Analytical Chemistry, Geochemistry, and Biochemistry Methods, Elsevier, 188 p.:

Reagan, M. T., and Moridis, G. J., 2007, Oceanic gas hydrate instability and dissociation under climate change scenarios: Geophysical Research Letters, v. 34, no. 22.

Riis, F., and Fjeldskaar, W., 1992, On the magnitude of the Late Tertiary and Quaternary erosion and its significance for the uplift of Scandinavia and the Barents Sea: NPF Special Publication, v. 1, no. 163-185.

Ruppel, C. D., and Kessler, J. D., 2017, The interaction of climate change and methane hydrates: Reviews of Geophysics, v. 55, no. 1, p. 126-168.

Seol, Y., and Kneafsey, T. J., 2011, Methane hydrate induced permeability modification for multiphase flow in unsaturated porous media: Journal of Geophysical Research: Solid Earth, v. 116, no. B8.

Slabon, P., Dorschel, B., Jokat, W., Myklebust, R., Hebbeln, D., and Gebhardt, C., 2016, Greenland ice sheet retreat history in the northeast Baffin Bay based on high-resolution bathymetry: Quaternary Science Reviews, v. 154, p. 182-198.

Sloan, E. D., and Koh, C. A., 1990, Clathrate hydrates of natural gases: New York, New York, Marcel Drekker, Marcel Drekker, 1-641 p.:

Stoll, R. D., and Bryan, G. M., 1979, Physical properties of sediments containing gas hydrates: Journal of Geophysical Research: Solid Earth, v. 84, no. B4, p. 1629-1634.

Stopler, D. A., Lawson, M., Davis, C. L., Ferreira, A. A., Santos Neto, E. V., Ellis, G. S., Lewan, M. D., Martini, A. M., Tang, Y., Schoell, M., Sessions, A. L., and Eiler, J. M., 2014, Formation temperatures of thermogenic and biogenic methane: Science, v. 344, no. 6191, p. 1500-1503.

Strout, J. M., and Tjelta, T. I., 2005, In situ pore pressures: What is their significance and how can they be reliably measured?: Marine and Petroleum Geology, v. 22, no. 1-2, p. 275-285.

Tasianas, A., Bünz, S., Bellwald, B., Hammer, Ø., Planke, S., Lebedeva-Ivanova, N., and Krassakis, P., 2018, High-resolution 3D seismic study of pockmarks and shallow fluid flow systems at the Snøhvit hydrocarbon field in the SW Barents Sea: Marine Geology, v. 403, p. 247-261.

Tasianas, A., Martens, I., Bünz, S., and Mienert, J., 2016, Mechanisms initiating fluid migration at Snøhvit and Albatross fields, Barents Sea: arktos, v. 2, no. 1.

Thorson, R. M., 2000, Glacial tectonics: a deeper perspective: Quaternary Science Reviews, v. 19, no. 14-15, p. 1391-1398.

Urlaub, M., Kratzke, I., and Hjelstuen, B. O., 2020, A numerical investigation of excess pore pressures and continental slope stability in response to ice-sheet dynamics: Geological Society, London, Special Publications, v. 500, no. 1, p. 255-266.

Van den Berg, J., Van de Wal, R., Milne, G., and Oerlemans, J., 2008, Effect of isostasy on dynamical ice sheet modeling: A case study for Eurasia: Journal of Geophysical Research: Solid Earth, v. 113, no. B5.

Welford, K., Peace, A., Geng, M., and Dickie, K., 2018, Crustal structure of Baffin Bay from constrained 3-D gravity inversion and deformable plate tectonic models: Geophysical Journal International, v. 214, no. 2, p. 1281-1300.

Wenger, L. M., Davis, C. L., and Isaksen, G. H., 2002, Multiple controls on petroleum biodegradation and impact on oil quality: SPE Reservoir Evaluation & Engineering, v. 5, no. 05, p. 375-383.

Whittaker, R. C., Hamann, R. E., and Pulvertaft, T. C. R., 1997, A New Frontier Province Offshore Northwest Greenland: Structure, Basin Development, and Petroleum Potential of the Melville Bay Area: AAPG Bulletin, v. 81, no. 6, p. 978-998.

Winsborrow, M. C., Andreassen, K., Corner, G. D., and Laberg, J. S., 2010, Deglaciation of a marine-based ice sheet: Late Weichselian palaeo-ice dynamics and retreat in the southern Barents Sea reconstructed from onshore and offshore glacial geomorphology: Quaternary Science Reviews, v. 29, no. 3-4, p. 424-442.

Wygrala, B., P., 1989, Integrated study of an oil field in the southern Po Basin, Northern Italy [PhD: University of Cologne, 328 p.

Zieba, K. J., and Grover, A., 2016, Isostatic response to glacial erosion, deposition and ice loading. Impact on hydrocarbon traps of the southwestern Barents Sea: Marine and Petroleum Geology, v. 78, p. 168-183.

Chapter 6 Appendix

Age Assignment Table								
Glacial cycle	Age (Ma)	Horizon (hz)	Layer	Erosion Map	Facies	Event Type	Glacial Event	Sub-layers
	0	a10-11						
			A10-11		50/50%	Deposition	Sed. Deposition	2
	0.1					Erosion	Deglaciation	
6	**0.15**					Hiatus	Stable Ice	
	0.35	Ice 6		Ice 6_map				
			Ice 6		Ice	Deposition	Ice Growth	5
	0.43					Hiatus	Hiatus	
	0.45	a8-9						
			A8-9		50/50%	Deposition	Sed. Deposition	3
	0.5					Erosion	Deglaciation	
5	**0.55**					Hiatus	Stable Ice	
	0.85	Ice 5		Ice 5_map				
			Ice 5		Ice	Deposition	Ice Growth	5
	0.98					Hiatus	Hiatus	
	0.1	a5-6-7						
			A5-6-7		50/50%	Deposition	Sed. Deposition	4
	1.1					Erosion	Deglaciation	
4	**1.2**					Hiatus	Stable Ice	
	1.5	Ice 4		Ice 4_map				
			Ice 4		Ice	Deposition	Ice Growth	5
	1.58					Hiatus	Hiatus	
	1.6	a3-4						
			A3-4		50/50%	Deposition	Sed. Deposition	4
	1.65					Erosion	Deglaciation	
3	**1.7**					Hiatus	Stable Ice	
	1.9	Ice 3		Ice 3_map				
			Ice 3		Ice	Deposition	Ice Growth	5
	1.98					Hiatus	Hiatus	
	2.0	a2						
			A2		50/50%	Deposition	Sed. Deposition	2
	2.05					Erosion	Deglaciation	
	2.15					Hiatus	Stable Ice	
2	**2.25**	Ice2		Mu-B & -C Half + Ice 2_map				
			Ice 2		Ice	Deposition	Ice Growth	5
	2.33					Hiatus	Hiatus	
	2..35	a1		Mu-B & -C Half_map				
			A1		50/50%	Deposition	Sed. Deposition	3
	2.4			Mu-B & -C Half_map		Erosion	Deglaciation	
1	**2.5**					Hiatus	Stable Ice	
	2.6	Ice1		Mu-B & -C + Ice 1_map				
			Ice 1		Ice	Deposition	Ice Growth	5
	2.68					Hiatus	Hiatus	
	2.7	b1		Mu-B & -C_map				

Appendix 6A. Age assignment table | The age assignment table used within PetroMod basin modelling software to simulate sediment redistribution and six cycles of glacial advance and retreat across the shelf. Erosion maps are used to add the ice thickness during glacial periods, in combination with paleo-water depth maps that control the depth of the ice and isostatic adjustments. The horizons and layers, sub-layers and facies defined here are shown on Fig. 6.4, and the evolution of the glacial model defined in this table can be seen on Fig. 6.5. Facies (50/50%) represents 50% sand and 50% shale.

7

Summary and Conclusions

The final chapter of this thesis summarises the principal findings of the research chapters presented, and provides perspectives on the wider implications of this research. A consideration of what key questions still remain unanswered is also provided, as well as the direction future research should take in order to continue developing our understanding in this field.

7.1. Summary of Results

The main aim of this thesis was to improve our understanding of the impacts of glaciation on petroleum systems. This was achieved by focussing on the Melville Bay region, offshore northwest Greenland, and by developing four key research aims.

7.1.1. Research Aim 1: Tectonostratigraphic evolution

The first research aim was to develop our understanding of the structure and stratigraphy of Melville Bay, and to improve our knowledge of basin evolution and the chronology and potential lithology of seismic stratigraphic packages. Understanding this framework and evolution will act as the foundation for understanding key elements of the contemporary nature and evolution of the petroleum systems; something that was integral to reaching the principal aim of this thesis. This research aim was studied within Chapters 2-5.

In Chapter 2, the first comprehensive analysis of a 1672 km^2 3D seismic reflection survey on the inner shelf of Melville Bay is provided, describing the structure and stratigraphy of the Melville Bay Ridge (MBR) and Melville Bay Graben (MBG). Previous to this work, only regional studies were available (Gregersen et al., 2019; 2013; 2016; Knutz et al., 2012; 2015; Whittaker et al., 1997), and this Chapter provides a more detailed description of the seismic stratigraphy in these areas, whilst improving our understanding of the chronology and evolution of key seismic packages, in particular, the likely age of sand deposition within mega-unit D2 during the mid-Eocene. The Chapter contains a detailed assessment of the identified mass transport deposit reservoir on the crest of the MBR ridge, which concluded that this package comprises of highly porous, gas-charged sands intercalated with shale layers and overlain by post-slide pelagic mudstones. The existence and genesis of polygonal fault networks within the overlying muddy stratigraphy was also described. Analysing and interpreting the deposition and deformation of the reservoir, and by conducting a landslide reconstruction, revealed important aspects of basin evolution, including interpretations of depositional environments during the Eocene and the rejuvenation of uplift and the southward tilting of the MBR, adding to other interpretations for Cenozoic uplift (Gregersen et al., 2019; Japsen et al., 2006).

In Chapter 3, our understanding of both the stratigraphy and structure of the MBR and MBG were improved further, including a more detailed structural interpretation of deep syn-rift and post-rift tectonic faults, as well as widespread polygonal fault networks (Gregersen et al., 2019). This work included the analysis of a second 5038 km^2 3D seismic reflection survey across the mid and outer shelf of Melville Bay, including the South Kivioq Basin (SKB) and the Melville Bay Trough Mouth Fan (MB-TMF), expanding the detailed subsurface description (Gregersen et al., 2013; Knutz et al., 2019; Newton et al., 2017). The study improved our understanding of lithology by identifying several sand prone potential reservoir horizons as well as likely high porosity and permeability carrier beds throughout both syn- and post-rift stratigraphy. Furthermore, our subsurface understanding in Melville Bay was also improved via estimations for both the shallow geothermal gradient (49 °C/km) and heat flow (70-90 mW/m2) using identified bottom simulating reflectors (BSRs). This provides the first publically available heat flow estimation on this part of the West Greenland margin (Lucazeau, 2019; Pye and Hyndman, 1972).

In Chapter 4, the 3D seismic geohazard assessment, conducted across the entire 3D seismic coverage in Melville Bay, provided a more detailed assessment of fault networks within the MBG, as well as the potential lithology of the shallow stratigraphy, focussing on the early depositional units of the MB-TMF and the contourite successions of mu-C and –B, adding to previous interpretations by Knutz et al. (2015); (2019). This included the detailed assessment and identification of mass transport deposits, glacigenic sediments, debris flows and potentially sandy horizons within areas of the post-rift stratigraphy that have been targeted by IODP Proposal 909 (Bennett et al., 2014; Newton et al., 2020; 2017).

Finally, in Chapter 5, a wide range of literature and regional data sources were used in combination with the seismic data studies of Chapters 2-4, to create a 2D petroleum systems model which represents a synthesis of the stratigraphic and structural framework across the Melville Bay margin. The chronology of events, as well as the nature of paleo-geometries defined by the back-stripping and decompaction process, improved our understanding of basin evolution since the Early Cretaceous (Gregersen et al., 2019; 2013; Japsen et al., 2006; Knutz et al., 2012). This, importantly, identified the substantial variation in subsidence rates between the MBG and SKB as well as the continued prominence and influence of the MBR throughout basin development. The model also predicts the porosity and permeability of the stratigraphy across the margin. Furthermore, a sensitivity analysis was conducted to test several parameters within the model, revealing the most likely characteristics of heat flow history, variations in fault permeability and the possible lithology characteristics of the mu-D1 regional seal.

7.1.2. Research Aim 2: Petroleum systems

The second research aim was to characterise the potential petroleum systems in Melville Bay, by identifying and describing key petroleum system elements, the contemporary distribution of hydrocarbons and the possible history of hydrocarbon generation and migration. Understanding the nature and evolution of the petroleum systems is an essential aspect to assessing how these systems may have been impacted by recent glaciations. This research aim was studied within Chapters 2-5.

In Chapter 2, the discovery of a 420 km^2, gas-charged submarine landslide deposit was reported, which presented some of the first seismic evidence for an existing petroleum system in Melville Bay, after regional assessments (Grecula et al., 2018; Gregersen, 2008; Gregersen et al., 2013; Whittaker et al., 1997). This reservoir is a key element of the petroleum systems in Melville Bay and within Chapter 2, direct hydrocarbon indicators and velocity estimations were used to estimate that the reservoir most likely contains gassy hydrocarbons. Furthermore, gas was interpreted to have charged all areas of the reservoir, despite its post-depositional break up into numerous, potentially isolated reservoir blocks, suggesting the reservoir charge most likely occurred from the underlying syn-rift sediments. These sediments exist within the MBR structure, up-dip from potential source kitchens within the deeper MBG (Gregersen et al., 2013; Nøhr-Hansen et al., 2018). This suggests an important migration mechanism, up-dip into the ridge structure via high porosity and permeability syn-rift carrier beds.

In Chapter 3, the first inventory of shallow gas and gas hydrates were provided for the northwestern part of the Greenland margin (Minshull et al., 2020), via the identification of numerous gas-related seismic amplitude anomalies within the uppermost 1-2 km of the stratigraphy. Documenting the occurrence of shallow gas and gas hydrate is important, as these deposits may represent drilling hazards, environmental concerns or even possibly a future energy source (Demirbas, 2010; Merey, 2016; Ruppel and Kessler, 2017). This work expanded our understanding of the contemporary distribution of hydrocarbons across the SKB, MBR and MBG areas (Gregersen et al., 2013; Whittaker et al., 1997), with gas being interpreted to exist within various trapping scenarios including as isolated pockets, beneath the base of the gas hydrate stability zone (GHSZ), within glacial clinoforms of the MB-TMF and finally, within the extensive reservoir described in Chapter 2. Gas hydrates were identified across an area of 537 km^2 via the identification of a discontinuous BSR that marks the base of the GHSZ. Chapter 3 also provides the first interpretation of the migration history of fluids across the region, using the relationship between structural and stratigraphic elements and the distribution and character of hydrocarbon anomalies. This

suggested that migration was significantly influenced by the underlying paleo-rift topography, as well as multiple shelf edge glaciations since ~2.7 Ma (Knutz et al., 2019); factors which probably caused the focussed hydrocarbon distribution in areas above the MBR, as well as the possibility of seal breach and leakage from the reservoir on the ridge crest; a process similar to that proposed in the Danish North Sea and Barents Sea (Goffey et al., 2016; Ostanin et al., 2017). Finally, near-seabed gas hydrate deposits were assessed to be relatively stable across the margin, with dissociation at the seabed being relatively unlikely even when considering current estimates of future global warming (Krey et al., 2009; Ruppel and Kessler, 2017; Stocker et al., 2014). In Chapter 4, the method for characterizing the present day distribution of hydrocarbons was presented, along with a more detailed analysis of the distribution and nature of seismic hydrocarbon anomalies within localised areas around IODP Proposal 909 site localities.

In Chapter 5, 2D petroleum systems modelling was used to predict most likely scenarios for the contemporary nature and evolution of the petroleum systems within Melville Bay. This included a detailed assessment of the condition and distribution of petroleum system elements, with particular focus given to the lithology and sealing efficiency of the mu-D1 regional seal (first described by Knutz et al. (2012), the likelihood of fluid migration through fault planes, and the possible distribution of source rock horizons that are thought to exist in Melville Bay (Bojesen-Koefoed, 2011; Cairn Energy PLC, 2011; Nøhr-Hansen et al., 2018). Both thermogenic and biogenic petroleum systems were tested within the model, with the results representing the first comprehensive frontier assessment of the generation, expulsion, migration, accumulation and preservation of hydrocarbons across the Melville Bay margin. Importantly, the model predicts a viable petroleum system fed by Cretaceous and Paleocene source rocks, with the maturation of these source rocks significantly influenced by variable subsidence rates between the MBG and SKB. Hydrocarbon migration and accumulation was shown to be influenced by extensive faults as well as the MBR structure, with the reservoir existing on the ridge crest predicted to contain methane gas, charged via Cretaceous syn-rift carrier beds from source kitchens on the flank of the MBG (Fig. 7.1) (Nøhr-Hansen et al., 2018). Additionally, biogenic hydrocarbon generation was shown to be a probable scenario in Melville Bay, and may represent the only reasonable method of creating the gas accumulations that are thought to exist within glacigenic sediments overlying the SKB. Lastly, gas hydrates were predicted to have been stable across the margin since at least 5.33 Ma.

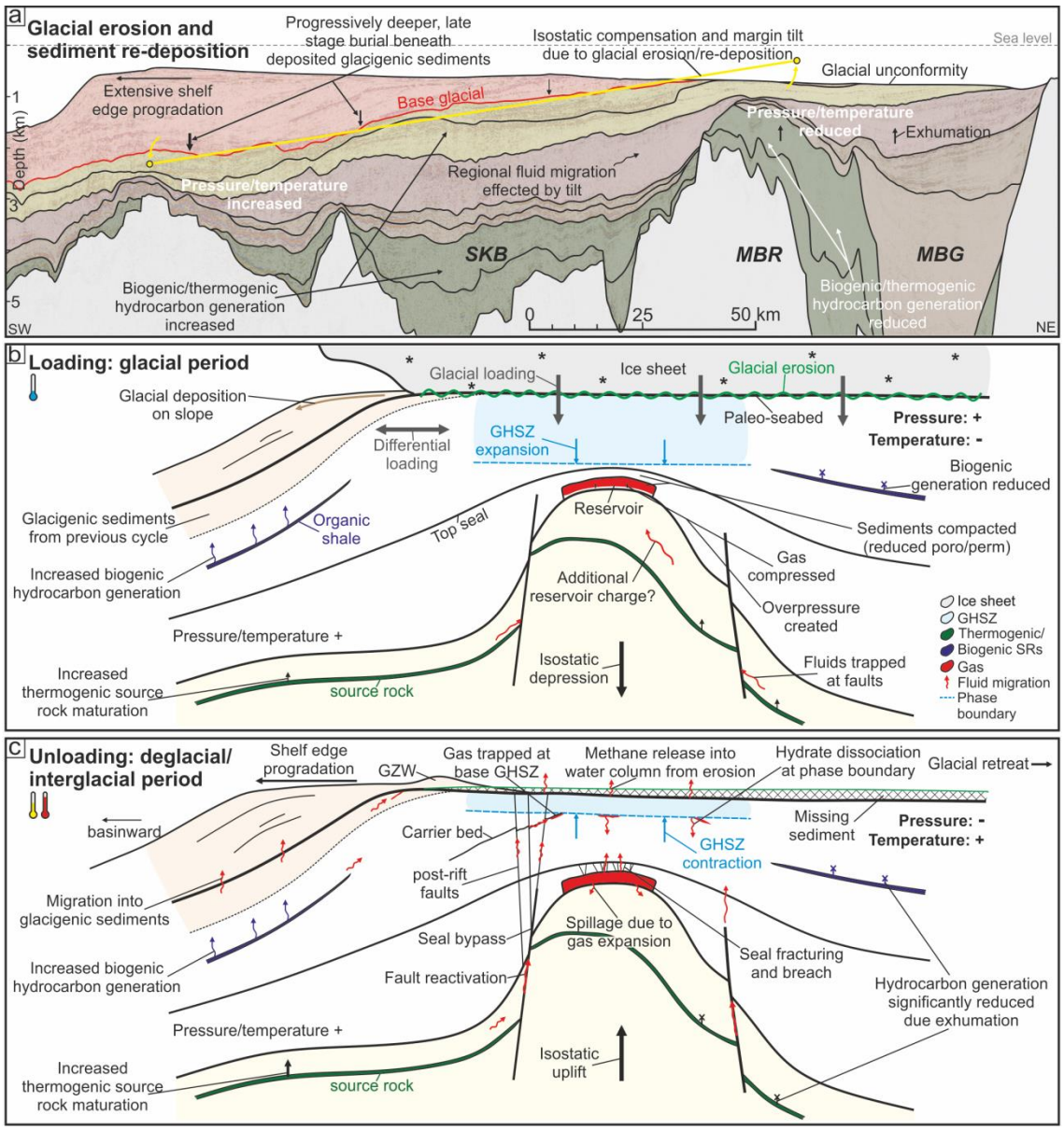

Figure 7.1. Synthesis of glacial impacts |a) A seismic cross section in depth across the Melville Bay margin displaying the impacts of glacial erosion, sediment re-deposition and isostatic compensation on margin evolution and subsurface conditions. Schematic synthesis diagrams displaying the impacts of glacial loading cycles on the underlying petroleum systems assessed within this thesis are shown on (b) and (c). (b) represents a glacial period with ice sheet expansion and loading on the shelf, whilst (c) represents a deglacial/interglacial period with glacial retreat and load removal. The schematic diagrams are not drawn to scale. Abbreviations used include South Kivioq Basin (SKB), Melville Bay Ridge (MBR), Melville Bay Graben (MBG), porosity (poro), permeability (perm), gas hydrate stability zone (GHSZ) and grounding zone wedge (GZW).

7.1.3. Research Aim 3: Impact of glaciation on margin evolution and subsurface

The third research aim was to improve our understanding of the influence that Pliocene-Pleistocene glaciations have had on both the evolution of the Melville Bay margin and subsurface conditions (pressure, temperature and sediment compaction) across the shelf. By understanding the severity, nature and timing of these changes, we can better

assess their potential impact on the petroleum systems within Melville Bay. This research aim was studied within Chapters 3-6.

In Chapter 3, the impact of glacial erosion on the inner shelf, the re-deposition of this sediment to the outer shelf as part of the MB-TMF (Knutz et al., 2019; Newton et al., 2017), and the tilting of the margin basinward as a consequence of these processes is discussed (Doré and Jensen, 1996; Løtveit et al., 2019). The study suggests that the glacial-redistribution of sediment led to the uplift and exposure of stratigraphy on the inner shelf and the subsequent additional burial and compaction of the stratigraphy on the outer shelf, with both processes effecting subsurface conditions and these structural changes likely being exacerbated by isostatic adjustments in response to the load redistribution (Kjemperud and Fjeldskaar, 1992; Zieba and Grover, 2016).

The first attempt to model these changes in burial, and therefore subsurface pressure and temperature conditions, on the West Greenland margin, were presented within Chapter 5. The model assesses the impact of removing 4-500 m of sediment thickness from the inner shelf by glacial erosion, and re-depositing this sediment to the outer shelf as part of the MB-TMF (Fig. 7.1) (Knutz et al., 2019; Newton et al., 2017). This simulated the basinward tilting of the margin since 2.7 Ma as a result of sediment redistribution (Doré and Jensen, 1996; Fjeldskaar and Amantov, 2018), with this tilt causing potential carrier beds within the stratigraphy west of the MBR to dip more steeply.

In Chapter 6, a 2D petroleum systems model is created that depicts the possible evolution of the Melville Bay margin throughout the period of glaciation. This model represents a novel method for testing the effects of glacial erosion, sediment re-deposition and crustal ice loading simultaneously. The model provides more detail towards estimating the influence glaciation has had on margin evolution and subsurface conditions (Cavanagh et al., 2006; Fjeldskaar and Amantov, 2018; Grassmann et al., 2010; Medvedev et al., 2019; Newton et al., 2020; 2017), with the model predicting substantial variations in subsurface pressure, temperature and sediment compaction as a result of glacial processes since ~2.7 Ma (Fig. 7.1). Exhumation on the inner shelf as a result of glacial erosion is estimated to have reduced pore pressure by ~5 MPa and temperatures by ~25 °C at the top of mu-D1. Whilst, sediment re-deposition to the outer shelf is predicted to have increased pore pressure by ~6.5 MPa and temperatures by ~15 °C within the same section. On top of these longer term effects, cycles of ice loading are estimated to have repeatedly increased pore pressures by ~5 MPa and temperatures by 5-6 °C beneath the ice, similar to that estimated by Cavanagh et al. (2006); Grassmann et al. (2010) and Johansen et al. (1996) on other glaciated margins. Temperature was predicted to not fully re-equilibrate during

interglacials, leading to a ~3 °C reduction throughout the last 2.7 Myr on the inner shelf. Pore pressure is also estimated to have increased by 3 MPa during the period of glaciation, but this is instead attributed to increased water depths, partly due to over-deepening through glacial erosion (Newton et al., 2017). Furthermore, ice loading is predicted to have increased sediment compaction, with the first cycle of glaciation reducing the porosity of the reservoir on the MBR crest, while also reducing the permeability (increasing effectiveness) of the overlying mu-D1 seal.

Finally, in both Chapters 3 and 4 (and Appendix A and B), several glacial geomorphological features are identified, described and mapped; improving our understanding of the impact glaciations have had on the evolution of the margin, including evidence for ice sheet grounding, glacial deposition and erosion of the seabed by both the ice sheet itself and icebergs calved off of the front of the ice margin (Bennett et al., 2014; Newton et al., 2021; 2020; 2017).

7.1.4. Research Aim 4: Modelling the impacts of glaciation

The final research aim of this thesis was to model the possible impacts of glacial erosion, sediment re-deposition and repeated ice loading on the Melville Bay petroleum systems, focussing on hydrocarbon generation, expulsion, migration, accumulation and preservation. Predicting and assessing these effects will help improve our understanding of the impacts of glaciation on petroleum systems; the main aim of this thesis. This research aim was studied within Chapters 3, 5 and 6.

In Chapter 3, an assessment into the history of fluid migration in the area proposed that both fluid migration and the contemporary distribution of hydrocarbons have been influenced by glaciations. Firstly, the tilting of the Melville Bay margin basinward due to glacial sediment redistribution, likely influenced fluid migration pathways across the mid-shelf, focussing fluids towards the inner shelf into areas above the MBR. Exhumation through glacial erosion, and repeated ice loading on the inner shelf, is suggested as a possible mechanism for fluid re-migration, similar to that observed in the North Sea and on the Norwegian margin (Corcoran and Doré, 2002; Goffey et al., 2016; Løtveit et al., 2011; Zieba and Grover, 2016). Fluid re-migration possibly occurred via the fracturing of the mu-D1 seal and the leakage of hydrocarbons from the reservoir on the MBR crest (Fig. 7.1), as well as fault reactivation providing pathways for seal bypass. Furthermore, glacial erosion and variable pressure and temperature conditions, due to repeated ice loading, are thought to have affected gas hydrate stability across the margin, similar to that proposed for other glaciated margins (Andreassen et al., 2017; Grassmann et al., 2010). Hydrate dissociation at the seabed only likely occurred as a result of glacial-erosion, as gas hydrate

hosting sediments were removed (Fig. 7.1). Otherwise, near-seabed hydrate deposits were estimated to be relatively stable due to large water depths (>650 m) (Ruppel and Kessler, 2017; Serov et al., 2017). Large variations in the thickness of the GHSZ are predicted as a result of considerable excursions in pressure and temperature conditions during glacial-interglacial cycles (Chand et al., 2012; Grassmann et al., 2010). This may have caused an expansion of the hydrate deposits during glaciation, and subsequent dissociation of gas hydrate at the phase boundary during periods of deglaciation, possibly contributing to the numerous free gas accumulations observed trapped beneath the phase boundary at present day.

In Chapter 5, one of the main impacts observed, when first attempting to model the effect of glacial erosion and sediment re-deposition, was the late onset of source rock maturation and hydrocarbon generation within the SKB; a factor that was predominantly attributed to increased burial, pressure and temperature beneath the re-deposited glacigenic sediments (Fig. 7.1) (Bojesen-Koefoed, 2011; Fjeldskaar and Amantov, 2018). Furthermore, glacial erosion on the inner shelf was predicted to cause the re-migration and loss of hydrocarbons at the seabed, with part of these fluids having leaked out of the reservoir on the crest of the MBR.

In Chapter 6, the 2D petroleum systems model was created primarily to test the potential impacts of glacial processes on the petroleum systems in Melville Bay (research aim 4). This study represents the first investigation into these effects on the Greenland margin (Fjeldskaar and Amantov, 2018; Medvedev et al., 2019). Multiple cross shelf glaciations since ~2.7 Ma (Knutz et al., 2019), and the associated variations in subsurface conditions throughout this period (research aim 3), were predicted to cause a wide range of effects to the underlying petroleum systems (Fig. 7.1). Firstly, hydrocarbon generation and expulsion is shown to significantly decrease due to erosion-related temperature reductions on the inner shelf, but contrastingly increase at the mid-to-outer shelf beneath the thick package of re-deposited glacigenic sediment. During glacial periods, beneath the ice load, thermogenic generation is shown to increase, but biogenic generation significantly decreases due to near surface temperature reductions deepening the biogenic maturity window. Hydrocarbon migration and reservoir leakage is more likely to occur during periods of deglaciation, as the lithostatic load is removed, but when increased fluid pressures may still persist (Goffey et al., 2016; Lund et al., 2009; Ostanin et al., 2017). This potentially led to the fracturing of the mu-D1 seal and leakage from the main reservoir during the first deglacial period. Gas within the reservoir has also likely experienced cyclic episodes of expansion and contraction throughout glacial and interglacial periods, possibly

impacting both reservoir volumes and leakage (Gray, 1987; Nyland et al., 1992; Tasianas et al., 2016).

Finally, glaciation is predicted to have impacted the gas hydrate deposits that exist across the Melville Bay margin, with reduced temperatures on the inner shelf due to erosion and ice loading, as well as deeper waters, causing an increase in hydrate stability and the phase boundary to deepen by ~150 m since 2.7 Ma. Pressure and temperature excursions as a result of cyclic ice loading and unloading, led to the repeated expansion of the gas hydrate stability zone by several hundred meters during glacial periods, before contracting during deglaciation, possibly resulting in hydrate dissociation at the base of the stability zone (Ostanin et al., 2017; Portnov et al., 2016; Serov et al., 2017). This expansion of hydrate stability has potentially also affected the main reservoir on the MBR crest, possibly causing reservoir gas to repeatedly convert to gas hydrate during glacial periods, before dissociating back into free gas during deglaciation; a process that may have reduced reservoir quality, hydrocarbon volumes and gas saturation (Collett, 1993; Lee et al., 2013). Importantly, gas hydrates are again predicted to have been stable at the seabed throughout the period of glaciation, but seabed dissociation likely did occur during the removal of ~4-500 m of gas hydrate hosting sediments due to glacial erosion; a process that may have released a significant volume of methane into the water column and potentially the atmosphere, possibly impacting the climate system (Krey et al., 2009; Portnov et al., 2016; Ruppel and Kessler, 2017).

7.2. Future Research Directions

This thesis has provided a detailed description of the stratigraphy, structure and potential petroleum systems across large areas of Melville Bay, including the Melville Bay Graben, Melville Bay Ridge and South Kivioq Basin. The majority of this research is based on the interpretation of seismic data and therefore, our knowledge of stratigraphic elements such as lithology and important aspects of the petroleum systems such as source rock distribution, fluid type and hydrocarbon saturation, is uncalibrated and thus uncertain. Part of this calibration data may be provided by the results of the Baffin Bay Scientific Coring Program – Expedition 344S led by Shell in 2012 (Acton, 2012), which was not available for this thesis. Future work to combine the shallow core results with the seismic data would allow a much greater understanding of the lithological properties of the shallow stratigraphy, and this knowledge could be expanded away from the site locations across Melville Bay. Additionally, this data would improve our understanding of the distribution and character of sampled Cretaceous source rock intervals (Nøhr-Hansen et al., 2018); knowledge that would reduce uncertainty within petroleum systems modelling studies.

Furthermore, additional calibration data may potentially be provided in the future, through sediment coring resulting from the possible expedition arising from IODP Proposal 909. This additional stratigraphic information should be used within future research to ground truth the current understanding of the stratigraphic framework from seismic studies. This data may also provide greater chronology of ice advance and retreat across the Melville Bay margin; information that could be used to refine petroleum systems models. The geohazard workflow presented in Chapter 4 which was used during the planning of IODP Proposal 909, should also be implemented within future scientific drilling proposals, to increase expedition safety and success. Finally, 3D seismic data also exists within the Tooq licence block (south of the study area) which were not available for this thesis, with this data potentially capturing the southern part of the Melville Bay Graben and the Upernavik Basin. Expanding the seismic interpretations and petroleum systems assessment from this thesis into the additional 3D data, would provide a more complete understanding of the Melville Bay region.

This thesis achieved its main research aim and provided an improved understanding of the impacts that glaciations can have on petroleum systems through both seismic studies and petroleum systems modelling. Our understanding of this complex interaction is not complete however, due to the large variations in both the nature of petroleum systems and glacial processes experienced across glaciated margins worldwide. It is therefore likely, that glaciations can cause a diverse range of impacts across differing glaciated margins. Therefore, to expand our understanding further, the results concerning Melville Bay from this thesis, should be used as an analogue, particularly the petroleum systems modelling approach described in Chapter 6, to create comparative studies across other sections of Melville Bay and importantly, across other glaciated margins worldwide. These studies for example, could focus on other hydrocarbon fields predicted to have been effected by glaciation in the past, such as the Troll gas field in the Norwegian North Sea (Gray, 1987; Medvedev et al., 2019; Nyland et al., 1992) and the Snøhvit field in the southwest Barents Sea (Ostanin et al., 2017; Tasianas et al., 2016). Additionally, a wider range of glacial scenarios could be tested to reflect the uncertainty of past glacial dynamics, particularly beyond the last glacial maximum. These efforts would increase our knowledge of the effects of glaciations further, whilst importantly, reducing the uncertainty of modelling the impacts of these effects on petroleum systems. These potential studies, along with this thesis, may then provide key information beneficial to both hydrocarbon exploration efforts and the modelling of past and future climate change.

Furthermore, testing the effect of glacial isostasy was limited in this research, due to the time dependent viscoelastic response of the Earth's mantle to the release in stress after ice load removal, meaning that isostatic legacies can cross different glacial-interglacial cycles (Lambeck et al., 1998). Such legacies are not well understood and come with significant uncertainties. Therefore, future modelling studies would benefit from a more detailed assessment into the impacts of both long term isostatic adjustments associated with sediment redistribution, and shorter time scale isostatic fluctuations associated with differential loading throughout glacial-interglacial cycles, such as Zieba and Grover (2016), Fjeldskaar and Amantov (2018) and Løtveit et al. (2019). This would likely involve the dedicated modelling of lithospheric stress during glacial loading periods, and may reveal a profound effect on the petroleum systems in Melville Bay, due to thick, grounded ice sheets having advanced to the shelf edge multiple times since ~2.7 Ma (Knutz et al., 2019; Newton et al., 2017). Additionally, the isostatic response to continued melting of the Greenland ice sheet in the future could also be considered, given that the sector of the ice sheet closest to Melville Bay is experiencing some of the largest mass losses across its entirety (Mouginot et al., 2019). Future isostatic change may continue to impact the petroleum systems further, and may represent a less studied implication of future climatic warming.

7.3. Implications and Concluding Remarks

The research presented within this thesis has provided detailed evidence of the stratigraphy, structure and potential petroleum systems of Melville Bay, offshore northwest Greenland, whilst importantly, improving our understanding of the impacts of glaciations on petroleum systems. This thesis shows that glaciations can have a substantial influence on the evolution and subsurface conditions across glaciated margins, through processes such as the erosion, transportation and re-deposition of sediment, as well as the repeated loading and unloading of the shelf during glacial-interglacial cycles. These processes can cause structural modifications associated with erosion, deposition and isostatic compensation across the margin, as well as significant variations in subsurface pressure, temperature and sediment compaction. These glacial-related changes are estimated to have a considerable effect on petroleum systems, affecting processes such as source rock maturation, as well as influencing hydrocarbon re-migration and reservoir leakage. Additionally, glaciations effect gas hydrate deposits, with variable pressure and temperature conditions effecting hydrate stability, possibly leading to hydrate dissociation at the phase boundary.

These findings are essential to improving our understanding of the complex interaction between repeated glaciations and petroleum systems, with this research providing a comparison to studies performed across the North Sea and Norwegian margin, e.g. Fjeldskaar and Amantov (2018); Løtveit et al. (2019) and Medvedev et al. (2019). The petroleum systems modelling approach presented in this thesis to test this interaction, also provides an important tool for future studies. Importantly, this thesis provides crucial considerations that will help improve the success and limit the safety risks associated with scientific drilling, as well as oil and gas exploration, especially if industry continues operating within challenging and environmentally sensitive, high latitude environments. Finally, this thesis provides an important analogue for studies concerning the interaction of petroleum systems and climate change, with the assessment of the sensitivity of such systems to environmental change, providing critical insight into how near-surface hydrocarbon accumulations may respond to past and future climate and oceanic warming.

References

Acton, G., 2012, Proceedings of the Baffin Bay Scientific Coring Program – Expedition 344S: Reporting by company consortium with eight companies led by Shell, p. 1-842.

Andreassen, K., Hubbard, A., Winsborrow, M., Patton, H., Vadakkepuliyambatta, S., Plaza-Faverola, A., Gudlaugsson, E., Serov, P., Deryabin, A., Mattingsdal, R., Mienert, J., and Bunz, S., 2017, Massive blow-out craters formed by hydrate-controlled methane expulsion from the Arctic seafloor: Science, v. 356, p. 948-953.

Bennett, R., Campbell, D. C., Furze, M. F., and Haggart, J. W., 2014, The shallow stratigraphy and geohazards of the Northeast Baffin Shelf and Lancaster Sound: Bulletin of Canadian Petroleum Geology, v. 62, no. 4, p. 217-231.

Bojesen-Koefoed, J. A., 2011, West Greenland Petroleum Systems – an Overview of Source Rocks and Oil Seepages and Their Implications for Offshore Petroleum Exploration: The Geological Survey of Denmark and Greenland.

Cairn Energy PLC, 2011, Greenland operational update [press release], p. 1-2.

Cavanagh, A. J., Di Primio, R., Scheck-Wenderoth, M., and Horsfield, B., 2006, Severity and timing of Cenozoic exhumation in the southwestern Barents Sea: Journal of the Geological Society, v. 163, no. 5, p. 761-774.

Chand, S., Thorsnes, T., Rise, L., Brunstad, H., Stoddart, D., Boe, R., Lagstad, P., and Svolsbru, T., 2012, Multiple episodes of fluid flow in the SW Barents Sea (Loppa High) evidenced by gas flares, pockmarks and gas hydrate accumulation: Earth and Planetary Science Letters, v. 331-332, p. 305-314.

Collett, T. S., 1993, Natural gas hydrates of the Prudhoe Bay and Kuparuk River area, north slope, Alaska: AAPG bulletin, v. 77, no. 5, p. 793-812.

Corcoran, D., and Doré, A., 2002, Top seal assessment in exhumed basin settings—Some insights from Atlantic margin and borderland basins, Norwegian Petroleum Society Special Publications, Volume 11, Elsevier, p. 89-107.

Demirbas, A., 2010, Methane hydrates as potential energy resource: Part 1 – Importance, resource and recovery facilities: Energy Conversion and Management, v. 51, no. 7, p. 1547-1561.

Doré, A. G., and Jensen, L. N., 1996, The impact of late Cenozoic uplift and erosion on hydrocarbon exploration: offshore Norway and some other uplifted basins: Global and Planetary Change, v. 12, no. 1-4, p. 415-436.

Fjeldskaar, W., and Amantov, A., 2018, Effects of glaciations on sedimentary basins: Journal of Geodynamics, v. 118, p. 66-81.

Goffey, G., Attree, M., Curtis, P., Goodfellow, F., Lynch, J., Mackertich, D., Orife, T., and Tyrrell, W., 2016, New exploration discoveries in a mature basin: offshore Denmark, *in* Bowman, M., and Levell, B., eds., Petroleum Geology of NW Europe: 50 Years of Learning – Proceedings of the 8th Petroleum Geology Conference: London, Geological Society.

Grassmann, S., Cramer, B., Delisle, G., Hantschel, T., Messner, J., and Winsemann, J., 2010, pT-effects of Pleistocene glacial periods on permafrost, gas hydrate stability zones and reservoir of the Mittelplate oil field, northern Germany: Marine and petroleum geology, v. 27, no. 1, p. 298-306.

Gray, D. I., 1987, Troll, *in* Spencer, A. M., ed., Geology of the Norwegian Oil and Gas Fields: London, Graham and Trotman.

Grecula, M., Wadsworth, S., Maloney, D., Lauferts, H., Cooke, G., Jones, A., and Stevanovic, S., Baffin Bay Elusive Plays: Geological Surprises of an Arctic Exploration Campaign, *in* Proceedings American Association of Petroleum Geology International Conference and Exhibition (ICE), London, UK, 2018, Volume 30548, p. 1-20.

Gregersen, G., Knutz, P. C., Nøhr-Hansen, H., Sheldon, E., and Hopper, J. R., 2019, Tectonostratigraphy and evolution of the West Greenland continental margin: Bulletin of the Geological Society of Denmark, v. 67, p. 1-21.

Gregersen, U., 2008, The north-east Baffin Bay region, offshore Greenland–a new frontier petroleum exploration region: Geological Survey of Denmark and Greenland (GEUS) Bulletin, v. 15, p. 65-68.

Gregersen, U., Hopper, J. R., and Knutz, P. C., 2013, Basin seismic stratigraphy and aspects of prospectivity in the NE Baffin Bay, Northwest Greenland: Marine and Petroleum Geology, v. 46, p. 1-18.

Gregersen, U., Knutz, P. C., and Hopper, J. R., 2016, New geophysical and geological mapping of the eastern Baffin Bay region, offshore West Greenland: Geological Survey of Denmark and Greenland Bulletin, v. 35, p. 83-86.

Japsen, P., Bonow, J. M., Green, P. F., Chalmers, J. A., and Lidmar-Bergstrom, K., 2006, Elevated, passive continental margins: Long-term highs or Neogene uplifts? New evidence from West Greenland: Earth and Planetary Science Letters, v. 248, no. 1-2, p. 330-339.

Johansen, H., Fjeldskaar, W., and Mykkeltveit, J., 1996, The influence of glaciation on the basin temperature regime: Global and Planetary Change, v. 12, no. 1-4, p. 437-448.

Kjemperud, A., and Fjeldskaar, W., 1992, Pleistocene glacial isostasy - implications for petroleum geology: NPF Special Publication, v. 1, p. 187-195.

Knutz, P. C., Gregersen, U., and Hopper, J. R., 2012, Late Paleogene Submarine Fans in Baffin Bay and North-West Greenland, 74th EAGE Conference and Exhibition incorporating EUROPEC 2012 Copenhagen, EAGE, p. 5.

Knutz, P. C., Hopper, J. R., Gregersen, U., Nielsen, T., and Japsen, P., 2015, A contourite drift system on the Baffin Bay–West Greenland margin linking Pliocene Arctic warming to poleward ocean circulation: Geology, v. 43, no. 10, p. 907-910.

Knutz, P. C., Newton, A. M. W., Hopper, J. R., Huuse, M., Gregersen, U., Sheldon, E., and Dybkjær, K., 2019, Eleven phases of Greenland Ice Sheet shelf-edge advance over the past 2.7 million years: Nature Geoscience, v. 12, p. 361-368.

Krey, V., Canadell, J. G., Nakicenovic, N., Abe, Y., Andruleir, H., Archer, D., Grubler, A., Hamilton, N. T. M., Johnson, A., Kostov, V., Lamarque, J., Langhorne, N., Nisbet, E. G., O'Neil, B., Riahi, K., Riedel, M., Wang, W., and Yakushev, V., 2009, Gas hydrates: entrance to a methane age or climate threat?: Environmental Research Letters, v. 4, p. 1-6.

Lambeck, K., Smither, C., and Johnston, P., 1998, Sea-level change, glacial rebound and mantle viscosity for northern Europe: Geophysical Journal International, v. 134, no. 1, p. 102-144.

Lee, J., Jung, J., Lee, M., Bahk, J.-J., Choi, J., Ryu, B.-J., and Schultheiss, P., 2013, Pressure core based study of gas hydrates in the Ulleung Basin and implication for geomechanical controls on gas hydrate occurrence: Marine and Petroleum Geology, v. 47, p. 85-98.

Løtveit, I. F., Fjeldskaar, W., and Sydnes, M., 2019, Tilting and flexural stresses in basins due to glaciations—An example from the Barents Sea: Geosciences, v. 9, no. 11, p. 474.

Løtveit, I. F., Gudmundsson, A., and Fjeldskaar, W., 2011, Effects of stress changes due to glacial erosion on reservoir excess pressure and fault-zone reactivation: EGU Gen. Assem.

Lucazeau, F., 2019, Analysis and mapping of an updated terrestrial heat flow data set: Geochemistry, Geophysics, Geosystems, v. 20, no. 8, p. 4001-4024.

Lund, B., Schmidt, P., and Hieronymus, C., 2009, Stress evolution and fault stability during the Weichselian glacial cycle: Swedish Nuclear Fuel and Waste Management Co.

Medvedev, S., Hartz, E. H., Schmid, D. W., Zakariassen, E., and Varhaug, P., 2019, Influence of glaciations on North Sea petroleum systems: Geological Society, London, Special Publications, v. 494, p. SP494-2018-2183.

Merey, S., 2016, Drilling of gas hydrate reservoirs: Journal of Natural Gas Science and Engineering, v. 35, p. 1167-1179.

Minshull, T. A., Marín-Moreno, H., Betlem, P., Bialas, J., Bünz, S., Burwicz, E., Cameselle, L., Cifci, G., Giustinaini, M., Hillman, J. I. T., Hölz, S., Hopper, J. R., Ion, G., León, R., Magalhaes, V., Makovsky, Y., Mata, M., Max, M. D., Nielsen, T., Okay, S., Ostrovsky, I., O'Neil, N., Pinheiro, L. M., Plaza-Faverola, A., Rey, D., Roy, S., Schwalenberg, K., Senger, K., Vadakkepuliyambatta, S., Vasilev, A., and Vázquez, J. T., 2020, Hydrate occurrence in Europe: A review of available evidence: Marine and Petroleum Geology, v. 111, p. 735-764.

Mouginot, J., Rignot, E., Bjørk, A. A., Van Den Broeke, M., Millan, R., Morlighem, M., Noël, B., Scheuchl, B., and Wood, M., 2019, Forty-six years of Greenland Ice Sheet mass balance from 1972 to 2018: Proceedings of the National Academy of Sciences, v. 116, no. 19, p. 9239-9244.

Newton, A. M. W., Huuse, M., Cox, D. R., and Knutz, P. C., 2021, Seismic geomorphology and evolution of the Melville Bugt Trough Mouth Fan, northwest Greenland: Quaternary Science Reviews, v. 255, p. 1-23.

Newton, A. M. W., Huuse, M., Knutz, P. C., Cox, D. R., and Brocklehurst, S. H., 2020, Repeated ice streaming on the northwest Greenland shelf since the onset of the Middle Pleistocene Transition: The Cryosphere Discuss., v. 2019, p. 1-18.

Newton, A. M. W., Knutz, P. C., Huuse, M., Gannon, P., Brocklehurst, S. H., Clausen, O. R., and Gong, Y., 2017, Ice stream reorganization and glacial retreat on the northwest Greenland shelf: Geophysical Research Letters, v. 44, p. 7826-7835.

Nøhr-Hansen, H., Pedersen, G. K., Knutz, P. C., Bojesen-Koefoed, J. A., Sliwinska, K. K., and Hovikoski, J., 2018, Potential Cretaceous source-rocks from the north-east Baffin Bay, West Greenland, AAPG Europe Regional Conference - Global Analogues of the Atlantic Margin: Lisbon, p. 1.

Nyland, B., Jensen, L. N., Skagen, J. I., Skarpnes, O., and Vorren, T., 1992, Tertiary uplift and erosion in the Barents sea: magnitude, timing and consequences, *in* Larsen, R. M., Brekke, H., Larsen, B. T., and Talleraas, E., eds., Structural and Tectonic modelling and its application to petroleum geology: Amsterdam, Netherlands, Elsevier Science Publishers, p. 153-162.

Ostanin, I., Anka, Z., and Di Primio, R., 2017, Role of faults in Hydrocarbon Leakage in the Hammerfest Basin, SW Barents Sea: Insights from seismic data and numerical modelling: Geosciences, v. 7, no. 2, p. 28.

Portnov, A., Vadakkepuliyambatta, S., Mienert, J., and Hubbard, A., 2016, Ice-sheet-driven methane storage and release in the Arctic: Nature communications, v. 7, no. 1, p. 1-7.

Pye, G. D., and Hyndman, R. D., 1972, Heat-flow measurements in Baffin Bay and the Labrador Sea: Journal of Geophysical Research, v. 77, no. 5, p. 938-944.

Ruppel, C. D., and Kessler, J. D., 2017, The interaction of climate change and methane hydrates: Reviews of Geophysics, v. 55, no. 1, p. 126-168.

Serov, P., Vadakkepuliyambatta, S., Mienert, J., Patton, H., Portnov, A., Silyakova, A., Panieri, G., Carroll, M. L., Carroll, J., and Andreassen, K., 2017, Postglacial response of Arctic Ocean gas hydrates to climatic amelioration: Proceedings of the National Academy of Sciences, v. 114, no. 24, p. 6215-6220.

Stocker, T. F., Qin, D., Plattner, G.-K., Tignor, M. M., Allen, S. K., Boschung, J., Nauels, A., Xia, Y., Bex, V., and Midgley, P. M., 2014, Climate Change 2013: The physical science basis. contribution of working group I to the fifth assessment report of IPCC the intergovernmental panel on climate change: Cambridge, UK, Cambridge University Press, p. 1-29.

Tasianas, A., Martens, I., Bünz, S., and Mienert, J., 2016, Mechanisms initiating fluid migration at Snøhvit and Albatross fields, Barents Sea: arktos, v. 2, no. 1.

Whittaker, R. C., Hamann, R. E., and Pulvertaft, T. C. R., 1997, A New Frontier Province Offshore Northwest Greenland: Structure, Basin Development, and Petroleum Potential of the Melville Bay Area: AAPG Bulletin, v. 81, no. 6, p. 978-998.

Zieba, K. J., and Grover, A., 2016, Isostatic response to glacial erosion, deposition and ice loading. Impact on hydrocarbon traps of the southwestern Barents Sea: Marine and Petroleum Geology, v. 78, p. 168-183.

Appendix A

Preamble

AMWN interpreted the data, wrote the manuscript and drafted the figures presented in this chapter. DRC assisted with interpretations, figure creation and manuscript writing. All authors reviewed the final manuscript.

This manuscript is published in the journal *The Cryosphere*:

Newton, A. M. W., Huuse, M., Knutz, P. C., and Cox, D. R., 2020, Repeated ice streaming on the northwest Greenland continental shelf since the onset of the Middle Pleistocene Transition, The Cryosphere, 14, pp. 2303–2312.

Repeated Ice Streaming on the Northwest Greenland Continental Shelf since the Onset of the Middle Pleistocene Transition

Andrew M. W. Newton[1,2], Mads Huuse[1,], Paul C. Knutz[3,], and David Cox[1]

[1]Department of Earth and Environmental Sciences, The University of Manchester

[2]School of Natural and Built Environment, Elmwood Building, Queens University Belfast, University Road, UK, BT7 1NN

[3]Geophysics Department, Geological Survey of Denmark and Greenland, Øster Voldgade 10, DK-1350 Copenhagen K, Denmark

Abstract

Ice streams provide a fundamental control on ice sheet discharge and depositional patterns along glaciated margins. This paper investigates ancient ice streams by presenting the first 3D seismic geomorphological analysis of a major glacigenic succession offshore Greenland. In Melville Bugt, northwest Greenland, six sets of landforms (five buried and one on the seafloor) have been interpreted as mega-scale glacial lineations (MSGLs) that provide evidence for extensive ice streams on outer palaeo-shelves. A gradual change in mean MSGL orientation and associated depocentres through time suggests that the palaeo-ice flow and sediment transport pathways migrated in response to the evolving submarine topography through each glacial–interglacial cycle. The stratigraphy and available chronology show that the MSGLs are confined to separate stratigraphic units and were most likely formed after the onset of the Middle Pleistocene Transition at ~1.3 Ma. The MSGL record in Melville Bugt suggests that since ~1.3 Ma, ice streams have regularly advanced across the continental shelf during glacial stages. High-resolution buried 3D landform records such as these have not been previously observed anywhere on the Greenland continental shelf margin and provide a crucial benchmark for testing how accurately numerical models are able to recreate past configurations of the Greenland Ice Sheet

1. Introduction

The northwest sector of the Greenland Ice Sheet (GrIS) is currently experiencing some of the largest mass losses across the ice sheet (Mouginot et al., 2019). During the Pleistocene the northwest sector has also been shown to have experienced major changes in ice margin extent through multiple glacial–interglacial cycles (Knutz et al., 2019). To better project the future evolution of the northwest Greenland Ice Sheet, and the GrIS as a whole, requires the reconstruction of past configurations of the ice sheet, the role and evolution through time of its ice streams, and an understanding of how the antecedent and evolving topography impacted ice flow patterns during past glacial stages. Typically, reconstruction involves using fragmented geological records to constrain or test numerical ice sheet models that attempt to map spatio-temporal changes in ice sheet extent and the dominant processes as the climate evolves across multiple glacial–interglacial cycles (Solgaard et al., 2011; Tan et al., 2018). Improving and building upon that fragmented geological record is, therefore, of considerable importance for helping to improve and calibrate these models – i.e. if models can accurately reconstruct the past, then we can have more confidence in what they project for the future.

Although much of the past offshore extent of the GrIS and its retreat is poorly resolved (Funder et al., 2011; Vasskog et al., 2015), there are some areas, such as the Uummannaq and Disko troughs in the west and the Kangerlussuaq, Westwind, and Norske troughs in the east and northeast of Greenland, that have been surveyed. Geophysical data and shallow marine cores have been used to document landforms from the Last Glacial Maximum (LGM) on the continental shelf, deglacial ages, and retreat styles – with retreat often punctuated by Younger Dryas stillstands and an intricate relationship between calving margins and ocean currents (Arndt et al., 2017; Dowdeswell et al., 2010; Hogan et al., 2016; Jennings et al., 2014; Sheldon et al., 2016). Seismic reflection data have been used to explore evidence of older glaciations and show that the GrIS repeatedly advanced and retreated across the continental shelves of west and east Greenland through much of the late Pliocene and Pleistocene (Hofmann et al., 2016; Knutz et al., 2019; Laberg et al., 2007; Pérez et al., 2018). These seismic data show that the GrIS extent has varied by hundreds of kilometres throughout the Pleistocene and offer additional constraining observations to borehole and outcrop data that provide conflicting evidence that Greenland could have been nearly ice-free or persistently ice-covered for parts of the Pleistocene (Bierman et al., 2016; Schaefer et al., 2016).

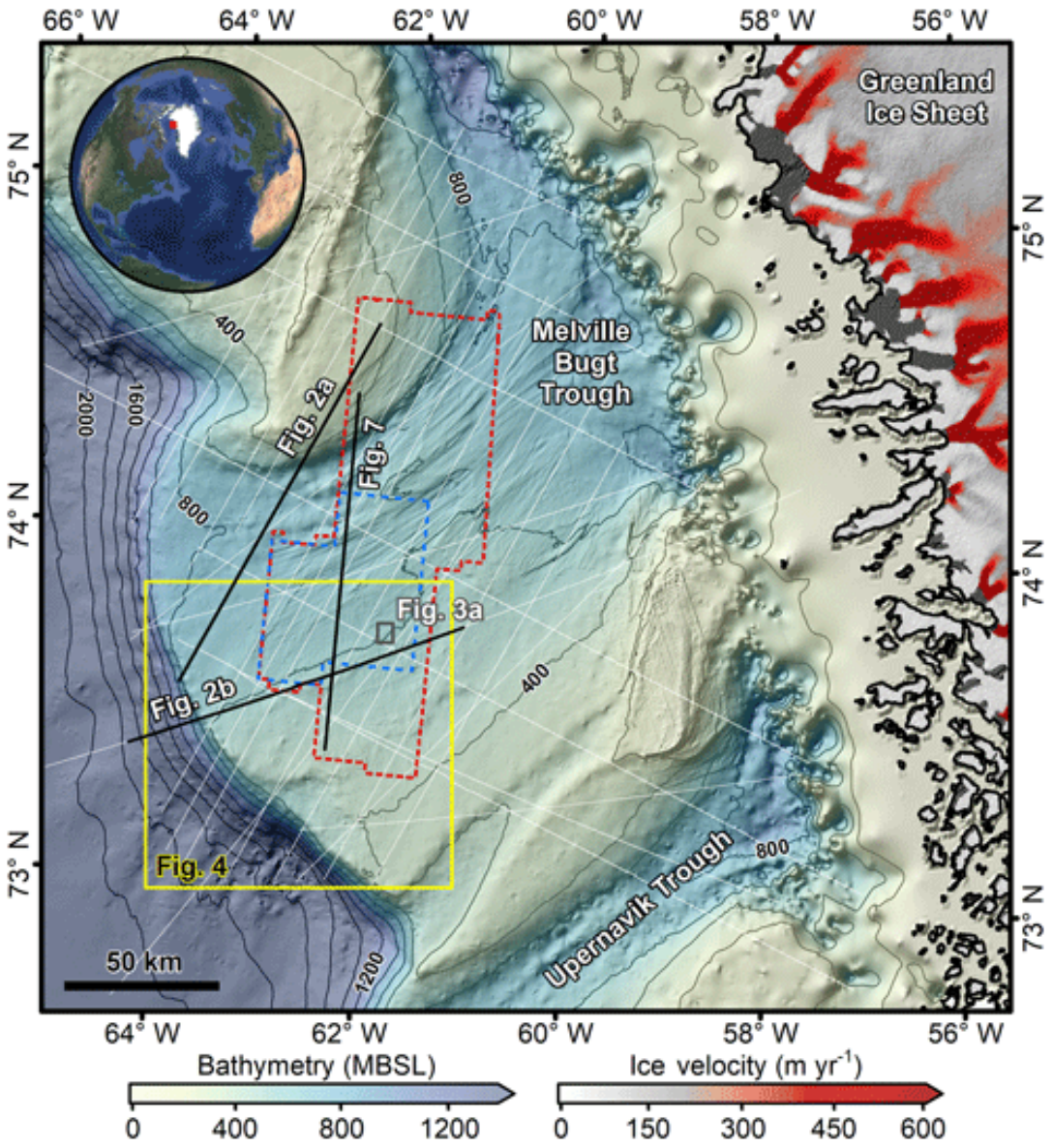

Figure 1. Seabed morphology and ice flow velocity | The grey bathymetric contours are every 200 m, and the dashed blue and red lines show the outline of the 3D seismic surveys (blue is a high-resolution subcrop of the original data that were reprocessed). The thin white lines show the locations of 2D seismic data. Mean ice velocity from MEaSUREs (see Joughin et al., 2010) shows contemporary outlet glaciers flowing into northeastern Baffin Bay. Bathymetry combined from Jakobsson et al. (2012), Newton et al. (2017), and Knutz et al. (2019). All figures plotted in UTM zone 21N. MBSL is metres below sea level.

To help understand long-term climatic changes, especially those associated with ice streams during glacial maxima, landforms observed on palaeo-seafloor surfaces mapped from 3D seismic data can provide information on past ice sheet geometries and ice-streaming locations. Landforms can be observed on surfaces preserved within trough-mouth fans (TMFs), typically deposited on the middle and upper continental slope, or on palaeo-shelf layers buried on the middle and outer continental shelf that built out as the TMF prograded (Ó Cofaigh et al., 2003). Here, for the first time offshore Greenland, buried glacial landforms preserved on palaeo-shelves are documented using 3D seismic

reflection data from Melville Bugt (Fig. 1). Whilst ice streams are thought to have been present in Melville Bugt since ~2.7 Ma (Knutz et al., 2019), these landforms provide new, direct, and detailed evidence of ice flow pathways for six episodes of ice stream advance onto the outer continental shelf of Melville Bugt from ~1.3 Ma.

2. Background

Ice streams are corridors of fast-flowing ice that can measure >20 km wide and be hundreds of kilometres long, with velocities of >400–500 m yr−1 (Bennett, 2003). Both in the present and in the geological past, ice streams have been important conduits for ice sheet mass redistribution and sediment delivery to ice sheet margins (Vorren and Laberg, 1997). Mega-scale glacial lineations (MSGLs) are elongated landforms (typically 1–10 km long) that form by the streamlining (Clark et al., 2003) or accretion of subglacial sediments (Spagnolo et al., 2016) beneath fast-flowing ice (Clark, 1993). This association is supported by observations of similar MSGL features beneath the present-day Rutford Ice Stream in West Antarctica (King et al., 2009). MSGLs thought to date to the LGM have been observed on the present-day seafloor of the Melville Bugt study area (Fig. 1) and typically measure 4–6 km long, 100–200 m wide, and 10–20 m high (Newton et al., 2017; Slabon et al., 2016). The MSGLs on the outermost continental shelf show that fast-flowing ice occupied the Melville Bugt Trough and reached the shelf edge, before retreating and experiencing changes in ice flow pathways, as is indicated by cross-cutting MSGLs on the middle continental shelf (Newton et al., 2017).

The glacial stratigraphy in Melville Bugt (Fig. 1) extends across an area of ~50 000 km2 and measures up to ~2 km thick. The succession has recorded advance and retreat of the northwest GrIS across the continental shelf multiple times since ~2.7 Ma and is subdivided into 11 major prograding units separated by regional unconformities (Knutz et al., 2019). The stratigraphy is partly age-constrained by a number of dates extracted from microfossil (~2.7 Ma) and palaeomagnetic (~1.8 Ma) data (Christ et al., 2020; Knutz et al., 2019). These dates suggest that whilst sediment accumulation likely varied over orbital and suborbital timescales, over periods longer than this (0.5–1.0 Myr) it did not change substantially and has been grossly linear through time since glacigenic deposition began (Knutz et al., 2019). In the northern part of the trough, topset preservation is limited due to more recent glacial erosion that has cut into the substrate (Fig. 2a), whereas in the south there is better preservation of aggradational topset strata (Fig. 2b) – i.e. palaeo-shelves where buried landforms might be found.

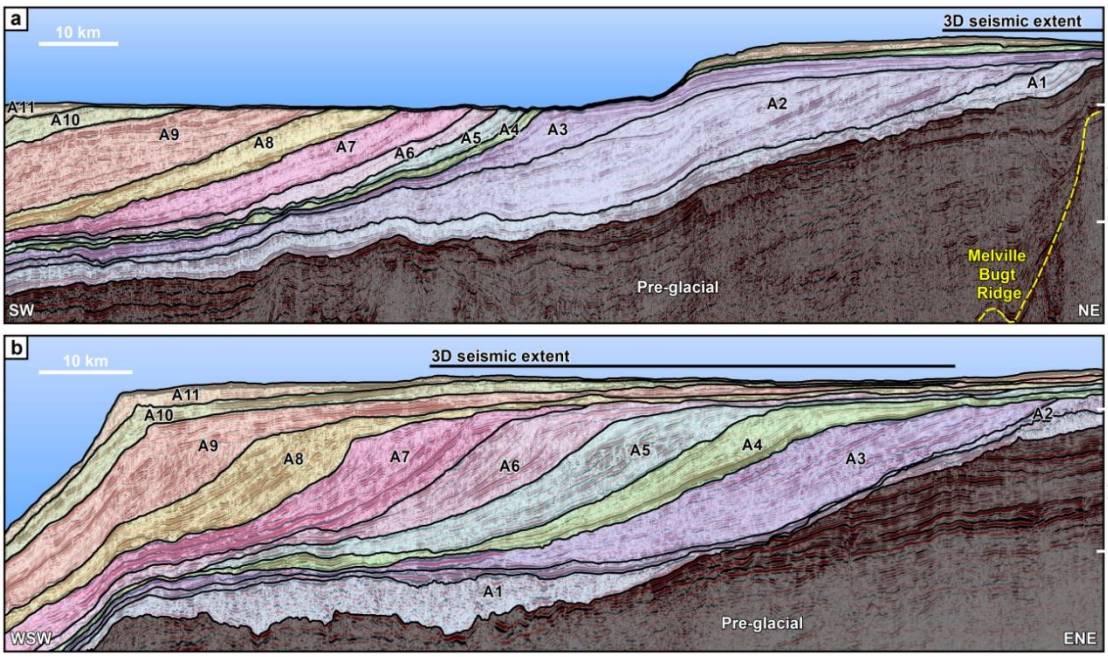

Figure 2. Seismic cross-section profiles through the glacigenic succession | The fan comprises 11 seismic stratigraphic units bounded by glacigenic unconformities formed since ~2.7 Ma (Knutz et al., 2019). The tentative chronology from Knutz et al. (2019) suggests that the palaeo-seafloor surfaces preserved within units A7–A9 likely cover a time period from ~1.3 to 0.43 Ma. This time period captures much of the Middle Pleistocene (781–126 ka) and the transition into it from ~1.3 Ma. Locations of the lines are shown in Fig. 1. TWT is two-way-travel time.

3. Methods

This study used industry 3D and 2D seismic reflection data from Melville Bugt, northwest Greenland (Fig. 1). The vertical resolution of the glacial succession is ~10–15 m and the horizontal resolution ~20–30 m – based on frequencies of ~30–50 Hz and a sound velocity of ~2–2.2 km s−1. Horizons were picked from within the 3D seismic data as part of a seismic geomorphological analysis (Posamentier, 2004), and gridded as 25 m × 25 m two-way-travel time surface maps – i.e. buried palaeo-seafloor maps. It is important to note that unlike traditional seafloor studies carried out on bathymetric data, these palaeo-seafloor surfaces will have subsided and compacted since being buried. This means that landform thicknesses likely represent a minimum estimate of their original morphology. Seismic attributes, including variance and root-mean-square (RMS) amplitude, were extracted across the surfaces to aid in visualising architectural elements and landforms. This study focused on identifying glacial landforms and used published examples to guide interpretation (e.g. Dowdeswell et al., 2016). Where possible, using the velocity model of Knutz et al. (2019), thickness maps were created for subunits derived from deposits that were stratigraphically linked to surfaces containing glacigenic landforms – e.g. correlative

slope deposits onlapping the profile of the glacially influenced clinoform reflection. These depocentre maps can be used to document where sediments have been eroded and deposited, providing insight into how depositional patterns may have changed in response to the evolution of ice stream pathways. In the absence of precise dating for each surface, the linear age model of Knutz et al. (2019) has been used to relatively date glacial landforms identified in the different prograding units.

4. Subglacial Landforms

Seismic geomorphological analysis of topset strata imaged in the 3D data showed four sets of buried streamlined features 5–15 km long and 200–300 m wide (Figs. 3 and 4). The landforms are typically 10–15 m high and although they are close to vertical seismic resolution limits (meaning that cross-sectional profiles are subtle), they are best observed in planform using the RMS amplitude or hillshaded surfaces. The streamlined features display a parallel concordance and are confined to individual palaeo-shelf layers within separate stratigraphic units, and their trend cross-cuts acquisition lines obliquely (Figs. 3 and 4). These features are interpreted as MSGLs due to their morphology (Spagnolo et al., 2014) and similarity to MSGLs observed on the local seafloor (Newton et al., 2017) and buried on other glaciated margins (e.g. Andreassen et al., 2007; Dowdeswell et al., 2006; Montelli et al., 2017; Rea et al., 2018).

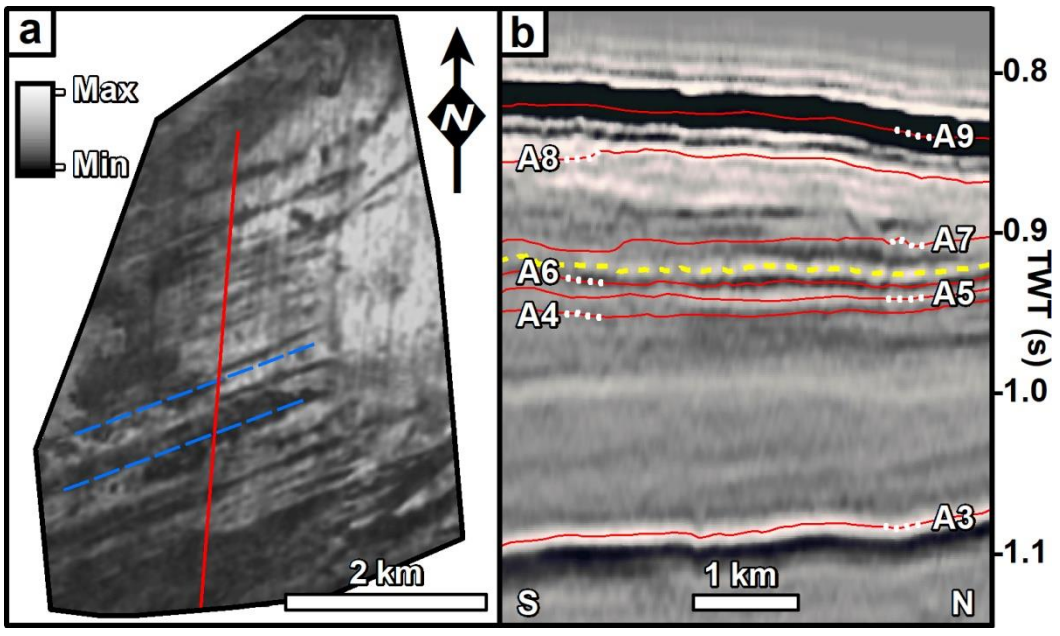

Figure 3. MSGL | (a) MSGL set 1, the oldest example of mega-scale glacial lineations (dashed blue lines), displayed as an RMS image observed from 3D seismic reflection data and within unit A7 (b). The colour bar represents RMS values. Note this surface is only partially preserved due to subsequent glacial erosion. For location see Fig. 1. (b) Seismic cross-section profile showing the stratigraphic position (dashed yellow line) of the surface imaged in panel (a). The red lines show the top surface of each unit in the glacigenic succession, and the dashed white lines are to help match the labels to surfaces in this condensed stratigraphy. The location of the cross-section profile is shown by the red line on (a).

MSGL set 1 is the oldest and is observed with an orientation of 254° on a partially preserved surface in the lowest part of a thinly developed topset section of unit A7 (~1.3–1.05 Ma; Fig. 3). It was not possible to confidently determine correlative slope deposits and the associated depocentre due to the limited spatial extent of their preservation. Rising through the stratigraphy, MSGL set 2 is observed in the upper part of unit A8 (~1.05–0.65 Ma; Fig. 4a, d), and the associated depocentre is located in the southwestern part of the study area and measures up to 250 m thick. All of the subunit depocentres show sediment thicknesses greater than 100 m and have been mapped from the slope deposits that are correlative to the adjacent palaeo-shelves. The slope deposits are typically comprised of onlapping chaotic seismic packages interpreted as stacked glacigenic debrites (Fig. 5; Vorren et al., 1989). MSGL set 2 has an average compass bearing of 225° (σ=5°) that aligns well with the maximum depocentre thickness (Fig. 4a). MSGL sets 3 and 4 are observed on separate surfaces preserved within the topset strata of unit A9 (~0.65–0.45 Ma; Fig. 4b, c, e, f), and their bearings show a gradual transition to 237° from the 225° observed in unit A8 (Fig. 6).

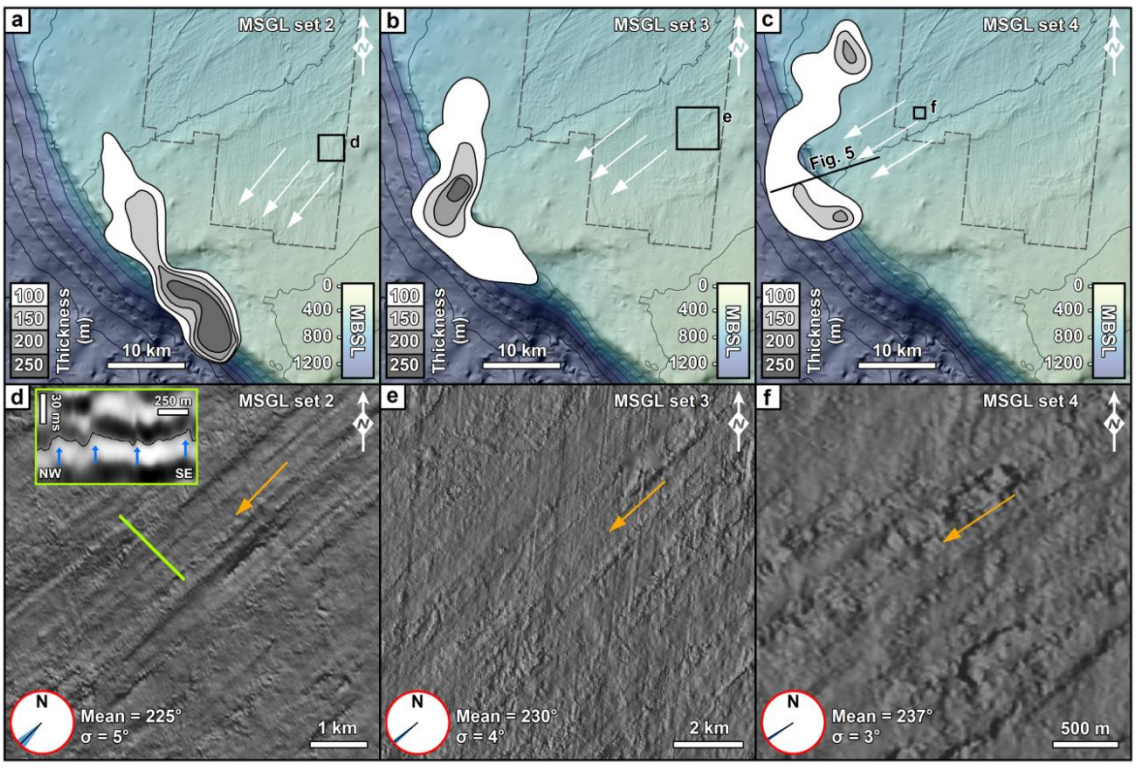

Figure 4. Buried MSGLs and associated TMF thickness maps | Panels (a) to (c) show the geographic location of MSGL sets 2–4 which are displayed as hillshade images on panels (d) to (f). The dashed grey line on panels (a) to (c) is the 3D seismic survey outline overlain on the contemporary seafloor; the white arrows show the inferred ice flow direction from the MSGLs, and the contoured outlines show the thickness of the sedimentary deposit associated with MSGL sets 2–4. Orange arrows on panels (d) to (f) show the inferred ice flow direction. On panel (d) the green line displays the location of the inset cross-section profile of the MSGL. Blue arrows point to the mounded features visible on the hillshade image. The red circles in panels (d) to (f) display average MSGL compass bearings (black line) and the standard deviation (surrounding blue

fan) for each panel. Location of panels (a) to (c) shown in Fig.1. The relative ages and stratigraphic positions of each MSGL set are discussed in the text and labelled in Fig. 6.

Although the 3D seismic data do not cover the distal part of the succession, by using examples of MSGLs that have been observed in 3D (Figs. 3, 4), the 2D seismic data were investigated for similar cross-sectional features. In unit A10 (~0.45–0.35 Ma) a reflection on the outer continental shelf shows a similar corrugated morphology, with heights of 10–15 m and widths of 200–300 m, to the MSGL pattern observed in the 3D data (Fig. 6b). The MSGLs documented in the 3D data also show that ice previously flowed towards this general area (Fig. 6c). The interpretation of the corrugated features as MSGL set 5 is less robust due to the lack of 3D data, and whilst it is not possible to unequivocally rule out that these features are something else, such as iceberg scours, an interpretation of MSGLs is supported by the location of these features in topset strata above the glacial unconformity that marks the top of unit A9, suggesting the presence of grounded and erosive ice on the outer continental shelf, conditions generally associated with MSGL formation.

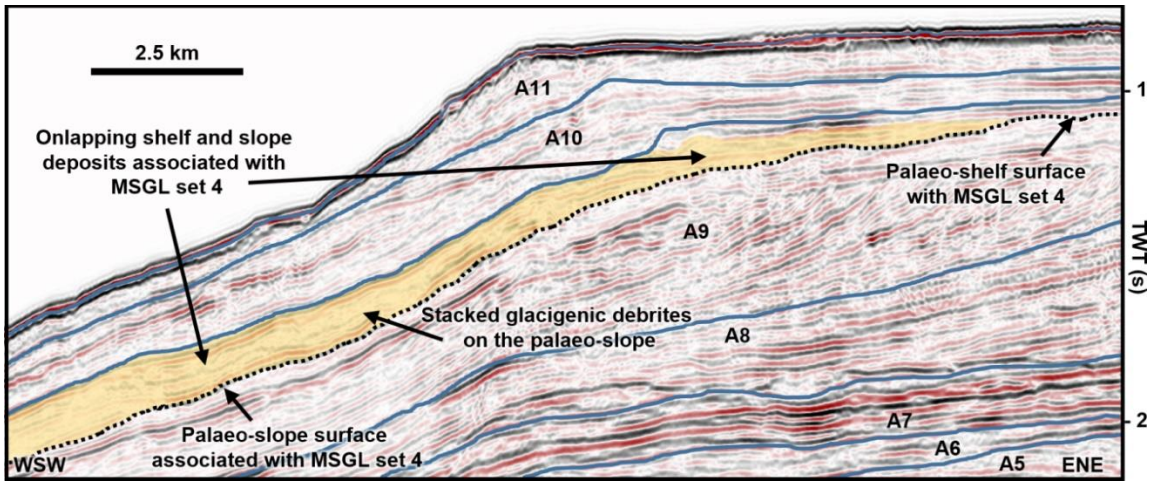

Figure 5. MSGL set 4 | Seismic cross-section profile showing the main glacigenic units and the palaeo-shelf surface (dotted line) where MSGL set 4 is observed. Onlapping and stacked debrite packages are interpreted to be genetically linked to deposition caused by the ice stream that formed this set of MSGLs and are used as an indicator of the broad depositional patterns displayed in Fig. 4c. Line location is shown in Fig. 4c.

The final set of MSGLs (set 6) is observed in unit A11 (~0.35–0 Ma) on the seafloor and provides evidence for a grounded ice stream on the outer continental shelf at the LGM (Newton et al., 2017; Fig. 6c). These MSGLs show cross-cutting evidence that allow for changes in ice flow patterns to be deduced. The oldest MSGLs on the seafloor suggest an ice flow towards the west-southwest that is parallel to the axis of the trough, whilst the younger MSGLs (i.e. those which cross-cut the older MSGLs) show an ice flow towards

the south-southwest, suggesting a change in ice flow during deglaciation (Newton et al., 2017).

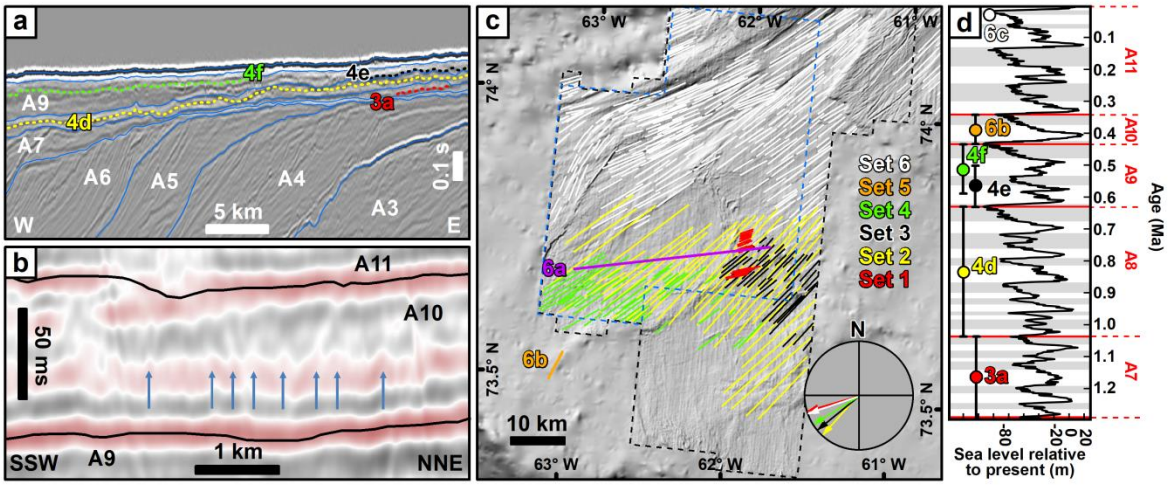

Figure 6. Distribution of MSGL | (a) Seismic cross-section profile showing the stratigraphic location of the surfaces shown in Figs. 3 and 4. The blue lines are the tops of the units shown in Fig. 2. The location of the lines is shown in panel (c). (b) Seismic cross-section profile from 2D seismic survey showing evidence for potential MSGLs (blue arrows) in unit A10 on the outer continental shelf. Seismic line location is shown in panel (c). (c) Digitised MSGL record from 3D seismic data. Set 6 represents the LGM record from Newton et al. (2017), and sets 1–5 are from the current study. The compass shows the mean bearings for each set of MSGLs with the exception of set 5 because it is not captured in 3D. (d) Possible age range for each MSGL surface observed within the glacigenic units of Knutz et al. (2019) and compared against the global sea level record (Miller et al., 2011). Grey bands are glacial stages. Note that in all the panels, the surfaces (a), digitised MSGL (c), mean flow bearings (c), and labels (d) are colour-coded to ease cross-referencing.

5. Paleo-ice Streams

The previous lack of 3D seismic data coverage means that prior to this study, ice stream landforms have not been observed for glacials preceding the LGM on the Greenland margin. Information on past ice flow patterns has, therefore, relied upon broad inferences from depocentre locations – i.e. areas where large volumes of sediment are associated with the general pathway of ice streams. Using the new seismic data, six sets of ice stream landforms have been documented – one on the seafloor, four buried surfaces imaged in 3D, and one captured in the 2D seismic data. The MSGL sets provide evidence for multiple ice-streaming events on the northwest Greenland continental shelf prior to, and including, the LGM. Limited chronological constraints are currently available to determine exact timings, but the available chronology suggests these features formed during six glacial stages after ~1.3 Ma (Knutz et al., 2019). Although no older MSGLs have been imaged on palaeo-shelves captured in the available 3D seismic data, ice streams are inferred to have operated in the area prior to ~1.3 Ma, based on the large volumes of sediment delivered to the margin (Knutz et al., 2019). It is noteworthy that the first

observations of MSGLs occur at the onset of a major change in the depositional patterns of the Melville Bugt and Upernavik TMFs. Unit A7 was deposited when the Melville Bugt and Upernavik TMFs combined to form an elongate depocentre up to 1 km thick. During the subsequent deposition of unit A8 the TMFs separated into discrete depocentres up to 700 m thick, signalling a possible reorganisation in ice flow in the region (Knutz et al., 2019). The reasons for this change are unresolved, but modification of the submarine topography brought about by glacigenic deposition and erosion, such as is presented here, may have forced adjustments in the ice sheet flow on the outer continental shelf due to changes in available accommodation.

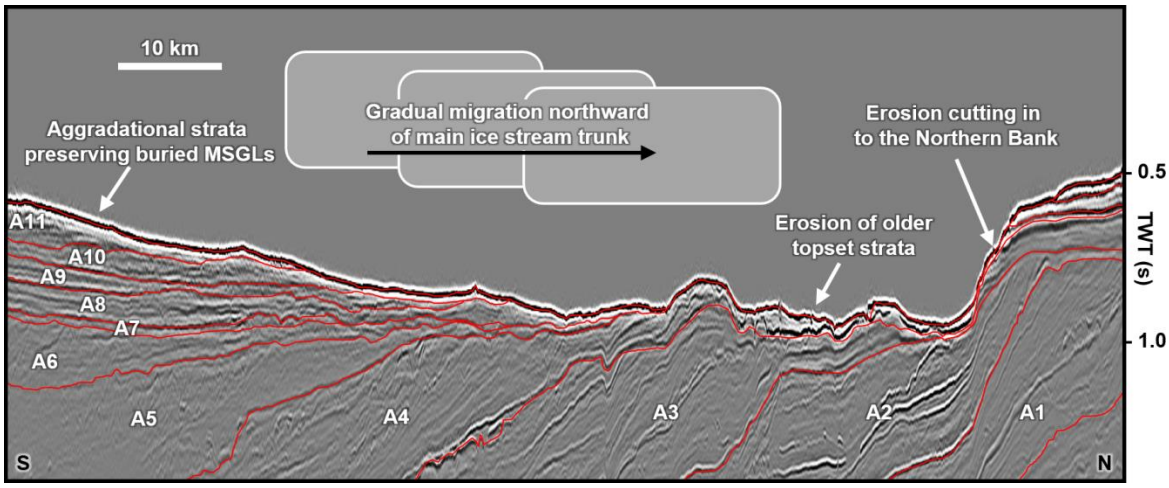

Figure 7. Topset preservation| Interpreted seismic strike cross-section profile across the continental shelf showing spatially variable preservation of topset deposits associated with the main depositional units. This variable preservation is thought to relate to the gradual migration of the ice stream away from the areas of higher topography that contain the aggradational strata. This northward migration of the ice stream pathways is also reflected by the erosion of the southern flank of the Northern Bank. Location of the line is shown in Fig. 1.

Switches in ice stream pathways on continental shelves between different glacial maxima have been observed on the mid-Norwegian margin, where new cross-shelf troughs were formed through the erosive action of ice (Dowdeswell et al., 2006). In contrast to the mid-Norwegian margin, the available data in Melville Bugt do not show evidence of buried cross-shelf troughs. The observations show changes in ice stream pathways that appear to have occurred more gradually between each MSGL set but remained focused within the confines of the pre-existing trough. The longevity of the Northern Bank and the significant overdeepening of the inner trough (see Newton et al., 2017) likely provided consistent topographic steering of ice streams on the inner continental shelf. On the outer continental shelf, deposition during the preceding glacial stage likely forced gradual ice stream migration northward due to this deposition reducing the available accommodation for subsequent glacial stages (Fig. 7). Thickness maps associated with MSGL sets 2–4

demonstrate this gradual, rather than extreme, shift in ice stream drainage pathways that is supported by 5–6° shifts in the mean orientation of each MSGL set from 225° during unit A8 time, to 237° during unit A9 time (Fig. 4). This shift continued at the LGM when the majority of MSGLs on the outer continental shelf – except for some cross-cutting related to deglaciation (Newton et al., 2017) – shows a mean orientation of ~248° (Fig. 6c).

The partial preservation of the different palaeo-shelves means ice margin fanning on the less topographically confined outer continental shelf cannot be definitively ruled out as an explanation for differing MSGL orientations. However, the observed metrics and depocentre migration provide complementary evidence that this was in response to a gradual migration of the main ice stream flow pathway – i.e. ice flow pathways gradually moved northward in a clockwise pattern from unit A8 onwards (~1 Ma). The gradual shift northward of the main ice stream pathway and its associated erosion meant that topset deposits in the south, with each passing glacial stage, were increasingly less impacted by the ice stream erosion, and therefore the landforms that they contained had a better chance of being preserved through subsequent glacial stages. The Melville Bugt Trough is the widest in Greenland (Newton et al., 2017), and it is possible that the preservation of these topsets is a consequence of this. The preservation suggests that whilst the main palaeo-ice stream trunks associated with each glacial stage were accommodated within the broad confines of the trough, the fast-flowing and most erosive ice did not occupy its full width – e.g. there are no MSGLs present for the LGM (set 6) in the southern part of the trough. The northward migration of the main ice stream pathway is also reflected by erosion and cutting into the deposits of the Northern Bank (Fig. 7). Although ice stream margin fanning or changes in upstream ice sheet controls cannot be ruled out, the gradual depocentre and MSGL migration suggests that deposition during successive glacial stages may have been sufficient to bring about small changes in flow directions and subsequent depositional patterns. Future ice sheet modelling can contribute to this discussion by exploring whether ice volume over northern Greenland would have been sufficient to maintain ice flux if the ice streams occupied the full width of the Melville Bugt Trough. To a lesser extent, it is possible that the Melville Bugt Ridge, an underlying tectonic structure which has previously generated accommodation in the southern part of the basin through differential subsidence (Cox et al., 2020; Knutz et al., 2019), could have contributed to reducing potential erosion of aggradational topsets by increasing palaeo-water depths to the point where ice grounding was significantly reduced or removed.

In the wider context of the whole GrIS, in east Greenland, sedimentological and geophysical evidence suggests that early in the Middle Pleistocene Transition (MPT – ~1.3

to 0.7 Ma) ice advanced across the continental shelf (Laberg et al., 2018; Pérez et al., 2019), whilst offshore southern Greenland documentation of increased ice-rafted detritus suggests a similar ice advance (St. John and Krissek, 2002). MPT ice sheet expansions have been documented in the Barents Sea (Mattingsdal et al., 2014), on the mid-Norwegian margin (Newton and Huuse, 2017), in the North Sea (Rea et al., 2018), and in North America (Balco and Rovey, 2010), highlighting a response of all major Northern Hemisphere ice sheets to a currently unresolved climate forcing. Although ice streaming in Melville Bugt continued after the MPT and through to the latest Pleistocene, some studies from lower-latitude areas of west and east Greenland show reduced ice stream erosion and deposition at this time (Hofmann et al., 2016; Pérez et al., 2018), perhaps suggesting the high-latitude locality of Melville Bugt or the overdeepened and bottlenecked geometry (topographic constraints) of the inner trough (Newton et al., 2017) helped promote conditions favourable for ice streaming.

The MSGL record presented here provides some additional insight into the contradictory records on the longevity of the GrIS. Schaefer et al. (2016) showed that cosmogenic signatures require ice-free periods during the Pleistocene and whilst these ice-free periods need not have occurred since 1.1 Ma, ice sheet loss could have occurred during or after the MPT. Ice stream evolution has been shown to have led to rapid ice sheet changes on other ancient ice sheets (Sejrup et al., 2016), and given that ~16 % of the GrIS currently drains into Melville Bugt (Rignot and Mouginot, 2012) the ice streams documented here could have contributed to major changes in ice sheet organisation and extent – indeed, the numerical model used by Schaefer et al. (2016) requires the early loss of the northwest GrIS during ice sheet collapse. Fully resolving issues like this requires numerical ice sheet models that are capable of reproducing fragmented geological evidence. For example, recent modelling exploring Pleistocene climate evolution (Willeit et al., 2019) provides palaeo-geographic maps of ice sheet extent that do not capture the ice sheet extent inferred from buried landform records on many glaciated margins (e.g. Rea et al., 2018), including Melville Bugt. Thus, there is currently a mismatch between modelling outputs and landform records. If these models are not able to recreate ice sheet extent, ice stream locations, and flow pathways that have been extracted from the geological record, then those models will require refinement before they can be used as a tool for projecting future GrIS evolution. These potential discrepancies underline how geological records, such as those presented here, provide crucial empirical constraints for modelling the GrIS across multiple glacial–interglacial cycles.

6. Conclusions

This study provides a seismic geomorphological analysis offshore northwest Greenland and documents, for the first time, several sets of buried MSGLs on the Greenland margin. The observation of different MSGL sets in separate stratigraphic layers confirms the presence of fast-flowing ice streams during at least six glacial maxima since the onset of the Middle Pleistocene Transition at ~1.3 Ma. These landform records show that grounded and fast-flowing ice advanced across the continental shelf to the palaeo-shelf edge of northwest Greenland, with each subsequent ice stream flow pathway being partly controlled by the deposits left behind by the ice streams that preceded it. This represents a first spatio-temporal insight into sediment deposition and ice flow dynamics of individual ice streams during glacial maxima since ~1.3 Ma in Melville Bugt. These results help to further emphasise why northwest Greenland would be suitable for future ocean drilling that will help to elucidate ice sheet and climate history of the region.

Acknowledgments

Andrew M. W. Newton was supported by the Natural Environment Research Council (NERC) and Cairn Energy. David R. Cox was supported by NERC and the British Geological Survey. Schlumberger and Esri are thanked for Petrel and ArcGIS software. All authors thank Cairn Energy and Shell for data and permission to publish. Simon H. Brocklehurst is thanked for pre-reviewing this work and offering valuable insights. Brice R. Rea, Lara F. Perez, the anonymous reviewer, and the editor Pippa Whitehouse are thanked for helpful comments and handling of the manuscript.

References

Andreassen, K., Ødegaard, C. M., and Rafaelsen, B.: Imprints of former ice streams, imaged and interpreted using industry three-dimensional seismic data from the south-western Barents Sea, in: Seismic geomorphology: applications to hydrocarbon exploration and production, edited by: Davies, R. J., Posamentier, H. W., Wood, L. W., and Cartwright, J. A., Geological Society Special Publication, London, UK, 151–169, 2007.

Arndt, J. E., Jokat, W., and Dorschel, B.: The last glaciation and deglaciation of the Northeast Greenland continental shelf revealed by hydro-acoustic data, Quaternary Sci. Rev., 160, 45–56, https://doi.org/10.1016/j.quascirev.2017.01.018, 2017.

Balco, G. and Rovey, C. W.: Absolute chronology for major Pleistocene advances of the laurentide ice Sheet, Geology, 38, 795–798, https://doi.org/10.1130/G30946.1, 2010.

Bennett, M. R.: Ice streams as the arteries of an ice sheet: Their mechanics, stability and significance, Earth-Sci. Rev., 61, 309–339, https://doi.org/10.1016/S0012-8252(02)00130-7, 2003.

Bierman, P. R., Shakun, J. D., Corbett, L. B., Zimmerman, S. R., and Rood, D. H.: A persistent and dynamic East Greenland Ice Sheet over the past 7.5 million years, Nature, 540, 256–260, https://doi.org/10.1038/nature20147, 2016.

Christ, A. J., Bierman, P. R., Knutz, P. C., Corbett, L. B., Fosdick, J. C., Thomas, E. K., Cowling, O. C., Hidy, A. J., and Caffee, M. W.: The Northwestern Greenland Ice Sheet During The Early Pleistocene Was Similar To Today, Geophys. Res. Lett., 47, e2019GL085176, https://doi.org/10.1029/2019GL085176, 2020.

Clark, C. D.: Mega-scale glacial lineations and cross-cutting ice-flow landforms, Earth Surf. Proc. Land., 18, 1–29, https://doi.org/10.1002/esp.3290180102, 1993.

Clark, C. D., Tulaczyk, S. M., Stokes, C. R., and Canals, M.: A groove-ploughing theory for the production of mega-scale glacial lineations, and implications for ice-stream mechanics, J. Glaciol., 49, 240–256, https://doi.org/10.3189/172756503781830719, 2003.

Cox, D. R., Huuse, M., Newton, A. M. W., Gannon, P., and Clayburn, J. A. P.: Slip Sliding Away: Enigma of Large Sandy Blocks within a Gas Bearing Mass Transport Deposit, Offshore NW Greenland, Am. Assoc. Petr. Geol. B., 104, 1011–1044, https://doi.org/10.1306/10031919011, 2020.

Dowdeswell, J. A., Ottesen, D., and Rise, L.: Flow switching and large-scale deposition by ice streams draining former ice sheets, Geology, 34, 313–316, https://doi.org/10.1130/G22253.1, 2006.

Dowdeswell, J. A., Ottesen, D., and Rise, L.: Rates of sediment delivery from the Fennoscandian Ice Sheet through an ice age, Geology, 38, 3–6, https://doi.org/10.1130/G25523.1, 2010.

Dowdeswell, J. A., Canals, M., Jakobsson, M., Todd, B. J., Dowdeswell, E. K., and Hogan, K. A.: Atlas of Submarine Glacial landforms: Modern, Quaternary and Ancient, Geological Society of London, London, UK, 2016.

Funder, S., Kjeldsen, K. K., Kjær, K. H., and O Cofaigh, C.: The Greenland Ice Sheet During the Past 300 000 Years: A Review, in: Developments in Quaternary Science, edited by: Ehlers, J., Gibbard, P. L., and Hughes, P. D., Elsevier, Amsterdam, the Netherlands, 699–713, 2011.

Hofmann, J. C., Knutz, P. C., Nielsen, T., and Kuijpers, A.: Seismic architecture and evolution of the Disko Bay trough-mouth fan, central West Greenland margin, Quaternary Sci. Rev., 147, 69–90, https://doi.org/10.1016/j.quascirev.2016.05.019, 2016.

Hogan, K. A., Ó Cofaigh, C., Jennings, A. E., Dowdeswell, J. A., and Hiemstra, J. F.: Deglaciation of a major palaeo-ice stream in Disko Trough, West Greenland, Quaternary Sci. Rev., 147, 5–26, https://doi.org/10.1016/j.quascirev.2016.01.018, 2016.

Jakobsson, M., Mayer, L., Coakley, B., Dowdeswell, J. A., Forbes, S., Fridman, B., Hodnesdal, H., Noormets, R., Pedersen, R., Rebesco, M., Schenke, H. W., Zarayskaya, Y., Accettella, D., Armstrong, A., Anderson, R. M., Bienhoff, P., Camerlenghi, A., Church, I., Edwards, M., Gardner, J. V., Hall, J. K., Hell, B., Hestvik, O., Kristoffersen, Y., Marcussen, C., Mohammad, R., Mosher, D., Nghiem, S. V., Pedrosa, M. T., Travaglini, P. G., and Weatherall, P.: The International Bathymetric Chart of the Arctic Ocean (IBCAO) Version 3.0, Geophys. Res. Lett., 39, L12609, https://doi.org/10.1029/2012GL052219, 2012.

Jennings, A. E., Walton, M. E., Ó Cofaigh, C., Kilfeather, A., Andrews, J. T., Ortiz, J. D., De Vernal, A., and Dowdeswell, J. A.: Paleoenvironments during Younger Dryas-Early Holocene retreat of the Greenland Ice Sheet from outer Disko Trough, central west Greenland, J. Quaternary Sci., 29, 27–40, https://doi.org/10.1002/jqs.2652, 2014.

Joughin, I., Smith, B. E., Howat, I. M., Scambos, T., and Moon, T.: Greenland flow variability from ice-sheet-wide velocity mapping, J. Glaciol., 56, 415–430, https://doi.org/10.3189/002214310792447734, 2010.

King, E. C., Hindmarsh, R. C. A., and Stokes, C. R.: Formation of mega-scale glacial lineations observed beneath a West Antarctic ice stream, Nat. Geosci., 2, 585–588, https://doi.org/10.1038/ngeo581, 2009.

Knutz, P. C., Newton, A. M. W., Hopper, J. R., Huuse, M., Gregersen, U., Sheldon, E., and Dybkjær, K.: Eleven phases of Greenland Ice Sheet shelf-edge advance over the past 2.7 million years, Nat. Geosci., 12, 361–368, https://doi.org/10.1038/s41561-019-0340-8, 2019.

Laberg, J. S., Guidard, S., Mienert, J., Vorren, T. O., Haflidason, H., and Nygård, A.: Morphology and morphogenesis of a high-latitude canyon; the Andøya Canyon, Norwegian Sea, Mar. Geol., 246, 68–85, https://doi.org/10.1016/j.margeo.2007.01.009, 2007.

Laberg, J. S., Rydningen, T. A., Forwick, M., and Husum, K.: Depositional processes on the distal Scoresby Trough Mouth Fan (ODP Site 987): Implications for the Pleistocene evolution of the Scoresby Sund Sector of the Greenland Ice Sheet, Mar. Geol., 402, 51–59, https://doi.org/10.1016/j.margeo.2017.11.018, 2018.

Mattingsdal, R., Knies, J., Andreassen, K., Fabian, K., Husum, K., Grøsfjeld, K., and De Schepper, S.: A new 6 Myr stratigraphic framework for the Atlantic-Arctic Gateway, Quaternary Sci. Rev., 92, 170–178, https://doi.org/10.1016/j.quascirev.2013.08.022, 2014.

Miller, K., Mountain, G., Wright, J., and Browning, J.: A 180-Million-Year Record of Sea Level and Ice Volume Variations from Continental Margin and Deep-Sea Isotopic Records, Oceanography, 24, 40–53, https://doi.org/10.5670/oceanog.2011.26, 2011.

Montelli, A., Dowdeswell, J. A., Ottesen, D., and Johansen, S. E.: Ice-sheet dynamics through the Quaternary on the mid-Norwegian continental margin inferred from 3D seismic data, Mar. Petrol. Geol., 80, 228–242, https://doi.org/10.1016/j.marpetgeo.2016.12.002, 2017.

Mouginot, J., Rignot, E., Bjørk, A. A., van den Broeke, M., Millan, R., Morlighem, M., Noël, B., Scheuchl, B., and Wood, M.: Forty-six years of Greenland Ice Sheet mass balance from 1972 to 2018, P. Natl. Acad. Sci. USA, 116, 9239–9244, https://doi.org/10.1073/pnas.1904242116, 2019.

Newton, A. M. W. and Huuse, M.: Late Cenozoic environmental changes along the Norwegian margin, Mar. Geol., 393, 216–244, https://doi.org/10.1016/j.margeo.2017.05.004, 2017.

Newton, A. M. W., Knutz, P. C., Huuse, M., Gannon, P., Brocklehurst, S. H., Clausen, O. R., and Gong, Y.: Ice stream reorganization and glacial retreat on the northwest Greenland shelf, Geophys. Res. Lett., 44, 7826–7835, https://doi.org/10.1002/2017GL073690, 2017.

Ó Cofaigh, C., Taylor, J., Dowdeswell, J. A., and Pudsey, C. J.: Palaeo-ice streams, trough mouth fans and high-latitude continental slope sedimentation, Boreas, 32, 37–55, https://doi.org/10.1080/03009480310001858, 2003.

Pérez, L. F., Nielsen, T., Knutz, P. C., Kuijpers, A., and Damm, V.: Large-scale evolution of the central-east Greenland margin: New insights to the North Atlantic glaciation history, Global Planet. Change, 163, 141–157, https://doi.org/10.1016/j.gloplacha.2017.12.010, 2018.

Pérez, L. F., Nielsen, T., Rasmussen, T. L., and Winsborrow, M.: Quaternary interaction of cryospheric and oceanographic processes along the central-east Greenland margin, Boreas, 48, 72–91, https://doi.org/10.1111/bor.12340, 2019.

Posamentier, H. W.: Seismic Geomorphology: Imaging Elements of Depositional Systems from Shelf to Deep Basin Using 3D Seismic Data: Implications for Exploration and Development, in: 3D Seismic Technology: Application to the Exploration of Sedimentary Basins, edited by: Davies, R. J., Cartwright, J. A., Stewart, S. A., Lappin, M., and Underhill, J. R., Geological Society of London, London, UK, 11–24, 2004.

Rea, B. R., Newton, A. M. W., Lamb, R. M., Harding, R., Bigg, G. R., Rose, P., Spagnolo, M., Huuse, M., Cater, J. M. L., Archer, S., Buckley, F., Halliyeva, M., Huuse, J., Cornwell, D. G., Brocklehurst, S. H., and Howell, J. A.: Extensive marine-terminating ice sheets in Europe from 2.5 million years ago, Sci. Adv., 4, eaar8327, https://doi.org/10.1126/sciadv.aar8327, 2018.

Rignot, E. and Mouginot, J.: Ice flow in Greenland for the International Polar Year 2008-2009, Geophys. Res. Lett., 39, L11501, https://doi.org/10.1029/2012GL051634, 2012.

Schaefer, J. M., Finkel, R. C., Balco, G., Alley, R. B., Caffee, M. W., Briner, J. P., Young, N. E., Gow, A. J., and Schwartz, R.: Greenland was nearly ice-free for extended periods during the Pleistocene, Nature, 540, 252–255, https://doi.org/10.1038/nature20146, 2016.

Sejrup, H. P., Clark, C. D., and Hjelstuen, B. O.: Rapid ice sheet retreat triggered by ice stream debuttressing: Evidence from the North Sea, Geology, 44, 355–358, https://doi.org/10.1130/G37652.1, 2016.

Sheldon, C., Jennings, A., Andrews, J. T., Ó Cofaigh, C., Hogan, K., Dowdeswell, J. A., and Seidenkrantz, M. S.: Ice stream retreat following the LGM and onset of the west Greenland current in Uummannaq Trough, west Greenland, Quaternary Sci. Rev., 147, 27–46, https://doi.org/10.1016/j.quascirev.2016.01.019, 2016.

Slabon, P., Dorschel, B., Jokat, W., Myklebust, R., Hebbeln, D., and Gebhardt, C.: Greenland ice sheet retreat history in the northeast Baffin Bay based on high-resolution bathymetry, Quaternary Sci. Rev., 154, 182–198, https://doi.org/10.1016/j.quascirev.2016.10.022, 2016.

Solgaard, A. M., Reeh, N., Japsen, P., and Nielsen, T.: Snapshots of the Greenland ice sheet configuration in the Pliocene to early Pleistocene, J. Glaciol., 57, 871–880, https://doi.org/10.3189/002214311798043816, 2011.

Spagnolo, M., Clark, C. D., Ely, J. C., Stokes, C. R., Anderson, J. B., Andreassen, K., Graham, A. G. C., and King, E. C.: Size, shape and spatial arrangement of mega-scale glacial lineations from a large and diverse dataset, Earth Surf. Proc. Land., 39, 1432–1448, https://doi.org/10.1002/esp.3532, 2014.

Spagnolo, M., Phillips, E., Piotrowski, J. A., Rea, B. R., Clark, C. D., Stokes, C. R., Carr, S. J., Ely, J. C., Ribolini, A., Wysota, W., and Szuman, I.: Ice stream motion facilitated by a shallow-deforming and accreting bed, Nat. Commun., 7, 10723, https://doi.org/10.1038/ncomms10723, 2016.

St. John, K. E. K. and Krissek, L. A.: The late Miocene to Pleistocene ice-rafting history of Southeast Greenland, Boreas, 31, 28–35, https://doi.org/10.1111/j.1502-3885.2002.tb01053.x, 2002.

Tan, N., Ladant, J. B., Ramstein, G., Dumas, C., Bachem, P., and Jansen, E.: Dynamic Greenland ice sheet driven by pCO2 variations across the Pliocene Pleistocene transition, Nat. Commun., 9, 4755, https://doi.org/10.1038/s41467-018-07206-w, 2018.

Vasskog, K., Langebroek, P. M., Andrews, J. T., Nilsen, J. E. Ø., and Nesje, A.: The Greenland Ice Sheet during the last glacial cycle: Current ice loss and contribution to sea-level rise from a palaeoclimatic perspective, Earth-Sci. Rev., 150, 45–67, https://doi.org/10.1016/j.earscirev.2015.07.006, 2015.

Vorren, T. O. and Laberg, J. S.: Trough mouth fans - Palaeoclimate and ice-sheet monitors, Quaternary Sci. Rev., 16, 865–881, https://doi.org/10.1016/S0277-3791(97)00003-6, 1997.

Vorren, T. O., Lebesbye, E., Andreassen, K., and Larsen, K. B.: Glacigenic sediments on a passive continental margin as exemplified by the Barents Sea, Mar. Geol., 85, 251–272, https://doi.org/10.1016/0025-3227(89)90156-4, 1989.

Willeit, M., Ganopolski, A., Calov, R., and Brovkin, V.: Mid-Pleistocene transition in glacial cycles explained by declining CO2 and regolith removal, Sci. Adv., 5, eaav7337, https://doi.org/10.1126/sciadv.aav7337, 2019.

B

Appendix B

Preamble

AMWN interpreted the data, wrote the manuscript and drafted the figures presented in this chapter. DRC assisted with interpretations and figure creation. All authors reviewed the final manuscript.

This manuscript is published in the journal *Quaternary Science Reviews*:

Newton, A. M. W., Huuse, M., Cox, D. R., and Knutz, P. C., 2021, Seismic geomorphology and evolution of the Melville Bugt Trough Mouth Fan, northwest Greenland, Quaternary Science Reviews, v. 255, pp. 1-23.

Seismic Geomorphology and Evolution of the Melville Bugt Trough Mouth Fan, Northwest Greenland

Andrew M. W. Newton[1, 2], Mads Huuse[1, 2], David R. Cox[1] and Paul C. Knutz[3]

[1]Department of Earth and Environmental Sciences, The University of Manchester

[2]School of Natural and Built Environment, Elmwood Building, Queens University Belfast, University Road, UK, BT7 1NN

[3]Geophysics Department, Geological Survey of Denmark and Greenland, Øster Voldgade 10, DK-1350 Copenhagen K, Denmark.

Abstract

Trough mouth fans on glaciated margins are a common sedimentary feature that contain a record of ice sheet advance and retreat across the continental shelf. This study uses 2D and 3D seismic reflection data across the Melville Bugt Trough Mouth Fan (MB-TMF), offshore northwest Greenland, to document its stratigraphic architecture, glacigenic landforms, and marine deposits. The MB-TMF stratigraphy is characterised by rapid progradation of the continental shelf (over 100 km since ~2.7 Ma) and heterogeneous truncation or subsidence of topset strata. The variable topset character relates to the repeated growth and retreat of the Greenland Ice Sheet across the shelf since ~2.7 Ma. Seismic geomorphology and facies analysis of the prograding clinoforms show repeated sequences of debris flow deposits and gullies that are taken to infer gravity-driven processes and the presence of meltwater-related hyperpycnal flows in areas proximal to the ice sheet on the outer shelf. Several sets of mega-scale glacial lineations confirm the presence and flow pathways of successive ice streams since ~1.3 Ma. Evolution of the MB-TMF can be summarised into four stages that were controlled by variations in ice sheet erosion, topographic forcing of ice stream flow, and changes in accommodation related to

glacigenic deposition and tectonic subsidence. These results show that during the Middle Pleistocene Transition there is an apparent switch from a meltwater-dominated depositional regime, to one with greater emplacement of materials by ice directly at the palaeo-shelf edge. These results provide significant new detail about the large-scale glacigenic and marine depositional processes during the repeated fluctuations of the northwest Greenland Ice Sheet into Melville Bugt since ~2.7 Ma.

1. Introduction

As the Greenland Ice Sheet (GrIS) adjusts to rising air temperatures and changes in ice sheet extent, velocity, and mass, it will influence global sea level and North Atlantic oceanography (Hanna et al., 2013; Joughin et al., 2014; Rahmstorf et al., 2015; Richter-Menge et al., 2016; Shepherd et al., 2012). Given that the GrIS has the potential to add ~7 m to global sea level if it were to fully melt (IPCC, 2013), understanding its long-term history is of global significance, even if only a small percentage of that sea level rise were realised. Despite the importance of understanding the evolution of the GrIS across multiple timescales, it is only with recent innovations in marine geophysical surveying that our understanding has begun to improve. Past research has mainly concentrated on certain parts of the Greenland margin such as Disko Bugt and Scoresby Sund (e.g. Hofmann et al., 2016, 2018; Hogan et al., 2016; Jennings et al., 2014; Laberg et al., 2013, 2018; Pérez et al., 2018), leaving the Melville Bugt region (Fig. 1) as poorly understood at a range of timescales. This is important because the northwest sector of the GrIS is experiencing some of the largest contemporary mass losses across the ice sheet (Mouginot et al., 2019) and it has been shown to have responded dynamically across multiple glacial-interglacial cycles in the past (Knutz et al., 2019).

Recent seafloor mapping in Melville Bugt has shown that ice extended to the shelf edge at the Last Glacial Maximum (Newton et al., 2017; Slabon et al., 2016, 2018), which is more extensive than the mid-shelf position previously inferred (Funder et al., 2011). Stratigraphic mapping of the Melville Bugt Trough Mouth Fan (MB-TMF) and the Upernavik TMF (Fig. 1) show that since ~2.7 Ma there were at least 11 major growth and retreat phases of the northwest GrIS, including the Last Glacial Maximum (Knutz et al., 2019). A number of these advances are further documented by 3D seismic data that show the presence of ice streams on the continental shelf since ~1.3 Ma (Newton et al., 2020). This has important implications for our understanding of the longevity of the GrIS across orbital timescales (e.g. Bierman et al., 2016; Schaefer et al., 2016).

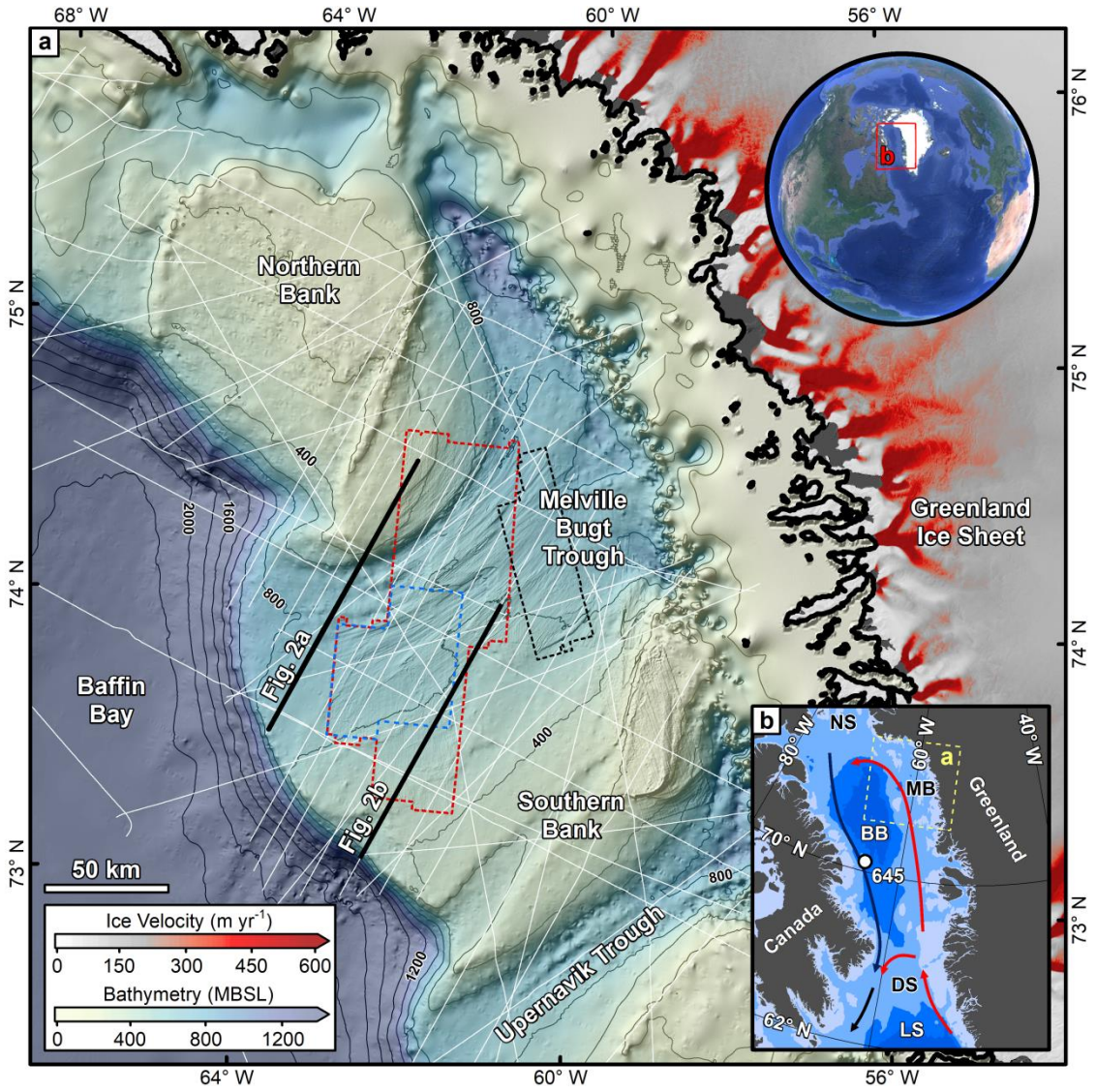

Figure 1. Study site area | (a) Bathymetry compilation of the Melville Bugt study site (continental shelf area) and northeastern part of Baffin Bay (basin area) from Newton et al. (2020). Ice velocity from Joughin et al. (2010). Bathymetric contours every 200 m. Red/blue dashed lines are the ANU 3D seismic volumes and black is PITU. White lines are the 2D seismic grid. (b) Simplified schematic showing the West Greenland (red), Baffin (gold), and Labrador (black) Currents. Abbreviations: Baffin Bay (BB), Davis Strait (DS), Labrador Sea (LS), Melville Bugt (MB), and Nares Strait (NS). Bathymetric layers, from light blue to dark, are 200 m, 1000 m, and 2000 m.

Fans such as the MB-TMF are a common feature on high-latitude glaciated margins and they can provide significant insights into ice sheet history (Vorren and Laberg, 1997). Although TMFs form at the mouth of cross-shelf troughs excavated by ice stream erosion, not all cross-shelf troughs are associated with a fan (e.g. Batchelor and Dowdeswell, 2014). During glacial advances across the continental shelf, large volumes of material can be delivered directly to the shelf edge through sediment-laden glacial meltwater or the direct emplacement of subglacial materials (Bellwald et al., 2020a; Ó Cofaigh et al., 2003; Vorren and Laberg, 1997). Dependent upon the antecedent morphology of the shelf and the relative proportions of different types of sedimentation, the TMF typically builds out into a

fan-shaped depocentre. This depocentre contains a record of glacial-interglacial fluctuations through time and provides an important resource for understanding the evolution of the margin and its association with glacial and marine processes through time. As a result of this insight, many studies have sought to understand the long-term evolution of TMFs and relate this back to environmental conditions and changes (e.g. Andreassen et al., 2007; King et al., 1996; Laberg et al., 2013; Rise et al., 2005).

This study provides a seismic geomorphological and glaciological analysis of the MB-TMF using 2D and 3D seismic reflection data to determine the dominant glacigenic and marine processes during margin progradation. These new results provide detailed mapping of the palaeo-slope units from the seismic data and build upon previous work on the regional seismic stratigraphy of the Melville Bugt and Upernavik TMFs (Knutz et al., 2019), and palaeo-shelf landforms previously described in Newton et al. (2020). Taking this new glaciological and oceanographic evidence together, and linking it with prior work, different processes are linked to seismic geomorphological features and facies to reconstruct the glacial and stratigraphic evolution of the MB-TMF since the late Pliocene.

2. Setting

Baffin Bay is an oceanic basin between West Greenland and Arctic Canada that is almost enclosed to the north but for shallow connections (<600 m) to the Arctic Ocean through the Nares Strait and the Canadian Arctic Archipelago (Fig. 1a). In the south it is connected to the North Atlantic via the Davis Strait and Labrador Sea. The Greenland continental shelf is dissected by cross-shelf troughs that extend to the shelf edge, where prominent bulges are interpreted as TMFs (Batchelor and Dowdeswell, 2014; Jakobsson et al., 2012). Troughs are typically 40-120 km wide with water depths of ~400-800 m. Melville Bugt is the largest of these troughs at ~300 km long, with water depths at the shelf edge of ~500 m that decrease to ~1000 m in the deepest part of the trough on the inner shelf (Fig. 1a). The trough is constrained by the Northern and Southern Banks either side, which have water depths of ~300-400 m. The Northern and Southern Banks are primarily a result of Neogene drift deposits and late Pliocene-Pleistocene glacigenic deposition. The Northern Bank is partly underpinned by the tectonic inversion structure the Melville Bugt Ridge (MBR) (Cox et al., 2020a; Knutz et al., 2019) (Fig. 1a, 2a, 3). Proximal to the coastline, Archaean-Proterozoic basement rocks are exposed at the seafloor or are covered by a thin veneer of glacial sediment (Freire et al., 2015; Henriksen et al., 2009).

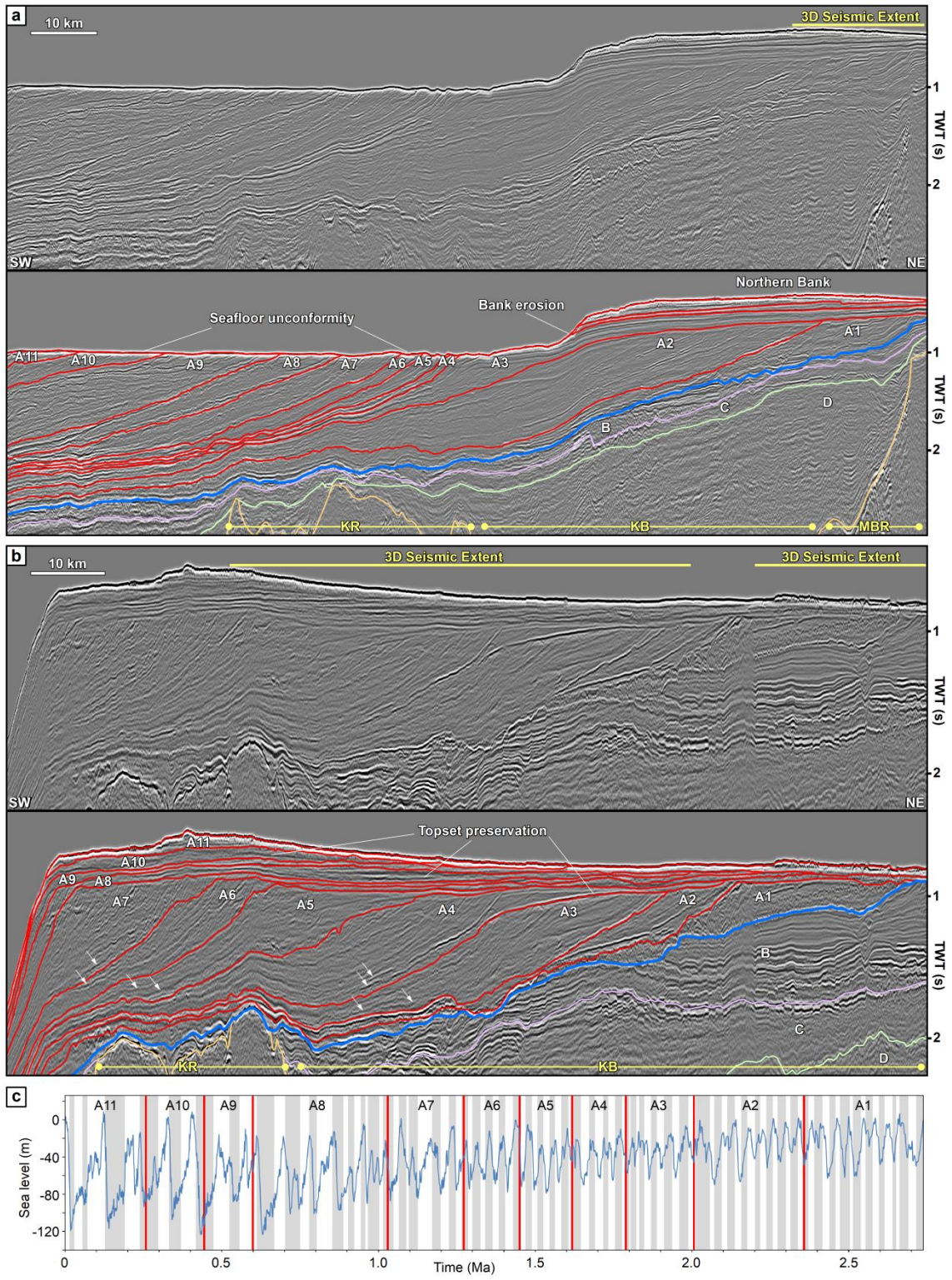

Figure 2. The MB-TMF | Uninterpreted and interpreted seismic dip lines (a) and (b) across the MB-TMF. The late Pliocene and Pleistocene succession is separated into 11 prograding units with variable topset preservation. Units B, C, and D represent the pre-glacial stratigraphy. KR, KB, and MBR are abbreviations for the Kivioq Ridge, Kivioq Basin, and Melville Bugt Ridge, respectively. The white arrows point to high amplitude reflections on the lower slopes that are discussed in the text. Locations of the lines are shown on Fig. 1. (c) Graph showing the global sea level record relative to the present (Miller et al., 2011) and estimated ages for the boundaries of the 11 prograding units of the MB-TMF (Knutz et al., 2019). The grey and white bands represent glacial and interglacial stages, respectively.

2.1 Geological History

The Melville Bugt graben is separated from the Kivioq Basin by the northwest-southeast trending Melville Bugt and Kivioq Ridges and has been infilled since the onset of rifting in the Cretaceous (Gregersen et al., 2013; Whittaker et al., 1997) (Fig. 2, 3). Paleocene seafloor spreading occurred in Baffin Bay before cessation during the late Eocene-Oligocene (Oakey and Chalmers, 2012; Whittaker et al., 1997). During the latest Paleogene or early Neogene uneven subsidence of the MBR has been documented in the study area (Cox et al., 2020a). Through the Neogene, compressional stresses led to several episodes of uplift and exhumation of West Greenland (Japsen et al., 2006; Oakey and Stephenson, 2008). From the mid-Miocene there is evidence for enhanced along-slope current-influenced deposition that ceased during the late Pliocene when Northern Hemisphere glaciation intensified (Knutz et al., 2015). There is limited lithological control on these environmental changes, with ODP Site 645 (Fig. 1b) recovering mudstone and muddy sandstones of early Miocene to Pliocene age underlying ~300 m of Pleistocene marine mudstones with ice-rafted detritus (IRD) (Cremer, 1989).

2.2 Oceanographic History

During the mid-Miocene, initiation of along-slope currents extending from the Davis Strait into Baffin Bay (Knutz et al., 2015; Nielsen et al., 2011) occurred at the same time as the Fram Strait opened and North Atlantic deep-water production increased (Engen et al., 2008; Poore et al., 2006). During the late Neogene, strong geostrophic circulation in Baffin Bay likely caused, or at least enhanced, heat advection to high-latitudes until the late Pliocene, when ice caps built up due to reduced poleward heat flux (Knutz et al., 2015; Li et al., 2015). The Pleistocene oceanography of northeastern Baffin Bay is poorly resolved due to turbidites, reworking, and calcite dissolution obscuring the palaeo-ecological record (Aksu et al., 1988; De Vernal et al., 1987). During the late Pliocene and Early Pleistocene, at ODP Site 645, deep-water production was reduced during glacial stages (Arthur et al., 1989; Jarrard and Arthur, 1989), with foraminifera and dinoflagellates reflecting northward advection of Subarctic surface waters to at least the Davis Strait at the onset of each glacial (Aksu et al., 1988). After this, Subarctic species reduction reflects a southward shift of perennial sea ice (Aksu et al., 1988). During interglacials, the Labrador Current and bottom-currents increased in strength (Hillaire-Marcel et al., 1994).

Contemporary circulation is cyclonic (Fig. 1b), with cold Nordic Sea water entering Baffin Bay via the northward-flowing West Greenland Current (WGC) (Cuny et al., 2002). The WGC bifurcates in the Davis Strait with a proportion flowing west to join the Labrador Current and the rest flowing northward. The WGC component that flows

northwards crosses the basin in northern Baffin Bay and joins the southward-flowing Baffin Current before re-joining with the other branch of the WGC and becoming a major constituent of the Labrador Current (Cuny et al., 2002; Melling et al., 2001). These conditions have prevailed since at least ~10-9 ka as ice sheet retreat opened the Nares Strait (England et al., 2006; Georgiadis et al., 2020; Jennings et al., 2011, 2019; Knudsen et al., 2008). Evidence for the latest onset of the WGC has shown that it may have been present, albeit with variable strength and pathways, since at least ~14 ka in Disko Bugt (Sheldon et al., 2016).

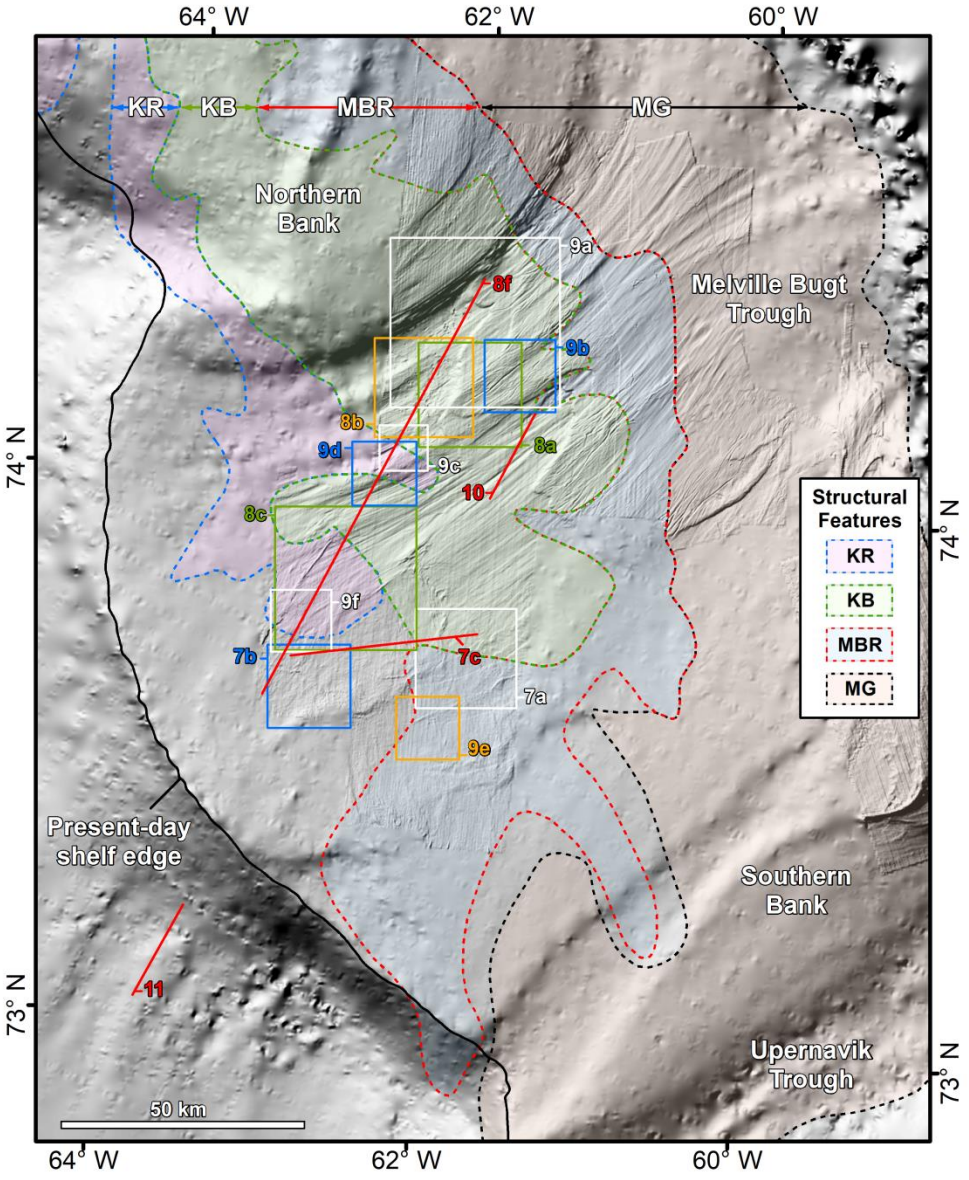

Figure 3. Data location map | Locations of the seismic profiles and surfaces presented in subsequent figures overlain onto a hillshade map of the modern bathymetry. The dashed outlines and semi-transparent polygons mark the underlying geological structure of the study area. The dashed outlines and associated arrows are colour-coded for ease of comparison. Abbreviations of the structural features are as follows: Kivioq Basin (KB), Kivioq Ridge (KR), Melville Graben (MG), and Melville Bugt Ridge (MBR), respectively.

2.3 Glacial History

IRD evidence suggests a more or less continuous presence of an ice cover on Greenland since ~18 Ma (Thiede et al., 2010). Geological and geophysical data offshore southeast and east Greenland show the repeated advance and retreat of grounded ice onto the continental shelf since the late Miocene (~7 Ma) (Larsen et al., 1994; Pérez et al., 2018), before increased observations of IRD in the late Pliocene suggest frequent marine-terminating ice developed from 3.5-2.5 Ma (St. John and Krissek, 2002). This is supported by geophysical evidence from West Greenland showing the onset of deposition of the Disko, Upernavik, and Melville Bugt TMFs during this period (Hofmann et al., 2016; Knutz et al., 2019). In Melville Bugt, 11 mega-advance and retreat cycles of the northwest GrIS since ~2.7 Ma have been documented, with a dynamic change in depositional patterns at ~1 Ma (see Knutz et al., 2019). This change coincides with the Middle Pleistocene Transition and increased observations of ice stream landforms (Newton et al., 2020). Despite these recent improvements in our knowledge, there is still uncertainty about where and how frequently the GrIS advanced and retreated across the continental shelf prior to the Last Glacial Maximum that spanned 24-16 ka (Alley et al., 2010; Funder et al., 2011).

At the Last Glacial Maximum the Laurentide, Greenland, and Innuitian ice sheets formed a continuous belt around northern Baffin Bay (Jennings et al., 2018), with the GrIS reaching the shelf-edge in Melville Bugt (Newton et al., 2017; Slabon et al., 2016). Deglaciation began at ~16-15 ka (Lecavalier et al., 2014) and this correlates with observations from Disko Bugt showing margin retreat from the shelf edge by ~15-14 ka, before advancing or stabilising during the Younger Dryas (Hogan et al., 2016; Jennings et al., 2014; Sheldon et al., 2016). In the Holocene, ice sheet margins in Melville Bugt had largely retreated to or behind their present position, where it now mainly consists of marine-terminating outlet glaciers (Fig. 1a) (Batchelor et al., 2018; Briner et al., 2013).

3. Data and Methods

This study uses industry 2D and 3D multi-channel seismic reflection data (Fig. 1-3). The 2D seismic data have a vertical resolution of ~14-19 m (frequencies of 26-30 Hz and velocities of 1650-1950 m s^{-1}) for unit A, the glacial interval between 200-800 milliseconds TWT (two-way-time) below the seafloor. The grid spacing of the 2D data is variable but individual lines are generally 10-30 km apart across the study area (Fig. 1a). The ANU and PITU 3D seismic surveys cover 8700 km^2 and 1,672 km^2, respectively. A full description of the collection and processing parameters for the surveys is presented in Cox et al. (2020b).

The vertical seismic resolution within the target interval is 13-22 m for the ANU survey (frequency 22-32 Hz and velocities of 1650-2100 m s^{-1}) and 13-30 m for the PITU survey (frequency 20-40 Hz and velocities of 2100-2400 m s^{-1}). The horizontal spacing for the surveys is 6.25 m (inline) x 50 m (crossline) (ANU) and 25 m (inline) x 12.5 m (crossline) (PITU). These surveys cover part of the late Pliocene and Pleistocene stratigraphy, with the most distal deposits at the shelf edge not captured. All of the seismic reflection data were phase shifted to ensure the seismic wavelet was symmetrical about zero time to reduce distortion and improve resolution. In this work, a normal SEG polarity is used, where a downward increase or decrease in acoustic impedance is displayed on seismic profiles as a black or white reflection, respectively. Conversion from time to depth was based on a simplified p-wave velocity of 1.48 km s^{-1} for the water column and 2.1 km s^{-1} for the glacial stratigraphy. There is currently no local well control on the margin, so these estimates are a reasonable approximation based on observations from the comparable Svalbard glaciated margin (Geissler et al., 2011; Geissler and Jokat, 2004).

The traditional approach to seismic sequence stratigraphy uses the delineation of bounding unconformities to understand relative sea level changes (Vail et al., 1977). However, unconformity bounded sequences can form from non-eustatic factors, especially on glaciated margins where ice sheet dynamics and isostasy impact shelf evolution (Powell, 1991; Powell and Cooper, 2002). The chronostratigraphic framework of 11 prograding units (Fig. 2) is extended from the framework mapped by Knutz et al. (2019) on the Melville Bugt and Upernavik TMFs. Using Schlumberger's Petrel 2017.1 software, the framework was established across the available data in this study to create bounding horizons (grid size of 500 m). The regional-scale seismic stratigraphy was supplemented with a seismic geomorphological analysis (cf. Posamentier, 2004) of vertical profiles, the main unit boundaries, and sub-unit palaeo-seafloor surfaces (i.e. traceable surfaces within the main units) from the 2D and 3D seismic data, in order to extract more detail on depositional processes at unit and sub-unit scales than has previously been documented. Palaeo-seafloors were picked from continuous amplitude reflections. This approach does not assume a specific *a priori* control to each surface, but instead establishes an allostratigraphic framework and an inventory of palaeo-seafloor surfaces for analysis of landforms. Variance (8 ms window) and RMS amplitude (8 ms window) volume attributes were generated from the 3D volume to aid landform identification. Spectral decomposition was also performed on the seismic frequency attribute within Geoteric 2018.3 and was displayed using a colour blend of 20 Hz (red), 30 Hz (green) and 45 Hz (blue) (equivalent to a tuning thickness of 22.5 m, 15 m, and 10 m at 1800 m s^{-1}, respectively). These values

were iteratively adjusted to determine the combination that allowed for the best imaging of thin-bed features.

In addition to this manual approach, a semi-automatic method was used to pick 3D seismic horizons with relative geological ages using Paleoscan 2017.1 (e.g. Daynac et al., 2016; Newton et al., 2018). This involves the auto-tracking of horizon surfaces and worked well for slope reflections but required manual editing of topsets where the stratigraphy was more complex. These horizon surfaces allow for the development of geological time-slices that obey the stratigraphic dip, rather than cross cut it like ordinary time-slices, and provide a quick insight into potentially important reflections that were then picked manually. Thus, only surfaces manually picked were used to document landform features in this study. All horizons were picked in Petrel and investigated as structure maps in 3D space under a range of lighting conditions and volume attribute displays. Once landforms were identified they were considered with depocentre and stratigraphic changes to explore the links between submarine processes and the wider evolution of the MB-TMF.

It is important to note that whilst the MB-TMF is the primary focus of this study, its evolution is closely linked with the Upernavik TMF to the south (Knutz et al., 2019) (Fig. 1, 4a). The availability of 3D seismic reflection data allows this study to use the existing framework derived from the 2D data to explore the depositional and erosional processes associated with the outbuilding of the MB-TMF at a higher spatial resolution. These 3D seismic data do not cover the entirety of the MB-TMF and, therefore, seismic geomorphological interpretations from the outer shelf are primarily derived from the 2D data and correlation with 3D surfaces mapped up-dip.

4. Results and Interpretation

4.1 Margin Architecture

The top surface of the 'B-unit' of Knutz et al. (2019) marks the base of the glacigenic succession in the MB-TMF that is investigated here (Fig. 2). The seismic data show that the total MB-TMF is up to ~2 km in thickness and covers an area of at least ~30,000 km^2 (Fig. 4). The deposition of this glacial prism has helped the shelf margin to prograde basinward by over ~100 km through the late Pliocene and Pleistocene with gradual changes in the progradation direction through time (Fig. 4a, 5). In the study area, 11 late Pliocene and Pleistocene seismic units have been mapped through the MB-TMF (Knutz et al., 2019), along with smaller intra-unit packages that make up these main units. These intra-units follow similar criteria to the main units but are more spatially restricted and are typically associated with specific landforms. The main units are bounded between high-amplitude

and laterally semi-continuous seismic reflections within the A-unit and are labelled A1-A11, from oldest to youngest (Fig. 2). Although the units generally show similar acoustic properties throughout their wedge-like geometries (e.g. alternation of discontinuous and low-amplitude lobes between high-amplitude and continuous reflections on the slope) there is a difference in margin architecture from north to south. In the north, topsets of units A1-A3 are (at least partly) preserved, whilst those for units A4-A11 are heavily truncated (Fig. 2a) and subcrop beneath a thin veneer of Late Pleistocene sediment. To the south, topsets associated with unit A3 become thicker, whilst topsets of units A4-A11 are extensively preserved and thicken (Fig. 2b).

The seismic character of unit A1 varies in dip and strike. In the north, the upper part of the unit is characterised by semi-continuous, high-amplitude reflections that are truncated in the area above the MBR by the top surface of unit A2 (Fig. 2a). Down-dip, chaotic facies are bounded above by a high-amplitude reflection marking the base of unit A2, and below by the base of the glacigenic succession. In the south, deposits on the upper slope are generally structureless and thin downslope (Fig. 2b). At the base of slope, unit A1 is a wedge-like unit with little internal structure (Fig. 2b and 4a) (Knutz et al., 2019).

Unit A2 shows a distinct change in the seismic character and is characterised by 30-40 km of shelf edge progradation to the southwest (Fig. 2a). The depocentre is concentrated over the northern-most part of the study area and reaches up to ~700-800 m in thickness (Fig. 4) before pinching out in the southern part of the fan (Fig. 2b). The unit is the only one that is significantly preserved beneath the Northern Bank. The internal architecture is different to unit A1 and shows numerous high-amplitude reflections separated by fragmented and lower-amplitude lobes (Fig. 2a). A number of prograding and aggrading topsets are partly preserved, but there is also a noticeable unconformity in the most northern part of the study area that marks the top of much of this unit (Fig. 2a).

Units A3-A9 display a sigmoidal geometry in which continued subsidence has preserved a number of palaeo-shelves, including the bounding surfaces of each unit (Fig. 2b). Each of these units typically displays high-amplitude reflections separated by stacks of lobate deposits. Units A3-A7 contain fan-like high-amplitude reflections at the base of the slope (white arrows in Fig. 2b). The topsets are typically characterised by laminated reflections in areas proximal to the palaeo-shelf edge.

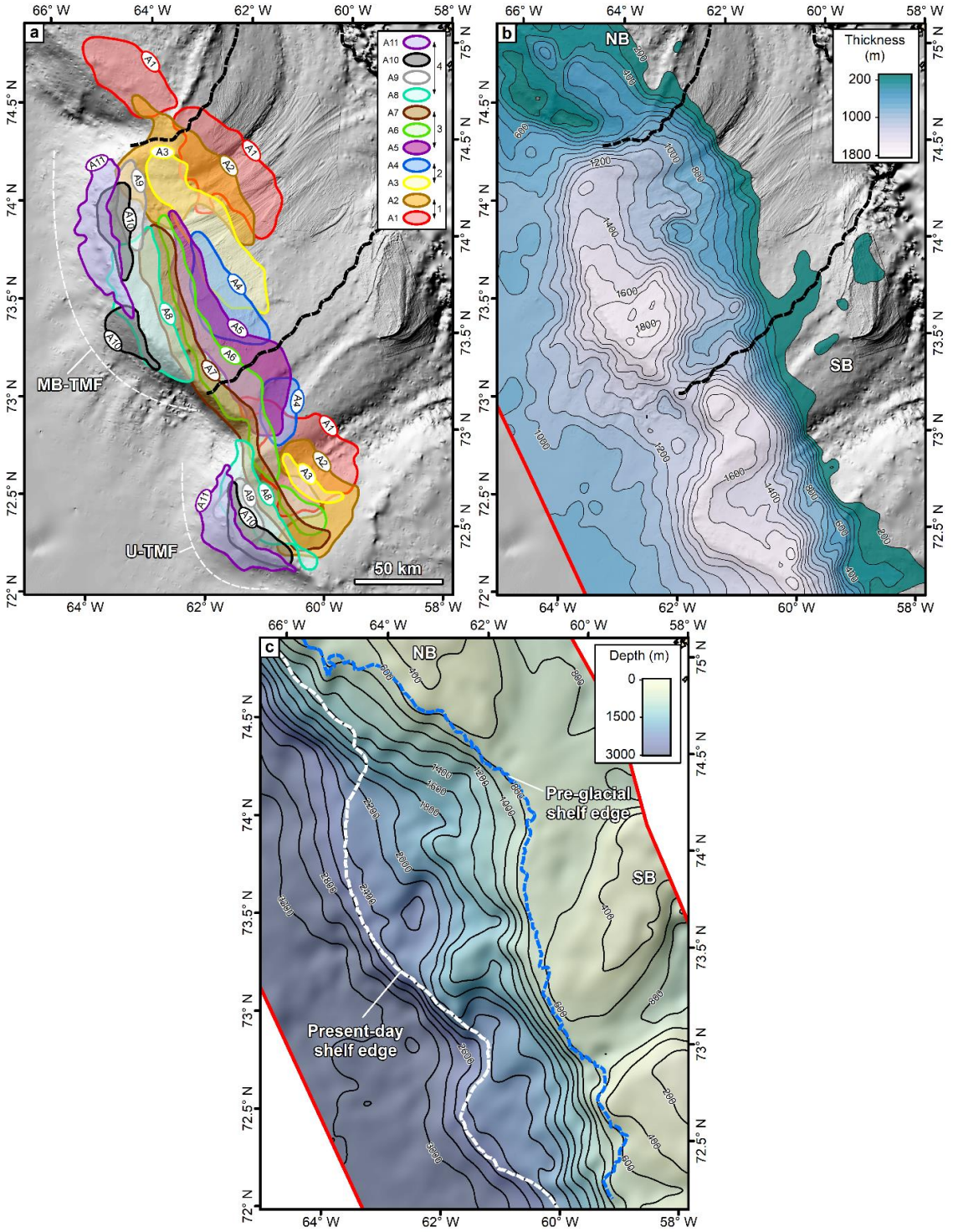

Figure 4. TMF depocentres | a) Depocentre locations for the main units within the Melville Bugt (MB-) and Upernavik (U-) TMF systems. The boundaries for each unit are the 300 m thick contour. The black dashed line shows the boundary of the contemporary trough; b) Semi-transparent isopach for the glacigenic succession overlain on a hillshade map of the modern bathymetry. The contours are every 100 m. Red line is the basinward limit of the data used to derive the thickness; c) A depth converted seafloor map of the base glacial surface showing the general morphology of the shelf prior to glaciation and at the present-day. Note that parts of the inner shelf cannot be reconstructed for this time period due to erosion of the record.

The depocentres of units A3-A7 show the margin prograded up to ~120 km to the southwest, with the depocentres generally becoming more elongate through time (Fig. 4a).

During the deposition of unit A5, the separate depocentres associated with the MB-TMF and the Upernavik TMF merge. As units A7-A9 were deposited the direction of progradation switches westward towards the basin (Fig. 4a, 5). The MB-TMF and Upernavik TMF systems also separate as unit A8 is deposited (Fig. 4a). During the accumulation of units A8-A11, the style of deposition in the south gradually switches from progradational to aggradational (Fig. 2b). This is also marked by a change from the elongate shape of the earlier unit depocentres to a more pronounced and localised deposition in front of the contemporary cross-shelf troughs as the progradation direction began to align with the contemporary shelf edge (Fig. 4a, 5).

4.2 Seismic Geomorphology

4.2.1 Grounding-zone Wedges

Two asymmetric wedges comprised of low-amplitude and semi-continuous reflections are observed on the palaeo-shelves of units A3 and A6 within the 3D data (Fig. 6a, 6b). The wedges are ~30-60 m high and measure 20-40 km long across the width of the trough (north-south) and 10-20 km to its length (west-east) (Fig. 6c). Basinward dipping reflections are observed within the two wedges, indicating that progradation was a dominant feature in their formation. Based on their asymmetric shape, these wedges are interpreted as grounding-zone wedges (GZWs) or ice-contact fans formed at the grounding-line of a marine-terminating ice margin (Alley et al., 1986; Anandakrishnan et al., 2007; Bellwald et al., 2020b; Dowdeswell and Fugelli, 2012). The lateral extent of these features and a lack of proximal meltwater channels suggest they are unlikely to be associated with point source deposition (i.e. ice-contact fan), and instead may represent a line-source mode of sediment delivery such as a GZW. GZWs are typically comprised of diamictic material delivered to the grounding-line via subglacial deformation of basal debris, subaqueous flows and meltwater plumes, or rainout of material from beneath an ice shelf (Anandakrishnan et al., 2007; Powell and Domack, 2002). The wedges have been deposited atop two of the main unit boundaries that represent glacial unconformities; suggesting that a grounded ice sheet created the unconformity before depositing the wedge. Both the wedges are deposited close to the palaeo-shelf edge of units A3 and A6, suggesting a stage of relative ice sheet stability on the outer shelf during their deposition.

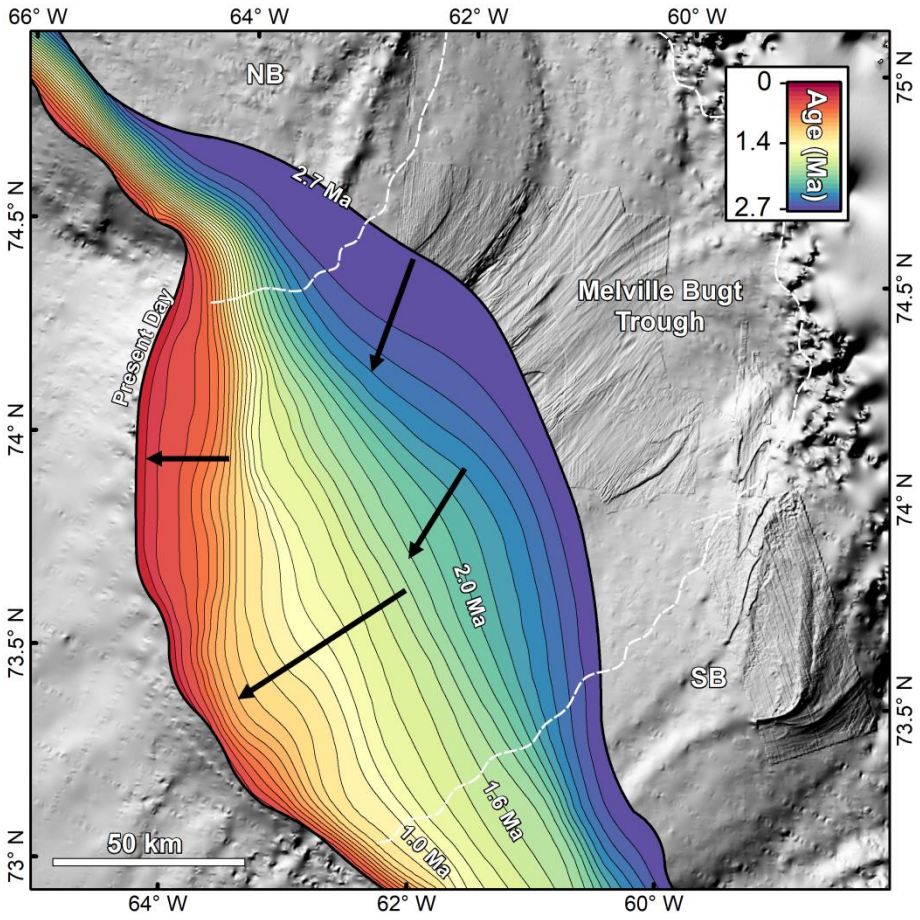

Figure 5. Progradation pattern of the MB-TMF overlying the bathymetry | This has been created by using the dates for the major units (Fig. 2c) as a time constraint and interpolation of the ages and shelf edge location in between. This allows for the position of the shelf edge to be estimated every 100 kyr (black contours) and demonstrates the broad, regional-scale pattern of shelf edge progradation. Selected ages have been added that relate to key stages in the fan evolution. The white dashed line shows the outline of the cross-shelf trough. Black arrows show changes in progradation direction through time.

4.2.2 Mega-scale Glacial Lineations

Within the ANU 3D seismic volume, several sets of linear features are observed on a number of palaeo-shelves (Fig. 7). These streamlined features are typically 5-15 km long and 200-300 m wide. Although these features are most clearly observed in planform, some of the largest features measure up to ~15 m high, though this is likely a minimum estimate of their form prior to burial and compaction. These landforms are similar to mega-scale glacial lineations (MSGL) that have been observed on the seafloor of the Melville Bugt cross-shelf trough (Newton et al., 2017), and many other glaciated margins (e.g. Dowdeswell et al., 2016). MSGL are thought to form from the streamlining or accretion of subglacial debris and are associated with fast-flowing ice streams and glacier surges (Clark, 1993; Spagnolo et al., 2016). The identification of MSGL can be used to reconstruct the locations of palaeo-ice streams in the geological record and concomitant glacial sediment

delivery pathways (e.g. Dowdeswell et al., 2006). The MSGL are observed in units A7-A11 (Fig. 7) and have been extensively detailed in Newton et al. (2020) – they are presented here using new imaging techniques (e.g. spectral decomposition) and are summarised because of their relevance to the overall evolution of the fan. The ice flow directions inferred from the MSGL suggest that ice was flowing toward the southwest. This corresponds well with the progradation pattern and the migration of the unit A8-A9 depocentres (Fig. 4a, 5) – suggesting palaeo-ice streams on the shelf impacted sedimentary processes during the deposition of these units. Although the 3D seismic data do not extend to the shelf edge, similar cross-sectional profiles of the MSGL are observable on some of the 2D seismic profiles and are taken as tentative evidence of buried MSGL in unit A10 (Newton et al., 2020). Most of the unconformities, including the main unit boundaries that have been interpreted as representing surfaces of glacial erosion, do not contain evidence of MSGL. The depocentre volumes associated with the fan, and a lack of other erosional features (e.g. fluvial incisions), are inconsistent with a mode of extensive erosion that is not glacial. Therefore, it would appear likely that the absence of MSGL represents either a lack of preservation of the original features prior to burial, or, limitations in seismic resolution allowing the features to be imaged after burial and subsequent compaction.

4.2.3 Gullies

All the seismic units captured in the ANU 3D seismic volume contain high-amplitude reflections that are separated by chaotic and discontinuous low-amplitude reflections. The high-amplitude reflections often lack topsets due to truncation by subsequent glacial erosion (Fig. 2a). RMS amplitude and spectral decomposition show that many of the sub-unit palaeo-slope surfaces have been incised by U- and V-shaped features 100-800 m wide, 15-35 m deep, and up to 40 km long (though length is restricted by survey size) (Fig. 8, 9). Larger incisions observed on the base glacial surface are discussed in section 4.2.5. These geometries appear fairly consistent and there are only minor increases downstream in either incision depth or width. Within the limits of the 3D seismic data, the majority of these features flow down from the uppermost parts of the preserved palaeo-slopes as branching systems (Fig. 8, 9). Non-branching features are observed but are less common and typically extend to the edge of the seismic survey, meaning that it is not possible to determine whether they merge with other features further down the slope. Whilst the majority of these features continue downslope to the margins of the seismic data, a small number appear to vanish on the palaeo-slope (e.g. Fig. 9f). Similar incisions are observed on 2D data from the outer shelf but appear to be less common from unit A8 onwards – albeit

with the caveat that 2D profile interpretation is more tentative due to interpretation of features on seismic profiles that are not strike-oriented and without 3D control.

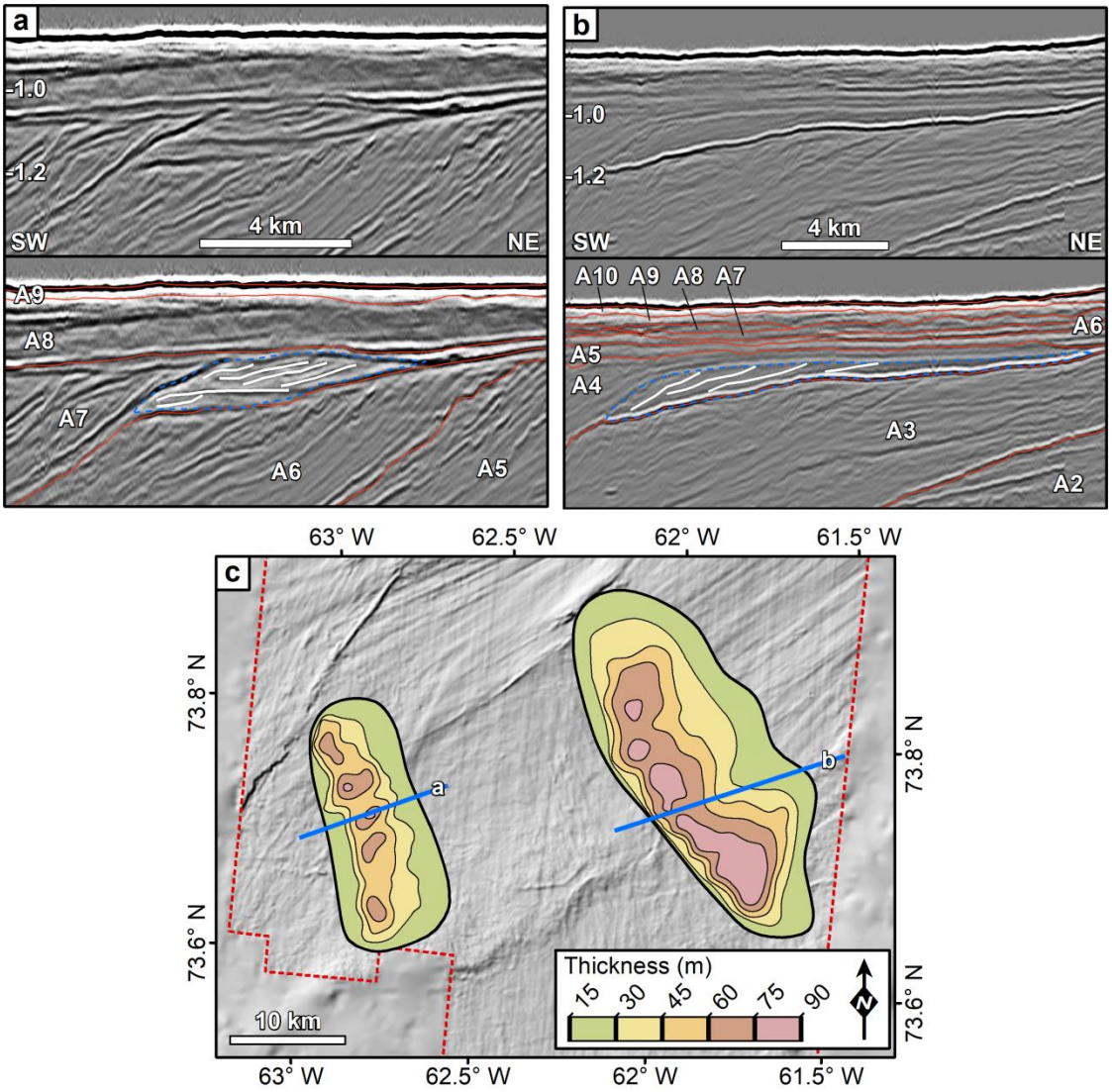

Figure 6. Grounding-zone wedges (GZWs) | a-b) Uninterpreted and interpreted seismic profiles showing examples of grounding-zone wedges atop the unconformities of units A6 and A3. The red lines are the main unit boundaries, whilst the blue dashed line indicates the cross-sectional profile of the wedges. White lines show internal geometry of the reflections. Profiles are located on panel (c). Vertical scales are in TWT (s); c) Depth converted thickness maps showing the extent and geometry of the wedge features. The locations of the two seismic lines are indicated by the blue lines and are overlain on a hillshade map of the contemporary seafloor. Note that the map shows the geometry of the wedges, not that they are on the same stratigraphic surface.

Gullies on glaciated margins are typically related to meltwater delivery at the ice sheet margin through long-term continuous supply or short-term glacial outburst floods (Gales et al., 2014; Noormets et al., 2009). Subglacial meltwater can typically entrain large sediment volumes and may become hyperpycnal flows which turn into erosional turbidity currents when this water is released at the grounding-line and cascades downslope (Bellwald et al., 2020a; Gales et al., 2014). These features are similar to gully features described on other

TMFs (Laberg et al., 2007; Noormets et al., 2009), including on the Disko TMF to the south of the study area (Ó Cofaigh et al., 2018). On the Disko TMF the gullies on the upper slope are mostly Type II gullies of Gales et al. (2013) – that is, they are typically non-branching, U-shaped, and are thought to relate to small-scale slope failure (Ó Cofaigh et al., 2018). The gullies observed on the MB-TMF cover all types of categories identified by Gales et al. (2013), with the most common being Type III – gullies that are branched, V-shaped, and related to sediment-meltwater – and to a lesser extent Type IV – gullies that are branched, U-shaped, and related to modification of gullies formed during a previous glacial advance. Modification of existing glacial gullies may be a source for some of the adjacent lobe deposits documented in section 4.2.4. The gullies are observed on surfaces reflecting an increase in downwards acoustic impedance, likely reflecting a transition from coarser to finer material. The gullies themselves display as low (RMS) amplitude features across this surface (Fig. 8b). This perhaps suggests that the infill of the gullies is more similar to the underlying sediment, causing a lower acoustic impedance contrast at the base of the gully, than compared to the rest of the surface (which displays higher RMS amplitude). This may suggest a gully infill consisting of finer-grained sediments.

On a number of the palaeo-slopes, small mounded features are found where a number of gullies branch together and appear to terminate (Fig. 8b). Whilst seismic resolution prevents imaging of any internal facies character (such as pressure ridges), the bulges at the base of the slope could reflect the accumulation of material excavated from the gullies as a fan (e.g. Ó Cofaigh et al., 2003) or a debris flow that utilised the gullies during erosive turbidity current flow (e.g. Bulat, 2005). Given that similar lobate features are observed elsewhere on the same surfaces, but do not appear to be connected to gullies, it is likely that these features are debris flow deposits rather than fans.

Although it is plausible that the gullies were formed without a proximal ice sheet, it is difficult to envisage how sediment-laden water could travel large distances across the shelf from the palaeo-coastline whilst maintaining sufficient energy to continue sediment entrainment, particularly without topographic constraints focusing flow. The close proximity of glacial unconformities and other glacial landforms in correlative deposits, indicating regular ice sheet advance to the palaeo-shelf edge, supports a meltwater process as the main factor during each episode of gully formation. Thus, meltwater processes appear to have persisted through much of the development of the MB-TMF and supports other work from West Greenland (e.g. Ó Cofaigh et al., 2018) suggesting that despite the high-latitude setting, meltwater processes have played a fundamental role in margin development. The coverage of the 3D seismic reflection data mean that there is also a

spatial limitation on mapping the extent of these features. However, on some of the 2D profiles, further down-dip there is evidence of incisional features (Fig. 10) that might suggest either a continuation of these gullies downslope or perhaps a transformation into channel-levee systems similar to recent work on the North Sea Fan (Bellwald et al., 2020a). The work there showed the importance of meltwater on TMF development and adds further support to the observations from the MB-TMF that meltwater processes were of fundamental importance.

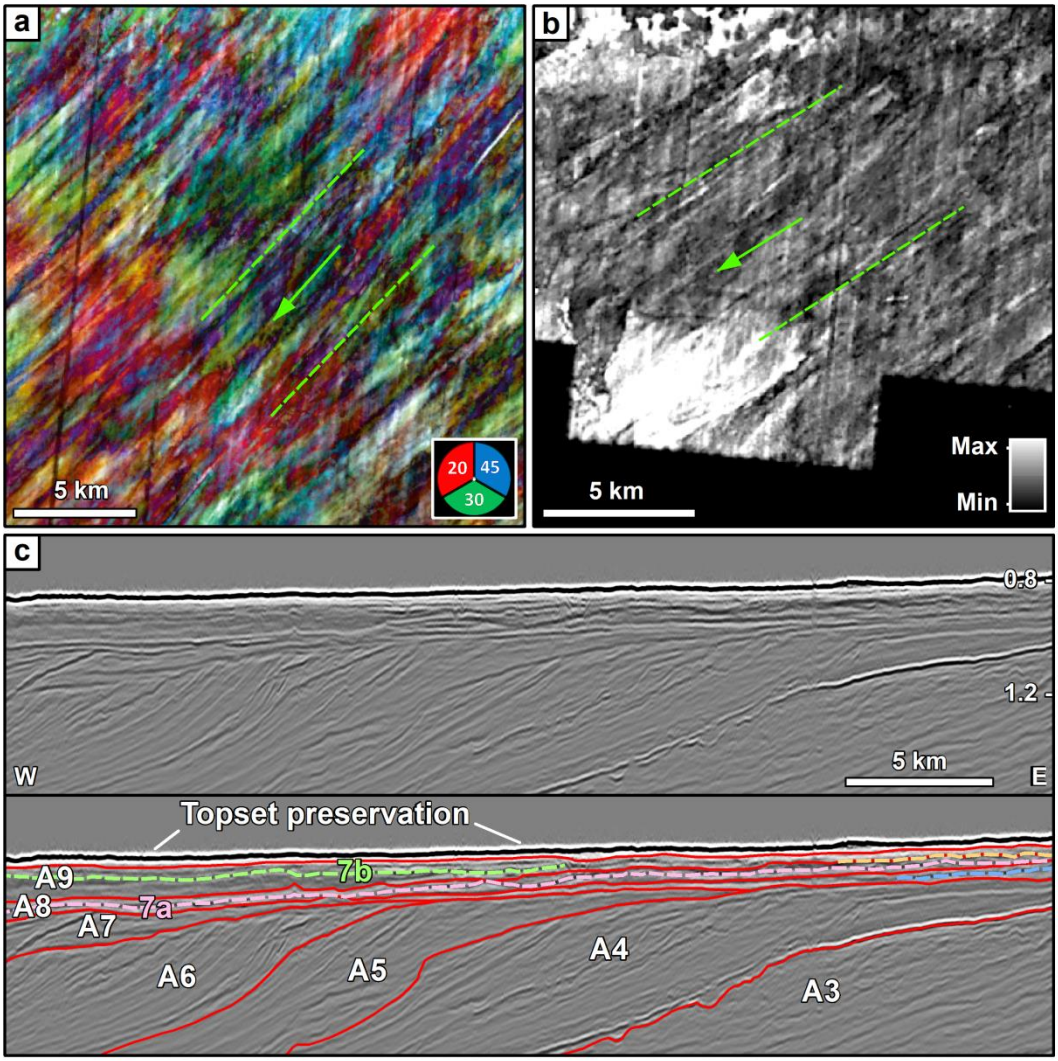

Figure 7. Mega-scale glacial lineations (MSGL) | a-b) Examples of mega-scale glacial lineations (MSGL) observed in units A8-A9. Spectral decomposition (a) and RMS amplitude (b) volume attributes. Colour scale in (a) is Hz. The dashed green lines show a number of digitised MSGL and arrows the inferred ice flow; c) Uninterpreted and interpreted seismic profile through the 3D seismic volume. The different coloured dashed lines indicate surfaces with MSGL and the red lines are the main unit boundaries. The stratigraphic locations of panels (a) and (b) are labelled. Location of seismic line is shown on Fig. 3. Vertical scales are in TWT (s).

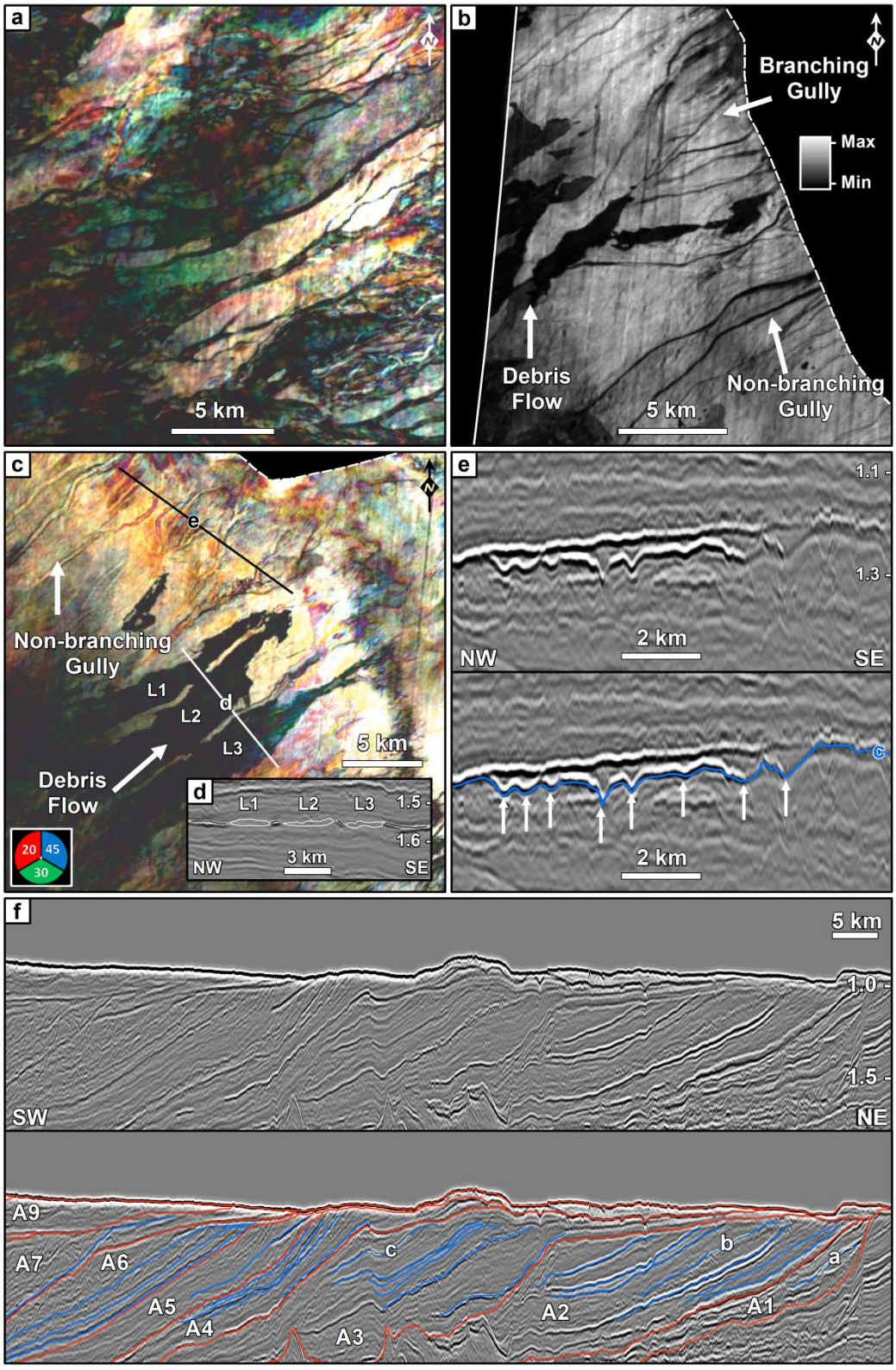

Figure 8. Gullies and debris flows | a) Gullies observed in unit A1 shown on a spectral decomposition (Hz) extraction – colour scale is shown on (c); b) Gullies in unit A2 displayed as a RMS amplitude extraction. Note the example of a branching gully system that appears to show a debris flow deposit downstream of the confluence of the gullies; c) Gullies and debris flow lobes observed in unit A3 displayed as a spectral decomposition extraction. Location of panel cross-sections (d) and (e) observed in unit A3 are shown; f) Uninterpreted and interpreted seismic profiles. The surfaces with gullies are indicated by blue lines and the red lines are the main unit boundaries. This profile is located on Fig. 3. Vertical scales are in TWT (s).

4.2.4 Debris Flow Deposits

Many of the gullied palaeo-slopes display lobate features that are typically best observed in plan-form (Fig. 8c). They are typically 2-5 km wide, extend downslope for 2-18 km and in cross-section the features are 10-20 m thick (limiting imaging of internal structures) (Fig. 8d). Two separate relationships are observed with the gullies: 1) some gullies have incised through the lobes, implying they are a later feature; and 2) some lobes begin where a number of the gullies terminate on the palaeo-slope (discussed above). These lobes are interpreted as debris flow deposits formed by the accumulation of material via gravity-driven movement of sediments from the shelf edge (Ó Cofaigh et al., 2003; Taylor et al., 2002).

Debris flow deposits observed on TMFs are typically interpreted as glacigenic debris flows (GDFs) that emanate from close to the grounding-line and extend downslope (e.g. Nygård et al., 2005; Ottesen et al., 2014). GDFs are commonly used to infer the presence of ice near the shelf edge. However, such an interpretation is potentially ambiguous given that debris flow deposits on non-glaciated margins show similar seismic characteristics (e.g. Beaubouef and Friedmann, 2000; Fanetti et al., 2008). Therefore, given that these lobate deposits are not on the upper palaeo-slope (since many of the upper slopes and topsets have been eroded and these features do not continue upslope to the truncation of the reflection), they may not be archetypical GDFs, but instead represent debris flows of previously deposited glacigenic material. This has an important implication for ice sheet reconstruction because the presence of proximal ice is not a prerequisite for this type of debris flow deposition.

Geomorphological evidence of meltwater gullies, GZWs, MSGL, and glacigenic unconformities regularly occur on the same or stratigraphically adjacent surfaces, providing complementary evidence that outer-shelf and shelf edge environments were proximal to the ice sheet margin. This suggests that the deposits are likely to represent the remobilisation of GDF deposits that were originally deposited by ice at the shelf edge. These types of flow deposits are common on many of the palaeo-slope surfaces throughout units A2-A7. In the latter units, from A8 onwards, there are similar features documented on the 2D seismic data that are observed with a greater frequency on the upper and middle palaeo-slopes and are interpreted, *sensu stricto*, as GDF deposits (Fig. 10). This increased documentation of GDFs, combined with a reduction in the number of gully observations from A8 onwards, perhaps signals a change in the dominant mode of deposition during MB-TMF evolution from meltwater-dominated to direct emplacement of glacigenic materials by ice located at the shelf edge. Interestingly, sedimentological

observations from the Scoresby Sund TMF in East Greenland show a similar depositional change at ~1.0 Ma, when glacimarine and marine deposition transitions into a dominance of debris flow deposition (Laberg et al., 2018).

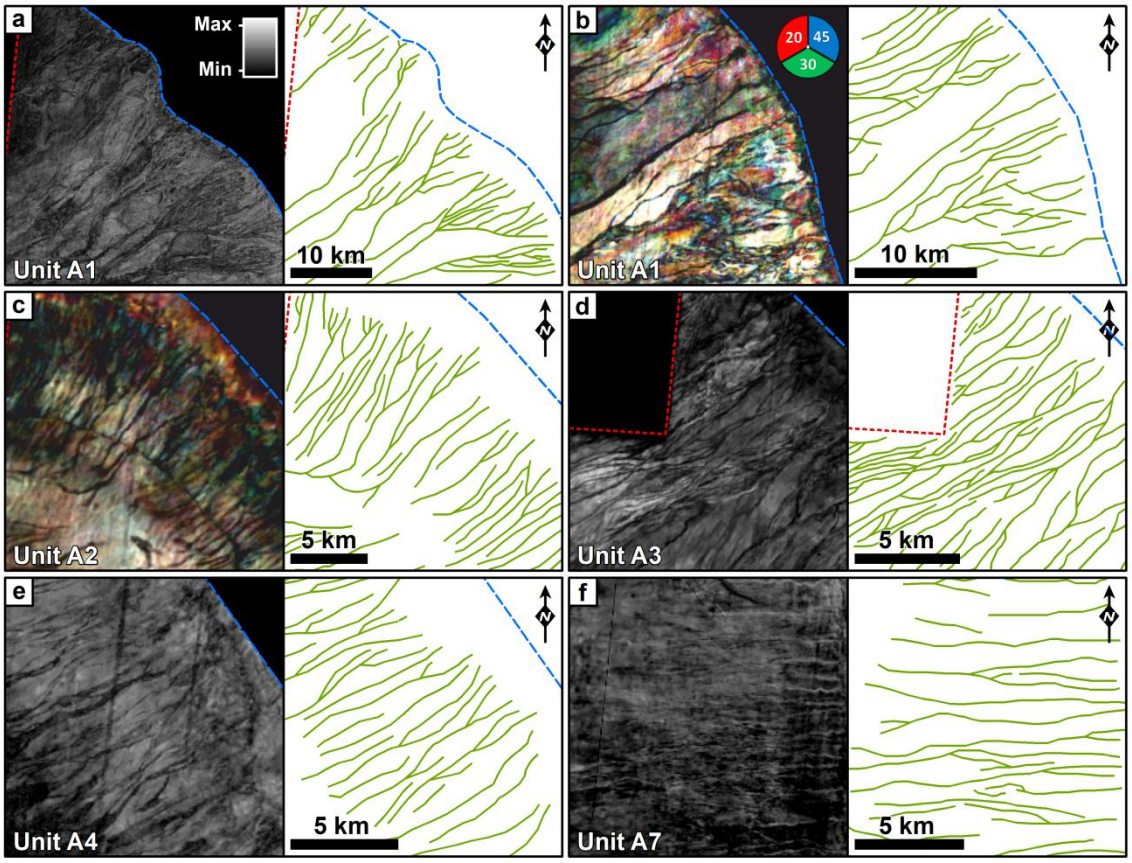

Figure 9. Gullied surfaces | (a, d, e, f) and spectral decomposition (b, c) maps. The blue dashed line shows the position of topset erosion for each surface and the red dashed line the outline of the 3D seismic volume. Green lines show a digitised record from the adjacent surfaces. Panel locations shown on Fig. 3. Note that the RMS amplitude and spectral decomposition (Hz) scales are the same for each panel.

4.2.5 Canyons

A number of canyon-like incisions are observed on the base glacial surface and measure 2-3 km wide and 100-150 m deep (Fig. 11). These features are at the edges of the 3D seismic data, limiting the documentation of their geometry and distribution. The inability to determine the full geometry or map the thalweg means that there is no conclusive evidence that the canyons are directly related to glacial meltwater and their genesis could instead be related to a relative sea level fall. The canyons were formed during the onset of the fan, thus they may represent one of the earliest glacial sea level regressions during the late Pliocene. Alternatively, these features may be related to local slope failure at the onset of glacial advance onto the continental shelf and could have continued to be cut by subsequent turbidity currents driven by sediment-laden glacial meltwater during the earliest

deposition of unit A1. More extensive data are required to fully image these features and determine their genesis, but it is proposed here that the lack of a fluvial sequence in the stratigraphy suggests the canyons are most likely of a proglacial origin.

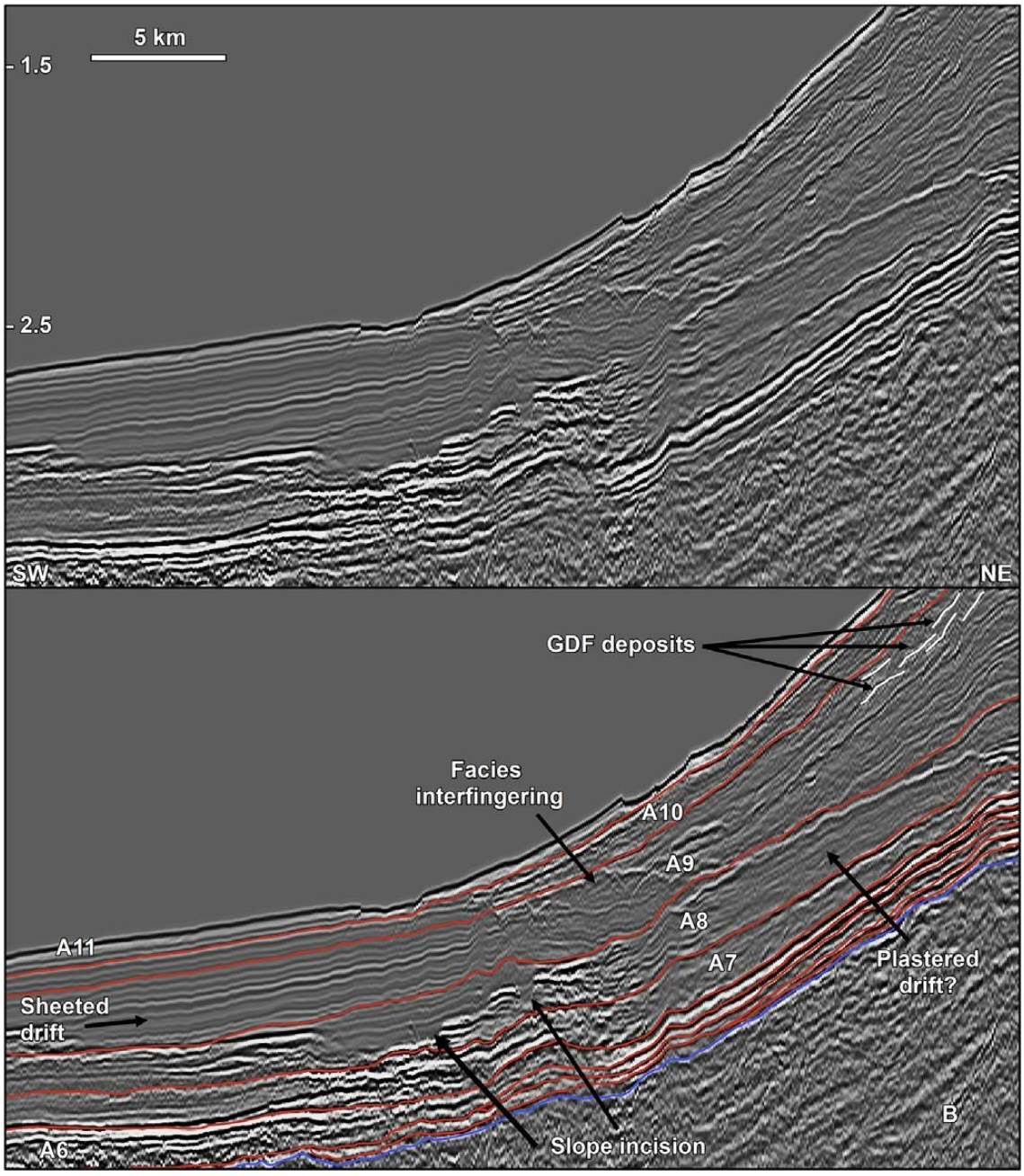

Figure 10. Drift deposits | Examples parallel wavy reflection interpreted as sheeted and plastered drift deposits, which would indicate oceanic current influence since the deposition of unit A7 onwards. For location see Fig. 3. Vertical scale is in TWT (s).

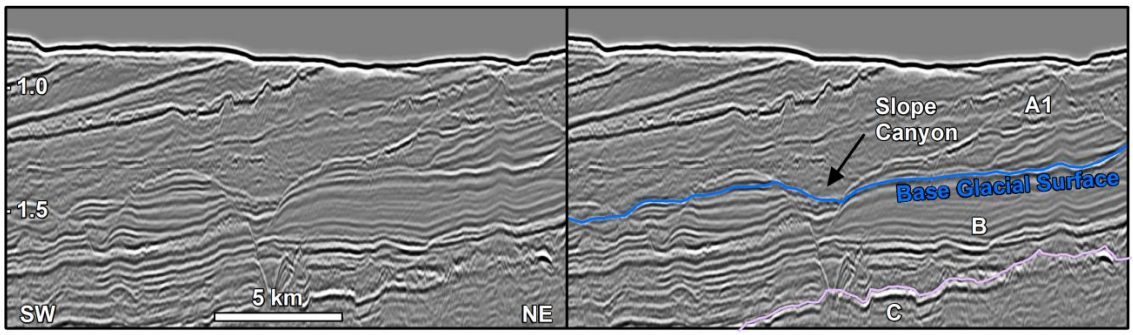

Figure 11. Canyons | Examples of canyons incised into the base glacial surface. These are thought to relate to the earliest glacial advances during the late Pliocene. Location shown on Fig. 3. Vertical scale is in TWT (s).

4.2.6 Basin Deposits

Within unit A8 a number of asymmetric mounded reflections that are dominantly aggradational, with occasional upslope migration, are observed in the lowermost palaeo-continental slope and typically onlap onto the top of unit A7 (Fig. 10). These have been interpreted as a drift-channel depositional system (Knutz et al., 2019) that reflects along-slope currents that have plastered deposition against the slope (e.g. Faugères et al., 1999; Rebesco et al., 2014). Downslope of the plastered drift in unit A8, a number of isolated incisions are interpreted as channel-like features possibly extending from slope gullies (Fig. 10). The lack of 3D seismic data on the outer shelf limits any analysis of potential connections between different incisions at the base of the slope, or with the gully systems observed upslope (section 4.2.3). The base of slope in units A9-A11 does not present the same amount of evidence for these incisions, but is instead characterised by laminated planar and wavy re- flections that typically onlap the palaeo-slope and are regularly intercalated with GDFs upslope (Fig. 10). These features could represent along-slope processes similar to sheet drift deposits observed on other margins (e.g. Knutz and Cartwright, 2003; Rebesco et al., 2014). Alternatively, the wavy geometry could indicate that these deposits are related to downslope processes in the form of turbidity currents, possibly relating to the upslope observations of gullies and GDFs. The different drift deposit geometries are not present on all dip profiles at the same stratigraphic level, and may represent either, or both, the presence of geostrophic or downslope currents since deposition of unit A7. More extensive data in this distal setting are required for a more confident interpretation on what processes led to the observed geomorphology.

4.2.7 Iceberg Scours

Although uncommon compared to their occurrence on other glaciated margins (e.g. Dowdeswell and Ottesen, 2013; Newton et al., 2018; Rafaelsen et al., 2002), a number of

linear and curvilinear furrows have been identified on several palaeo-seafloors preserved in all units (Fig. 12). These features are typically 200-400 m wide and 2-10 km long. Incision depth is difficult to estimate as the features are best observed in planform, but larger furrows are up to 20 m deep. The furrows on the slope can be distinguished from gullies as they occur parallel to the slope contours (i.e. along-slope rather than downslope), whilst one set of furrows is splayed and on a preserved palaeo-shelf (Fig. 12d). The furrows are interpreted as iceberg scours formed from the temporary grounding of an iceberg (Brown et al., 2017; Woodworth-Lynas et al., 1985). As the iceberg is moved by ocean and tidal currents (or glacial drainage proximal to the ice margin), it leaves behind an erosional record of the iceberg trajectory (e.g. Newton et al., 2016; Todd et al., 1988). As the scours are generally parallel to the shelf edge, it suggests the local currents were moving northward in north-eastern Baffin Bay, albeit with a reduced intensity, as indicated by the lack of along-slope deposits until unit A8. On the palaeo-shelf, the fan-like scours are probably associated with icebergs floating away from the calving margin (Fig. 12d), their trajectory being driven by meltwater outflow or tidal flow away from the margin, or perhaps the swell from a subsequent calving event. Most scours are observed on upper palaeo-continental slopes, suggesting that the ice sheet margin was located near the shelf edge and was sufficiently thick to calve icebergs greater than the water depth or wide enough that if they overturned they impacted the seafloor. The lack of scours on the palaeo-shelves compared to the slope may suggest that during any ice margin retreat or stillstands on the outer shelf, melt was more dominant than calving, or that any icebergs which were calved were typically smaller or disintegrated quickly. It is also a possibility that the icebergs that formed some of these scours may have been sourced from elsewhere on the margin. For example, they might have travelled north via weakened ocean currents from the Disko Bugt area, where deep draft icebergs are known to have scoured seafloor depths of ~1 km (Kuijpers et al., 2007).

5. Evolution of the Melville Bugt TMF

The late Cenozoic record of Greenland glaciation has primarily been captured from IRD recorded in offshore boreholes. Although seismic stratigraphic and borehole data have shown the GrIS extended offshore during the late Miocene (St. John and Krissek, 2002; Larsen et al., 1994; Pérez et al., 2018), it was only during the latest Neogene that glaciation is thought to have intensified. IRD from several ODP Sites (642-645, 907, and 911) from around Greenland and the North Atlantic suggest Northern Hemisphere glaciations initially expanded offshore from ~3.4-3.3 Ma and intensified after ~2.8 Ma (Jansen et al., 2000; St. John and Krissek, 2002). The base of the MB-TMF indicates the onset of TMF

deposition at ~2.7 Ma (Knutz et al., 2019) and this is supported by sedimentary records showing an increased occurrence of IRD from this time onwards (Cremer, 1989; Wolf and Thiede, 1991). Although there are limited dates (Christ et al., 2020; Knutz et al., 2019) for constraining the MB-TMF evolution, four main stages of fan development are derived from linear sedimentation rates between these dates, as well as complementary relationships between depositional patterns, glacigenic unconformities, and the seismic geomorphology.

5.1 Stage 1 – 2.7-2.0 Ma

During Stage 1, unit A1 was deposited (Fig. 4a, 13a-c) with an onset of TMF deposition at ~2.7 Ma based on correlation with Knutz et al. (2019). Only a small part of the upslope portion of this unit is preserved and contained within the 3D seismic data and this reveals a glacigenic unconformity and evidence of gullies on the palaeo-slope – showing the influence of ice sheet processes during the deposition of the earliest unit. The more extensive seismic reflection dataset used by Knutz et al. (2019) shows a large depocentre that extends basinward of the 3D data studied here. Down-dip a chaotic pattern observed on seismic profiles (Fig. 2b) is reminiscent of downslope-dominated deposition, which is possibly linked to formation of the gullies in the Northern Bank area and excavation of a number of palaeo-canyons beneath the modern day trough (Fig. 11). The fragmented nature of the depocentre (Fig. 4a) indicates that these deposits could have been sourced from different areas along the margin.

An extensive grounded ice sheet, supported by IRD observations (Cremer, 1989), would have moved over unlithified marine sediments that could have been remobilised down the palaeo-continental slope, reworking the Neogene drift and graben infill material that comprised part of the Northern Bank (Fig. 13b). It is possible that the initial glaciations on Greenland might have helped transport large volumes of regolith beyond the coastline and into the marine setting, contributing to the accumulation of unlithified sediments with low shear strength properties that were vulnerable to failure and glacigenic transport. The fragmentation of these depocentres can be correlated to the pre-glacial, Neogene morphology of the shelf, where topographic depressions down-dip appear to have been preferentially infilled first and slope canyons used as the main sediment pathways from the shelf to the basin (Fig. 4c, 11).

Unit A2 was deposited during this stage and is broadly correlative with the increases in IRD observed across the wider North Atlantic at ~2.4 Ma (Jansen and Sjøholm, 1991) and expansions of the Laurentide and European Ice Sheets at a similar time (Balco et al., 2005;

Rea et al., 2018). On the palaeo-continental slope there are frequent observations of continuous and high-amplitude reflections from the 3D seismic data that show the repeated presence of gullies (Fig. 8). Gullies, iceberg scours, and the glacial unconformity that marks the top of unit A2, again suggest the presence of a marine-terminating ice sheet at the shelf edge and the proximal delivery of material and/or sediment-laden meltwater during and after peak glaciation (i.e. when the ice was located at the palaeo-shelf edge and during the earliest stages of retreat from it). The depocentre of unit A2 is well-preserved beneath the modern Northern Bank, highlighting its Pleistocene longevity. This depocentre also shows a southward shift, rather than a basinward shift, in depocentre location as accommodation on the pre-glacial stratigraphy begins to be infilled.

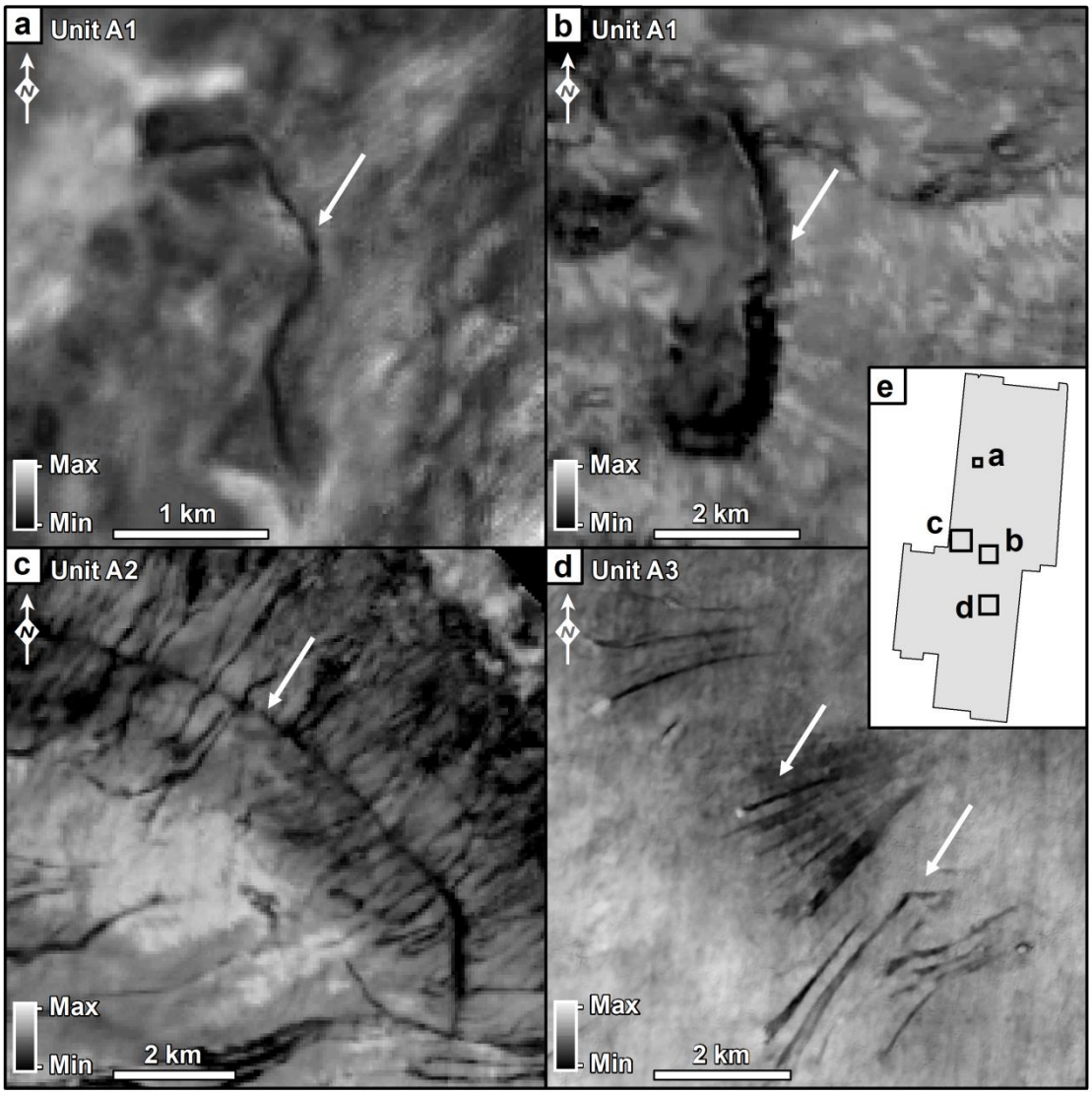

Figure 12. Iceberg Scours | Examples of iceberg scours displayed as RMS amplitude extractions: a-b) isolated iceberg scours; c) scour cross-cutting gullies on the slope; d) collection of fan-like scours on the palaeo-shelf of unit A3; and e) location of the panels in the ANU 3D seismic survey. Arrows pointing at the features of interest (i.e. the black curvi-linear features with minimum RMS amplitude values).

During this first stage of TMF development, units A1-A2 were deposited adjacent to the two banks in the north and south (Fig. 13a). The later erosion of the Melville Bugt Trough means that it is not possible to fully determine the precise geometry of the shelf morphology prior to the onset of glaciations. However, given that the depocentres of unit A1 appears to have built out from the Northern and Southern Banks, it is possible that the topography here was higher than the adjacent areas and could have acted as potential pinning points for early glacial advance, or even the inception of local ice domes (Fig. 4c, 13a-c). Ice sheet reconstructions from the Last Glacial Maximum on the mid-Norwegian and Antarctic Peninsula margins provide a reasonable analogue for such a reconstruction in Melville Bugt (e.g. Lavoie et al., 2015; Ottesen et al., 2005). The Neogene drift and sedimentary deposits in the graben may also have allowed one of the earliest ice sheets to erode into the sediments once the ice had traversed harder crystalline basement rocks to the east. This preferential erosion of the sedimentary substrate may have aided initial reworking of the proximal topography leading to the formation of a proto-trough (Fig 13b) – though it is likely this was fully initiated much later on.

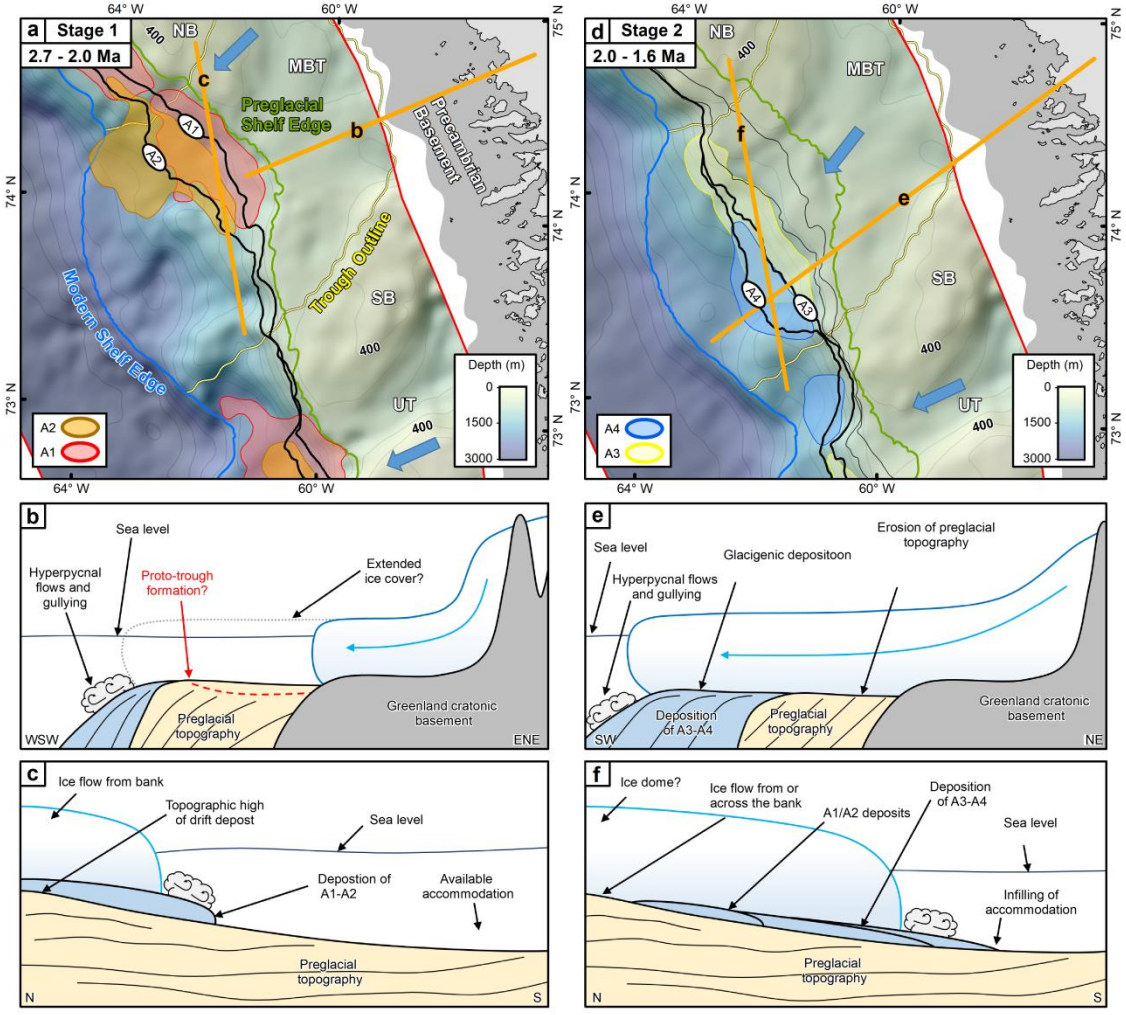

Figure 13. Stage 1 and 2 of MB-TMF evolution | Schematic model showing the first two stages of the stratigraphic and glaciological evolution of the MB-TMF. The coloured polygons on the maps relate to the depocentres shown on Fig. 4a and the black lines show the location of the palaeo-shelf edge at the end of the deposition of that unit. The thick blue arrows show the dominant direction of ice flow and progradation during deposition of the units. The cartoons show a hypothetical cross-section of the TMF at various stages during the fan formation. Location of each hypothetical cross-section is presented on the previous planform schematic. The underlying bathymetry in each map is a depth-converted surface of the seafloor topography at the beginning of the deposition of the youngest unit – e.g. in (a) the topography is for the base of the glacial succession and in (b) it is for the top of unit A2. The light grey contours are for the underlying topography and are measured every 200 m.

5.2 Stage 2 – 2.0-1.6 Ma

Units A3-A4 show ~40-50 km of progradation during Stage 2 that reflects a sustained period of shelf glaciation (Fig. 13d-f). This corresponds with further increases in IRD and reductions in sea surface and deep-water temperatures across the North Atlantic from 2.0-1.6 Ma (Bates et al., 2014; Henrich and Baumann, 1994; Krissek, 1989; Lawrence et al., 2009, 2010). Other seismic records of glaciated margins (e.g. Northwest Europe) show increased margin progradation and evidence of expanded grounded glaciation at a similar time (Montelli et al., 2017; Ottesen et al., 2012; Rea et al., 2018; Rise et al., 2005). These units contain frequent observations of gullied surfaces (Fig. 8, 9) that are related to the delivery of sediment-laden meltwater to the slope by ice grounded at, or proximal to, the palaeo-shelf edge (Fig. 13d-f). The depocentres migrate southwards away from the present day Northern Bank area (Fig. 4a) and their elongate shapes show material was delivered as a line source, rather than a point source, suggesting a wide ice margin.

Based on the observed depocentre migration (Fig 4a, 5), it appears that ice extended sufficiently far offshore that it advanced across the sedimentary deposits in the graben – as is indicated by the gullying and observation of a GZW atop the unit A3 unconformity. Ice dome presence on the Northern and Southern Banks could have helped facilitate ice stream flow in the area in between the domes, leading to the full onset of ice stream erosion into the preglacial sedimentary prism and formation of the Melville Bugt Trough. As a result, if the proto-trough was not initiated during Stage 1, it was likely initiated during Stage 2. The deposition of units A1-A2 also served to reduce accommodation adjacent to the banks (i.e. space in which sediments could accumulate) such that ice in the Melville Bugt Trough was then steered to the south of the Northern Bank where units A3 and A4 were deposited above the available accommodation in the southwest. Thus, topographic focusing and/or ice domes on the banks would have forced ice flow south of the Northern Bank into the proto-trough, leading to a positive feedback where ongoing erosion would deepen the bathymetry between the cratonic basement and the area between the banks – leading to further drawdown of ice into the trough.

The pinning and divergence of ice flow to the south of the bank may have been aided by accommodation changes related to topographic adjustment of the underlying MBR. If the ridge was uplifted in the north, as is hinted at by erosion and progressively steeper-dipping reflections onlapping the northern part of the ridge (Knutz et al., 2019), syn-depositional adjustment of the ridge could have increased the topographic barrier of the Northern Bank area – leading to further focusing of ice flow southward. The continued erosion and deepening of the trough implies that the ice sheet must have been grounded on the continental shelf at this time.

5.3 Stage 3 – 1.6-1.0 Ma

During Stage 3 the deposition of Units A5-A7 (Fig. 14a-c) are correlated with intensification of glaciation around the Northern Hemisphere (Knies et al., 2009; Rea et al., 2018), culminating with the onset of the Middle Pleistocene Transition that began at ~1.3 Ma (Head and Gibbard, 2005). Although the dominant progradation direction was toward the southwest, the shelf edge also prograded westward, away from the coastline, meaning that ice would have had an extra 20-30 km to travel in order to reach the palaeo-shelf edge after the deposition of each unit. Slope gullies and debris flow deposits are observed on many of the Stage 3 clinoforms – suggesting ice sheets provided a long-lived control on depositional processes and that the ice cover was capable of maintaining enough mass to extend across the increasing distances to the shelf edge.

Through time, the effect of glacial deposition and the continued presence of the Neogene deposits and early glacial units that comprise the Northern and Southern Bank areas, and potential ice domes above them, still controlled the distribution of available accommodation and concomitant ice flow pathways. With the south-western movement of each depocentre infilling available accommodation on the pre-existing topography, it is likely that ice continued to flow into the area between the cratonic basement and the two banks, leading to further erosion of the trough (Fig. 14b). As the depocentre of the MB-TMF migrated southward, the fan eventually merged with the Upernavik TMF before separating (Fig. 14c), with sediment delivery then focused in front of the two contemporary troughs (Knutz et al., 2019). This suggests that the contemporary morphology of the study area was largely constructed by this time.

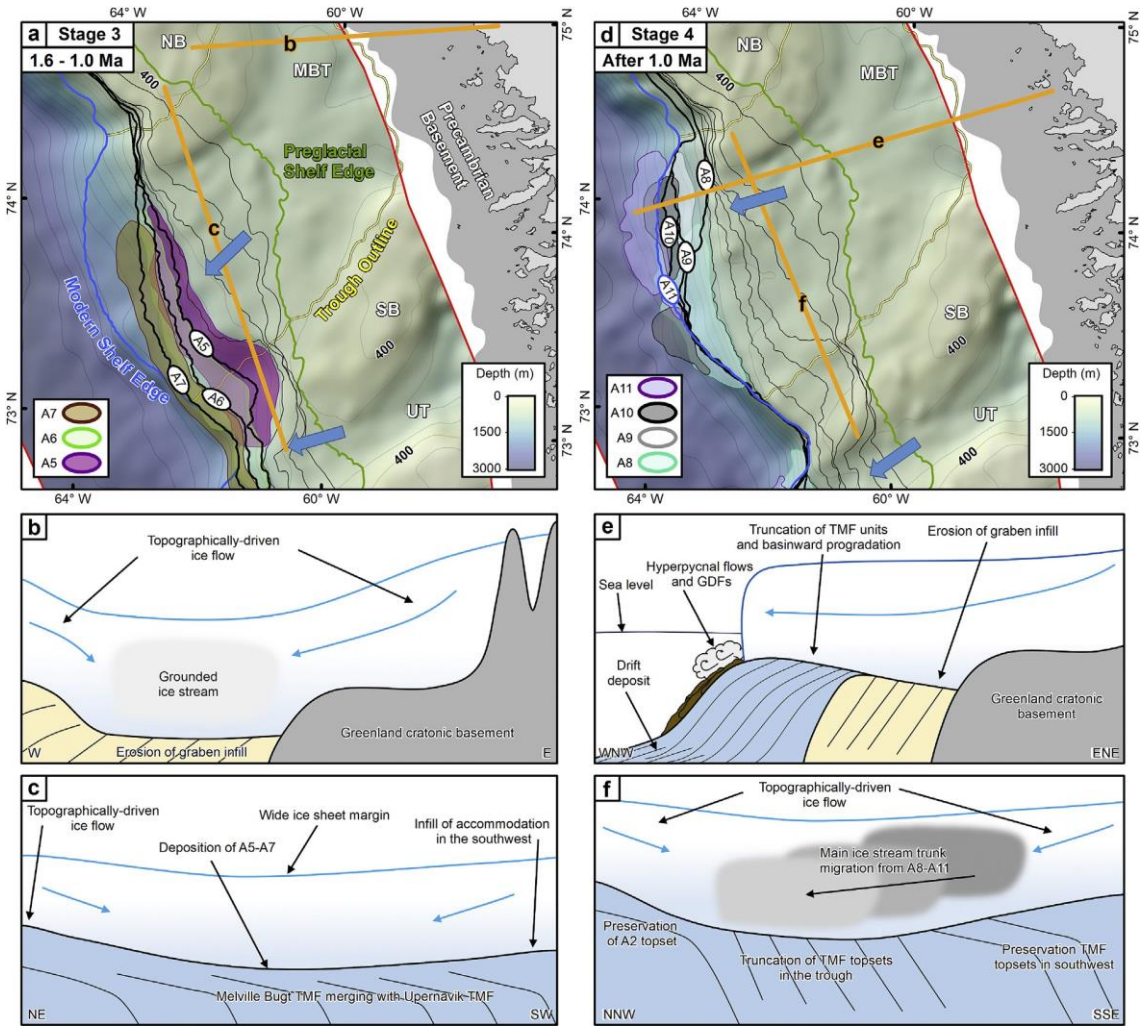

Figure 14. Stage 3 and 4 of MB-TMF evolution | Schematic model showing the third and fourth stages of the stratigraphic and glaciological evolution of the MB-TMF. The coloured polygons on the maps relate to the depocentres shown on Fig. 4a and the black lines show the location of the palaeo-shelf edge at the end of the deposition of that unit. The thick blue arrows show the dominant direction of ice flow and progradation during deposition of the units. The cartoons show a hypothetical cross-section of the TMF at various stages during the fan formation. Location of each hypothetical cross-section is presented on the previous planform schematic. The underlying bathymetry in each map is a depth converted surface of the seafloor topography at the beginning of the deposition of the youngest unit – e.g. in (a) the topography is the top of unit A4 and in (b) it is for the top of unit A7. The light grey contours are for the underlying topography and are measured every 200 m. Abbreviations are as follows Melville Bugt Trough (MBT), Northern Bank (NB), Southern Bank (SB), Upernavik Trough (UT). Note that on schematics (b), (c), and (f) the main ice flow is perpendicular to the cross-section (i.e. out of the page).

The amalgamation of the depocentres and their subsequent separation, may be a result of changes in ice flow patterns fundamentally controlled by the availability of accommodation on the shelf. At the start of Stage 3 there was still available accommodation to the west of the Southern Bank (Fig. 14a). As the depocentres merged, this accommodation was infilled and the onset of basinward progradation then began as the Southern Bank, and a potential ice dome above it, separated the ice stream flow into the two separate troughs. The forcing of depocentre splitting due to accommodation limitations is supported by MSGL from unit A7 onwards (Fig. 7) that demonstrate a

gradual shift northwards in ice stream flow within the Melville Bugt Trough (Newton et al., 2020).

5.4 Stage 4 – After 1.0 Ma

The last phase of TMF evolution is thought to date from ~1.0 Ma through to the last glacial cycle (Fig. 14d-f). This correlates well with records for the most extensive Pleistocene glaciations around the Northern Hemisphere (Jansen et al., 2000; Knies et al., 2009; Thierens et al., 2012). After the deposition of unit A7, it appears that the underlying Neogene topography between the two banks either side of the contemporary Melville Bugt Trough had been infilled (Fig. 14e, f). This also marks the time when the Upernavik TMF fully separates from the MB-TMF. Palaeo-shelves preserved in units A8-A9 contain MSGL (Fig. 7) confirming the presence of palaeo-ice streams within the Melville Bugt Trough. These ice streams flowed through the excavated trough and reflect ice funnelling into the area from adjacent areas of higher topography and the coastline. This is captured by small changes in ice stream flow directions that are indicated by the MSGL preserved in units A8-A10 (Newton et al., 2020). It is the material delivered by these ice streams and separation of ice flow that instigated basinward progradation from ~1.0 Ma.

Although the ice sheet flow during the deposition of units A9-A11 is toward the basin, the Stage 3 glacial deposits adjacent to the Southern Bank likely provided a topographic barrier that contributed to the northward component of depocentre migration (Fig. 4a). From the deposition of unit A9 onwards, the shelf architecture shows aggradation in the southern part of the study area (Fig. 2b). During the Middle and Late Pleistocene glaciations the magnitudes of sea level change were larger than any other part of the late Pliocene and Pleistocene (Lisiecki and Raymo, 2005; Miller et al., 2011). Consequently, during peak glacials, the banks were almost certainly covered by ice domes frozen to the bed, limiting subglacial erosion and helping to maintain the positive topographic relief of the banks through time (e.g. Lavoie et al., 2015; Ottesen et al., 2005). Bank preservation, combined with ice stream erosion within the trough (i.e. the seafloor unconformity), would have increased the local topographic gradient and encouraged ice flow from the banks and mainland toward the trough. The aggradational topset deposits observed in the south also thin out toward the northern part of the trough where they have been truncated by the northward movement of ice stream erosion (Fig. 2, 14f). These observations support the hypothesis that ice domes on the banks helped to promote their protection from glacial erosion, whilst also helping to control ice flow pathways into the trough.

During this period, the seismic facies and architecture of distal deposits provides evidence for continued down-slope movement of sediment through gullies and debris flow deposits, but it also provides potential evidence for along-slope processes. Although it is not certain due to the lack of data coverage, a sedimentary wedge onlapping the palaeo-slope during the deposition of unit A8 could be interpreted as a plastered contourite drift reflecting along-slope processes (Fig. 10). From the deposition of unit A9 to present, a planar sheeted drift deposit observed downslope of this feature provides possible evidence for both along-slope and downslope currents during the latest period of glaciation (Fig. 11). Deposits further up the slope from both types of drift are intercalated with GDFs.

The Miocene-Pliocene stratigraphy of the region shows that Baffin Bay was an important passageway for northward flowing currents that helped bring warmth to the higher latitudes of the study area (Knutz et al., 2015). In contrast, an along-slope influence on the Pleistocene drift-channel system must reflect the deep water circulation in Baffin Bay. The current age model for the seismic stratigraphy (Knutz et al., 2019) suggests that the drift accumulated during the last million years or so. Alternatively, Early Pleistocene contourite build-ups were obliterated by erosion and were reworked into the mass transport deposit underlying the drift-channel system. Nevertheless, it is possible that the drift accumulation is related to enhanced glacial-interglacial cycles that began after the Middle Pleistocene Transition. A better under- standing of its palaeoceanographic significance will require more high-resolution data that can elucidate the relative contributions of along-slope and downslope processes to these strata.

The intercalated GDFs also have possible palaeo-glaciological significance due to the apparent decrease in slope incisions during units A8-A11. The older units, A1-A7 contain multiple examples of slope gullying and although GDF deposits are occasionally present, they are considerably more frequent in the stratigraphy deposited since ~1.0 Ma, which itself appears to show reduced evidence of gullying (notwithstanding the limitations of data coverage). This perhaps indicates that the Early Pleistocene ice sheet in this region had a larger component of meltwater sedimentary processes than compared to the Middle and Late Pleistocene. This may reflect the larger ice sheets in the Middle and Late Pleistocene having a greater volume of ice above equilibrium line altitudes and more discharge occurring via iceberg calving. Similar observations of this shift in slope depositional patterns have been observed on the mid-Norwegian margin and in East Greenland (Laberg et al., 2018; Montelli et al., 2018; Ottesen et al., 2012). In these areas the Middle Pleistocene Transition stratigraphy records a change from the dominance of meltwater related deposition earlier in the record, to the emplacement of glacigenic materials directly at the

shelf edge in the form of GDFs during the latter. Recent work from the lower latitude North Sea Fan has shown that meltwater was a crucial component of TMF development during the Late Pleistocene (Bellwald et al., 2020a). During Stage 4 of the MB-TMF development, although they decrease in frequency compared to the older units, evidence of slope incisions in the younger stratigraphy perhaps suggests meltwater-related sedimentation was, similarly, still an important process (Fig. 10).

5.5 Topset Preservation

Across the MB-TMF topset, preservation is variable (Fig. 2), with the topsets of units A3-A11 having been preserved in the south and only the topset of unit A2 preserved in the north. Two possible mechanisms can be invoked to account for this spatial variation: 1) the MBR and recent tectonic adjustments (perhaps related to landscape modification and isostatic compensation) through the Pleistocene glaciations led to the preferential uplift of the northern part of the MBR and subsidence in the south; or 2) there was a general subsidence through time of glacigenic sediments which provided the main control on accommodation. In the distal parts of many TMF systems, outer palaeo-shelves are preserved by subsidence of rapidly deposited glacigenic sediments and inner shelf uplift due to erosion and isostatic compensation (ten Brink et al., 1995; Hjelstuen et al., 2004; Vorren and Laberg, 1997). Whilst this could account for the general preservation of topsets, it does not account for the spatial variation in topset erosion and it is proposed here that this relates to the interplay between glacigenic sediment deposition and the routing of ice streams.

After the deposition of units A7-A8, the available Neogene accommodation was infilled and the shelf edge was broadly aligned to the coastline. This infilling of the outermost part of the Southern Bank also provided a major topographic barrier to the south (Fig. 4a), in addition to the Northern Bank. Regardless of adjustments of the MBR, the older units in the north would have likely naturally subsided through time – potentially resulting in a south-north gradient. This contrasts to the onset of MB-TMF where accommodation was located in the area adjacent to the Southern Bank (Fig. 4c), leading to a north-south gradient. This "see-saw" in accommodation appears to have been one of the main controls on depositional patterns. Differential movements of the MBR may have helped facilitate initial preservation through uplift of the Northern Bank area and subsidence of the area to the south, forcing a dominance of south-westward progradation from unit A3 onwards. Thus, accommodation changes related to the MBR may be superimposed on general accommodation changes from sediment compaction. The interplay between relative basin movements, ice sheet processes, sediment pathways, and the ability of ice sheets to modify

the topography and in turn have their flow influenced by those topographic changes, provided the dominant control on depositional patterns. The influence of ice sheets in modifying large-scale shelf morphology has previously been shown on the mid-Norwegian margin (Dowdeswell et al., 2006; Newton and Huuse, 2017), where changes in accommodation through different glaciations influenced ice and sediment pathways during each subsequent glaciation.

5.6 Landscape Evolution

The frequency and extent of GrIS advances during the Early Pleistocene raises broad questions about our understanding of Northern Hemisphere glaciations. Oxygen isotope records have been used as a proxy for ice sheet volume and sea level changes throughout the Pleistocene, with glacial stages in the Early Pleistocene characterised by smaller ice sheet volumes and lower magnitude sea level drops compared to the Middle-Late Pleistocene (Lisiecki and Raymo, 2005; Miller et al., 2011). However, an increasing number of geological observations have shown that during many Early Pleistocene glacial stages, the Laurentide and European Ice Sheets were comparable, at least in areal extent, to those in the Middle-Late Pleistocene (e.g. Balco et al., 2005; Rea et al., 2018). Adding a more extensive Early Pleistocene GrIS to this has potential implications for sea level and ice volume proxies – i.e. how can Early Pleistocene ice sheets be similar in extent to those in the Middle-Late Pleistocene when oxygen isotope records suggest that Early Pleistocene ice volumes were significantly smaller?

Previous work has suggested low-slung and slippery Early Pleistocene ice sheets could have facilitated increased ice extent without impacting the ice volumes inferred from proxy records (Rea et al., 2018). This could hypothetically explain why there appears to be an abundance of glacial meltwater during TMF progradation during the Early Pleistocene, as more of the ice margin may have been below the equilibrium line altitudes of a low-slung and slippery ice sheet. A similar scenario to North America, where a thick layer of regolith provided low basal friction that facilitated ice sheet expansion (e.g. Clark and Pollard, 1998), could also contribute to extensive Early Pleistocene ice sheets in Greenland. This is perhaps supported by unit A1, which is partly characterised by a mass transport complex that may be related to a major transfer of weathered material to the basin. A key issue is how quickly the weathered material could be transported and how much was removed – i.e. whether regolith was removed in one glaciation or several. Mineralogical evidence derived from ODP Site 645 (Fig. 1b) suggest removal may have taken place over much of the Early Pleistocene, before culminating in the Middle Pleistocene Transition, when older sediments derived from weathered continental deposits changed to younger sediments

sourced from crystalline bedrock (Andrews, 1993; Thiebault et al., 1989). This could provide a mechanism that contributed to the repeated advance of Early Pleistocene ice sheets in Greenland that are documented in this study. This issue also feeds back into contemporary discussions about the longevity of the GrIS (Bierman et al., 2016; Schaefer et al., 2016). If part of northwest Greenland did experience long periods without an ice sheet, then it is possible the regolith could have been sufficiently renewed to facilitate low-slung and slippery ice sheets during the next glaciation. Whether sufficient regolith could have been both generated and accumulated across the mountainous terrain of Melville Bugt during an interglacial, rather than being transported elsewhere by fluvial or glaci-fluvial processes, is a further complicating factor. Additionally, if regolith accumulation cannot be achieved during one interglacial, a more limited ice sheet would be required for one or more of the subsequent glacial stages in order for sufficient material to accumulate, having implications for finger-printing sea level fluctuations during the Pleistocene.

It is generally assumed that the Laurentide Ice Sheet provided the dominant control on sea level during the Pleistocene and that contributions from Greenland were probably somewhat consistent through time as they were constrained by the areal extent of the continental shelf (e.g. Batchelor et al., 2019; Margold et al., 2015). Whilst this is still likely to be the case, the results presented here show that the GrIS repeatedly advanced to the outer shelf margin of Melville Bugt during many glacial stages of the Pleistocene. Cosmogenic radionuclide dating studies have also suggested that Greenland might have experienced interglacial periods during the Pleistocene when the ice sheet was considerably smaller than present (Schaefer et al., 2016). Thus, the GrIS has clearly evolved dynamically through the Pleistocene and if these ice sheet advances were not characterised by low-slung and slippery ice sheets, as hypothesised above, then they would have had a greater influence on the global sea level record than has previously been assumed. This raises the intriguing possibility of major fluctuations in the relative contributions of the different Northern Hemisphere ice sheets through time – i.e. during different glacials or glacial-interglacial transitions the ice sheets may account for different proportions of total ice volume, albeit with a continued dominance from the Laurentide Ice Sheet. Unravelling the character of these palaeo-ice sheets, whether they were low-slung and slippery or something more similar to the Last Glacial Maximum, will provide new information on not just ice sheet evolution, but also how glacial-interglacial sea level contributions from the different ice sheets might have varied and how these observations compare with, and potentially contradict, global sea level records.

The limited preservation of topset strata and the lack of borehole control across the MB-TMF and on most glaciated margins, make these contradictions between landform and proxy records (currently) difficult to resolve. Improving our understanding of glaciations prior to the last one will require a combination of numerical landscape evolution models that are designed to explore the onshore-offshore source-to-sink dynamics and geological analysis of sediments comprising TMFs in order to ground-truth ancient erosional and depositional ice sheet processes and how they compare to global sea level records and other proxy records of environmental change.

6. Conclusions

The MB-TMF is a ~2.7 Myr long archive of glacial-interglacial changes measuring up to ~2 km in thickness. In this study, a seismic stratigraphic and geomorphological analysis of the fan reveals an abundance of buried glacier-influenced landforms and deposits. These features highlight how existing and evolving topographic changes through time influenced the availability of accommodation and controlled ice sheet flow and resulting depositional patterns. Deposits emplaced by downslope gravitational processes are common throughout the stratigraphy, suggesting a long-lived influence of glacigenic processes (e.g. meltwater hyperpycnal flows) at the shelf edge, or proximal to it, during many glacial stages. After ~1.0 Ma the interglacial stages were likely characterised by an increase in northward heat transport. The excellent preservation of topsets across different parts of the MB-TMF, and the large volume of sediments that make up the fan, appear to provide a near-continuous record of glacigenic and marine depositional processes since ~2.7 Ma. The apparent lack of a major time gap in the depositional history of the fan means that these sedimentary records likely contain a long-term composite record of ice sheet, atmospheric, and oceanographic changes through the late Pliocene and Pleistocene. The seafloor unconformity and gently dipping strata mean that these records could be accessed by ocean drilling to relatively shallow depths across the fan. Such records would build on the seismic geomorphological reconstruction here and help to develop understanding on the evolution of the GrIS further.

Acknowledgements

The authors are grateful to TGS (2D), Cairn Energy (PITU), and Shell (ANU) for providing the seismic data used within this study. AMWN was supported by the Natural Environment Research Council (NERC grant reference number NE/K500859/1) and Cairn Energy whom funded his PhD. AMWN also thanks the British Society for Geomorphology for providing a postgraduate research grant that enabled visiting and collaborating with the Geological Survey of Denmark and Greenland during this project. DRC was funded by the NERC Centre for Doctoral Training in Oil & Gas (grant reference number NE/M00578X/1) and the British Geological Survey (BGS) via the British University Funding Initiative (studentship number: S356). Schlumberger, Eliis, Geoteric, and ESRI are thanked for providing software. Simon H. Brocklehurst is thanked for comments on the earliest stages of this work. The authors would like to sincerely thank Benjamin Bellwald and an anonymous reviewer for taking the time to offer such detailed and insightful comments on the paper, especially in the context of the current health crisis

References

Aksu, A. E., Mudie, P. J., Macko, S. A. and de Vernal, A.: Upper Cenozoic history of the Labrador Sea, Baffin Bay, and the Arctic Ocean: A paleoclimatic and paleoceanographic summary, Paleoceanography, 3, 519–538, doi:10.1029/PA003i005p00519, 1988.

Alley, R. B., Blankenship, D. D., Bentley, C. R. and Rooney, S. T.: Deformation of till beneath ice stream B, West Antarctica, Nature, 322, 57–59, doi:10.1038/322057a0, 1986.

Alley, R. B., Andrews, J. T., Brigham-Grette, J., Clarke, G. K. C., Cuffey, K. M., Fitzpatrick, J. J., Funder, S., Marshall, S. J., Miller, G. H., Mitrovica, J. X., Muhs, D. R., Otto-Bliesner, B. L., Polyak, L. and White, J. W. C.: History of the Greenland Ice Sheet: paleoclimatic insights, Quat. Sci. Rev., 29, 1728–1756, doi:10.1016/j.quascirev.2010.02.007, 2010.

Anandakrishnan, S., Catania, G. A., Alley, R. B. and Horgan, H. J.: Discovery of till deposition at the grounding line of Whillans Ice Stream, Science (80-.)., 315, 1835–1838, doi:10.1126/science.1138393, 2007.

Andreassen, K., Ødegaard, C. M. and Rafaelsen, B.: Imprints of former ice streams, imaged and interpreted using industry three-dimensional seismic data from the south-western Barents Sea, in Seismic geomorphology: applications to hydrocarbon exploration and production, edited by R. J. Davies, H. W. Posamentier, L. W. Wood, and J. A. Cartwright, pp. 151–169, Geological Society Special Publication., 2007.

Andrews, J. T.: Changes in the silt- and clay-size mineralogy of sediments at Ocean Drilling Program site 645B, Baffin Bay, Can. J. Earth Sci., 30, 2448–2452, doi:10.1139/e93-211, 1993.

Arthur, M. a., Srivastava, S. P., Kaminski, M., Jarrard, R. and Osler, J.: Seismic stratigraphy and history of deep circulation and sediment drift development in Baffin Bay and the Labrador Sea, Proc. Ocean Drill. Program, Sci. Results, 957–988, doi:10.2973/odp.proc.sr.105.118.1989, 1989.

Balco, G., Rovey, C. W. and Stone, J. O. H.: The first glacial maximum in North America, Science (80-.)., 307, 222, doi:10.1126/science.1103406, 2005.

Batchelor, C. L. and Dowdeswell, J. A.: The physiography of High Arctic cross-shelf troughs, Quat. Sci. Rev., 92, 68–96, doi:10.1016/j.quascirev.2013.05.025, 2014.

Batchelor, C. L., Dowdeswell, J. A. and Rignot, E.: Submarine landforms reveal varying rates and styles of deglaciation in North-West Greenland fjords, Mar. Geol., 402, 60–80, doi:10.1016/j.margeo.2017.08.003, 2018.

Batchelor, C. L., Margold, M., Krapp, M., Murton, D. K., Dalton, A. S., Gibbard, P. L., Stokes, C. R., Murton, J. B. and Manica, A.: The configuration of Northern Hemisphere ice sheets through the Quaternary, Nat. Commun., doi:10.1038/s41467-019-11601-2, 2019.

Bates, S. L., Siddall, M. and Waelbroeck, C.: Hydrographic variations in deep ocean temperature over the mid-Pleistocene transition, Quat. Sci. Rev., 88, 147–158, doi:10.1016/j.quascirev.2014.01.020, 2014.

Beaubouef, R. T. and Friedmann, S. J.: High-resolution seismic/sequence stratigraphic framework for the evolution of Pleistocene intra slope basins, western Gulf of Mexico: Depositional models and reservoir analogs, in Deep-water reservoirs of the world: Gulf Coast Section SEPM 20th Annual Research Conference, edited by P. Weimer, R. M. Slatt, J. Coleman, N. C. Rosen, H. Nelson, A. H. Bouma, M. J. Styzen, and D. . Lawrence, pp. 40–60, SEPM., 2000.

Bierman, P. R., Shakun, J. D., Corbett, L. B., Zimmerman, S. R. and Rood, D. H.: A persistent and dynamic East Greenland Ice Sheet over the past 7.5 million years, Nature, 540, 256–260, doi:10.1038/nature20147, 2016.

Briner, J. P., Håkansson, L. and Bennike, O.: The deglaciation and neoglaciation of upernavik isstrøm, greenland, Quat. Res., 80, 459–467, doi:10.1016/j.yqres.2013.09.008, 2013.

ten Brink, U. S., Schneider, C. and Johnson, A. H.: Morphology and Stratal Geometry of the Antarctic Continental Shelf: Insights from Models, in Geology and seismic stratigraphy of the Antarctic margin, edited by A. . Cooper, P. . Barker, and G. Brancolini, pp. 1–24, American Geophysical Union., 1995.

Brown, C. S., Newton, A. M. W., Huuse, M. and Buckley, F.: Iceberg scours, pits, and pockmarks in the North Falkland Basin, Mar. Geol., 386, 140–152, doi:10.1016/j.margeo.2017.03.001, 2017.

Bulat, J.: Some considerations on the interpretation of seabed images based on commercial 3D seismic in the Faroe-Shetland Channel, Basin Res., 17, 21–42, doi:10.1111/j.1365-2117.2005.00253.x, 2005.

Christ, A. J., Bierman, P. R., Knutz, P. C., Corbett, L. B., Fosdick, J. C., Thomas, E. K., Cowling, O. C., Hidy, A. J. and Caffee, M. W.: The Northwestern Greenland Ice Sheet During The Early Pleistocene Was Similar To Today, Geophys. Res. Lett., 47, e2019GL085176, doi:10.1029/2019GL085176, 2020.

Clark, C. D.: Mega-scale glacial lineations and cross-cutting ice-flow landforms, Earth Surf. Process. Landforms, 18, 1–29, doi:10.1002/esp.3290180102, 1993.

Clark, P. U. and Pollard, D.: Origin of the middle Pleistocene transition by ice sheet erosion of regolith, Paleoceanography, 13, 1–99999, doi:10.1029/97PA02660, 1998.

Cox, D. R., Huuse, M., Newton, A. M. W., Gannon, P. and Clayburn, J. A. P.: Slip Sliding Away: Enigma of Large Sandy Blocks within a Gas Bearing Mass Transport Deposit, Offshore NW Greenland, Am. Assoc. Pet. Geol. Bull., 104(5), 1011–1043, 2020a.

Cox, D. R., Knutz, P. C., Campbell, D. C., Hopper, J. R., Newton, A. M. W., Huuse, M. and Gohl, K.: Geohazard detection using 3D seismic data to enhance scientific drilling site selection, Sci. Drill., 28, 1-27, doi:10.5194/sd-28-1-2020, 2020b.

Cremer, M.: Texture and Microstructure of Neogene-Quaternary Sediments, ODP Sites 645 and 646, Baffin Bay and Labrador Sea, in Proceedings of the Ocean Drilling Program, 105 Scientific Results, edited by S. P. Srivastava, M. A. Arthur, B. Clement, and et al., pp. 7–20, ODP, College Station, TX., 1989.

Cuny, J., Rhines, P. B., Niiler, P. P. and Bacon, S.: Labrador Sea Boundary Currents and the Fate of the Irminger Sea Water, J. Phys. Oceanogr., 32, 627–647, doi:10.1175/1520-0485(2002)032<0627:lsbcat>2.0.co;2, 2002.

Daynac, N., Lacaze, S. and Pauget, F.: Interpretation of complex faulted deposits in the North Sea using the relative geological time model, First Break, 34, 55–62, 2016.

De Vernal, A., Hillaire-Marcel, C., Aksu, A. E. and Mudie, P. J.: Palynostratigraphy and chronostratigraphy of Baffin Bay deep sea cores: Climatostratigraphic implications, Palaeogeogr. Palaeoclimatol. Palaeoecol., 61, 97–105, doi:10.1016/0031-0182(87)90042-3, 1987.

Dowdeswell, J. A. and Fugelli, E. M. G.: The seismic architecture and geometry of grounding-zone wedges formed at the marine margins of past ice sheets, Bull. Geol. Soc. Am., 124, 1750–1761, doi:10.1130/B30628.1, 2012.

Dowdeswell, J. A. and Ottesen, D.: Buried iceberg ploughmarks in the early Quaternary sediments of the central North Sea: A two-million year record of glacial influence from 3D seismic data, Mar. Geol., 344, 1–9, doi:10.1016/j.margeo.2013.06.019, 2013.

Dowdeswell, J. A., Ottesen, D. and Rise, L.: Flow switching and large-scale deposition by ice streams draining former ice sheets, Geology, 34, 313–316, doi:10.1130/G22253.1, 2006.

Dowdeswell, J. A., Canals, M., Jakobsson, M., Todd, B. J., Dowdeswell, E. K. and Hogan, K. A.: Atlas of Submarine Glacial landforms: Modern, Quaternary and Ancient, Geological Society of London., 2016.

Engen, Ø., Faleide, J. I. and Dyreng, T. K.: Opening of the Fram Strait gateway: A review of plate tectonic constraints, Tectonophysics, 450, 51–69, doi:10.1016/j.tecto.2008.01.002, 2008.

England, J., Atkinson, N., Bednarski, J., Dyke, A. S., Hodgson, D. A. and Ó Cofaigh, C.: The Innuitian Ice Sheet: configuration, dynamics and chronology, Quat. Sci. Rev., 25, 689–703, doi:10.1016/j.quascirev.2005.08.007, 2006.

Fanetti, D., Anselmetti, F. S., Chapron, E., Sturm, M. and Vezzoli, L.: Megaturbidite deposits in the Holocene basin fill of Lake Como (Southern Alps, Italy), Palaeogeogr. Palaeoclimatol. Palaeoecol., 259, 323–340, doi:10.1016/j.palaeo.2007.10.014, 2008.

Faugères, J. C., Stow, D. A. V., Imbert, P. and Viana, A.: Seismic features diagnostic of contourite drifts, Mar. Geol., 162, 1–38, doi:10.1016/S0025-3227(99)00068-7, 1999.

Freire, F., Gyllencreutz, R., Greenwood, S. L., Mayer, L., Egilsson, A., Thorsteinsson, T. and Jakobsson, M.: High resolution mapping of offshore and onshore glaciogenic features in metamorphic bedrock terrain, Melville Bay, northwestern Greenland, Geomorphology, 250, 29–40, doi:10.1016/j.geomorph.2015.08.011, 2015.

Funder, S., Kjeldsen, K. K., Kjær, K. H. and O Cofaigh, C.: The Greenland Ice Sheet During the Past 300,000 Years: A Review, in Developments in Quaternary Science, edited by J. Ehlers, P. L. Gibbard, and P. D. Hughes, pp. 699–713, Elsevier, Amsterdam., 2011.

Gales, J. A., Larter, R. D., Mitchell, N. C. and Dowdeswell, J. A.: Geomorphic signature of Antarctic submarine gullies: Implications for continental slope processes, Mar. Geol., 337, 112–124, doi:10.1016/j.margeo.2013.02.003, 2013.

Gales, J. A., Leat, P. T., Larter, R. D., Kuhn, G., Hillenbrand, C. D., Graham, A. G. C., Mitchell, N. C., Tate, A. J., Buys, G. B. and Jokat, W.: Large-scale submarine landslides, channel and gully systems on the southern Weddell Sea margin, Antarctica, Mar. Geol., 348, 73–87, doi:10.1016/j.margeo.2013.12.002, 2014.

Geissler, W. H. and Jokat, W.: A geophysical study of the northern Svalbard continental margin, Geophys. J. Int., 158, 50–66, doi:10.1111/j.1365-246X.2004.02315.x, 2004.

Geissler, W. H., Jokat, W. and Brekke, H.: The Yermak Plateau in the Arctic Ocean in the light of reflection seismic data-implication for its tectonic and sedimentary evolution, Geophys. J. Int., 187, 1334–1362, doi:10.1111/j.1365-246X.2011.05197.x, 2011.

Georgiadis, E., Giraudeau, J., Jennings, A., Limoges, A., Jackson, R., Ribeiro, S. and Massé, G.: Local and regional controls on Holocene sea ice dynamics and oceanography in Nares Strait, Northwest Greenland, Mar. Geol., 422, 106115, doi:10.1016/j.margeo.2020.106115, 2020.

Gregersen, U., Hopper, J. R. and Knutz, P. C.: Basin seismic stratigraphy and aspects of prospectivity in the NE Baffin Bay, Northwest Greenland, Mar. Pet. Geol., 46, 1–18, doi:10.1016/j.marpetgeo.2013.05.013, 2013.

Hanna, E., Navarro, F. J., Pattyn, F., Domingues, C. M., Fettweis, X., Ivins, E. R., Nicholls, R. J., Ritz, C., Smith, B., Tulaczyk, S., Whitehouse, P. L. and Jay Zwally, H.: Ice-sheet mass balance and climate change, Nature, 498, 51–59, doi:10.1038/nature12238, 2013.

Head, M. J. and Gibbard, P. L.: Early-Middle Pleistocene transitions: an overview and recommendation for the defining boundary, in Early-Middle Pleistocene Transitions: The Land-Ocean Evidence, edited by M. J. Head and P. L. Gibbard, pp. 1–18, Geological Society of London., 2005.

Henrich, R. and Baumann, K. H.: Evolution of the Norwegian Current and the Scandinavian Ice Sheets during the past 2.6 m.y.: evidence from ODP Leg 104 biogenic carbonate and terrigenous records, Palaeogeogr. Palaeoclimatol. Palaeoecol., 108, 75–94, doi:10.1016/0031-0182(94)90023-X, 1994.

Henriksen, N., Higgins, A. K., Kalsbeek, F., Christopher, T. and Pulvertaft, R.: Greenland from Archaean to Quaternary: Descriptive text to the 1995 geological map of Greenland, 1:2 500 000. 2nd edition., 2009.

Hillaire-Marcel, C., Vernal, A. de, Bilodeau, G. and Wu, G.: Isotope stratigraphy, sedimentation rates, deep circulation, and carbonate events in the Labrador Sea during the last ~ 200 ka, Can. J. Earth Sci., 31, 63–89, doi:10.1139/e94-007, 1994.

Hjelstuen, B. O., Sejrup, H. P., Haflidason, H., Nygård, A., Berstad, I. M. and Knorr, G.: Late Quaternary seismic stratigraphy and geological development of the south Vøring margin, Norwegian Sea, Quat. Sci. Rev., 23, 1847–1865, doi:10.1016/j.quascirev.2004.03.005, 2004.

Hofmann, J. C., Knutz, P. C., Nielsen, T. and Kuijpers, A.: Seismic architecture and evolution of the Disko Bay trough-mouth fan, central West Greenland margin, Quat. Sci. Rev., 147, 69–90, doi:10.1016/j.quascirev.2016.05.019, 2016.

Hofmann, J. C., Knutz, P. C., Kjær, K. H., Nielsen, T. and Ó Cofaigh, C.: Glacial and submarine processes on the shelf margin of the Disko Bay Trough Mouth Fan, Mar. Geol., 402, 33–50, doi:10.1016/j.margeo.2017.12.001, 2018.

Hogan, K. A., Ó Cofaigh, C., Jennings, A. E., Dowdeswell, J. A. and Hiemstra, J. F.: Deglaciation of a major palaeo-ice stream in Disko Trough, West Greenland, Quat. Sci. Rev., 147, 5–26, doi:10.1016/j.quascirev.2016.01.018, 2016.

IPCC: Working Group I Contribution to the IPCC Fifth Assessment Report - Summary for Policymakers, Clim. Chang. 2013 Phys. Sci. Basis, doi:10.1017/CBO9781107415324.004, 2013.

Jakobsson, M., Mayer, L., Coakley, B., Dowdeswell, J. A., Forbes, S., Fridman, B., Hodnesdal, H., Noormets, R., Pedersen, R., Rebesco, M., Schenke, H. W., Zarayskaya, Y., Accettella, D., Armstrong, A., Anderson, R. M., Bienhoff, P., Camerlenghi, A., Church, I., Edwards, M., Gardner, J. V., Hall, J. K., Hell, B., Hestvik, O., Kristoffersen, Y., Marcussen, C., Mohammad, R., Mosher, D., Nghiem, S. V., Pedrosa, M. T., Travaglini, P. G. and Weatherall, P.: The International Bathymetric Chart of the Arctic Ocean (IBCAO) Version 3.0, Geophys. Res. Lett., 39, L12609, doi:10.1029/2012GL052219, 2012.

Jansen, E. and Sjøholm, J.: Reconstruction of glaciation over the past 6 Myr from ice-borne deposits in the Norwegian Sea, Nature, 249, 600–603, doi:10.1038/349600a0, 1991.

Jansen, E., Fronval, T., Rack, F. and Channell, J. E. T.: Pliocene-pleistocene ice rafting history and cyclicity in the Nordic seas during the last 3.5 myr, Paleoceanography, 15, 709–721, doi:10.1029/1999PA000435, 2000.

Japsen, P., Bonow, J. M., Green, P. F., Chalmers, J. A. and Lidmar-Bergström, K.: Elevated, passive continental margins: Long-term highs or Neogene uplifts? New evidence from West Greenland, Earth Planet. Sci. Lett., 248, 330–339, doi:10.1016/j.epsl.2006.05.036, 2006.

Jarrard, R. D. and Arthur, M. A.: Milankovitch Paleoceanographic Cycles in Geophysical Logs from ODP Leg 105, Labrador Sea and Baffin Bay, in Proceedings of the Ocean Drilling Program, 105 Scientific Results, edited by S. P. Srivastava, M. A. Arthur, B. Clement, and E. Al., pp. 757–772, ODP., 1989.

Jennings, A. E., Sheldon, C., Cronin, T., Francus, P., Stoner, J. S. and Andrews, J.: The Holocene History of Nares Strait, Oceanography, 24, 26–41, 2011.

Jennings, A. E., Walton, M. E., Ó Cofaigh, C., Kilfeather, A., Andrews, J. T., Ortiz, J. D., De Vernal, A. and Dowdeswell, J. A.: Paleoenvironments during Younger Dryas-Early Holocene retreat of the Greenland Ice Sheet from outer Disko Trough, central west Greenland, J. Quat. Sci., 29, 27–40, doi:10.1002/jqs.2652, 2014.

Jennings, A. E., Andrews, J. T., Ó Cofaigh, C., St-Onge, G., Belt, S., Cabedo-Sanz, P., Pearce, C., Hillaire-Marcel, C. and Calvin Campbell, D.: Baffin Bay paleoenvironments in the LGM and HS1: Resolving the ice-shelf question, Mar. Geol., 402, 5–16, doi:10.1016/j.margeo.2017.09.002, 2018.

Jennings, A. E., Andrews, J. T., Oliver, B., Walczak, M. and Mix, A.: Retreat of the Smith Sound Ice Stream in the Early Holocene, Boreas, 48, 825–840, doi:10.1111/bor.12391, 2019.

St. John, K. E. K. and Krissek, L. A.: The late Miocene to Pleistocene ice-rafting history of Southeast Greenland, Boreas, 31, 28–35, doi:10.1111/j.1502-3885.2002.tb01053.x, 2002.

Joughin, I., Smith, B. E., Howat, I. M., Scambos, T. and Moon, T.: Greenland flow variability from ice-sheet-wide velocity mapping, J. Glaciol., 56, 415–430, doi:10.3189/002214310792447734, 2010.

Joughin, I., Smith, B. E., Shean, D. E. and Floricioiu, D.: Brief communication: Further summer speedup of jakobshavn isbræ, Cryosphere, 8, 209–214, doi:10.5194/tc-8-209-2014, 2014.

King, E. L., Sejrup, H. P., Haflidason, H., Elverhøi, A. and Aarseth, I.: Quaternary seismic stratigraphy of the North Sea Fan: Glaciallyfed gravity flow aprons, hemipelagic sediments, and large submarine slides, Mar. Geol., 130, 293–315, doi:10.1016/0025-3227(95)00168-9, 1996.

Knies, J., Matthiessen, J., Vogt, C., Laberg, J. S., Hjelstuen, B. O., Smelror, M., Larsen, E., Andreassen, K., Eidvin, T. and Vorren, T. O.: The Plio-Pleistocene glaciation of the Barents Sea-Svalbard region: a new model based on revised chronostratigraphy, Quat. Sci. Rev., 28, 812–829, doi:10.1016/j.quascirev.2008.12.002, 2009.

Knudsen, K. L., Stabell, B., Seidenkrantz, M. S., Eiríksson, J. and Blake, W.: Deglacial and Holocene conditions in northernmost Baffin Bay: Sediments, foraminifera, diatoms and stable isotopes, Boreas, 37, 346–376, doi:10.1111/j.1502-3885.2008.00035.x, 2008.

Knutz, P. C. and Cartwright, J.: Seismic stratigraphy of the West Shetland Drift: Implications for late Neogene paleocirculation in the Faeroe-Shetland gateway, Paleoceanography, 18, 1–17, doi:10.1029/2002PA000786, 2003.

Knutz, P. C., Hopper, J. R., Gregersen, U., Nielsen, T. and Japsen, P.: A contourite drift system on the Baffin Bay-West Greenland margin linking Pliocene Arctic warming to poleward ocean circulation, Geology, 43, 907–910, doi:10.1130/G36927.1, 2015.

Knutz, P. C., Newton, A. M. W., Hopper, J. R., Huuse, M., Gregersen, U., Sheldon, E. and Dybkjær, K.: Eleven phases of Greenland Ice Sheet shelf-edge advance over the past 2.7 million years, Nat. Geosci., 2019.

Krissek, L. A.: Late Cenozoic records of ice-rafting at ODP sites 642, 643, and 644, Norwegian Sea: onset, chronology, and characteristics of glacial/interglacial fluctuations, in Proc. ODP. Sci. Results 10, edited by O. Eldholm, J. Thiede, E. Taylor, and E. Al., pp. 61–74, ODP., 1989.

Laberg, J. S., Guidard, S., Mienert, J., Vorren, T. O., Haflidason, H. and Nygård, A.: Morphology and morphogenesis of a high-latitude canyon; the Andøya Canyon, Norwegian Sea, Mar. Geol., 246, 68–85, doi:10.1016/j.margeo.2007.01.009, 2007.

Laberg, J. S., Forwick, M., Husum, K. and Nielsen, T.: A re-evaluation of the pleistocene behavior of the scoresby sund sector of the greenland ice sheet, Geology, 41(12), 1231–1234, doi:10.1130/G34784.1, 2013.

Laberg, J. S., Rydningen, T. A., Forwick, M. and Husum, K.: Depositional processes on the distal Scoresby Trough Mouth Fan (ODP Site 987): Implications for the Pleistocene evolution of the Scoresby Sund Sector of the Greenland Ice Sheet, Mar. Geol., 402, 51–59, doi:10.1016/j.margeo.2017.11.018, 2018.

Larsen, H. C., Saunders, A. D., Clift, P. D., Beget, J., Wei, W., Spezzaferri, S., Ali, J., Cambray, H., Demant, A., Fitton, G., Fram, M. S., Fukuma, K., Gieskes, J., Holmes, M. A., Hunt, J., Lacasse, C., Larsen, L. M., Lykke-Andersen, H., Meltser, A., Morrison, M. L., Nemoto, N., Okay, N., Saito, S., Sinton, C., Stax, R., Vallier, T. L., Vandamme, D. and Werner, R.: Seven million years of glaciation in Greenland, Science (80-.)., 264, 952–955, doi:10.1126/science.264.5161.952, 1994.

Lavoie, C., Domack, E. W., Pettit, E. C., Scambos, T. A., Larter, R. D., Schenke, H. W., Yoo, K. C., Gutt, J., Wellner, J., Canals, M., Anderson, J. B. and Amblas, D.: Configuration of the Northern Antarctic Peninsula Ice Sheet at LGM based on a new synthesis of seabed imagery, Cryosphere, 9, 613–629, doi:10.5194/tc-9-613-2015, 2015.

Lawrence, K. T., Herbert, T. D., Brown, C. M., Raymo, M. E. and Haywood, A. M.: High-amplitude variations in north atlantic sea surface temperature during the early pliocene warm period, Paleoceanography, 24, PA2218, doi:10.1029/2008PA001669, 2009.

Lawrence, K. T., Sosdian, S., White, H. E. and Rosenthal, Y.: North Atlantic climate evolution through the Plio-Pleistocene climate transitions, Earth Planet. Sci. Lett., 300, 329–342, doi:10.1016/j.epsl.2010.10.013, 2010.

Lecavalier, B. S., Milne, G. A., Simpson, M. J. R., Wake, L., Huybrechts, P., Tarasov, L., Kjeldsen, K. K., Funder, S., Long, A. J., Woodroffe, S., Dyke, A. S. and Larsen, N. K.: A model of Greenland ice sheet deglaciation constrained by observations of relative sea level and ice extent, Quat. Sci. Rev., 102, 54–84, doi:10.1016/j.quascirev.2014.07.018, 2014.

Li, X., Jiang, D., Zhang, Z., Zhang, R., Tian, Z. and Yan, Q.: Mid-Pliocene westerlies from PlioMIP simulations, Adv. Atmos. Sci., 32, 909–923, doi:10.1007/s00376-014-4171-7, 2015.

Lisiecki, L. E. and Raymo, M. E.: A Pliocene-Pleistocene stack of 57 globally distributed benthic δ 18O records, Paleoceanography, 20, PA1003, doi:10.1029/2004PA001071, 2005.

Margold, M., Stokes, C. R. and Clark, C. D.: Ice streams in the Laurentide Ice Sheet: Identification, characteristics and comparison to modern ice sheets, Earth-Science Rev., 143, 117–146, doi:10.1016/j.earscirev.2015.01.011, 2015.

Melling, H., Gratton, Y. and Ingram, G.: Ocean circulation within the North Water polynya of Baffin Bay, Atmos. - Ocean, 39, 301–325, doi:10.1080/07055900.2001.9649683, 2001.

Miller, K., Mountain, G., Wright, J. and Browning, J.: A 180-Million-Year Record of Sea Level and Ice Volume Variations from Continental Margin and Deep-Sea Isotopic Records, Oceanography, 24, 40–53, doi:10.5670/oceanog.2011.26, 2011.

Montelli, A., Dowdeswell, J. A., Ottesen, D. and Johansen, S. E.: Ice-sheet dynamics through the Quaternary on the mid-Norwegian continental margin inferred from 3D seismic data, Mar. Pet. Geol., 80, 228–242, doi:10.1016/j.marpetgeo.2016.12.002, 2017.

Montelli, A., Dowdeswell, J. A., Ottesen, D. and Johansen, S. E.: 3D seismic evidence of buried iceberg ploughmarks from the mid-Norwegian continental margin reveals largely persistent North Atlantic Current through the Quaternary, Mar. Geol., 399, 66–83, doi:10.1016/j.margeo.2017.11.016, 2018.

Mouginot, J., Rignot, E., Bjørk, A. A., van den Broeke, M., Millan, R., Morlighem, M., Noël, B., Scheuchl, B. and Wood, M.: Forty-six years of Greenland Ice Sheet mass balance from 1972 to 2018, Proc. Natl. Acad. Sci., doi:10.1073/pnas.1904242116, 2019.

Newton, A. M., Huuse, M., Knutz, P. and Cox, D. R.: Repeated ice streaming on the northwest Greenland shelf since the onset of the Middle Pleistocene Transition, Cryosph., 14, 2303–2312, doi:10.5194/tc-2019-268, 2020.

Newton, A. M. W. and Huuse, M.: Late Cenozoic environmental changes along the Norwegian margin, Mar. Geol., 393, 216–244, doi:10.1016/j.margeo.2017.05.004, 2017.

Newton, A. M. W., Huuse, M. and Brocklehurst, S. H.: Buried iceberg scours reveal reduced North Atlantic Current during the stage 12 deglacial, Nat. Commun., 7, doi:10.1038/ncomms10927, 2016.

Newton, A. M. W., Knutz, P. C., Huuse, M., Gannon, P., Brocklehurst, S. H., Clausen, O. R. and Gong, Y.: Ice stream reorganization and glacial retreat on the northwest Greenland shelf, Geophys. Res. Lett., 44(15), 7826–7835, doi:10.1002/2017GL073690, 2017.

Newton, A. M. W., Huuse, M. and Brocklehurst, S. H.: A Persistent Norwegian Atlantic Current Through the Pleistocene Glacials, Geophys. Res. Lett., 45(11), 5599–5608, doi:10.1029/2018GL077819, 2018.

Nielsen, T., Andersen, C., Knutz, P. C. and Kuijpers, A.: The Middle Miocene to Recent Davis Strait Drift Complex: Implications for Arctic-Atlantic water exchange, Geo-Marine Lett., 31, 419–426, doi:10.1007/s00367-011-0245-z, 2011.

Noormets, R., Dowdeswell, J. A., Larter, R. D., Ó Cofaigh, C. and Evans, J.: Morphology of the upper continental slope in the Bellingshausen and Amundsen Seas - Implications for sedimentary processes at the shelf edge of West Antarctica, Mar. Geol., 258, 100–114, doi:10.1016/j.margeo.2008.11.011, 2009.

Nygård, A., Sejrup, H. P., Haflidason, H. and Bryn, P.: The glacial North Sea Fan, southern Norwegian Margin: Architecture and evolution from the upper continental slope to the deep-sea basin, Mar. Pet. Geol., 22, 71–84, doi:10.1016/j.marpetgeo.2004.12.001, 2005.

Ó Cofaigh, C., Taylor, J., Dowdeswell, J. A. and Pudsey, C. J.: Palaeo-ice streams, trough mouth fans and high-latitude continental slope sedimentation, Boreas, 32, 37–55, doi:10.1080/03009480310001858, 2003.

Ó Cofaigh, C., Hogan, K. A., Jennings, A. E., Callard, S. L., Dowdeswell, J. A., Noormets, R. and Evans, J.: The role of meltwater in high-latitude trough-mouth fan development: The Disko Trough-Mouth Fan, West Greenland, Mar. Geol., 402, 17–32, doi:10.1016/j.margeo.2018.02.001, 2018.

Oakey, G. N. and Chalmers, J. A.: A new model for the Paleogene motion of Greenland relative to North America: Plate reconstructions of the Davis Strait and Nares Strait regions between Canada and Greenland, J. Geophys. Res. Solid Earth, 117, B10401, doi:10.1029/2011JB008942, 2012.

Oakey, G. N. and Stephenson, R.: Crustal structure of the Innuitian region of Arctic Canada and Greenland from gravity modelling: Implications for the Palaeogene Eurekan orogen, Geophys. J. Int., 173(1039–1063), doi:10.1111/j.1365-246X.2008.03784.x, 2008.

Ottesen, D., Dowdeswell, J. A. and Rise, L.: Submarine landforms and the reconstruction of fast-flowing ice streams within a large Quaternary ice sheet: The 2500-km-long Norwegian-Svalbard margin (57°-80°N), Bull. Geol. Soc. Am., 117, 1033–1050, doi:10.1130/B25577.1, 2005.

Ottesen, D., Dowdeswell, J. A., Rise, L. and Bugge, T.: Large-scale development of the mid-Norwegian shelf over the last three million years and potential for hydrocarbon reservoirs in glacial sediments, in Glaciogenic Reservoirs and Hydrocarbon Systems, edited by M. Huuse, J. Redfern, D. P. Le Heron, R. J. Dixon, A. Moscariello, and J. Craig, pp. 53–73, Geological Society of London., 2012.

Ottesen, D., Dowdeswell, J. A. and Bugge, T.: Morphology, sedimentary infill and depositional environments of the Early Quaternary North Sea Basin (56°-62°N), Mar. Pet. Geol., 56, 123–146, doi:10.1016/j.marpetgeo.2014.04.007, 2014.

Pérez, L. F., Nielsen, T., Knutz, P. C., Kuijpers, A. and Damm, V.: Large-scale evolution of the central-east Greenland margin: New insights to the North Atlantic glaciation history, Glob. Planet. Change, 163, 141–157, doi:10.1016/j.gloplacha.2017.12.010, 2018.

Poore, H. R., Samworth, R., White, N. J., Jones, S. M. and McCave, I. N.: Neogene overflow of Northern component water at the Greenland-Scotland ridge, Geochemistry, Geophys. Geosystems, 7, Q06010, doi:10.1029/2005GC001085, 2006.

Posamentier, H. W.: Seismic Geomorphology: Imaging Elements of Depositional Systems from Shelf to Deep Basin Using 3D Seismic Data: Implications for Exploration and Development, in 3D Seismic Technology: Application to the Exploration of Sedimentary Basins, edited by R. J. Davies, J. A. Cartwright, S. A. Stewart, M. Lappin, and J. R. Underhill, pp. 11–24, Geological Society of London., 2004.

Powell, R. and Domack, G. W.: Modern glaciomarine environments, in Modern and Past Glacial Environments, edited by J. Menzies, pp. 445–486, Butterworth-Heinemann., 2002.

Powell, R. D.: Grounding-line systems as second-order controls on fluctuations of tidewater termini of temperate glaciers, in Glacial marine sedimentation; Paleoclimatic significance, edited by J. B. Anderson and G. M. Ashley, pp. 75–93, Geological Soceity of America, Boulder, Colorado., 1991.

Powell, R. D. and Cooper, J. M.: A glacial sequence stratigraphic model for temperate, glaciated continental shelves, in Glacier-Influenced Sedimentation on High-Latitude Continental Margins, edited by J. A. Dowdeswell and C. Ó Cofaigh, pp. 215–244, Geological Society of London., 2002.

Rafaelsen, B., Andreassen, K., Kuilman, L. W., Lebesbye, E., Hogstad, K. and Midtbø, M.: Geomorphology of buried glacigenic horizons in the Barents Sea from three-dimensional seismic data, in Glacier-Influenced Sedimentation on High-Latitude Continental Margins, vol. 203, edited by J. A. Dowdeswell and C. Ó Cofaigh, pp. 259–276., 2002.

Rahmstorf, S., Box, J. E., Feulner, G., Mann, M. E., Robinson, A., Rutherford, S. and Schaffernicht, E. J.: Exceptional twentieth-century slowdown in Atlantic Ocean overturning circulation, Nat. Clim. Chang., 5, 475–480, doi:10.1038/nclimate2554, 2015.

Rea, B. R., Newton, A. M. W., Lamb, R. M., Harding, R., Bigg, G. R., Rose, P., Spagnolo, M., Huuse, M., Cater, J. M. L., Archer, S., Buckley, F., Halliyeva, M., Huuse, J., Cornwell, D. G., Brocklehurst, S. H. and Howell, J. A.: Extensive marine-terminating ice sheets in Europe from 2.5 million years ago, Sci. Adv., 4(6), doi:10.1126/sciadv.aar8327, 2018.

Rebesco, M., Hernández-Molina, F. J., Van Rooij, D. and Wåhlin, A.: Contourites and associated sediments controlled by deep-water circulation processes: State-of-the-art and future considerations, Mar. Geol., 352, 111–154, doi:10.1016/j.margeo.2014.03.011, 2014.

Richter-Menge, J. A., Overland, J. E. and Mathis, J. T.: Arctic Report Card 2016 Arctic Report Card 2016. http://www.arctic.noaa.gov/Report-Card., Arct. Rep. Card, 2016.

Rise, L., Ottesen, D., Berg, K. and Lundin, E.: Large-scale development of the mid-Norwegian margin during the last 3 million years, Mar. Pet. Geol., 22, 33–44, doi:10.1016/j.marpetgeo.2004.10.010, 2005.

Schaefer, J. M., Finkel, R. C., Balco, G., Alley, R. B., Caffee, M. W., Briner, J. P., Young, N. E., Gow, A. J. and Schwartz, R.: Greenland was nearly ice-free for extended periods during the Pleistocene, Nature, 540, 252–255, doi:10.1038/nature20146, 2016.

Sheldon, C., Jennings, A., Andrews, J. T., Ó Cofaigh, C., Hogan, K., Dowdeswell, J. A. and Seidenkrantz, M. S.: Ice stream retreat following the LGM and onset of the west Greenland current in Uummannaq Trough, west Greenland, Quat. Sci. Rev., 147, 27–46, doi:10.1016/j.quascirev.2016.01.019, 2016.

Shepherd, A., Ivins, E. R., Geruo, A., Barletta, V. R., Bentley, M. J., Bettadpur, S., Briggs, K. H., Bromwich, D. H., Forsberg, R., Galin, N., Horwath, M., Jacobs, S., Joughin, I., King, M. A., Lenaerts, J. T. M., Li, J., Ligtenberg, S. R. M., Luckman, A., Luthcke, S. B., McMillan, M., Meister, R., Milne, G., Mouginot, J., Muir, A., Nicolas, J. P., Paden, J., Payne, A. J., Pritchard, H., Rignot, E., Rott, H., Sørensen, L. S., Scambos, T. A., Scheuchl, B., Schrama, E. J. O., Smith, B., Sundal, A. V., Van Angelen, J. H., Van De Berg, W. J., Van Den Broeke, M. R., Vaughan, D. G., Velicogna, I., Wahr, J., Whitehouse, P. L., Wingham, D. J., Yi, D., Young, D. and Zwally, H. J.: A reconciled estimate of ice-sheet mass balance, Science (80-.)., 338, 1183–1189, doi:10.1126/science.1228102, 2012.

Slabon, P., Dorschel, B., Jokat, W., Myklebust, R., Hebbeln, D. and Gebhardt, C.: Greenland ice sheet retreat history in the northeast Baffin Bay based on high-resolution bathymetry, Quat. Sci. Rev., 154, 182–198, doi:10.1016/j.quascirev.2016.10.022, 2016.

Slabon, P., Dorschel, B., Jokat, W. and Freire, F.: Bedrock morphology reveals drainage network in northeast Baffin Bay, Geomorphology, 303, 133–145, doi:10.1016/j.geomorph.2017.11.024, 2018.

Spagnolo, M., Phillips, E., Piotrowski, J. A., Rea, B. R., Clark, C. D., Stokes, C. R., Carr, S. J., Ely, J. C., Ribolini, A., Wysota, W. and Szuman, I.: Ice stream motion facilitated by a shallow-deforming and accreting bed, Nat. Commun., 7, 10723, doi:10.1038/ncomms10723, 2016.

Taylor, J., Dowdeswell, J. A., Kenyon, N. H. and Ó Cofaigh, C.: Late Quaternary architecture of trough-mouth fans: debris flows and suspended sediments on the Norwegian margin, in Glacier-Influenced Sedimentation on High-Latitude Continental Margin, edited by J. . Dowdeswell and C. Ó Cofaigh, pp. 55–71, Geological Society of London., 2002.

Thiebault, F., Cremer, M., Debrabant, P., Foulon, J., Nielsen, O. B. and Zimmerman, H.: Analysis of sedimentary facies, clay mineralogy, and geochemistry of the Neogene-Quaternary sediments in Site 645, Baffin Bay, Proc., Sci. results, ODP, Leg 105, Baffin Bay Labrador Sea, 105, 83–100, doi:10.2973/odp.proc.sr.105.111.1989, 1989.

Thierens, M., Pirlet, H., Colin, C., Latruwe, K., Vanhaecke, F., Lee, J. R., Stuut, J. B., Titschack, J., Huvenne, V. A. I., Dorschel, B., Wheeler, A. J. and Henriet, J. P.: Ice-rafting from the British-Irish ice sheet since the earliest Pleistocene (2.6 million years ago): Implications for long-term mid-latitudinal ice-sheet growth in the North Atlantic region, Quat. Sci. Rev., 44, 229–240, doi:10.1016/j.quascirev.2010.12.020, 2012.

Todd, B. J., Lewis, C. F. M. and Ryall, P. J. C.: Comparison of trends of iceberg scour marks with iceberg trajectories and evidence of paleocurrent trends on Saglek Bank, northern Labrador Shelf, Can. J. Earth Sci., 25, 1374–1383, doi:10.1139/e88-132, 1988.

Vail, P. R., Mitchum, R. M., Todd, R. G., Widmier, J. M., Thompson III, S., Sangree, J. B., Bubb, J. N. and Hatlelid, W. G.: Seismic stratigraphy and global changes of sea-level, in Seismic Stratigraphy - Applications to Hydrocarbon Exploration, edited by C. E. Payton, pp. 49–212, American Association of Petroleum Geologists., 1977.

Vorren, T. O. and Laberg, J. S.: Trough mouth fans - Palaeoclimate and ice-sheet monitors, Quat. Sci. Rev., 16, 865–881, doi:10.1016/S0277-3791(97)00003-6, 1997.

Whittaker, R. C., Hamann, N. E. and Pulvertaft, T. C. R.: A new frontier province offshore northwest Greenland: Structure, basin development, and petroleum potential of the Melville Bay area, Am. Assoc. Pet. Geol. Bull., 81, 978–998, 1997.

Wolf, T. C. W. and Thiede, J.: History of terrigenous sedimentation during the past 10 m.y. in the North Atlantic (ODP Legs 104 and 105 and DSDP Leg 81), Mar. Geol., 101, 83–102, doi:10.1016/0025-3227(91)90064-B, 1991.

Woodworth-Lynas, C. M. T., Simms, A. and Rendell, C. M.: Iceberg grounding and scouring on the Labrador Continental Shelf, Cold Reg. Sci. Technol., 10, 163–186, doi:10.1016/0165-232X(85)90028-X, 1985.

C

Appendix C

Preamble

DRC and AMWN both wrote the manuscript and drafted the figures presented in this chapter. MH assisted with figure creation and reviewed the final manuscript.

This manuscript is published in an Elsevier textbook:

Cox, D. R., Newton, A. M. W., and Huuse, M., 2020, An introduction to seismic reflection data: acquisition, processing and interpretation, in Scarselli, N., Adam, J., and Chiarella, D., eds., Regional Geology and Tectonics – Volume 1: Principles of Geologic Analysis, Second Edition, Elsevier, Amsterdam, Netherlands, Chapter 22, pp. 571-603.

An Introduction to Seismic Reflection Data: Acquisition, Processing and Interpretation

David R. Cox[1], Andrew M. W. Newton[1, 2] and Mads Huuse[1, 2]

[1]Department of Earth and Environmental Sciences, The University of Manchester

[2]School of Natural and Built Environment, Elmwood Building, Queens University Belfast, University Road, UK, BT7 1NN

Abstract

Knowledge of the subsurface can be ascertained from outcrop extrapolation, drilling, mining and geophysical measurements. Geophysical techniques help us to fully understand the evolution of sedimentary basins by creating images of the subsurface. This is especially important in basins where either the trend of the stratigraphy or the lack of outcrop creates great uncertainty on what the geological record is beneath the surface. The most common and versatile method used to image the subsurface is the reflection seismic method applied in either two-dimensional lines or three-dimensional volumes. This involves the generation and transmission of sound waves into the subsurface where it is then refracted or reflected at the interface between rocks with different physical properties or rocks that contain different fluid types. The energy that returns to the surface is then recorded and processed to create an acoustic image of the subsurface. In this chapter, the physical background and general workflow, from the collection of seismic data to its interpretation, are presented.

1. Introduction

Subsurface imaging is a key component of basin analysis across a range of scales. Subsurface basin analysis is particularly important in areas with few outcrops or where relatively flat-lying stratigraphy provides only a limited temporal context from exposed rocks (Allen and Allen, 2013). The integration of subsurface and surface geological information has clear implications for palaeo-environmental reconstruction and resource exploitation. A range of methods have been developed for subsurface characterization,

including gravity and magnetics (Hinze et al., 2013), seismic reflection (Ashcroft, 2011), borehole data (Tiab and Donaldson, 2015) and the surface geology of dipping strata (Lisle et al., 2011). Whilst these methods are useful, especially when integrated and considered collectively, their value is often limited by vertical and horizontal resolution.

The reflection seismic method is the most commonly used technique for imaging the subsurface (Ashcroft, 2011, Sheriff and Geldart, 1995). The technique involves the transmission of a sound wave into the subsurface, which is then refracted and reflected at the interface between rocks of different physical properties according to the acoustic impedance (AI) contrast and incidence angle. Once the energy returns to the surface, it is recorded and processed to create an image of what the subsurface 'sounds like'. Geologists and geophysicists use these images to examine how basins developed and changed through time. The data can provide insights on stratigraphy, subsurface structure, rock physical properties and contrasts, the presence and migration of fluids, the presence of igneous and sedimentary intrusions and their emplacement/deformation history as well as past geomorphological agents.

In this chapter, the physical background behind the seismic reflection method is discussed. In subsequent sections, a general workflow is presented that spans the initial collection of the seismic data, through to how the results are processed to generate seismic images and eventually used for interpretation.

1.1 The Reflection Seismic Method

Creating an interpretable seismic image of the subsurface first involves generating sound waves that are transmitted into the Earth (as seismic waves) and returned to the surface as reflections originating from boundaries (reflectors) that represent changes in the physical properties of rock or sediment layers or anomalous fluid accumulations. In reflection seismology, the reflected waves are detected by receivers which measure energy and arrival time with a huge redundancy for each source and midpoint, allowing for the accurate imaging of subsurface geological interfaces.

Three types of seismic waves can be generated by a source: P (longitudinal) waves, S (transverse) waves and boundary waves (Fig. 1). Compressional waves (P-waves) have a backward and forward particle motion and propagate via compressional and dilational uniaxial strain, parallel to the wave propagation direction. Shear waves (S-waves) have a particle motion that is side to side with propagation perpendicular to the direction of wave travel. Boundary waves are low-velocity, low-frequency surface waves with a complex particle motion (Bolt, 1982).

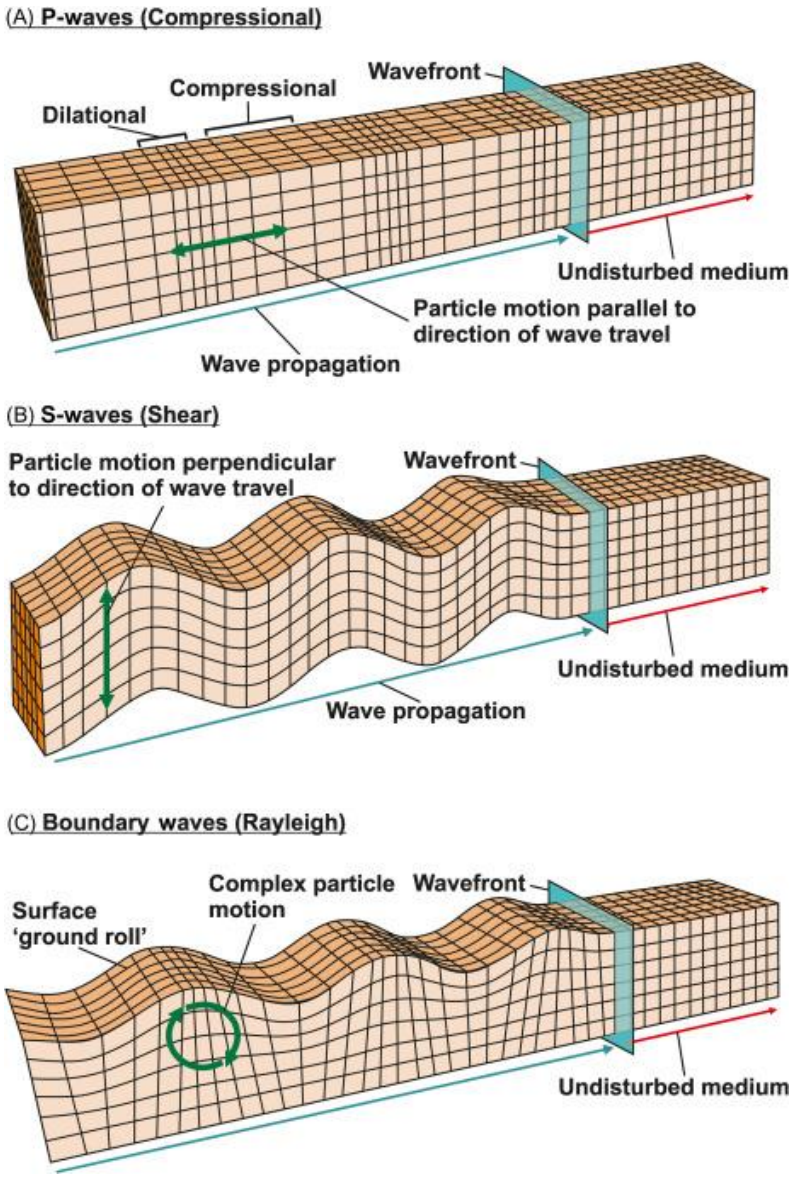

Figure 1. Types of seismic waves | Schematic diagram illustrating the mechanisms of seismic wave propagation through the Earth's medium. Three types of seismic waves are compared: (A) compressional waves (P-waves); (B) shear waves (S-waves) and (C) boundary (Rayleigh) waves. Modified from Bolt, (1982).

Historically, seismic surveying only measured vertical ground motion created by the higher-velocity P-waves. However, S-waves also give important information about the subsurface. Modern surveys therefore use multicomponent receivers that measure all three seismic waves, albeit at the expense of greater data acquisition and processing costs (Dondurur, 2018). An example of the benefit of multiwave recording is being able to use the ratio of VP/VS (P-wave velocity/S-wave velocity) (Fig. 1) to determine Poisson's ratio. This can provide a diagnostic indicator of potential lithologies through velocity variations (Domenico, 1984).

Surveys are typically designed to either record reflected or refracted waves (Fig. 2). Within the oil and gas industry, reflection surveys are commonly used with refraction

surveys typically reserved for the imaging of deep structures or for near-surface applications where detailed velocities are needed. More information on refraction seismology is provided in Musgrave (1967).

The propagation of seismic waves can be visualized as either wavefronts or raypaths. A wavefront represents the outward propagation of the seismic wave from the source. This propagation is determined by the velocity of the surrounding rock and is used to illustrate the 3D nature of wave propagation and reflection in the subsurface. Raypaths simply represent one direction of wave propagation from the source and are commonly used to illustrate imaging principles and for simplified seismic modelling schemes.

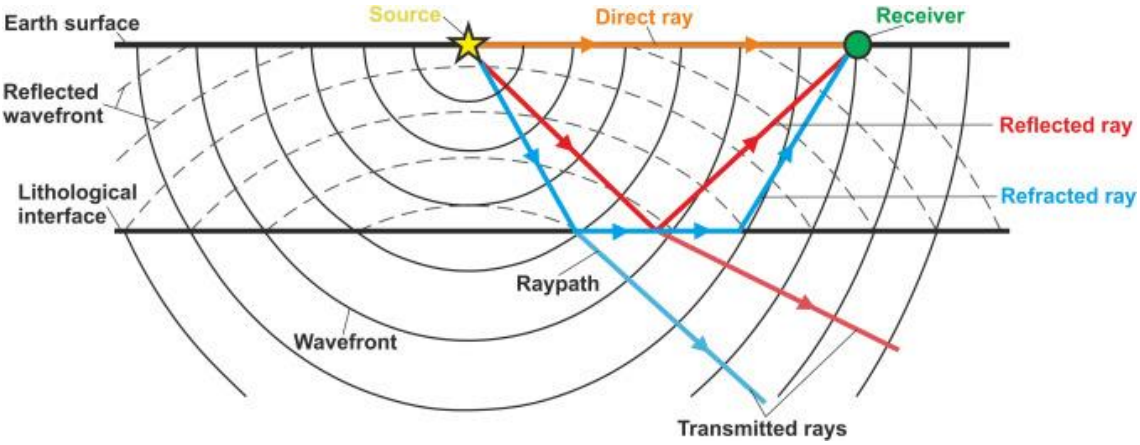

Figure 2. Wavefronts and raypaths | Diagram showing the basic pathway of a seismic wave that is produced by the source, reflected or refracted at the lithological interface and subsequently recorded by the receiver at the surface. The travel direction of the seismic wave is represented simply by raypaths but also by wavefronts which depict the three-dimensional (3D) nature of wave propagation. Based on Ashcroft, (2011).

Each point of the wavefront is represented by a seismic wavelet. A wavelet is a one-dimensional (1D) pulse created by the seismic source that has a measurable amplitude, frequency, period and phase, and it is these characteristics that determine the character of the seismic reflection that is recorded (Fig. 3).

- Amplitude: the maximum extent of the oscillation (vibration through the Earth),
- Frequency: the number of crests of a wave that move past a given point in a given unit of time,
- Period: the time taken for a complete oscillation to pass a given point, and
- Phase: the angular difference between peak amplitude of a seismic wavelet and reference time, usually 0.

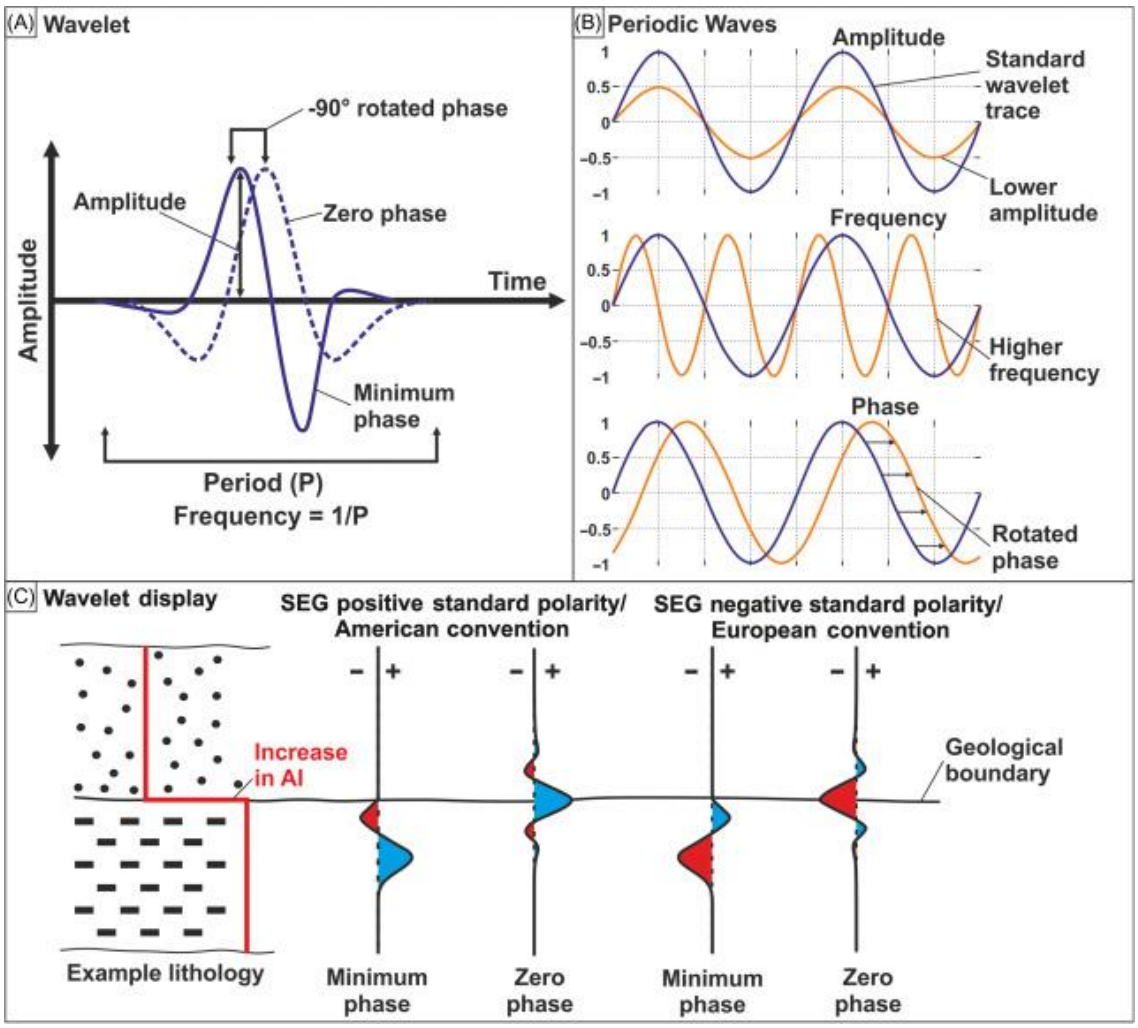

Figure 3. Wavelet theory and polarity | (A) Diagram showing the measurable characteristics of a wavelet; (B) three graphs that show the effect of varying the amplitude, frequency and phase of a seismic wave; (C) diagram that depicts the polarity conventions used for displaying seismic data. This includes SEG positive standard (American) and negative standard (European) polarity display for both minimum-phase and zero-phase wavelets. Modified from Sheriff and Geldart, (1995).

A wavelet recorded at the surface will indicate the difference in AI across a reflector via a compressional or dilational initial (P-wave) response. Assigning compression or dilation of the wavelet to either positive or negative values for display is determined by polarity. The Society of Exploration Geophysicists (SEG) (Thigpen et al., 1975) defines the two types of polarity convention used for displaying seismic data using minimum-phase or zero-phase wavelets as either 'positive standard polarity' (American polarity) or 'negative standard polarity' (European Polarity) (Fig. 3). For an American positive polarity display, an increase in AI with depth (such as water bottom) will be registered as negative reflection amplitudes and therefore display the onset of compression as a trough to the left of the central trace line (Fig. 3). For a zero-phase wavelet, an increase in AI with depth will be represented by a central positive peak. Alternatively, in Europe and the rest of the world,

SEG negative polarity display (or 'reverse polarity') defines the onset of compression from an increase in AI to display as a positive peak, with a zero-phase wavelet displaying as a central negative trough (Fig. 3C) (Thigpen et al., 1975).

Additionally, the two polarity conventions also define the colour recommended to be used for peaks and troughs in seismic data display (Fig. 3C), although the choice of colour may vary by interpreter preference or depending on what features are being interpreted. According to SEG standard, American positive polarity display, a peak will be coloured blue with a trough red. This colour scheme is opposite for European, SEG negative polarity display, with peaks displaying as red and troughs as blue. Understanding the phase and polarity of the data and the colour convention used allows the interpreter to determine whether the reflection coefficient (RC) across a reflector is positive or negative simply from the colour of the associated reflection in the seismic image.

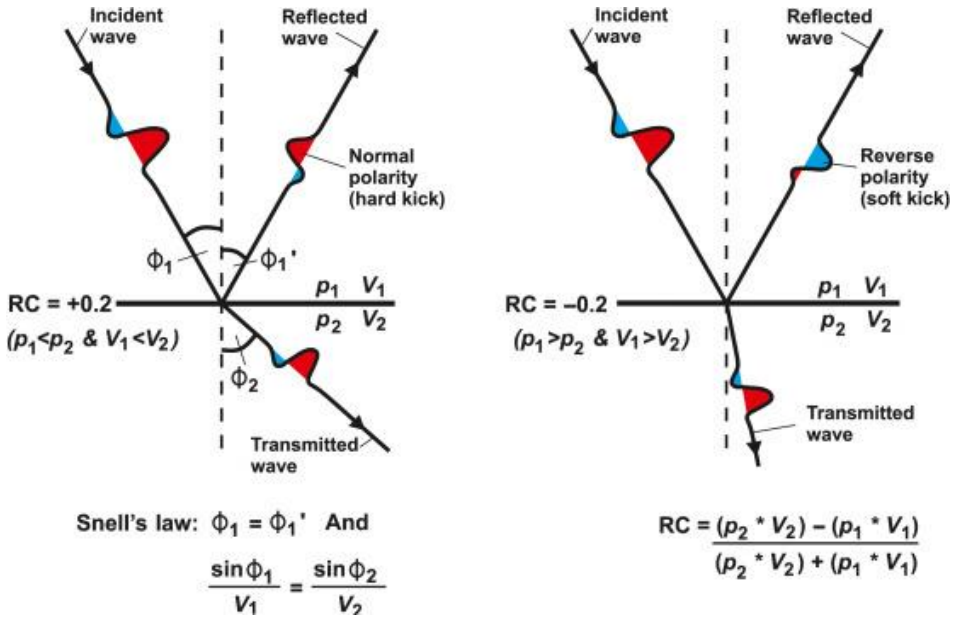

Figure 4. Reflection coefficient (RC) and polarity reversal | Diagram highlighting the effect of differing RCs (positive and negative) at lithological boundaries on the returned wavelet polarity. The diagram also highlights Snell's law that defines the relationship between the angle of incidence and reflectance as well as calculating the angle of refraction for a transmitted wave. Zoeppritz's equation shows how the reflectivity coefficient is calculated via the change in velocity (V) and density (ϱ) at each geological interface. Modified from Ashcroft, (2011).

The polarity of the reflection created by the geological interface (reflector) is determined by the downward change in the 'acoustic impedance' of the rocks (i.e. the opposition to the flow of acoustic energy). The AI of a rock is defined as a product of density (ϱ) and P-wave velocity (V) [AI=(ϱ×V)]. The difference of AI between two rock types can also be expressed as the reflection coefficient (RC), which gives the ratio of amplitude between the reflected wave and the incident wave. The RC at an interface is

calculated using Zoeppritz's equation, which uses the differing AI values of the two layers (Fig. 4).

When a layer of low AI overlies a layer of high AI, the boundary has a 'positive reflection coefficient' (Fig. 3 and 4). A compressional wavelet reflecting back from this interface would experience no change in polarity and this can be described as a 'hard kick'. However, when the boundary is said to have a 'negative reflection coefficient' with a layer of high AI overlying a layer of low AI, the polarity of the reflection is reversed and can be described as a 'soft kick' (Fig. 4).

The RC (difference in AI between layers) also controls the proportion of the seismic wave energy that is reflected back towards the surface from an interface. If the RC is positive, that percentage of the energy will be reflected back as the same polarity wavelet (e.g. RC of +0.1 will cause 10% of the energy to be reflected upwards and no polarity change). The same applies to a negative RC, although this time the polarity of the wavelet will be reversed. In addition to this, the initial wave and the reflected wave will be symmetric to a line perpendicular to the boundary [i.e. the angle of incidence (Φ1) will equal the angle of reflection (Φ1')]. This is the first rule of Snell's law (Fig. 4). Most of the seismic energy is still transmitted downwards at an interval and will be refracted at that boundary. The angle of refraction for the transmitted wave can be calculated using Snell's law (Fig. 4). Overall, the reflected energy is small, especially at increasing depth, meaning the receivers have to be extremely sensitive to minor changes in acoustic energy.

1.2 Seismic Resolution

The wavelet is also one of the principal components in determining the vertical resolution of seismic data, which is a measure of how far apart two geological boundaries have to be before they can be detected as separate events. This resolution limit is often one-fourth of the dominant wavelength, which is determined by the frequency of the wavelet and the velocity of the rock unit.

- Wavelength: $\lambda = V / F$ (wavelength = velocity / frequency)
- Vertical seismic resolution: $\lambda / 4$ (wavelength / 4)

The vertical seismic resolution generally decreases with depth due to a reduction of the wavelet frequency (as high frequencies are reflected by relatively shallow reflectors) and an increase in velocity (often due to compaction). This increases both the wavelength and the minimum thickness between two rock units that is required for a unit to be detected on seismic data.

The thickness at which two geological boundaries are no longer recorded as separate events is termed the 'tuning thickness'. When the bed thickness is within this tuning range for a certain dominant frequency and velocity, amplitude interference will occur, causing brightening or dampening of the amplitudes due to constructive or destructive interference between the responses from the two events. The frequency dependence of tuning is exploited by the spectral decomposition technique which aims to enhance the reflection response in the thin reservoir case (see 'Seismic interpretation' section). Tuning also occurs for zero-phase data where the sidelobes of a negative reflection can interfere with the peak of a positive one. Attempts to minimize this effect led to the development of the broadband seismic method (see 'Acquisition of reflection seismic data' section).

The horizontal resolution is coarser than the vertical resolution due to acquisition effects and imperfect processing algorithms and velocity models. The un-migrated Fresnel zone (the area on a boundary which energy is reflected from) width is an indicator for horizontal resolution and depends (similarly to vertical resolution) on the wavelength (λ). In the case of perfect 3D migration, the migrated Fresnel zone width is $\lambda/2$. The horizontal resolution of high quality 3D migrated data is thus limited to $\lambda/2$ or the acquisition line spacing, which ever is greater. Examples of attempts to reduce the Fresnel zone width and increase horizontal resolution include reducing line spacing during acquisition (see 'Acquisition of reflection seismic data' section) and through migration during processing (see 'Seismic processing' section). More information on seismic resolution and tuning can be found in Ashcroft (2011), Brown (2011), Roden et al. (2017) and Sheriff and Geldart (1995).

2. Acquisition of reflection seismic data

The collection of reflection seismic data is a time-consuming and expensive process requiring meticulous planning and consideration of issues, such as geography (topography and weather), politics, economics, technology, workforces and timescales, all of which must be conducive for data collection. In this section, the background on the acquisition of terrestrial and marine two-dimensional (2D) and 3D seismic reflection surveys is presented. The discussion below is designed to provide an understanding of the parameters and equipment used in reflection seismology. A more detailed insight can be found from dedicated textbooks such as Sheriff and Geldart (1995), Yilmaz (2001), Ashcroft (2011) and Wencai (2013).

1.1 Terrestrial Surveys

When planning a land-based survey, the first considerations are to establish the geological objectives (i.e. what results are desired), what data are already available (e.g. existing boreholes) and what difficulties may arise from attempting to collect and integrate new data. In an ideal 2D seismic survey, acquisition lines would be parallel and perpendicular to the actual (or perceived) dip of the strata or trend of important geological structures. These lines should be equally spaced, straight and extend beyond the immediate area of interest to allow for migration of the reflections during processing (see 'Seismic processing' section). The exact spacing should consider the wavelengths and dips associated with subsurface folds and faults (that may only be partially known from gravity, magnetic or existing seismic data) to ensure they can be effectively imaged. However, depending upon the exact geographical setting (topography, infrastructure, rivers and environmental sensitivity), the desired grid may not be possible. To reduce costs (land-based surveys are typically the most expensive) and ensure the collection of useful data, potential operational problems will be resolved before data collection begins, although amendments may be required on an ad hoc basis (Kumar et al., 2006).

Once the survey has been designed, data collection can begin. Collection typically starts with a source that is capable of producing a band of repeatable frequencies. Since the 1950s, the most common terrestrial source of energy is Vibroseis – a truck with a metal plate that can be lowered onto the ground (Fig. 5A). These plates vibrate for ~20 seconds, generating a known seismic signal that starts at a low frequency and increases through the 'sweep' (each interval of signal generation). Several Vibroseis trucks are often used together in order to create sufficient seismic energy from each sweep (Yilmaz, 2001). The consistent signals generated, combined with the minimal disturbance compared to explosive sources (see below), mean that Vibroseis can be used in sensitive areas and even on existing infrastructure such as roads (Fig. 5A). In processing of Vibroseis data, the long sweep of the pulse is recorded at the source to enable deconvolution of the reflected signal by the source signal in order to achieve a similarly sharp final reflection image as would have been achieved with an explosive source.

Another source of energy for reflection seismic surveys is the use of large detonations, using explosives such as dynamite, which can create large outputs of elastic energy. Dynamite is typically placed into a borehole tens of metres below the surface before a controlled explosion occurs. Unless the survey is in an area with steep terrain or poor accessibility where it is either impossible or prohibitively expensive to use Vibroseis, explosive sources are rarely used due to the destructive nature, security ramifications,

uncontrollable bandwidths and time consumption for preparing different shots. Thus, for most locations, Vibroseis is the energy source of choice.

Figure 5. Reflection seismic sources | (A) Image of a Vibroseis truck. Note that the more gentle nature of Vibroseis source generation means that the vibrating plate has been planted on the existing infrastructure – that is the road. (B) Images of marine source equipment: (i) example of airguns used in a marine seismic survey to generate the energy source via highly pressurized air and (ii) spool containing a marine seismic streamer cable. These streamers contain the hydrophones (grey areas on the cable). (iii) A selection of birds that are used to help control the depth of the streamer cable by adjustments of the angle of the fins. Image (A) from Nuclear Waste Management Organization, (2018).

Additional equipment is required to receive and measure the seismic response that is generated. For land-based surveys, a geophone converts ground motion into an electrical voltage. Geophones record both compressional and transverse body waves (i.e. the P- and S-waves) and surface waves. Each geophone is part of a wider set of evenly spread geophones (often 100+) that are planted into the ground (using a spike) and connected via a cable or using mobile phone technology. The necessity to plant geophones means that special consideration needs to be given if the substrate is not conducive (e.g. exposed

bedrock). Such issues should be considered during the initial planning of the survey. A survey typically consists of hundreds (or thousands) of geophones with an optimized distribution to reduce potential noise in the data (e.g. ground roll – where the signal travels along the surface layer) (Stone, 1994).

Once a source pulse has been generated and the signal received, it is then recorded digitally. Traditionally, data have been recorded digitally onto magnetic field tapes where each receiver channel (i.e. each geophone) is sampled in sequential order. The seismic signal is recorded onto high-quality recording instruments at a set interval, often every 2–4 milliseconds. The data are typically recorded in an industry standard format that has been defined by the SEG (see 'The reflection seismic method' section).

A crucial component for any survey is providing topographic and geographic context for the recordings. Field geometry is recorded using a global positioning system (GPS), which maps the precise locations of sources (when generated) and receivers. This means that during processing, corrections can be applied (e.g. statics – see 'Seismic processing' section), so issues such as landscape topography can be accurately accounted for, allowing for the true shape of the subsurface to be presented. A geographical context also allows other data sets (e.g. boreholes or legacy seismic data) to be presented in the correct positions relative to new data (Yilmaz, 2001).

2.2. Marine Surveys

Planning a marine survey requires similar geological considerations as for terrestrial surveys (e.g. depth and orientation of targets, stratal dips), although the logistics are often less complex and surveying more efficient. Unique considerations include the bathymetry and potential unseen obstacles below the sea surface such as pipelines, reefs, shipwrecks or icebergs, as well as the impact of a seismic survey on marine fauna and oceanographic factors such as currents that may deflect the equipment array when travelling through the water. Logistical planning also needs to provide sufficient notice to shipping authorities so that other vessels can avoid trailing equipment (see below). Reducing traffic also allows for potential noise in the data to be minimized.

The exact survey set-up plays an important role in what type of vessel is used. For example, if extra-long cables and a large crew are required, then it will require a vessel capable of facilitating this. The vessel will likely be responsible for generating, receiving and recording the seismic signals. Though academic vessels may be modified for seismic work, industry vessels are often custom-built. This means that industry vessels can both generate

the data and be designed with characteristics that allow for noise reduction from issues such as inclement weather (Dondurur, 2018).

In a marine survey, the vessel movement complicates the generation of a repeatable and consistent signal. The most common marine seismic source is produced from airguns (Fig. 5B-i), which release a shot of compressed air into the water every 4–8 seconds (or longer if the interval of interest is deeper). Typically, this involves an array of different sized guns (cylinder size affects the frequency range of the signal) that are fired at the same time to reduce potential noise in the data. Previously, water guns were used following a similar principle (i.e. compressed water), but they are less common because they produce a limited frequency, which impacts seismic resolution.

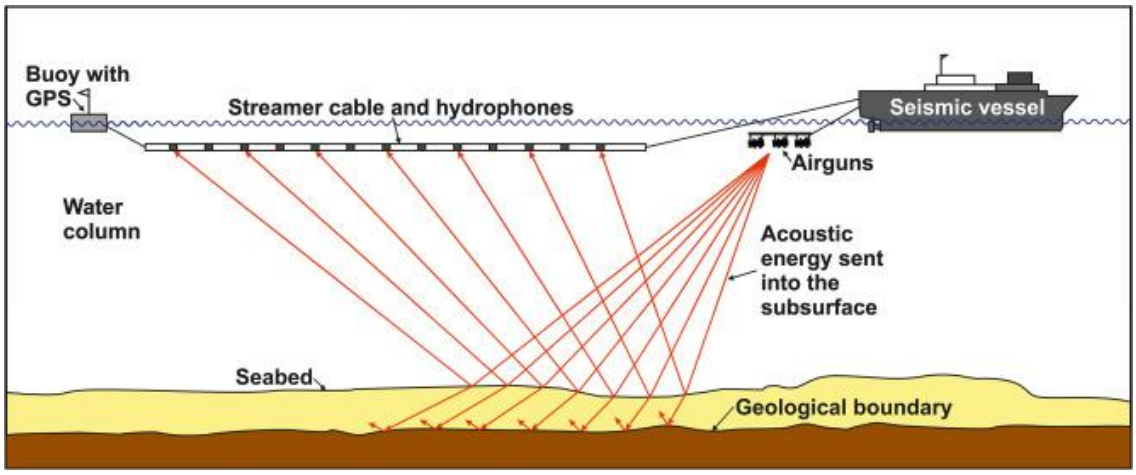

Figure 6. 2D marine survey | Simple schematic showing the general set-up for a 2D marine seismic reflection survey. The acoustic pulse created by airguns, travels into the subsurface and reflects off the main geological boundaries. This reflected energy is then recorded by hydrophones within the streamer cable and relayed back to the vessel. Note that the image is not drawn to scale.

A hydrophone receiver converts changes in water pressure, after signal generation, into an electrical voltage. Similar to terrestrial surveys, extensive lengths of cables are required to collect the data that will be recorded at intervals of 2–4 milliseconds. In marine surveys, these are called streamers and can be several kilometres long (Fig. 5B-ii). Each streamer contains many individual hydrophones that are grouped into receiver groups, typically 6.25–12.5 m apart. To ensure the streamer floats near to the water surface, it is partly filled with buoyant fluids. To keep the streamer at a set depth, a combination of weights, clamped along the streamer, and wing attachments ('birds') are used. Birds allow the depth to be controlled by varying the fin angle (much like an aircraft) or by adjusting the speed of the vessel (Fig. 5B-iii). At the end of the streamer, a buoy with a GPS unit marks the end of the equipment array. The streamer and airguns trail behind the boat as it moves through the water and collects data for set time intervals, typically 8-12 seconds for oil industry

seismic data and 1-2 seconds for site investigation seismic data, after the firing of the source (Fig. 6) (Dondurur, 2018).

The time series of noise and signal received by the hydrophones travels down the streamer cable or via telemetry back to the vessel where it is recorded. The data are recorded on similar equipment and in similar formats to that described for terrestrial surveys, but also include navigation information and geographical data about the position of the streamer relative to the location of the vessel. Similar to terrestrial seismic data, the geographic data are important for post-cruise processing of the raw data so that optimal imaging can be achieved.

2.3. Three-dimensional Surveys

Whilst 2D seismic surveys provide the key data set for regional studies and significantly improve our understanding of the subsurface, it is important to consider that the 2D seismic profile is a cross section of a 3D Earth, generated using omnidirectionally propagating waves. This can result in seismic signals being recorded from adjacent areas and may lead to unreliable interpretations (i.e. out-of-plane energy can be incorporated into the seismic line). Also, large grid spacing between 2D lines (often ~1 km) can cause spatial aliasing of features leading to the misinterpretation of 3D geometries (Cartwright and Huuse, 2005). With technological improvement and the desire to reduce risks associated with hydrocarbon exploration, 3D seismic data have revolutionized subsurface geological knowledge (Cartwright and Huuse, 2005, Dorn, 1998). Though 3D seismic data are more expensive to collect, the data allow for better mapping of faults, geomorphological features, reservoir blocks, imaging of the true structural dip (2D may only provide the apparent dip) and 2–3 orders of magnitude better lateral resolution.

Planning a 3D seismic survey, whether onshore or offshore, must consider the same issues discussed previously. However, due to the increased field efforts that will be required and the greater expense, the survey design will be more complex. In a terrestrial 3D seismic survey, the geophones are laid out in a series of parallel lines (topography and infrastructure dependent) and the source (i.e. Vibroseis) is carried out at an orthogonal angle to these parallel lines (Fig. 7A). This single recording is known as a 'patch' and once complete, the subsurface response will be recorded again at the next, partially overlapping, patch. In marine 3D seismic surveys, the data are collected in swaths a few hundred metres wide and orientated in the direction of travel of the seismic vessel (Fig. 7 and 8). Ordinarily, this is achieved by deploying several streamers behind the boat, which are then spread out by vanes. Alternatively, multiple vessels carrying different sets of streamers may be used. That

said, using multiple vessels to collect marine 3D seismic data is uncommon because modern purpose-built seismic vessels are capable of deploying up to 20 streamers at a time with more than 1 km between the outermost streamers (Dondurur, 2018).

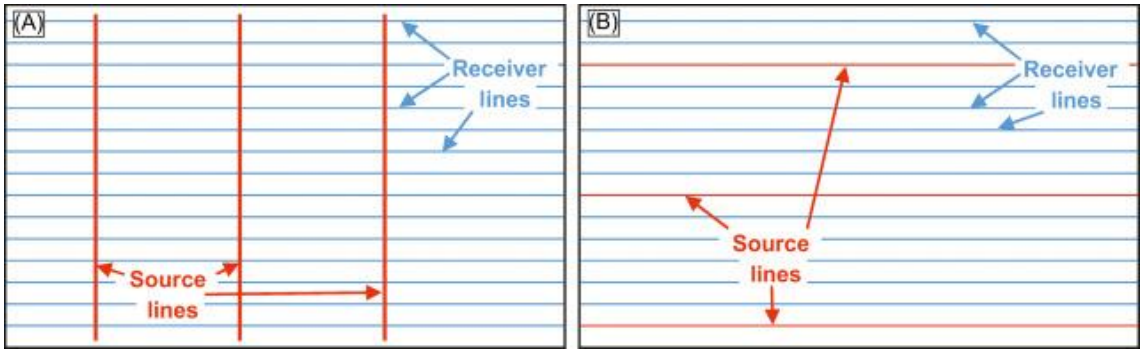

Figure 7. 3D terrestrial survey design | (A) Example of patches of data collection that are typically used in terrestrial 3D seismic reflection data collection; (B) examples of swaths of data collected in marine 3D seismic reflection data.

In order to image the 'true' 3D geometry of the subsurface, the seismic survey is subdivided into smaller cells (known as bins) that may be square (e.g. 25 by 25 m or 12.5 by 12.5 m) or rectangular (e.g. 18.75 by 37.5 m). The traces generated during acquisition are gathered in a specific bin depending on the common midpoint (CMP) between the source and the different receivers. This means that the bin contains traces that have different azimuths, 'offsets' and angles to the direction of the line. As more traces are assigned to the bin (the number of traces is known as the 'fold'), the resolution increases when the traces are stacked and migrated to generate the final trace for each bin. As the acquisition of the 3D survey continues, the signal/noise ratio increases proportionally to the square root of the number of traces per bin (Fig. 8). In parts of the survey with a low fold, further shooting may be required to complete the grid, most likely at the end of the survey rather than returning at a later date (Vermeer, 2012).

As improved methods have allowed for cheaper 3D seismic reflection data collection, there has been a growing use of 'four-dimensional (4D) surveys', where a number of 3D seismic surveys across the same area are collected at different times. Repeated surveying allows for fluid movement to be monitored during extraction of hydrocarbons or injection of, for example, CO2 into the subsurface. The results from a 4D study allow for infill wells to be better sited so that unproductive parts of a reservoir can be targeted (Landrø, 2015, Lumley, 2010).

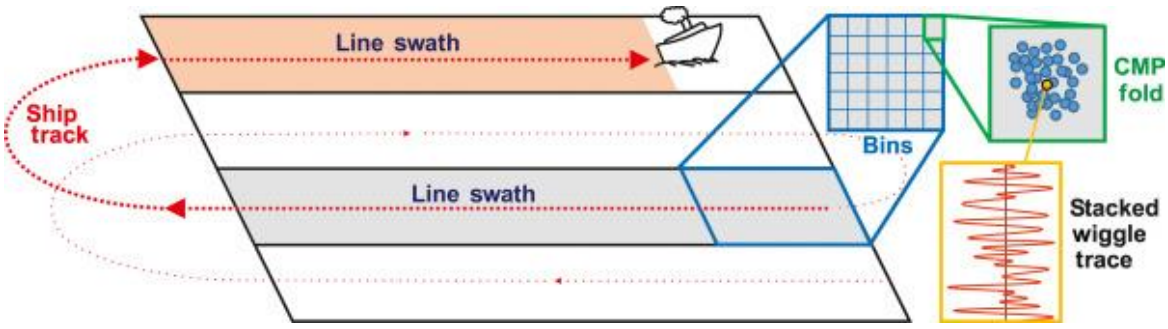

Figure 8. 3D marine survey | Simplified schematic showing how marine 3D seismic reflection data are collected for marine surveys. The example binning shows the amount of data contained within each bin and how, once processed, these traces can be combined to provide a stacked wiggle trace for each individual bin. Note that the binning is similar for terrestrial 3D seismic reflection data collection, but the azimuthal range is much greater for land geometries as depicted in Fig. 7.

2.4 Broadband Seismic

In seismic reflection surveying, the resolution depends on the dominant frequency, whereas the bandwidth of the seismic data determines the wavelets peak to sidelobe ratio. The use of broad bandwidth seismic aims to provide better resolution data that allows the imaging of thinner and more subtle geological features. Broadband seismic data can be acquired in various ways to minimize the interference between primary and multiple reflections, for example using variable depth–towed streamers or using hydrophones with directional recording of the wavefield. Increasing higher frequencies creates a sharper central peak of the wavelet by increasing the dominant frequency, whilst increasing lower frequencies suppresses the amplitude of the wavelet sidelobes, causing the wavelet to look more like a spike (Fig. 9). This wavelet, created through broadening the amplitude spectrum, is closer to the ideal seismic response from a formation boundary and is used to create clearer and more accurate images of the subsurface (Fig. 9B). Broadband seismic methods have led to successful exploration of subtle stratigraphic traps, the delineation of structural closures and importantly provided better resolution data that are less susceptible to tuning effects and provide more detailed images of thin reservoirs and a better basis for seismic inversion (see 'Impedance inversion' section) workflows (Fig. 9B) (Duval, 2012).

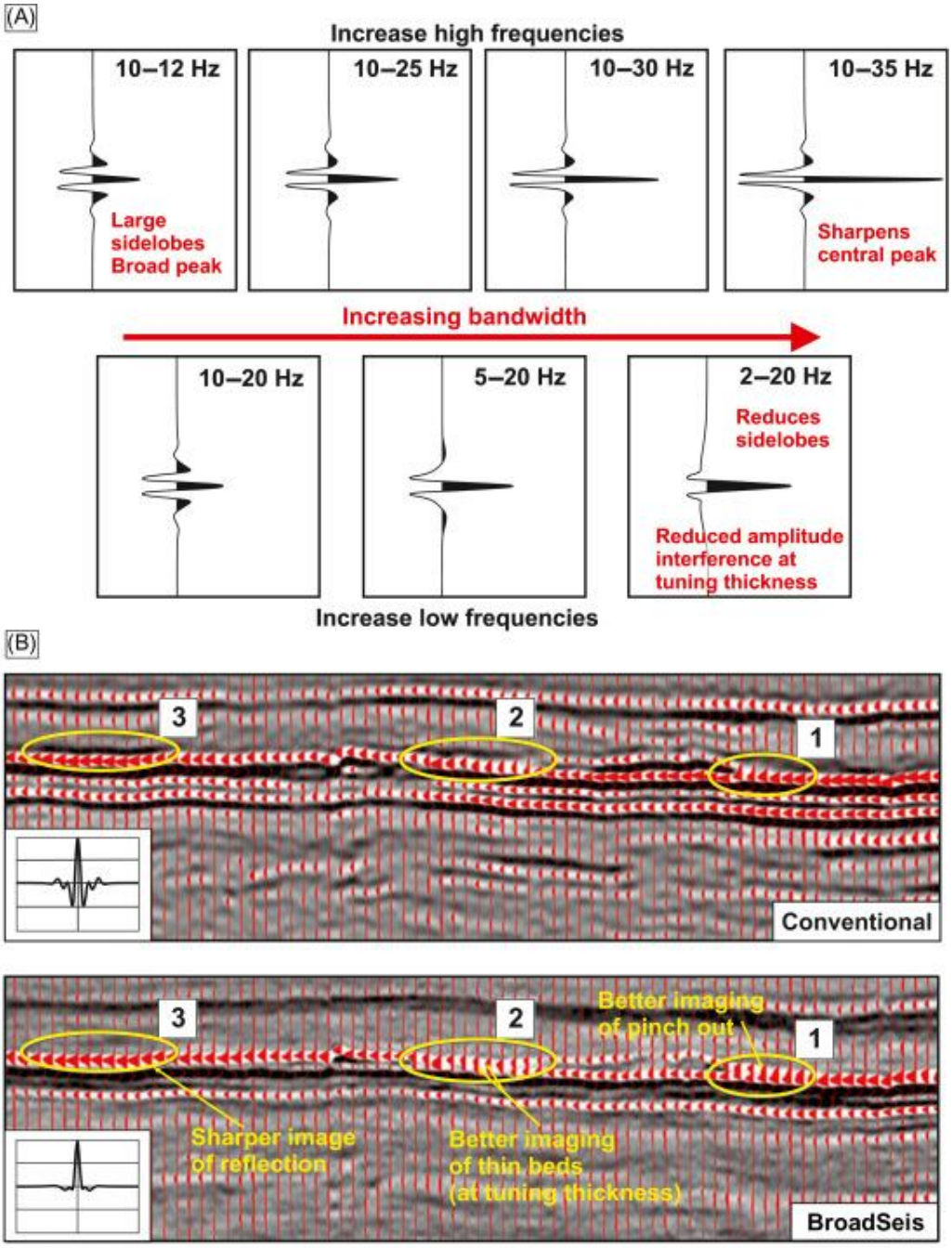

Figure 9. Broadband seismic | The effect of broad bandwidth seismic acquisition on the seismic wavelet and the subsequent quality and resolution of the seismic image. (A) Effect of frequency content on the relative peak/sidelobe amplitudes of a zero-phase wavelet. Increasing the high-frequency content increases the dominant frequency, sharpens the central wavelet peak and reduces sidelobe energy whilst increase in low frequencies dramatically reduces sidelobe energy. (B) Conventional versus broadband (BroadSeis) seismic data from the North Sea showing the more accurate imaging of pinch outs (1), thin beds (2) and subsurface reflections (3) in broadband data. Modiefied from Duval, (2012).

3. Seismic Processing

The raw recorded data provided by reflection seismic acquisition are not immediately suitable for interpretation. The data must be processed to create an accurate and interpretable image. This involves a number of assumptions and processing steps that are

designed to remove noise, minimize artefacts, improve resolution and simplify the data to aid efficient and accurate interpretation. The most basic steps in the reflection seismic method assume an isotropic and horizontally bedded Earth structure, which is virtually never fully realistic (and would not be particularly interesting), although more advanced and iterative processing workflows place more emphasis on the measurements and any irregularities to provide more accurate subsurface images and models (e.g. Robein, 2010). The processing steps applied and the sequence of these steps may differ from data set to data set due to different processing conventions or different company workflows. Seismic processing steps can be categorized into four functions: data preparation, data correction, data reduction and data enhancement. The steps within these functions and a typical workflow sequence are shown in Fig. 10, although it is important to remember that additional steps may be included, omitted or re-sequenced (as noted above). Modern processing workflows are often highly iterative, requiring multiple repeated and refined stages of model building and correction to ensure the best possible final image, especially in structurally complex areas. The processing workflow illustrated herein represents the basic steps and the reader should be aware that far more advanced and computationally intensive processing workflows are nowadays commonplace and increasingly being a matter for integrated teams of geologists/geophysicists, mathematicians and physicists.

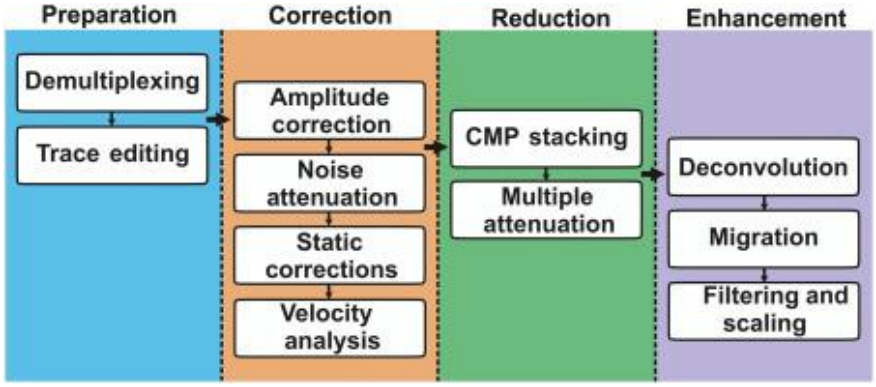

Figure 10. Highly simplified processing workflow | Workflow showing the common steps taken to process field seismic data to create an interpretable image. The steps are grouped into preparation, correction, reduction and enhancement. Note that steps can be omitted, re-sequenced or new steps added depending on the data, schedule and desired quality of result. Additionally, modern processing increasingly involves data being migrated into depth in the prestack domain. Adapted from Dondurur, (2018).

The section below aims to provide a basic understanding of each of the key steps used within seismic data processing that are shown in Fig. 10. A more detailed insight can be found through dedicated textbooks such as Mari et al. (1999), Yilmaz (2001), Dondurur (2018) and Mousa (2019).

3.1 Data Preparation

3.1.1 Demultiplexing

Seismic data are often transferred from the field in a multiplexed format (either SEG-A or SEG-D formats) with the seismic traces remaining in time order from all the receivers at a given time. This data need to be demultiplexed, which will reformat the traces to be in 'trace sequential format' (SEG-Y or SEG-X formats) that provides the traces for all the times for each given receiver (Dondurur, 2018).

3.1.2 Trace Editing

Some traces may need to be flagged for editing or removal due to errors that have occurred during recording, storage or transfer. These errors may include highly noisy traces (due to bad connections or electrical interference), duplicated traces, large data spikes, dead traces (no signal) or polarity reversals (Dondurur, 2018).

3.2 Data Correction

3.2.1 Amplitude Corrections

The seismic waveform, and therefore the wavelet, suffers degradation through time in the subsurface that causes the received reflection amplitude to be weak and difficult to observe. This degradation is caused by effects such as the spherical divergence of sound waves as energy is spread across the wavefront. Additionally, energy absorption, internal reflecting between rock layers (multiples) and unreturned reflections (scattering) also cause degradation. Finally, transmission losses occur at each interface (discussed in 'The reflection seismic method' section) further weakening the reflection signal.

To combat this degradation and to allow efficient imaging of reflections, gain correction is applied. This increases the amplitude of the traces by the mathematical slope of the decay through time. The correction is often calculated using specimen source traces that allow a standard correction curve to be applied for a particular survey (Yilmaz, 2001).

3.2.2 Noise Attenuation

Noise in the seismic record can occur from a number of natural and anthropogenic sources, as discussed in 'Acquisition of reflection seismic data' section. It can cause dilution of the seismic section, reduced resolution and errors in future processing steps such as migration and stacking. Certain coherent, linear noise sources can be anticipated and removed in initial field processing or via automatic noise removal software packages. However, due to the complex diversity of noise sources during acquisition, additional noise attenuation steps are often required.

The most common method of random noise attenuation is a bandpass filter which will remove unwanted low and high frequencies prone to noise whereas an F-K filter can be used to remove coherent noise created by marine acquisition equipment and ground roll. Due to noise interfering with the signal in the normal time-distance domain (t-x), the shot record must be converted into F-K domain to separate the two, allowing attenuation without affecting the desired signal. This domain considers the frequency of the sampled time (F) versus the wavenumber of the sampled distance (K). The shot record in F-K can be analysed by using a 2D digital Fourier transform. Typically, seismic reflection signal will have high F values and low K values, whereas coherent noise will oppositely have low F values and high K values. This allows for noise to be separated and removed from the seismic signal via a filter in the F-K domain (Yilmaz, 2001). More information on noise attenuation and the use of Fourier transforms can be found in Mousa (2019), Elboth et al. (2010) and Rabiner and Gold (1975).

3.2.3 Static Corrections

Static corrections involve a bulk time shift of certain seismic traces to allow accurate comparison of traces throughout a survey. A common application of static correction is to adjust all traces to a common surface reference datum, often mean sea level. This is usually required due to changes in topography in land surveys or due to alterations in gun and streamer depths or tidal changes during marine acquisition. Another common static correction removes the effect on velocity caused by shallow unconsolidated layers found above true bedrock, known as the 'weathering layer' (Yilmaz, 2001).

3.2.4 Velocity Analysis (normal move-out and dip move-out)

The application of appropriate static corrections allows the accurate calculation of velocity corrections of deeper reflections in a process termed normal move-out (NMO) correction (Fig. 11). CMP gathers record nonzero-offset data and NMO corrections allow the data to be corrected to the plane of zero offset. This removes the effect caused by increased travel time due to increased offset between source and receiver (Fig. 11). This increased travel time causes CMP-recorded reflections to be displayed as hyperbolic reflections away from the zero-offset trace (Fig. 11). The CMP is the point on the surface equidistant between the source and receiver. The point directly below this at the reflector depth is known as the common depth point (CDP) and its surface projection only matches the CMP exactly for a perfectly isotropic and horizontally layered Earth (Fig. 11A). For each source location, a number of CMPs are sampled equivalent to the number of receivers and spaced at half the receiver spacing. This gives rise to the 'shot-gather' in which each

trace belongs to a different CMP. The process of CMP sorting sorts out which traces belong to which CMPs and allows the display of the component gather traces for individual CMPs before velocity analysis, correction and stacking (Fig. 11).

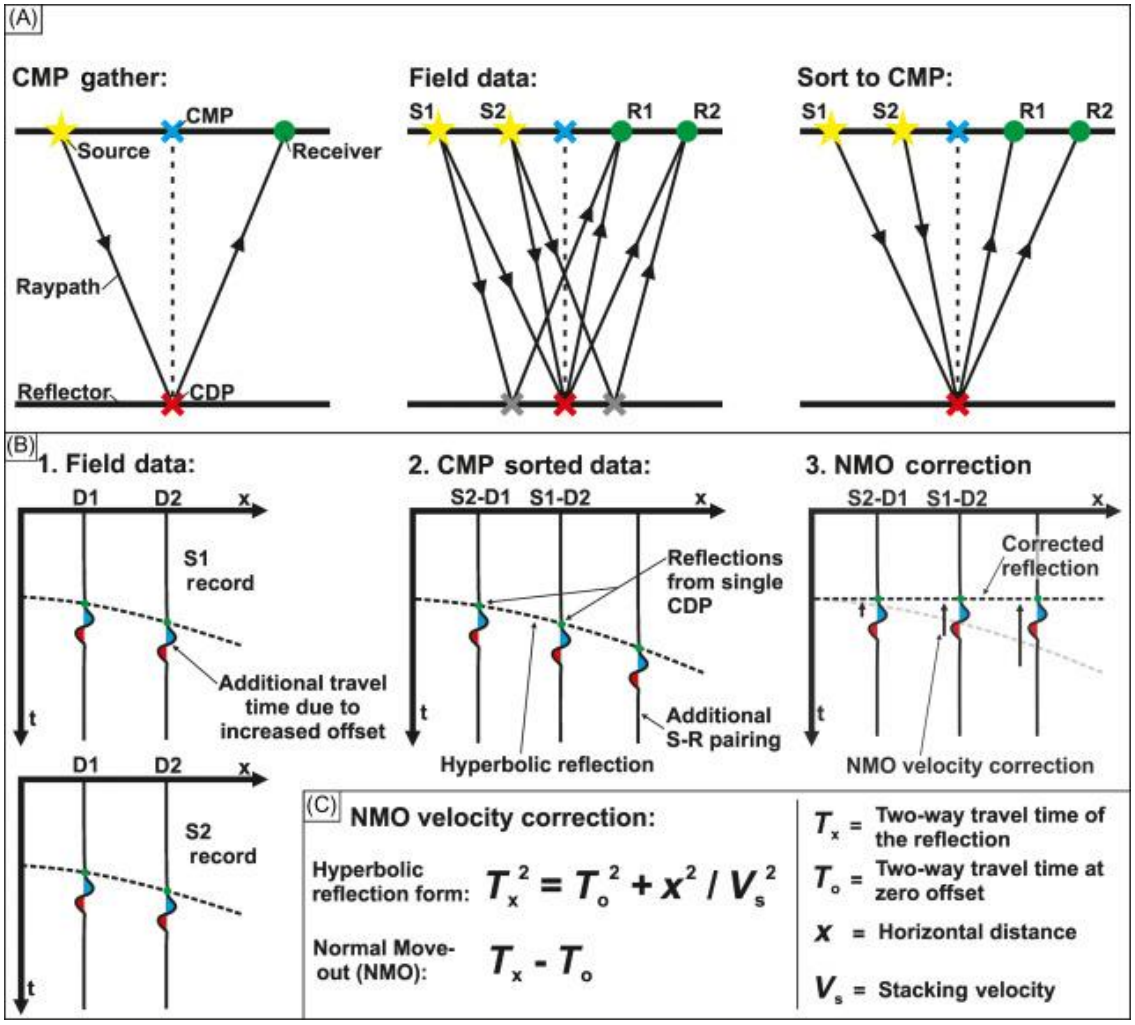

Figure 11. Velocity analysis and normal move-out (NMO) | (A) Diagrams that depict the use of common midpoint (CMP) gathers and source and receiver pairings during acquisition. Field data are sorted into single CMP gathers for each common depth point (CDP) for simplicity; (B) a series of graphs displaying the distance from the source and the time recorded for both field data and CMP-sorted wavelets. The increased travel time between source and receiver pairing with increased offset (shown in A) causes a time delay on the wavelet that causes the reflection to plot as a hyperbolic curve. NMO is used to correct this by applying a stacking velocity that returns the reflection hyperbola into its correct position for any given time and offset; (C) equations that calculate the form of the hyperbolic reflection and NMO. Importantly, Vst is the stacking velocity required to correct the hyperbolic reflection into its correct position. Based on Ashcroft, (2011).

A sampled reflection forms a hyperbolic curve due to the increase in time taken for the sound to reach the more distant receivers. The mathematical form of the reflection hyperbola allows the calculation of the stacking velocity (Vst) (Fig. 11C). The stacking velocity is calculated from the geometric information known from the acquisition geometry and two-way travel time (TWT) recording for each trace and the time shift necessary to

correct the reflection hyperbola to its horizontally aligned position for any given time and offset. This correction is known as NMO. Once applied, it will cause appropriately corrected reflections to appear horizontal on a 'corrected gather' (Fig. 11B and C).

It is often not quite this simple, however, as a reflection boundary is rarely completely horizontal and the velocity structure in each layer is rarely completely isotropic. A dipping reflector will cause there to be no common reflecting point on the sampled boundary. To overcome this, a process called dip move-out (DMO) is applied to create an apparent common reflection point and add a dip-dependent variable to the stacking velocity. DMO will then be dip-independent and will apply the necessary time shift for a more accurate stack. DMO can be applied using a number of methods (explained in more detail within Yilmaz, 2001 and Hale, 1984) that are usually applied after NMO corrections. Lateral velocity variations within the subsurface traversed by the seismic waves in a particular CMP gather will give rise to subtle variations in the NMO that may require an additional processing step termed residual move-out to be carried out before stacking to provide perfectly crisp images. This process gives additional granularity to the velocity model resulting from the standard DMO and NMO velocity analysis (e.g. Yilmaz, 2001).

3.2.5 Migration

Imaging complex geological features and structures in the subsurface can often cause a significant difference between the true location of a reflector within the subsurface and where it is represented in a seismic reflection section. This is due to the assumption that the minimum time reflection is derived from directly beneath the receiver (CDP), when in fact it can be reflected and diffracted at differing angles towards the receiver due to the variable dip of reflectors (Fig. 12). This can lead to the inaccurate imaging and decreased spatial resolution of such features on un-migrated seismic sections, including synclinal 'bow-tie' reflections and the apparent broadening of anticlines in un- or imperfectly migrated sections (Fig. 12).

Seismic migration is the process that attempts to overcome this problem by geometrically re-locating seismic events in space and time back into their true subsurface position. The migration process can be timely and expensive, but the development of computer migration algorithms has dramatically increased the use and efficiency of the process. When processing 3D seismic data, energy to the receiver from 'out-of-plane events' must also be considered through the application of 3D migration. The three main migration algorithms commonly used are Kirchhoff, finite difference and F-K. In cases where migration is not completely successful, prestack depth migration (PSDM) can be

used to yield a better result and is often used in areas of salt diapirism. Full-waveform inversion (FWI) is another approach that is gaining popularity due to its improved image quality and associated highly accurate velocity model, allowing much more use to be made of the velocities in the interpretation of the subsurface properties. More detail on the migration process, algorithms and PSDM can be found in Yilmaz (2001) and Jones et al. (2008).

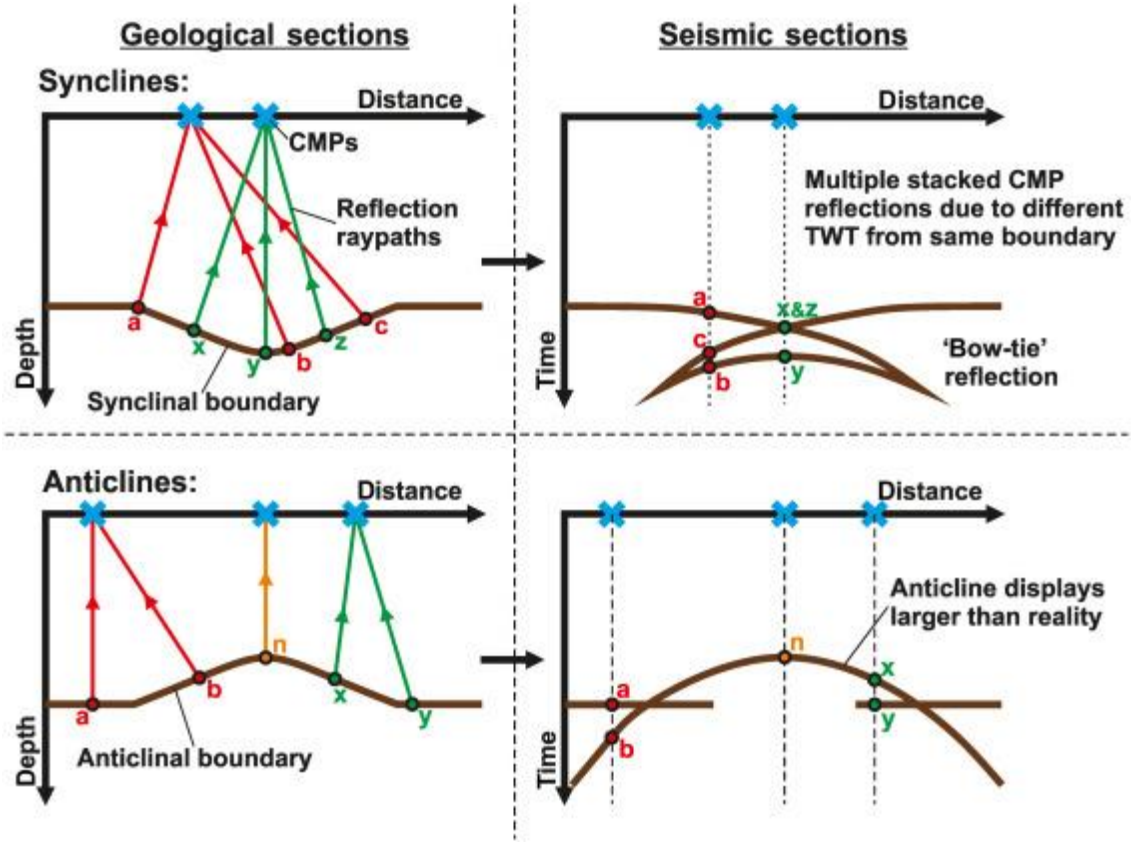

Figure 12. Migration | Schematic diagrams that show the effect of more complex geological features on seismic acquisition. The use of common midpoint (CMP) gathers assumes that the minimum time reflection is derived from directly beneath the receiver (the CDP); this causes a difference between where the energy is plotted on seismic sections and its true location in the subsurface. This causes commonly observed features in the seismic such as bow-tie reflections and enlarged anticlines. The process of migration aims to correct this and return the seismic event back to its true subsurface location in space and time. Modified from Etris et al., (2002).

3.3 Data reduction and enhancements

3.3.1 Common Midpoint Stacking

Velocity analysis (NMO and DMO) and the associated corrections cause the reflections for a CMP to appear horizontal on the corrected CMP gathers. The traces in each gather can now be added together or 'stacked' to create a series of stacked traces, one per gather. CMP stacking causes the enhancement of primary reflections and the reduction of random noise and multiples. The wavelet signal/noise ratio is amplified by a factor equivalent to the

square root of the number of traces summed. Additionally, multiples (see the next section) are not fully corrected during NMO and DMO and remain imaged as curved hyperbolas (see Velocity Analysis). This will cause them to have misaligned peaks that will not amplify during stacking and will instead be suppressed relative to perfectly corrected primary reflections. Once stacked, a requirement for further processing steps may become apparent. The traces can, therefore, be unstacked to apply the process before re-completing CMP stacking.

3.3.2 Multiple Attenuation and Deconvolution

Multiple reflections and reverberations can be created by the downward reflection of the primary reflected source at shallower AI contrasts. If this secondary reflected wavelet is then once again reflected at the deeper AI boundary and returns to the receiver, it will be recorded as a multiple reflection (Fig. 13). Multiples are classified into two classes: long-path multiples, the most obvious of which are commonly recognized as reflections that are twice the TWT, twice the dip and reversed polarity from the primary reflector; and short-path multiples that typically complicate deeper primary reflections through short-path reverberations (Fig. 13).

Multiples that remain post-CMP stacking can be attenuated using techniques that predict their periodicity or difference in move-out velocities from that of primary reflections in the CMP domain. Methods used include wavefield prediction and subtraction, filtering and predictive deconvolution. More information on all three methods is provided by Chunyan et al. (2003). Deconvolution works by convolving the seismic trace with the predicted noise or multiple signal to remove it, leaving, ideally, only the primary reflection signal within the deconvolved trace. This form of deconvolution is applied through a filter and forms the basis of the commonly used predictive deconvolution method that attenuates short-period multiples by predicting the periodicity of reverberations created by water bottom and shallow reflectors (Sheriff and Geldart, 1995; Yilmaz, 2001).

After the removal of multiples and the boosting of the reflected wavelets through deconvolution, a final stage of deconvolution can be applied. Wavelet deconvolution is aimed at changing the trace signal from minimum to zero phase (see 'The reflection seismic method' section). The benefit of this is to ensure the peak amplitude of the recorded reflection occurs at the point of impedance contrast (the lithological boundary). This helps to counteract the blurring of reflected wavelets by using a clean zero-phase wavelet spike that has a large amplitude and short time duration, aiding accurate interpretation (see

'Seismic interpretation' section). To convert the wavelet to zero phase, the source wavelet must be known. This can be gained either by measuring the seismic source (wavelet synthesis) or by statistical extraction in the frequency domain (wavelet extraction). Once the minimum-phase wavelet is known, it can be deconvolved with the seismic trace to produce the zero-phase wavelet (Dondurur, 2018; Mousa, 2019).

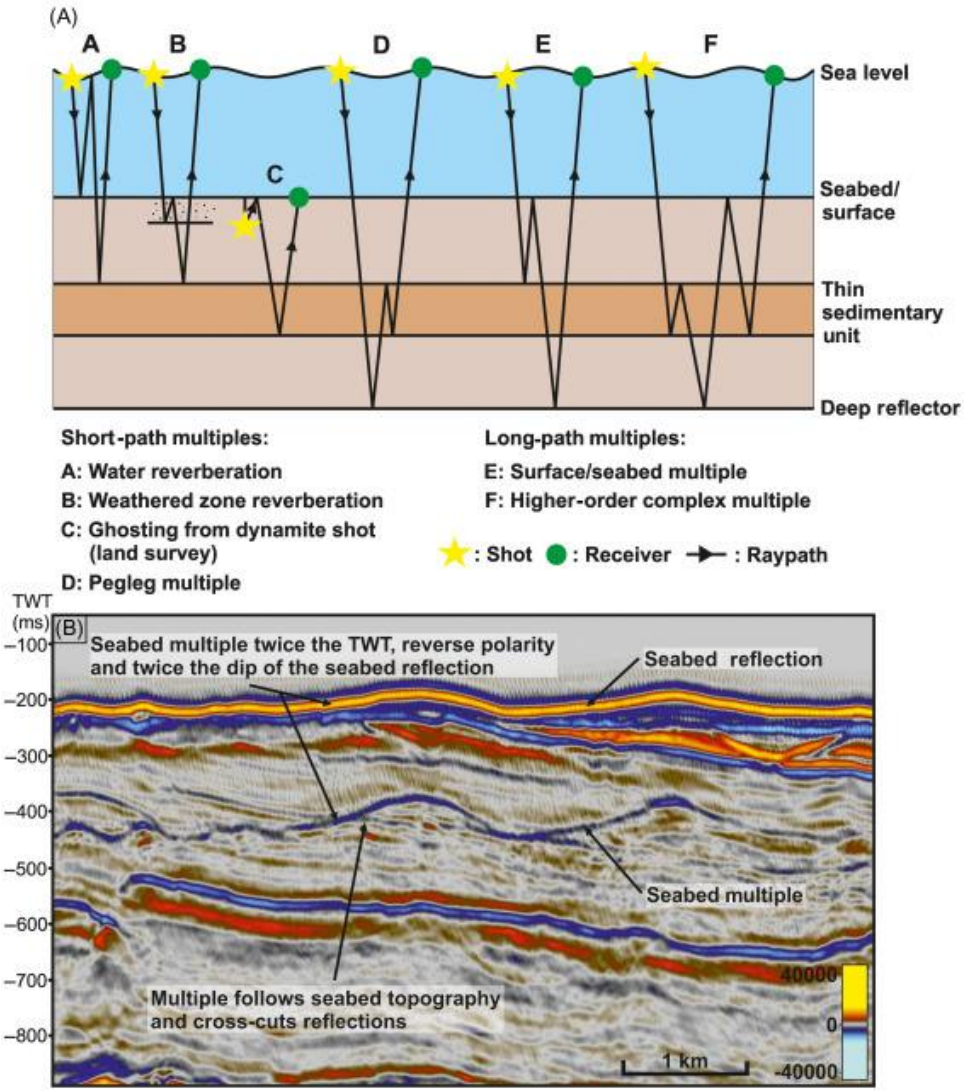

Figure 13. Multiples | The cause and effect of multiples in seismic data. (A) Simple schematic that depicts the various types of both long- and short-path multiple reflections that can occur between the seismic source production and receiver recording. These multiples are a form of noise on seismic data and can cause complication in both further processing and interpretation and therefore need to be attenuated via methods such as wavefield prediction, filtering and predictive deconvolution. (B) Seismic cross section showing a long-path seabed multiple that is created due to the returning seabed reflection reflecting downwards at the sea level before re-reflecting at the seabed and being recorded by the receiver. This causes a multiple reflection to occur at twice the two-way time of the seabed that displays both reverse polarity and twice the dip. (A) Diagram based on Keary et al., (2002). (B) Seismic courtesy of the Oil and Gas Authority (open source).

3.4 Filtering and Scaling

The final step prior to digital output and display is typically the application of a frequency filter to attempt to reduce the effect of white noise on the signal. Various types of frequency filters can be used, with the most common being a bandpass filter that zeroes all frequencies outside a desired range. The data are converted to the frequency domain via a Fourier transform before application.

Once the processing steps are complete, the parameters can be chosen for effective display of the seismic section either on paper or on a workstation. Once displayed, additional seismic attribute steps (such as gain correction) can be applied to reduce noise further or to equalize shallow and deep reflections. Spectral whitening is another post-processing adjustment sometimes applied to boost the high-frequency amplitudes as a means of compensating for increased high-frequency attenuation with increased travel time.

4. Seismic Interpretation

Once the data have been processed, they are ready for interpretation. A brief overview of seismic interpretation is provided and those interested in further reading should refer to a number of seminal texts that provide significant background on interpreting seismic reflection data and converting that into geological knowledge – for example Payton (1977), Badley (1985), Avseth (2005), Brown (2011) and Simm and Bacon (2014). Similar to the planning of the seismic surveys, the detail and time spent on interpretation will depend on the desired end objectives. For example, a structural geologist may only be interested in large-scale tectonic features (e.g. faults, key surfaces), whereas an energy company may want to develop a subsurface model of hydrocarbon sources, seals and reservoirs, requiring detailed understanding of sedimentary facies and physical properties.

Traditionally, seismic reflection data were interpreted on paper with interpretations laboriously annotated on paper maps. However, contemporary workstations allow the combination of multiple 2D and 3D data sets in one project – for example a basin-scale study may contain 1000 s km of 2D data and 10,000 s km2 of 3D data. These projects are often created using specially designed seismic interpretation software that can display various seismic intersections (In-lines, X-lines, arbitrary lines and Z-slices) in both 2D and 3D (Fig. 14). Although depth-domain interpretation is becoming more commonplace, a typical seismic display is usually presented in the time domain where depth is provided as TWT (the time taken for the original source to reach the geological interval, be reflected

and then received). Other features such as horizontal scales, intersecting seismic lines and colour bars are also often displayed alongside the seismic image (Fig. 14). Creating a project in a suitable coordinate reference system for the geographic location and study area size, and loading up the seismic data ready for analysis, along with other forms of data such as geophysical borehole or geographical data, is the first step in the workflow towards the development of a final geological model (Fig. 15).

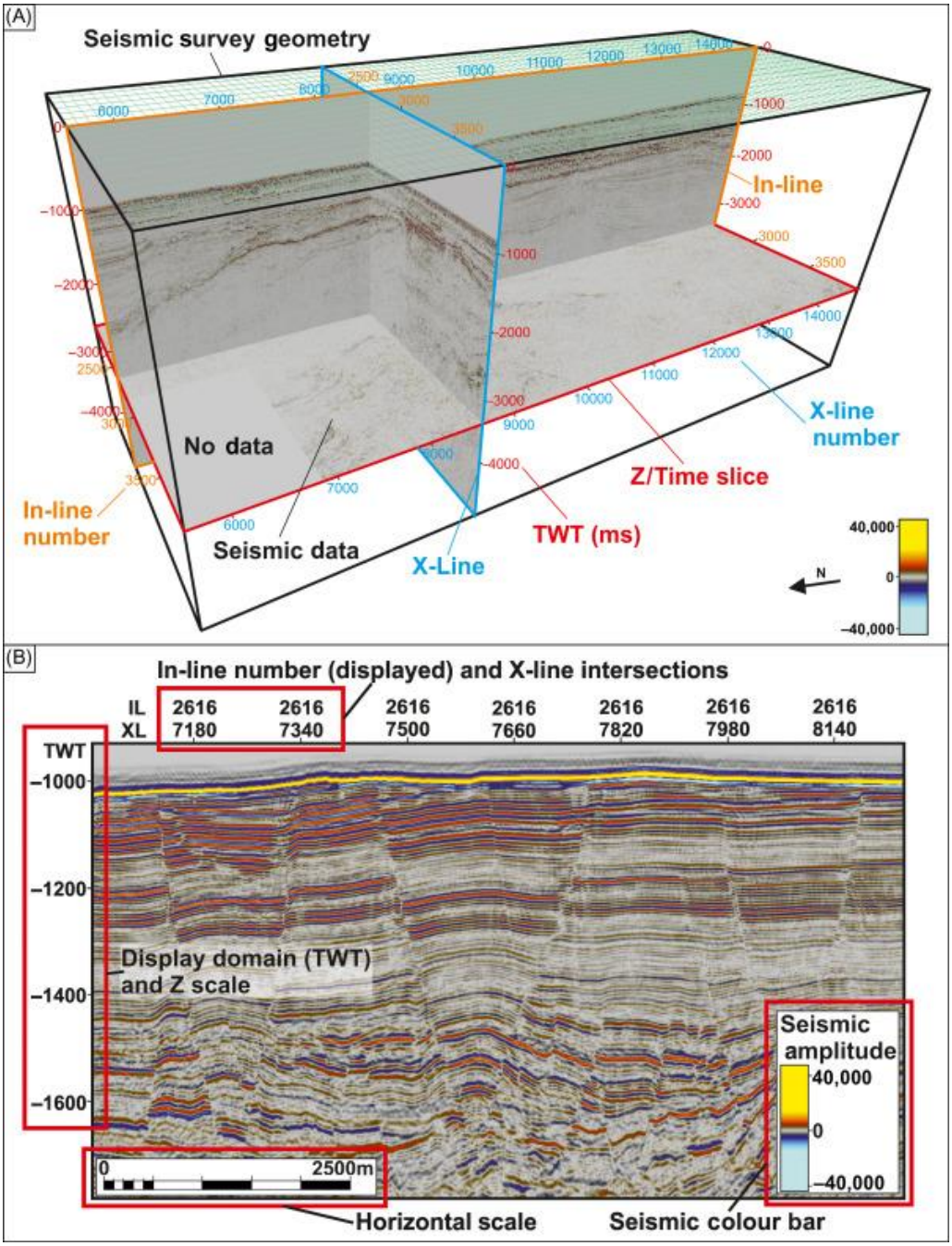

Figure 14. Seismic grid display | Seismic data displayed on a workstation within interpretation software. (A) 3D seismic cube display showing the survey geometry, typical intersections including In-line, X-line and Z-slice and common annotations such as depth in TWT (milliseconds) and In-line and X-line intersection number; (B) In-line intersection view typically used for interpretation. Seismic data are usually displayed in the time domain with two-way time provided depth. Other features that are commonly displayed are horizontal scales, colour bars to show polarity and seismic intersections. Seismic courtesy of Cairn Energy PLC.

Once the data have been compiled, a quality assessment is performed to observe any initial issues that need to be rectified. Carrying out the assessment at the start means that any problematic issues do not propagate through the interpretation. Considerations include ensuring the data set is located correctly, identifying any obvious artefacts (such as multiples and migration issues, see 'Seismic processing' section) and whether the resolution is sufficient. It is also important to determine the phase and polarity (see 'The reflection seismic method' section) of the seismic data to understand what the reflections are showing. In projects that contain a large amount of data, it is often necessary to establish a reference data set so that other data sets with depth misties or different polarity/phase conventions can be converted.

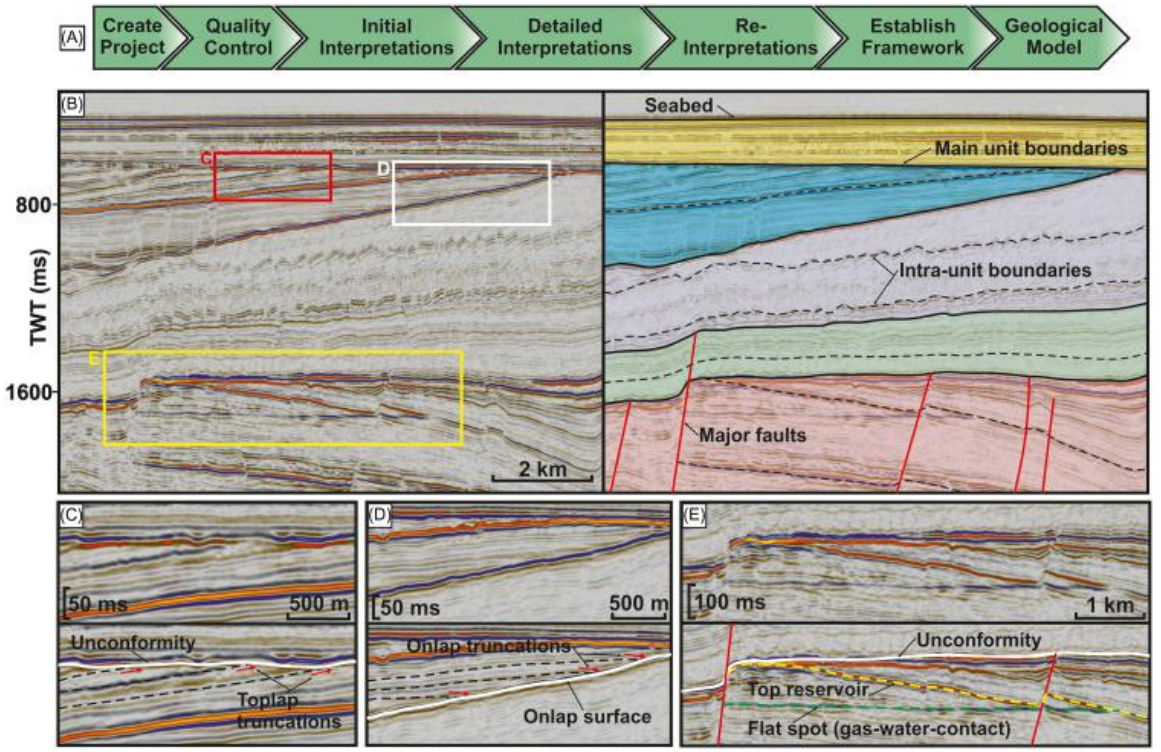

Figure 15. Seismic interpretation workflow | (A) Schematic workflow showing the steps of seismic interpretation required to build towards understanding the subsurface and creating an accurate geological model; (B) an uninterpreted and interpreted seismic section (in two-way time) depicting the interpretation process of documenting key reflections, geological units and faults; (C, D and E) uninterpreted and interpreted enlarged sections of the seismic cross section from B, showing more detailed interpretation methods such as identifying reflection relationships and terminations that may represent unconformities or sequence boundaries as well as hydrocarbon related features. Seismic courtesy of NPD.

If geophysical borehole data are available within the seismic coverage, then a seismic-well tie (SWT) can be conducted before seismic interpretation begins. This process bridges the gap between geological information from the well (in depth) and geophysical information from the seismic data (typically in two-way time). The main aim of this process

is to calibrate depth values to the TWT (time domain) for the geophysical logs so that they accurately match the seismic data. Geological information interpreted from the logs such as lithology, reservoir properties and formation age can then be correlated with the different seismic packages, facies and horizons. Importantly, this process may highlight key packages or horizons within the seismic data that can be focused upon during interpretation, such as unconformities, reservoir zones or fluid contacts.

The SWT process involves the creation of a synthetic seismogram from well log data that can be accurately tied to the seismic data, thus creating an accurate time–depth relationship (TDR) (Fig. 16). The process involves five main steps (shown below) but each of these steps can vary depending on the data available and the level of accuracy and confidence required in the SWT result.

1. Checkshot data are used to time-convert the well (create depth values in TWT) and create an initial (but often inaccurate) TDR.
2. A sonic log (higher-resolution velocity data) is calibrated using the checkshot data and is used to time-convert the well, creating a secondary and slightly more accurate TDR.
3. An AI log and reflectivity series (RCs) (Fig. 16) are created from the calibrated sonic and density logs.
4. A wavelet that represents the seismic trace must either be generated analytically or extracted from the seismic data. This is then convolved with the reflectivity series to create a synthetic seismogram (Fig. 16).
5. The synthetic seismogram is then 'tied' to a single or several seismic traces located at the well path, using a minimum of adjustments. This fine-tuning of the relationship between the well data created synthetic trace (originally from depth data) and seismic data (in time) creates an accurate TDR that is used to conduct a final time conversion of the well. The borehole and seismic data are now tied, and an accurate transfer of geological and geophysical information can be completed.

Once data quality control, assurance and the SWT process are complete (dependent on data availability), the initial interpretation can begin. This typically involves documenting the presence of key reflections and units (e.g. sequence boundaries), structural elements (e.g. faults) and geomorphological features (e.g. channels) and, if possible, unravels the basic depositional setting (Fig. 15). This is typically done by quickly scanning through the data to understand large-scale patterns and areas requiring further analysis.

The most time-consuming part of the interpretation process is often the detailed mapping of key faults and reflections – which are often termed 'horizons' during interpretation. The detail with which these are mapped will depend on the desired outcomes. This type of analysis is based on the assumption that seismic reflections follow geological time lines and that different depositional settings can be defined within a succession of conformable strata that are genetically linked – see Payton (1977). By exploring how seismic reflections vary (e.g. amplitude, geometry, terminations) (Fig. 15) and what relationships are evident between different facies, architectures and unconformities within a sedimentary succession, it should be possible to document the chronology of basin infill, erosional processes and the interaction between accommodation and sediment supply. Integrating core and borehole data can aid in the interpretation of different reflections by relating seismic character to specific lithologies.

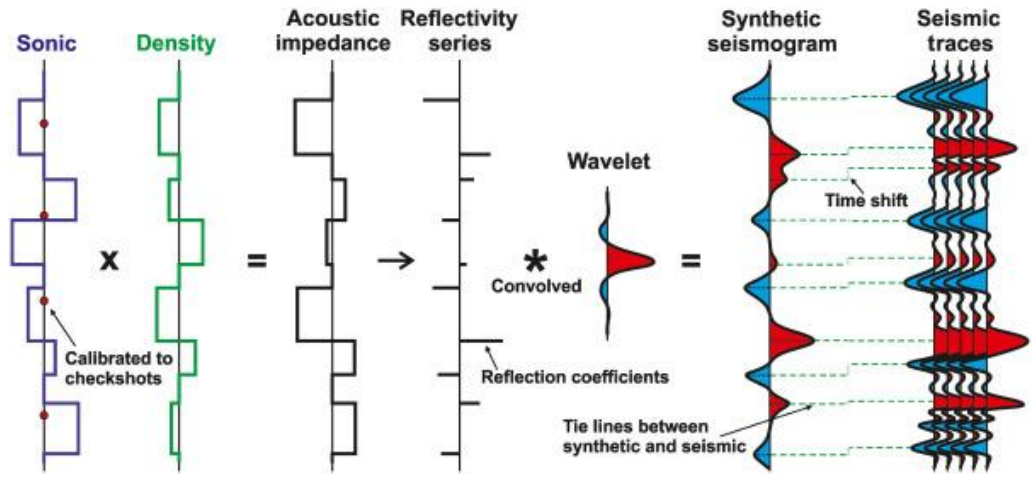

Figure 16. Seismic-well tie | A workflow showing the seismic-well tie process. Sonic and density logs are combined to create an AI log, which defines the reflection coefficients at subsurface boundaries and is used to create a reflectivity series. This is then convolved with a seismic wavelet to create a synthetic seismogram. The seismogram can then be stretched and squeezed in an attempt to tie it to the real seismic data. This process creates a time–depth relationship for the well that allows the time conversion of log data and the transfer of information between the depth and time domains.

Deciding which horizons are important depends on the above rationale and whether they have either a seismic stratigraphic or geomorphological significance (or both). After the faults and horizons have been picked (this can often be achieved manually, semi-automatically or automatically), thickness and structure maps can be generated to explore how depositional and erosional patterns changed through time. This may also include generating geobodies of specific geomorphological or structural features (e.g. channels, salt diapirs, sedimentary or igneous intrusions, etc.) (Fig. 17). It is important to remember that there are no specific seismic reflection characteristics that can be used as a unique indication of a particular type of geological facies. Thus it is often the case that more

questions may arise through further analysis, which may eventually lead to re-interpretation (Fig. 15).

Often interpretation will involve the interpreters looking at other seismic attributes (e.g. coherency, variance, sweetness, amplitude versus angle, etc.) and post-processing methods (e.g. spectral decomposition and blending of various attributes) to create volumes tuned to emphasize specific subsurface aspects such as structure, lithology or fluid presence. Attributes display derivatives of the seismic measurement and are usually based on time, amplitude or frequency. An attribute can be created for a full 3D seismic volume and utilized within a software package using viewing planes and filters. Attribute display style is determined by the colour bar which is often modified in an attempt to tease out extra information from certain seismic parameters (Froner et al., 2013). A popular volume attribute to use during interpretation is windowed trace to trace variance (or coherence) which will highlight horizontal or strata-normal discontinuities in amplitude throughout the seismic cube, therefore, clearly highlighting the location of faults and other discontinuities facilitating their accurate interpretation (Fig. 18). Surface attributes are also commonly used to provide additional information on structural, stratigraphic and reservoir elements across a specific interpreted horizon. An example of this is shown by using both amplitude and time attributes to identify glaciogenic landforms within buried stratigraphy (Fig. 19). Most attributes are derived from poststack seismic data; however, certain attributes use prestack data, such as amplitude versus angle (AVA) (see 'Amplitude versus angle analysis' section). Detailed information on seismic attributes can be found in Brown (2011).

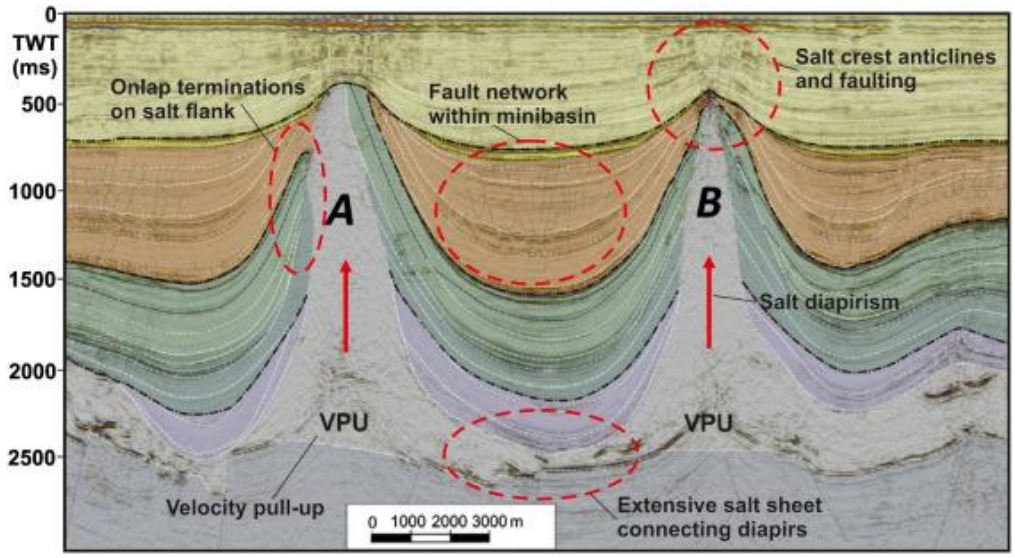

Figure 17. Complex seismic interpretations | Two-way time seismic intersection displaying complex subsurface features imaged in seismic data such as salt diapirs, mini-basins, polygonal fault networks and velocity pull-up due to increased velocities within salt. Seismic interpretation steps have been completed and key horizons, geological units and faults are displayed. The image importantly shows the difference in seismic

character between the subsurface sediments (layered coloured units) and the salt bodies (not coloured). Mage modified from Harding and Huuse, (2015).

Detailed interpretation and the utilization of many forms of seismic attribute are commonplace within subsurface geoscience studies. In petroleum exploration, there is a particular focus on direct hydrocarbon indicators (DHIs) that occur as anomalous amplitudes and, sometimes, high-frequency attenuation due to a change in pore fluids within the rocks (Fig. 20). Due to the uncertainties involved in the prediction of viable petroleum accumulations prior to drilling, the presence of DHIs can be the difference between an exploration well being drilled or not. Nevertheless, DHIs are often challenging to interpret accurately and a clear understanding of the rock properties and their seismic expression is required to differentiate between lithological and fluid effects. Basic rock physics rules and awareness of pitfalls such as multiple reflections, diagenetic flat spots and low-saturation gas effects and how to test for these can help improve the utility of DHI observations (e.g. Hilterman, 2001; Simm and Bacon, 2014).

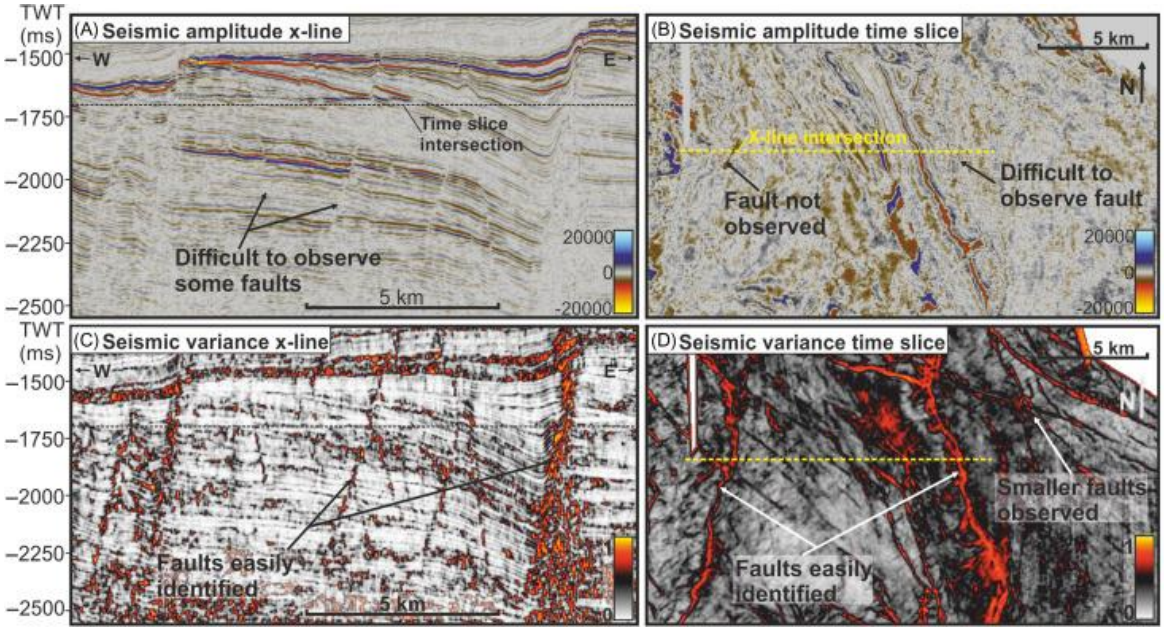

Figure 18. Faults | A comparison of a seismic x-line intersection (A) and a time slice intersection (B) displaying seismic amplitude with a seismic x-line intersection (C) and time slice intersection (D) displaying the seismic variance attribute. Note the enhanced imaging and increased resolution of vertically extensive features such as faults on the variance attribute display when compared to a traditional seismic amplitude display. This increased resolution aids the identification and accurate tracking of fault features and is therefore used extensively during structural interpretation of seismic data. Seismic courtesy of NPD.

Due to the variation in AI between reservoir and seal, as well as different fluid types, a range of DHIs may be observed:

- Bright spot: A local increase in 'soft' seismic amplitude caused by the increase of RC due to hydrocarbon fluids. Bright spots are commonly caused by gas within clastic reservoirs that causes a decrease in velocity from the overlying seal unit, increasing the negative impedance contrast and brightening the top-sand reflection.
- Dim spot: Low-porosity sandstones or carbonates can often cause large impedance contrasts from the overlying shale. Hydrocarbons will cause a velocity and density reduction within the sands; however, this may not decrease enough to reverse the RC polarity. Therefore, the reduced AI contrast between reservoir and seal will reduce the seismic amplitude, creating a 'dim spot'.
- Flat spot: In subsurface reservoirs, because of their relative densities, gas is found above oil, which is found above water/brine. The contact between the different fluids in a dipping reservoir will form crosscutting hard reflections due to the downward relative increases in velocity and density of the pore fluids. The reflection amplitude is greater in highly porous reservoirs due to their low matrix stiffness and high pore fluid content.
- Polarity reversal: In intermediate porosity reservoirs, the addition of hydrocarbon fluids can decrease the AI of the reservoir to become less than the overlying seal. This then causes the top reservoir reflection to change polarity. The top reservoir polarity will reverse in areas that are below the hydrocarbon column and filled with water, thus marking the fluid contact.
- Velocity push-down (velocity shadow): Hydrocarbon fluids cause a reduction in velocity that increases travel times through a reservoir. This can cause seismic reflections to be 'pushed-down' and appear deeper than they are in reality.
- Fluid flow features: The movement (and subsequent trapping along the path) of low-density hydrocarbon fluids can often be observed through seismic anomalies. Gas chimneys are examples of this where hydrocarbons have leaked from a deep reservoir to the subsurface resulting in a low-velocity, low-amplitude gas cloud in the seismic data. Other examples of anomalous fluid flow features include fluid pipes, fault flags and pockmarks. More information on fluid flow features can be found in Hilterman (2001), Cartwright et al. (2007), Huuse et al., 2010, Brown, 2011.

Once interpretation is complete, the interpreter can begin creating or building upon an existing geological framework that characterizes present-day subsurface geology and attempts to explain the depositional and deformational history of the area that led to its

formation. For industry purposes, this framework may include an outline of important features such as reservoir limits, seal extent, sweet spots for drilling and potential subsurface hazards. This information may also be developed into a 3D reservoir model that attempts to recreate subsurface reservoir properties as accurately as possible to allow for field development simulations that test the effects of hydrocarbon production and/or fluid injection.

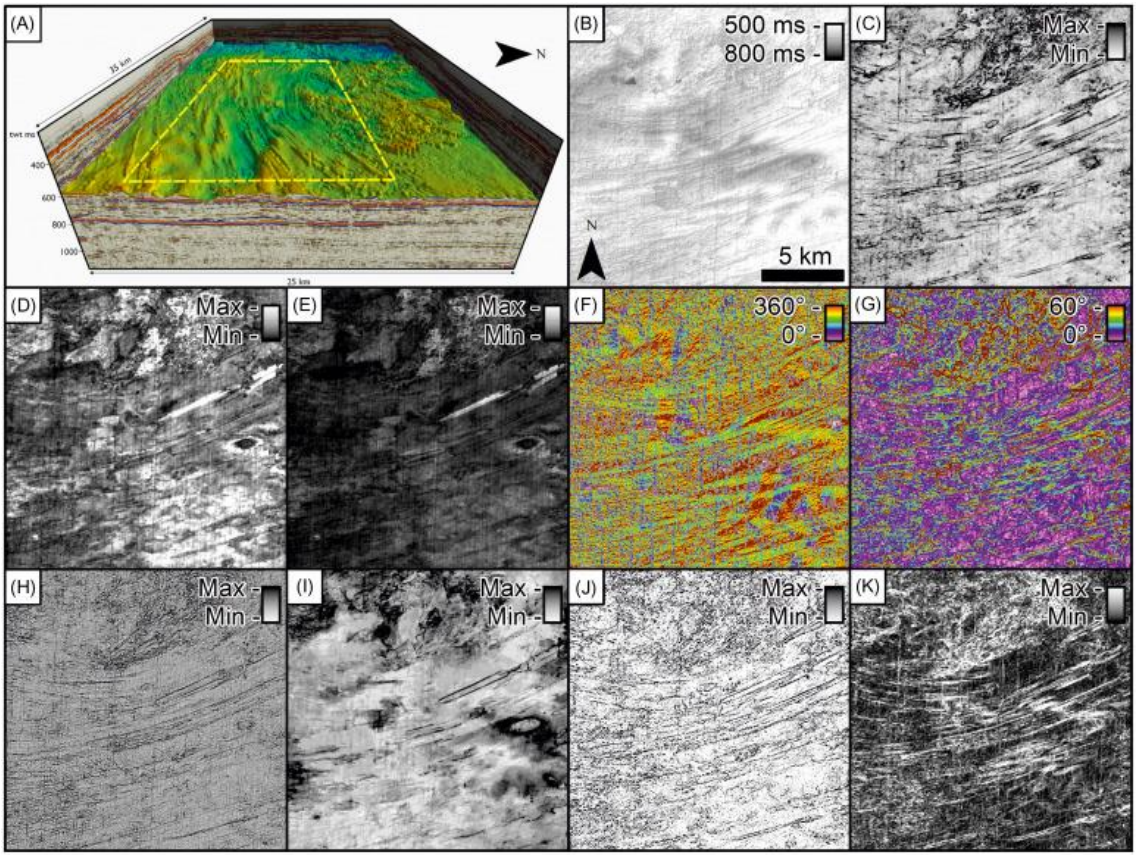

Figure 19. Seismic attributes | Multiple seismic attributes can be used to identify and analyse buried glaciogenic landforms. (A) 3D perspective view of 3D seismic sections and auto-tracked horizon showing a set of well-developed mega-scale glacial lineations as a two-way time surface. The following panels show how these features appear using different attributes. The additional attributes include: (B) shaded relief, (C) variance, (D) root mean–square (RMS) amplitude with a window of 4 milliseconds, (E) RMS amplitude with a window of 8 milliseconds, (F) surface azimuth, (G) surface dip, (H) curvature, (I) 3D edge enhancement, (J) dip deviation and (K) dip illumination. The scale in panel (B) is the same for panels (C–K). From Newton, (2017).

4.1 Advanced Techniques

4.1.1 Depth Conversion

Seismic reflections typically display the TWT of reflectors in the subsurface from the datum. The conversion of this information into the depth domain, via the process of 'time-to-depth' conversion, is required for quantitative assessment of parameters such as subsidence and trap and fluid volumes. Depth imaging allows for direct comparison to well

data (without depth to time conversion) and allows a more accurate and realistic imaging and understanding of the subsurface geology, provided the velocity model is realistic and migration algorithms sufficiently robust. Importantly, this allows for interpretations and 3D reservoir models, built from these interpretations, to be displayed in depth. This aids the accuracy of volumetric calculations, whilst allowing the precise planning of exploration, appraisal or development wells (Al-Chalabi, 2014).

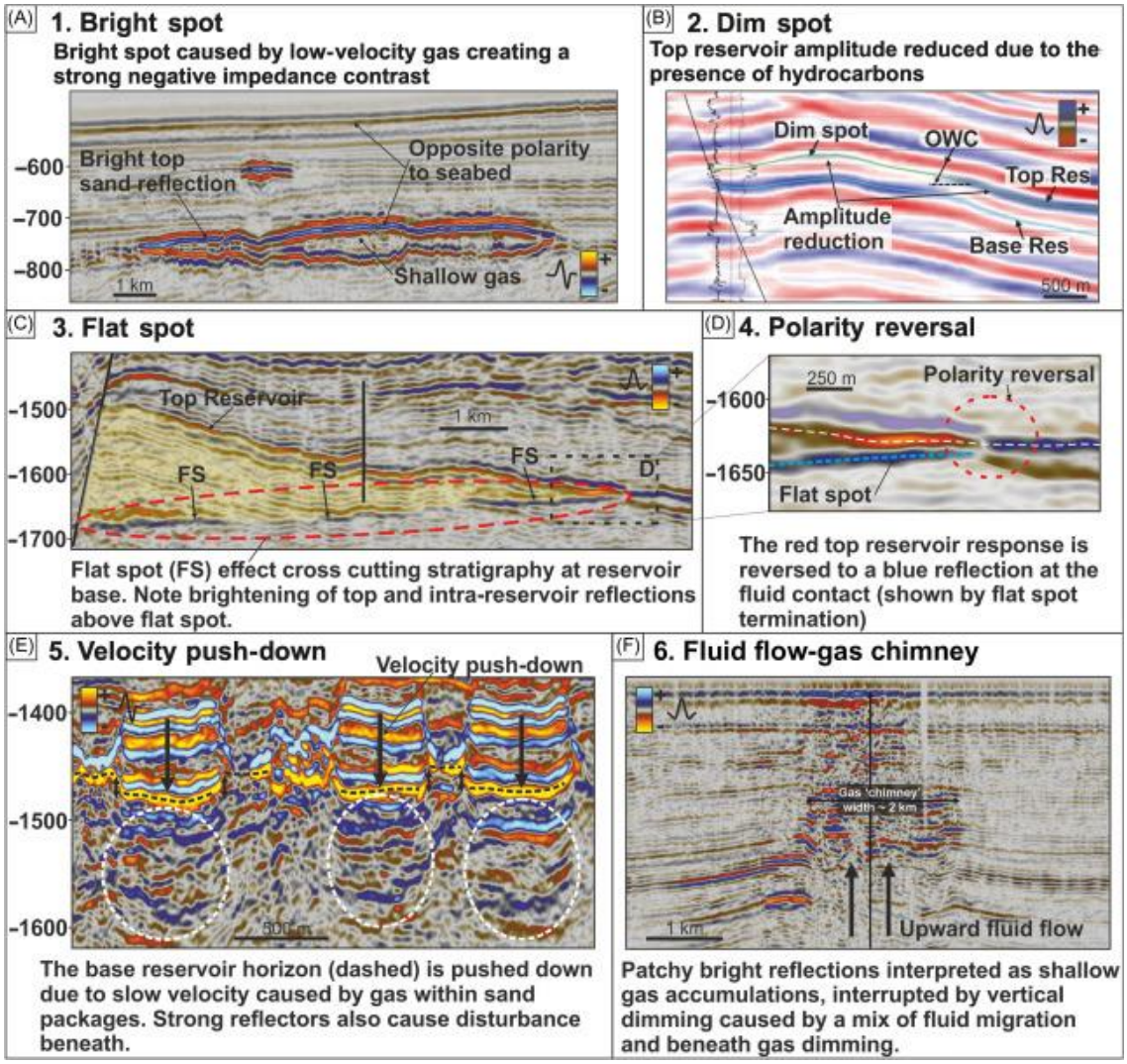

Figure 20. Direct hydrocarbon indicators (DHIs) | Direct hydrocarbon indicators (DHIs) observed within seismic data. (A) Bright spot caused by low-velocity gas creating a negative impedance contrast at the top reservoir. (B) Dim spot caused by the reduction of reflectivity coefficient due to the presence of hydrocarbons in the reservoir pore space. The AI variation, however, is not strong enough to create a polarity reversal. (C) Flat spot created by the presence of hydrocarbons creating a positive reflection coefficient at the fluid contact which is observed as a near-horizontal reflection that crosscuts stratal reflections within the reservoir. (D) Polarity reversal caused by the presence of hydrocarbons in the reservoir affecting the reflectivity coefficient at the top reservoir horizon. The polarity switch is observed at the edge of the reservoir at the fluid contact or the onset of non-reservoir. (E) Velocity push-down of the base reservoir horizon due to reduced velocities within a hydrocarbon filled reservoir causing reflections to plot deeper than reality. A strong reflection disturbance is also depicted beneath the reservoir likely due to the presence of hydrocarbons. (F) Upward migration of hydrocarbons as a gas chimney. This feature is characterized by discontinuous bright reflections (shallow gas) that are often surrounded by dimmed amplitudes (migrating fluids). (A, C, D and F) seismic courtesy of NPD. (B) modified from Wokcik et al., (2016). (E) seismic courtesy of Cairn Energy PLC.

The process of depth conversion can either be applied to prestack seismic data, poststack seismic data or directly to interpretation objects. The method chosen depends on the complexity of the geology (and therefore the velocity field), budget and time. All depth conversion methods require knowledge of the velocity field through a time-depth relationship (TDR). This can be provided by several methods:

- A 'checkshot survey' that measures P-wave velocity from a conventional source by using a geophone that is lowered down the wellbore.
- A 'vertical seismic profile', which is acquired in a similar manner to a densely spaced checkshot survey, sometimes with varying source locations, to create a narrow seismic section at the borehole location and immediate surroundings.
- Stacking velocities can be calculated directly from the seismic data during the NMO processing step (see 'Seismic processing' section). Interval velocities between reflectors can then be calculated from the stacking velocities using a Dix conversion (Dix, 1955).
- Regional velocities provided by nearby locations or published data can be used when no direct measurement data are available.
- Prestack migration velocity modelling.
- FWI approaches integrating the prestack migration seismic velocity information with well data in an iterative process to create a highly detailed and realistic velocity field.

It is worth noting that the provided velocities may have varying accuracy and the use of certain types may be suitable over others. For example velocity data recorded within the well are extremely detailed in the close vicinity of the well but susceptible to borehole conditions, casing, invasion by drilling fluids, cycle skipping, and become less representative with increasing offset (Rider and Kennedy, 2011).

The velocity information provided via these methods is often used to create a velocity model, which will be used within the depth conversion process (Fig. 21). Velocity models range from using a single TDR velocity function from a single well (1D) to the use of multi-well velocity function maps (2D) and layered models with lateral velocity variations (3D), which can either be constructed by the interpreter or, as is becoming more prevalent, by the processing workflow involved in FWI (e.g. Jones et al., 2013).

Many methods of depth conversion using velocity models are available that range in complexity, accuracy and time. However, depth migrations using processing velocities are often considered the most accurate method of creating a depth image and will often enhance resolution (Fig. 21). This is due to many more variables being considered during velocity analysis (NMO and DMO – see 'Seismic processing' section) and the migration of seismic energy into its correct location. This process will often involve depth migration to help reach the most accurate result possible. This is usually performed on prestack data and is termed PSDM. Additional information on depth conversion can be found in dedicated texts such as Al-Chalabi (2014) and Jones et al. (2008).

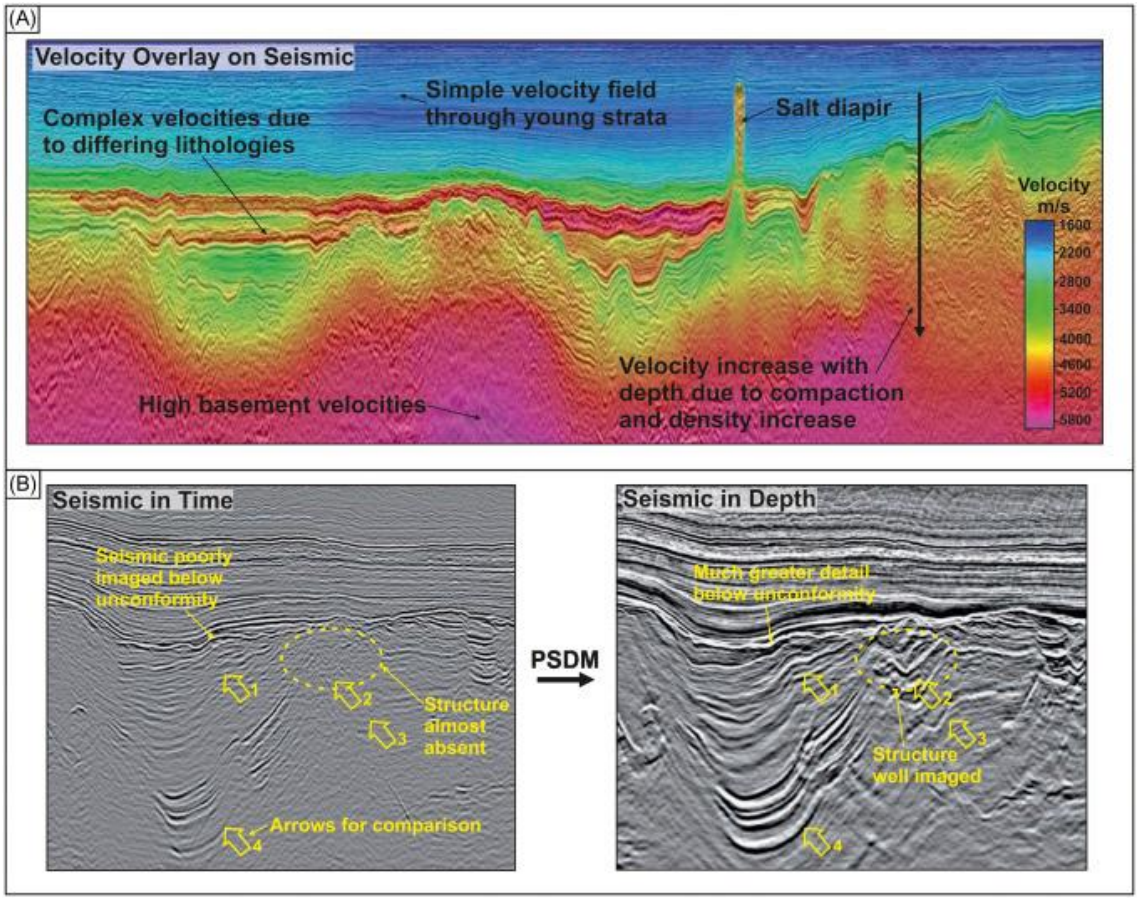

Figure 21. Depth conversion | Velocity models and poststack depth migration. (A) Velocity field from a created velocity model overlying a seismic intersection that highlights the complex nature of velocities within the subsurface and the detail required on a regional and local scale to achieve an accurate conversion; (B) comparison between vintage prestack time-migrated (PSTM) seismic (left) and prestack depth-migrated (PSDM) seismic (right). The PSDM processing created a much more accurate image of the subsurface in depth, which in particular shows much-improved resolution beneath the unconformity. Modified from Hollingworth et al., (2015).

4.1.2 Amplitude versus Angle Analysis

Amplitude versus angle (AVA) analysis is a technique that is commonly used within the petroleum exploration industry for the detection of hydrocarbons, identifying lithology and

for analysing fluid parameters. The technique derives from the simpler amplitude versus offset (AVO) technique, which only requires geometry information from the acquisition geometry. AVA in contrast uses the processing velocity information and ray tracing calculations of incidence angle to calculate amplitudes as a function of incidence angle and is thus much more representative of the angle-dependent RC. Both approaches are based on the understanding that P-wave RCs (and therefore reflection amplitude) at a boundary vary with the angle of incidence (see 'The reflection seismic method' section). This variation has a direct relationship to the relative values of Poisson's ratio (Domenico, 1984) of the separated media. When the below medium is gas-filled sand, the Poisson's ratio is shown to exhibit anomalously low values which result in an increase of the P-wave RC with increasing offset. This increase in amplitude with offset facilitates the detection of gas sands (Castagna and Backus, 1993). Additionally, the characteristically low VP/VS ratio (shown by the low Poisson's ratio) can aid the distinction between gas sand layers and other low-impedance layers such as brine sands and coals. Finally, with the aid of empirical relationships between S-wave velocity (VS) and the P-wave velocity for varying rock types, the AVO and AVA approaches provide information towards lithology identification.

AVA and AVO analyses are completed using prestack seismic data. The differing 'angle of incidence' is provided by various angle-stack volumes [typically 0–15 degrees (near stack) 15–30 degrees (mid-stack) 30–45 degrees (far stack) 45–60 degrees (ultra-far stack)], which are provided by the seismic processor. The angle stacks are used in comparison to observe the change in amplitude with offset. The AVA and AVO methods are still developing and being increasingly used within the hydrocarbon industry. An example of this is the use of AVA within seismic inversion studies (see below), which allow improved lithology description and better discrimination of fluid type and contacts. The theory of AVA and AVO analysis and examples of their application can be found in Ojha and Sain (2007a), Ojha and Sain (2007b), Castagna and Backus (1993), Castagna and Swan (1997) and Zhang and Brown (2001).

4.1.3 Impedance Inversion

Seismic impedance inversion is the process of transforming seismic reflection data into a pseudo-AI data set. This AI data can provide a quantitative rock-property description of a reservoir and therefore additional information to seismic data. As AI is a product of rock density and P-wave velocity, it can be closely related to rock properties such as lithology, porosity and fluid fill. Therefore, AI inversion models can be used to delineate hydrocarbon fluids and often form the basis of generating 3D facies and petrophysical properties that can be populated into 3D reservoir models for flow simulations.

Prior to inversion, well log data should be examined for relationships between AI (calculated from density and sonic logs) and logs that show reservoir properties (porosity) and fluid effects (neutron density). This pre-inversion analysis informs the interpreter of expected results, whilst lowering the risk of false assumptions. The basis of the inversion process involves the deconvolution of the seismic trace with the seismic wavelet to create a reflection series, which is then converted into a relative AI trace. This process is completed for every trace in the seismic cube, resulting in a relative AI cube. This can be made into an absolute AI volume by adding the low-frequency trend provided by the AI data in the well data (which can be supplemented by the processing velocity trends) (Fig. 22). The end result will have uncertainties due to imperfections in the input data, the use of well versus seismic-derived velocities, nonstationary wavelets and a non-representative background AI model. But it can nonetheless be helpful in giving an insight into subsurface AI variations that can be related to other rock properties such as porosity (Fig. 22).

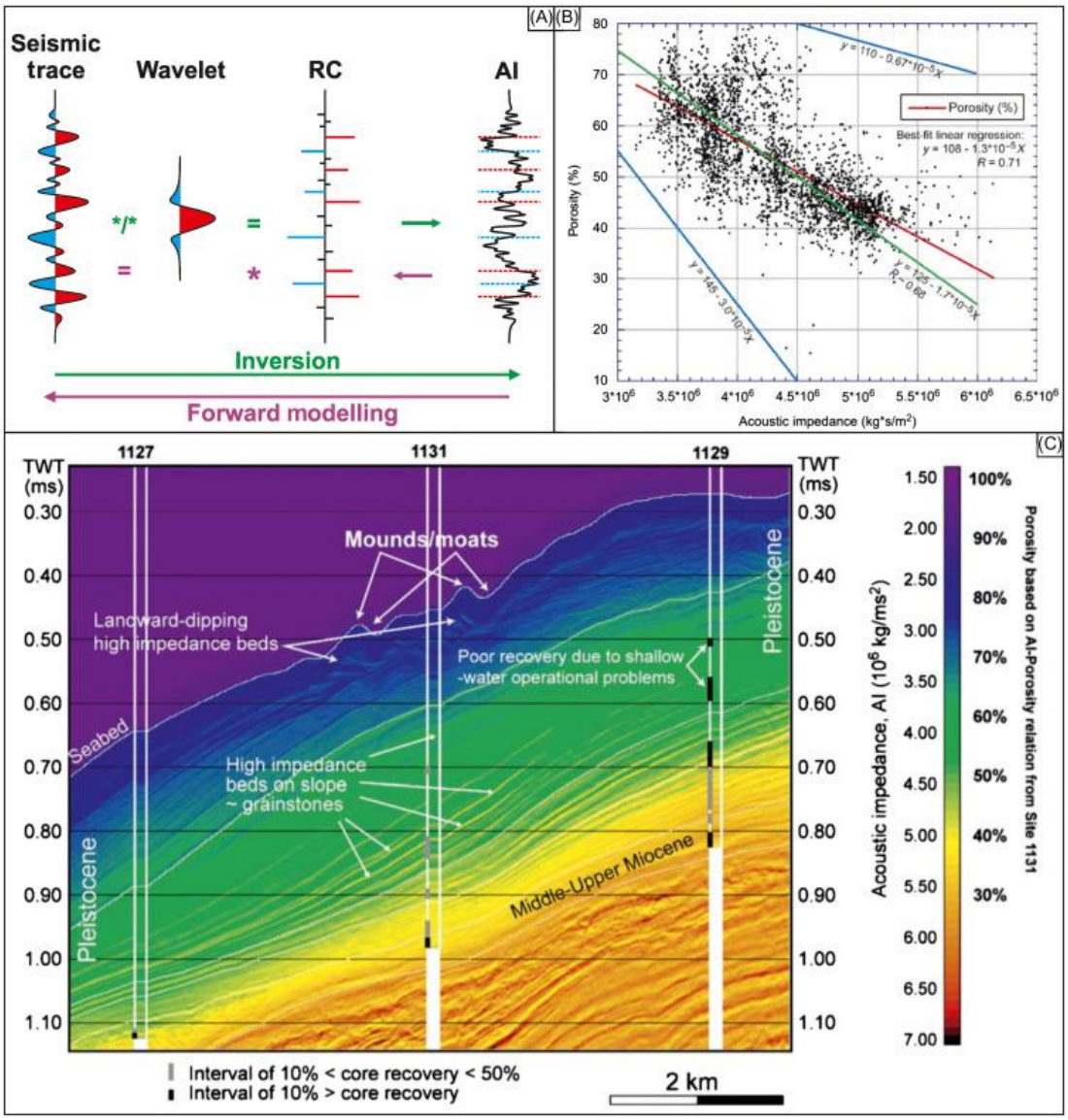

Figure 22. Acoustic Impedance (AI) inversion | (A) Diagram showing the basis of the inversion process with the seismic trace being deconvolved with a wavelet to create a reflection coefficient series which can be converted into an AI log; (B) a cross-plot showing the relationship between AI and porosity. The large scatter of data points is in part caused by poor borehole conditions during data collection. Well log data that give reservoir properties are examined for relationships between AI prior to inversion to inform the interpreter of the expected result; (C) a 2D AI section that shows the varying trend of AI with depth and highlights high-impedance sand beds. High porosity values identify the water column and unconsolidated sediments with impedance-derived porosity decreasing as a function of depth below seabed. The inverted section displays an absolute rock property (AI), which can be directly related to porosity, using the relationship given in (B), which could not be ascertained from the relative impedance changes indicated by the original seismic reflection data. Modified from Huuse and Feary, (2005).

However simple this may seem, there are additional complexities regarding wavelet removal from the seismic trace, resulting in a number of inversion methods being available. These methods are either deterministic or geostatistical and can be applied to either poststack, prestack or angle-stack data. Commonly used inversion methods include recursive inversion (poststack), sparse-spike inversion (poststack) and elastic-impedance inversion (prestack or angle stack). Method selection is usually determined by the number of wells, quality of log data, frequency of seismic data and, importantly, what you seek to learn from the inversion (Brown, 2011, Russell and Hampson, 2006).

Once the inversion process and quality control of the result are complete, interpretation (usually property extraction) can begin. The interpreter must remember that the AI cube represents a change in rock properties and not simply an interface as in seismic data. This will allow the interpretation of known relationships between AI and lithological parameters (from well analysis and published material), where the whole cube can be analysed using cut-off filters and cross-plots. Targets of interest may become apparent and can be extracted as geobodies giving 3D information on the extent of the target zone. This information can then be directly transferred into the model building process and identified variations in lithological properties can be included in volumetric calculations. More information on the theory and application of impedance inversion can be found in Brown (2011), Russell and Hampson (2006) and Latimer et al. (2000).

4.1.4 Forward Modelling

Forward modelling of seismic data is a technique that creates synthetic seismic models from known geological information. This can be in 1D, 2D or 3D and is often created to simulate the result of a seismic survey and more specifically to estimate the expected seismic expression of a geological feature or fluid effect. The forward modelling process uses a rock physical model as input and the result is often compared to fully processed seismic sections to verify the interpretation that was used to create the geological model. If required, alterations to the interpretation can be made before running the process again to

reach a closer match. Forward seismic modelling is used in a variety of subsurface interpretation and modelling applications including SWT, fluid substitution, AVA modelling, survey design, reservoir model validation, etc. (Simm and Bacon, 2014).

The basic theory of forward seismic modelling is the inverse of seismic inversion (Fig. 22), where an RC is provided by the geological model before being convolved with a source wavelet to create a synthetic seismogram. As with inversion, the process is often more complex than this. Reasons for this include the variation of input data (geological model), estimation of source wavelet and the simulation of the effects associated with seismic theory such as wave refraction, velocity reduction and the inclusion of migration calculations due to dip and 'out-of-plane' structures. There are two main classes of numerical forward modelling methods: ray tracing and wave equation methods. Both can be applicable depending on the underlying data types (differing dimension, type of gather, simulated data). Ray tracing methods often provide accurate travel times and amplitudes with low to medium processing time. However, reflection calculations are only made along the minimum time path within the model. Wave equation methods allow the simultaneous calculation of propagation and reflection throughout the whole model at a cost of additional processing time. Two commonly used wave equation methods are the Kirchhoff method and finite difference method. Additional information and examples of seismic forward modelling can be found within Anderson and Cardimona (1995), Janson and Fomel (2011) and Grippa et al. (2019).

4.1.5 Spectral Decomposition

The seismic reflection time series arising from subsurface geological features will be characterized by a limited range of frequencies with an overall dominant frequency, usually defined as either the frequency of peak amplitude or the frequency mid-way between the high- and the low-frequency cut-offs (Badley, 1985). Specific dominant frequencies will enhance the reflection response of beds with certain thicknesses and velocities that define these beds as being within the tuning range, creating an amplitude response greater than the amplitudes from a single interface. This effect is exploited by the spectral decomposition technique that breaks down the seismic signal into different narrow frequency sub-bands, each with a characteristic tuning thickness for a particular velocity. These frequency sub-bands are then analysed to reveal specific interferences within the seismic bandwidth that are often masked when using the full seismic bandwidth stack. This technique allows high-resolution imaging and more accurate identification of lithological heterogeneities and fluid effects (Bahorich and Farmer, 1995).

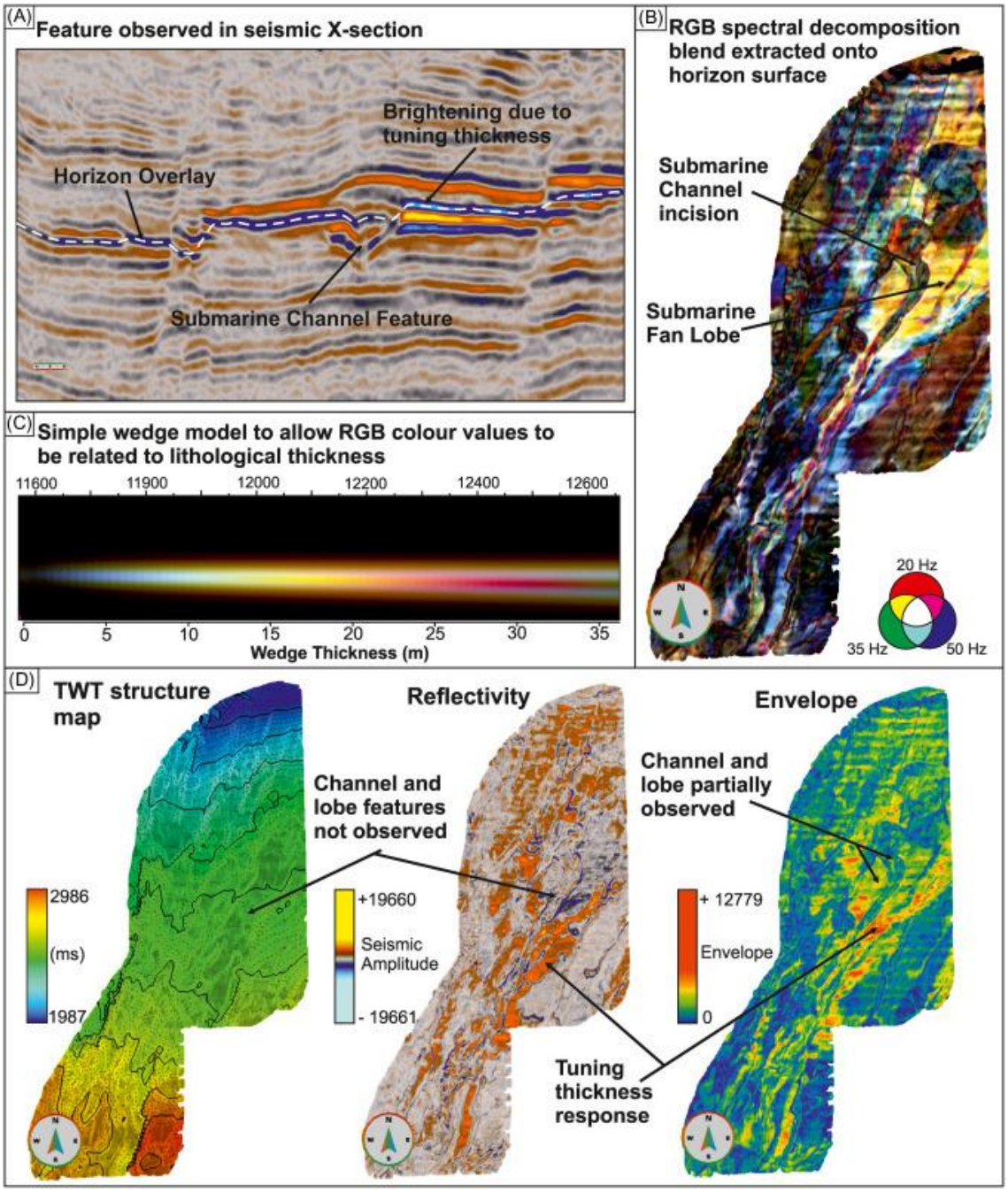

Figure 23. Spectral decomposition | Spectral decomposition and colour blending enhance the interpretation of seismic data where target elements are near the tuning thickness. Colour blending extracted seismic frequency attributes equivalent to the expected tuning thicknesses will create an enhanced and clearer image of the feature. This is illustrated by the enhanced imaging of a submarine channel incision cutting a submarine fan lobe on the (RGB) colour blend when compared to conventional seismic reflection data and attribute analysis. (A) TWT seismic cross section showing the interpreted horizon; (B) RGB spectral decomposition colour blend showing the enhanced image; (C) wedge model showing the colour display of differing tuning thicknesses; (D) TWT structure map, seismic reflectivity extraction and envelope attribute extraction on the interpreted horizon showing the poor imaging of the submarine channel and lobe features. Data and images courtesy of ffA and Geoteric.

The basic workflow of spectral decomposition first involves preparing the data to best reveal lithological or fluid properties. This may involve selecting a subset 'zone of interest', noise reduction or completing spectral balancing, which removes the wavelet shape from

the seismic, leaving just interferences (Chopra and Marfurt, 2016). It is also important to maintain a broad signal bandwidth to preserve resolution (especially with high frequencies). Several sub-band frequency cubes will then be extracted from the full-bandwidth seismic cube at key frequencies. Choosing which frequencies to extract depends on the overall resolution and frequency distribution of the seismic cube as well as the depth, impedance contrast and complexity of the target. The extracted frequency cubes can then be spectrally blended together using either the red green blue or cyan magenta yellow colour models (each frequency cube is assigned to a set colour and blended with the others). Colour composite images can then be extracted from the blend for analysis, usually at Z-slice intervals or draped onto horizon interpretations (Fig. 23). The use of the colour-bar blending allows frequency interference trends to be observed across three specific frequencies at once, which may highlight trends that remained hidden in conventional full-bandwidth seismic. Common 'hidden' features that are exposed by using this technique include channel bodies (Fig. 23), gas sands and pinch-out sands. These features can often be masked within the seismic data due to being below the vertical seismic resolution or displaying as anomalously bright amplitudes due to being at the tuning thickness (when two events below the seismic resolution constructively interfere to cause an anomalously bright amplitude) (Fig. 23).

Features creating the tuning thickness anomaly, such as the submarine fan lobe on Fig. 23, will often not display effectively in conventional full-bandwidth seismic data or through seismic attributes such as the envelope (Fig. 23D). However, the spectral decomposition technique is able to extract the frequency disturbance and display a more effective and accurate image of the body (Fig. 23B). Additionally, a wedge model can be used to assign certain thicknesses of the unit to set colours within the colour blend (Fig. 23C), thus furthering our understanding of the body whilst extending the effectiveness of the spectral decomposition technique. Further detail on spectral decomposition methods is provided by Castagna and Sun (2006) and Brown (2011).

4.1.6 Semi-automated Horizon Picking

A recent innovation in 3D and 2D seismic analysis is the semi-automation of seismic horizon picking (Fig. 24). Software packages that offer this process follow similar workflows, whereby after importing the seismic data, an algorithm is run that attempts to track every possible horizon and attributes a relative geological age – for example Daynac et al. (2016). Depending upon the type of geological setting and its stratigraphic complexity, the geological model created by the captured horizon picks can then be refined by the interpreter in problematic areas such as those around faults or areas that have

experienced folding (e.g. perhaps around salt diapirs). Once the geological model has been refined so that all horizons are geologically accurate (Fig. 24), a stack of horizons can then be created. This horizon stack allows the user to scroll through the horizons in a manner that is similar to scrolling through time slices in a 3D seismic cube. However, the key difference with the horizon stack is that it allows the user to scroll through chronostratigraphically defined surfaces that reflect the geological structure rather than cross-cutting it. This is an evolving area in seismic interpretation science and as it becomes more widespread in its use, it will help to create a more efficient workflow that helps interpreters to more quickly identify areas of interest, both in terms of hydrocarbons and wider basin evolution understanding. As things currently stand, significant user input is still required to properly and accurately interpret problematic geological areas such as those referred to above, but, nonetheless, these new types of software have the potential to revolutionize seismic interpretation workflows.

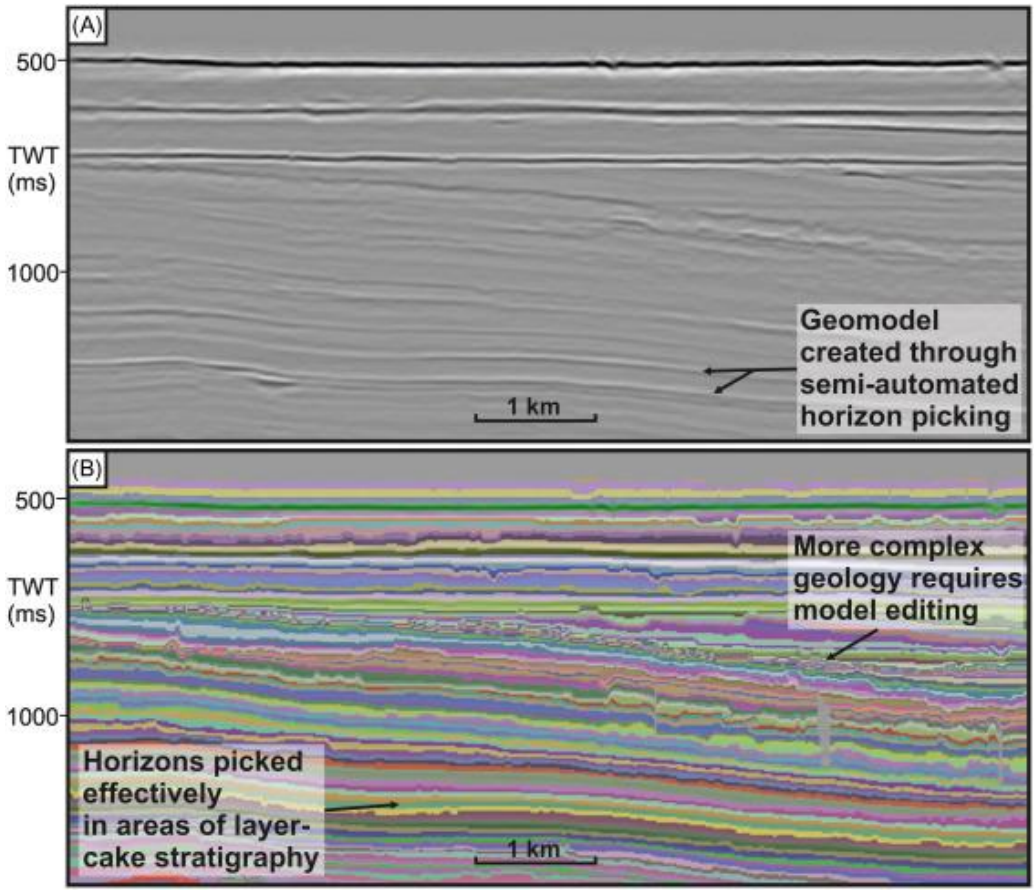

Figure 24. Semi-automated horizon picking | An example of semi-automatic horizon picking from the PaleoScan software. The model grid requires user input to refine and correct the interpretation. (A) Uninterpreted seismic data; (B) refined model grid that is used to create the horizon stack and generate surfaces for geomorphological analysis. Modified from Newton et al., (2018).

4.1.7 Geographical Information Systems

The use of a geographical information system (GIS) has typically been restricted to topics such as geography and geomorphology. However, the increasing nature of cross-discipline collaboration has led to a growing appreciation of the benefits of GIS for integrating subsurface information. This may include palaeo-geographic reconstructions, 3D geological cartography, or the use of geostatistical and geospatial processing tools that can provide further insight. These tools mean that seismic surfaces, fault systems and channels (among other features) can be imported from seismic interpretation software into a GIS where they can be interrogated in a dedicated geospatial and geostatistical domain. Furthermore, it is becoming increasingly common for GIS functionalities to be incorporated into interpretation packages – for example Petrel, Kingdom, Decision Space, etc.

Some examples of how GIS has been used to improve the analyses of seismic reflection data include: (1) Newton et al. (2018), who generated geospatial information from erosional features in the Norwegian Sea, from multiple horizon surfaces to reconstruct a 2.5 Myr record of palaeo-oceanography, (2) Cox et al. (2020) reconstructed the geometry, pattern and previous connectivity of a submarine landslide before it occurred offshore Northwest Greenland and (3) Rea et al. (2018) combined seismic reflection data with borehole, core and ocean-climate modelling to redefine our understanding of glaciation in the North Sea. These examples show how geological and geophysical data can be stored or combined to generate meaningful outputs that would previously have been unmanageable outside of a dedicated GIS package.

5. Summary

This chapter outlines the background, acquisition and interpretation of seismic reflection data in geological and geophysical studies. This method allows scientists to examine the Earth's subsurface to understand how basins have evolved through time and determine what this means for both subsurface prospectivity and utilisation. Whether the data are 2D or 3D, seismic reflection surveys can provide a wealth of information on basin structure, stratigraphy, lithology and subsurface fluids. The benefits of this are even greater when combined with other data sets, such as petrophysical data from boreholes, to provide an integrated model of the subsurface. Since the first generation of controlled-source seismic data almost 100 years ago, these data sets have provided a unique insight across a range of different subsurface studies, from crustal dynamics to contemporary current-induced sediment waves. The explosive growth in the spatial coverage and imaging quality

of 3D seismic surveys both on- and offshore has led to vastly improved basinal insights and exploration successes and has also enabled insights into fundamental Earth processes ranging from mantle and crustal-scale processes, through sedimentology, fluid flow and climate change. The recent growth in the use of 4D seismic data has led to additional improvements in understanding the life cycles of fluid and gas reservoirs. Improvements in computer processing power and the sensitivity of acquisition equipment will likely continue as higher-resolution and better-processed data sets become available, and interpretation will be increasingly effective as it is assisted by semi-automated approaches, providing unprecedented insights into subsurface geology.

Acknowledgements

DRC and AMWN would like to thank the Natural Environment Research Council and the British Geological Survey (DRC only) for funding their PhD and postdoctoral research [Grant numbers: DRC: NE/M00578X/1 (NERC) and S356 (BGS); AMWN: NE/R013675/1]. All authors would like to thank the providers of software packages and data sets, which have contributed to the writing of this chapter and finally to thank the editors for inviting us to contribute to this book.

References

Al-Chalabi, M., 2014, Principles of Seismic Velocities and Time-to-Depth Conversion: Houten, The Netherlands, EAGE Publications, 488 p.

Allen, P. A., and J. R. Allen, 2013, Basin Analysis: Principles and Application to Petroleum Play Assessment: Oxford, Wiley-Blackwell, 632 p.

Anderson, N. L., and S. Cardimona, 1995, Forward Seismic Modeling: The Key to Understanding Reflection Seismic and Ground Penetrating Radar (GPR) Techniques, *in* U. o. M.-R. Department of Geology and Geophysics, ed., Rolla, MO, USA.

Ashcroft, W., 2011, A Petroleum Geologist's Guide to Seismic Reflection: Oxford, Wiley-Blackwell, 176 p.

Avseth, P., 2005, Quantitative Seismic Interpretation: Applying rock physics tool to reduce interpretation risk: Cambridge, Cambridge University Press, 373 p.

Badley, M. E., 1985, Practical seismic interpretation: Boston, MA, USA, IHRDC Press.

Bahorich, M., and S. Farmer, 1995, 3-D seismic discontinuity for faults and stratigraphic features: The coherence cube: The Leading Edge, v. 14, p. 1021-1098.

Bolt, B. A., 1982, Inside the Earth: San Fransisco, WH Freeman and Co., 191 p.

Brown, A. R., 2011, Interpretation of Three-Dimensional Seismic Data: Oklahoma, USA, American Association of Petroleum Geologists and the Society of Exploration Geophysicists.

Cartwright, J. A., and M. Huuse, 2005, 3D seismic technology: the geological 'Hubble': Basin Research, v. 17, p. 1-20.

Castagna, J. P., and M. M. Backus, 1993, Offset-Dependent Reflectivity-Theory and Practice of AVO Analysis: Investigations in Geophysics: Tulsa, OK, USA, Society of Exploration Geophysics.

Castagna, J. P., and S. Sun, 2006, Comparison of spectral decomposition methods: First Break, v. 24.

Castagna, J. P., and H. W. Swan, 1997, Principles of AVO crossplotting: The Leading Edge, v. 16, p. 337-344.

Chopra, S., and K. J. Marfurt, 2016, Spectral decomposition and spectral balancing of seismic data: The Leading Edge, v. 35, p. 176-179.

Chunyan, X., J. C. Bancroft, R. J. Brown, and C. Zhihong, 2003, Multiple suppression: A literature review, CREWES Research Report, Consortium for Research in Elastic Wave Exploration Seismology.

Cox, D. R., M. Huuse, A. M. W. Newton, P. Gannon, and J. Clayburn, In Press, Slip Sliding Away: Enigma of Large Sandy Blocks within a Gas Bearing Mass Transport Deposit, Offshore NW Greenland: AAPG Bulletin.

Daynac, N., S. Lacaze, and F. Pauget, 2016, Interpretation of complex faulted deposits in the North Sea using the relative geological timemodel: First Break, v. 34, p. 55-62.

Dix, C. H., 1955, Seismic Velocities from Surface Measurements: Geophysics, v. 20, p. 68-86.
Domenico, S. N., 1984, Rock lithology and porosity determination from shear and compressional wave velocity: Geophysics, v. 49, p. 1188-1195.
Dondurur, D., 2018, Acquisition and Processing of Marine Seismic Data, Elsevier, 606 p.
Dorn, G. A., 1998, Modern 3-D seismic interpretation: The Leading Edge, v. 17, p. 1262-1262.
Duval, G., 2012, How broadband can unlock the remaining hydrocarbon potential of the North Sea: First Break, v. 30, p. 85-91.
Elboth, T., I. V. Presterud, and D. Hermansen, 2010, Time-frequency seismic data de-noising: Geophysical Prospecting, v. 58, p. 441-453.
Etris, E. L., N. J. Crabtree, J. Dewar, and S. Pickford, 2002, True depth conversion: more than a pretty picture: CSEG Recorder, v. 26, p. 11-22.
Froner, B., S. J. Purves, J. Lowell, and J. Henderson, 2013, Perception of visual information: the role of colour in seismic interpretation: First Break, v. 31, p. 29-34.
Grippa, A., A. Hurst, G. Palladino, I. Icopini, I. Lecomte, and M. Huuse, 2019, Seismic imaging of complex geometry: Forward modeling of sandstone intrusions: Earth and Planetary Science Letters, v. 513, p. 51-63.
Hale, D., 1984, Dip-moveout by Fourier transform: Geophysics, v. 49, p. 741-757.
Harding, R., and M. Huuse, 2015, Salt on the move: Multi stage evolution of salt diapirs in the Netherlands North Sea: Marine and Petroleum Geology, v. 61, p. 39-55.
Hilterman, F. J., 2001, Seismic Amplitude Interpretation: Distinguished Instructor Series No. 4: Tulsa, OK, Society of Exploration Geophysicists, 244 p.
Hinze, W. J., v. F. R. R. B., and A. H. Saad, 2013, Gravity and Magnetic Exploration : Principles, Practices, and Applications: Cambridge, Cambridge University Press.
Hollingworth, S., O. Pape, C. Purcell, E. Kaszycka, T. Baker, J. Cowley, G. Duval, and L. Twigger, 2015, Setting new standards for regional understanding – mega-scale broadband PSDM in the North Sea: First Break, v. 33, p. 75-79.
Huuse, M., and D. A. Feary, 2005, Seismic inversion for acoustic impedance and porosity of Cenozoic cool-water carbonates on the upper continental slope of the Great Australian Bight: Marine Geology, v. 215, p. 123-134.
Huuse, M., C. A.-L. Jackson, P. V. Rensbergen, R. J. Davies, P. B. Flemings, and R. J. Dixon, 2010, Subsurface sediment remobilization and fluid flow in sedimentary basins: an overview: Basin Research, v. 22, p. 342-360.
Janson, X., and S. Fomel, 2011, 3-D forward seismic model of an outcrop-based geocellular model: Concepts in Sedimentology and Paleontology, v. 10, p. 87-106.
Jones, C. E., M. Evans, A. Ratcliffe, G. Conroy, R. Jupp, J. I. Selvage, and L. Ramsey, 2013, Full Waveform Inversion in a Complex Geological Setting - A Narrow Azimuth Towed Streamer Case Study from the Barents Sea, 75th EAGE Conference & Exhibition incorporating SPE EUROPEC 2013, London, UK.
Jones, I. F., R. I. Bloor, B. L. Biondi, and J. T. Etgen, 2008, Prestack Depth Migration and Velocity Model Building: Geophysics Reprint Series: Tulsa, Oklahoma, USA, Society of Exploration Geophysics.
Keary, P., M. Brooks, and I. Hill, 2002, An Introduction to Geophysical Exploration: Oxford, Wiley-Blackwell, 272 p.
Kumar, A., P. Barua, and B. P. Sarma, 2006, Problems and Challenges in Conducting Seismic Survey Operations in Logistically Difficult Hilly and Rugged Terrain of the Foothills of Uttaranchal – A Case Study, 6th International Conference & Exposition on Petroleum Geophysics, Kolkata.
Landrø, M., 2015, 4D Seismic, *in* K. Bjørlykke, ed., Petroleum Geoscience: Berlin, Heidelberg, Springer.
Latimer, R. B., R. Davidson, and P. V. Riel, 2000, An interpreter's guide to understanding and working with seismic-derived acoustic impedance data: The Leading Edge, v. 19, p. 242-256.
Lisle, R. J., P. Brabham, and J. W. Barnes, 2011, Basic Geological Mapping: Oxford, Wiley-Blackwell.
Lumley, D., 2010, 4D seismic monitoring of CO2 sequestration: The Leading Edge, v. 29, p. 113-240.
Mari, J., F. Glangeaud, and F. Coppens, 1999, Signal processing for geologists & geophysicists: Paris, Editions Technip, 480 p.
Mousa, W. A., 2019, Advanced digital signal processing of seismic data: Cambridge, UK, Cambridge University Press.
Musgrave, A., 1967, Seismic Refraction Prospecting: Seismic Refraction Prospecting, Society of Exploration Geophysics.
Newton, A., 2017, Seismic geomorphology of glaciated margins, University of Manchester.
Newton, A. M. W., M. Huuse, and S. H. Brocklehurst, 2018, A persistent Norwegian Atlantic Current through the Pleistocene glaciations: Geophysical Research Letters, v. 45, p. 5599-5608.
Nuclear Waste Management Organization, 2018, Image of vibroseis truck, Online, NWMO.
Ojha, M., and K. Sain, 2007a, Seismic amplitude versus angle (AVA) responses from a bottom simulating reflector of various gas-hydrates models: Geohorizons, v. 12, p. 22-26.

Ojha, M., and K. Sain, 2007b, Seismic velocities and quantification of gas-hydrates from AVA modeling in the western continental margin of India: Marine Geophysical Researches, v. 28, p. 101-107.
Payton, C. E., 1977, Seismic stratigraphy: applications to hydrocarbon exploration: Oklahoma, USA, American Association of Petroleum Geologists.
Rabiner, L. R., and B. Gold, 1975, Theory and application of digital signal processing: Englewood Cliffs, NJ, Prentice-Hall Inc., 777 p.
Rea, B. R., A. M. W. Newton, R. Harding, R. M. Lamb, M. Bigg, G. R. Spagnolo, M. Huuse, S. H. Brocklehurst, P. Rose, F. A. Buckley, J. Cater, S. Archer, M. Halliyeva, J. Basell, J. Howell, and D. Cornwell, 2018, An Early Pleistocene record of extensive and repeated marine-based glaciation on the NW European margin: Science Advances, v. 4, p. 149-179.
Rider, M., and M. Kennedy, 2011, The geological interpretation of well logs: Edinburgh, Rider-French Consulting Ltd., 432 p.
Robein, E., 2010, Seismic Imaging: A Review of the Techniques, their Principles, Merits and Limitations: Houten, The Netherlands, EAGE Publications.
Roden, R., T. A. Smith, P. Santogrossi, D. Sacrey, and G. Jones, 2017, Seismic interpretation below tuning with multiattribute analysis: The Leading Edge, v. 36, p. 330-339.
Russell, B., and D. Hampson, 2006, The old and the new in seismic inversion: CSEG Recorder, v. 31, p. 5-11.
Sheriff, R. E., and L. P. Geldart, 1995, Exploration Seismology: New york, Cambridge University Press, 592 p.
Simm, R., and M. Bacon, 2014, Seismic amplitude: an interpreter's handbook: Cambridge, UK, Cambridge University Press.
Stone, D. G., 1994, Designing Seismic Surveys in Two and Three Dimensions: Reference Series: Tulsa, OK, Society of Exploration Geophysics.
Thigpen, B. B., A. E. Dalby, and R. Landrum, 1975, Report on Subcommittee on Polarity Standards: Geophysics, v. 40, p. 694-699.
Tiab, D., and E. C. Donaldson, 2015, Petrophysics : theory and practice of measuring reservoir rock and fluid transport properties: Oxford, Gulf Professional Publishing.
Vermeer, G. J. O., 2012, 3D Seismic Survey Design: Geophysical Reference Series No. 12: Tulsa, OK, Society of Exploration Geophysics.
Wencai, Y., 2013, Reflection Seismology: Theory, Data Processing and Interpretation: Amsterdam, Elsevier.
Wojcik, K. M., I. S. Espejo, A. M. Kalejaiye, and O. K. Umahi, 2016, Bright spots, dim spots: Geologic controls of direct hydrocarbon indicator type, magnitude, and detectability, Niger Delta Basin: Interpretation, v. 4, p. SN45-SN69.
Yilmaz, O., 2001, Seismic Data Analysis: Processing, Inversion, and Interpretation of Seismic Data¨: Investigations in Geophysics, v. 1: Tulsa, OK, USA, Society of Exploration Geophysics.
Zhang, H., and R. J. Brown, 2001, A Review of AVO analysis, CREWES Research Report, Consortium for Research in Elastic Wave Exploration Seismology.